2006

Jointless and Smoother Bridges: Behavior and Design of Piles

Robert J. Frosch
frosch@purdue.edu

Voraniti Chovichien

Katrinna Durbin

David Fedroff

Final Report

FHWA/IN/JTRP-2004/24

JOINTLESS AND SMOOTHER BRIDGES: BEHAVIOR AND DESIGN OF PILES

By

Robert J. Frosch
Principal Investigator
Professor of Civil Engineering

and

Voraniti Chovichien
Katrinna Durbin
David Fedroff

Graduate Research Assistants

School of Civil Engineering
Purdue University

Joint Transportation Research Program
Project No. C-36-56XX
File No. 7-4-49
SPR-2393

Conducted in Cooperation with the
Indiana Department of Transportation
and the Federal Highway Administration

Purdue University
West Lafayette, IN 47907
January 2006

INDOT Research

TECHNICAL *Summary*

Technology Transfer and Project Implementation Information

TRB Subject Code: 25-1 Bridges *January 2006*
Publication No.: FHWA/IN/JTRP-2004/24 *Final Report*

Jointless and Smoother Bridges: Behavior and Design of Piles

Introduction

Integral abutment bridges have been used in the United States for decades. These structures eliminate expensive expansion joints by utilizing the end bent to accommodate the total thermal movement of the bridge. Due to their complexity of response, these bridges are designed based upon experience, and a rational design specification has not been developed. Furthermore, the interaction of the abutment, pile, and soil remains uncertain. A better understanding regarding the behavior of this system is needed. The objective of this research is to evaluate the behavior of the integral abutment-pile system and evaluate any limitations of its use. A goal of the research is to develop minimum design and detailing recommendations. Two phases were conducted: a field investigation and an experimental investigation. In both phases, analytical and parametric studies were performed to further understand the behavior of this structural system. Based on the research performed here, design recommendations are provided regarding the design of the pile system as well as limitations on the overall length for this structural type.

Findings

Based on the results of the field, experimental, and analytical studies, the following recommendations are provided. In general, these recommendations are directed towards the pile behavior.

1. Piles sizes should be selected to provide adequate axial capacity while minimizing their bending resistance along the longitudinal axis of the bridge. This selection provides for maximum ductility response while minimizing stresses at the abutment-pile connection.

2. Piles should be oriented about their weak axis. This orientation provides for maximum ductility response while minimizing stresses at the abutment-pile connection.

3. Axial load should be limited to $0.25f_yA_s$ for H piles and $0.25f_yA_s + 0.4f'_cA_c$ for CFT piles. This axial load level which is currently stipulated by AASHTO based on pile driving stresses provides adequate displacement response and ductility. Higher stress levels demonstrate a lower ductility capacity.

4. The minimum embedment length of 15 in. often specified for pile embedment should be increased and/or confinement steel should be provided. Additional research in this regard is needed to quantify the effect, but it is recommended that a minimum of 24 in. be provided at this time. Significant deterioration of the pile-abutment connection occurred for the larger pile sections that can limit the response and behavior of the pile-abutment system.

5. A minimum pile length below ground is required to prevent displacement at the pile base. The minimum length depends on pile size as well as soil type and is provided as follows:

Table 8.1: Minimum Pile Length

Pile Size	Minimum Depth (ft)	
	Clay	Sand
HP10	30	25
HP12	35	25
HP14	40	30
CFT14	50	35

6. Bridges designed considering the above recommendations can be constructed up to a maximum total length of 500 ft for both steel and concrete superstructures. This recommendation is based on consideration of structures with skews less than 30 degrees. The length limit was selected to limit local pile buckling and provide for a bridge life of 100 years. Lengths longer than this limit are possible if the bridge deck casting which provides continuity for the integral bridge is conducted at temperatures less than 60° F. For temperatures in the range of 40 - 50° F, the bridge length can be extended to 770 ft. Casting at moderate temperatures should be encouraged.

Implementation

The recommendations provided through this study can be easily implemented to improve the performance of integral abutment bridges and extend the benefits of integral and jointless design to a larger number of structures. Implementation should proceed primarily through the INDOT Design Division through changes in design requirements provided in the design manual.

There are many benefits from the use of jointless, integral bridges. The elimination of joints and bearings reduces maintenance costs as well as results in a smoother pavement. Smoother bridges result in a reduction in live load impact, improved riding quality, and reduced snowplow damage. Experience in Indiana as well as other states has demonstrated that integral bridges result in an increased service life and a substantial savings to INDOT in construction as well as life-cycle costs. This improved performance and resulting cost savings can now be extended to a larger number of structures.

.

Contacts

For more information:

Prof. Robert J. Frosch
Principal Investigator
Purdue University School of Civil Engineering
West Lafayette IN 47907
Phone: (765) 494-5904
Fax: (765) 496-1105
E-mail: frosch@ecn.purdue.edu

Indiana Department of Transportation
Division of Research
1205 Montgomery Street
P.O. Box 2279
West Lafayette, IN 47906
Phone: (765) 463-1521
Fax: (765) 497-1665

Purdue University
Joint Transportation Research Program
School of Civil Engineering
West Lafayette, IN 47907-1284
Phone: (765) 494-9310
Fax: (765) 496-7996
E-mail: jtrp@ecn.purdue.edu
http://www.purdue.edu/jtrp

TECHNICAL REPORT STANDARD TITLE PAGE

1. Report No.	2. Government Accession No.	3. Recipient's Catalog No.
FHWA/IN/JTRP-2004/24		

4. Title and Subtitle	5. Report Date
Jointless and Smoother Bridges: Behavior and Design of Piles	January 2006
	6. Performing Organization Code

7. Author(s)	8. Performing Organization Report No.
Robert Frosch, Voraniti Chovichien, Katrinna Durbin, David Fedroff	FHWA/IN/JTRP-2004/24

9. Performing Organization Name and Address	10. Work Unit No.
Joint Transportation Research Program 1284 Civil Engineering Building Purdue University West Lafayette, IN 47907-1284	
	11. Contract or Grant No. SPR-2393

12. Sponsoring Agency Name and Address	13. Type of Report and Period Covered
Indiana Department of Transportation State Office Building 100 North Senate Avenue Indianapolis, IN 46204	Final Report
	14. Sponsoring Agency Code

15. Supplementary Notes

Prepared in cooperation with the Indiana Department of Transportation and Federal Highway Administration.

16. Abstract

Integral abutment bridges have been used in the United States for decades. By eliminating expensive expansion joints, the piles supporting the end bent accommodate the total thermal movement of the bridge. Currently, integral bridges are designed based upon experience, and a rational design specification has not been developed. Furthermore, the interaction of the abutment, pile, and soil remains uncertain. A better understanding regarding the behavior of this system is needed. The objective of this research is to evaluate the behavior of the integral abutment-pile system and evaluate any limitations of its use. To achieve this objective, two phases of research were conducted. The first phase was a field study that investigated the in-service pile behavior of four integral abutment bridges. The second phase was an experimental study that was used to evaluate the capability of piles typically used in integral abutment bridges. Nine low-cycle, large amplitude lateral displacement pile tests were conducted. Throughout both phases, analytical investigations were also conducted. To develop simplified modeling techniques that sufficiently account for soil-pile interaction, the piles supporting abutments were analytically modeled and calibrated based on the field and experimental results. A parametric study was also performed with variables including pile type, pile orientation, axial load, pile length, and soil type. The results of these phases were evaluated and design recommendations were developed based on these results. Overall, the design recommendations provide for an extension in the length limits often used for integral bridges. The extension of these limits can result in a reduction in bridge construction and maintenance costs for a large number of structures that cannot currently be built using this structural system.

17. Key Words	18. Distribution Statement
Bridge, Bridge Design, Integral Abutment, Jointless, Piles	No restrictions. This document is available to the public through the National Technical Information Service, Springfield, VA 22161

19. Security Classif. (of this report)	20. Security Classif. (of this page)	21. No. of Pages	22. Price
Unclassified	Unclassified	534	

ACKNOWLEDGEMENTS

This work was supported by the Joint Transportation Research Program (JTRP) administered by the Indiana Department of Transportation (INDOT) and Purdue University through contract SPR-2393. The support of the Indiana Department of Transportation (INDOT) and the Federal Highway Administration (FHWA) are thankfully recognized. The authors would like to thank to Dr. Tommy Nantung from the INDOT Division of Research for his support throughout the project. Thanks are extended to members of the Study Advisory Committee for their participation and helpful comments throughout the project. These members include Naveed Burki, Khalil Dughaish, Jaffar Golkhajeh, Keith Hoernshemeyer, Jim Karr, Randy Strain, and Mike Wenning. Finally, thanks are extended to Stephen Weintraut, Scott Newbolds, Jerry D. Ritchie, and Dan Clark for providing information and thoughtful comments throughout this project.

TABLE OF CONTENTS

Page

Page

LIST OF TABLES

LIST OF FIGURES

CHAPTER 1: INTRODUCTION

1.1 Introduction

In traditional bridge construction, expansion and bearing joints are installed at selected locations along the bridge. These joints are often costly to purchase, install, maintain, and repair. In addition, corrosion damage to the joint can occur from salt, moisture, and accumulated dirt. Snow plows often damage or loosen the joint hardware (Wasserman, 1996). Due to these problems, elimination of joints is desirable. A jointless structure can be achieved using an integral abutment bridge. This bridge type uses short stub type abutments that are rigidly connected to the bridge deck without joints. A typical integral abutment is illustrated in Figure 1.1.

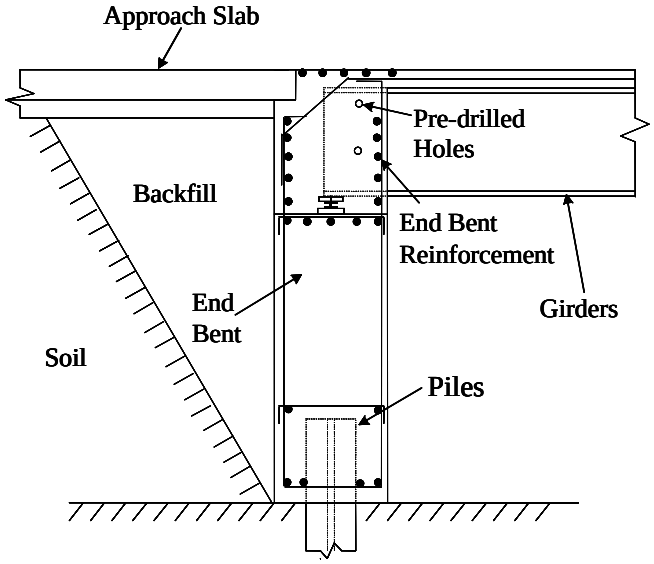

Figure 1.1: Cross-Section of a Typical Integral End Bent (Durbin, 2001)

1.2 Overview of Integral Abutment Bridges

Integral abutment bridges have several advantages over traditional bridges including:

- Integral abutment bridges are more economical because of the elimination of expensive expansion joints and the reduction in maintenance costs (Steel Bridges, 1993).
- Integral abutment bridges improve riding quality because of the elimination of joints.
- The construction of integral abutment bridges is more rapid than that of traditional bridges because of the use of only a single row of vertical (not battered) piles. Fewer piles and less forming are typically required.
- As reported by Burke (1993), integral abutment bridges are simple to design and time-efficient to analyze. A continuous superstructure including girders is simplified as a continuous horizontal frame member. Also, the piles and piers can be represented by vertical members.
- Integral abutments provide for improved seismic performance.

Even though integral abutment bridges have many advantages, a number of issues should be considered. By eliminating joints, the end abutments must accommodate the total thermal movement of the bridge. This movement can be estimated by Equation 1-1.

$$\Delta L = \alpha(\Delta T)L \qquad (1\text{-}1)$$

where:

ΔL = change in bridge length due to temperature change, in.

α = material coefficient of thermal expansion, 1/°F

ΔT = change in temperature, °F

L = total bridge length, in.

While the abutments and piles resist longitudinal movement of the superstructure, additional stresses or secondary stresses due to shrinkage, creep, settlement, temperature, and earth pressure can occur in the girders and piles. Problems occurring in integral abutment bridges can be briefly summarized as follows:

- Differential support settlements induce additional shears and moments in the deck, girders, and piles.
- Temperature-induced movement of the abutment can cause settlement of the approach slab (Arsoy, 1999).
- Daily temperature change causes bending moments in the bridge girders.
- High passive earth pressures behind the abutment can damage the bridge abutments while resisting movement.
- Pile stresses in the abutment can reach or exceed yield, induce plastic hinging, and consequently reduce the axial capacity of the pile.

As reported by Russell (1994), the interaction of abutment, soil, and superstructure still remains unknown. The soil-pile relationship under cyclic bridge movement is also uncertain. Moreover, there are no available methods for estimating the magnitude and distribution of passive pressure forces. Better understanding regarding the behavior of pile and soil should be investigated.

Due to concerns regarding secondary effects, a Technical Advisory of the Federal Highway Administration (FHWA, 1980) suggested length limits for integral abutment bridges in 1980. The limits were set as follows: 300-ft for steel bridges, 500-ft for cast-in-place concrete bridges, and 600-ft for prestressed concrete bridges. However, as reported by Burdette, et al. (2002), the Tennessee Department of Transportation (TDOT) has used longer lengths for integral abutment bridges. Wasserman provides several recommendations about pile configuration, pile orientation, anchorage of beam to pile cap, and backfill (Wasserman, 1996). These recommendations are provided based on field experience. Piles, for example, are recommended to be driven vertically and in only one row to achieve the highest extent of flexibility to accommodate cyclic thermal movements. As reported by Wasserman, there is disagreement regarding pile orientations; fifteen states orient the pile for strong-axis bending, while thirteen states

orient the pile for weak-axis bending. To reduce pile stresses, the piles may be driven through a pre-bored hole approximately twice the diameter of the pile. The pre-bored hole is recommended to be 8-ft in depth below the abutment beam and backfilled with loose sand (Wasserman, 1996). As noted, there are a variety of recommendations that are based solely on field experience. In addition, these recommendations often vary considerable with diametrically opposed recommendations provided from state to state.

1.3 Pile Considerations

1.3.1 Pile Design

Pile design for integral abutment bridges is based on a variety of assumptions and is often specified by state standards or guidelines. In general, the following methods are used:

1. Pile design considers only axial loads.
2. Pile design accounts for bending stresses due to temperature effects, but ignores backfill resistance.
3. Pile design incorporates soil-pile interaction based on results from specified computer programs such as LPILE (Reese, 2000).

1.3.2 Pile Type

Some states specify steel H piles (HP); other states specify concrete-filled steel tube piles (CFT), while others use prestressed concrete piles.

1.3.3 Pile Orientation

Besides design considerations and pile types, pile orientations vary from state to state. Orienting the H piling for weak-axis bending offers the least resistance and facilitates pile-head bending for fixed head conditions. However, due to the potential for flange buckling, the total lateral displacement is more limited than when the piling is oriented in strong-axis bending.

1.4 INDOT Standards

In Indiana, according to Bridge Design Memorandum #233 and #243 (INDOT, 1992a and INDOT 1992b), bridge lengths are limited to 250-ft for steel bridges and 300-ft for prestressed concrete bridges with a maximum skew angle of 30°. For reinforced concrete integral bridges, the maximum bridge length is 200-ft regardless of the skew. Only steel H piles or 14-in. diameter concrete-filled steel tube piles are permitted for use in integral abutment bridges. Steel H piles are recommended to be oriented in weak-axis bending to minimize pile bending stresses. Furthermore, the axial stress on the pile should be no more than 9 ksi. The Bridge Design Memorandums are provided in Appendix A. INDOT also allows jointless bridges up to a 454 degree skew as long as the bridge length doesn't exceed 150 ft (45 m).

1.5 Objectives and Scope

There is interest in extending the length limitations for integral abutment bridges in Indiana to take advantage of the benefits of integral construction for an increased number of structures. Therefore, the objective of this research is to develop minimum design and detailing recommendations to allow extension of the current length limitations. Integral bridges are in general considered limited by the capability of the piles to accommodate thermal movements. To achieve this objective, this study will:

1. Investigate the in-service pile behavior of integral abutment bridges.
2. Develop simplified modeling techniques that sufficiently account for soil-pile interaction. Soil-pile interaction will be based on measured in-field response.
3. Evaluate the capability of the pile types used in Indiana to support axial load while subject to low-cycle, large-amplitude lateral displacements.

CHAPTER 2: FIELD INVESTIGATION

2.1 Introduction

Four bridges were instrumented to observe the in-service behavior of integral abutment bridges as well as the behavior of the piles supporting these structures. Structures instrumented as part of the research include the SR249 over US12 bridge, two I65 over SR25 bridges, and the SR18 over Mississinewa River bridge. General details of the bridges are tabulated in Table 2.1. This chapter discusses both the instrumentation scheme and the response of the piles.

Table 2.1: General Details of the Bridges

	SR249 over US 12	**I65 over SR25**	**SR18 over Mississinewa River**
Total Length (ft)	990	152	367
Skew Angle (degrees)	13	25	8
Number of Spans	10	2	5
Span Length (ft)	86.6, 3@98.4, 114.8, 4@101.7, 86.6	2@76	62, 3@81, 62
Number of Girders	4	7	5
Girder Type	Prestressed Concrete Bulb Tee	W36x150 Steel	Prestressed Concrete Bulb Tee
Pile Type and Bending Orientation	HP14x89 (Strong Axis)	Six HP12x53 (Weak Axis) and Four CFT14.5	CFT14
Total Number of Piles	6 (Bent1) and 5 (Bent 11)	10 (Both Bents)	10 (Both Bents)
Date Instrumented	Spring 2000	Summer 2000	Summer 2003

2.2 SR249 over US12 Bridge

The first integral abutment bridge instrumented is located on SR249 over US12 in Portage Township, Indiana (Figure 2.1). The bridge (Structure #12-64-2673) is located near I65, 1.51 miles to the South of US30 and is a continuous, composite, prestressed concrete, bulb-tee bridge with ten spans. The bridge has a skew angle of 13˚ 11′ (13.183˚) relative to the abutments and has a total bridge length of 990 ft. A plan view of the bridge is presented in Figure 2.2. This bridge was selected because its total bridge length exceeded the INDOT length limitation of 300 ft for a prestressed concrete, integral abutment bridge. The bridge consists of varying span dimensions that include: 86.6 ft (26.4 m), 3@98.4 ft (3@30.0 m), 114.8 ft (35.0 m), 4@101.7 ft (4@31.0 m), and 86.6 ft (26.4 m). A typical cross section of the bridge is shown in Figure 2.3. It should be noted that this structure was designed using metric dimensions, hence, the irregular U.S. customary units.

Figure 2.1: SR249 over US12 Bridge

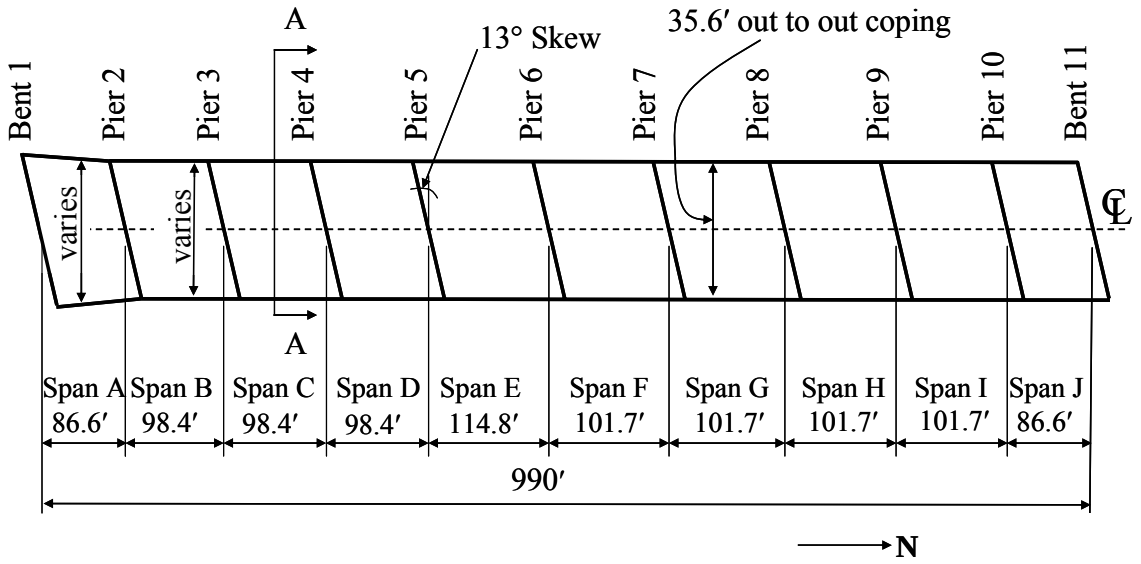

Figure 2.2: Plan View (SR249 over US12)

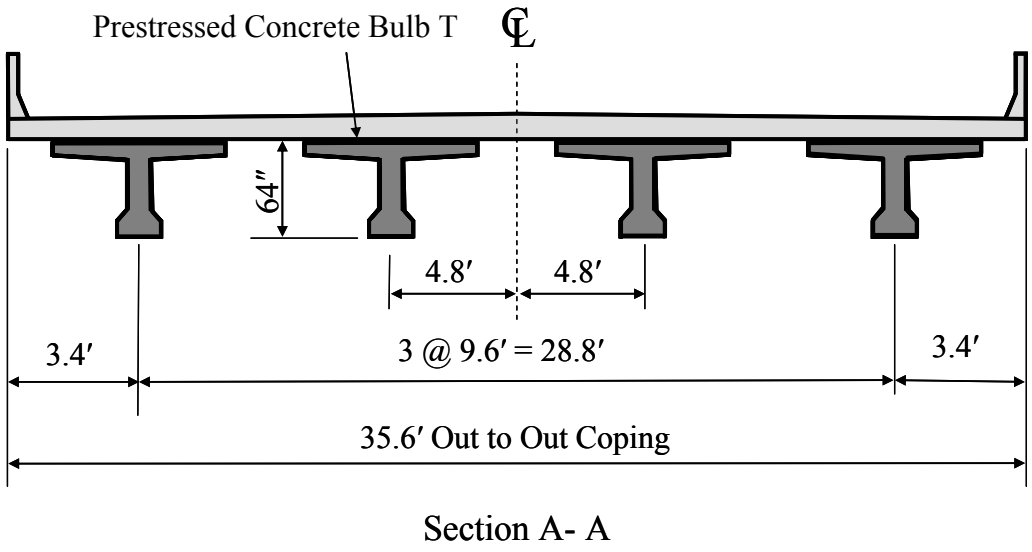

Figure 2.3: Typical Cross Section (Section A-A of Figure 2.2) (SR249 over US12)

2.2.1 End Bent/Pile Design

2.2.1.1 End Bent

The end bents are supported on steel HP14x89 (HP360x132-SI) piles embedded 18 in. (450 mm) into the end bent pile cap. A single row of six piles supports Bent 1, and a single row of five piles supports Bent 11 as shown in Figure 2.4. Piles were oriented to provide strong axis bending with respect to the longitudinal axis of the bridge. The total pile length is approximately 131 ft (40 m) for piles on Bent 1, and all piles were driven to a bearing capacity of 245 tons (2182 kN) according to the INDOT pile driving record provided in Appendix B. The total pile length is approximately 164 ft (50 m) for piles on Bent 11, and all piles were driven to a bearing capacity of 240 tons (2143 kN). Figure 2.5 illustrates the piles included in Bents 1 and 11. The piles are embedded 1.5 ft in the abutment. The pile length below ground is approximately 113 ft and 143 ft for piles on Bents 1 and 11, respectively. An expanded polystyrene (EPS) was placed behind the end bents (Figure 2.6). The EPS fill was used to eliminate the effect of passive earth pressure on the end bents. Consequently, the piles are unsupported above ground. End bent details of the bridge are included in Appendix C.

2.2.1.2 Pile Design

All piles were designed considering both the vertical loads and the horizontal thermal movement. The axial load consisted of the dead load of the abutment, bridge deck, girder, and live load. The live load was based on HS20-44 truck and Michigan Truck Train loading No. 5 with distribution in accordance with the 16th Edition of the AASHTO Standard Specifications (1996). H piles bending about their strong axis were selected because of the greater allowable stress permitted by the AASHTO specifications for this bending direction. The piles had 0.5 in. (13 mm) thick by 1 ft (300 mm) high expanded polystyrene placed around the pile in the abutment to simulate a pinned connection.

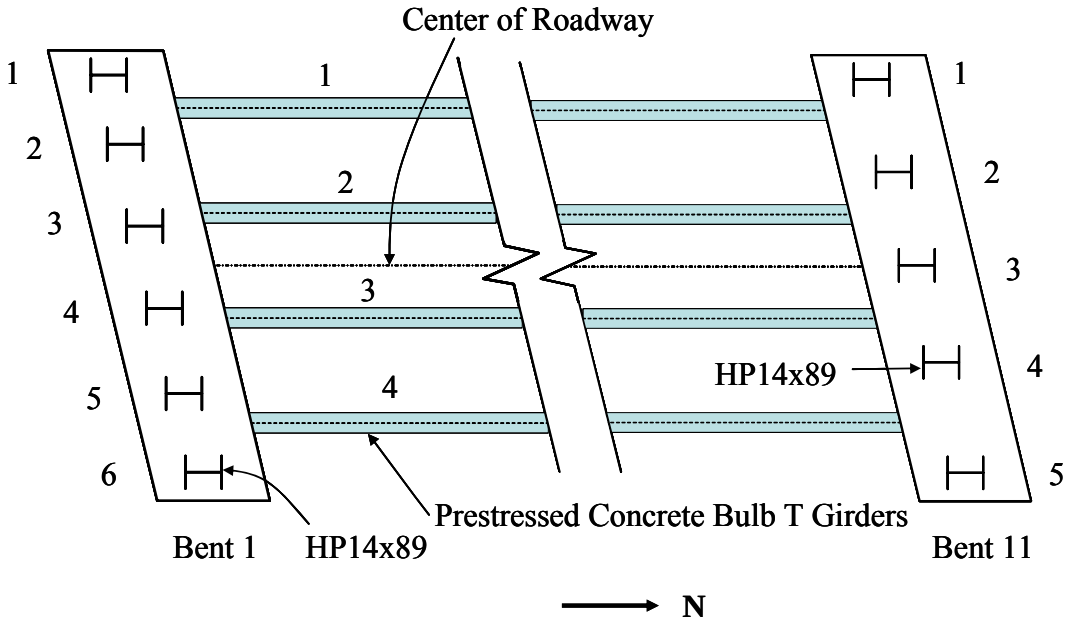

Figure 2.4: Bents 1 and 11 Plan Views (SR249 over US12)

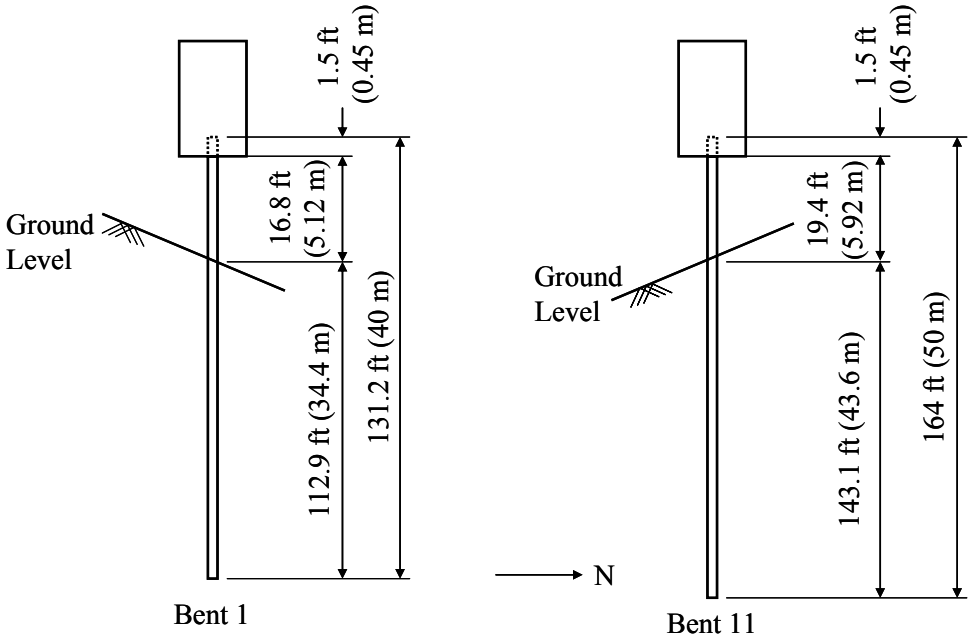

Figure 2.5: Typical Pile Length (SR249 over US12)

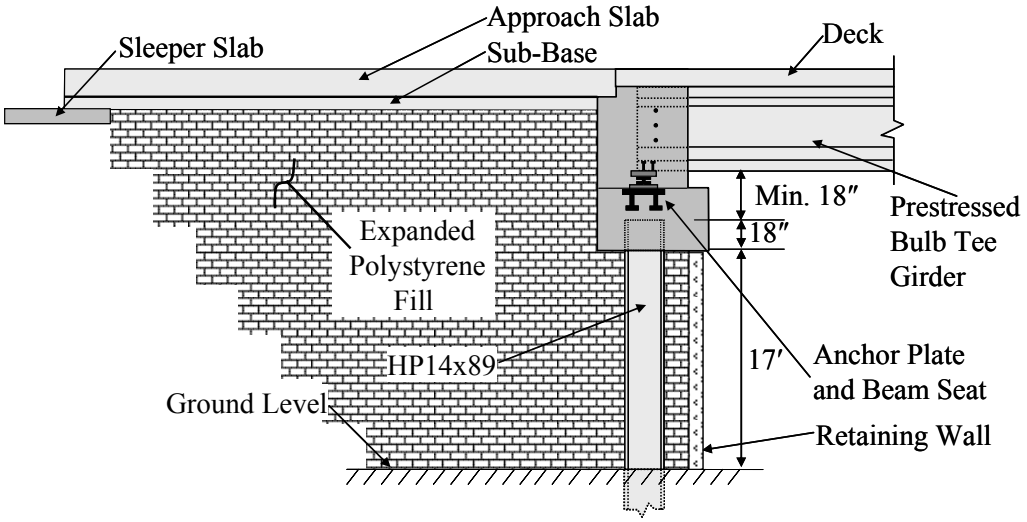

Figure 2.6: Expanded Polystyrene (SR249 over US12)

2.2.1.3 Soil Borings

The soil boring plan is provided in Figure 2.7. Soil boring No. 1 and 10 (TB-1 and TB-10) are representative of soils at Bents 1 and 11 as tabulated in Tables 2.2 and 2.3, respectively. The value of N from the Standard Penetration Test (SPT) indicates the average number of blows required to drive a 1.375 in. inner diameter (I.D.), 2 in. outer diameter (O.D.) split spoon sampler 12 in. by means of a 140 lb weight falling 30 in. The ground water table was measured 4.2 ft from ground level for Bent 1, while it was 5.9 ft from ground level for Bent 11. Soil profiles for Bents 1 and 11 are shown in Figure 2.8.

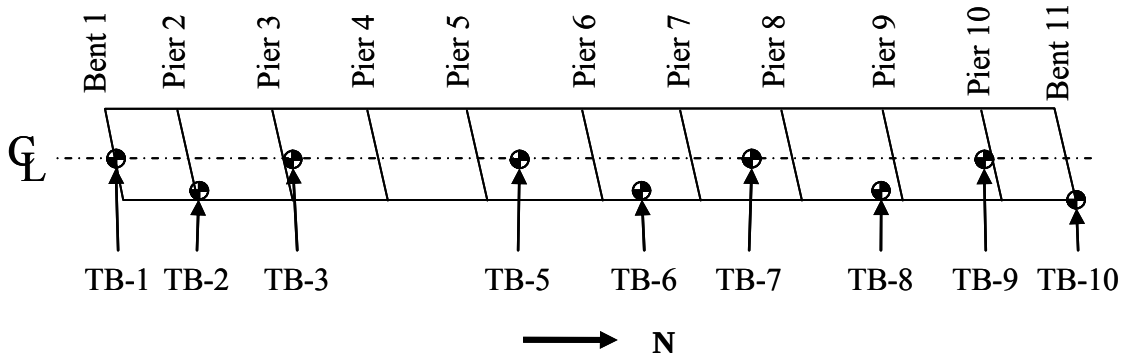

Figure 2.7: Soil Boring Plan (SR249 over US12)

Table 2.2: Soil Boring Data from TB-1 for Bent 1 (SR249 over US12)

Depth from Ground Level (ft)		N	SOIL TYPE
0	3	-	Gravelly sand, dark brown (visual)
2.5	10	18	SAND, medium dense, moist to wet after 4.6 ft, brown to gray after 6.9 ft
10	15	2	PEAT, moist, black with occasional sand seams (visual)
15	20	0	MARL, moist, dark gray
20	35	14	SAND, medium dense to loose, wet, gray
35	45	2	MARL, moist, dark gray
45	60	19	SAND, medium dense, wet, gray, with occasional thin silty clay seams (visual)
60	65	21	SILTY LOAM, very stiff wet, gray
65	75	36	SAND, dense, wet, gray
75	80	13	SILTY LOAM, medium dense, wet, gray
80	100	47	SAND, dense to very dense, wet, gray, occasional thin silty clay seams.
100	110	14	CLAY, hard to stiff, moist, gray
110	115	-	SAND, very dense, wet, gray (visual)
115	130	56	SILTY LOAM, hard, moist, gray

Table 2.3: Soil Boring Data from TB-10 for Bent 11 (SR249 over US12)

Depth from Ground Level (ft)		N	SOIL TYPE
0	10	11	SAND, medium dense to very loose, moist to wet, brown, occasional thin peat seams from 3.6 ft to 7.9 ft
10	15	-	MARL, moist, dark gray (visual)
15	35	19	SAND, medium dense, wet, gray
35	40	-	PEAT, moist, black (visual)
40	45	4	MARL, moist, dark gray
45	55	14	SAND, medium dense, wet, gray
55	60	8	SILTY LOAM, loose, wet, gray
60	85	36	SAND, medium dense to very dense, wet, gray, occasional thin silty loam seams
85	100	19	SILTY CLAY, very stiff to medium stiff, moist, gray, occasional thin to interbedded fine sand and silt seams
100	115	18	SILTY LOAM, very stiff, moist, gray, occasional thin sand seams
115	120	32	SAND, dense, wet, gray
120	140	39	SILTY LOAM, hard, moist, gray, occasional thin sand seams

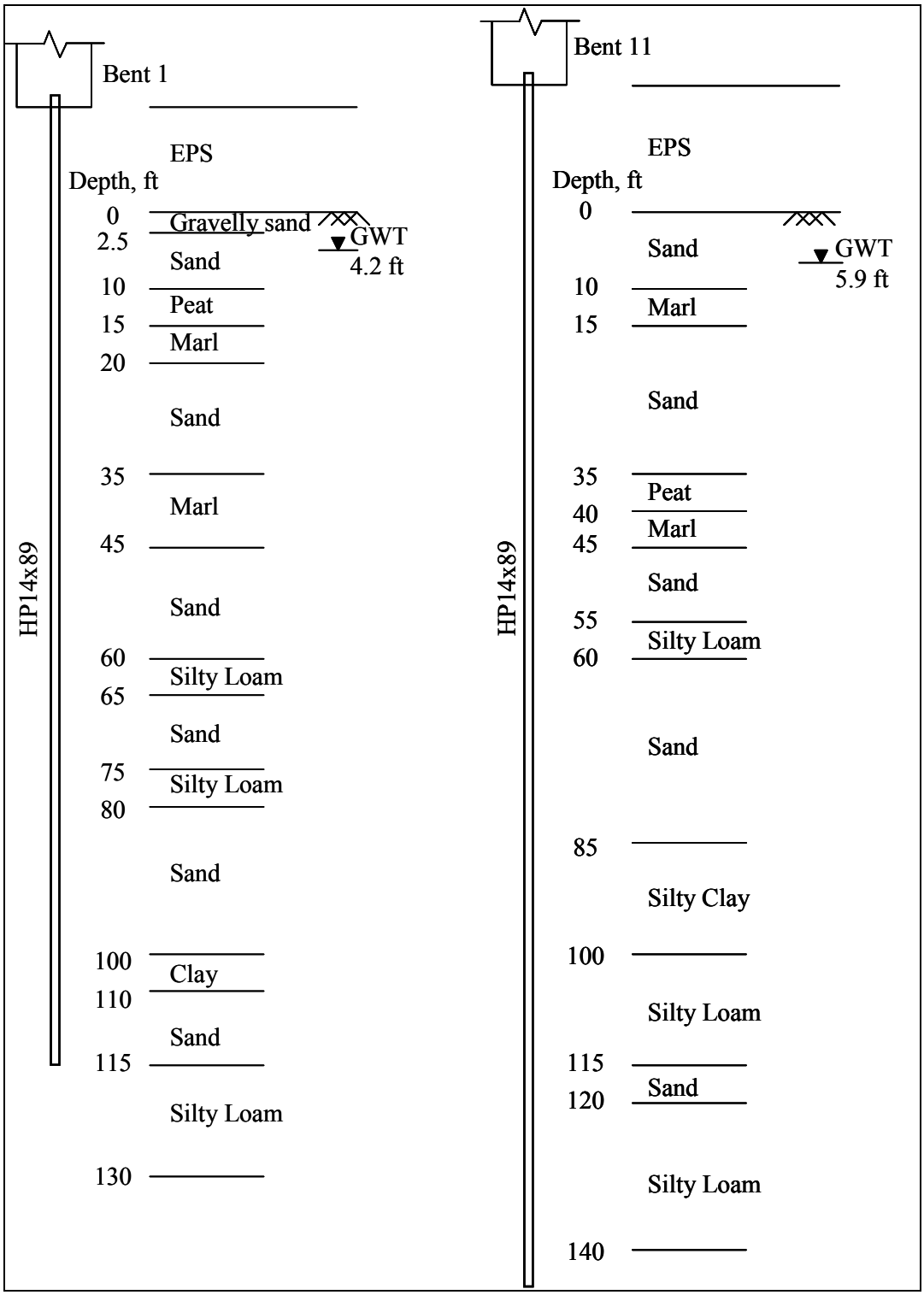

Figure 2.8: Soil Profile (SR249 over US12)

2.2.2 Structural Materials

2.2.2.1 Concrete

According to Bridge Design Memorandum #246 (INDOT, 1992c), the superstructure shall be Class C concrete with a 28-day design compressive strength (f_c') of 4,000 psi. However, for the SR249 over US12 bridge, INDOT Class C concrete was used for both the superstructure and the substructure for Bents 1 and 11. Structural concrete for piers excluding footings was INDOT Class A (f_c' = 3,500 psi.), while INDOT Class B concrete (f_c' = 3,000 psi) was used for footings. The bridge deck was cast in phases which began on September 16, 1999 and finished on October 11, 1999. The complete construction sequence is provided in Appendix D.

2.2.2.2 Piles

The HP14x89 piles were supplied in accordance with AASHTO M 183 (INDOT Standard Specifications, 1999).

2.2.3 Instrumentation Design

The objective of the bridge instrumentation was to investigate the behavior of the end bents and piles. Since direct movement of the end bent displacement was not possible, these displacements will be extrapolated from data obtained in combination from instrumentation provided on the end bents as well as instrumentation of adjacent piers. Details of the instrumentation scheme provided across the bridge including the bents, piles, and piers are discussed.

2.2.3.1 Bent Instrumentation

Bents 1 and 11 were instrumented similarly, and the instrumentation scheme for these end bents is shown in Figure 2.9. All instruments were manufactured by Geokon, Inc. A tiltmeter (Model 6350) was used to measure the rotation of the abutment and was located at the center of the abutment, 20 in. below the bottom of Girder 3 (Figure 2.10). A tiltmeter was located on the north side of Bent 1 and on the south side of Bent 11. In

addition, a crackmeter (Model 4420) with a capacity of 6 in. and a gage length of 27 in. was used to measure the displacement of the girder relative to the abutment. The crackmeter was connected at the bottom of Girder 3 and the abutment (Figure 2.10). All instruments incorporate thermistors that enable temperatures to be monitored along with the gages.

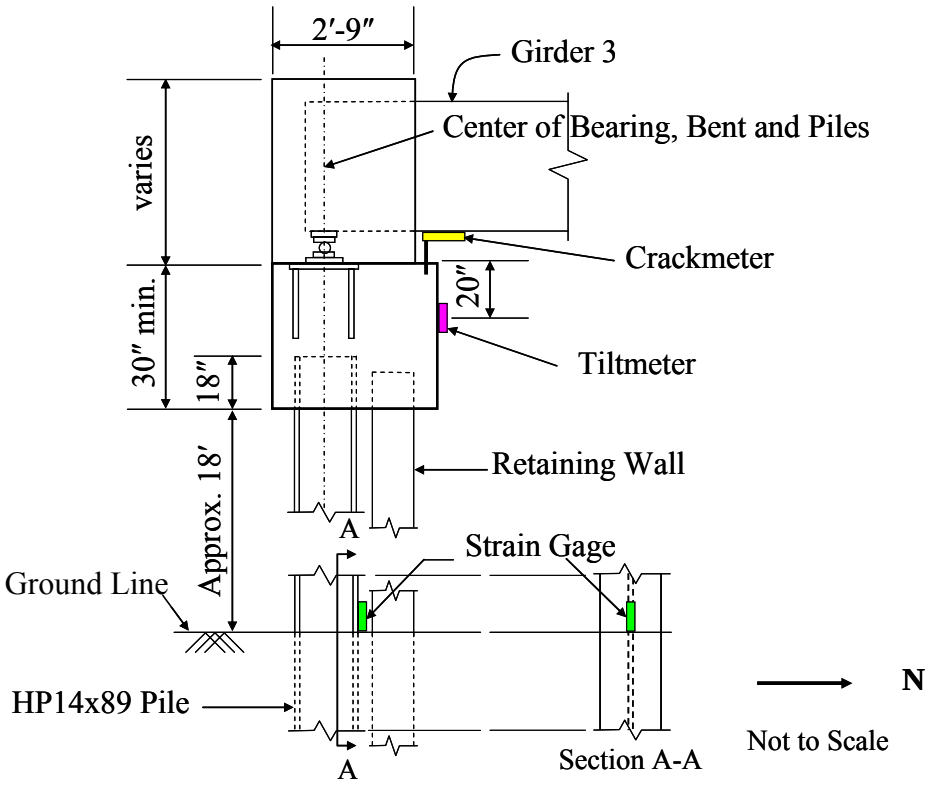

Figure 2.9: End Bent Instrumentation (SR249 over US12)

2.2.3.2 Pile Instrumentation

The behavior of the piles supporting the integral abutment was of particular interest. To investigate the behavior of the piles, strain gages (Model VK-4100) were installed on the piles of each end bent at ground level (at the bottom of the expanded polystyrene (EPS) fill level) as shown in Figure 2.11. Strain gages were spot welded at the center of the pile flange on the north face of the flange on Bent 1 and on the south face of the flange on Bent 11 as illustrated in Section A-A in Figure 2.9.

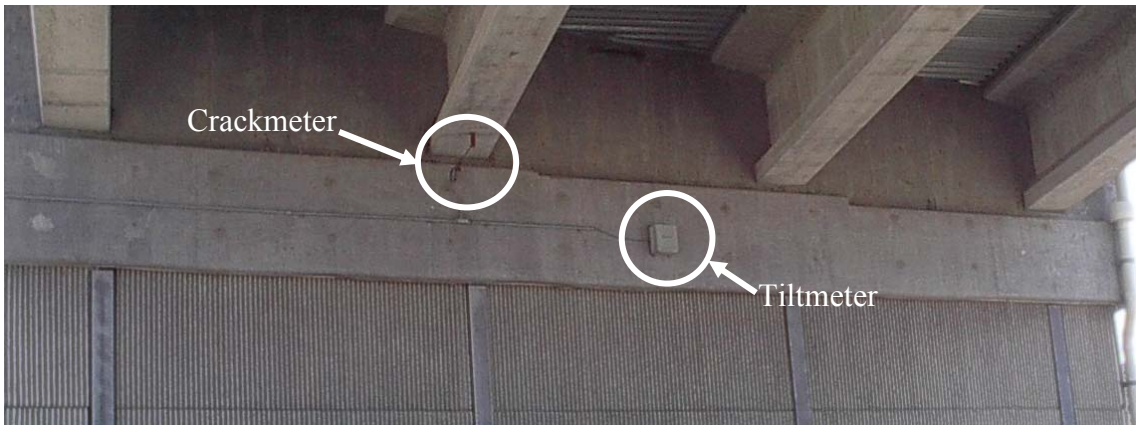

Figure 2.10: Crackmeter and Tiltmeter Locations on Bent 1 (SR249 over US12)

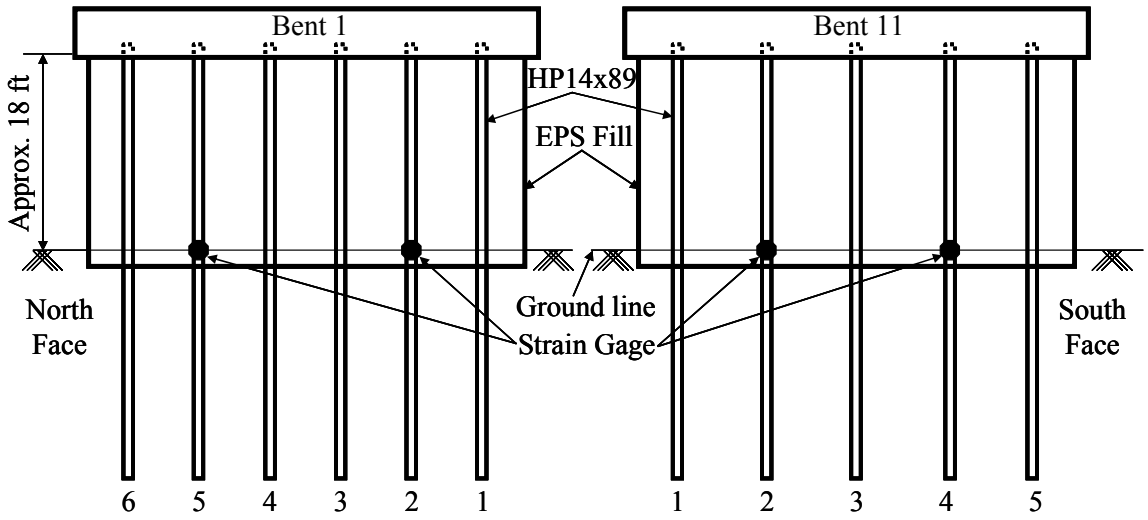

Figure 2.11: Pile Instrumentation (SR249 over US12)

2.2.3.3 Pier Instrumentation

Several of the piers were selected for instrumentation to evaluate movement of the piers as well as to enable estimation of the end bent movement. Rebar strain gages, crackmeters, and tiltmeters were used to determine movement at the top of the pier. Figure 2.12 shows the locations of tiltmeters and crackmeters on Pier 2. End bent movements were extrapolated from the calculated pier movements.

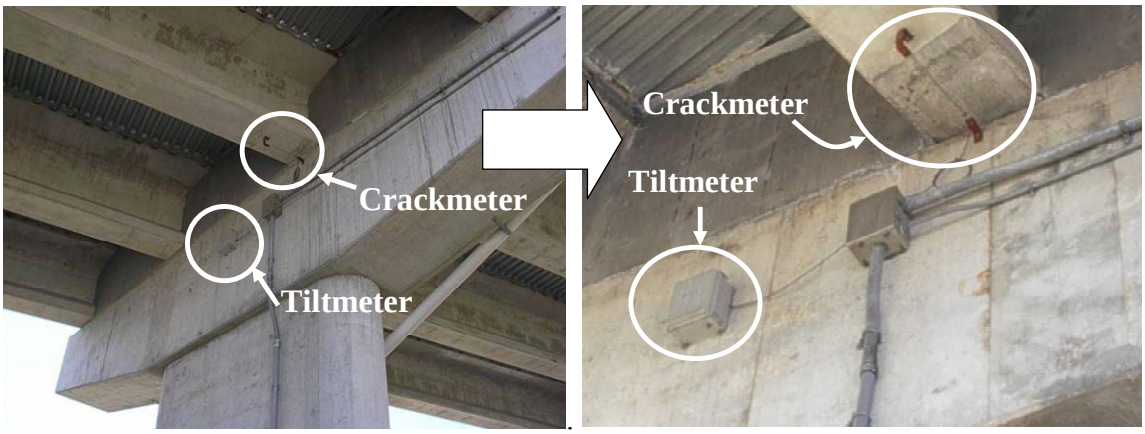

(a) Top of Pier 2 (b) Top of Pier 2

(c) Bottom of Pier 2 (d) Top of Pier 2 (East Side)

Figure 2.12: Tiltmeter and Crackmeter Locations (SR249 over US12)

2.2.3.3.1 Piers 2 and 10

Piers 2 and 10 were instrumented identically (Figure 2.13). A crackmeter was used to measure the displacement of Girder 3 relative to the pier to evaluate relative movement between the pier and the girder as well as to enable an estimate of the movement of the end bents. Rotations were measured by the tiltmeters at the base and pier top. These gages were used to evaluate footing rotations and pier top rotations such that the deflection of the pier could be estimated based on calculations. Tiltmeters on both Piers 2 and 10 were mounted on the south and east faces (Figure 2.13) to measure rotations about both axes of the pier to enable evaluation of the effect of bridge skew.

In addition, six rebar strain gages (Model 4911) were provided around the perimeter of the base of the pier to determine the magnitude of axial and bending forces resisted by the pier (Figure 2.14). These gages were installed at sister bars adjacent to the actual rebar. The combination of these gages was used to determine the forces experienced by the piers as well as their deflections.

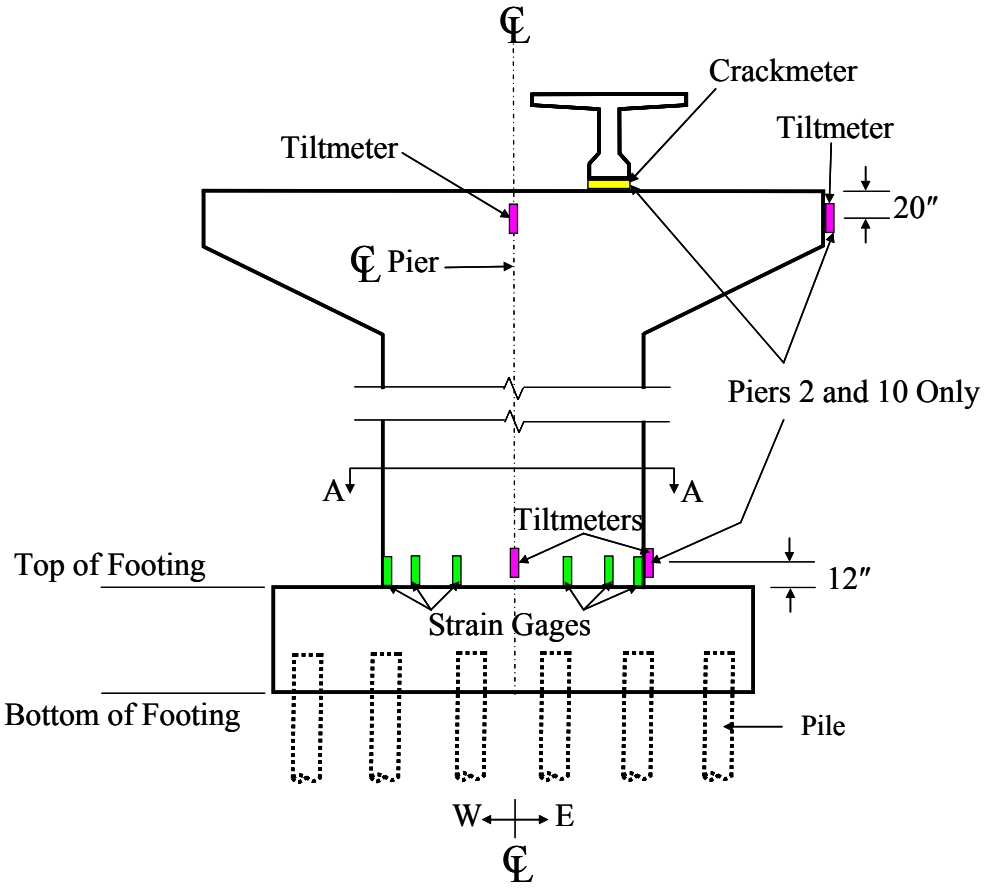

Figure 2.13: Pier Instrumentation (SR249 over US12)

2.2.3.3.2 Piers 3, 4, and 5

Piers 3, 4, and 5 were instrumented identically. Tiltmeters were located at the top and bottom on the south face (Figure 2.13). Furthermore, rebar strain gages were located at the base similar to Piers 2 and 10, with the exception that gages were not located on the east and west faces (Figure 2.14). The instrumentation of the SR 249 over US 12 bridge is summarized in Figure 2.15.

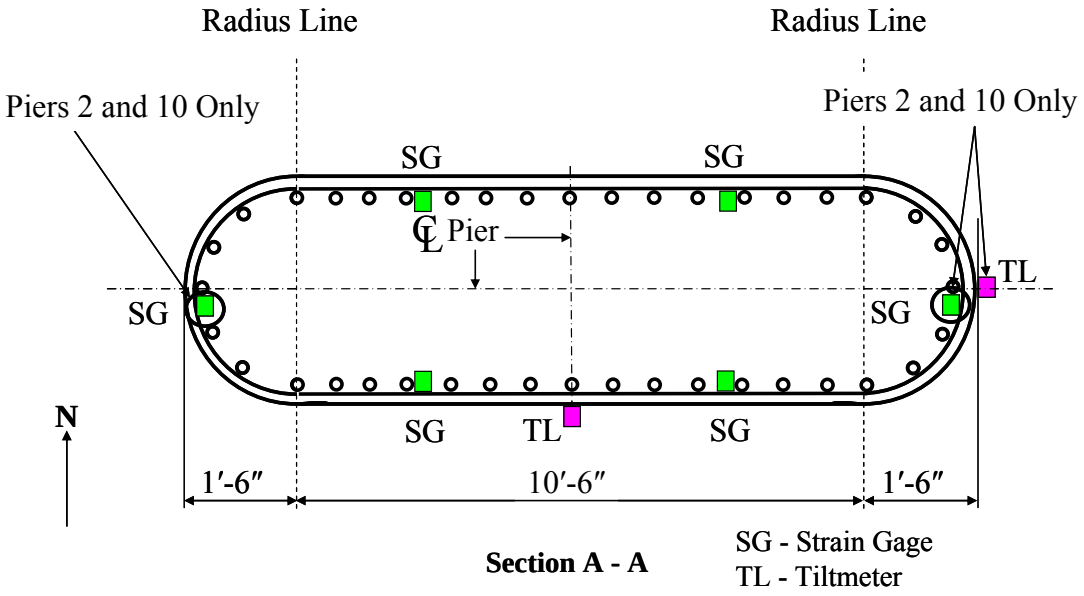

Figure 2.14: Strain Gages and Tiltmeter Locations (Section A-A of Figure 2.13) (SR249 over US12)

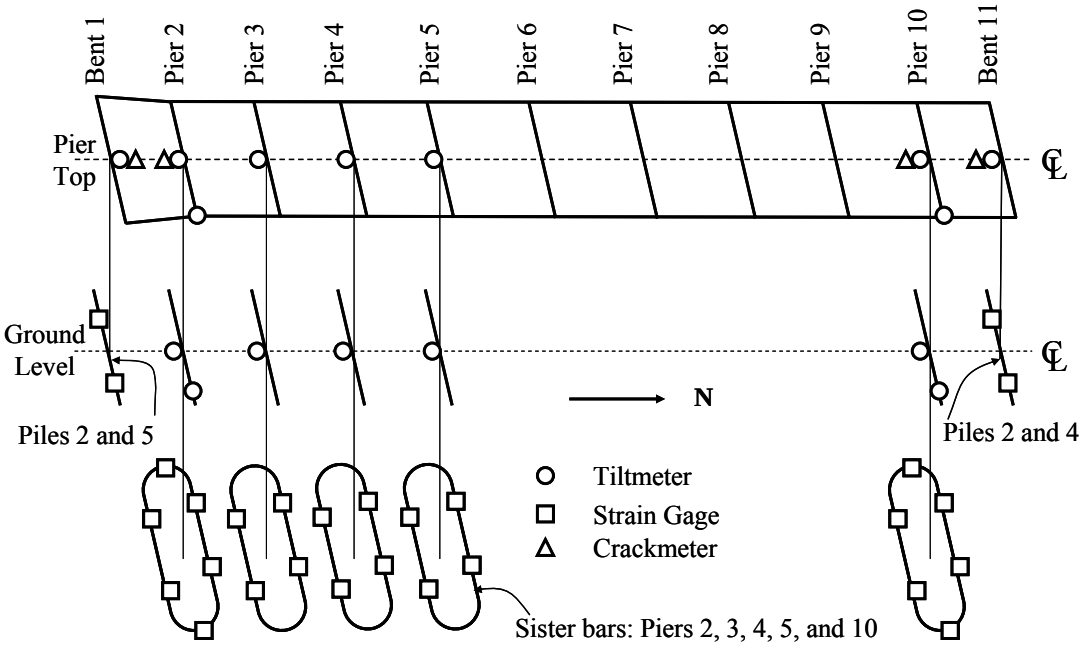

Figure 2.15: Bridge Instrumentation (SR249 over US12)

2.2.4 Data Acquisition

A Model 8020 MICRO-10 Datalogger and four Model 8032 Multiplexers provided by Geokon Inc. were required to record the data from the instruments previously discussed. It should be noted that tiltmeters and crackmeters were installed after the bridge was cast, while strain gages were installed before casting. The initial reading date of each multiplexer is shown in Table 2.4. All gages were zeroed at the initial reading date and read hourly. Therefore, the values recorded from all gages are relative to the day that gages started reading.

Table 2.4: Multiplexers (SR249 over US12)

Multiplexer	Gages	Initial Reading Date
1	- All tiltmeters	May 17, 2000 at 11:00AM
2	- Rebar strain gages on Piers 2, 3, and 10	June 7, 2000 at 9:00AM
3	- Rebar strain gages on Piers 4 and 5 - All crackmeters	June 7, 2000 at 9:00AM
4	- Pile strain gages on Bents 1 and 11 - Temperature gages	June 7, 2000 at 9:00AM

2.2.4.1 Problems

Problems with the instrumentation system for the SR249 over US12 bridge began on August 18, 2000 as summarized in Table 2.5. The system was reinstalled and failed on July 23, 2001. Figure 2.16 provides a summary of the inoperable gage locations. Solid shapes indicate that the gage has been malfunctioning since July 23, 2001.

Rebar strain gages started reading on June 7, 2000 and a large number of gages (Figure 2.16) failed on July 23, 2001. Recorded data beyond July 23, 2001 is not considered reliable; therefore, only data from June 7, 2000 to July 23, 2001 will be considered in this research.

Table 2.5: Instrumentation Problem (SR249 over US12)

Date	Event
May 17, 2000	All tiltmeters were zeroed and started reading.
June 7, 2000	All rebar strain gages, all pile strain gages, and all crackmeters were zeroed and started reading. All temperature gages started reading.
August 18, 2000	A modem was installed incorrectly causing all gages to malfunction. All gages read off-scale.
December 8, 2000	The system was back on-line and functioning properly.
July 23, 2001	All gages read off-scale due to a problem with a multiplexer board. The datalogger was subsequently removed from the bridge and repaired by INDOT.
April 10, 2002	The system was repaired and Multiplexers 1, 2, and 3 were operational. However, the data obtained from the bridge was very sporadic.
April 20, 2002	The complete system failed.
April 25, 2002	Multiplexers 1 and 2 became operational.
May 9, 2002	Multplexers 3 and 4 became operational. Although all multiplexers were operational, several gages were out-of-range due to damage to the recharging system.
May 13, 2002	The multiplexers were removed and repaired by INDOT.
May 29, 2002	The datalogger was removed and sent to Campbell Scientific for repair.
July 2, 2002	The datalogger was reinstalled with a reconfigured charging system. Unfortunately, only Multiplexer 1 was operable and only the thermistors in the tiltmeters provided reliable data. Some tiltmeter data were out-of-range. The boards in Multiplexers 2, 3, and 4 had electrical damage. Lightning was suspected.
July 18, 2002	All crackmeters and seven tiltmeters on the bridge were malfunctioning. All temperature gages were no longer in-service. Five rebar strain gages failed.

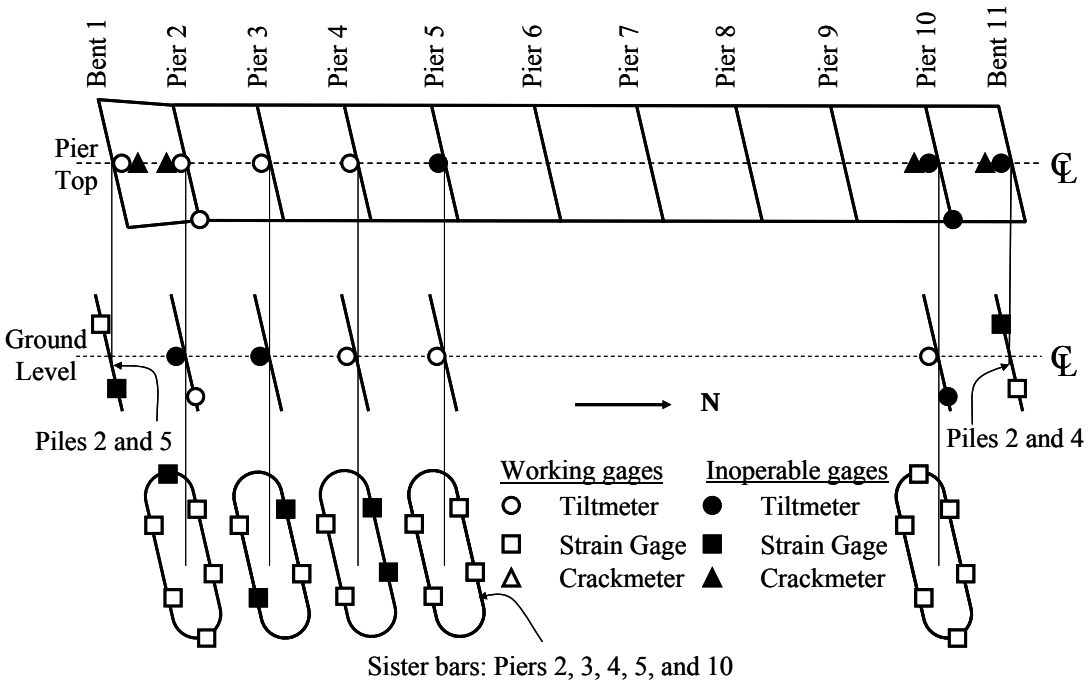

Figure 2.16: Malfunctioning Gage Locations (SR 249 over US12)

2.3 I65 over SR25 Bridges

Due to the number of malfunctioning gages on the SR249 over US12 bridge, INDOT Bridges #I-65-176-5543C (I65 over SR25) in Tippecanoe County were selected to investigate the general behavior of an integral abutment bridge. These bridges were chosen for study because they are considered typical integral bridges and their length and skew met current INDOT limitations.

Two identical bridges, one northbound and one southbound structures were instrumented. These bridges are located approximately 15 miles from Purdue University in Lafayette, Indiana. The bridges are two-span continuous, with seven-W36x150 steel girders supporting the concrete deck (Figure 2.17). The bridges have a total length of 152 ft and a skew angle of 25° relative to the abutments (Figure 2.18). An elevation view of the bridge is shown in Figure 2.19.

Figure 2.17: I65 over SR25 Northbound Structure

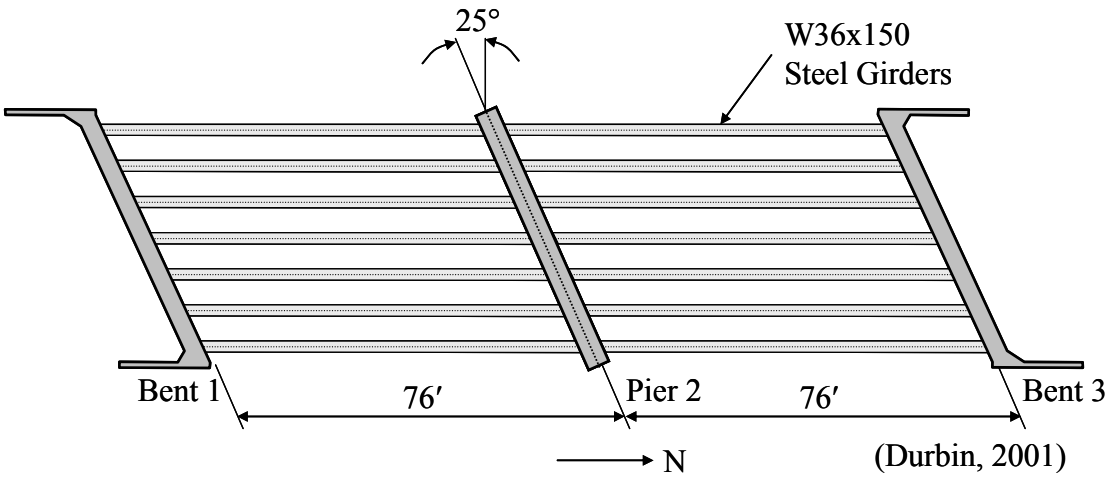

Figure 2.18: Plan View (I65 over SR25)

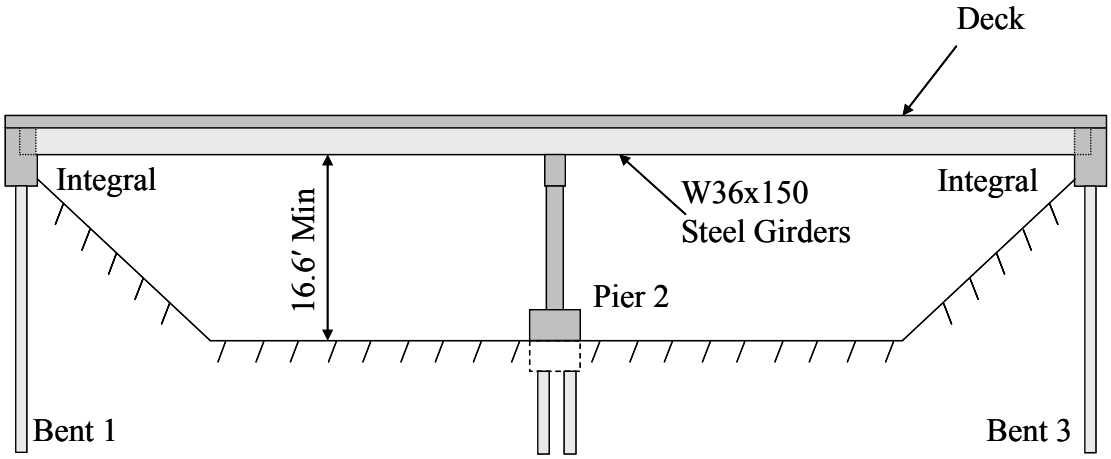

Figure 2.19: Profile View (I65 over SR25)

2.3.1 End Bent/Pile Design

2.3.1.1 End Bent

A single row of ten piles supports each abutment. Six HP12x53 steel piles bending about their weak axis and four 14 ½ in. diameter concrete-filled steel tube piles with a wall thickness of ¼ in. (CFT14.5x0.25) support each end bent. Because this project was a rehabitation, the four CFT piles were reused from the existing construction and the six H piles were added. The total pile length was approximately 42 ft, and the

piles were driven to a bearing capacity of 100 tons according to the INDOT Pile Driving Record provided in Appendix B. The piles were embedded 2 ft into the abutment as shown in Figure 2.20. Therefore, the pile length below ground level was approximately 40 ft. End bent details of the bridge are included in Appendix C.

2.3.1.2 Pile Design

All piles were designed for axial load only. The axial load consisted of the dead load of the abutment, bridge deck, girder, and wingwall. The live load was based on HS20-44 truck loading in accordance with the 16th Edition of the AASHTO Standard Specifications (1996).

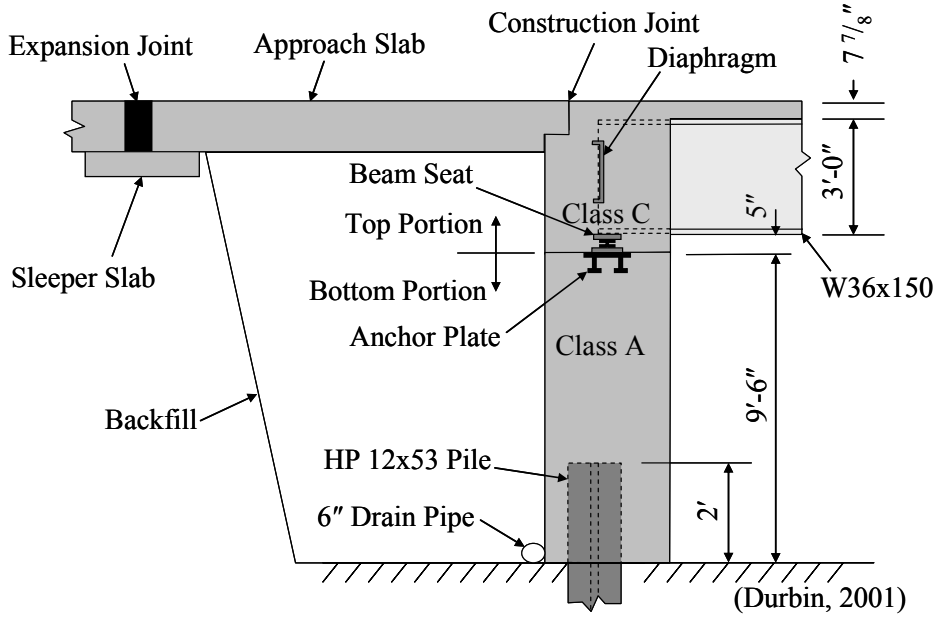

Figure 2.20: Profile View of Integral End Bent (I65 over SR25)

2.3.1.3 Soil Borings

Soil borings were located at Bent 1 and Pier 2 for the southbound structure as well as at Pier 2 and Bent 3 for the northbound structure. Soil boring plans are provided in Figure 2.21. The soil boring logs are summarized in Tables 2.6 - 2.9. The SPT values are also provided. Soil borings No. 1 and 4 (TB-1 and TB-4) were considered as a representative soil profile for the southbound and northbound structures, respectively.

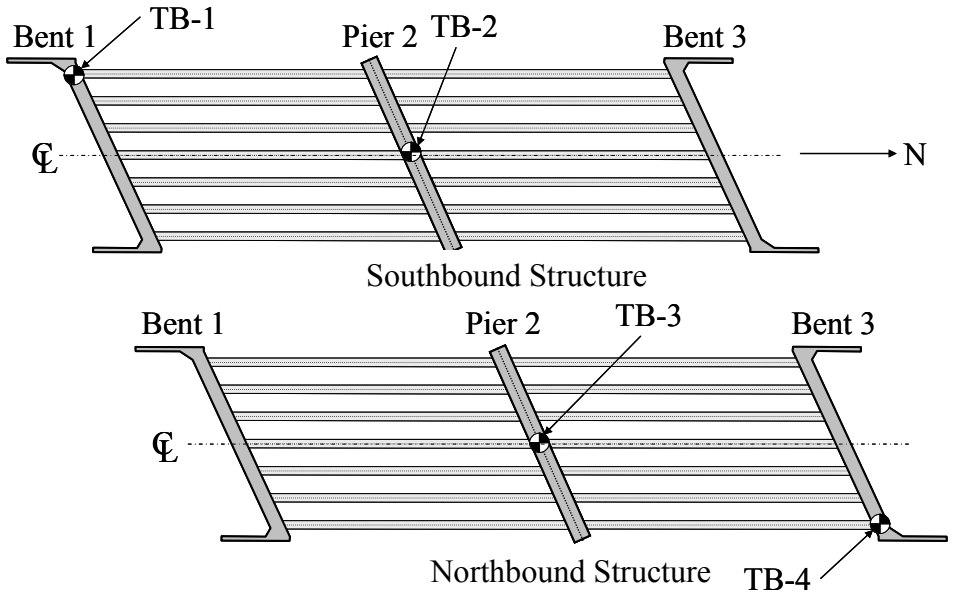

Figure 2.21: Soil Boring Plan (I65 over SR25)

Table 2.6: Soil Boring Log Data from TB-1 (I65 over SR25)

Depth from Ground Level (ft)		N	Soil Type
0.0	1.0	5	Gray moist soft sandy clay, trace of organic material
1.0	5.5	6	Brown loose fine to medium sand
5.5	22.5	27	Brown medium dense fine to medium gravel with some fine to medium sand, large gravel noted
22.5	26.5	*	Gray dense fine to medium sand, thin layers of silty clay
26.5	30.0	29	Gray very hard clay loam, trace of fine sand and gravel

* Cored boulder

Note: Ground water table was 6.5 ft below ground level

Table 2.7: Soil Boring Log Data from TB-2 (I65 over SR25)

Depth from Ground Level (ft)		N	Soil Type
0	8	26	Brown moist medium dense sand and gravel - Fill Top soil noted at 8 feet
8	16	15	Brown medium dense medium sand, a little clay
16	22	2	Brown loose medium sand
22	32.5	27	Brown medium dense coarse sand and gravel.
32.5	34	99*	Gray moist very hard clay loam, trace of small gravel

* 4 in. Penetration

Note: Ground water table was 22.5 ft below ground level

Table 2.8: Soil Boring Log Data from TB-3 (I65 over SR25)

Depth from Ground Level (ft)		N	Soil Type
0	7.5	35	Brown moist medium dense sand and gravel - Fill
7.5	8	-	Topsoil
8	17	6	Brown loose mediumsand, a little clay
17	28	28	Brown medium dense, medium to coarse sand and small gravel
28	45	99	Gray moist very hard clay loam, trace of small gravel, seam of sand and gravel at 38 ft

Note: Ground water table was 8.5 ft below ground level

Table 2.9: Soil Boring Log Data from TB-4 (I65 over SR25)

Depth from Ground Level (ft)		N	Soil Type
0	1	-	Top soil
1	8	6	Brown moist loose medium sand, a little clay
8	22	25	Brown medium dense coarse sand and small to medium gravel
22	30	99	Gray moist very hard clay loam, trace of small gravel

Note: Ground water table was 10 ft below ground level

2.3.2 Structural Materials

2.3.2.1 Concrete

INDOT Class A concrete (f'_c = 3,500 psi) was used for the substructure for the bottom portion of the abutment. Structural concrete for the superstructure which consisted of the top portion of the abutment and the bridge deck was INDOT Class C (f'_c = 4,000 psi).

The deck of the northbound structure was poured on August 15, 2000 from 7:00AM to 2:00PM, while the deck of the southbound structure was poured on October 18, 2000 from 7:30AM to 1:30PM. The construction sequence of this bridge is provided in Appendix D.

2.3.2.2 Piles

According to INDOT Standard Specifications (1999), all HP12x53 piles were supplied in accordance with AASHTO M 183. Material data for the existing CFT14.5x0.25 piles was not available. It is estimated based on typical practice that the piles were ASTM A252, Grade 2 or 3.

2.3.3 Instrumentation Design

Both the northbound and southbound structures were instrumented to investigate the end abutment and pile response.

2.3.3.1 Northbound Structure

On the northbound structure, Micro-Measurements ¼″ foil strain gages (CEA-06-250UN-350) were installed on the piles as shown in Figure 2.22 to evaluate the pile behavior. On Bent 1, gages were attached to Piles 2, 6, and 7 while gages were installed on Piles 2, 4, and 6 on Bent 3. All gages were installed at ground level (Figure 2.23) as the maximum stress was expected to occur at this location. Omega Type T 24 AWG solid thermocouple wire was installed on Girder 7 at midspan as illustrated in Figure 2.22 to provide ambient air temperature measurements.

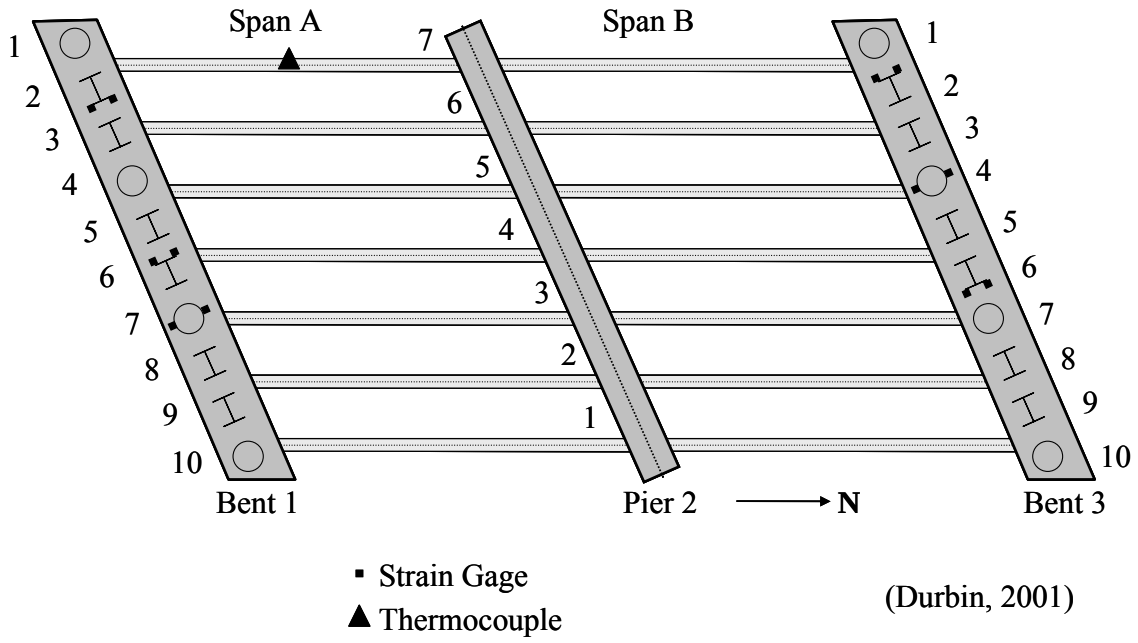

Figure 2.22: Strain Gage and Thermocouple Locations on Northbound Structure (I65 over SR25)

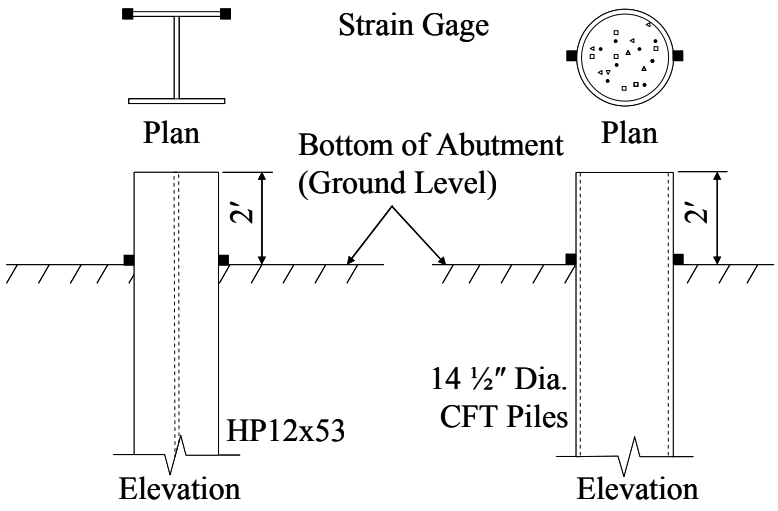

Figure 2.23: Strain Gage Location on Pile on Northbound Structure (I65 over SR25)

2.3.3.2 Southbound Structure

The southbound structure was instrumented to determine the longitudinal and transverse movement of the abutment as well as the response of the piles. In general, the instrumentation of this structure concentrated on the movement of the end bent. The locations of strain gages and potentiometers incorporated into the structure are shown in Figure 2.24. Micro-Measurements ¼″ foil strain gages (CEA-06-250UN-350) were installed on the edge of each flange of two HP12x53 piles (Piles 6 and 9) at the bottom of the abutment to measure biaxial bending of the piles. Figure 2.25 shows an elevation view of the end bent instrumentation. The strain gages were installed at the bottom of the abutment (Figures 2.26 and 2.27) where maximum pile stresses were expected.

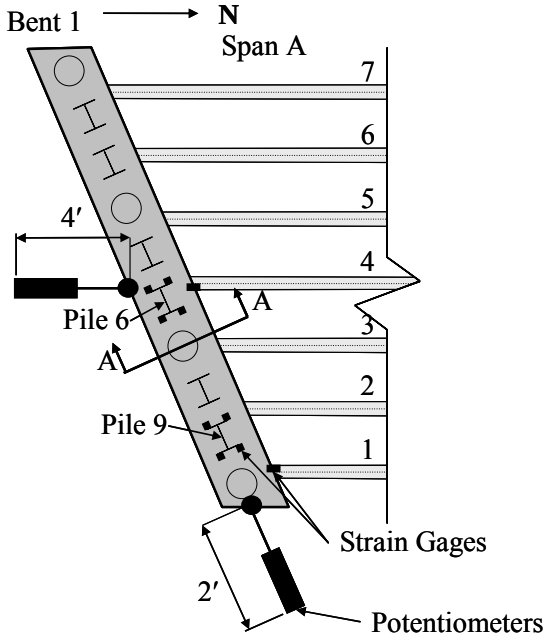

(Durbin, 2001)

Figure 2.24: Strain Gage and Potentiometer Locations on Southbound Structure (I65 over SR25)

In addition, two linear motion potentiometers (Maurey Instrument Corp. #M1326-3-103) were installed to measure the movement of the abutment (Figure 2.24). These potentiometers have a displacement capacity of 3 in. The longitudinal motion

potentiometer was placed approximately 4 ft behind the south face of the abutment (Figure 2.28) and the transverse motion potentiometer was placed approximately 2 ft east of the abutment. Only Bent 1 for the southbound structure was instrumented.

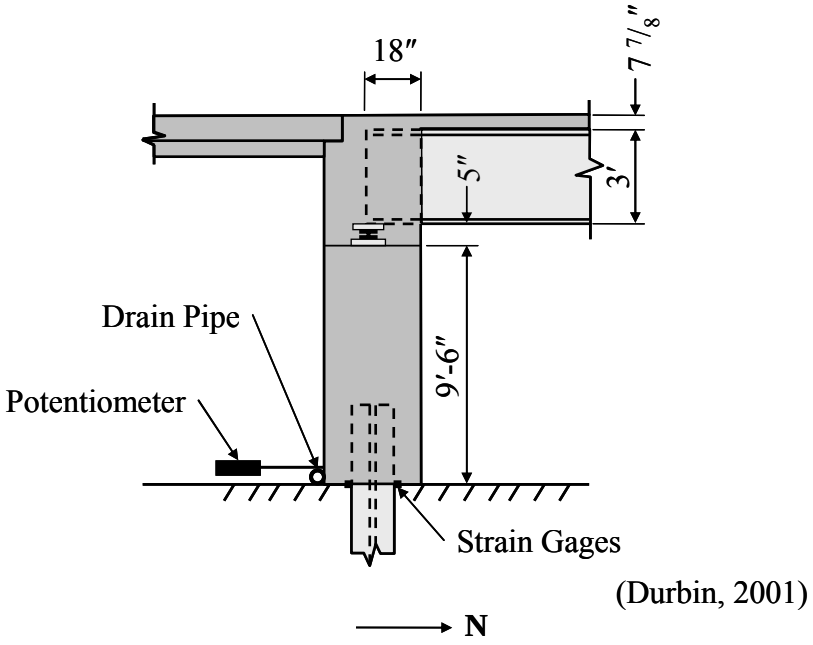

Figure 2.25: End Bent Elevation View on Southbound Structure (I65 over SR25)

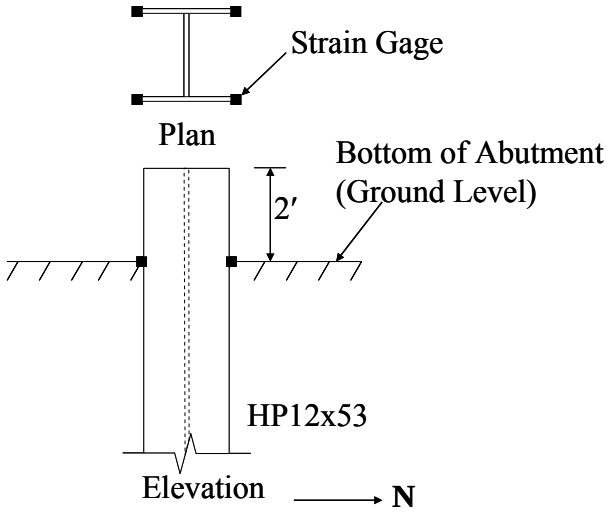

Figure 2.26: Pile Strain Gage Locations on Southbound Structure (I65 over SR25)

Figure 2.27: Strain Gages on H Pile (I65 over SR25)

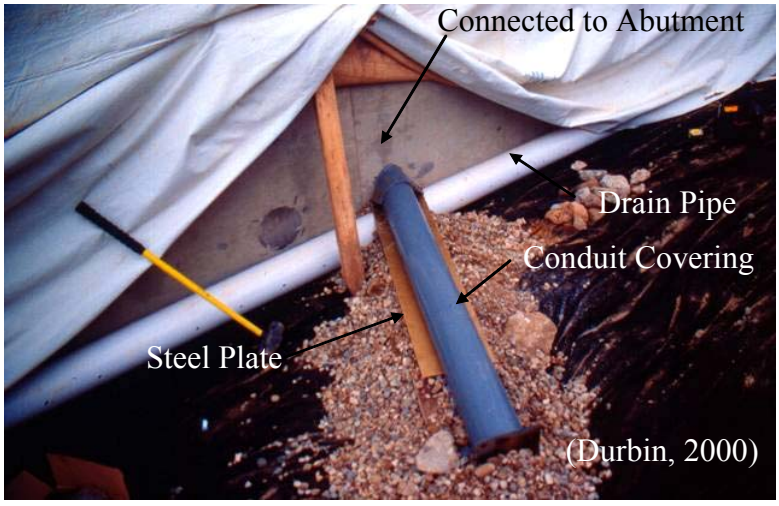

Figure 2.28: Linear Potentiometer Protected with Conduit (I65 over SR25)

2.3.4 Data Acquisition

To monitor the strain gages, thermocouples, and potentiometers on the bridge, a Campbell Scientific datalogger system (CR10X) with AM416 multiplexers was selected.

On the northbound structure, all gages were zeroed and began reading every 15 minutes on August 14, 2000, the day before deck casting. On January 17, 2001, the time interval was changed to hourly.

On the southbound structure, all gages were read hourly. The initial readings for various gages were taken at various times. The longitudinal potentiometer was zeroed on September 24, 2000, strain gages were zeroed on October 6, 2000, and the transverse potentiometer was zeroed on October 18, 2000.

2.3.4.1 Problems

Data from the southbound structure between May 13, 2002 and July 30, 2002 were not available because of a battery failure. All initial zero readings were unable to be recovered; therefore, beyond this date, the initial reading was estimated based on thermal response and historical data.

2.4 SR18 over Mississinewa River Bridge

As previously discussed, extensive problems with the SR249 over US12 bridge led to incomplete data for that structure. To make up for this deficiency, the SR18 over Mississinewa River Bridge (Figure 2.29) was also selected for instrumentation. There are several reasons for selecting this structure.

1. The bridge was designed and constructed according to typical integral abutment details.
2. The bridge exceeded the length limitation of INDOT and could provide much needed data regarding bridge length.
3. The skew of the structure was small. Therefore the research could focus on the effects of bridge length.

Figure 2.29: SR18 over Mississinewa River Bridge

To better understand the soil-pile-abutment-system, the five-span, continuous prestressed, concrete bulb-tee integral bridge was instrumented. The construction and instrumentation were part of Project No. STP/132-5 which was a bridge rehabilitation of Structure 18-27-4518D. This bridge is located east of the city of Marion in Grant County, Indiana on the westbound lanes of State Road 18 crossing the Mississinewa River. The total bridge length is 367 ft (Figure 2.30) with a skew angle of 8°. A typical cross section is presented in Figure 2.31.

2.4.1 End Bent/Pile Design

2.4.1.1 End Bent

Each abutment is supported by ten 14-in. diameter concrete-filled steel tube piles with a wall thickness of 0.312 in. (CFT14.0x0.312). The average pile length for Bent 1 was 20.8 ft with all piles driven to a bearing capacity of 112.5 tons. For Bent 6, the average pile length was 27 ft with the piles driven to 100 tons according to INDOT Pile Driving Record provided in Appendix B. The piles are embedded 1.25 ft in the abutment. End bent details of the bridge are included in Appendix C.

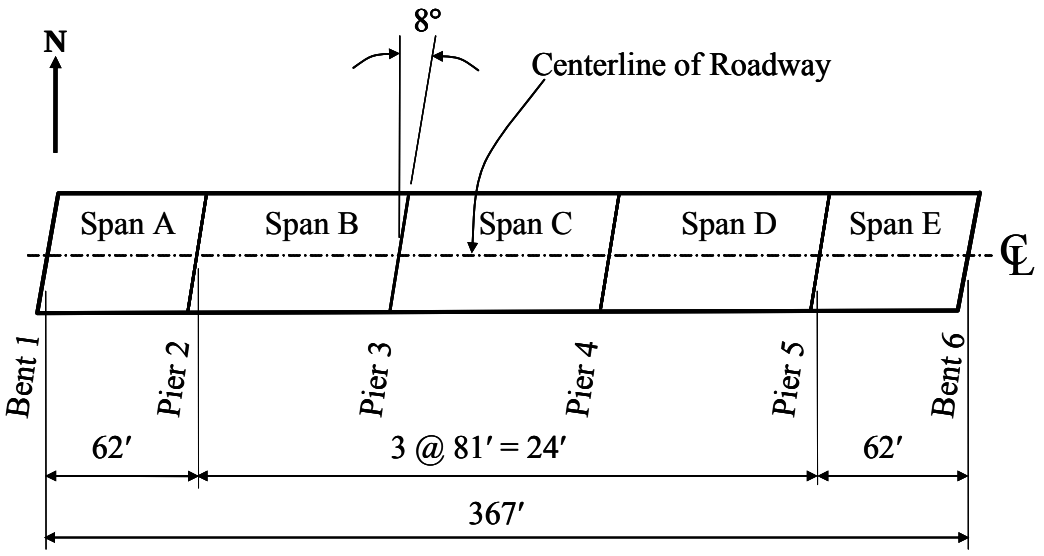

Figure 2.30: Plan View (SR18)

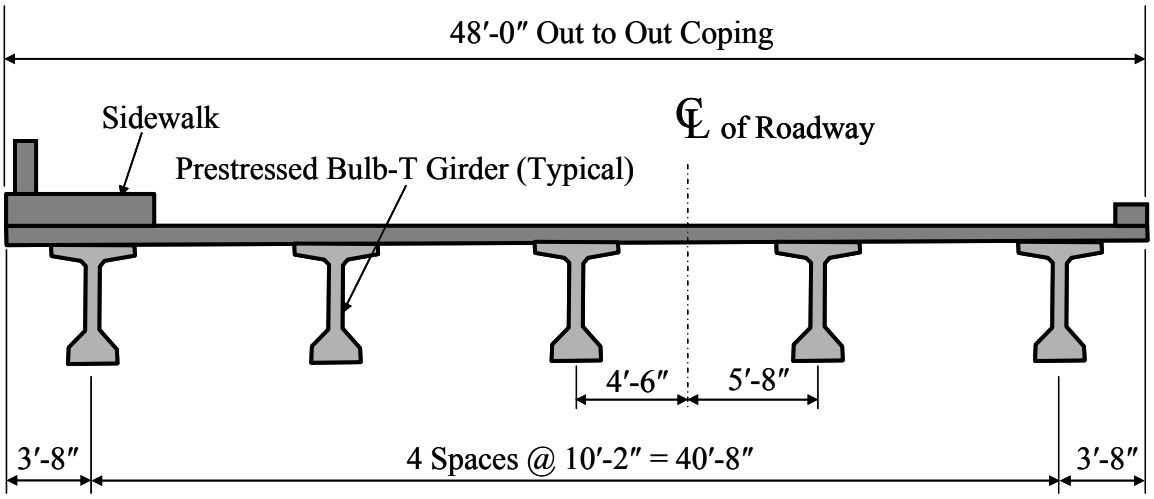

Figure 2.31: Typical Cross Section (SR18)

2.4.1.2 Pile Design

All piles were designed for axial load only. Axial loads consisted of dead loads from the abutment, bridge deck, girder, and diaphragm as well as live loads. Live load was based on HS20-44 loading with impact load (including consideration of lane load) based on 16th Edition of the AASHTO Standard Specification.

2.4.1.3 Soil Borings

Soil borings were located near each end bent as illustrated in Figure 2.32. Soil boring logs for Bents 1 and 6 are summarized in Tables 2.10 and 2.11. The ground water table was located 33.5 ft below ground level at Bent 1. At Bent 6, the ground water table was not observed at the maximum boring depth of 35 ft. The soil profiles for Bents 1 and 11 are presented in Figure 2.33 compared to Pile 6, which is approximately 23.5 ft long and are embedded 1.25 ft in the abutment; therefore, the pile length below ground level is approximately 22.25 ft

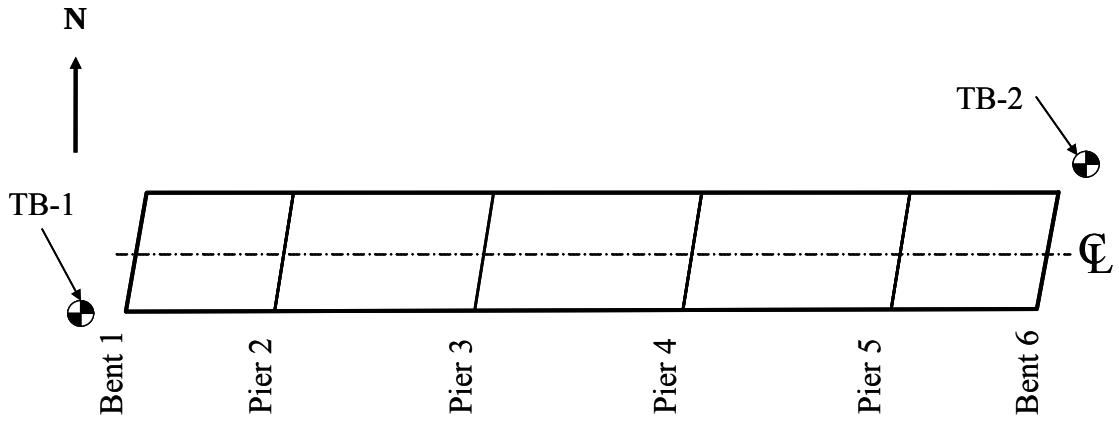

Figure 2.32: Soil Boring Plan (SR18)

Table 2.10: Soil Boring Data (TB-1) on Bent 1 (SR18)

Depth from Ground Level (ft)		N	SOIL TYPE
0.0	0.5	-	Asphalt
0.5	1.4	-	Concrete
1.4	2.9	17	SILTY LOAM, Slightly Moist, Stiff, Tan
2.9	5.0	23	SILTY CLAY LOAM, Stiff, Slightly Moist, Gray
5.0	10.0	20	SILTY LOAM + some sand + gravel, Stiff, Slightly Moist, Brown
10.0	15.0	21	SILTY LOAM, Stiff, Slightly Moist, Tan
15.0	20.0	16	SILTY CLAY LOAM, Stiff, Slightly Moist, Grayish Brown, Medium
20.0	25.0	15	SILTY LOAM,Medium stiff, Slightly Moist, Gray
25.0	30.0	6	SILTY LOAM, Soft, Moist, Gray,
30.0	35.0	47	SILTY LOAM, Soft, Gray
35.0	45.0	78	SILTY LOAM, Hard, Dry, Gray

Table 2.11: Soil Boring Data (TB-2) on Bent 6 (SR18)

Depth from Ground Level (ft)		N	SOIL TYPE
0.0	0.6	-	Asphalt
0.6	1.2	-	Concrete
1.2	2.7	19	SILTY LOAM, Stiff, Slightly Moist, Brown
2.7	8.0	28	SANDY LOAM, Medium Dense, Slightly Moist, Gray
8.0	10.0	16	SILTY LOAM, Medium Stiff, Slightly Moist, Brown
10.0	15.0	8	SANDY LOAM, Loose, Slightly Moist, Brown
15.0	20.0	12	SAND, Loose, Slightly Moist, Tan
20.0	25.0	19	SAND + some gravel, Medium Dense, Moist, Brown
25.0	30.0	63	SILTY LOAM, Hard, Slightly Moist, Gray
30.0	35.0	112	SILTY CLAY LOAM + Gravel, Hard, Dry, Gray

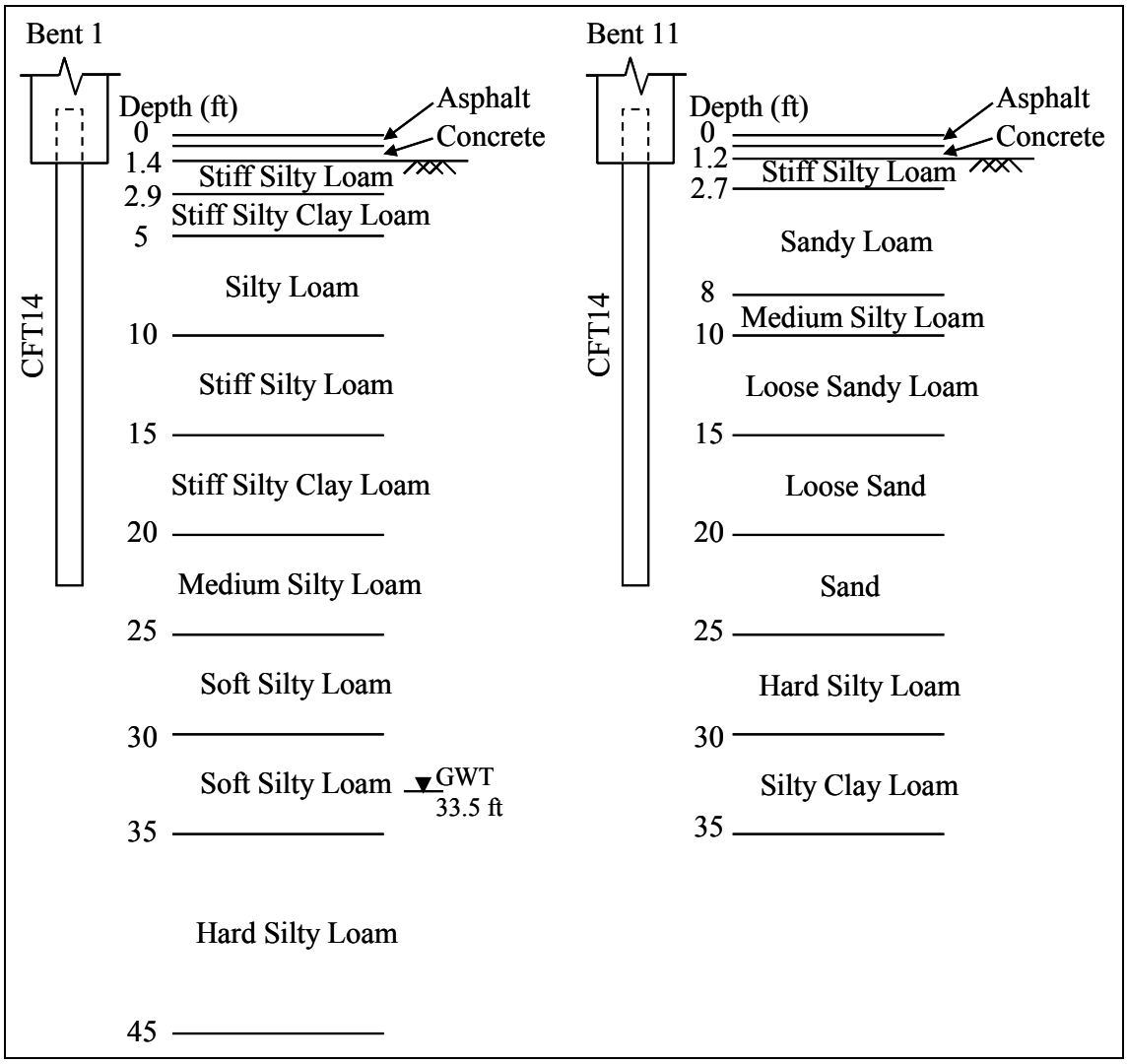

Figure 2.33: Soil Profiles on Bents 1 and 6 (SR18)

2.4.2 Structural Materials

2.4.2.1 Concrete

INDOT Class A concrete (f'_c = 3,500 psi) was used in all bents and piers while INDOT Class C concrete (f'_c = 4,000 psi) was used in the superstructure. INDOT Class B concrete (f'_c = 3,000 psi) was used for the footings. The bridge deck was cast on September 26, 2003 and opened to traffic on November 25, 2003. The construction sequence for this bridge is provided in Appendix D.

2.4.2.2 Piles

According to INDOT Standard Specifications (1999), the CFT14 rounded steel pipe shells were supplied in accordance with ASTM A252, Grade 2.

2.4.3 Instrumentation Design

2.4.3.1 Bent Instrumentation

To evaluate the abutment movement, tiltmeters and convergence meters were provided on Bents 1 and 6. All instruments were manufactured by Geokon Inc. A tiltmeter (Model 6350) was installed vertically on the face of end bent located 18 in. from the bottom at the center of the abutment (Figure 2.34).

To evaluate the longitudinal abutment movement, a convergence meter or displacement meter (Model 4425) was installed behind the abutment (Figure 2.35). The transducer end of the convergence meter was attached to a reference pile using an eye bolt. The rod end of the convergence meter was attached to the back of the end bent using an eye bolt anchored into the concrete. The convergence meter was oriented horizontally and operated perpendicular to the abutment. The convergence meter was used to measure the relative displacement between the end bent and the reference pile to determine the longitudinal abutment movement. The locations of the convergence meters, tiltmeters, and pile strain gages are shown in Figures 2.35 and 2.36.

Figure 2.34: Tiltmeter Location (SR18)

Figure 2.35: Convergence Meter (SR18)

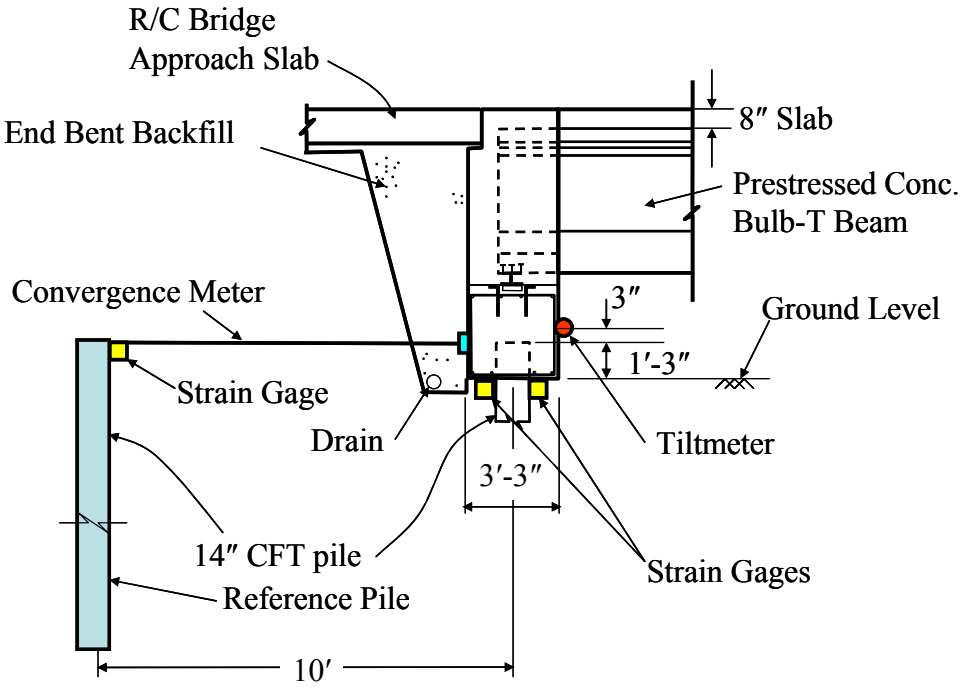

Figure 2.36: End Bent Instrumentation (SR18)

To measure the air temperature, three temperature gages (Model 4700) were installed on the bridge. One temperature gage was located at the mid-height of the concrete bridge deck between Bent 1 and Pier 2. Another gage located between Pier 5 and Bent 6 was also installed between the bottom of the deck and the bottom of the girder to prevent exposure to direct sunlight. The girder temperature gage was used to measure ambient temperature while the deck temperature gages were used to determine the rate at which the structure responded to air temperature changes.

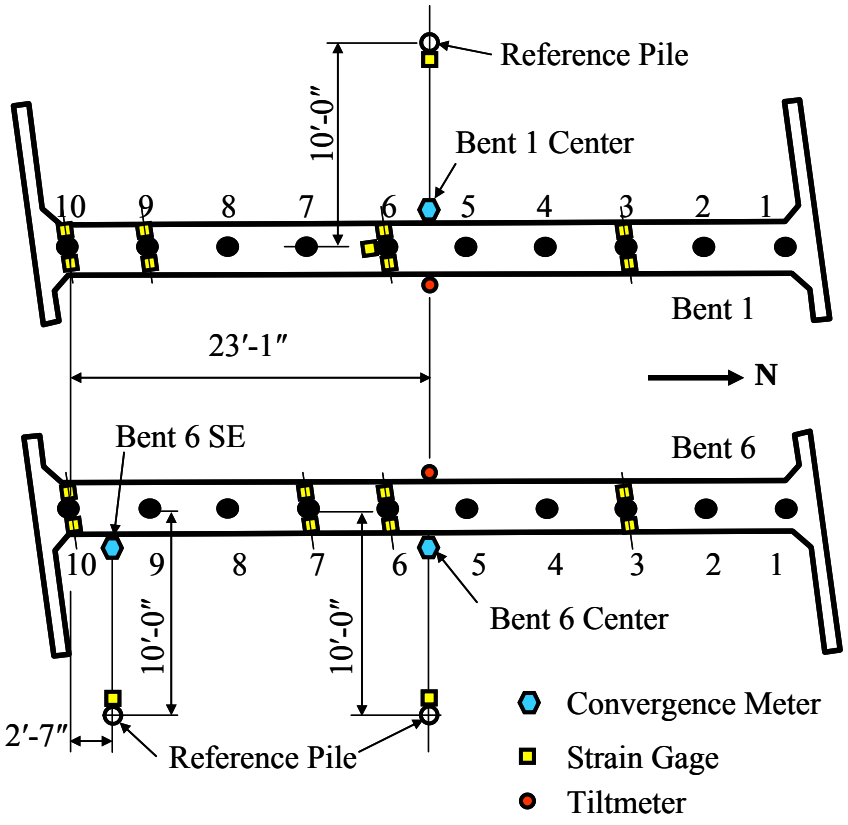

Figure 2.37: Pile Instrumentation (SR18)

2.4.3.2 Pile Instrumentation

Vibrating wire strain gages (Model VK-4100) were installed on piles, not only at ground level but also along the length of Pile 6 on Bent 1 (Figure 2.37), to evaluate the in-service, soil-structure response and to determine the response of the entire pile rather than only at the base of the abutment. Strain gages on Piles 3, 9, and 10 on Bent 1 as well as Piles 3, 6, 7, and 10 on Bent 6 were located on both the east and west faces at ground level to evaluate the pile behavior at the abutment-pile connection.

Strain gages on Pile 6 of Bent 1 were located at and below ground level as shown in Figure 2.38. All strain gages were attached to the pile by spot welding and were protected by steel angles (Figure 2.39). All strain gages except the ones at ground level were installed prior to pile driving to provide the strain profile along the length of the pile enabling investigation of the overall pile behavior. The strain gages at ground level were

installed after driving. These gages on Pile 6 allow calculation of pile bending down the length of the pile and estimate of the deflected shape. Strain gages on the south face were installed to provide redundancy, locate the neutral axis, and evaluate out-of-plane movement of the pile.

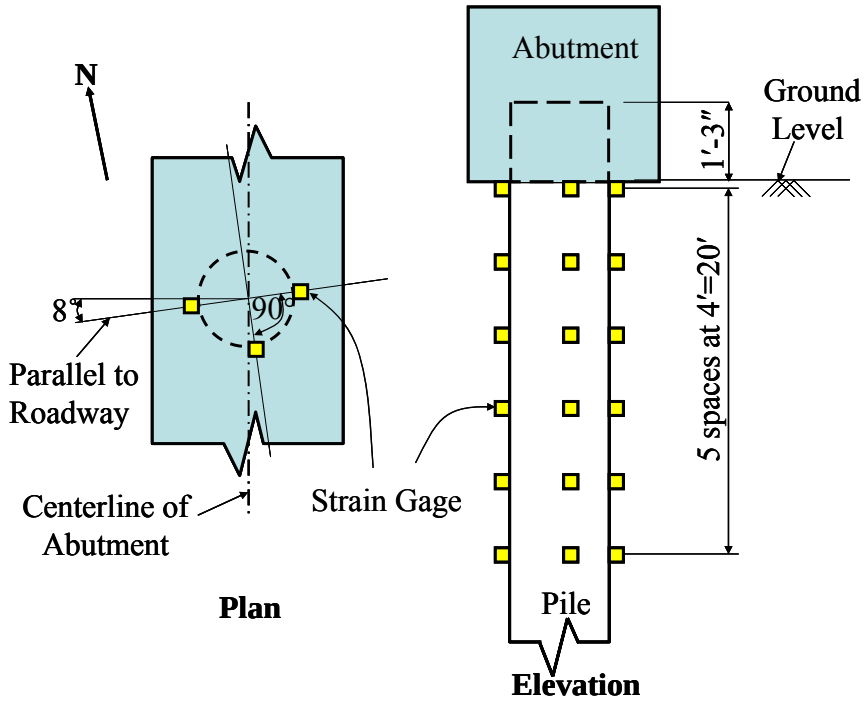

Figure 2.38: Strain Gages along the Pile Length (SR18)

To ensure that the gages on Pile 6 were installed at the correct depth, the other nine piles for that bent were driven first. While significant variation in pile length to achieve adequate bearing were observed, a reasonable estimate was obtained. Figure 2.40 shows the variation of the pile length that occurred for Bent 1. The pile prior to cut-off are shown in Figure 2.41. The pile was cut to the designed length so that the gages were properly located. The final instrumented pile length was 23.5 ft with 15 in. embedded in the abutment.

(a) Pile Strain Gage (b) Spot Welding

Figure 2.39: Pile Instrumentation (SR18)

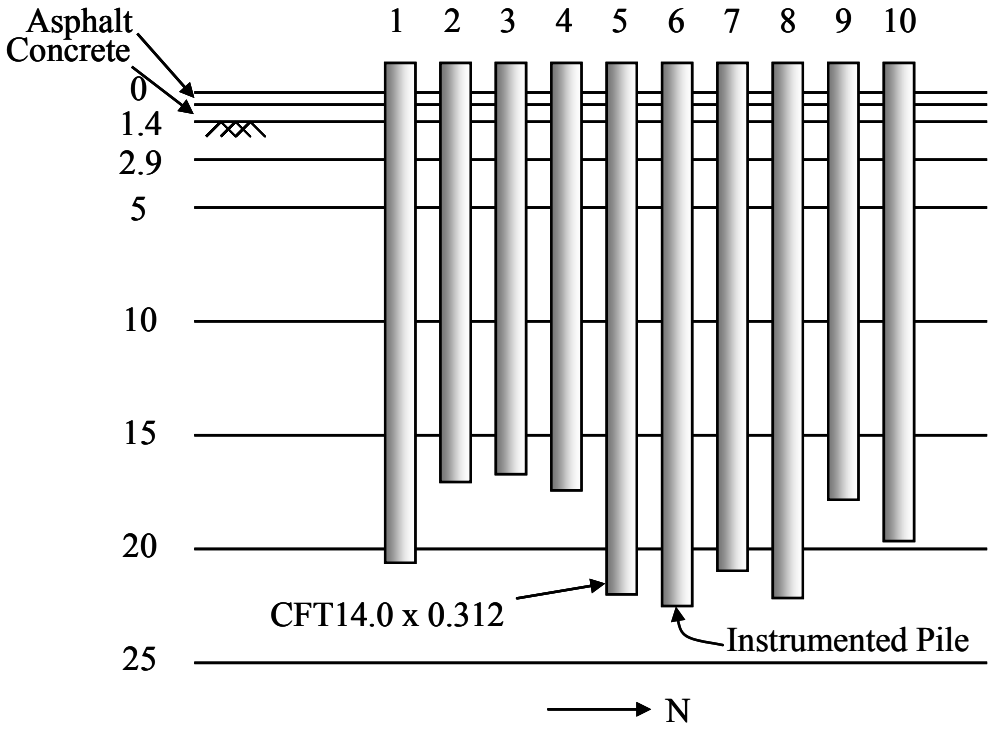

Figure 2.40: Variation of the Pile Length - Bent 1 (SR18)

Figure 2.41: Piles before Cut Off - Bent 1 (SR18)

2.4.4 Data Acquisition

All data was recording using a Geokon datalogger (Model 8020 Micro-10) along with several multiplexers (Model 8032). The gages on both end bents were zeroed and started reading hourly as listed in Table 2.12. To provide increased lightning protection, lightning arrestor boards (LAB-3) were also installed between the sensors and the multiplexers.

Table 2.12: Zeroed/Started Reading (SR18)

Gages	Zeroed/Started Reading	
	Bent 1	Bent 6
Pile Strain Gage	July 17, 2003	June 18, 2003
Convergence Meter	July 22, 2003	June 20, 2003
Tiltmeter	July 22, 2003	June 20, 2003

CHAPTER 3: FIELD RESULTS

3.1 Introduction

To evaluate the pile and abutment behavior of the four bridges discussed in Chapter 2, the field results were analyzed. Data recorded by the bent, pile, and pier instrumentation were used to estimate bent movements, determine deflected shapes of pile, and better understand the pile and abutment behavior of those bridges. In addition, the piles supporting abutments were analytically modeled, and the results from these analyses were calibrated with the field results.

3.2 SR249 over US12 Bridge

Due to problems with the datalogger system, data from most of the instruments are reliable only until July 23, 2001. Beyond this date, only temperature data is available. Therefore, data provided by tiltmeters, strain gages, and crackmeters will be considered only from June 7, 2000 to July 23, 2001.

3.2.1 Temperature

Air temperature was monitored by several thermistors across the structure. All thermistors read approximately the same value; therefore, the temperature from the tiltmeter on Bent 1 is considered as the representative ambient temperature. The temperature over time is shown in Figure 3.1. As noted, the breaks in the data are due to problems with the datalogger system. Since temperature data provided by the instruments began reading from June 7, 2000 after the bridge was cast, the construction temperature was obtained from data reported during construction. The construction

temperature was calculated from the daily low and high temperature throughout the casting period as provided in Table 3.1. Also tabulated in Table 3.2, are the construction as well as the maximum, and minimum temperatures over the time of the study. The average daily low and high construction temperatures were 45° and 68° F; however, the construction temperature was assumed to be equal to 60° F for simplicity as the exact temperature distribution over the construction sequence was not available.

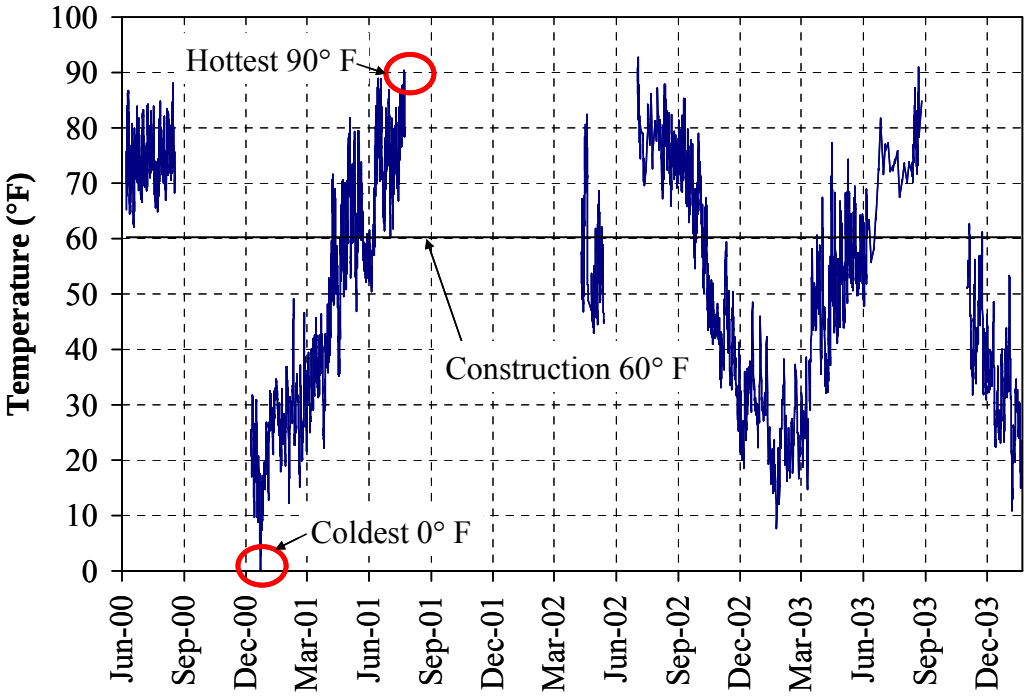

Figure 3.1: Air Temperature (SR249 over US12)

3.2.2 Rotations of the Abutment

Tiltmeters were used to measure the rotations of the abutment. Tiltmeters were located on the north side of Bent 1 and on the south side of Bent 11 as discussed in Section 2.2.3.1. Only rotations between June 2000 and July 2001 are considered due to the problem with the data acquisition system. Since the data acquisition system was connected to an external power source, electric interference or noise can be observed by the jumps in the data over the course of a day. The average rotations of Bents 1 and 11 were calculated to filter the noise as illustrated in Figures 3.2 and 3.3. The average

rotations were calculated considering the rotations four hours before and after the given time. The sign convention is illustrated in Figure 3.4. Positive rotation indicates that the abutment rotates inward or contracts and negative rotation indicates that the abutment rotates outward or expands. The rotations of both bents were almost identical and range from -0.1 to 0.1 degrees. In other words, the top of the abutment moved approximately 0.2 in. relatively to the bottom of the abutment considering the height of the abutment to be approximately equal to 9.84 ft (3 m). The results indicate that the abutment does not rotate significantly but rather translates during expansion and contraction.

Table 3.1: Construction Temperature (SR249 over US12)

Date	Section Cast	Daily Temperature (°F)	
		Low	High
September 10, 1999	Bent 1	45	77
September 16, 1999	Span A (East)	47	74
September 20, 1999	Span B	41	68
September 20, 1999	Span A (West)	41	68
September 23, 1999	Span C/D	49	75
October 1, 1999	Span E/F	41	76
October 6, 1999	Span G/H	42	58
October 8, 1999	Span J, Bent 11	52	56
October 11, 1999	Span I	45	64
Average		45	68

Table 3.2: Air Temperature (SR249 over US12)

Temperature Type	Temperature (°F)	Date
Construction	60	"Average" over September 10, 1999 to October 11, 1999
Maximum	90	July 22, 2001 at 16:00
Minimum	0	December 22, 2000 at 8:00

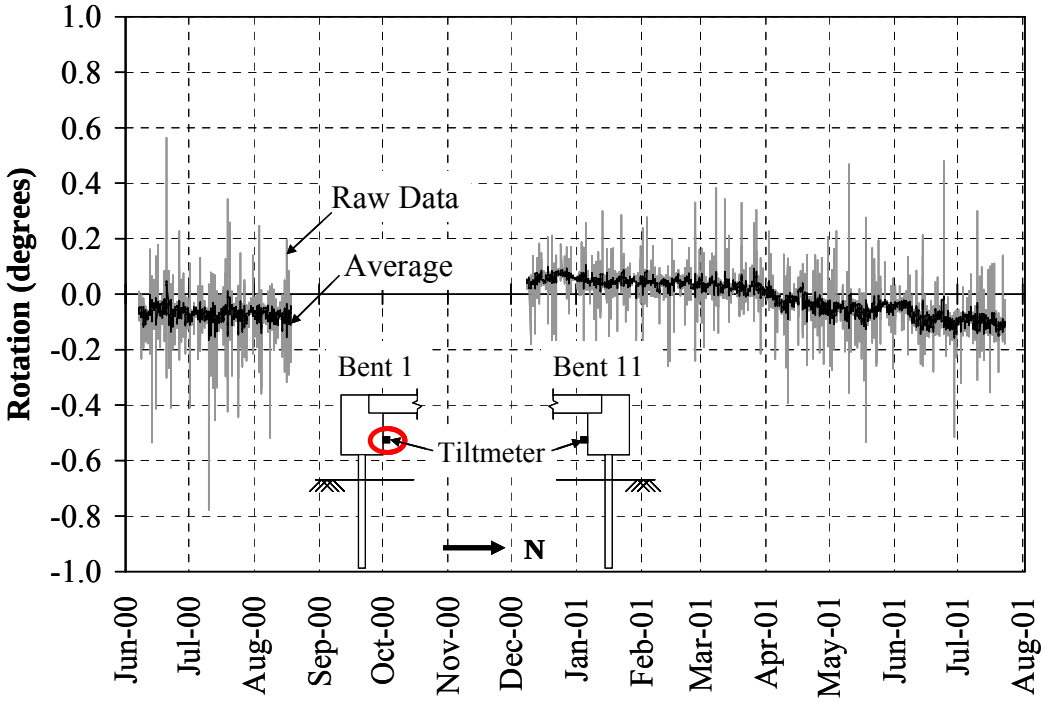

Figure 3.2: Rotations of Bents 1 (SR249 over US12)

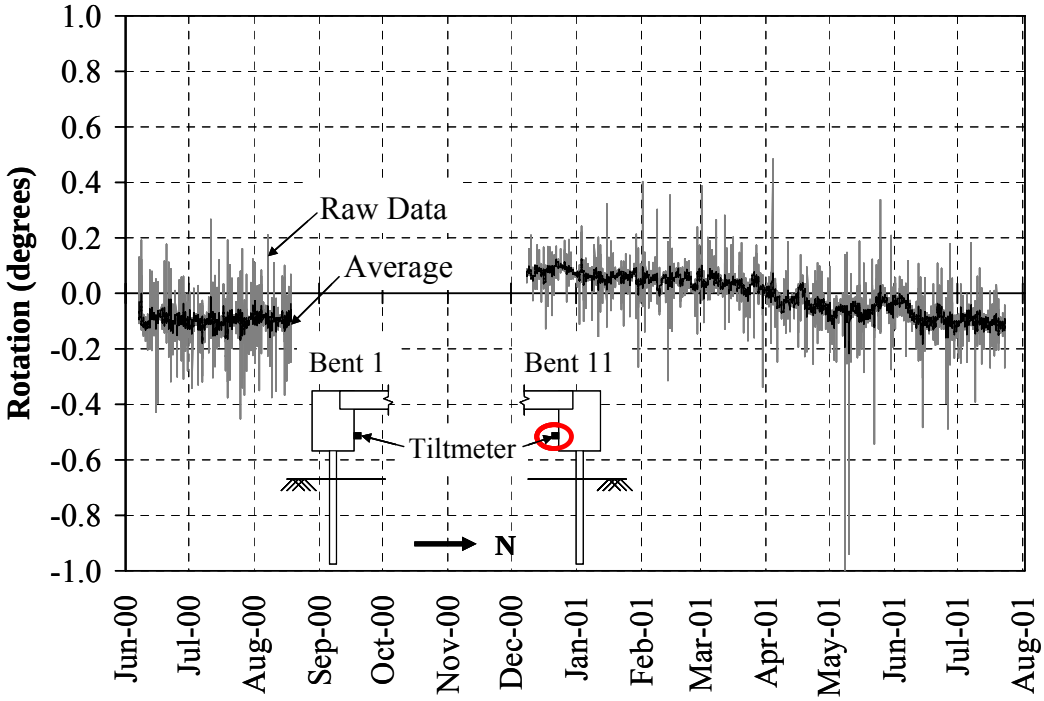

Figure 3.3: Rotations of Bent 11 (SR249 over US12)

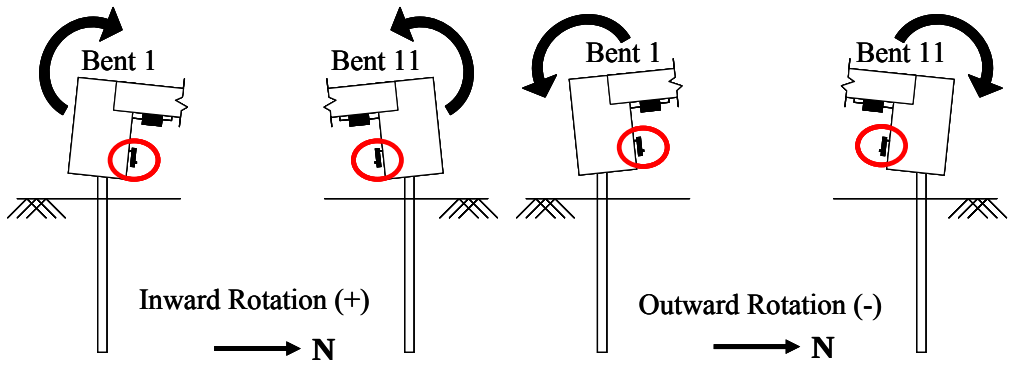

Figure 3.4: Sign Convention for Tiltmeter (SR249 over US12)

3.2.3 Relative Displacement

Crackmeters were used to measure the relative displacement between the girder and the abutment as well as between the girder and the pier. The sign convention for the crackmeters is illustrated in Figure 3.5. A positive sign indicates extension of the crackmeter or physically that the girder is moving away from the abutment. A negative sign indicates shortening, the abutment and girder are moving close together. The results from the crackmeters on Bents 1 and 11 are shown in Figure 3.6. Disregarding the erratic jumps, the crackmeter data from Bents 1 and 11 are essentially identical. The results indicate that as the temperature increased or the bridge expanded, the relative displacement between the girder and the abutment decreased. The relative displacement varied from approximately 0.04 in. during contraction to -0.02 in. during expansion indicating very small relative movement between the abutment and the girder. Thus, it can be concluded that the abutment and the girder moved together during expansion and contraction phases; in other words, it is appropriate to consider the abutment-girder connection as rigid.

The results from crackmeters on Piers 2 and 10 shown in Figure 3.7 indicate that Girder 3 moved very little relative to Pier 2. However, larger relative movement was observed at Pier 10. The larger movement resulted from both the pile detail and the construction. The girders were designed to move separately from the pier cap through the installation of a Styrofoam liner between the girder and the pier cap. However, this is

strong evidence that the girder remained bonded to Pier 2, but this connection broke free at Pier 10. Figure 3.8 shows spalling of concrete at Pier 10 indicating that the girder moved relative from the pier cap.

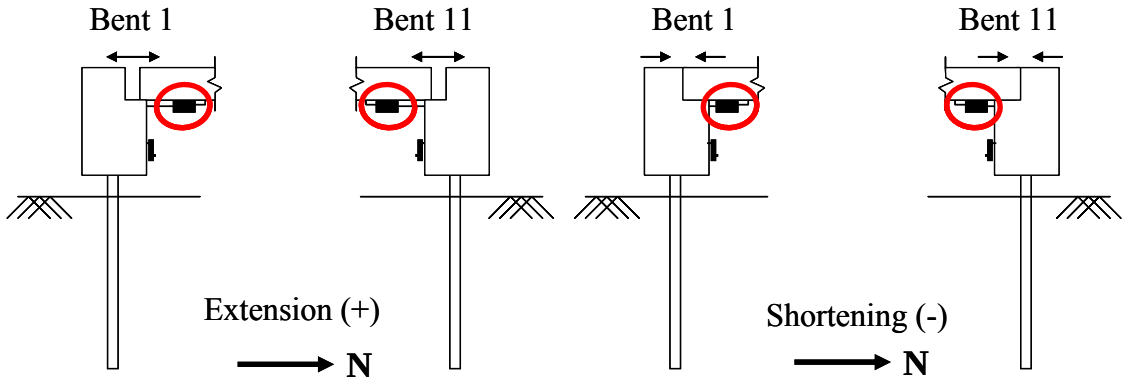

Figure 3.5: Sign Convention for Crackmeter (SR249 over US12)

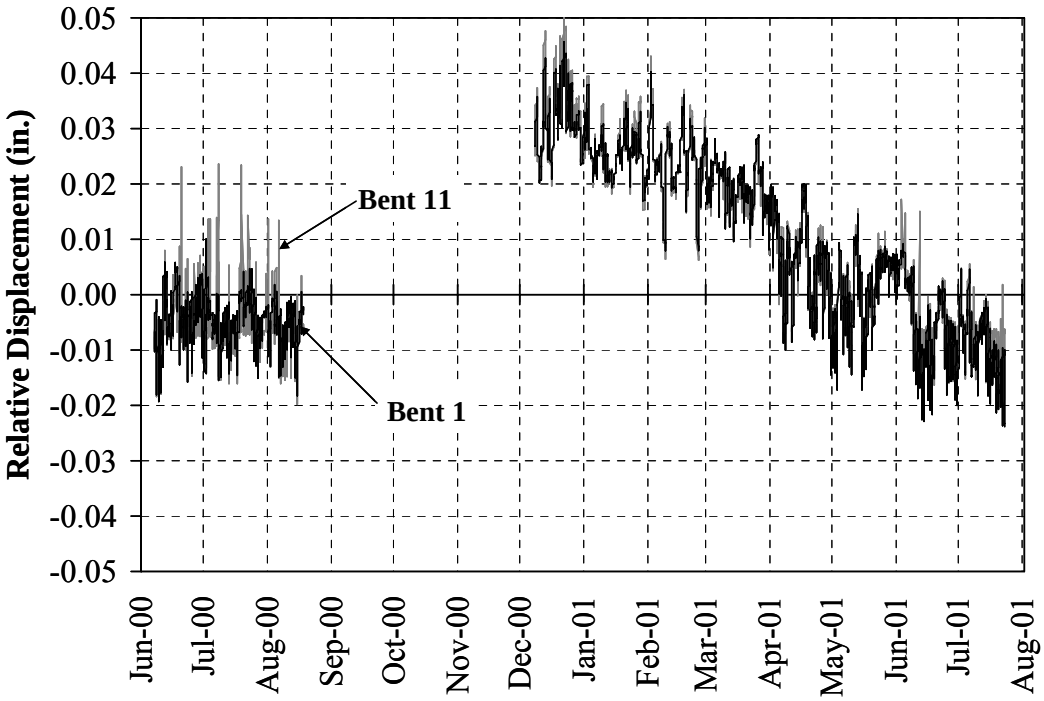

Figure 3.6: Relative Displacement on Bents 1 and 11 (SR249 over US12)

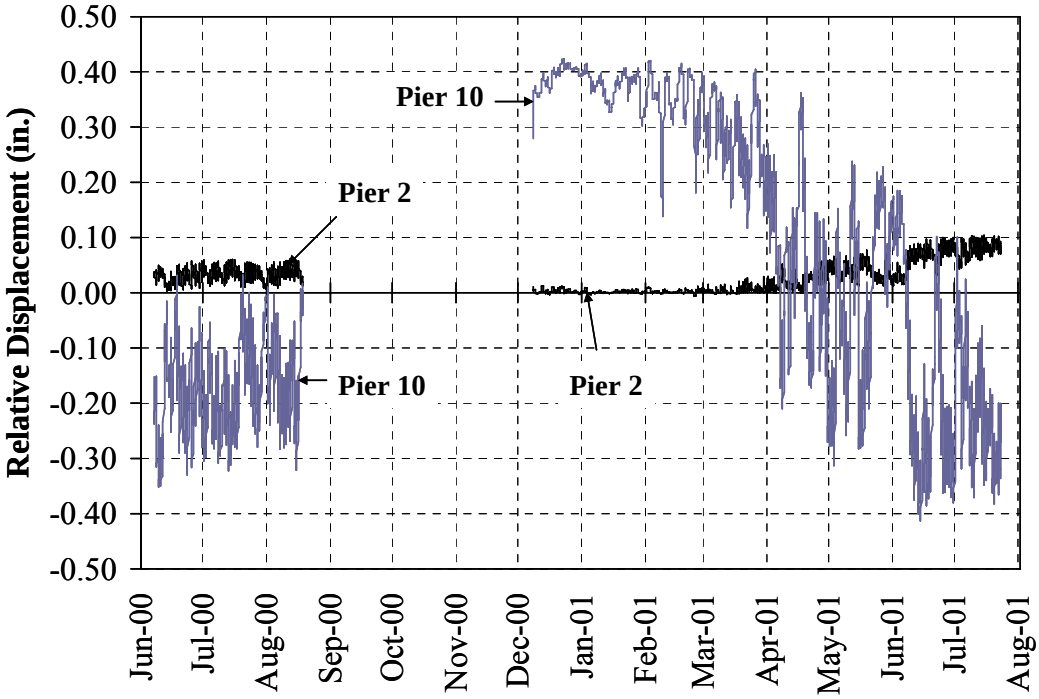

Figure 3.7: Relative Displacement on Piers 2 and 10 (SR249 over US12)

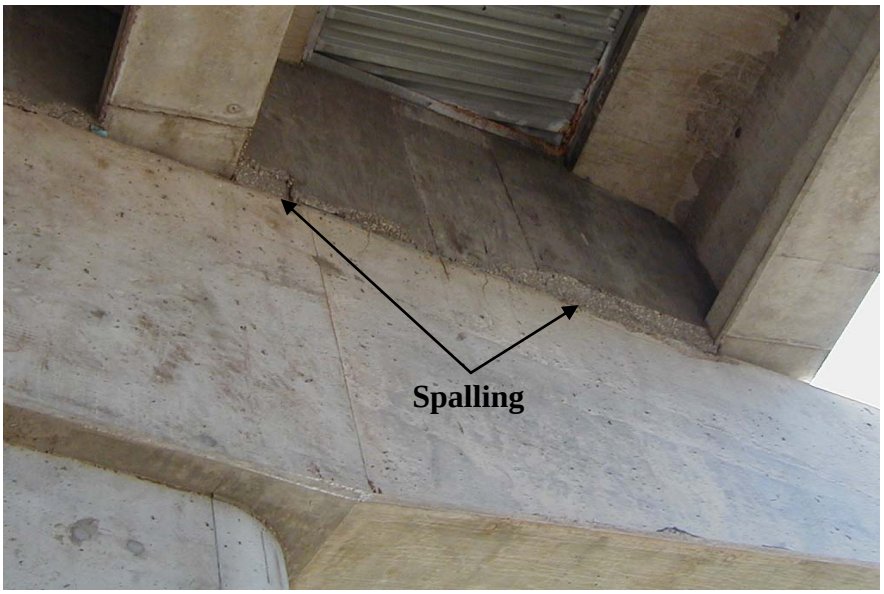

Figure 3.8: Spalling of Concrete at Pier 10 Cap (SR249 over US12)

3.2.4 Pier Strains

Strain gages were installed on sister bars at various locations as described in Section 2.2.3.3. The rebar strain data at the base of Piers 2, 3, 4, 5 and 10 are shown in Figures 3.9 to Figure 3.13, respectively. The strain gages measured positive strain for tension and negative strain for compression. The strain gages located on the same face of the pier (NW-NE, SW-SE) as well as the neutral axis gages (E-W) provided almost identical readings. The strain results indicate that during the contraction phase, the north side of the base of Piers 2, 3, 4, and 5 experienced in compression, while the south side of the base of Piers 2, 3, 4, and 5 experienced in tension. On the other hand, during the expansion phase, the north side of the base of Piers 2, 3, 4, and 5 experienced in tension while the south side of the base of Piers 2, 3, 4, and 5 experienced in compression. Strain gages on Pier 10 measured strain in the opposite direction to the strains measured on Piers 2. For instance, while the north side of Pier 2 was in tension, the north side of Pier 10 was in compression and vice versa. Figure 3.14 illustrates the deformed shape of the piers observed during the contraction phase.

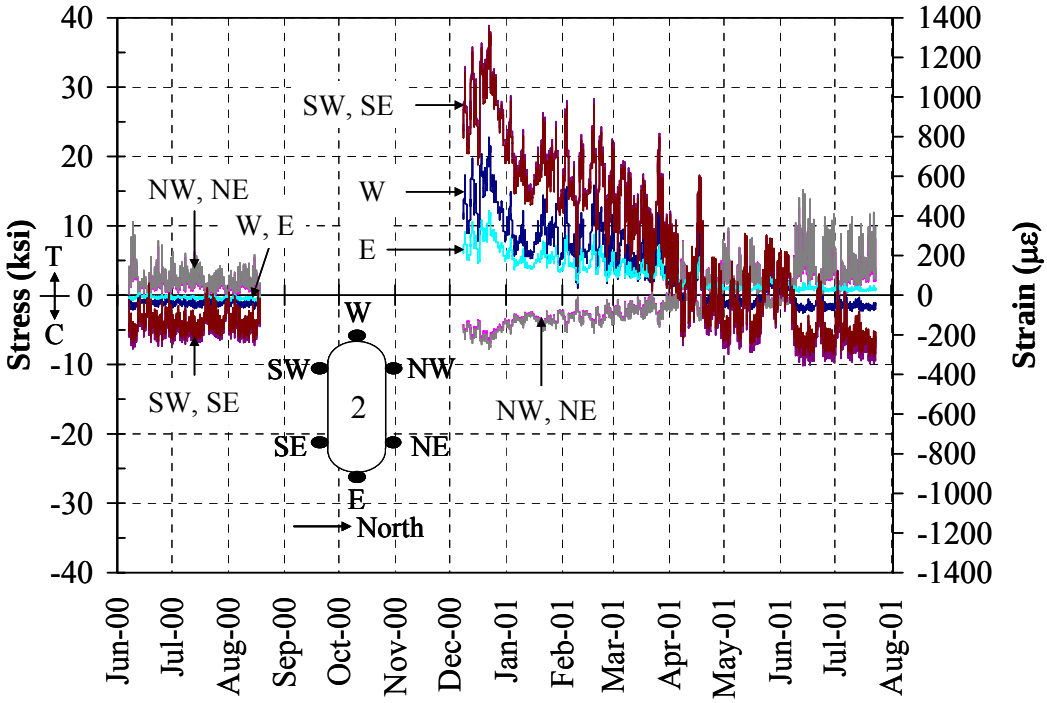

Figure 3.9: Strains and Stresses at the Base of Pier 2 (SR249 over US12)

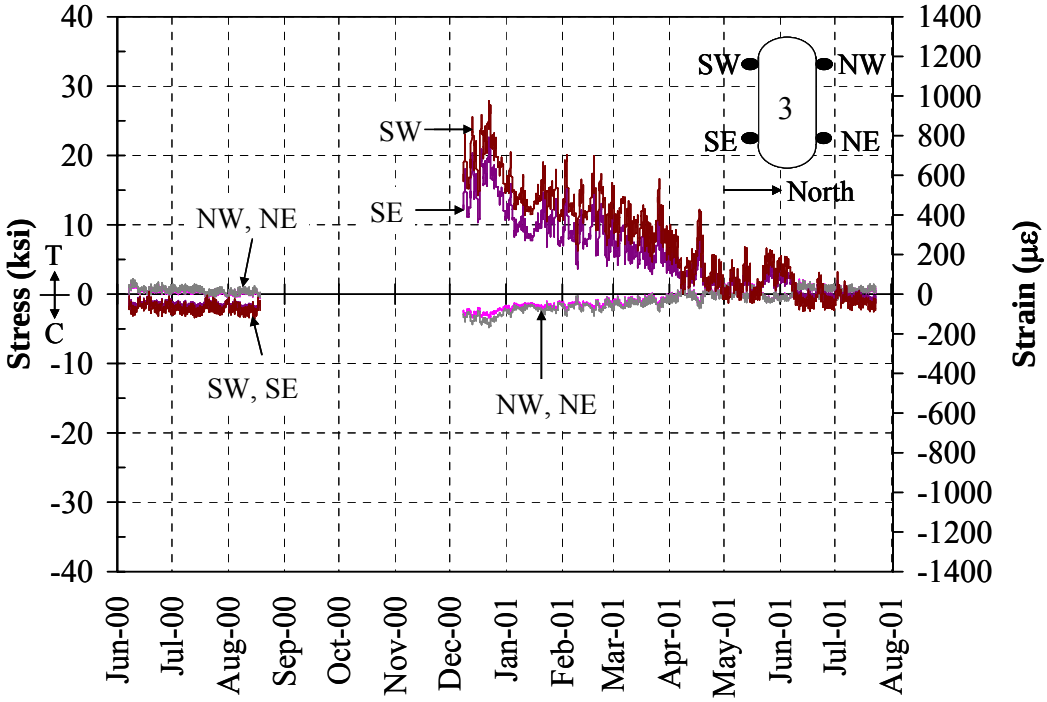

Figure 3.10: Strains and Stresses at the Base of Pier 3 (SR249 over US12)

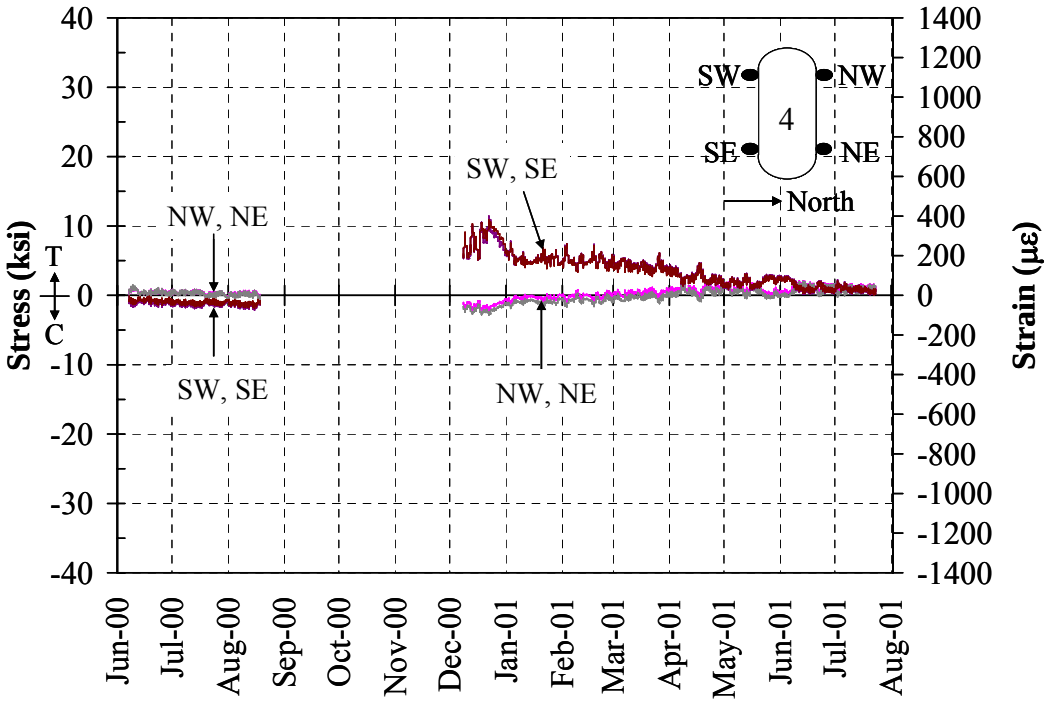

Figure 3.11: Strains and Stresses at the Base of Pier 4 (SR249 over US12)

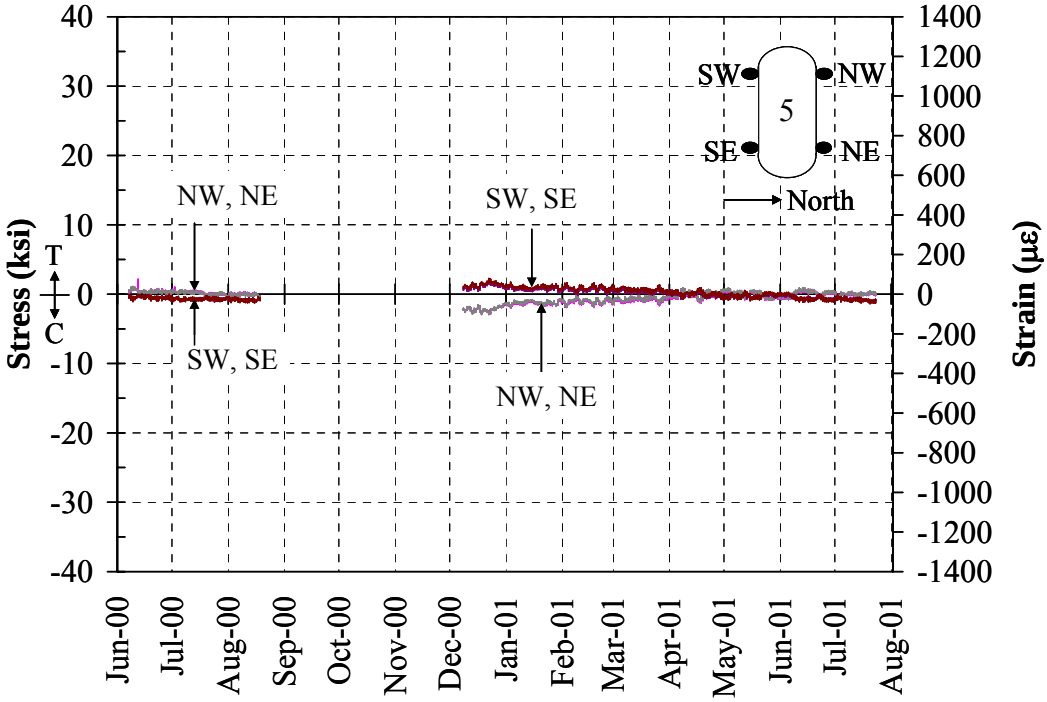

Figure 3.12: Strains and Stresses at the Base of Pier 5 (SR249 over US12)

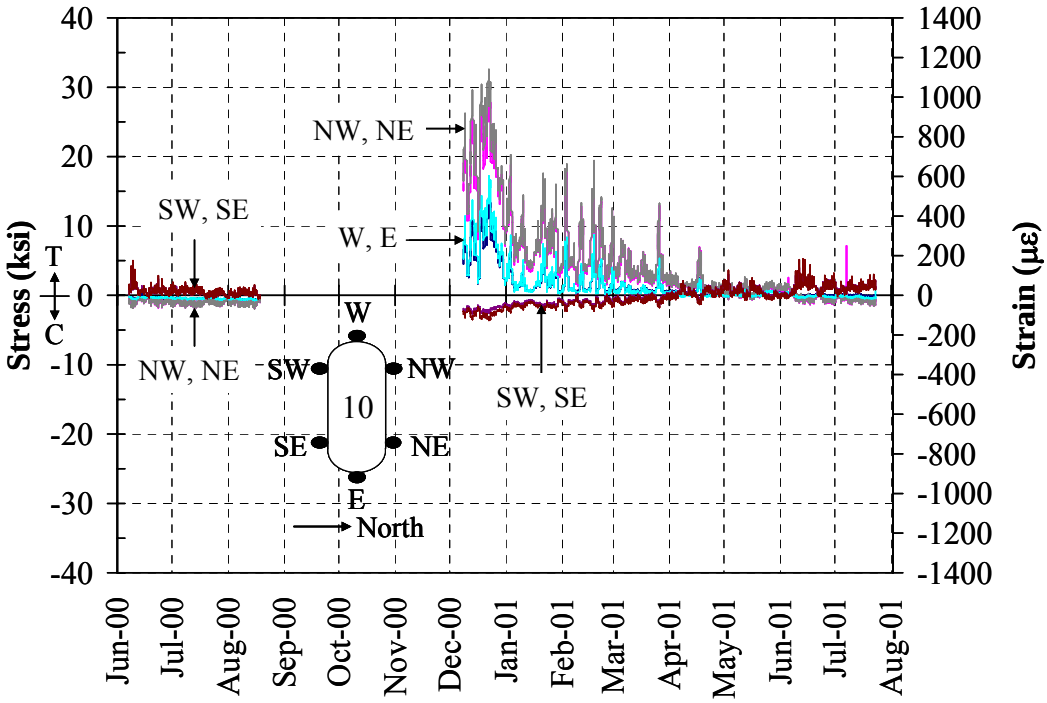

Figure 3.13: Strains and Stresses at the Base of Pier 10 (SR249 over US12)

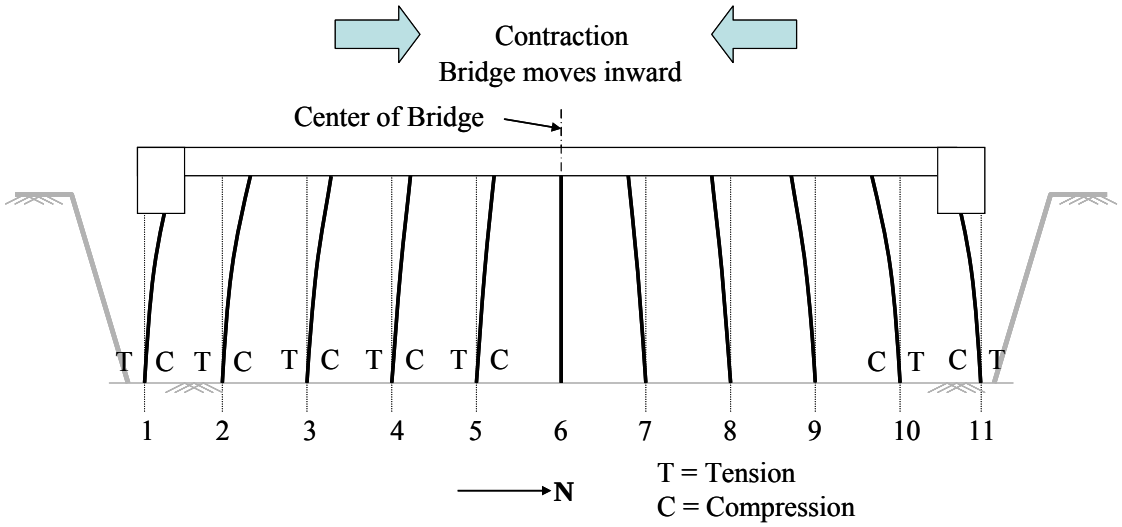

Figure 3.14: Contraction Phase (SR249 over US12)

3.2.5 Pile Strains

Strain gages were installed on the piles as described in Section 2.2.3.2. Strains and stresses of the piles on Bents 1 and 11 on the north face at ground level are presented in Figure 3.15. While electrical noise is evident in the measurements, the trend of the strains and stresses on the piles for both bents was similar. Measurements from Pile 5 for Bent 1 and Pile 2 for Bent 11 are not shown since these gages malfunctioned. It can be noticed that the pile strain of Bent 11 is relatively higher than that of Bent 1 during the contraction period. The maximum tensile stresses were approximately 6 and 8 ksi for Bents 1 and 11, respectively, while the maximum compressive pile stresses were approximately 4 and 17 ksi for Bents 1 and 11, respectively. The higher bending stresses for Bent 11 are likely explained because the girder/pier connection at Pier 10 had broken free while that of Pier 2 was still locked together. The interior face of the piles at ground level experienced tension during the expansion phase and compression during the contraction phase (Figure 3.14). Since expanded polystyrene (EPS) was applied on the top of the pile embedded in the abutment, it cannot be determined from this measurement whether the abutment-pile connection behaves fully rigid or pinned. In addition, the bending mode of the pile cannot be determined from this measurement alone.

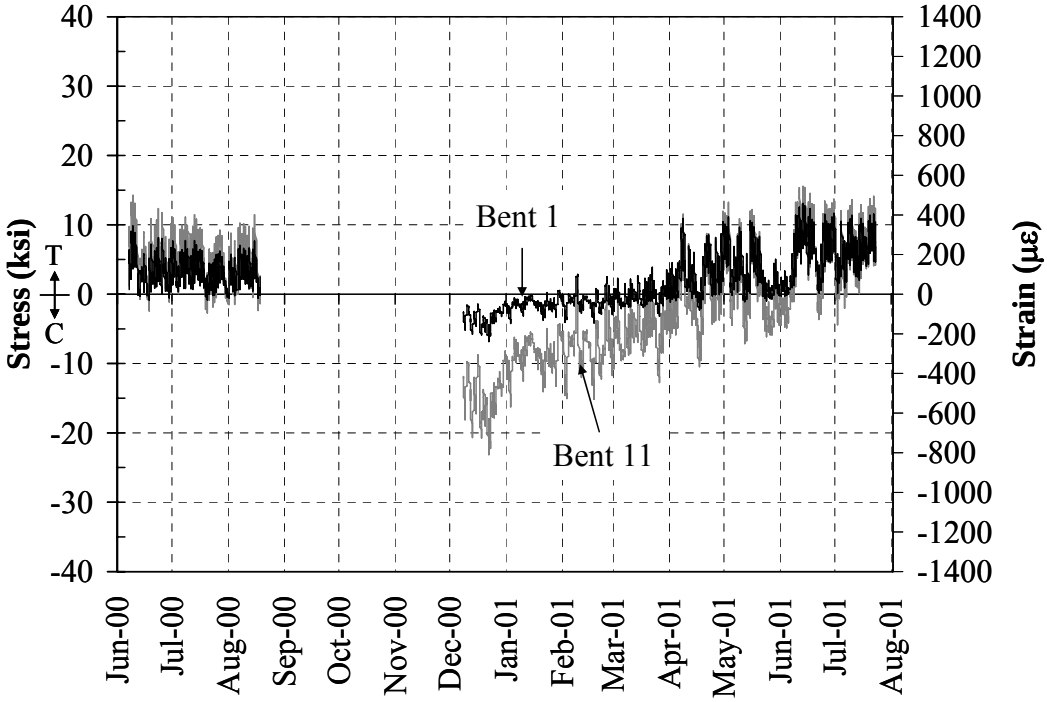

Figure 3.15: Stresses and Strains on Piles Supporting Bents 1 and 11

(SR249 over US12)

3.3 I65 over SR25 Bridge

The instrumentation of I65 over SR25 included both the northbound and southbound structures. Strain gages, thermocouples, and linear potentiometers were installed on the bridges as described in Chapter 2. The measurements provide useful data to evaluate the pile and abutment behavior.

3.3.1 Temperature

The air temperature was measured by a thermocouple located on Beam 7 at midspan and is plotted in Figure 3.16. The results over the three year period shown compare well with average high and low temperature for Lafayette, IN, based on historical data provided by the Weather Channel (www.weather.com). Table 3.3 summarizes construction, maximum, and minimum temperatures for the I65 over SR25 site during the duration of the study.

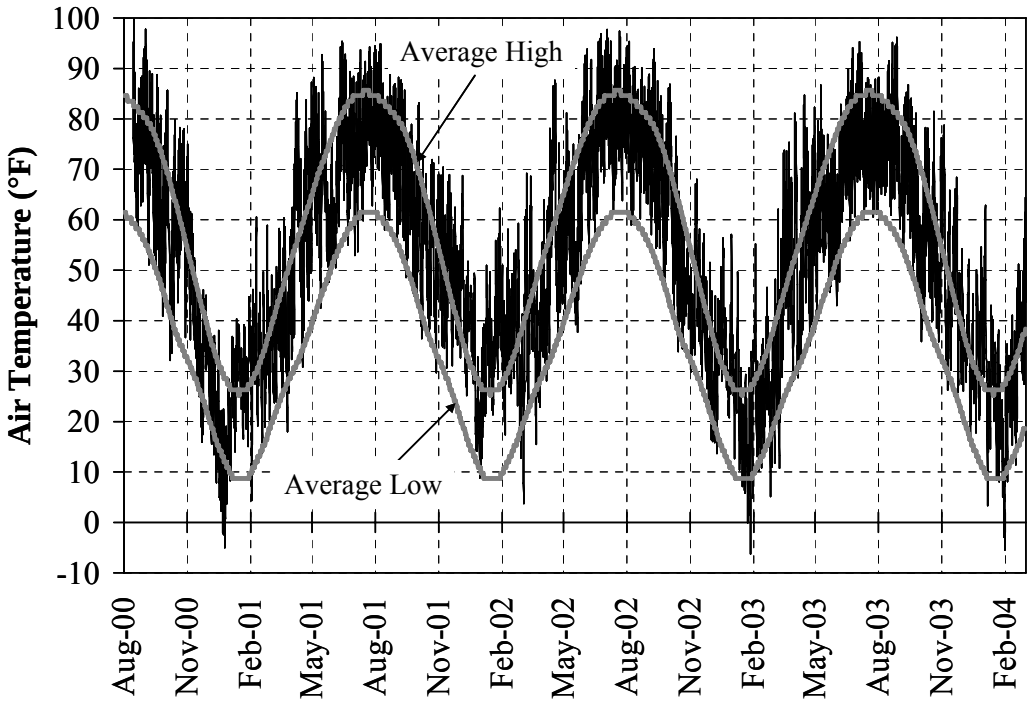

Figure 3.16: Air Temperature (I65 over SR25)

Table 3.3: Air Temperature (I65 over SR25)

Temperature Type	Temperature (°F)	Date
Construction	85	August 15, 2000
Maximum	100	September 1, 2000 at 16:00
Minimum	-7	December 25, 200 at 19:00

Southbound Structure

Temperature Type	Temperature (°F)	Date
Construction	58	October 18, 2000
Maximum	98	July 3, 2002 at 16:00
Minimum	-7	December 25, 2000 at 19:00

3.3.2 Abutment Movement

The movement of Bent 1 on the southbound structure was measured by both longitudinal and transverse linear potentiometers as described in Section 2.3.3.2. The movement recorded by the longitudinal potentiometer is shown in Figure 3.17. Water infiltration may have occurred for this instrument causing abrupt changes in the recorded measurement. That data was adjusted by removing the sudden jumps which provided reasonable results. Due to the erratic behavior of the gage especially following March 2001, the data was replotted only illustrating the results from September 2000 to March 2001 in Figure 3.18. From September 2000 to December 2000, it is observed that the bridge contracts as the temperature decreases. From January 2001 to March 2001, the bridge expanded due to the slight increase in temperature. After March 2001, the gage was problematic resulting in erratic jumps in the data.

The transverse movement of the end bent was adjusted and is presented in Figure 3.19. Neglecting the erratic jumps, the results reveal that the transverse movement due to bridge skew is minimal (Figure 3.20). As previously done for the longitudinal gage, this figure concentrates on the initial results from September 2000 to March 2001. The results from both the transverse and longitudinal gages should be considered with caution due to their performance issues and considering that data correction was necessary.

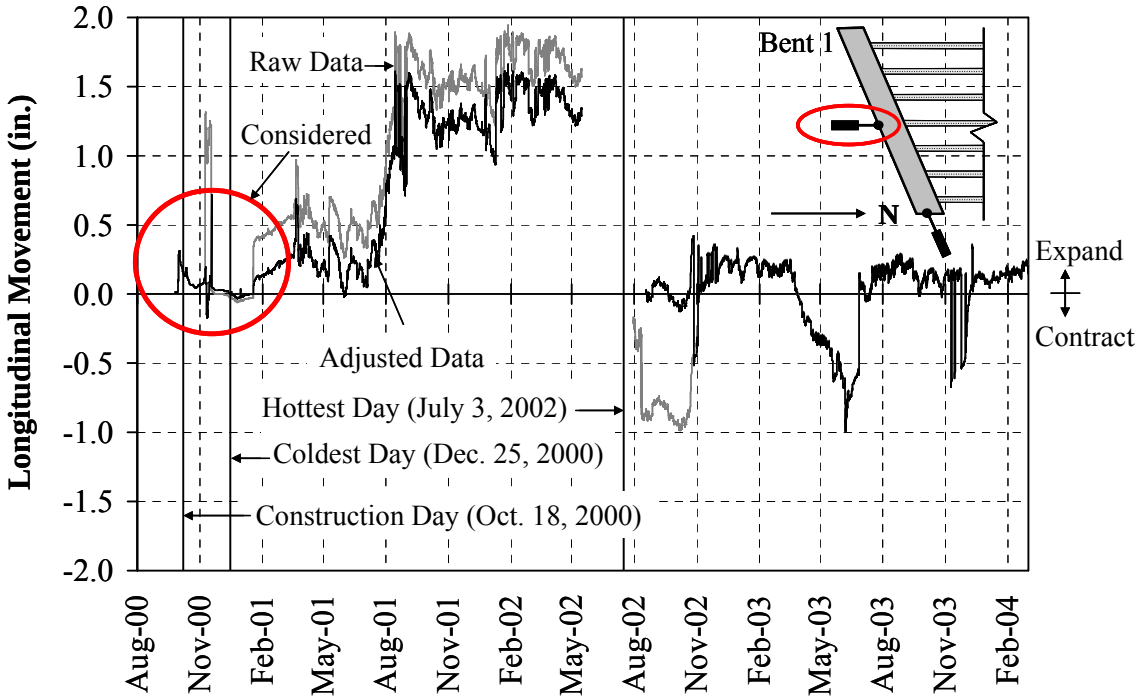

Figure 3.17: Longitudinal Movement (I65 over SR25)

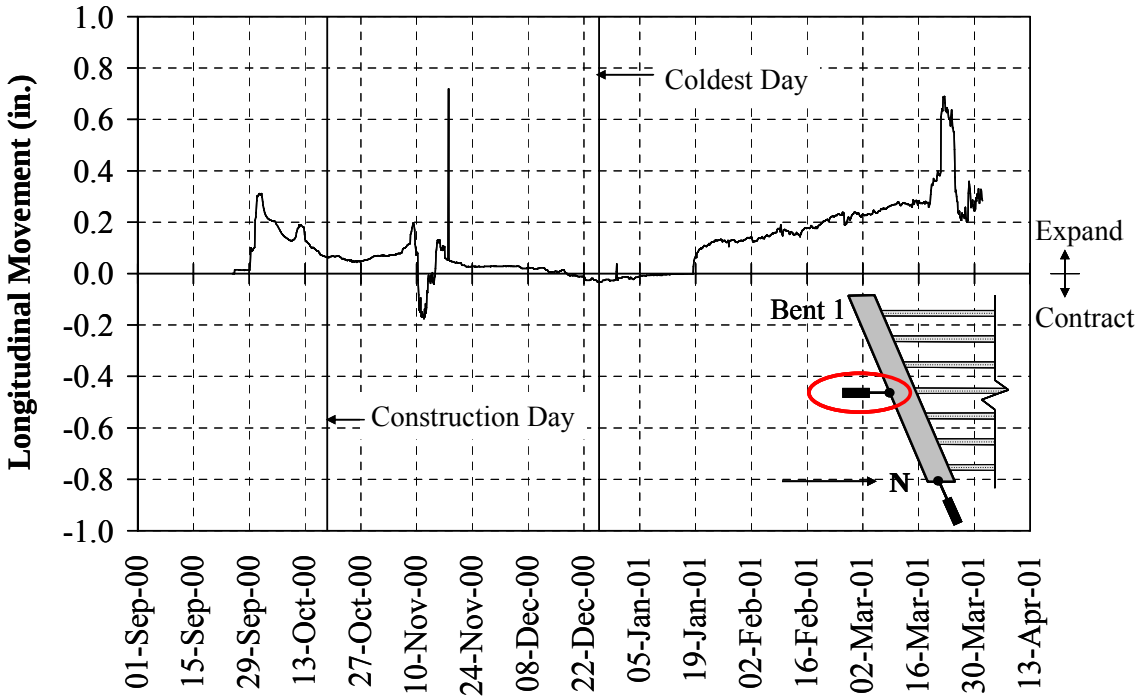

Figure 3.18: Initial Longitudinal Movement (I65 over SR25)

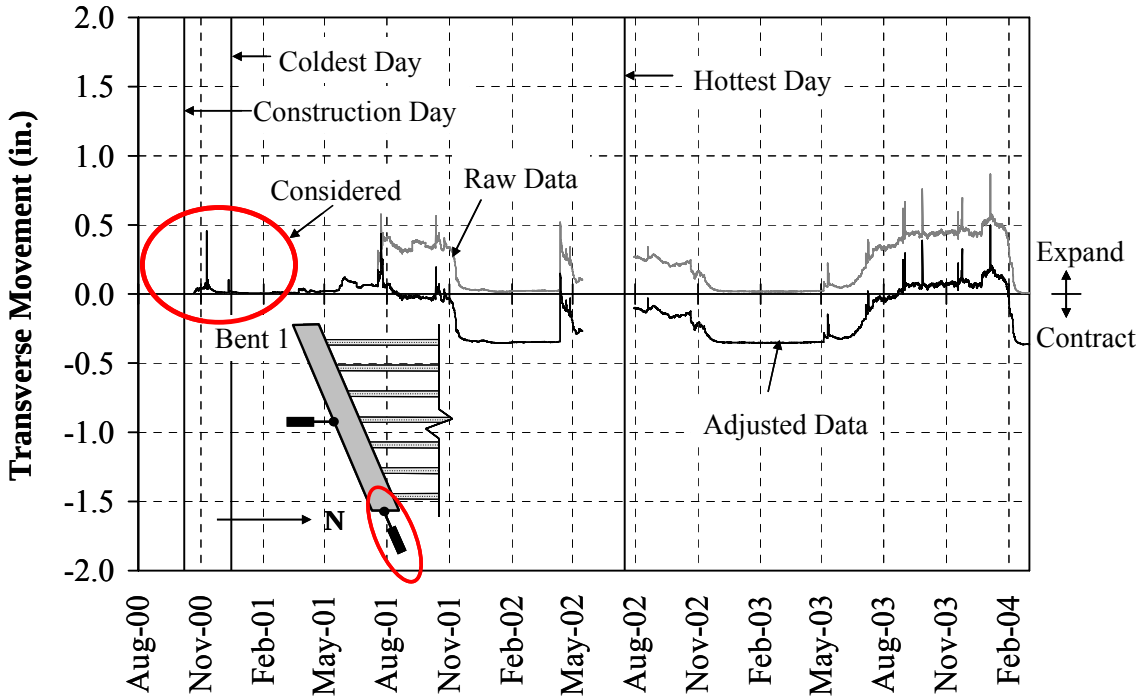

Figure 3.19: Transverse Movement (I65 over SR25)

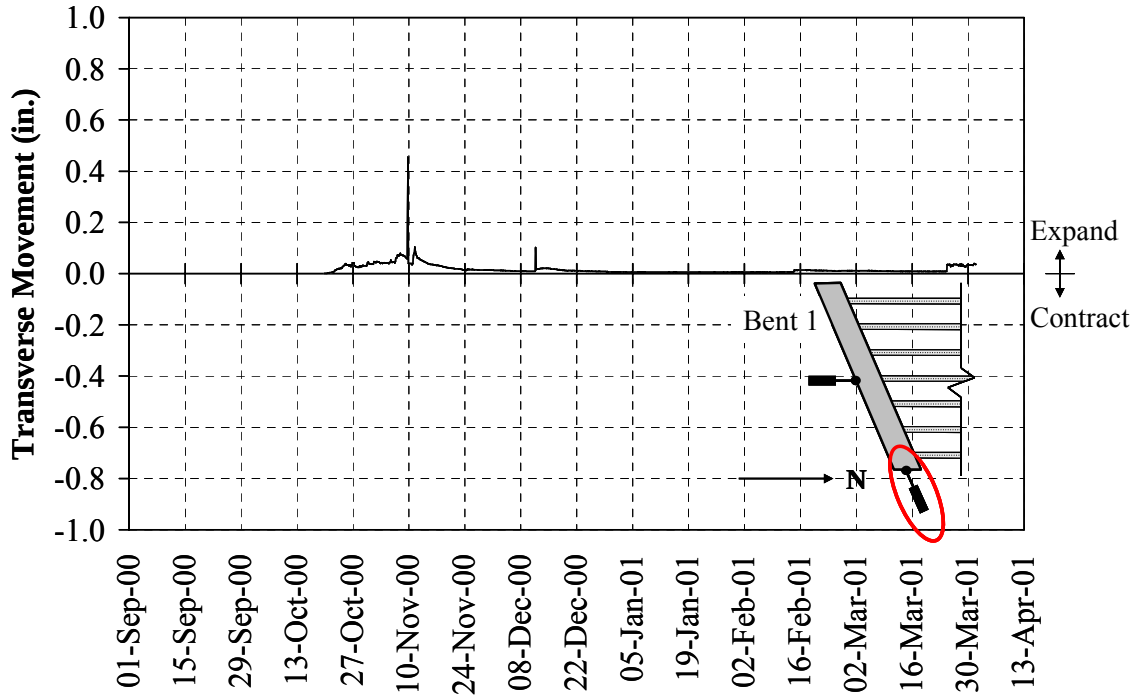

Figure 3.20: Initial Transverse Movement (I65 over SR25)

3.3.3 Pile Strains

Pile strains were monitored at different locations as described in Sections 2.3.3.2. Figure 3.21 shows the strain gage locations on Piles 6 and 9 supporting Bent 1 of the southbound structure. Due to a loss of battery power, data between approximately May 2002 and August 2002 were lost as well as the initial zero readings. Therefore, the magnitudes of strains after August 2002 are not highly reliable. For Pile 9, only the gage on the SW flange was still functioning over the duration of the study; therefore, data from this pile is not considered. Based on these problems, the results from Pile 6 are considered only from August 2000 to May 2002.

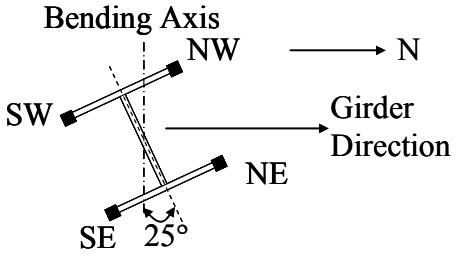

Figure 3.21: Strain Gage Locations on Piles 6 and 9 (Bent 1, Southbound Structure of I65 over SR25)

The strain on Pile 6 at the NE and NW locations is plotted in Figure 3.22 while the strain on Pile 6 at the SE and SW locations is shown in Figure 3.23. During contraction (approximately August through December), strains on the north face experienced tension while strains on the south face experienced compression. Moreover, as the temperature increased and the bridge expanded (approximately January through September), strains on the north face indicated compression while strains on the south face were in tension. This behavior indicates that the pile bent in double curvature during the expansion and contraction phases.

It is noted that the bending axis of the piles is neither about the weak nor strong axis, but rather about the 25° axis. As anticipated, during the expansion phase, the maximum tension strain occurred on the NE flange while the maximum compression strain occurred on the SW flange. The piles were essentially loaded in the direction of the girders as shown in Figure 3.21.

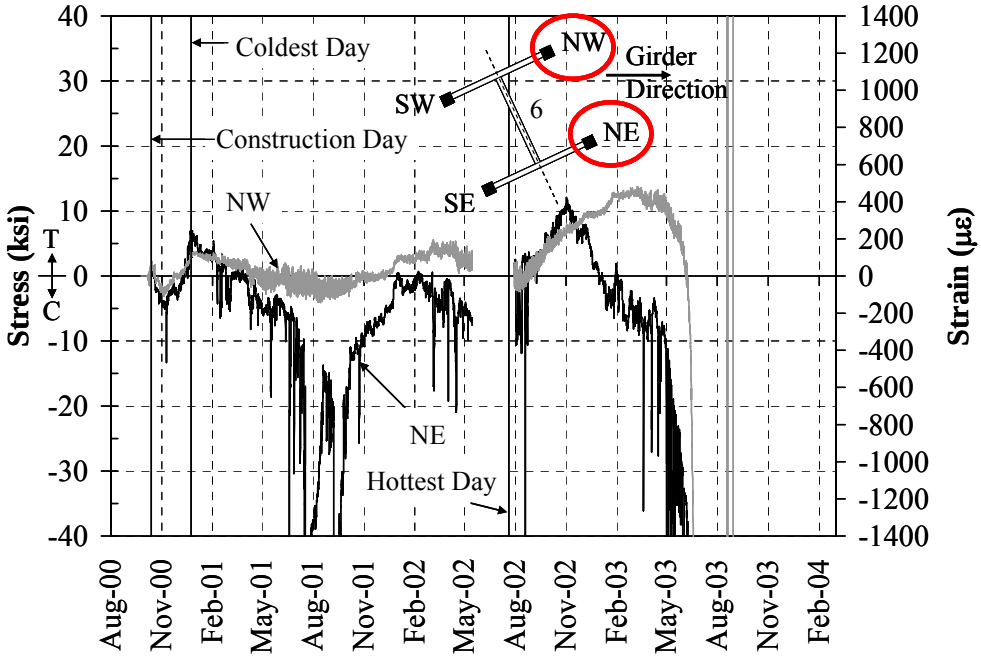

Figure 3.22: Strain at NW and NE Locations on Pile 6 (Bent 1, Southbound Structure of I65 over SR25)

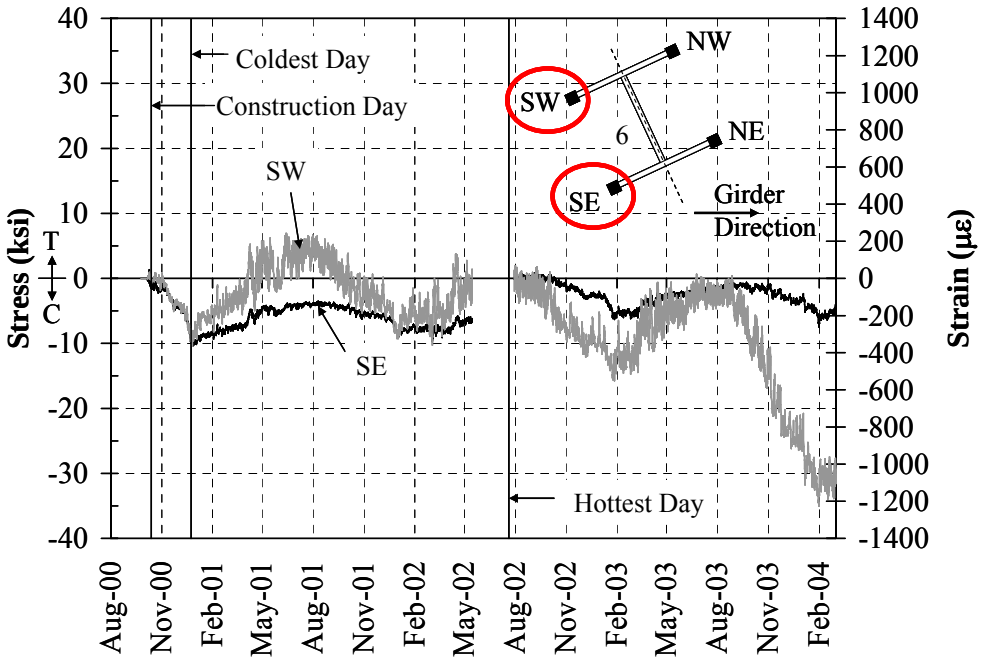

Figure 3.23: Strain at SW and SE Locations on Pile 6 (Bent 1, Southbound Structure of I65 over SR25)

During the coldest period, the south face of the pile experienced a compressive stress of approximately 10 ksi, while the pile experienced tensile stresses of approximately 6 ksi at the NE flange and 3 ksi at the NW locations. Neglecting the gage at the NE location due to off-scale readings, the NW and SE flanges experienced compression of 3 and 4 ksi, respectively during the expansion phase (August 2001), while the SW flange experienced tension of 6 ksi.

The recorded strains for Pile 7, Bent 1 on the northbound structure which is a CFT pile is shown in Figure 3.24. Due to the low strain recorded by the gages on the south face, it was considered not reliable. It is suspected that debonding of this gage occurred following installation. Based on the results of the north gage, however, double curvature behavior was observed. For instance, the north gage experienced tension during contraction (cold periods) and compression during expansion (hot periods). This behavior is in agreement with that observed for the H piles.

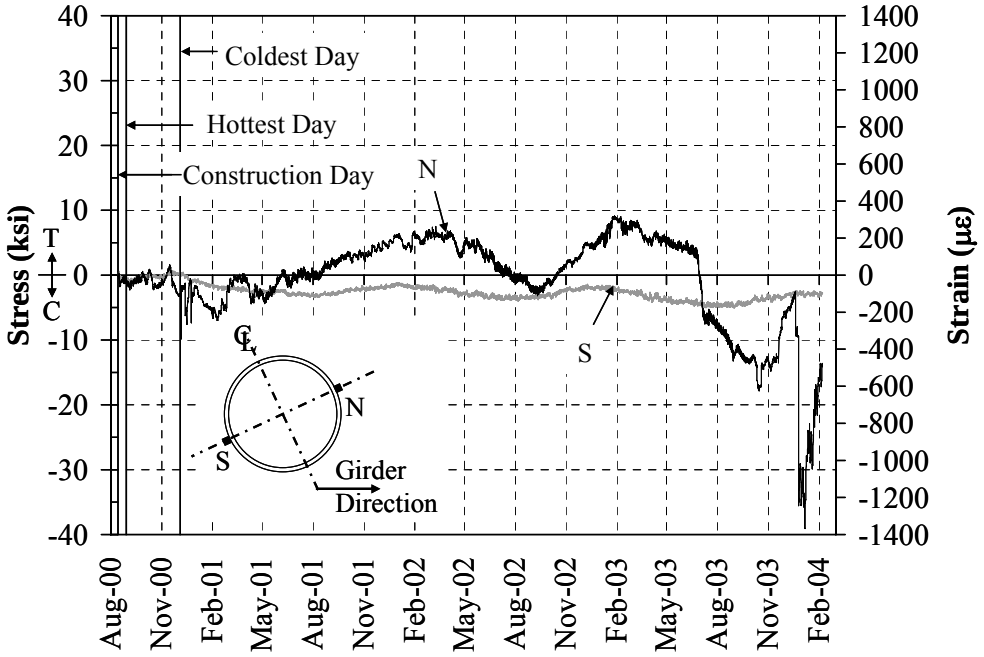

Figure 3.24: Strain on the North and South Locations on Pile 7 (Bent 1, Northbound Structure of I65 over SR25)

3.4 SR18 over Mississinewa River Bridge

The SR18 over Mississinewa River bridge was instrumented to compensate for the incomplete data from SR249 over US12 and I65 over SR25. The instruments on Bent 6 were installed in June 2003, while those on Bent 1 were installed in July 2003 as described in Chapter 2. Because the bridge deck was cast on September 26, 2003, only data between September 26, 2003 and March 9, 2004 are interpreted in the following section. Data in this period represent the behavior of the piles and abutments during the contraction phase. It should be noted that the instrumentation systems were connected to external power that initiated electrical noise in the signals beginning December 2, 2003. The problem was resolved on February 23, 2003.

3.4.1 Temperature

The temperature on the SR18 bridge was measured by temperature gages located on a girder and in the deck between Pier 5 and Bent 6 as shown in Figure 3.25. The temperature measured by both gages was almost identical. The response of the deck is slower than that of the girder. The construction, maximum, and minimum temperatures are summarized in Table 3.4.

3.4.2 Rotations of the Abutment

The rotation of the abutment was measured by tiltmeters located on the east and west faces of Bents 1 and 6, respectively. The rotations of the abutments were filtered by taking the average of the data recorded between the time interval four hours before and four hours after the desired measurement time. The filtered rotations of both bents are plotted in Figure 3.26. The results indicate that Bents 1 and 6 translated and hardly rotated.

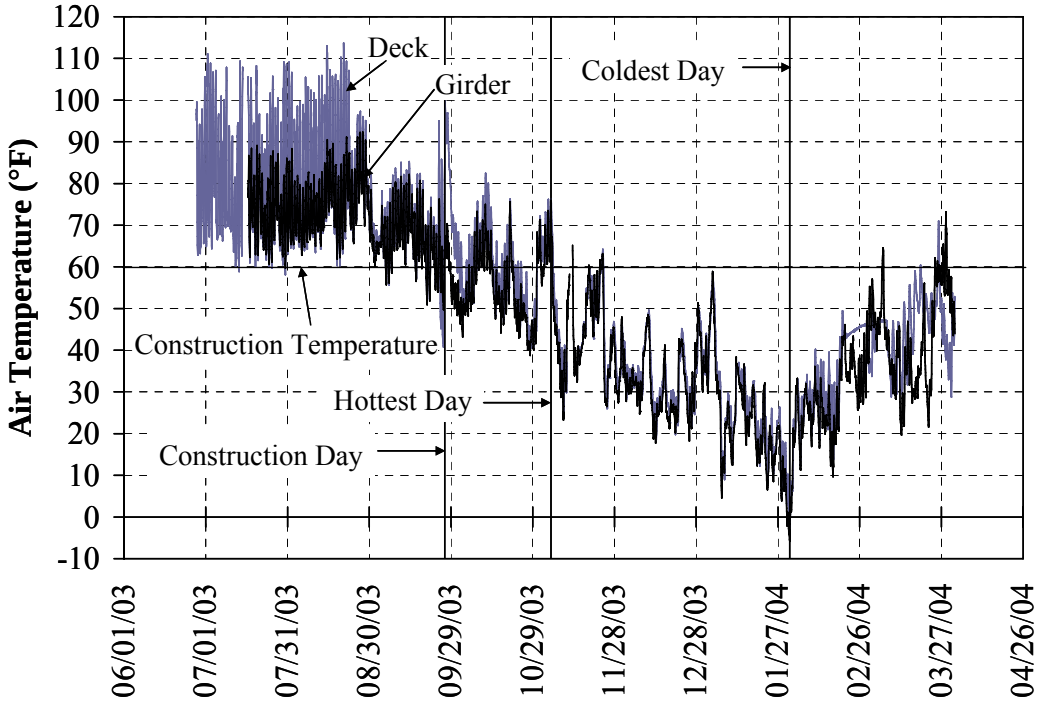

Figure 3.25: Air Temperature (SR18)

Table 3.4: Air Temperature (SR18)

Temperature Type	Temperature (°F)	Date
Construction	60	September 26, 2003
Maximum	76	November 4, 2003 at 16:00
Minimum	-6	January 31, 2004 at 8:00

3.4.3 Abutment Movement

The movements of the abutments were measured by convergence meters in different locations as discussed in Section 2.4.3. The abutment movements of Bents 1 and 6 are plotted in Figure 3.27. The convergence meters were slightly moved from the zero position before casting of the bridge deck. If the data are zeroed immediately prior to casting, however, the results are essentially identical (Figure 3.28). These results indicate that the abutment movement corresponds well with temperature. For instance, as the temperature decreases (contraction phase), both abutments move toward each other as anticipated.

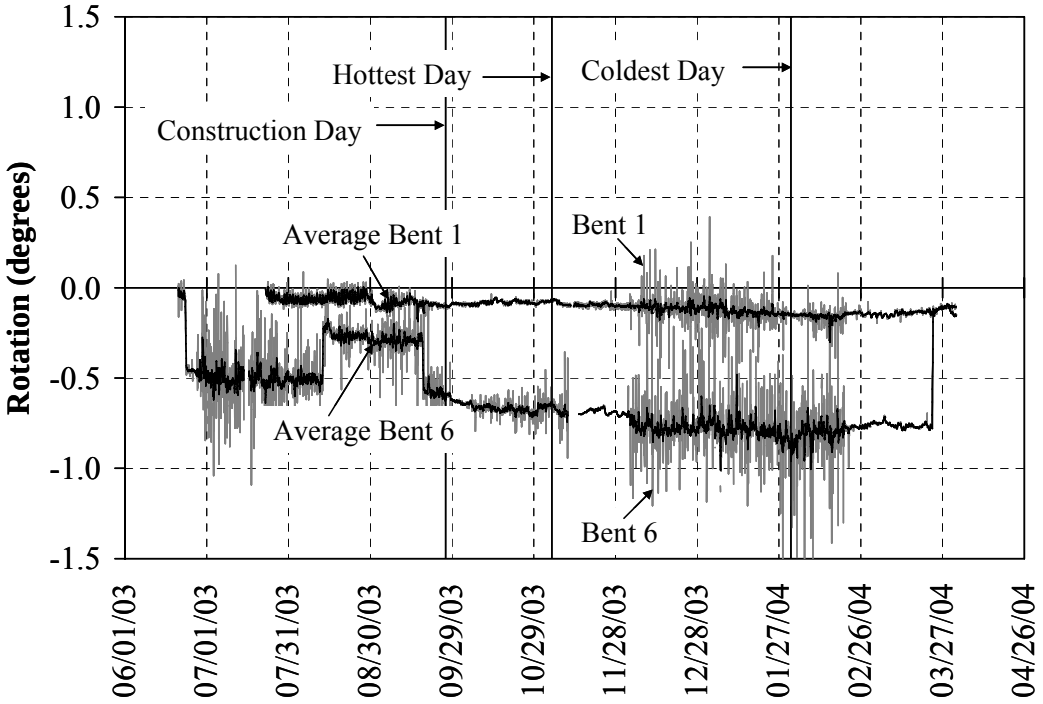

Figure 3.26: Rotations of the Abutment (SR18)

The measured movement of Bent 1 was compared to the thermal movement calculated according to Equation 3-1 as shown in Figure 3.29. The expansion and contraction longitudinal movements of Bents 1 and 6 on the hottest and coldest days obtained from the field were also compared to the calculated thermal movement in Table 3.5. It can be seen that the calculated abutment movements are greater than the measured values. This difference is most likely due to backfill restraint, pile resistance, and friction from the approach slab.

$$\Delta L = \alpha(\Delta T)L \qquad (3\text{-}1)$$

where:

α = thermal coefficient of concrete, taken as 6.0×10^{-6} /°F;

ΔT = change in temperature, taken as 16° F on the hottest day and 66° F on the coldest day;

L = half of the total span length, taken as 367 ft/2 = 183.5 ft.

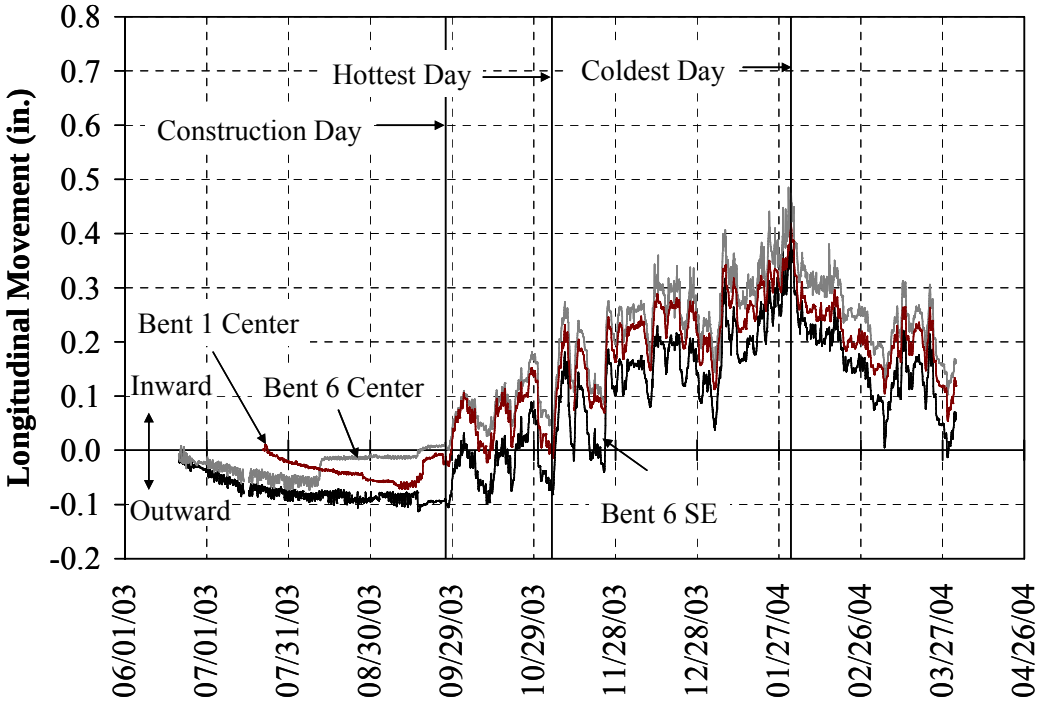

Figure 3.27: Abutment Movement (SR18)

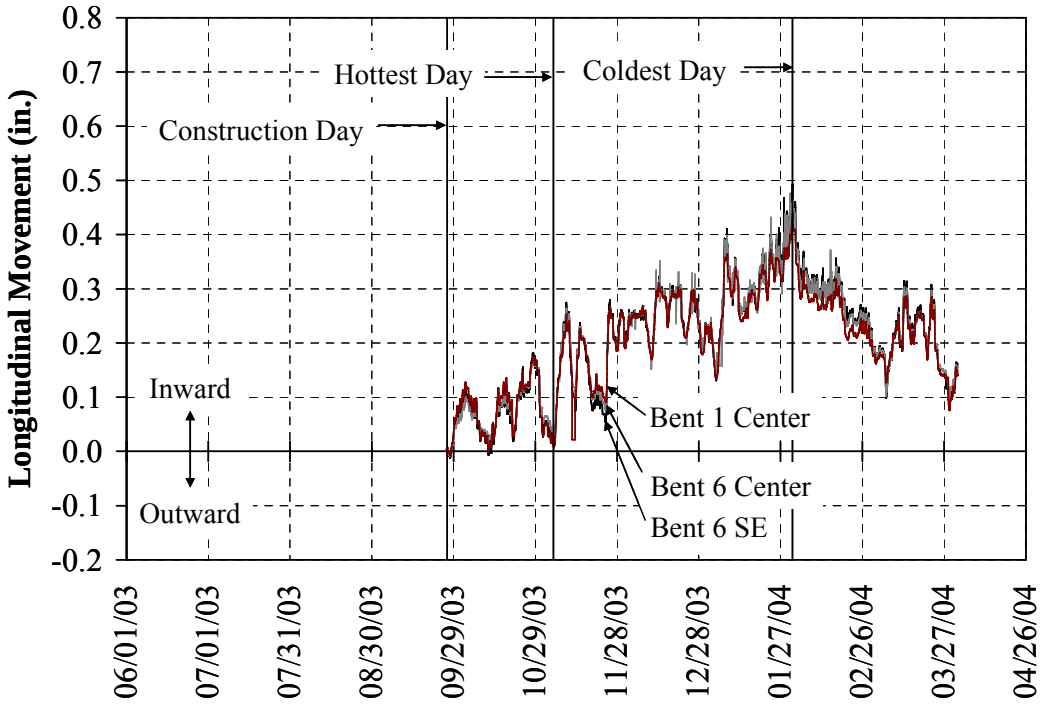

Figure 3.28: Adjusted Longitudinal Movement (SR18)

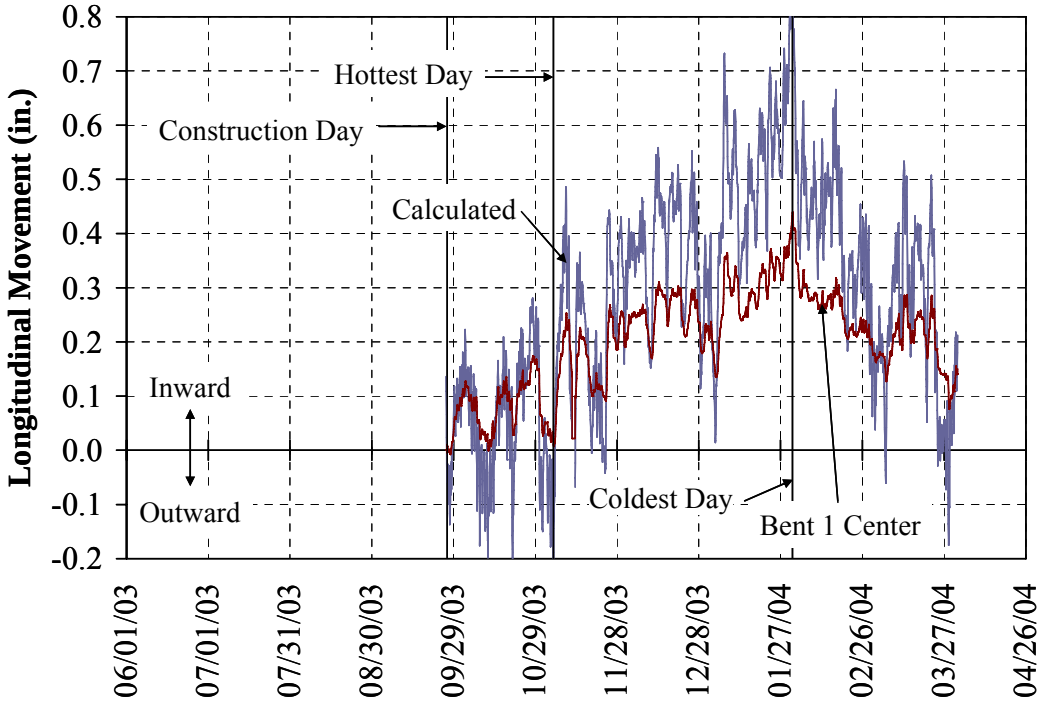

Figure 3.29: Calculated vs. Measured Movements (SR18)

Table 3.5: Abutment Movement (SR18)

Movement (in.)	Bent 1	Bent 6	Calculated
Expansion	0.07	0.03	0.19
Contraction	0.41	0.46	0.80

3.4.4 Pile Strains

Strain gages were installed on the piles of Bents 1 and 6 as illustrated in Section 2.4.3.2. The data for Bent 1 are available beginning July 17, 2003 (zeroed), while the data for Bent 6 are available beginning June 18, 2003. The data are presented until March 31, 2004.

As previously discussed, strain gages were installed along the length of Pile 6 (Bent 1) on the east, west, and south faces of the pile. These results are presented in Figures 3.30, 3.31, and 3.32, respectively. It should be noted that a strain gage located on the west face at a depth of 20 ft below ground level was damaged during driving.

In general, strain on the east and west faces at each depth are almost mirror images of one another. It is evident that the pile is sensitive to temperature change. As the temperature dropped, the pile on the east face at ground level experienced tension while the pile on the west face experienced compression. The strain profile along the pile length clearly indicates double curvature bending.

On the coldest day (January 31, 2004), Pile 6 of Bent 1 experienced 14 ksi of tension on the east face and 14 ksi of compression on the west face (Figures 3.30 and 3.31). Stresses on the east and west locations at a depth of 4, 8, 12, and 16 ft were progressively lower. On the east side of the pile, the stress at a depth of 20 ft was typically between the stresses that occurred at a depth of 4 ft and 8 ft (Figure 3.30). No data were recorded at the 20 ft depth at the west location because the gage was lost while driving (Figure 3.31).

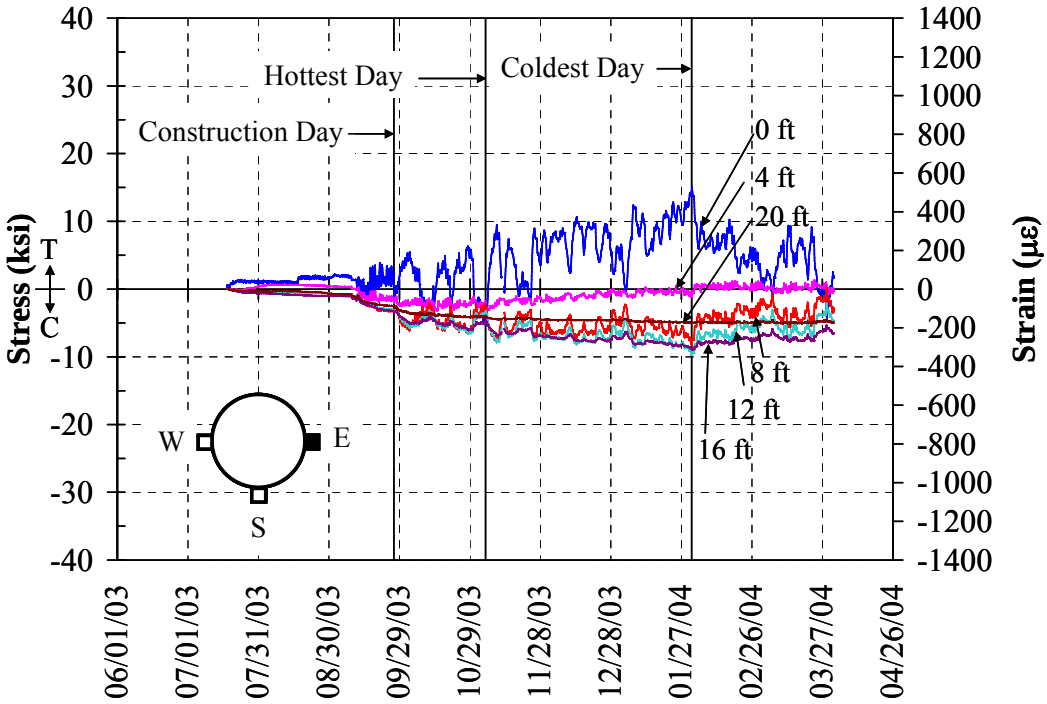

Figure 3.30: Strain at the East Locations on Pile 6, Bent 1 (SR18)

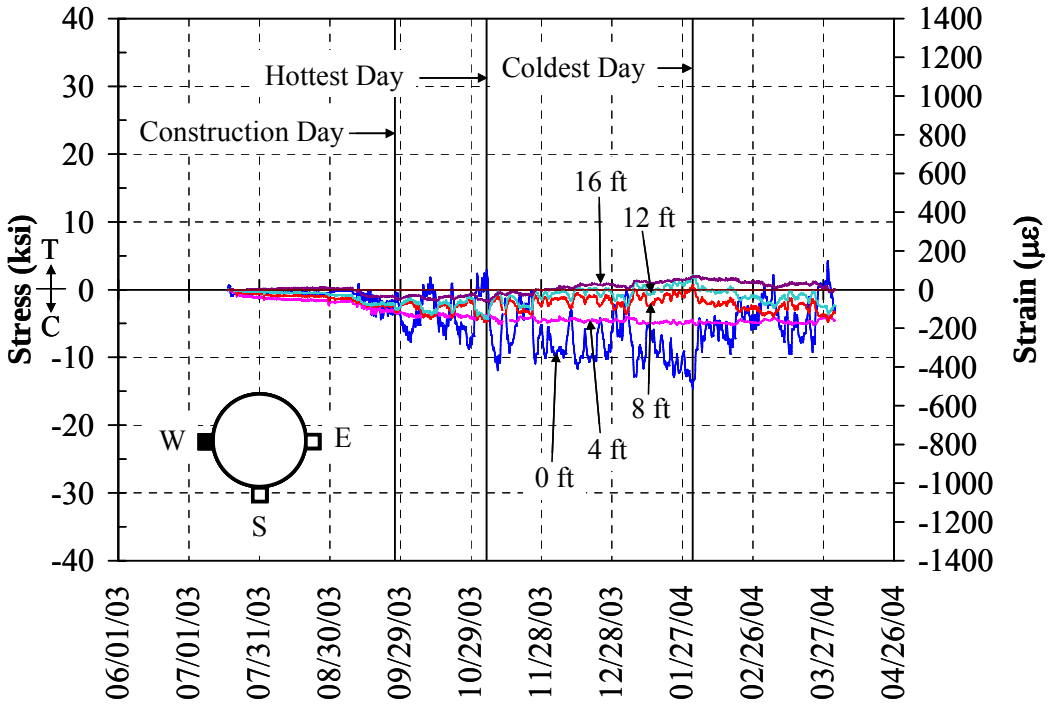

Figure 3.31: Strain at the West Locations on Pile 6, Bent 1 (SR18)

The south strains over the depth of the pile below ground were nearly constant after casting of the bridge deck while the strains at the ground level fluctuated slightly. Stresses on the south face have been fairly constant in the range of 2 to 4 ksi in compression. Axial stress induced by the weight of the beam, deck, diaphragm, precast, abutment, and live load was estimated to be equal to 2.6 ksi. A comparison of the measured stresses with the calculated dead/live load stresses indicates that the gages are performing well and providing reasonable results. Furthermore, it appears that the gages located on the south face are essentially located at the neutral axis as designed (Figure 3.32).

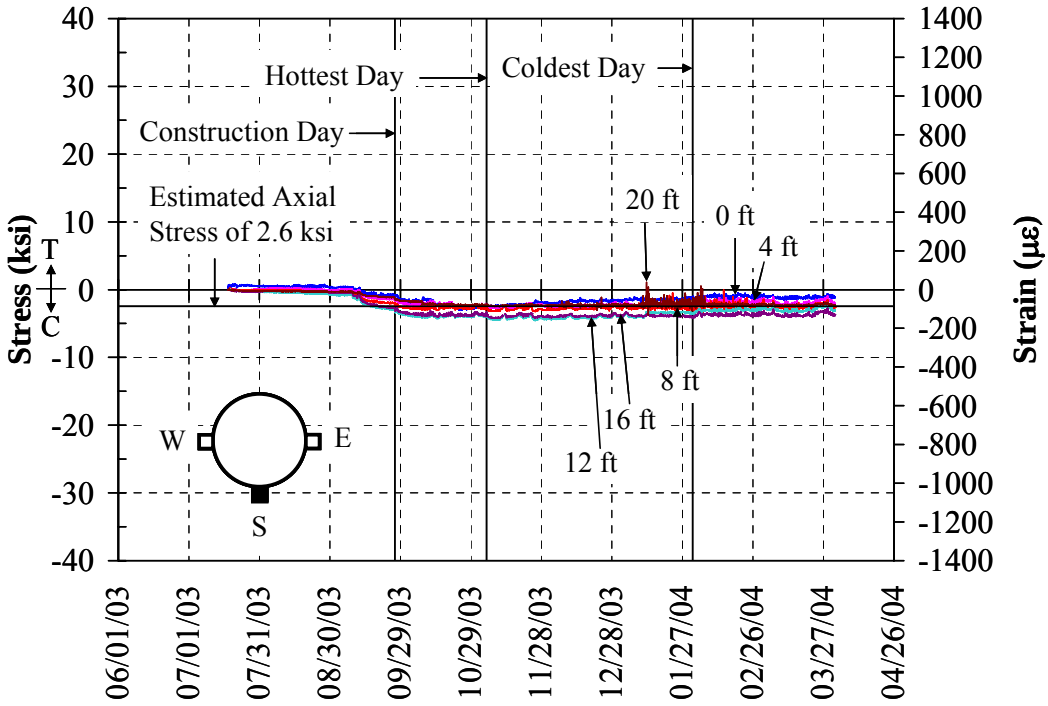

Figure 3.32: Strain at the South Locations on Pile 6, Bent 1 (SR18)

The gages located on Piles 3, 9, and 10 on Bent 1 and Piles 3, 7, and 10 on Bent 6 were positioned at ground level on both the east and west locations as described in Section 2.4.3.2. At each location, the gages on the piles responded identically with temperature changes.

For Bent 1, variations can be observed in the east measurements (Figure 3.33); however, the measurements from the west face were almost identical (Figure 3.34). The maximum pile stress measured on the west face was 15 ksi of compression while the maximum on the east face was 35 ksi of tension.

For Bent 6, strains at the east and west locations were mirror images of each other (Figures 3.35 and 3.36). The maximum and minimum stresses at ground level on the piles on Bent 6 were observed to be in the range of approximately ±20 ksi.

The readings obtained from the strain gages located at ground level also support double curvature pile bending.

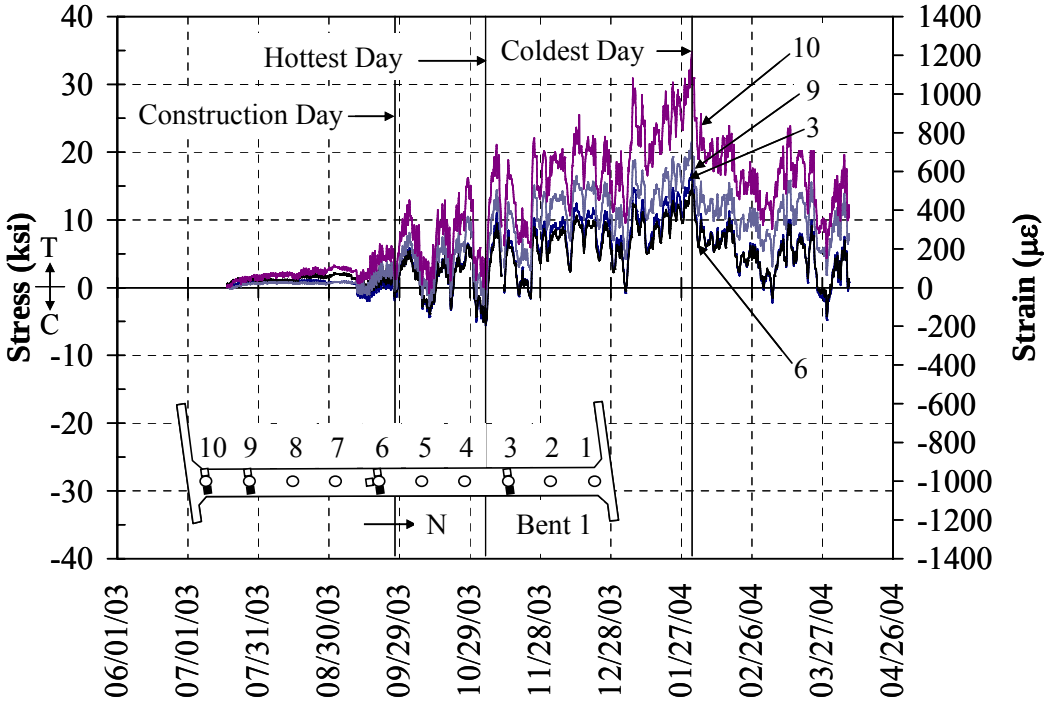

Figure 3.33: Pile Strains, East Face, Bent 1 (SR18)

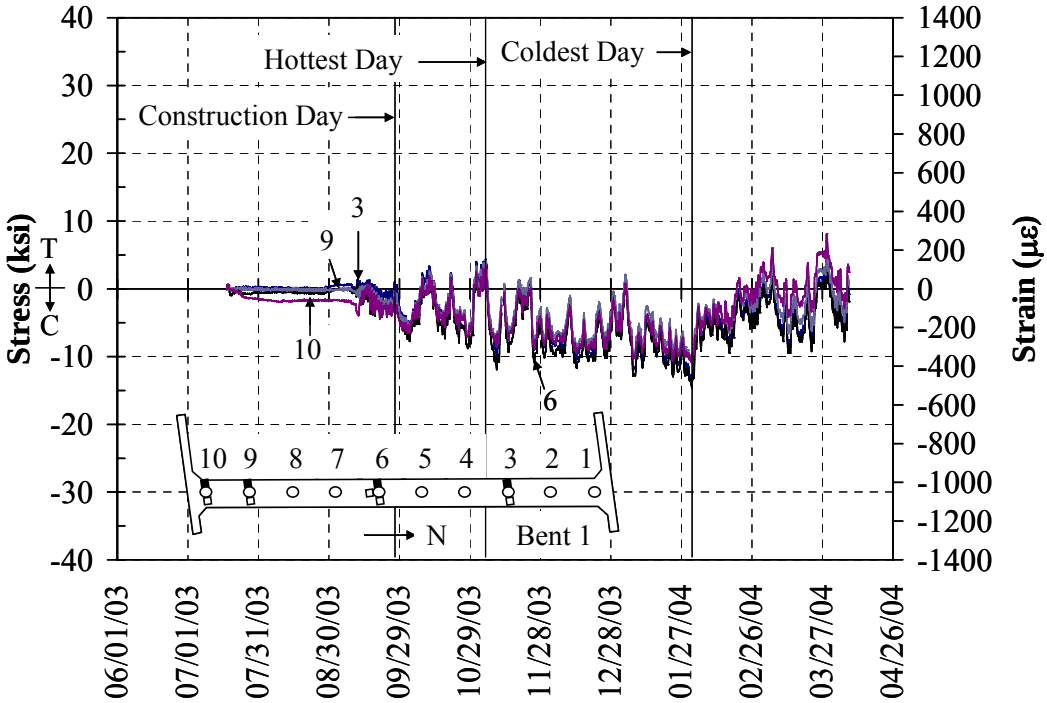

Figure 3.34: Pile Strains, West Face, Bent 1 (SR18)

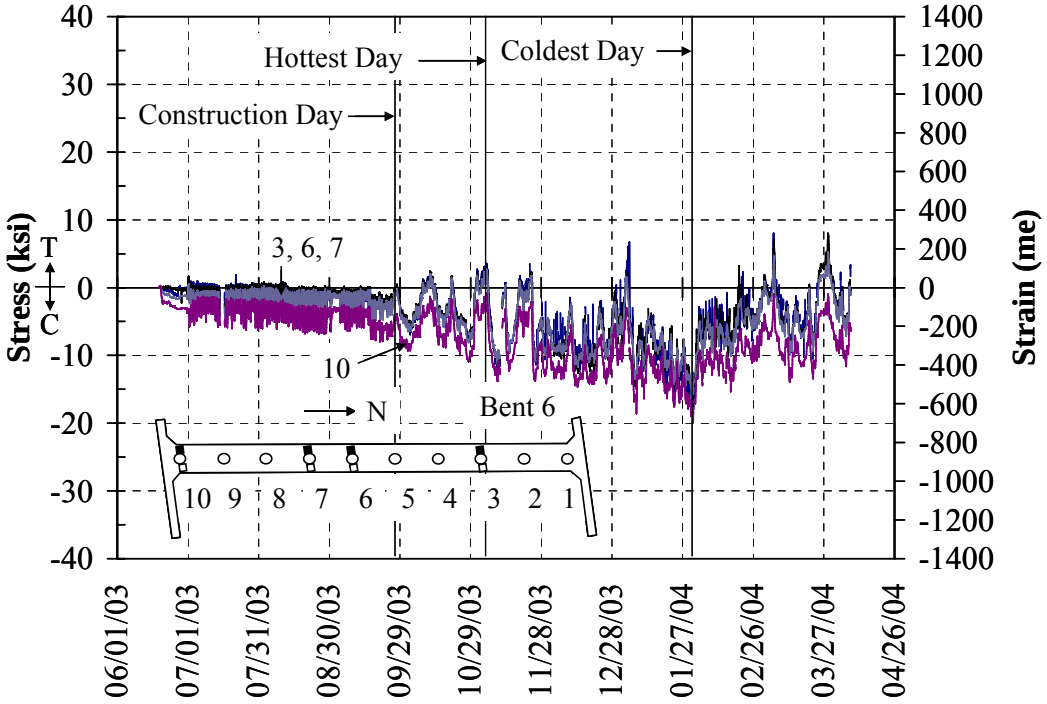

Figure 3.35: Pile Strains, East Face, Bent 6 (SR18)

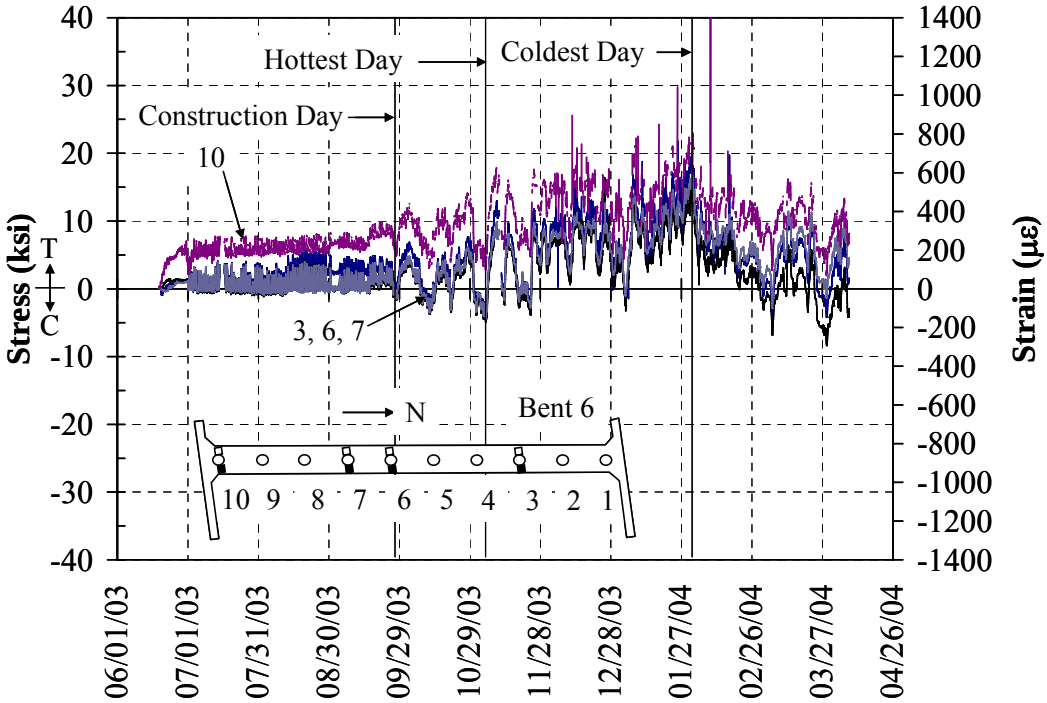

Figure 3.36: Pile Strains, West Face, Bent 6 (SR18)

3.5 Analysis of End Bent and Pile Movement

3.5.1 SR249 over US12 Bridge

The rebar strain gages on sister bars at the base of the piers were used to calculate the pier movement. Deflections at the top of the piers were calculated based on these recorded strains. Finally, the bent movements were extrapolated from the pier movements. Details of this analysis are presented in the following sections.

3.5.1.1 Pier Cross Section

The pier cross section used in the SR249 over US12 bridge is presented in Figure 3.37. A simplified pier cross section was used for calculation purposes as shown Figure 3.38. Considering this section, the moment-curvature relationship was determined (Figure 3.39). The compressive concrete strength, f_c', was taken as 3,500 psi representative of the Class A concrete used in the piers. The steel yield strength, f_y, was assumed to be 60,000 psi. The details of the simplified cross section are tabulated in Table 3.6.

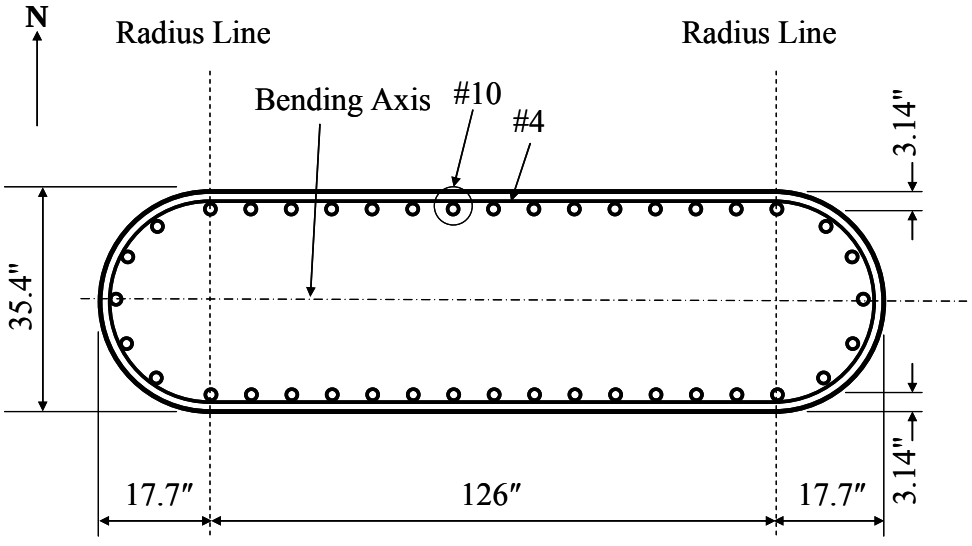

Figure 3.37: Pier Cross Section (SR249 over US12)

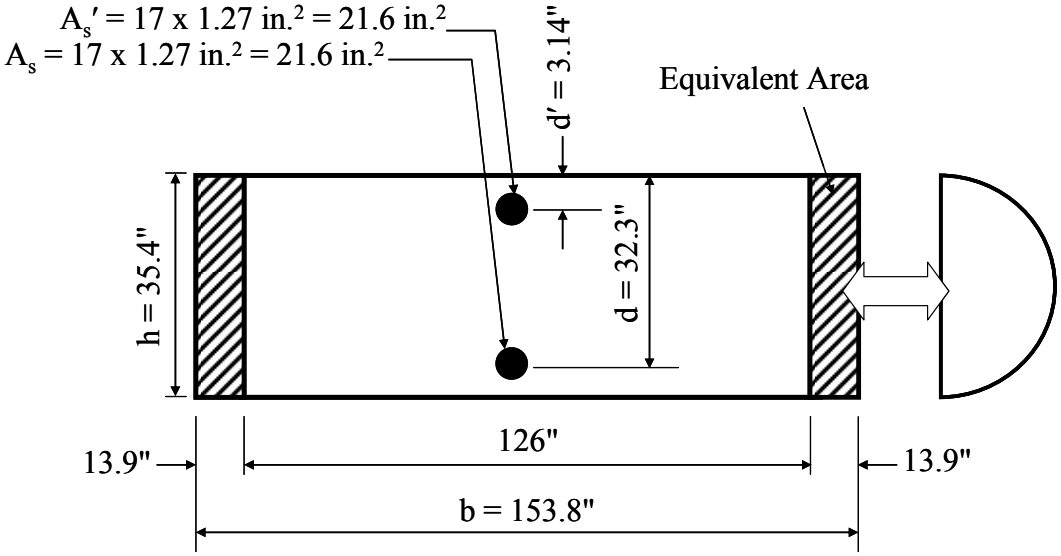

Figure 3.38: Simplified Pier Cross Section (SR249 over US12)

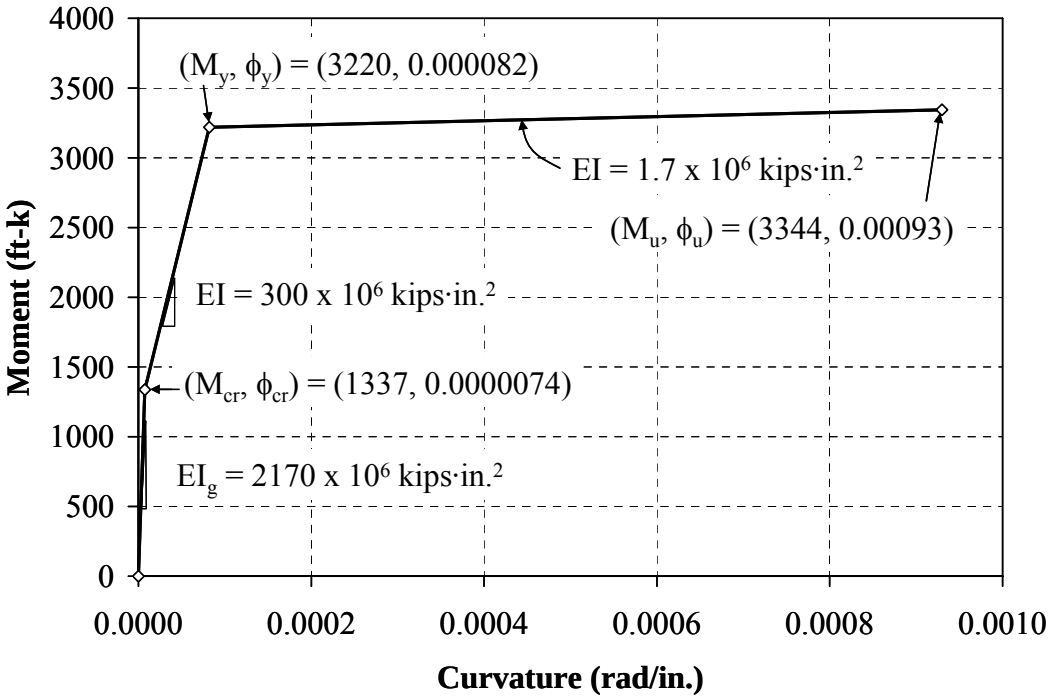

Figure 3.39: Moment-Curvature Relationship of Pier Cross Section

(SR249 over US12)

Table 3.6: Simplified Pier Cross Section Details (SR249 over US12)

Details	Values
Concrete Strength, f_c'	3500 psi
Steel Yield Strength, f_y	60000 psi
Concrete Modulus of Elasticity, E_c	3372 ksi
Steel Modulus of Elasticity, E_s	29000 ksi
Moment of Inertia of the Gross Uncracked Section, I_g	640293 $in.^4$
Moment of Inertia of the Cracked Section Transformed to Concrete, I_{cr}	16207 $in.^4$
Moment at Cracking, M_{cr}	1337 ft-k
Moment at First Yield, M_y	3220 ft-k
Moment at Ultimate, M_u	3344 ft-k
Curvature at Cracking, ϕ_{cr}	7.4×10^{-6} rad/in.
Curvature at First Yield, ϕ_y	82×10^{-6} rad/in.
Curvature at Ultimate, ϕ_u	930×10^{-6} rad/in.

3.5.1.2 Pier Movement

The piers were modeled as cantilever columns with a fixed end at the base subjected to a lateral load at the top as shown in Figure 3.40. The height of the pier, L, was 30.35 ft. A first order analysis was performed with the assumption of that the pier axial load does not affect the moment-curvature relationship. The top pier movement was calculated using strains obtained from rebar strain gages at the base of the piers as described below:

a) Average strains per day were determined.

b) Curvature was computed using the average strains on the north and south faces.

$$\phi = \frac{\text{Average strain at the north face - Average strain at the south face}}{\text{Distance between the north and south gages = 29.16 in.}}$$

c) Moment at the base of the pier was determined from the calculated curvature in Step b) using the moment-curvature relationship presented in Figure 3.39.

d) The lateral load, H, at the top of the pier was calculated from the moment at the base, M_{base}, divided by the height of the pier, L.

e) Moments along the pier height were calculated by applying the lateral load at the top of the pier.
f) Curvatures along the pier height were calculated using the moment-curvature relationship of the pier cross section shown in Figure 3.39
g) The lateral movements of the pier top, Δ, were computed using the moment-area theorem. The deflection was calculated using the moment of area under the curvature relationship about the top of the pile.

3.5.1.3 Abutment Movement

The end bent movements of the SR249 over US12 were extrapolated from the pier movements calculated in Section 3.5.1.2. The movement of Bent 1 was extrapolated from the calculated movement at the top of Piers 2 and 3 (Figure 3.41) plus the relative displacements measured by the crackmeters located at the top of Bent 1 and Pier 2 (Figures 3.6 and 3.7). The movement of Bent 11 was extrapolated from the movement at the top of Pier 10 and the movement at the center of the bridge taken as zero (Figure 3.42) plus the relative displacements measured by crackmeters located at the top of Pier 10 and Bent 11 (Figures 3.6 and 3.7). Due to the problems with the data acquisition system, only data between June 7, 2000 and July 23, 2001 were considered.

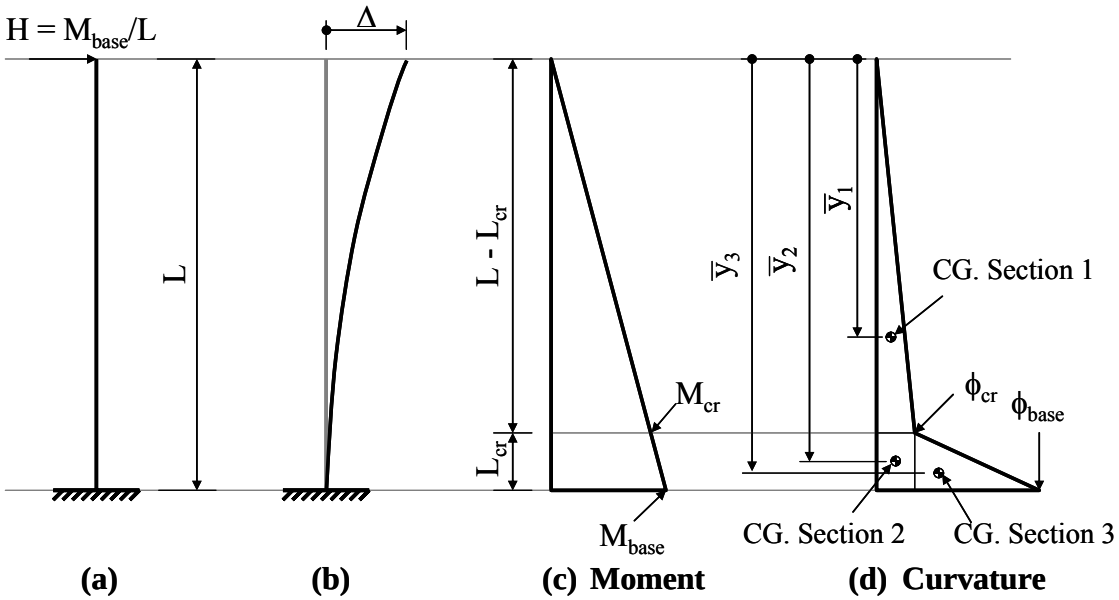

where:

H = lateral load, kips

M_{base} = moment at the base of the pier, ft-kips

ϕ_{base} = curvature at the base of the pier, rad/in.

M_{cr} = moment at cracking, ft-k

ϕ_{cr} = curvature at cracking, rad/in.

L = height of the pier, ft

L_{cr} = distance from the fixed end to the moment at cracking, so called "crack height," ft

Δ = lateral displacement at the pier top, in.

$\bar{y}_1, \bar{y}_2, \bar{y}_3$ = moment arm from the free end to the centroid of the section No. 1, 2, and 3, respectively, ft

Figure 3.40: Pier Model (SR249 over US12)

To compare the extrapolated bent movements with the thermal movement, the average temperature per day was calculated as shown in Figure 3.43. The thermal movements can be calculated by Equation 3-1,

$$\Delta L = \alpha(\Delta T)L \quad (3\text{-}1)$$

where:

ΔL = bridge movement, in.

α = coefficient of thermal expansion of concrete, taken as 6.0×10^{-6} /°F.

ΔT = change in temperature, °F, the reference temperature was taken as 65° F for the first day rebar strain gages started reading (June 7, 2000 at 9:00AM).

L = half of the total bridge length taken as 990 ft/2 = 495 ft.

Because the EPS backfill is behind the abutment, earth pressures do not exist behind the end bent to resist movement. Theoretically, the bridge should expand and contract corresponding to temperature ($\Delta L = \alpha(\Delta T)L$). The comparison between extrapolated movements and calculated thermal movements of Bents 1 and 11 is shown in Figures 3.44 and 3.45, respectively. The graphs show that the movement of Bents 1 and 11 corresponds well to temperature; however, the extrapolated movement on Bent 1 is slightly lower than the calculated thermal movement. This difference is likely due to the locking of the girders with Pier 2 as discussed in Section 3.2.3. As mentioned, the girders connecting to Pier 10 had been unlocked. Locking of the girders with the piers causes lateral forces to be resisted by the piers and reduces overall displacement at the end bent.

To provided an example, on the coldest day (December 22, 2000), the average temperature was 4° F while the measured lowest temperature reading was 0° F. Based on the average temperature, the calculated thermal movements of Bents 1 and 11 were computed by Equation 3-1. The comparison between the extrapolated and calculated values is tabulated in Table 3.7. The table shows the small difference between the extrapolated and calculated values of the movements. This smaller movement is expected likely due to the lateral resistance provided by the piles and restraint along the bridge length provided by the piers.

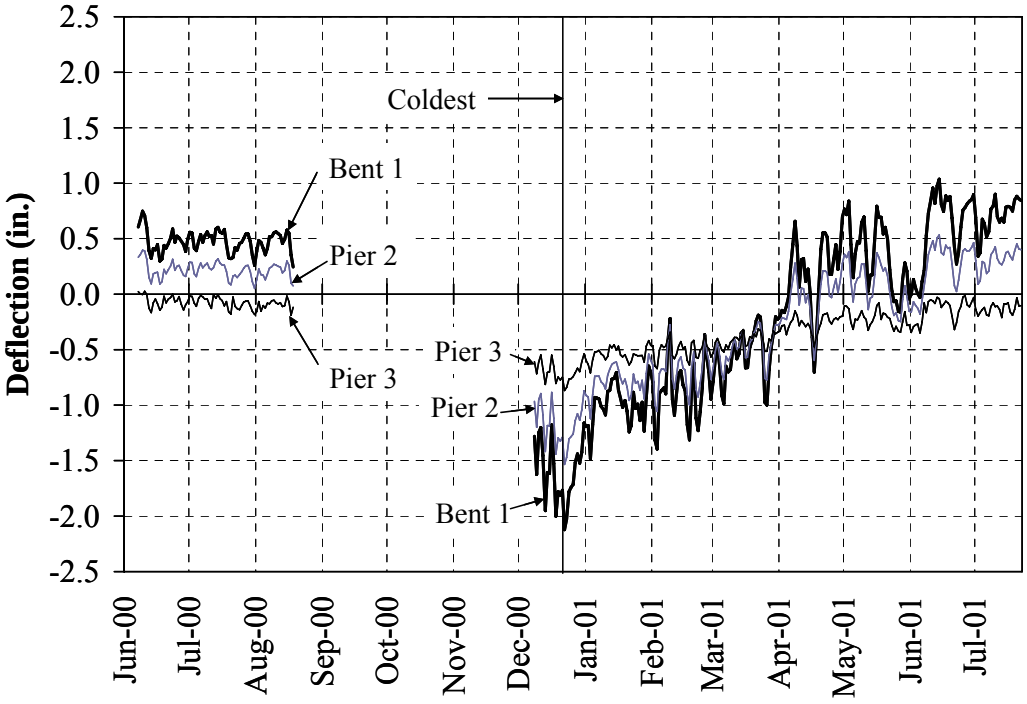

Figure 3.41: Extrapolation of Bent 1 Movement (SR249 over US12)

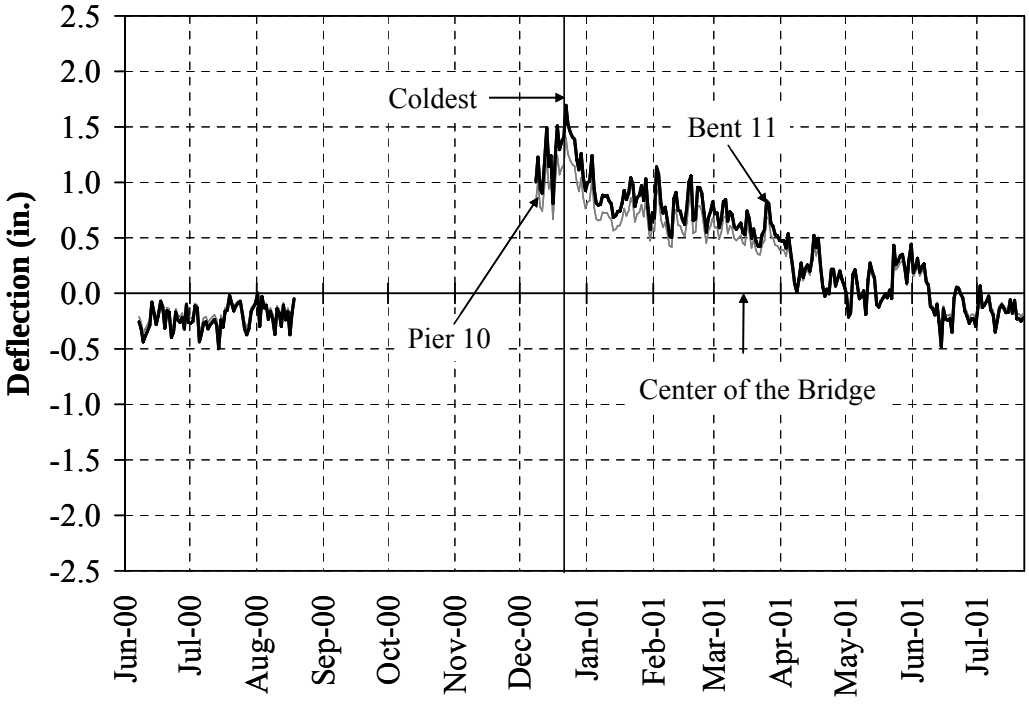

Figure 3.42: Extrapolation of Bent 11 Movement (SR249 over US12)

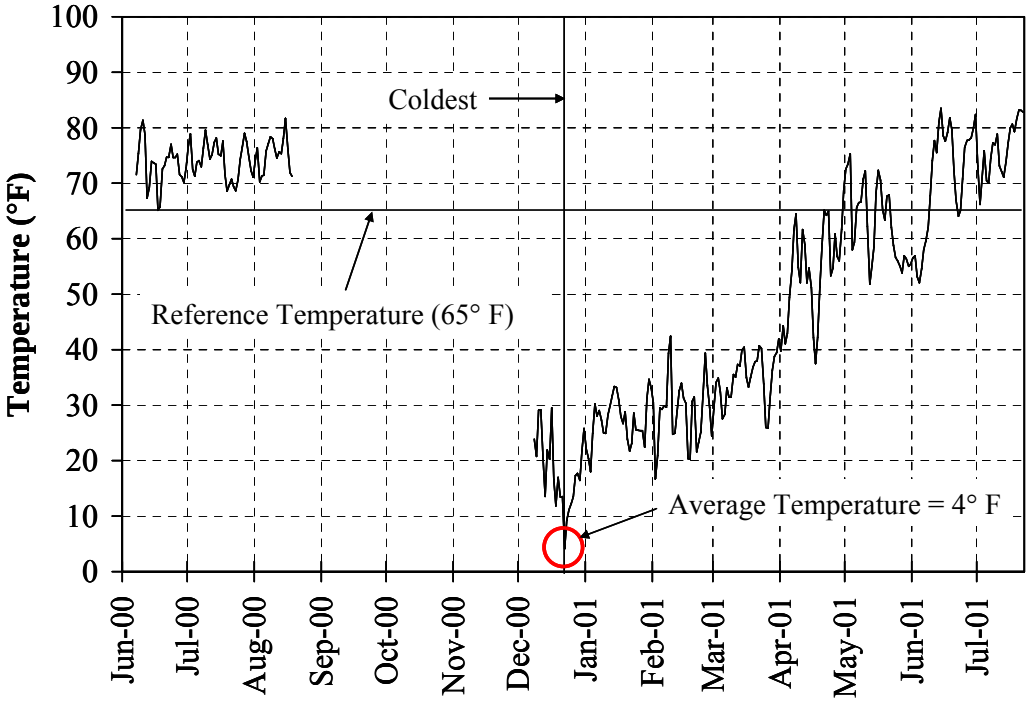

Figure 3.43: Average Daily Air Temperature (SR249 over US12)

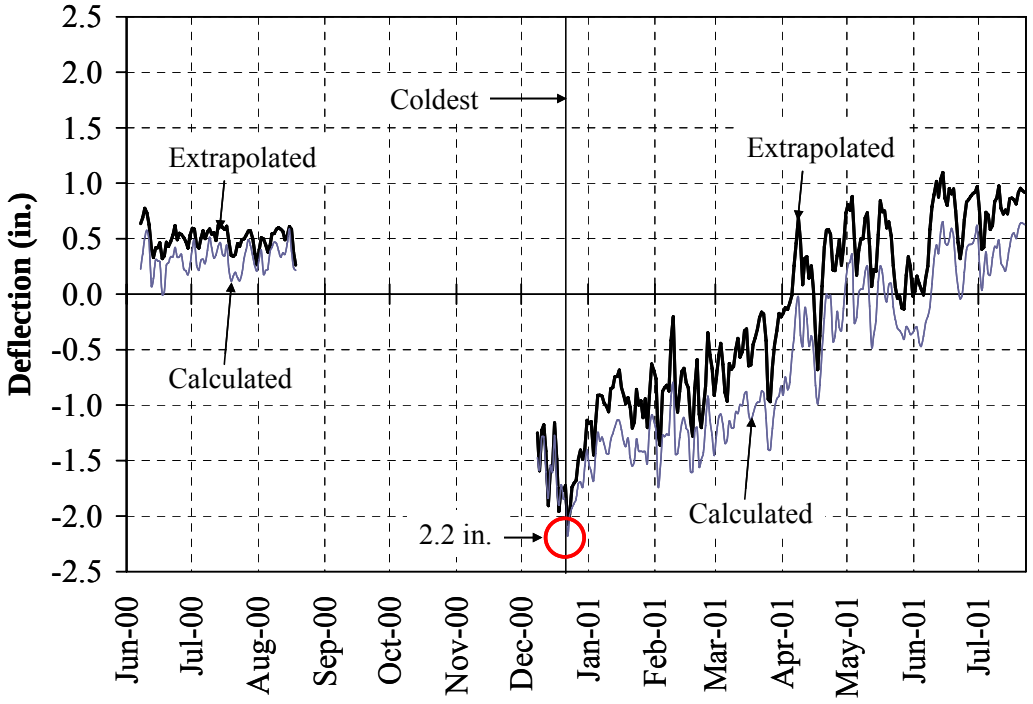

Figure 3.44: Extrapolated and Calculated Movement of Bent 1 (SR249 over US12)

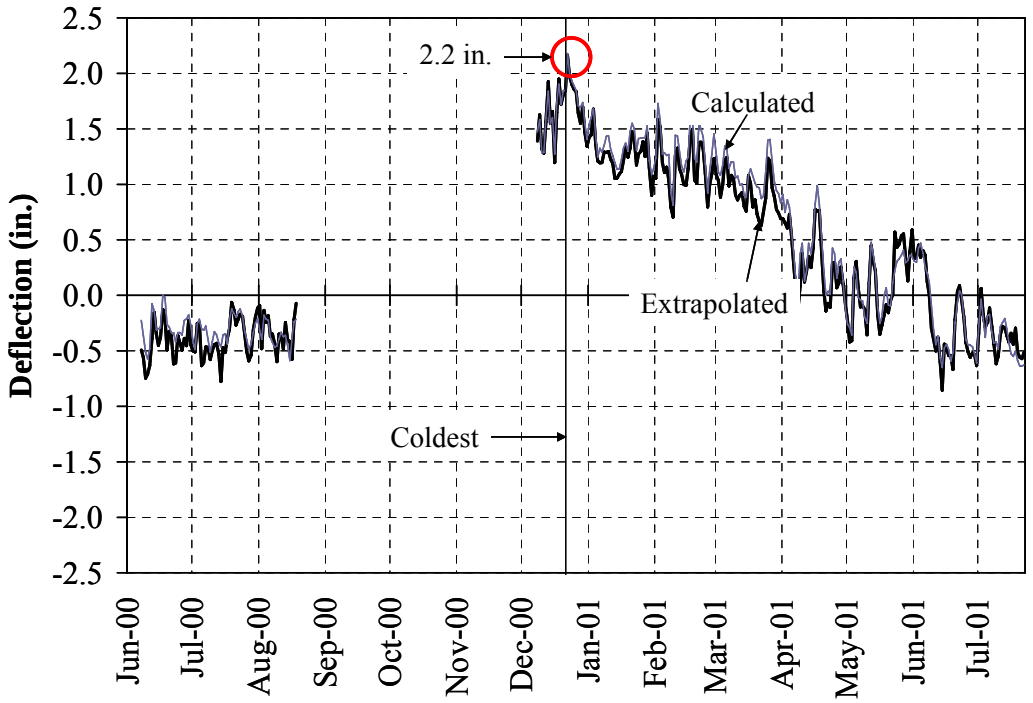

Figure 3.45: Extrapolated and Calculated Movement of Bent 11 (SR249 over US12)

Table 3.7: Comparison between Extrapolated and Calculated Movements (in.)

Bent 1				
Displacement extrapolated from Piers 2 and 3	**Relative displacement from crackmeter at Bent 1**	**Relative displacement from crackmeter at Pier 2**	**Total displacement**	**Theoretical movement**
2.12	+0.05 Ext.	+0.01 Ext.	2.17	2.20

Bent 11				
Displacement extrapolated from Piers 10 and center of the Bridge	**Relative displacement from crackmeter at Bent 11**	**Relative displacement from crackmeter at Pier 10**	**Total displacement**	**Theoretical movement**
1.70	+0.05 Ext.	+0.40 Ext.	2.15	2.20

3.5.2 I65 over SR25 Bridge

The longitudinal movement measured by the linear potentiometer is compared to the calculated movement based on Equation 3-1, where the reference temperature is taken as the construction temperature of the southbound structure (T = 58° F), the coefficient of thermal expansion of steel, α, is taken as 6.5 x 10^{-6} /°F, and the half of the total bridge length, L, is taken as 152 ft/2 = 76 ft. The comparison of the calculated movement and measured movement of the abutment is presented in Figure 3.46. As discussed in Section 3.3.2, only the trend of the measured movement should be considered, not the magnitude due to water infiltration. The graph indicated that the end bent movement corresponding to temperature changes, but this movement was not very sensitive to temperature changes.

3.5.3 SR18 over Mississinewa River Bridge

To better understand the behavior of piles supporting integral end bents, strain gages were installed along the length of Pile 6 of Bent 1 as described previously.

Recorded strains were used to determine the deflected shape of the pile. For this analysis, data between September 26, 2003 and March 31, 2004 were considered.

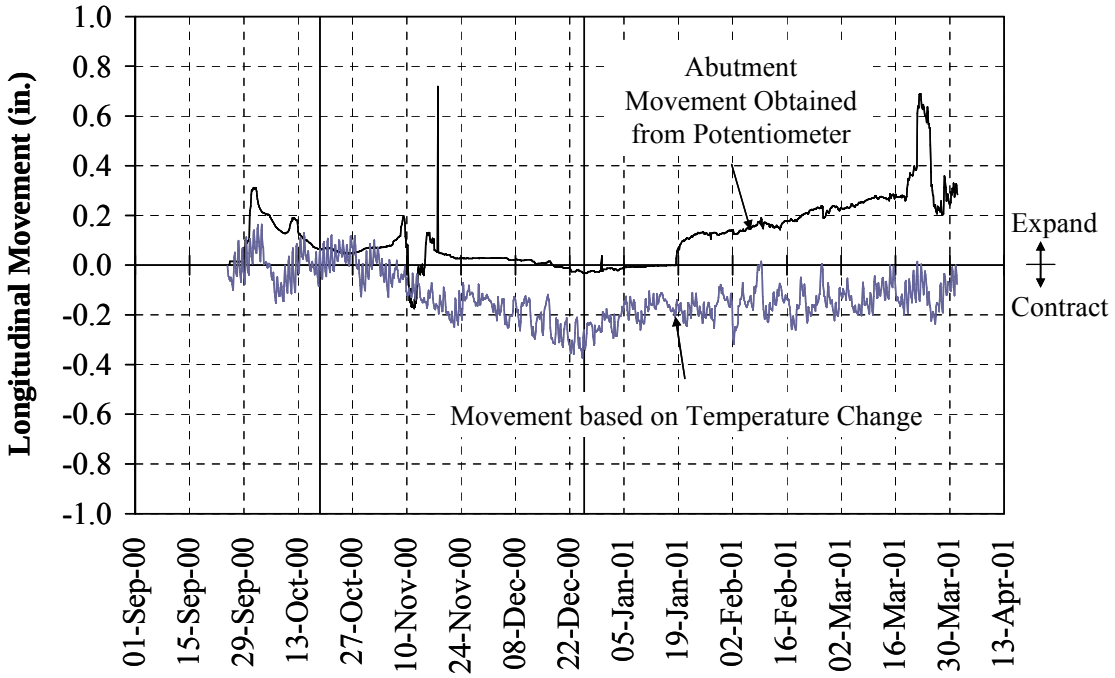

Figure 3.46: Comparison of Measured and Calculated Movements (I65 over SR25)

3.5.3.1 Stresses and Strains along the Pile Length

Stresses and strains on the east, west, and south faces of Pile 6 of Bent 1 over various temperature changes are plotted in Figures 3.47, 3.48, and 3.49, respectively. Stresses and strains along the pile length over various temperature change ranges, ΔT, were determined by grouping the strain according to the temperature range. The average strains of each temperature range were calculated. The increment of the temperature change range is 10° F ± 5% except for ΔT equal to 0° F. At ΔT = 0° F, the range considered was from -1 to 1° F. The temperature ranges are shown in Table 3.8. It is noted that the construction temperature was considered as 60° F, and all temperature changes are referenced from this temperature.

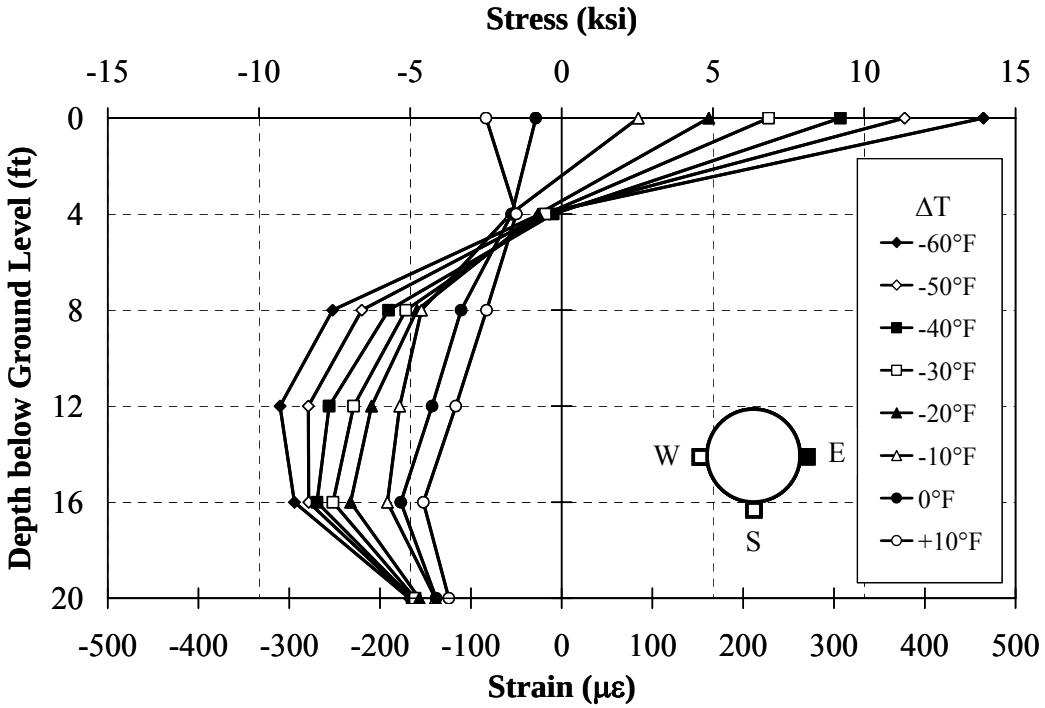

Figure 3.47: Stresses and Strains on Pile 6 on East Face (SR18)

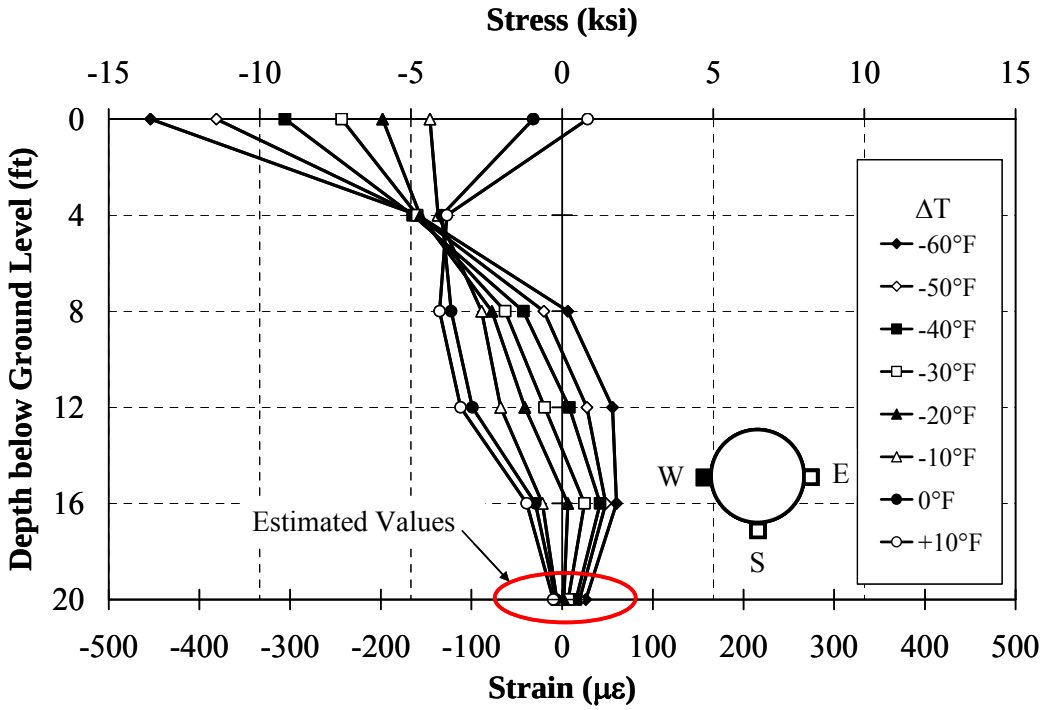

Figure 3.48: Stresses and Strains on Pile 6 on West Face (SR18)

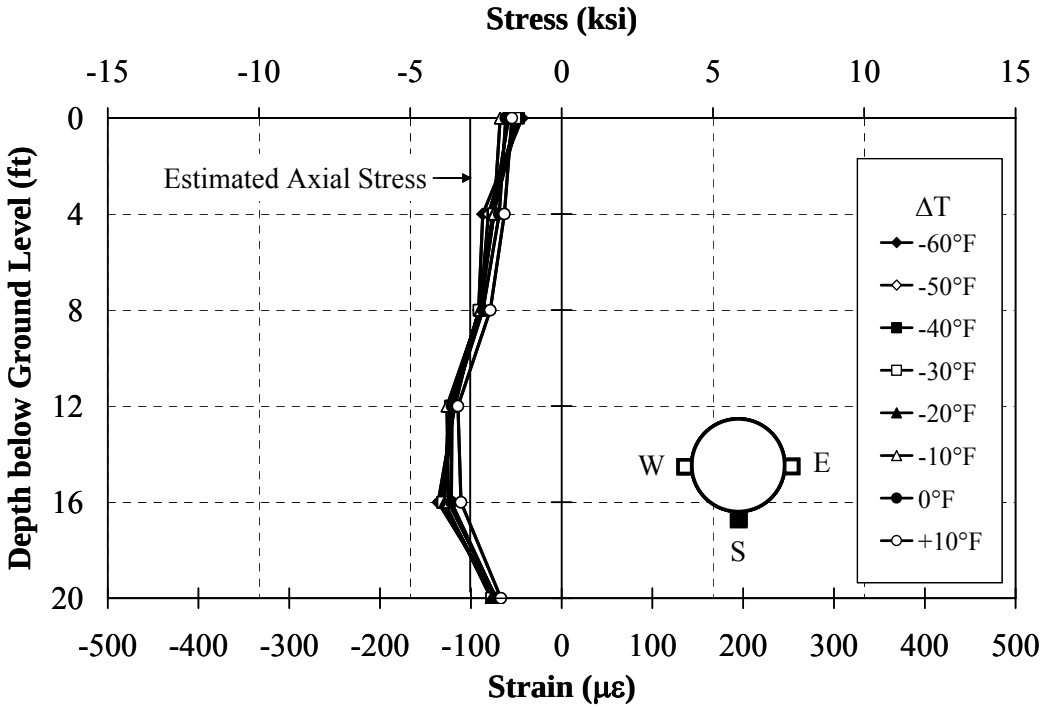

Figure 3.49: Stresses and Strains on Pile 6 on South Face (SR18)

Table 3.8: Temperature Change Range (SR18)

ΔT (°F)	Range (°F)	
-60	-63.0	-57.0
-50	-52.5	-47.5
-40	-42.0	-38.0
-30	-31.5	-28.5
-20	-21.0	-19.0
-10	-10.5	-9.5
0	-1.0	1.0
+10	10.5	9.5

It appears that the difference in stresses from the east and south face is almost equal to the difference in stresses from the west and south face. In other words, plane sections remain plane. It is noted that no data were recorded by the west strain gage at a depth of 20 ft below ground level due to damage during driving. However, stresses and strains on the west gage at a depth of 20 ft below ground level were estimated using the values from the east and south gages (Figure 3.48). These values were estimated assuming that plane sections remain plane.

Strains on the south gages were not zero because of the contribution of axial load (Figure 3.49). The axial load consists of dead loads from the abutment, bridge deck, girder, and diaphragm as well as highway live loads. An analysis was performed to determine the reasonableness of the measured values. A design axial load of approximately 80 kips was applied to each pile. The axial load was distributed to both the steel shell and the concrete core based on their relative axial stiffness. Therefore, an axial load of 35 kips was distributed to the steel shell area of 13.4 in.^{2}, while an axial load of 45 kips was distributed to the concrete core area of 140.5 in.^{2} This resulted in an average axial stress of 2.6 ksi on the steel shell that was calculated by dividing the axial load on the shell by its area as illustrated in Figure 3.50. The calculated value compares fairly well with the measured values (Figure 3.49).

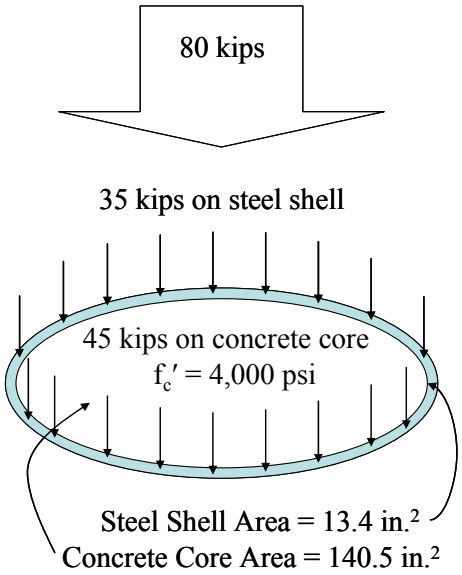

Figure 3.50: Axial Load Distribution (SR18)

3.5.3.2 Deflection of Pile 6

The pile was assumed to have a horizontally guided support at the top and a hinged support at the bottom. The top of the pile is free to translate but does not rotate, while the bottom of the pile is allowed to rotate without translation as illustrated in Figure 3.51. To determine deflections of the pile, curvatures were determined from strains on the east and west faces as illustrated in Figure 3.52. The curvatures were computed according to Equation 3-2.

$$\phi = \frac{SG_E - SG_W}{O.D.} \tag{3-2}$$

where:

ϕ = curvature, rad/in.

SG_E = strain on the east face, in./in.

SG_W = strain on the west face, in./in.

O.D. = outer diameter = 14 in.

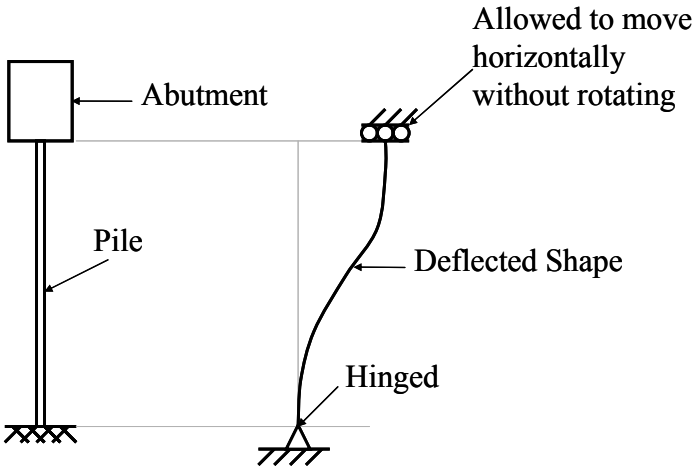

Figure 3.51: Assumption of Pile Movement

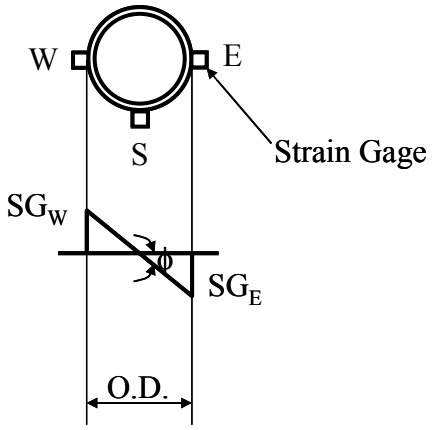

Figure 3.52: Computation of Curvature

Curvatures on Pile 6 over various temperature change ranges were plotted in Figure 3.53. The bottom of the pile is located at a depth of 22.25 ft; therefore, strain gages were not installed at this location. The curvatures at this depth were assumed to be zero. As shown, the pile is clearly bending in double curvature.

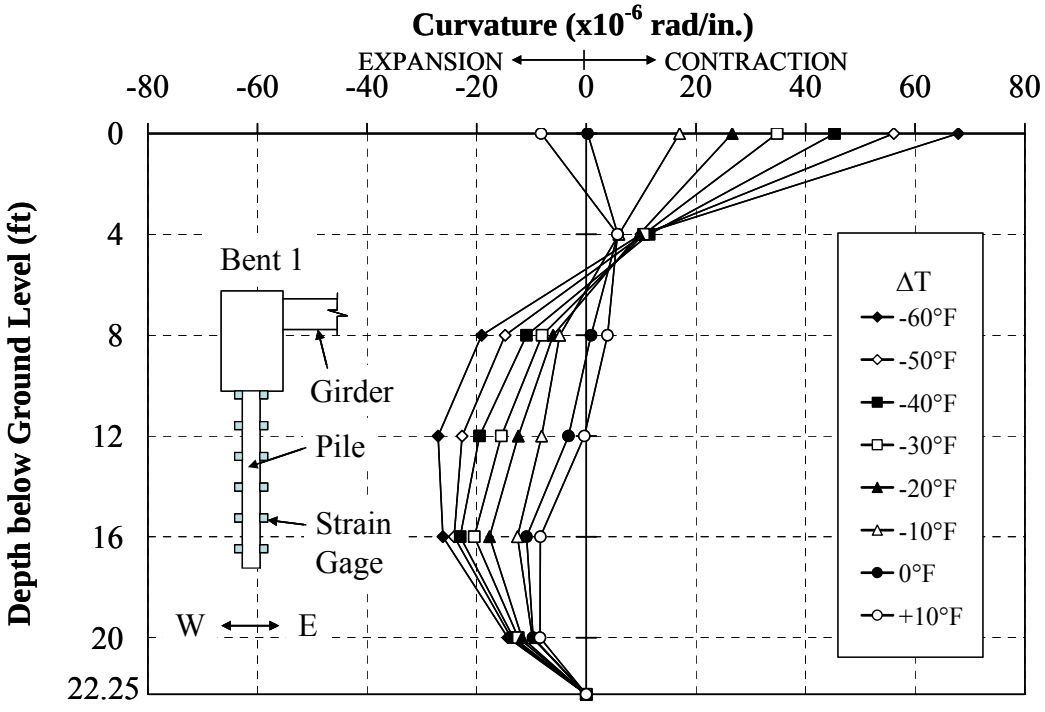

Figure 3.53: Curvature on Pile 6 over Various Changes in Temperature (SR18)

Deflections along the pile depth were computed by integrating the moment of the area under the curvature diagram considering the deflection measured at the pile top as measured by the convergence meter located at the center of Bent 1. Details of the computation of the deflected shape are provided in Appendix E. The deflected shape of Pile 6 over various temperature change ranges were estimated as shown in Figure 3.54. The estimated deflected shapes correspond very well to the temperature change, ΔT. Double curvature bending occurs with the inflection point located between a depth of 4 and 8 ft. The deflection at the bottom of the pile is zero as assumed in the calculation. This displacement at this depth was not measured.

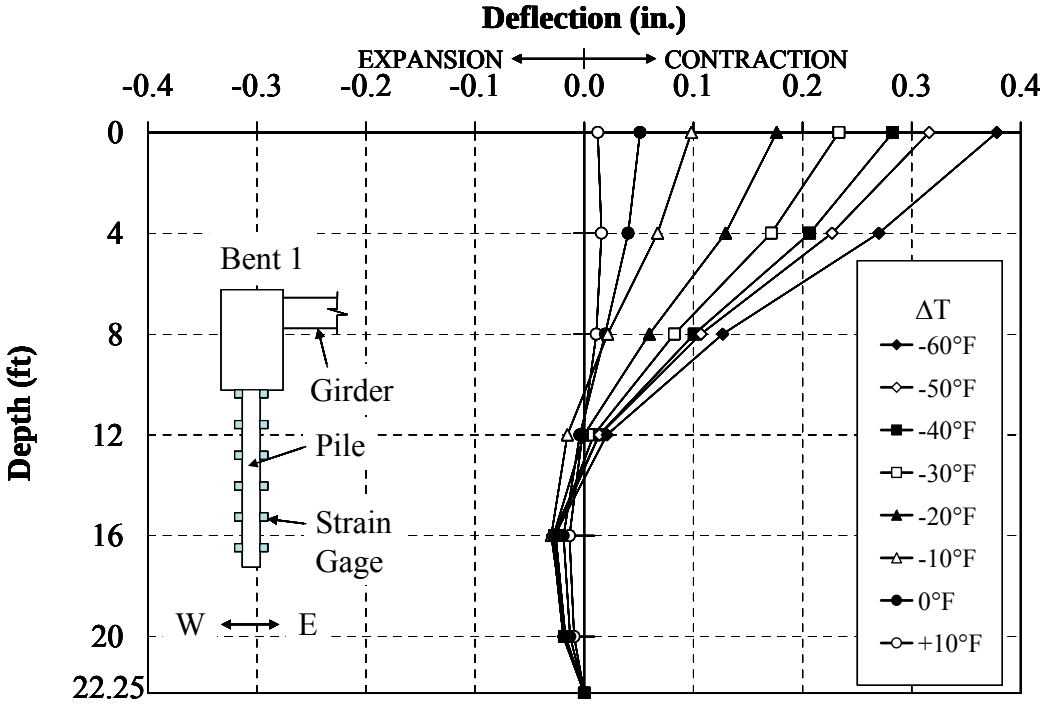

Figure 3.54: Deflection of Pile 6 over Various Changes in Temperature (SR18)

The estimated deflections at the top of Pile 6 were compared to the thermal movement calculated by Equation 3-1,

$$\Delta L = \alpha(\Delta T)L \qquad (3\text{-}1)$$

where:

α = coefficient of thermal expansion of concrete, taken as 6.0×10^{-6} /°F

ΔT = change in temperature, taken as -60, -50, -40, …, +10° F

L = half of the total span length, taken as 367 ft/2 = 183.5 ft.

The comparison of the deflections obtained from the convergence meter at the center of Bent 1 and the thermal movements calculated by Equation 3-1 is presented in Figure 3.55. It can be noticed that the deflections from the convergence meter are approximately half of the thermal movements. This difference is possibly due to restraint provided by the backfill, pile, and friction from the approach slab.

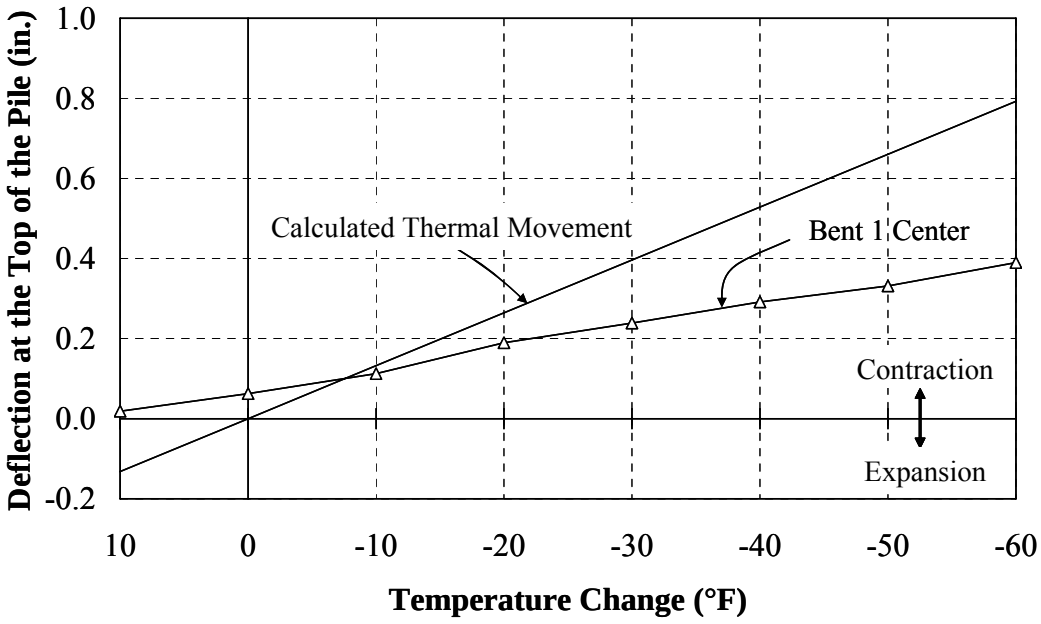

Figure 3.55: Deflection at the Top of Pile 6 (SR18)

CHAPTER 4: ANALYSIS OF FIELD RESULTS

4.1 Introduction

To evaluate the bridge data, two computer programs were used to model piles for the SR249 over US12 bridge, the I65 over SR25 bridge, and the SR18 over Mississinewa River bridge. The deflected shapes and moments along the pile length were calculated. Bridge data from SR249 over US12 and I65 over SR25 were not sufficient to estimate deflections and moments along the pile length, while strain data from SR18 provided enough information to approximate deflections and moments along the pile length. Therefore, only deflected shapes and moments on pile of SR18 calculated using strains can be compared to the results calculated using the two computer models.

Parametric studies were performed to determine the minimum acceptable pile length to be provided for typical integral abutment bridges. Variables include lateral displacement, axial load level, pile length, pile type, pile orientation, and soil type. Conclusions of the parametric studies are presented, and design recommendations are provided.

4.2 P-y Curve

The p-y curve presents the relationship between the lateral soil pressure against the pile (force per unit length of pile) and the corresponding lateral pile displacement. The soil characteristics in the soil-pile system are represented by the p-y curves. The p-y curve is dependent upon many variables such as soil type, shear strength parameters, moisture conditions, effective stress, stress history, and loading conditions (Welch and Reese, 1972). The p-y curves are different for short term static loading, sustained load,

cyclic loading, and dynamic loading. This study will consider only short term static loading which is considered appropriate for the pile response investigated here. A typical p-y curve is presented in Figure 4.1.

In the actual case of a laterally loaded pile, the soil response is usually nonlinear. As shown in Figure 4.1, the initial portion of the curve at a specific depth is a straight line, as defined by the initial soil modulus or initial soil stiffness, $E_{si}(z)$. The value of the initial soil modulus may vary with lateral deflection, y, and with the depth of the pile, z. A set of p-y curves along the pile length as illustrated in Figure 4.2 indicates that p-y curves are dependent upon the depth below ground surface.

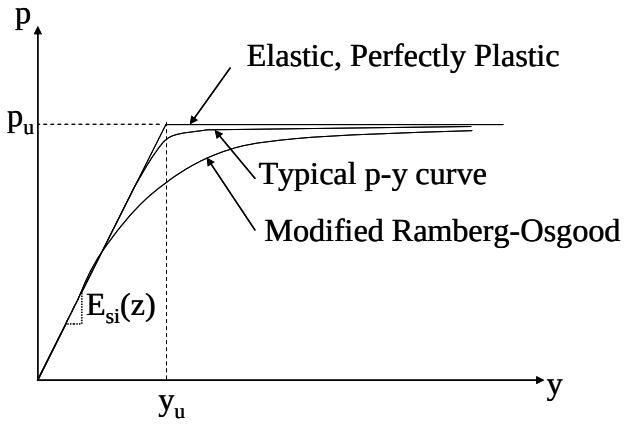

where:

p = soil resistance in units of force per linear length.

y = deflection of the pile perpendicular to the axis in units of length.

p_u = ultimate soil resistance in units of force per linear length.

y_u = ultimate deflection corresponding to p_u in units of length.

$E_{si}(z)$ = initial soil modulus or initial soil stiffness at the depth z in units of force per unit area.

Figure 4.1: Typical p-y Curve

The modified Ramberg-Osgood model can be used to approximate the p-y soil resistance and displacement curve for use in finite element analysis (Greimann, 1987). For convenience, the p-y curve can be assumed to be elastic, perfectly plastic as illustrated in Figure 4.1.

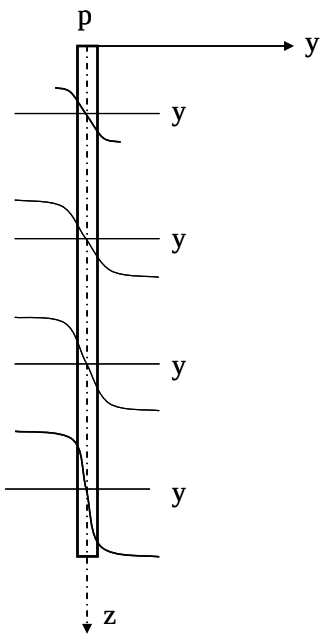

Figure 4.2: Set of p-y Curves (Reese et al., 1974)

4.2.1 Clay Model

Reese (1958) developed an expression for the ultimate soil resistance for clay, and Matlock (1970) modified the expression for soft, stiff, and very stiff clay. According to Griemann (1987), the ultimate soil resistance, $p_u(z)$, and the initial soil modulus, $E_{si}(z)$, for soft clay and stiff clay are given by Equations 4-1 and 4-2, respectively.

$$p_u(z) = \text{ lesser of } \begin{cases} \left[3 + \dfrac{\gamma}{c_u} z + \dfrac{0.5}{B} z\right] \cdot c_u B \\ 9 c_u B \end{cases} \tag{4-1}$$

$$E_{si}(z) = \frac{p_u}{y_{50}} \tag{4-2}$$

The ultimate soil resistance, $p_u(z)$, and the initial soil modulus, $E_{si}(z)$, for very stiff clay are given by Equations 4-3 and 4-4, respectively.

$$p_u(z) = \text{ lesser of } \begin{cases} \left[3 + \dfrac{\gamma}{c_u} z + \dfrac{2}{B} z\right] \cdot c_u B \\ 9 c_u B \end{cases} \tag{4-3}$$

$$E_{si}(z) = \frac{p_u}{2y_{50}} \tag{4-4}$$

where:

p_u = ultimate soil resistance, kips/ft.

γ = effective unit soil weight, lb/ft^3 or use γ = 50, 60, and 65 lb/ft^3 for soft, stiff, and very stiff clay, respectively (Griemann, 1987).

c_u = undrained shear strength from tri-axial test or use the values given in Table 4.1.

B = dimension of the pile parallel to bending axis, ft, as shown in Figure 4.3. For example,

B is the width of H pile, b_f, for the strong axis pile bending.

B is the depth of H pile, d, for weak axis pile bending.

B is outer diameter, O.D., for concrete-filled steel tube piles.

z = depth of a spring from soil surface, ft.

y_{50} = displacement at one-half ultimate soil resistance, ft. Taken as $2.5B\varepsilon_{50}$ for soft and stiff clay, and $2.0B\varepsilon_{50}$ for very stiff clay (Griemann, 1987).

ε_{50} = axial strain at one-half peak stress difference from triaxial test; or use 0.02, 0.01, and 0.005 for soft, stiff, and very stiff clay, respectively (Reese et al., 2000a and Reese et al., 2000b).

The p-y curve for soft and stiff clays proposed by Matlock (1970) is shown in Figure 4.4. The p-y curve for soft and stiff clays can be determined using Equation 4-5. The value of p remains constant beyond $y = 8y_{50}$.

$$p = 0.5\left(\frac{y}{y_{50}}\right)^{\frac{1}{3}} \cdot p_u \tag{4-5}$$

where:

p = generalized soil resistance, kips/ft.

p_u = ultimate soil resistance, kips/ft.

y = generalized displacement, ft.

y_{50} = displacement at one-half ultimate soil reaction, ft.

Table 4.1: Undrained Shear Strength and Soil Modulus Parameter for Clays (Reese et al., 2000b)

Clay Type	Undrained Shear Strength, c_u	Average c_u	k (lb/in.^{3})
Soft	250 - 500 psf 1.74 - 3.47 psi	375 psf 2.6 psi	30
Medium	500 - 1000 psf 3.47 - 6.94 psi	750 psf 5.2 psi	100
Stiff	1000 - 2000 psf 6.94 - 13.9 psi	1500 psf 10.4 psi	500
Very Stiff	2000 - 4000 psf 13.9 - 27.8 psi	3000 psf 20.8 psi	1000
Hard	4000 - 8000 psf 27.8 - 55.6 psi	6000 psf 41.7 psi	2000

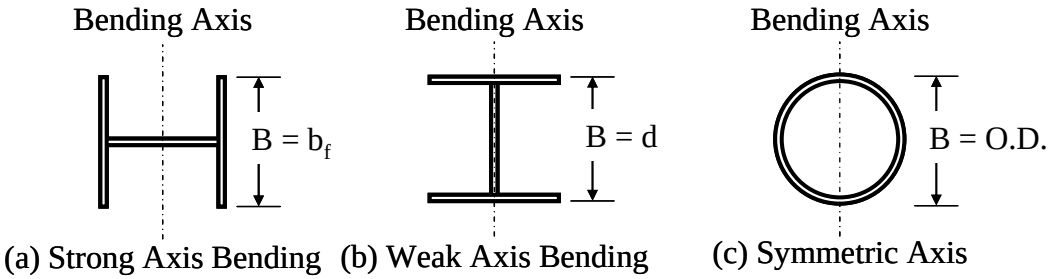

Figure 4.3: Definition of the Width, B

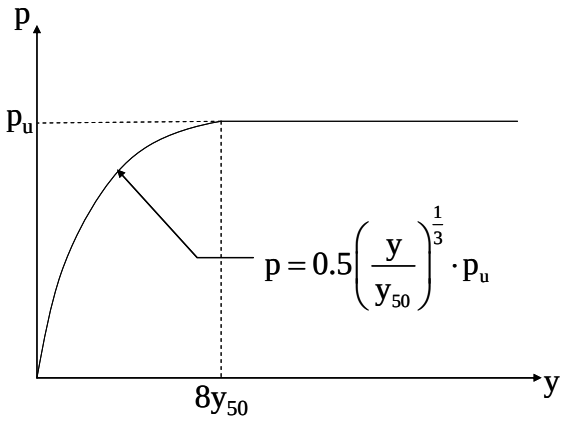

Figure 4.4: Typical p-y Curve for Soft Clay and Stiff Clay

Very stiff clay as modeled by Reese and Welch (1975) is shown in Figure 4.5. The p-y curve for very stiff clay can be determined using Equation 4-6. The value of p remains constant beyond $y = 16y_{50}$.

$$p = 0.5\left(\frac{y}{y_{50}}\right)^{\frac{1}{4}} \cdot p_u \tag{4-6}$$

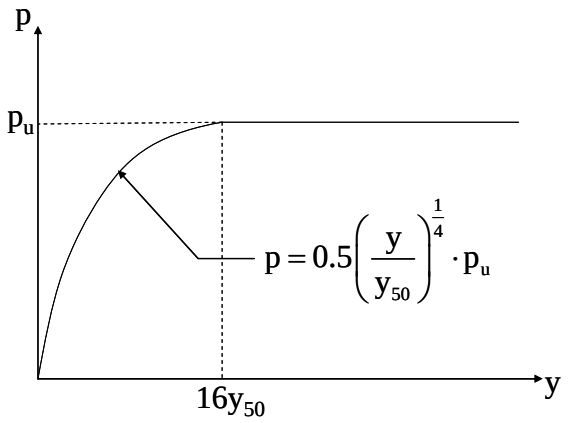

Figure 4.5: Typical p-y Curve for Very Stiff Clay

4.2.2 Sand Model

If values of Young's modulus of soil, E_m, were not obtained from laboratory tests, Terzaghi (1955) suggested numerical values for E_m as a function of the unit weight and relative density of sand (Equation 4-7). Based on experiments, E_m is suggested to be zero at the ground surface and increases linearly with depth. The initial slope or soil modulus of the p-y curve, $E_{si}(z)$, is defined by Equation 4-8.

$$E_m = J\gamma z \tag{4-7}$$

$$E_{si}(z) = \frac{E_m}{1.35} = \frac{J\gamma z}{1.35} \tag{4-8}$$

where:

E_m = Young's Modulus for the soil, lb/ft^2.

γ = average effective unit weight, lb/ft^3.

z = depth to p-y curve, ft.

J = 200, 600, and 1500 for loose, medium, and dense sand, respectively.

$E_{si}(z)$ = initial slope or soil modulus of the p-y curve at the depth z, kips/ft^2.

Reese et al. (1974) proposed the ultimate soil resistance per unit length of the pile given by the smaller of p_{st} in Equation 4-9 and p_{sd} in Equation 4-10. Equation 4-9 is used for computing the ultimate resistance near the ground surface, and Equation 4-10 is used for computing the ultimate resistance well below the ground surface. The computational procedure of the p-y curves for sand is provided in Appendix F.

$$p_{st} = \gamma z\left[\frac{K_o z\tan\phi\sin\beta}{\tan(\beta-\phi)\cos\alpha}+\frac{\tan\beta}{\tan(\beta-\phi)}(B+z\tan\beta\tan\alpha)\right.$$
$$\left.+K_0 z\tan\beta(\tan\phi\sin\beta-\tan\alpha)-K_A B\right] \quad (4\text{-}9)$$

$$p_{sd} = K_A B\gamma z(\tan^8\beta-1)+K_0 B\gamma z\tan\phi\tan^4\beta \quad (4\text{-}10)$$

where:

α = $\frac{\phi}{3}$ for loose sand, $\frac{\phi}{2}$ for medium or dense sand (Welch and Reese, 1972, Bowman, 1958, and Parker and Reese, 1971).

β = $45°+\frac{\phi}{2}$ (Mohr-Coulomb Theory).

γ = unit weight of soil, lb/ft^3.

z = depth from soil surface, ft.

ϕ = angle of internal friction, degrees.

K_0 = coefficient of earth pressure at rest = 1-sin ϕ (Greimann, et al., 1987).

K_A = active earth pressure coefficient, taken as $\tan^2(45°- \phi/2)$.

4.3 LPILE PLUS

LPILE PLUS Version 4.0 (Reese et al., 2000a and Reese et al., 2000b) is a computer program for the analysis of piles and drilled shafts under lateral loads. Soil springs in LPILE PLUS are modeled by lateral resistance-displacement curves or p-y curves. For LPILE PLUS, Matlock's (1970) approach was used to model soft clay while Reese and Welch's (1975) approach was used to model stiff clay and very stiff clay. Reese et al's (1974) approach was used to model the p-y curve for sand.

For LPILE PLUS, $E_{si}(z)$ is defined by Equation 4-11. The values of k recommended by Terzaghi (1955) are shown in Table 4.2. Reese et al. (1974) reported that the values of k for submerged sand from a test performed at Mastang Island are higher than the values reported by Terzaghi (1955); therefore, the values of k provided in Table 4.3 are used for the LPILE PLUS analysis.

$$E_{si}(z) = kz \tag{4-11}$$

where:

$E_{si}(z)$ = initial soil modulus at the depth z, lb/in.^{2}

k = soil modulus parameter, lb/in.^{3}

z = depth to p-y curve, in.

Table 4.2: Terzaghi's Values of k for Submerged Sand (Terzaghi, 1955)

Relative Density	Loose	Medium	Dense
Terzaghi's k (lb/in.^{3})	2.6-7.7	7.7-26	26-51

Table 4.3: Recommended Values of k (lb/in.^{3}) (Reese et al., 1974)

Sand	Relative Density		
	Loose	Medium	Dense
Submerged	20	60	125
Dry	25	90	225

LPILE PLUS performs a nonlinear analysis to determine deflected shapes and moments along the pile length. LPILE PLUS solves the problem of a laterally loaded pile with any arbitrary variation of pile stiffness or soil modulus along pile depth. An iterative solution method is used with values of the initial soil modulus, $E_{si}(z)$, adjusted until the values of soil resistance, p, and deflection, y, obtained in the solution are compatible with the external applied load.

4.3.1 Soil Models (LPILE PLUS)

4.3.1.1 Clay Model

The p-y curves of clay in LPILE PLUS are modeled in accordance with Section 4.2.1. The undrained shear strength, c_u, and soil modulus parameter, k, are provided in Table 4.1.

4.3.1.2 Sand Model

The p-y curves of sand in LPILE PLUS are modeled in accordance with Section 4.2.2.

4.3.2 Equivalent Diameter

The recommendations for p-y curves are based strongly on the results of experiments with cylindrical shapes. At the outset, it can be assumed that the soil in the flanges of H piles will move with the pile and that it will behave as a rectangular shape. The equivalent diameter of the pile, d_e, can be computed by finding a circular section with the same area as the rectangular section (Figure 4.6). Thus, the circular area of $\pi d_e^2/4$ is set to be equal to $b_f \cdot d$. Finally, the equivalent diameter can be solved. If the equivalent diameter, d_e, is greater than b_f or d, the lower value will be used. For CFT piles, the outer diameter, O.D., is used as the actual diameter (d_e = O.D.).

4.3.3 Transformed Section

Concrete-filled steel tube piles were transformed into an equivalent steel pile to determine pile properties (Figure 4.7). The concrete section of the pile was transformed to an equivalent steel section using the modular ratio, n, given by Equation 4-12. To replace the area of concrete with an area of steel having the same axial stiffness, AE, the equivalent steel section diameter, d_e, is computed by dividing the concrete section diameter, I.D., by n.

$$n = E_s/E_c \tag{4-12}$$

where:

E_s = modulus of elasticity of steel, ksi (E_s = 29,000 ksi)

E_c = modulus of elasticity of concrete, ksi ($E_c = 57\sqrt{f'_c}$)

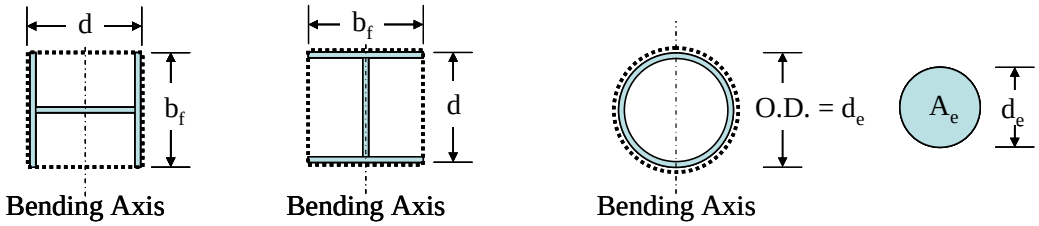

(a) Strong Axis Bending (b) Weak Axis Bending (c) Symmetric Axis (d) Equivalent Area

Figure 4.6: The Computation of Equivalent Diameter and Equivalent Area

The moment of inertia of the equivalent steel section, I_e, is the summation of the moment of inertia of the steel ring, $I_{steel\ ring}$, and the transformed steel section, $I_{transformed}$.

$$I_e = I_{steel\ ring} + I_{transformed} \tag{4-13}$$

$$I_{steel\ ring} = \frac{\pi}{64}\left(O.D.^4 - I.D.^4\right) \tag{4-14}$$

$$I_{transformed} = I_y = \frac{1}{4}\pi a^3 b = \frac{1}{4}\pi\left(\frac{I.D.}{2}\right)^3\left(\frac{I.D.}{2n}\right) \tag{4-15}$$

where:

a, b = major and minor axes, in.

O.D. = outer diameter, in.

I.D. = inner diameter, in.

4.4 SAP2000

SAP2000, a finite element program, was also used to model the piles. Piles were modeled as a beam-column element with springs positioned along the length representing the soil-spring stiffness. The pile was subjected to the same axial load and lateral displacement as used in LPILE PLUS. Deflected shapes and moments of the piles were determined and compared to the results analyzed using LPILE PLUS.

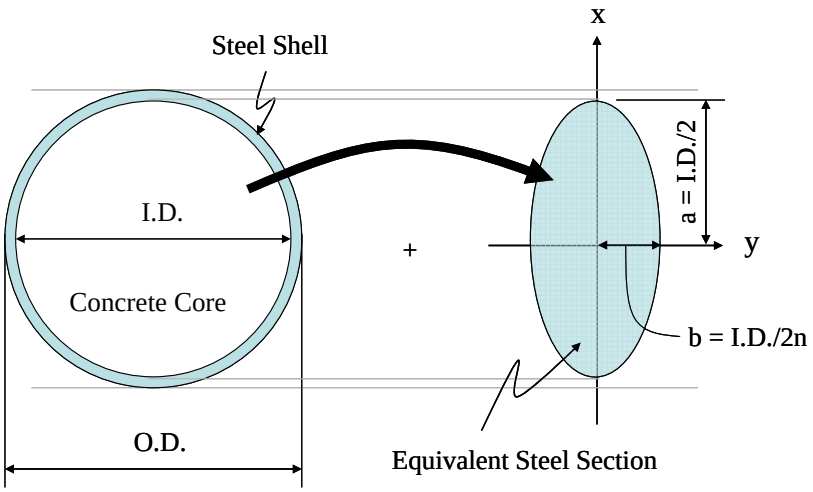

Figure 4.7: Transformed Concrete-Filled Steel Section

4.4.1 Elastic Soil Spring Method

Pile behavior is depended upon pile type, pile size, pile orientation, and the influence of soil surrounding the pile. The piles can be modeled using the equivalent cantilever pile method (Abendroth et al., 1989, Davisson, 1970, Greimann et al., 1987, and Girton et al., 1991) or using the elastic soil spring method (Wolde-Tinsae et al., 1982, Greimann et al., 1986, and Greimann et al., 1987). Because the actual pile length was used in the model and the lateral stiffness of the soil was calculated at each node level

along the pile member, according to Durbin (2001), the elastic soil spring method is recommended for modeling integral abutment piles because of its accuracy and various utilizations. For example, one pile length is used to determine the maximum moment, horizontal displacement, and elastic stability of the pile, whereas different lengths are required for each of these calculations in the equivalent cantilever method.

The effect of soil on pile behavior is represented by a series of Winkler springs continuous along the pile length. A Winkler's spring assumes no interaction between the different soil springs as the pile is displaced. Soil springs are applied over the length of the pile below ground level. Each spring has a stiffness based on the soil type, pile size, and depth from ground surface. Greimann (1987) provides equations for calculating the spring stiffness values for different soil types. Sand and clay models are discussed in the following sections.

For all analyses, the ground water table (GWT) was assumed to be at ground level unless otherwise stated. This is a conservative assumption. The initial spring stiffness values also known as soil modulus, $E_{si}(z)$, varied along the length of the pile and can be calculated based on Sections 4.2.1 and 4.2.2. The stiffness of individual soil springs spaced over the length of the pile, k(z), is calculated by multiplying the soil spring stiffness, $E_{si}(z)$, by a distance equal to half of the spring spacing above and below the specific spring ($s_1/2$ and $s_2/2$, respectively). The distinction between initial soil stiffness, $E_{si}(z)$, and soil spring stiffness, k(z), is illustrated in Figure 4.8. The soil spring applied on the pile along the pile depth, k(z), can be calculated by Equation 4-16.

$$k(z) = E_{si}(z) \cdot s \tag{4-16}$$

where:

$E_{si}(z)$ = soil spring at the depth of z, kips/ft.

s = spring spacing, ft. Equal to $s_1/2 + s_2/2$.

s_1, s_2 = half of the spacing above and below the spring, ft.

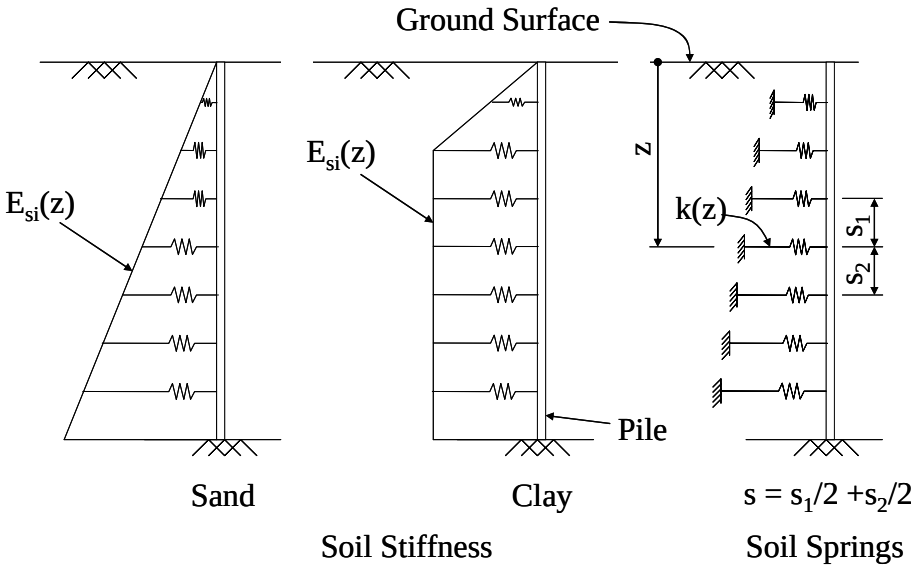

Figure 4.8: Initial Soil Stiffness and Soil Spring Stiffness

4.4.2 Soil Models (SAP2000)

4.4.2.1 Clay Model

The initial soil stiffness of clay, $E_{si}(z)$, was determined according to Section 4.2.1 along with the undrained shear strength given in Table 4.1.

4.4.2.2 Sand Model

The initial soil stiffness of sand, $E_{si}(z)$, was determined according to Section 4.2.2.

4.4.3 Transformed Section

The concrete-filled steel tube piles were transformed in accordance with Section 4.3.3 to determine the moment of inertia.

4.5 LPILE PLUS vs. SAP2000

The difference between LPILE PLUS and SAP2000 is that LPILE PLUS uses nonlinear p-y curves to iteratively calculate the deflections and moments along the pile length, while the SAP2000 models only use the initial slope of the p-y curve, $E_{si}(z)$, which is linear. For large lateral displacements, the nonlinear soil springs are more reasonable.

4.6 Analytical Bridge Models

4.6.1 SR249 over US12 Bridge

Due to insufficient field data to verify the deflected shape of the pile supporting the end bents, the deflected shape cannot be estimated using the field data. However, the deflected shapes estimated by LPILE PLUS and SAP2000 are presented and compared to each other. In addition, the magnitude of strains at the ground level of the pile is compared with the analytical results.

4.6.1.1 Pile Model

HP14x89 piles bending about their strong axis were modeled for the piles supporting both end bents. For convenience, the pile lengths for all models were slightly modified from the actual length to ease positioning of the soil springs. For Bent 1, the total length of the piles was modified to be 133.5 ft (the actual total pile length for Bent 1 is approximately 131 ft). The piles of both Bents 1 and 11 are embedded 1.5 ft in the abutment. The pile length above ground level is 17 ft measured from the ground surface to the bottom of the abutment; therefore, the pile length below ground level in the model is 115 ft (Figure 4.9). For Bent 11, the total length of the piles is assumed to be 165.5 ft (the actual total pile length for Bent 11 is 164 ft). The pile length above ground level is 19 ft measured from the ground surface to the bottom of the abutment; therefore, the pile length below ground level in the model is 145 ft (Figure 4.9).

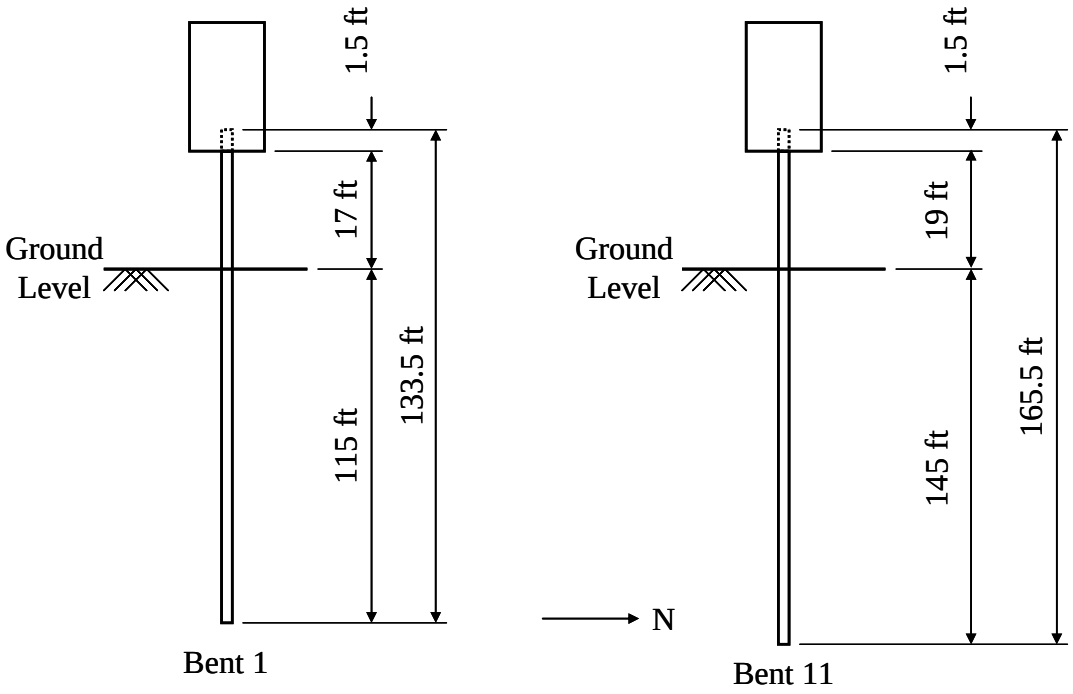

Figure 4.9: Pile Length for Piles of Bents 1 and 11 (SR249 over US12)

Since the piles embedded in the abutment are surrounded by expanded polystyrene to provide for a pin connection, the pile was modeled to have a roller support at the top and a hinged support at the bottom as illustrated in Figure 4.10. A roller support allows the pile to translate horizontally and rotate, and a hinged support allows the pile to rotate without translation. In reality, however, the abutment-pile connection likely behaves in-between a hinged and a fixed support. Therefore, a horizontally-guided support was also analyzed at the top of the pile. The horizontally-guided support allows the pile to translate horizontally without rotation. As shown in Figure 4.10, depths (z) are measured from the ground level. Positive values indicate below ground level and negative values indicate above ground level.

Each pile was subjected to an axial load of 200 kips according to calculations provided by the bridge designer (Section 2.2.1.2). The pile was subjected to a lateral movement of 2.2 in. based on the thermal movement calculated by Equation 4-17.

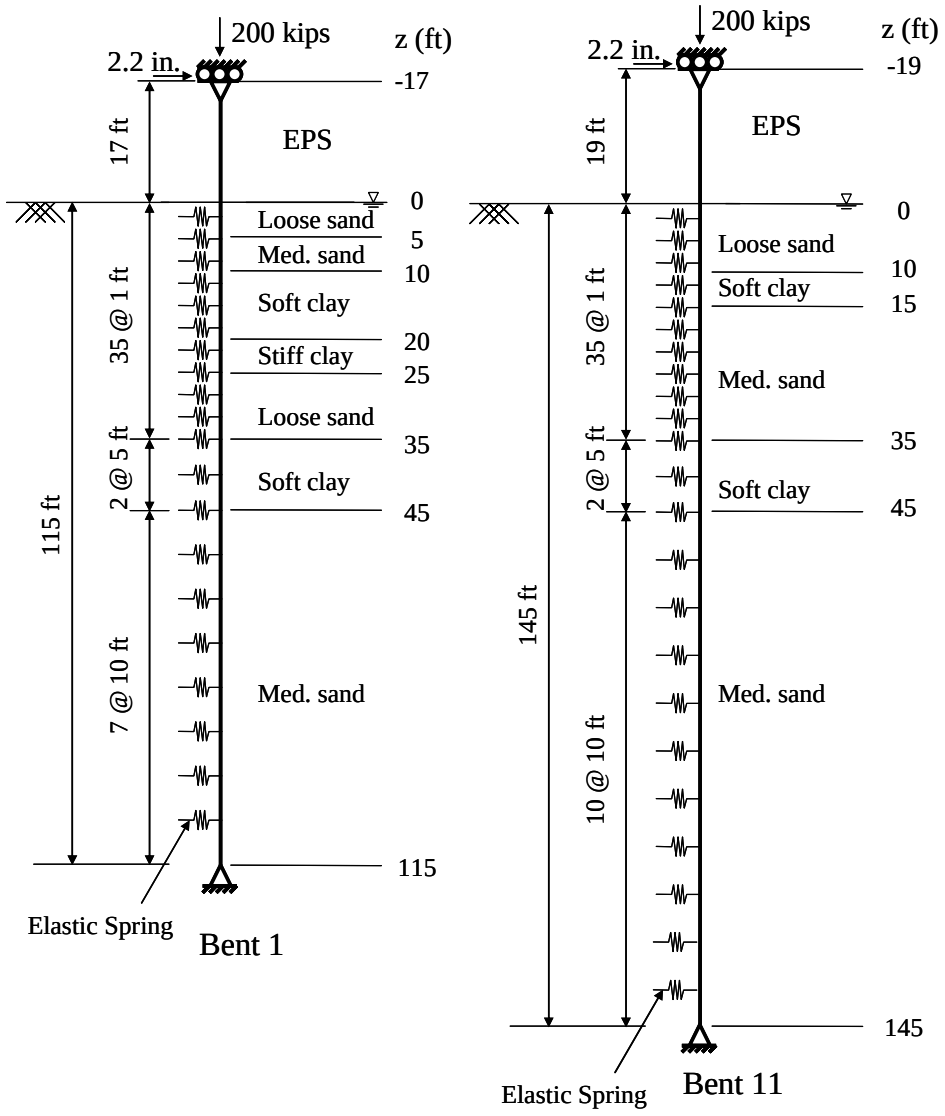

Figure 4.10: Pile Models for Bents 1 and 11 (SR249 over US12)

$$\Delta L = \alpha(\Delta T)L \qquad (4\text{-}17)$$

where:

α = coefficient of thermal expansion for concrete taken as $6x10^{-6}$ /°F.

ΔT = temperature change of 60° F taken on the coldest day (December 22, 2000 at 8:00AM).

L = half of the total bridge length taken as 990 ft/2 = 495 ft.

For LPILE PLUS, the cross-sectional area, A, equivalent diameter, d_e, and moment of inertia, I, of the pile were calculated and are listed in Table 4.4. The pile section properties are provided in Table 4.5. The modulus of elasticity of steel was assumed to be equal to 29,000 ksi.

Table 4.4: Input for LPILE Program (SR249 over US12)

Pile Section	A (in.^{2})	d_e (in.)	I (in.^{4})
HP14x89	26.1	6.2	904

Table 4.5: HP14x89 Cross Section Properties

Pile Section	A (in.^{2})	d (in.)	t_w (in.)	b_f (in.)	t_f (in.)	I_x (in.^{4})	I_y (in.^{4})	S_x (in.^{3})	S_y (in.^{3})	Z_x (in.^{3})	Z_y (in.^{3})
HP14x89	26.1	13.8	0.615	14.7	0.615	904	326	131	44.3	146	67.7

4.6.1.2 Soil Model

Soil surrounding the piles on both end bents was simplified as illustrated in Figure 4.10. Table 4.6 provides soil properties used in the analysis for Bents 1 and 11. As indicated in Figure 4.10, elastic springs were placed on the pile elements every foot for the first 35 ft below the ground level, every 5 ft for the next 10 ft, and every 10 ft for the rest of the pile length. For this analysis, the ground water table was assumed to be at ground level. The actual ground water table was approximately 4.2 ft and 5.9 ft below ground level for Bents 1 and 11, respectively. The spring stiffness for SAP2000 models was calculated according to Section 4.4.2 and the values of the soil spring stiffness are provided in Appendix G.

Table 4.6: Soil Properties on Bents 1 and 11 (SR249 over US12)

BENT 1							
Begin Depth (ft)	**End Depth (ft)**	**Soil Type**	**γ (lb/ft^3)**	**k (lb/in.^{3})**	**ϕ (degrees)**	**c_u (lb/in.^{2})**	**ε_{50} (in./in.)**
0	5	loose sand	55	20	30	-	-
5	10	med. sand	60	60	35	-	-
10	20	soft clay	50	30	-	2.6	0.02
20	25	stiff clay	60	500	-	10.4	0.01
25	35	loose sand	55	20	30	-	-
35	45	soft clay	50	30	-	2.6	0.02
45	115	med. sand	60	60	35	-	-

BENT 11							
Begin Depth (ft)	**End Depth (ft)**	**Soil Type**	**γ (lb/ft^3)**	**k (lb/in.^{3})**	**ϕ (degrees)**	**c_u (lb/in.^{2})**	**ε_{50} (in./in.)**
0	10	loose sand	55	20	30	-	-
10	15	soft clay	50	30	-	2.6	0.02
15	35	med. sand	60	60	35	-	-
35	45	soft clay	50	30	-	2.6	0.02
45	145	med. sand	60	60	35	-	-

4.6.1.3 Results

4.6.1.3.1 Deflected Shapes

The deflected shapes for the piles of Bents 1 and 11 are presented in Figures 4.11 and 4.12, respectively. The deflected shapes calculated using LPILE PLUS and SAP2000 correlate well. Differences in the deflected shape occur because the soil spring stiffness using LPILE PLUS is slightly stiffer than that used in the SAP2000 analysis. As illustrated in Table 4.7, for the pile models with a roller at the top of the pile, the average inflection point depths determined from the deflected shapes are 21.9 ft and 23.5 ft for Bents 1 and 11, respectively. For the pile models with a fixed support at the top of the pile, the average inflection point depths are 2.3 and 2.9 ft above ground level for Bents 1 and 11. The difference in the inflection point depths occurs because the pile models with

a roller support at the top of the pile bend in single curvature, while the pile models with a fixed support at the top of the pile bend in double curvature. Therefore, the inflection point depths of the pile models with a fixed support are higher than those with a roller support. These results indicate that the inflection point depth varies from -2.3 ft to 23.5 ft.

The location where lateral movement of the pile does not occur was also determined. A comparison of the depth that provides zero lateral displacement is presented in Table 4.8. The depths that provide zero lateral displacement do not change significantly. On average, this depth was calculated as 28.5 ft.

4.6.1.3.2 Moment vs. Depth

The moments along the pile length for Bents 1 and 11 are presented in Figures 4.13 and 4.14, respectively. The results indicate good correlation between the two analysis methods. The moments at ground level obtained from both analyses were compared with calculated moments from strain gages on Pile 5 of Bent 1 and Pile 2 of Bent 11 as tabulated in Table 4.9. Since strain gages on piles were zeroed and started reading after the bridge was cast, all strain values are relative. The strain values were assumed to be caused by flexure only. Strain on the opposite face of the pile was assumed to equal to the same value as the strain read by the gage on the other face but of different sign. The values of strains on the coldest day (December 22, 2000 at 8:00AM) were approximately 240 με and 800 με of Bents 1 and 11, respectively. Based on these assumptions, moments at ground level were calculated to be 75 ft-k on Bent 1 and 250 ft-k on Bent 11. One can note that the strain gage on Pile 2 of Bent 11 was not reliable because strain decreased very significantly compared to that of Pile 5 of Bent 1 during cold weather and changed to approximately the same value of strain of Bent 1 during warm weather as indicated in Figure 3.15. Therefore, only moment calculated from the strain gage on Pile 5 of Bent 1 will be considered. It appears that the moments at ground level calculated based on the strain gage measurement is between those calculated based on the roller- and fixed-support models. However, this abutment-pile connection behaves closer to a hinged connection rather than a fixed connection.

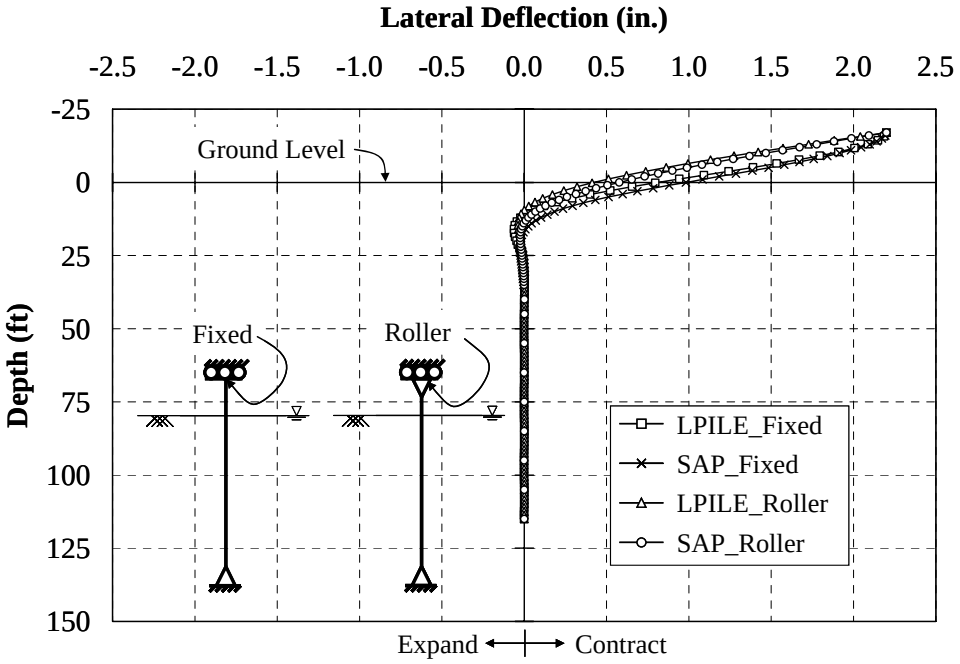

Figure 4.11: Deflected Shape of the Pile of Bent 1 (SR249 over US12)

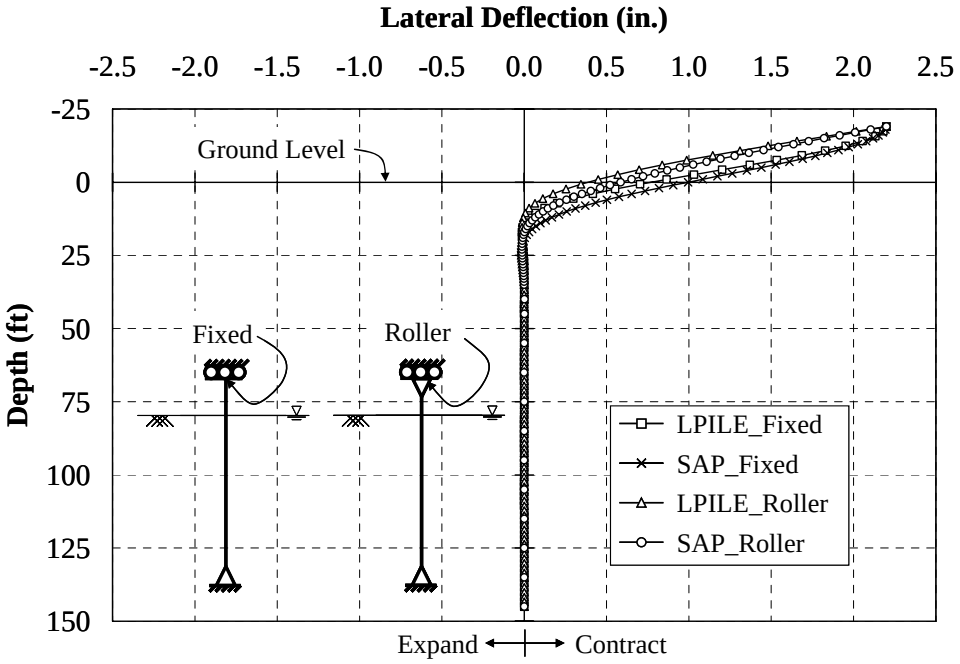

Figure 4.12: Deflected Shape of the Pile of Bent 11 (SR249 over US12)

Table 4.7: Inflection Point (SR249 over US12)

Bent	Inflection Point for Roller Model* (ft)		
	LPILE	SAP	Average
1	19.7	24.0	21.9
11	19.1	27.9	23.5

Bent	Inflection Point for Fixed Model* (ft)		
	LPILE	SAP	Average
1	-2.7	-1.8	-2.3
11	-3.7	-2.1	-2.9

* Depths measured from ground surface. Positive indicates depth below ground

Table 4.8: Depth of Zero Lateral Displacement (SR249 over US12)

Bent	Depth of Zero Lateral Displacement for Roller Models (ft)		
	LPILE	SAP	Average
1	23.9	31.0	27.5
11	22.0	30.0	26.0

Bent	Depth of Zero Lateral Displacement for Fixed Models (ft)		
	LPILE	SAP	Average
1	27.9	35.0	31.5
11	25.3	33.0	29.2

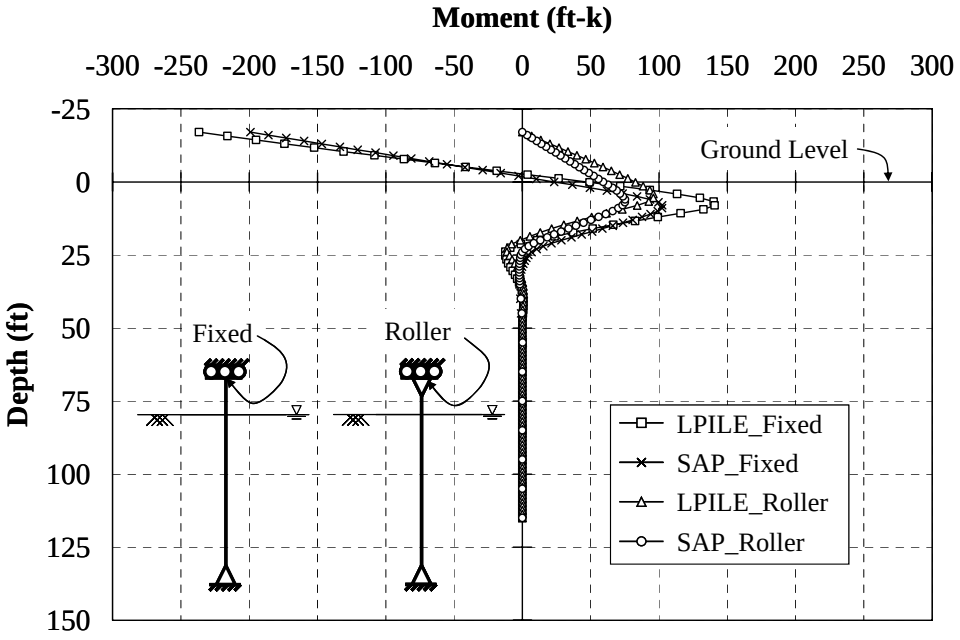

Figure 4.13: Moment vs. Depth of the Pile of Bent 1 (SR249 over US12)

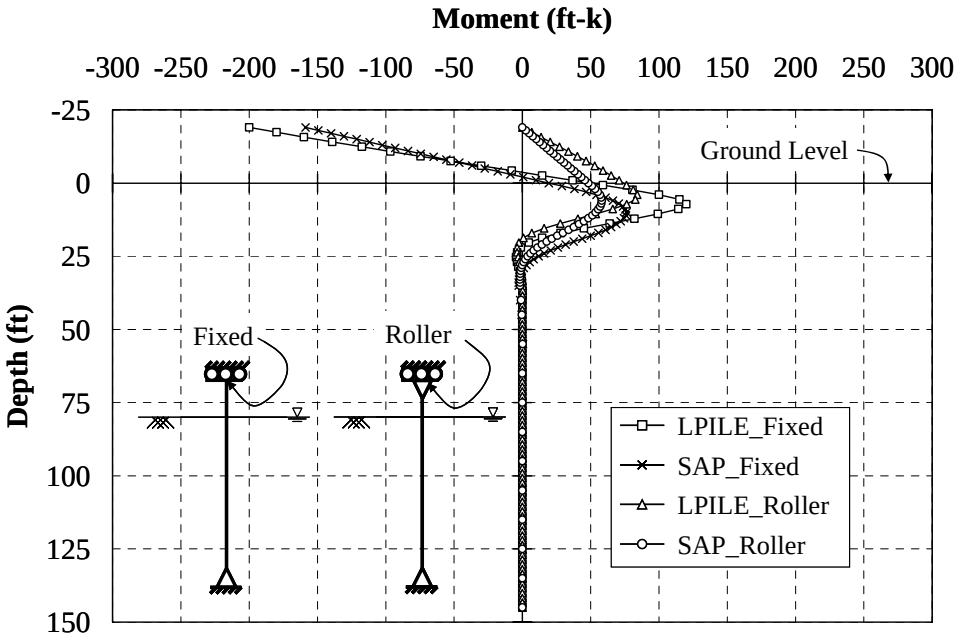

Figure 4.14: Moment vs. Depth of the Pile of Bent 11 (SR249 over US12)

Table 4.9: Moments at Ground Level (SR249 over US12)

Bent	Moment at Ground Level of Roller Models (ft-k)		
	LPILE	SAP	Strain Gage
1	82	59	75
11	74	48	253*

Bent	Moment at Ground Level of Fixed Models (ft-k)		
	LPILE	SAP	Strain Gage
1	47	23	75
11	50	19	253*

***** Questionable Value

4.6.2 I65 over SR25 Bridges

Due to insufficient field data to verify the deflected shape of the pile supporting the end bents, the deflected shape cannot be estimated using the field data. However, the estimated deflected shapes from the LPILE PLUS and SAP2000 analyses are presented and compared. In addition, the magnitude of strains at the base of the abutment is compared with the analytical results.

4.6.2.1 Pile Model

HP12x53 piles bending about their weak axis and CFT14.5x0.25 piles were modeled for the piles supporting the end bent. An approximate total pile length of all end bents is 42 ft, and the piles were embedded 2 ft in the abutment; therefore, the pile length below ground level is 40 ft. According to Durbin (2001), since the abutments only translate over temperature change, only the pile length below ground line will be considered.

The pile was modeled having a horizontally-guided support at the top and a pin connection at the bottom as illustrated in Figure 4.15. The total axial load applied on the ten piles of each bent is 156 kips according to bridge design calculations (Section 2.3.1.2). The H piles were subjected to an axial load of 11.1 kips, while the CFT piles were subjected to an axial load of 21.9 kips based on the axial stiffness of each pile. The piles were subjected to a lateral movement of 0.55 in. calculated by Equation 4-17,

$$\Delta L = \alpha(\Delta T)L \qquad (4\text{-}17)$$

where:

α = coefficient of thermal expansion for steel taken as 6.5×10^{-6} /°F.

ΔT = temperature change of 92° F taken on the coldest day for the northbound structure (December 25, 2000 at 19:00).

L = half of the total bridge length, taken as 152 ft/2 = 76 ft.

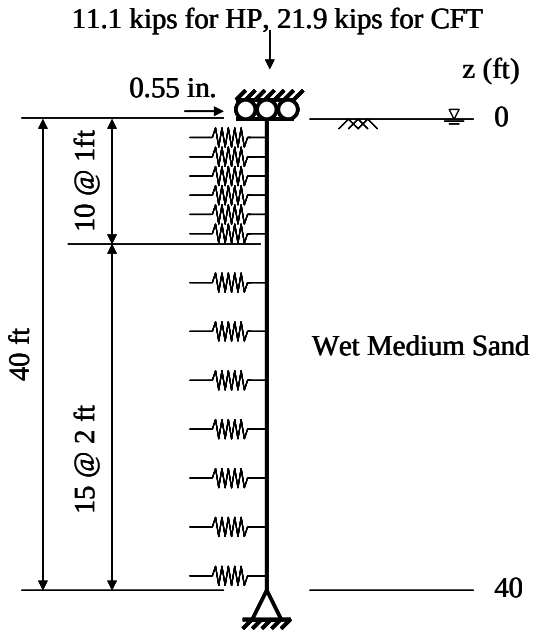

Figure 4.15: Pile Model (I65 over SR25)

For the LPILE PLUS model, the equivalent area and moment of inertia of the CFT piles and the equivalent diameter of the H piles were computed and are listed in Table 4.10. The specified compressive strength of concrete, f'_c is taken as 4,000 psi (INDOT Class C concrete), and the specified yield strength of steel is taken as 60 ksi for the H piles and 35 ksi for the CFT piles, respectively. The modulus of elasticity of concrete and steel is assumed to be 3,605 ksi and 29,000 ksi, respectively.

Table 4.10: Summary of Pile Properties for LPILE

Pile Section	A (in.^{2})	d (in.)	I (in.^{4})
HP12x53	15.5	11.8*	127
CFT	30.3**	14.5	519**

* equivalent diameter, ** transformed section

For the SAP2000 model, cross-sectional properties are required. The H pile cross section properties are provided in Table 4.11, and the CFT pile cross section properties are provided in Table 4.12.

Table 4.11: Cross Section Properties of HP12x53

Pile Section	A (in.^{2})	d (in.)	t_w (in.)	b_f (in.)	t_f (in.)	I_x (in.^{4})	I_y (in.^{4})	S_x (in.^{3})	S_y (in.^{3})	Z_x (in.^{3})	Z_y (in.^{3})
HP12x53	15.5	11.8	0.435	12.0	0.435	393	127	66.7	21.1	74.0	32.2

Table 4.12: Cross Section Properties of CFT14.5x0.25

Pile Section	Outer Diameter (in.)	Inner Diameter (in.)	Wall Thickness (in.)
CFT14.5x0.25	14.5	14.0	0.25

4.6.2.2 Soil Model

The analysis models considered the HP12x53 and CFT14.5 piles embedded 40 ft in a medium density sand. Elastic springs were placed along the pile length to represent soil resistance. For this analysis, the ground water table was assumed to be at ground level, and the effective unit weight of medium sand was therefore assumed to be 60 lb/ft^3. One can note that the actual ground water table varied from 6.5 ft to 22.5 ft below ground level. A summary of the soil properties for both LPILE PLUS and SAP2000 models is listed in Table 4.13. For the SAP2000 models, elastic springs were placed on the pile elements every foot for the first 10 ft below the ground level and every 2 ft for the next 30 ft as indicated in Figure 4.15. The soil spring stiffness was determined according to Section 4.4.2.2 and is listed in Appendix G.

Table 4.13: Soil Properties (I65 over SR25)

Begin Depth (ft)	End Depth (ft)	Soil Type	γ (lb/ft^3)	k (lb/in.^{3})	ϕ (degrees)
0	40	Med. Sand	60	60	35

4.6.2.3 Results

4.6.2.3.1 Deflected Shapes

The deflected shapes of the H and CFT piles are presented in Figures 4.16 and 4.17, respectively. For both pile types, the deflected shapes from LPILE PLUS and SAP2000 provide good correlation. Again, it should be noted that the soil models in LPILE PLUS are slightly stiffer than those used for the SAP2000 analysis. As shown in Table 4.14, the inflection points for both models are fairly constant with an average of 4.6 ft for the H piles and 6.1 ft for the CFT piles. The depths of zero lateral displacement are listed in Table 4.15. The depth of zero displacement based on the SAP2000 analysis is deeper than that based on LPILE PLUS.

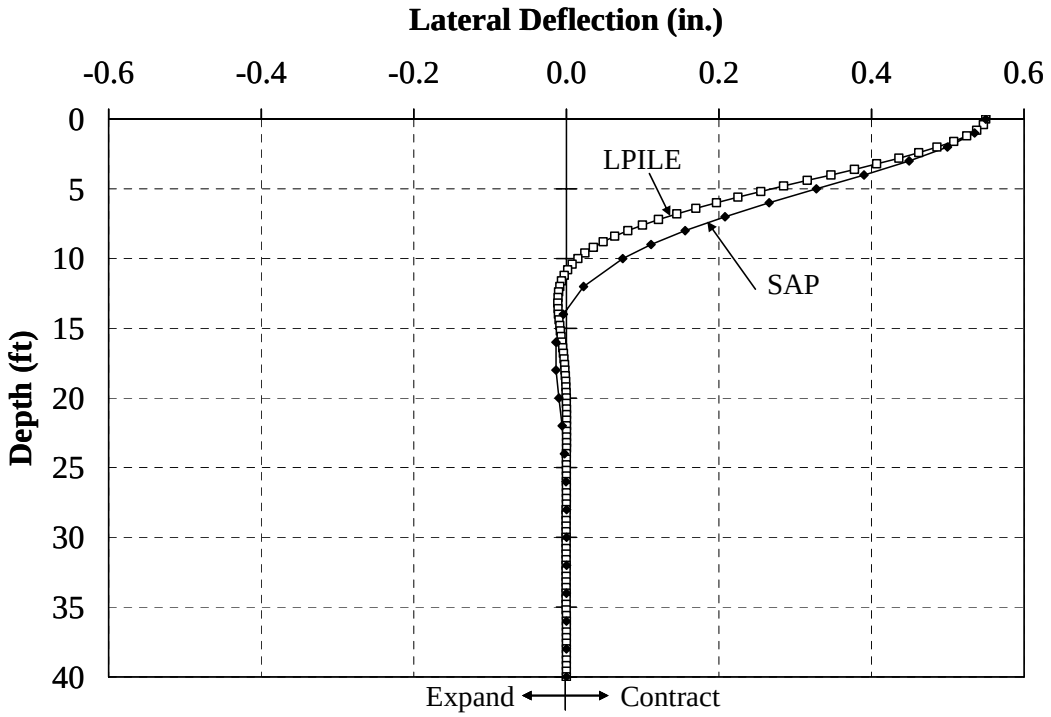

Figure 4.16: Deflected Shape of the H Pile (I65 over SR25)

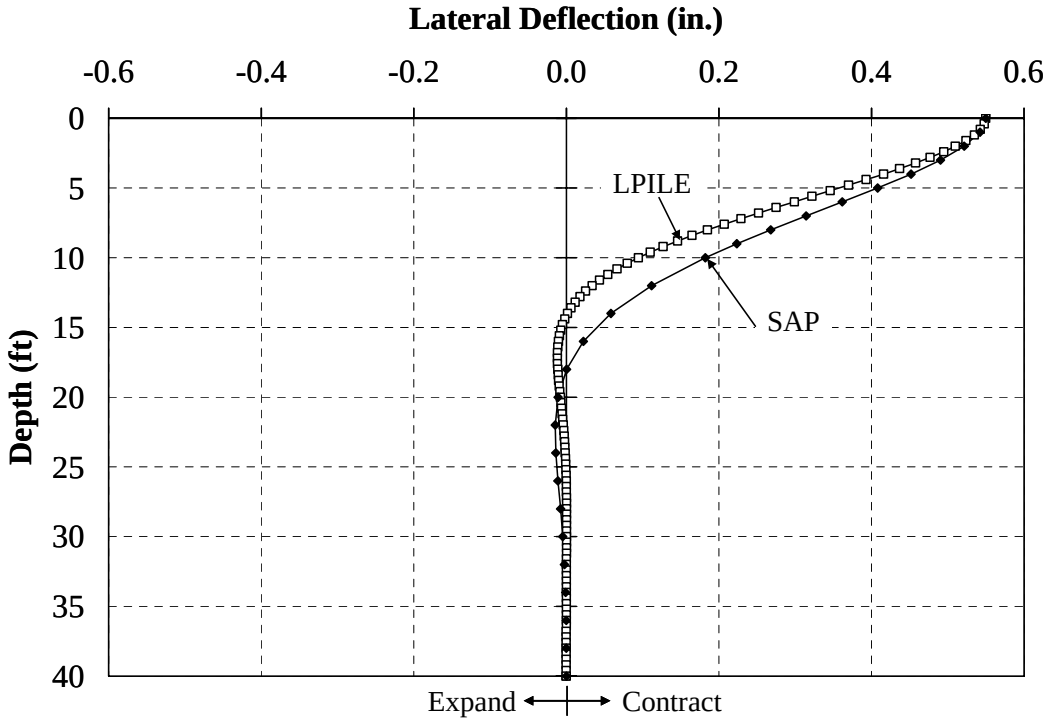

Figure 4.17: Deflected Shape of the CFT Pile (I65 over SR25)

Table 4.14: Inflection Point (I65 over SR25)

Pile Section	Inflection Point (ft)		
	LPILE	SAP	Average
HP12x53	4.3	4.9	4.6
CFT14.5	5.6	6.5	6.1

Table 4.15: Depth of Zero Lateral Displacement (I65 over SR25)

Pile Section	Depth of Zero Lateral Displacement (ft)		
	LPILE	SAP	Average
HP12x53	16.4	23.0	19.7
CFT14.5	21.6	29.0	25.3

4.6.2.3.2 Moment vs. Depth

The moments along the pile length for the H and CFT piles calculated using LPILE PLUS and SAP2000 are presented in Figures 4.18 and 4.19, respectively. The moment curves obtained by both analysis methods have the same trend. The moments calculated using LPILE PLUS are slightly higher than analyzed using SAP2000. This results from the smaller depth of zero displacement noted in the LPILE analysis. The depth that the pile does not rotate, defined as the depth of zero rotation, is listed in Table 4.16. As shown, the depth of zero rotation is approximately the same according to both methods. A comparison of the moments at ground level is tabulated in Table 4.17. The moments at ground level calculated from strain gages on Piles 2, 6, and 7 of the south end of the northbound structure are -28, -10, and 8 ft-k which are much less than the moments calculated based on this analysis. It should be noted that Piles 2 and 6 of the south end of the northbound structure are H piles, while Pile 7 is a CFT pile. The difference in moments is likely due to softening of the soil surrounding the piles caused by cyclic response or possible softening of the abutment-pile connection.

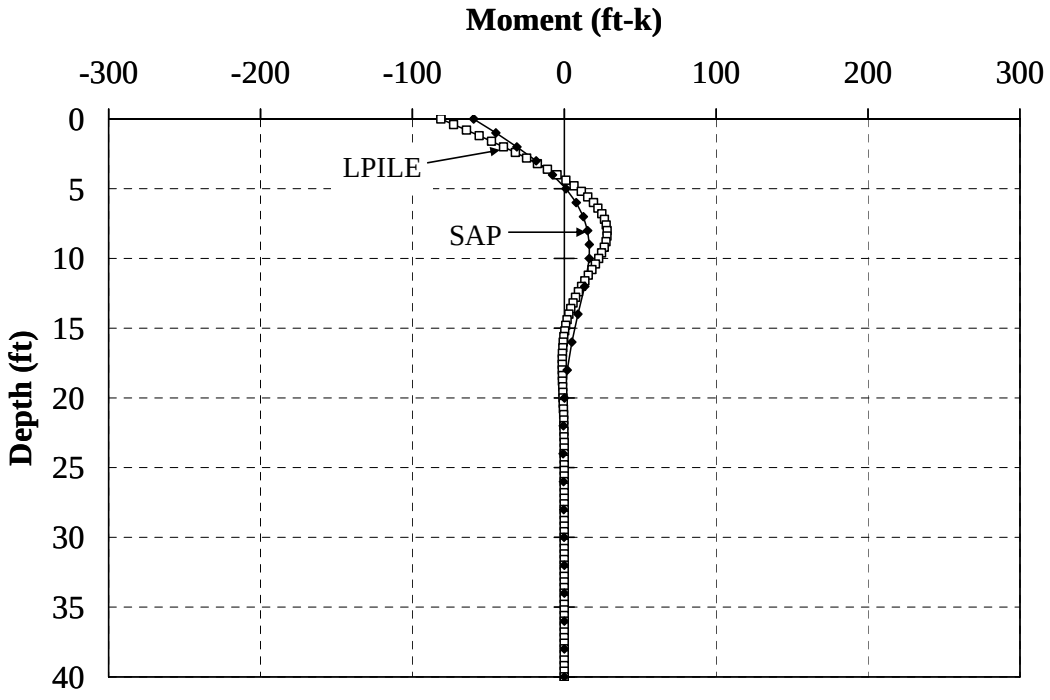

Figure 4.18: Moment vs. Depth of the H Pile (I65 over SR25)

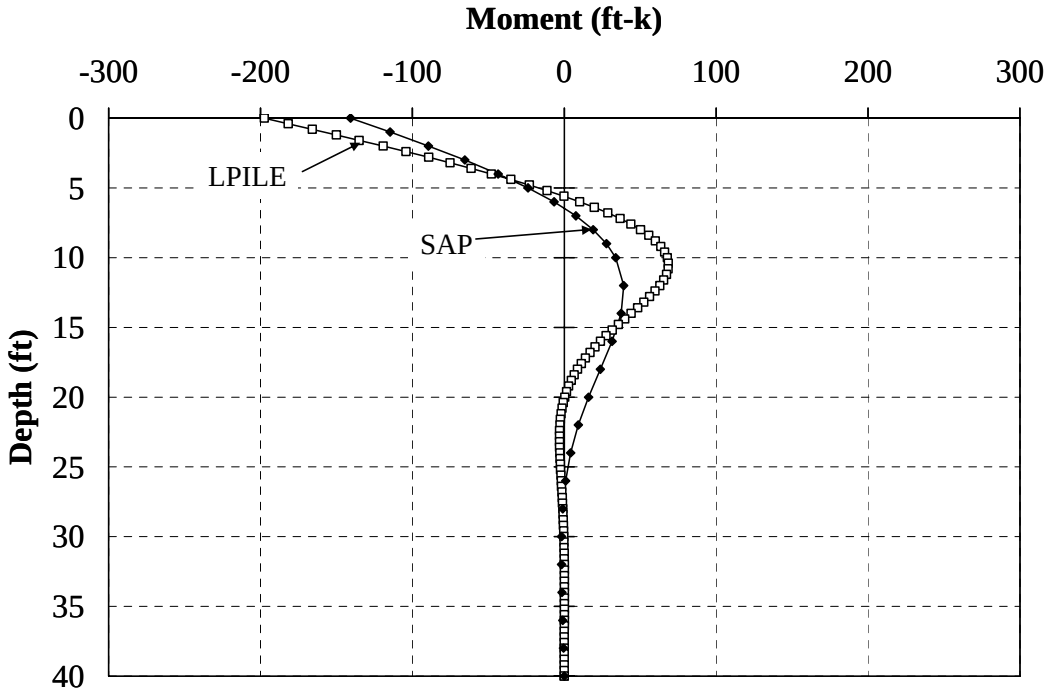

Figure 4.19: Moment vs. Depth of the CFT Pile (I65 over SR25)

Table 4.16: The Depth of Zero Rotation (I65 over SR25)

Pile Section	Depth of Zero Rotation (ft)		
	LPILE	SAP	Average
HP12x53	20.0	20.0	20.0
CFT14.5	28.0	27.0	27.5

Table 4.17: Moments at Ground Level (I65 over SR25)

Pile Section	Moment at Ground Level (ft-k)		
	LPILE	SAP	Average
HP12x53	-81	-60	-70
CFT14.5	-198	-141	-169

4.6.3 SR18 over Mississinewa River Bridge

Pile 6 of Bent 1 was modeled in two different soil types. The deflected shapes and moments along the length of the pile were calculated using LPILE PLUS and SAP2000 and compared. Due to nearly complete strain data obtained along the length of this pile, the calculated deflections and moments were also compared with the deflections and moments calculated using strain data from the bridge.

4.6.3.1 Pile Model

The 14-in. concrete-filled steel tube pile having a 14-in. outer diameter and 0.312-in. wall thickness (CFT14.0x0.312) was modeled. The total length of the pile as driven in the field is 23.50 ft. The pile was embedded 15 in. into the abutment, and thus the pile length below ground level is 22.25 ft (267 in.). This value was used in the analysis (Figure 4.20). The specified compressive strength of concrete was 4,000 psi (INDOT Class C), while the specified yield strength of steel was 35 ksi according the ASTM A252 Grade 2 steel. The modulus of elasticity of concrete and steel are 3,605 ksi and 29,000 ksi, respectively.

The CFT14 pile was modeled having a horizontally-guided support at the top and a hinge at the bottom as illustrated in Figure 4.20. The pile was subjected to axial load of

80 kips according to bridge design calculations (Section 2.4.1.2) and a lateral movement of 0.38 in. based on measurements provided by the convergence meter at 0° F (maximum temperature change, ΔT = -60° F).

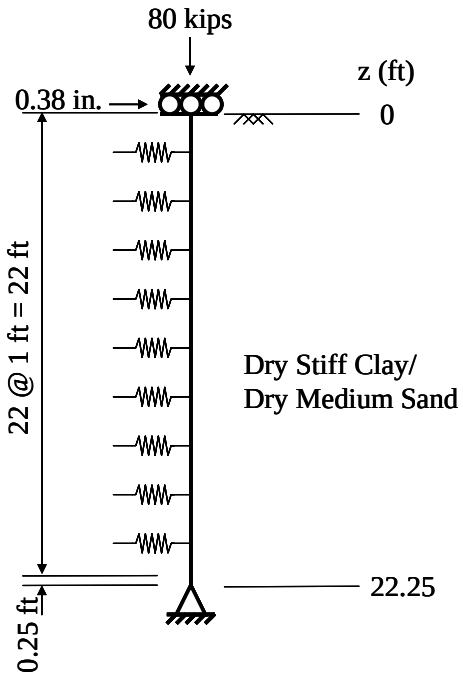

Figure 4.20: Pile Model (SR18)

For both LPILE PLUS and SAP2000 models, the transformed section of CFT pile was needed. The equivalent area, outer diameter, and moment of inertia of the equivalent steel section were computed and are listed in Table 4.18

Table 4.18: Cross Section Properties of CFT14

Pile Section	A_e (in.^{2})	d (in.)	I_e (in.^{4})
CFT14.0x0.312	30.9	14.0	510

4.6.3.2 Soil Model

Soils surrounding the pile consist of mostly silt, which is a combination of sand and clay. Soil spring models are not available in the present literature; therefore, two different analysis cases were considered. The first case considered is dry medium density

sand, and the second case is dry stiff clay. These cases were considered most similar to the in-site strength of soil as obtained from the soil borings. For each case, soil surrounds the pile from ground level to the bottom of the pile. The ground water level was measured deeper than 22.25 ft from ground level. Therefore, the unit weight of dry medium sand and dry stiff clay is assumed to be 120 lb/ft.^{3} The soil properties tabulated in Table 4.19 are used for both the LPILE and SAP models. For SAP models, elastic springs were placed on the pile elements every foot along the pile length as indicated in Figure 4.20. The soil spring stiffnesses were calculated according to Section 4.4.2 and are provided in Appendix G.

Table 4.19: Soil Properties (SR18)

Case	Begin Depth (ft)	End Depth (ft)	Soil Type	γ (lb/ft^3)	k (lb/in.^{3})	ϕ (degrees)	c_u (lb/in.^{2})	ε_{50} (in./in.)
I	0	22.25	Med. Sand	120	60	35	-	-
II	0	22.25	Stiff Clay	120	500	-	10.4	0.01

4.6.3.3 Results

4.6.3.3.1 Deflected Shapes

Comparisons of the deflected shapes of the pile embedded in dry medium sand and dry stiff clay are presented in Figures 4.21 and 4.22, respectively. The deflected shapes calculated using LPILE PLUS and SAP2000 correlate very well. The model for both dry medium sand and dry stiff clay used in LPILE PLUS is slightly stiffer than that used in the SAP2000 analysis. It can be seen that both models slightly underestimate the measured deflected shape for both soil types. It can be concluded, however, that the analytical results in general are in excellent agreement with the results from the strain gages. The inflection points are tabulated in Table 4.20. The inflection points obtained from the two models are fairly constant. On average, the inflection point is located approximately 5 ft from the ground level which corresponds to the location of inflection point expected based on the strain gage measurements.

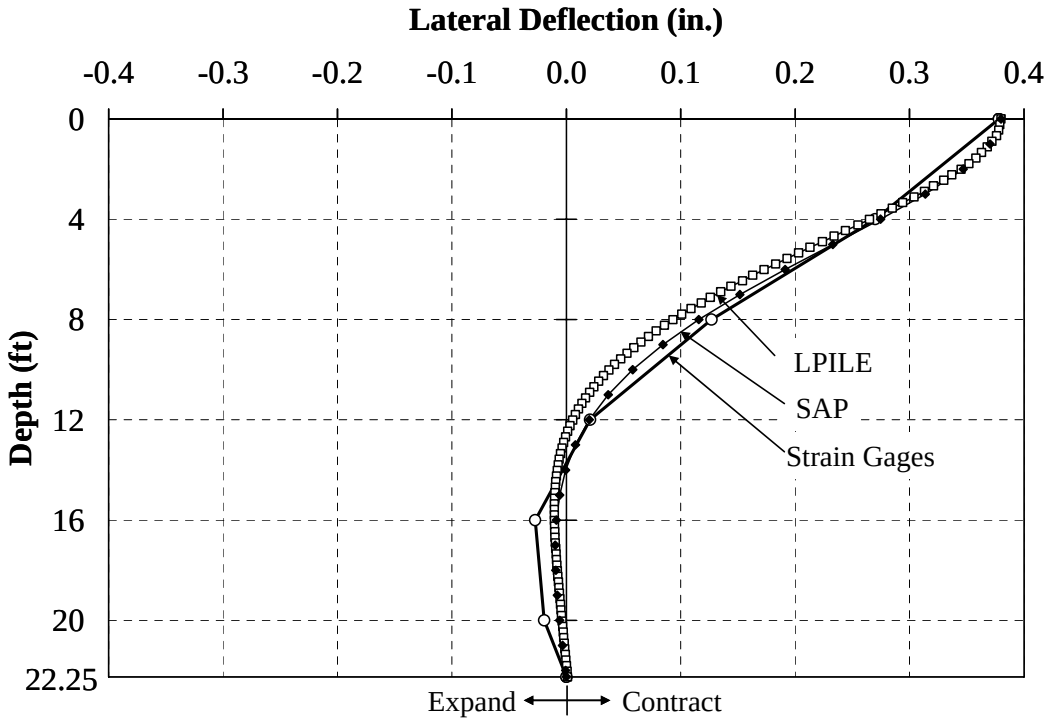

Figure 4.21: Deflected Shape of the Pile surrounding in Dry Medium Sand (SR18)

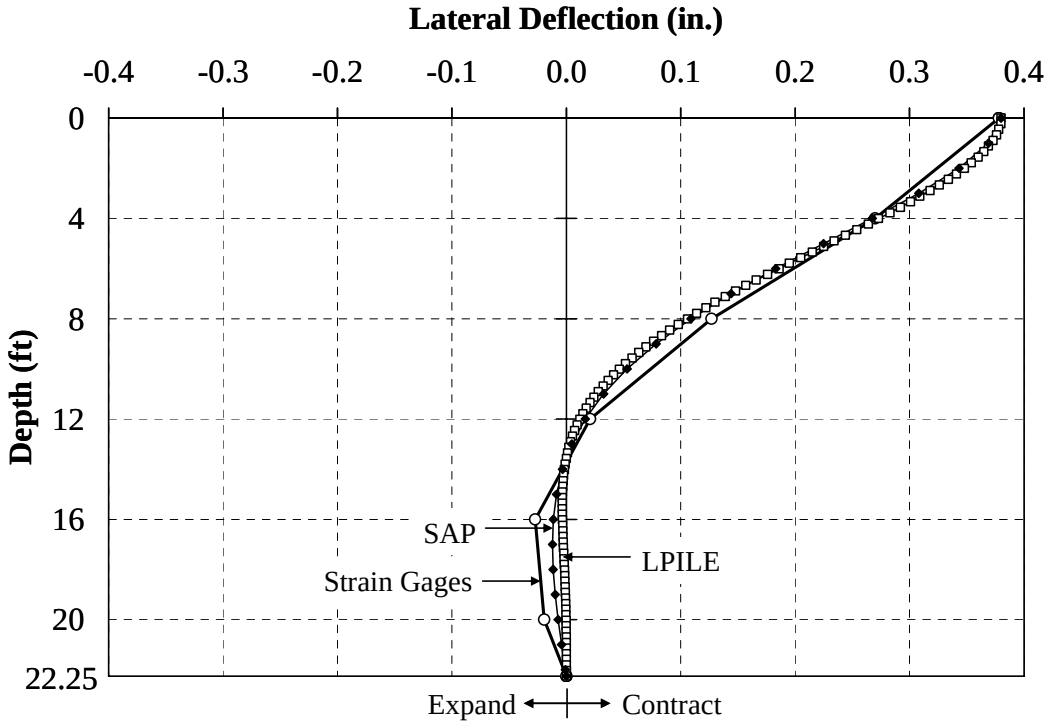

Figure 4.22: Deflected Shape of the Pile surrounding in Dry Stiff Clay (SR18)

Table 4.20: Inflection Point (SR18)

Soil Type	Inflection Point (ft)			
	LPILE	SAP	Average	Strain Gages
Dry Medium Sand	4.8	5.0	4.9	Between 4 and 8
Dry Stiff Clay	5.1	4.7	4.9	Between 4 and 8

4.6.3.3.2 Moment vs. Depth

Moments along the pile length calculated using LPILE PLUS and SAP2000 are presented in Figures 4.23 and 4.24, respectively. Moments calculated using both analysis methods provide the same trend. The results indicate that above the depth of approximately 13 ft, both dry medium sand and dry stiff clay models used in LPILE PLUS is slightly stiffer than that used in the SAP2000 analysis. The strain gage measurements also suggest that the soil spring stiffnesses are overestimated. Below the depth of approximately 13 ft, both soil models used in LPILE PLUS are less stiff than that used in the SAP2000 analysis and that determined from the strain gage measurements. Moments at ground level estimated using the two models were compared to the moments calculated using measured strains from Pile 6 as shown in Table 4.21. For both soil cases, the results show that the calculated moments at ground level using strain values are approximately 50% less than those obtained based on analysis. The difference may be caused by softening of the soil near ground level or softening of the abutment-pile connection which reduces the moment at ground level. It can be observed that above a depth of approximately 13 ft, the analyses overestimated the bending moments while they underestimated the moment below this depth.

Based on these results, it appears that from ground level to a depth of approximately 13 ft, the analytical soil models are slightly stiffer than the actual soils in the field while below a depth of approximately 13 ft, the soil models are softer than those present in the field. Overall, both analysis methods calculated the deflected shapes well. However, the bending moment was slightly overestimate.

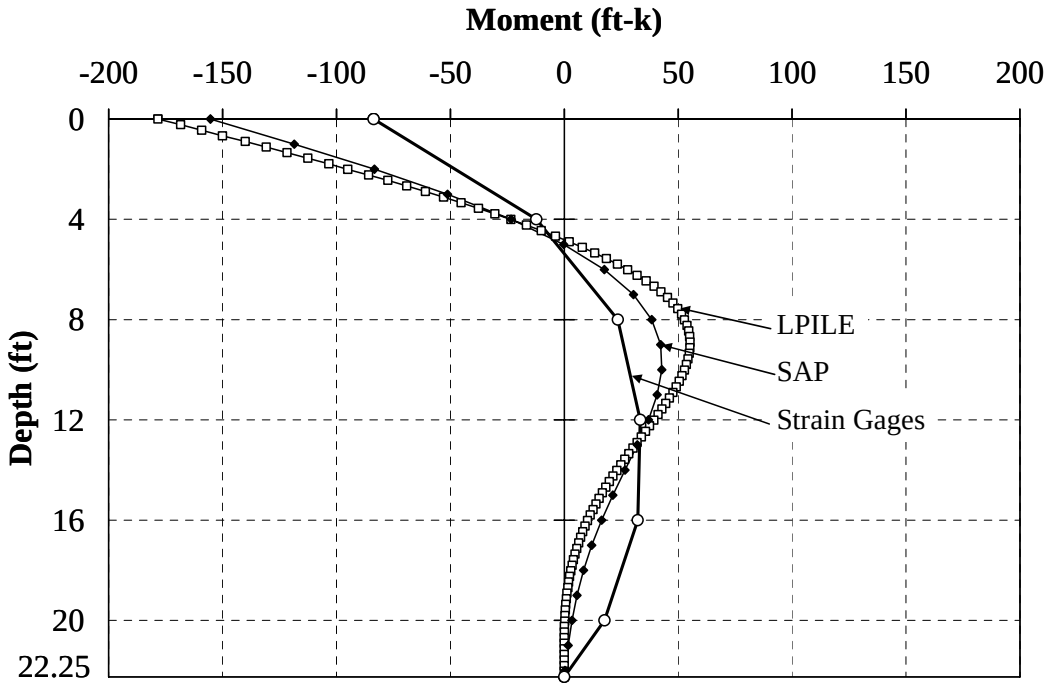

Figure 4.23: Moment vs. Depth of the Pile in Dry Medium Sand (SR18)

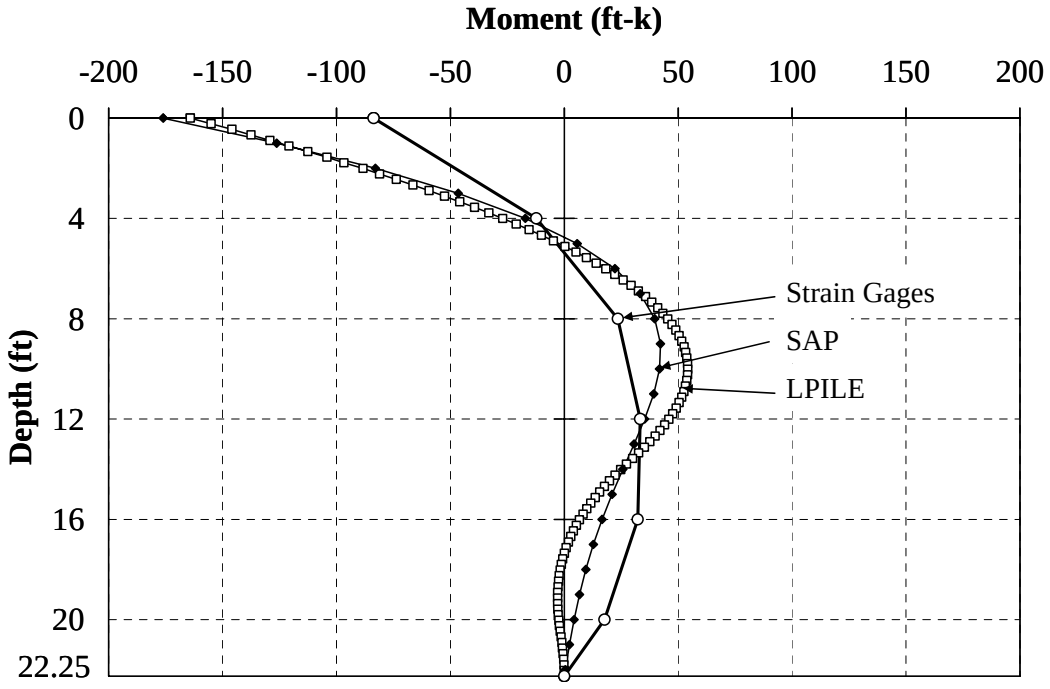

Figure 4.24: Moment vs. Depth of the Pile in Dry Stiff Clay (SR18)

Table 4.21: Moment at Ground Level (SR18)

Soil Type	Moment at Ground Level (ft-k)			
	LPILE	SAP	Average	Strain Gages
Dry Medium Sand	178	155	167	84
Dry Stiff Clay	164	176	170	84

4.7 Parametric Study

To evaluate the behavior of typical piles used in Indiana bridge construction, piles were modeled with a horizontally-guided support at the top of the pile. This support condition is representative of normal abutment-pile connection details and provides a reasonable model of actual behavior. According to the results described earlier in this chapter, LPILE PLUS provides results approximately the same as from the SAP2000 analysis. Therefore, all parametric studies were performed using LPILE PLUS due to the ease of use of this analysis package.

4.7.1 Variables

The parametric study investigated the effect of the following variables: lateral displacement, axial load, pile length, pile type, pile orientation, and soil type.

4.7.1.1 Lateral Displacement

Lateral movements, ΔL, of 1, 2, and 4 in. were investigated for all pile models unless otherwise stated. These lateral movements were calculated based on Equation 4-17,

$$\Delta L = \alpha(\Delta T)L \qquad (4\text{-}17)$$

where:

α = coefficient of thermal expansion of steel, taken as 6.5×10^{-6} /°F.

ΔT = temperature change, taken as 25, 50, and 100° F.

L = half of the total bridge length, taken as 1000 ft/2 = 500 ft.

4.7.1.2 Axial Load

According to INDOT Memorandum #233 (INDOT, 1992a), piles used in integral end bents shall be stressed to no more than 9 ksi. To evaluate the effect of the axial load, axial stresses of 0, 9, and 18 ksi were investigated unless otherwise stated.

4.7.1.3 Pile Length

In typical bridge construction, piles are driven until they reach a hard soil layer or their required bearing capacity. Even though the pile reaches a given depth based on axial capacity, the pile length may not be long enough to provide fixity at the bottom of the pile considering lateral displacements. To evaluate the appropriate length, L, such that the pile does not displace or rotate at the bottom, piles with lengths varying from 15 to 100 ft were analyzed with the assumption of that the bearing capacity of the pile is sufficient.

4.7.1.4 Pile Type

According to INDOT Memorandums #233 and #243 (INDOT, 1992a and INDOT, 1992b), only steel H pile and steel-encased concrete (SEC) or concrete-filled steel tube (CFT) pile shall be permitted for integral end bents. HP10x42 and HP12x53 piles are the most common H pile sections, while HP14x89 can be used for higher load capacities. In addition, CFT piles with an outer diameter of 14 in. and with a wall thickness of 0.213, 0.250, and 0.312 in. (CFT14x0.213, CFT14x0.250, and CFT14x0.312) are suggested according to INDOT Memorandum #243 (INDOT, 1992b). Therefore, two types of piles were investigated: steel H piles including HP10x42, HP12x53, and HP14x89 and CFT piles including CFT14x0.213 and CFT14x0.312 piles. The pile type and size were considered to evaluate the minimum pile lengths that can be provided for the piles recommended by INDOT. Section properties for these piles are provided in Table 4.22.

Table 4.22: Section Properties in Parametric Study*

Pile Type	Bending Axis	A ($in.^2$)	d_e (in.)	I ($in.^4$)	A_s ($in.^2$)	P (kips)
HP10x42	Weak	12.4	9.7	71.7	12.4	112
	Strong	12.4	10.1	210	12.4	112
HP12x53	Weak	15.5	11.8	127	15.5	140
	Strong	15.5	12.0	393	15.5	140
HP14x89	Weak	26.1	13.8	326	26.1	235
	Strong	26.1	14.7	904	26.1	235
CFT14x0.203	-	26.8	14.0**	418	8.8	79
CFT14x0.312	-	30.9	14.0**	510	13.4	120

*Cross sectional area and moment of inertia of CFT sections are based on steel transformed section

**Equivalent diameter of CFT section is equal to its outer diameter

4.7.1.5 Pile Orientation

According to INDOT Memorandum #233 (INDOT, 1992a), piles bending about their weak axis are recommended. However, piles in some integral bridges are oriented for bending about the strong axis (for example, the SR249 over US12 bridge). Therefore, H piles bending about both weak and strong axes as well as CFT piles bending about one symmetric axis were analyzed. The moments of inertia of each section are provided in Table 4.22.

4.7.1.6 Soil Type

To simplify the parametric study, each pile was modeled to be embedded in one soil layer. Two soil types considering various strengths were used in the analyses. Soil types include clay (soft, stiff, very stiff) and sand (loose, medium, dense). The properties of these soil types are provided in Table 4.23. The ground water table is assumed to be at ground level for all analyses; therefore the effective unit weight of soil is used. This is a conservative assumption. The effective unit weight of soil, γ, and the friction angle, ϕ, are in accordance with Greimann (1987). The values of the parameter, k, are based on Reese et al. (1974). The undrained shear strength, c_u, and the strain, ε_{50}, are as suggested by the LPILE PLUS User's manual (Reese et al., 2000b).

Table 4.23: Soil Properties in Parametric Study

Soil Type	Soil Consistence	γ (lb/ft^3)	k (lb/in.^{3})	ϕ (degrees)	c_u (lb/in.^{2})	ε_{50} (in./in.)
Clay	Soft	50	30	-	2.6	0.020
	Stiff	60	500	-	10.4	0.010
	Very Stiff	65	1000	-	20.8	0.005
Sand	Loose	55	20	30	-	-
	Medium	60	60	35	-	-
	Dense	65	125	40	-	-

4.7.2 Results of Parametric Study

Axial load, pile length, pile orientation, and pile type are of interest in evaluating their effect on the deflected shape and bending moment along the length of the pile as well as the inflection point depth, the zero lateral deflection depth, and the zero moment depth of the pile.

4.7.2.1 Effect of Axial Load

Piles for the SR249 over US12 and the SR18 over Mississinewa River bridges were modeled to evaluate the effect of axial load on the deflected shape and bending moment along the length. It should be noted that that LPILE PLUS accounts for of P-Δ effects.

The model of the pile of Bent 1 of SR249 over US12 described in Section 4.6.1 was used. The top of the pile was modeled with a roller. The pile was subjected to lateral displacement of 2.2 in. based on the extrapolated end bent movement in Section 3.5.1.3 and to an axial load of 0, 200, and 400 kips (0, 7.7, 15.4 ksi). The axial load of 200 kips was based on the bridge design calculations in Section 2.2.1.2. Soil properties are provided in Table 4.6. The results are presented in Figures 4.25 and 4.26.

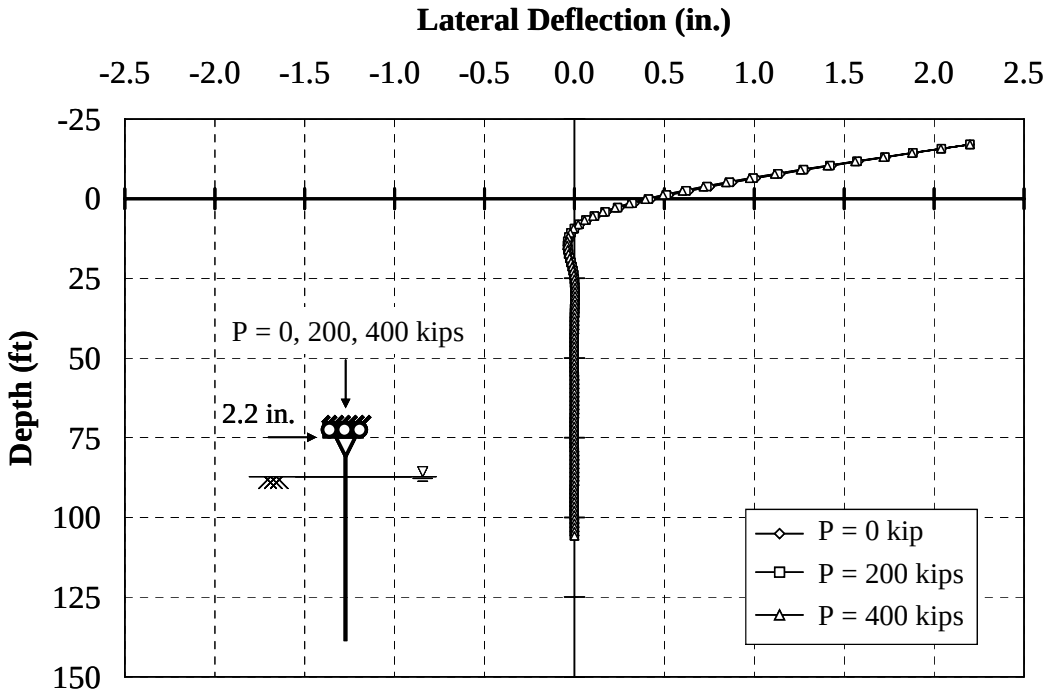

Figure 4.25: Effect of Axial Load on Lateral Deflection (SR249 over US12)

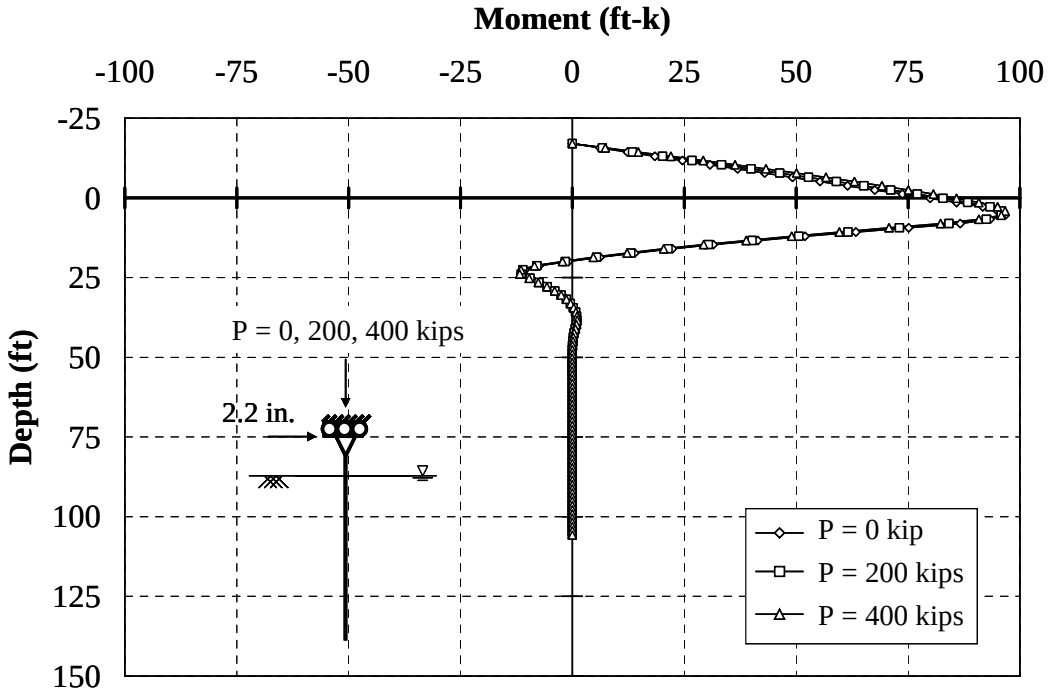

Figure 4.26: Effect of Axial Load on Bending Moment (SR249 over US12)

Another example is the pile for SR18 over the Mississinewa River. The pile was modeled with a horizontally-guided support at the top of the pile. The pile embedded in medium sand was subjected to lateral displacements of 0.38 in. and 4.0 in. Soil properties are provided in Table 4.23. The lateral displacement of 0.38 in. is the average bridge movement measured by the convergence meter located at the center of Bent 1 of the SR18 bridge during a temperature change ranging from -63° F to -57° F (ΔT = -60° F). The large lateral displacement of 4 in. is calculated based on Equation 4-17, where ΔT is taken as 100° F for a hypothetical 1000 ft bridge. Axial stresses of 0, 9, and 18 ksi (P = 0, 121, and 242 kips) were applied at the top of the pile. The results are presented in Figures 4.27 and 4.28. Based on both of these analyses, the axial load has an insignificant effect on both the deflected shape and bending moment along the length of the pile.

4.7.2.2 Effect of Pile Length

The effect of pile length was evaluated. Of particular interest was the length required such that the lateral displacement and rotation at the bottom of the pile were eliminated. To illustrate the effect of length, an analysis was performed for an HP12x53 pile embedded in a medium sand, bending about its weak axis, and subjected to an axial stress of 9 ksi and a lateral displacement of 4 in. at the top. The deformed shape and bending moment diagram of the pile for various pile lengths are presented in Figures 4.29 and 4.30, respectively. From this analysis, it can be seen that a pile length greater than 22 ft is required to eliminate lateral displacement and a pile length greater than 25 ft is required to eliminate rotation at the bottom of the pile. This analysis was also performed for other pile sections and soil conditions to evaluate minimum pile lengths.

For convenience, the pile length that eliminates lateral displacement is defined as the final zero deflection depth. The pile length that eliminates rotation is defined as the final zero moment depth. These terms are used to differentiate between other locations that produce zero displacement and moment.

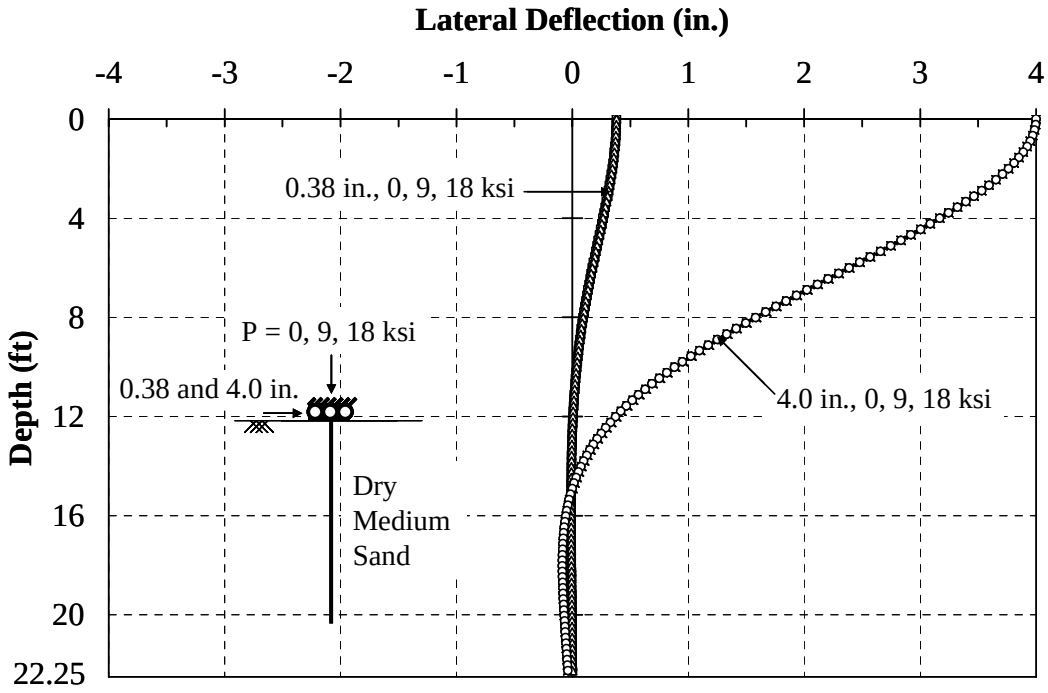

Figure 4.27: Effect of Axial Load on Lateral Deflection (SR18)

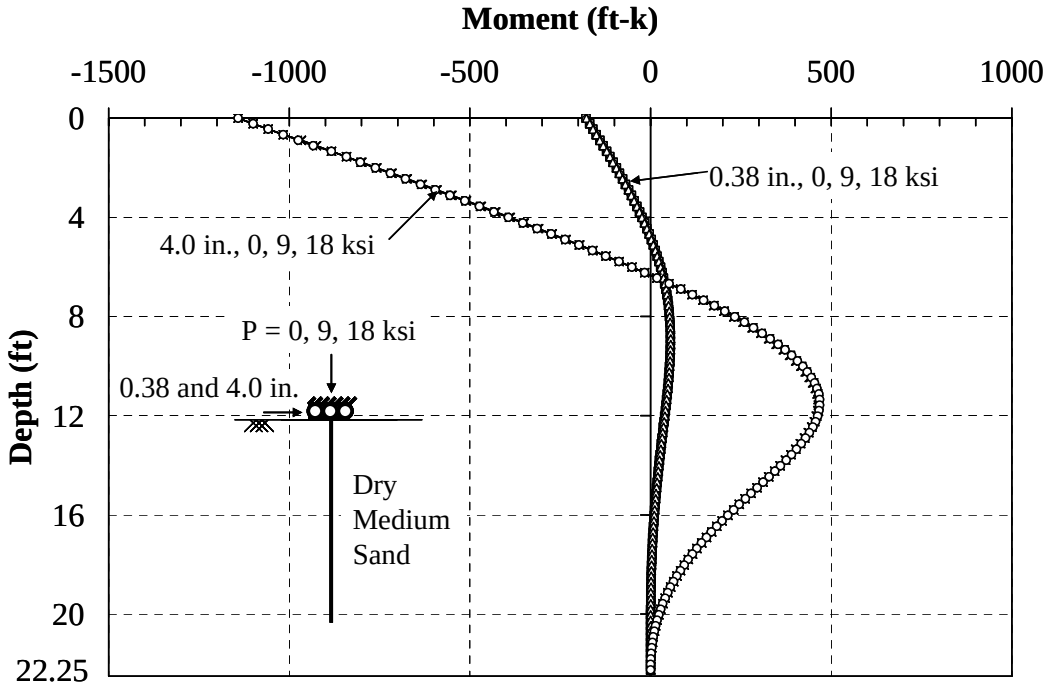

Figure 4.28: Effect of Axial Load on Bending Moment (SR18)

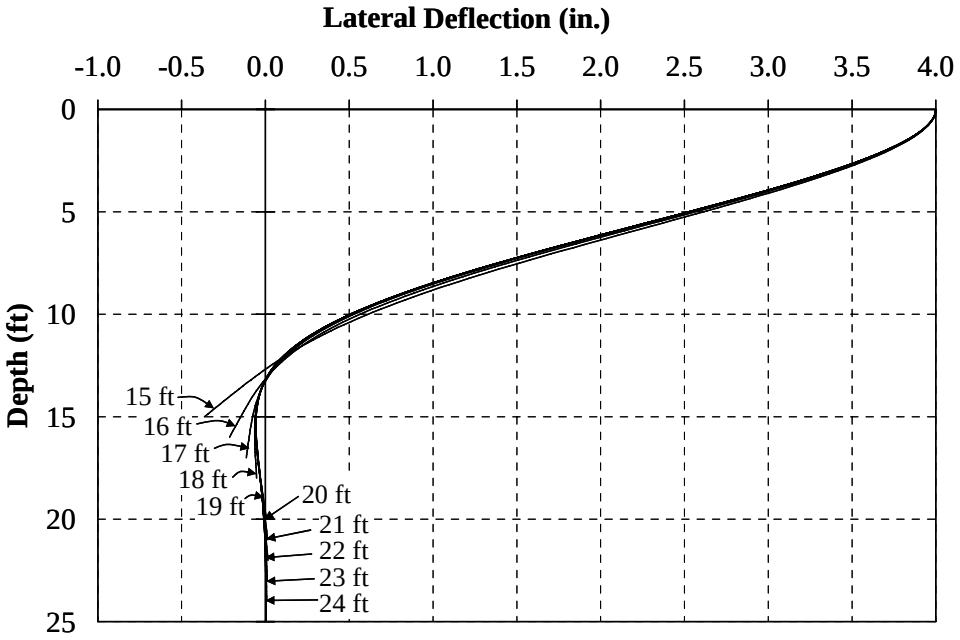

Figure 4.29: Deflected Shape of the Pile with Various Pile Lengths

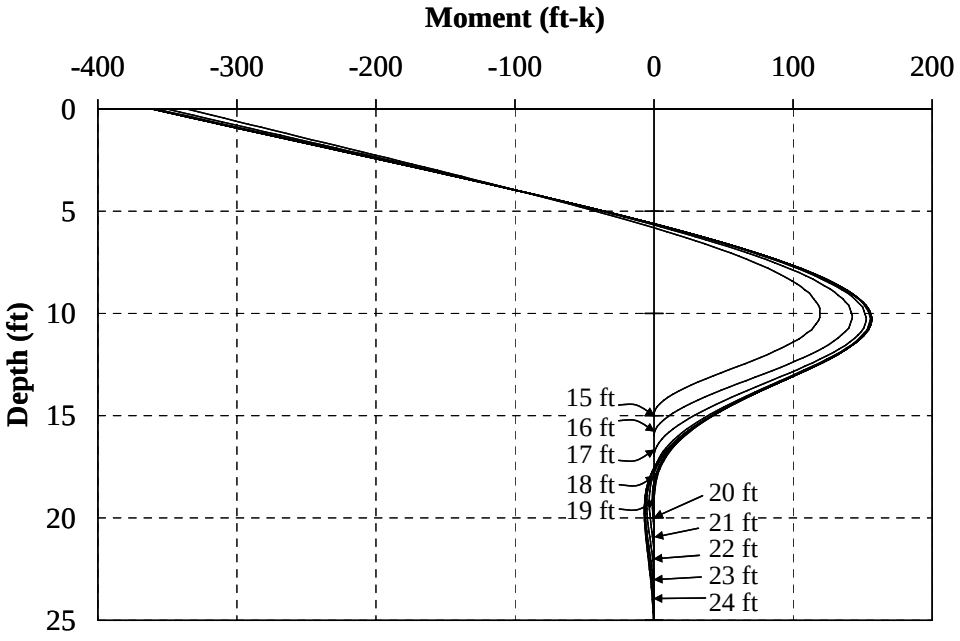

Figure 4.30: Moment of the Pile with Various Pile Lengths

4.7.2.3 Depth of Inflection Point

The depth to the inflection point was evaluated since this point is of interest in developing the experimental program for this research program. This depth is significant in that it is the location where bending moment is zero along the pile length.

The depth to the inflection point of HP10x42, HP12x53, and HP14x89 piles are presented in Figures 4.31, 4.32, and 4.33, respectively, while the depth to the inflection point of CFT14x0.213 and CFT14x0.312 piles are presented in Figure 4.34. Several conclusions can be reached.

1. For the same pile section, the results indicate that the inflection points of a pile embedded in various soil types are fairly constant. As the soil becomes softer, the inflection point moves slightly deeper.
2. For different pile orientations, bending about the strong axis (stiffer) provides a deeper inflection point than bending about the weak axis (less stiff).
3. For the same pile section but subjected to different tip lateral displacements (as the lateral displacement increases from 1 in. to 4 in.), the inflection point is located deeper.
4. Considering all pile analyzed, the inflection points range from 4 to 12 ft below ground level.

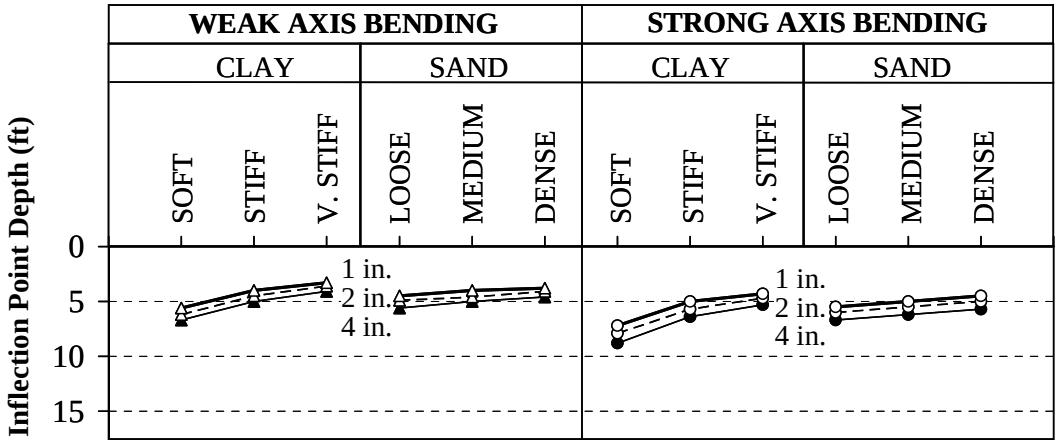

Figure 4.31: Inflection Point Depth of HP10x42

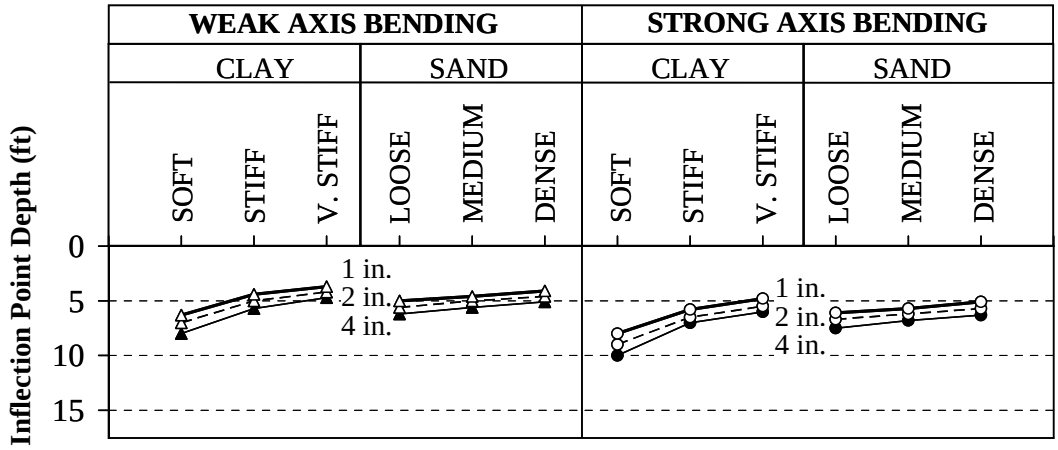

Figure 4.32: Inflection Point Depth of HP12x53

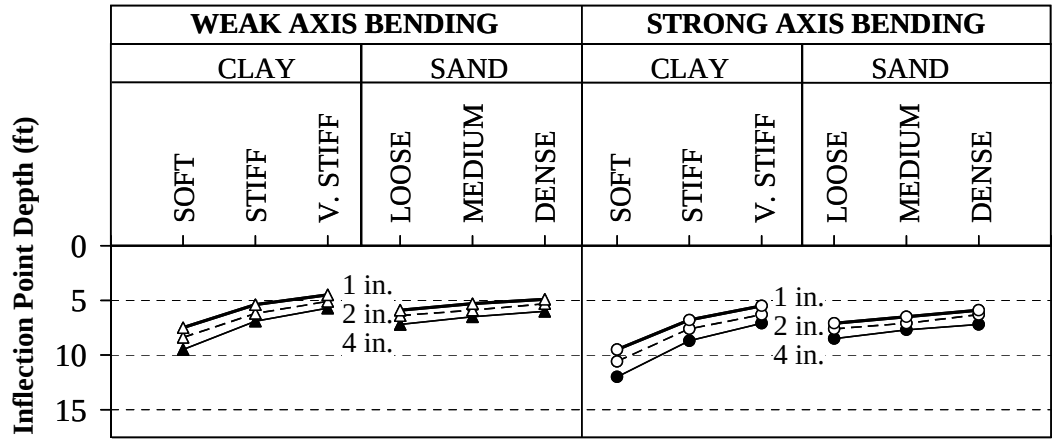

Figure 4.33: Inflection Point Depth of HP14x89

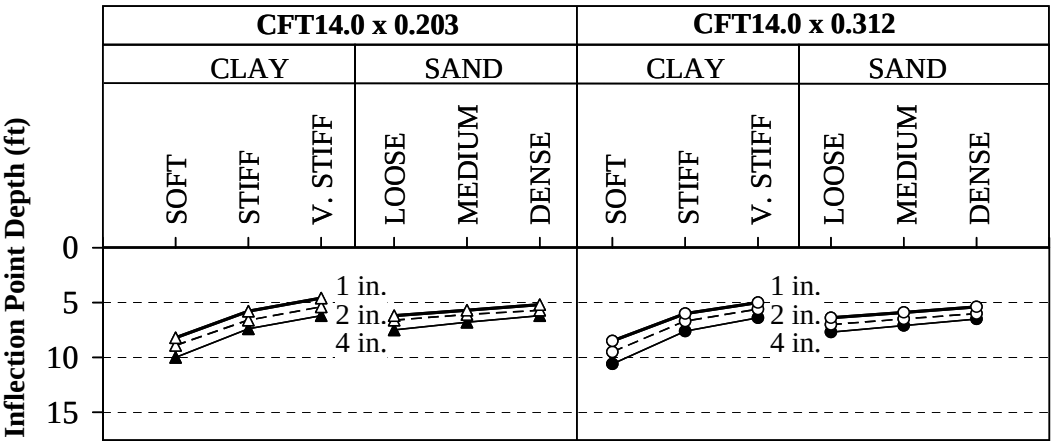

Figure 4.34: Inflection Point Depth of CFT14

4.7.2.4 The Final Zero Deflection and Zero Moment Depths

The final zero deflection depths of HP10x42, HP12x53, and HP14x89 are presented in Figures 4.35, 4.36, and 4.37, respectively, while the final zero deflection depths of CFT14x0.213 and CFT14x0.312 are presented in Figure 4.38. The final zero moment depths of HP10x42, HP12x53, and HP14x89 are presented in Figures 4.39, 4.40, and 4.41, respectively, while the final zero moment depths of CFT14x0.213 and CFT14x0.312 are presented in Figure 4.42.

The final zero deflection and zero moment depths are influenced by soil type, bending axis or stiffness of the pile, and tip lateral displacement in the same manner as the inflection depth. It can be noted, however, that soil type plays more a significant role in the final zero deflection and the final zero moment depths. For example, as the stiffness of the soil increases, the inflection point depth is fairly constant (Figures 4.31 – 4.34), while the final zero deflection depth and the final zero moment depth change significantly. Considering the same pile section, clay provides a more significant effect on the final zero deflection depth than that provided by sand.

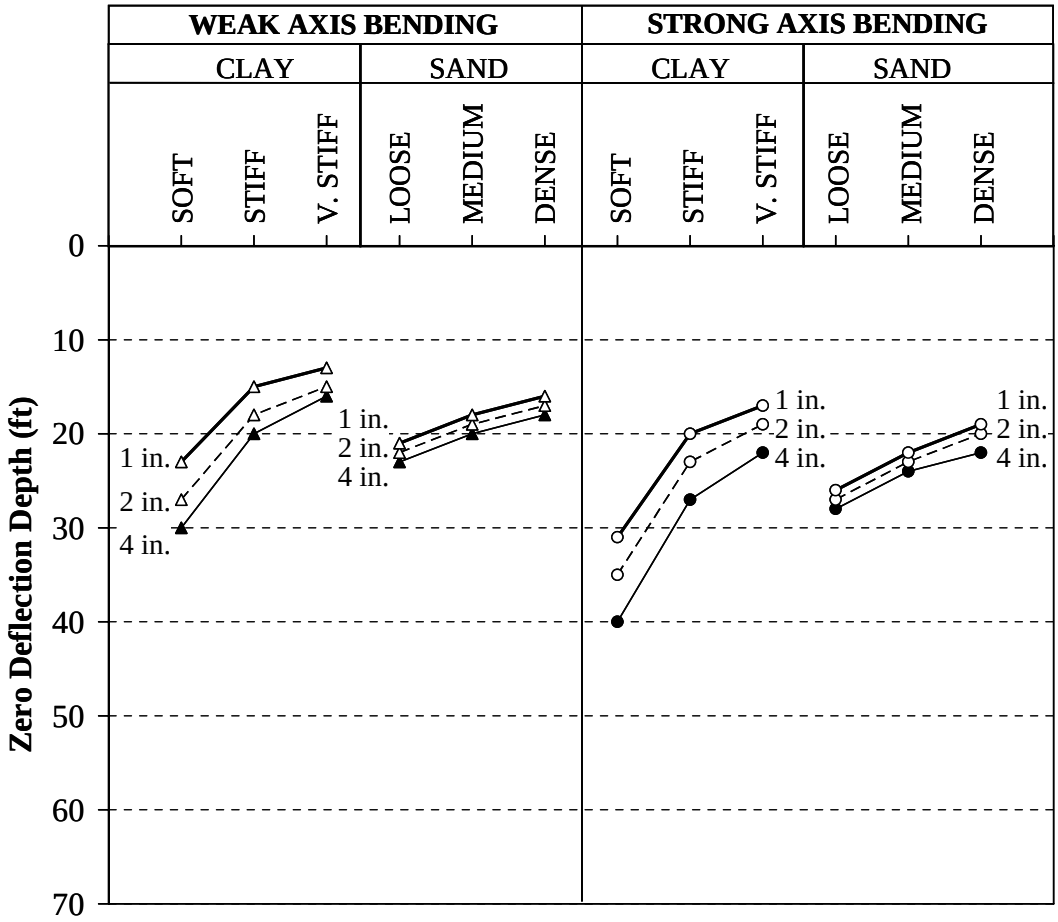

Figure 4.35: Zero Deflection Depth of HP10x42

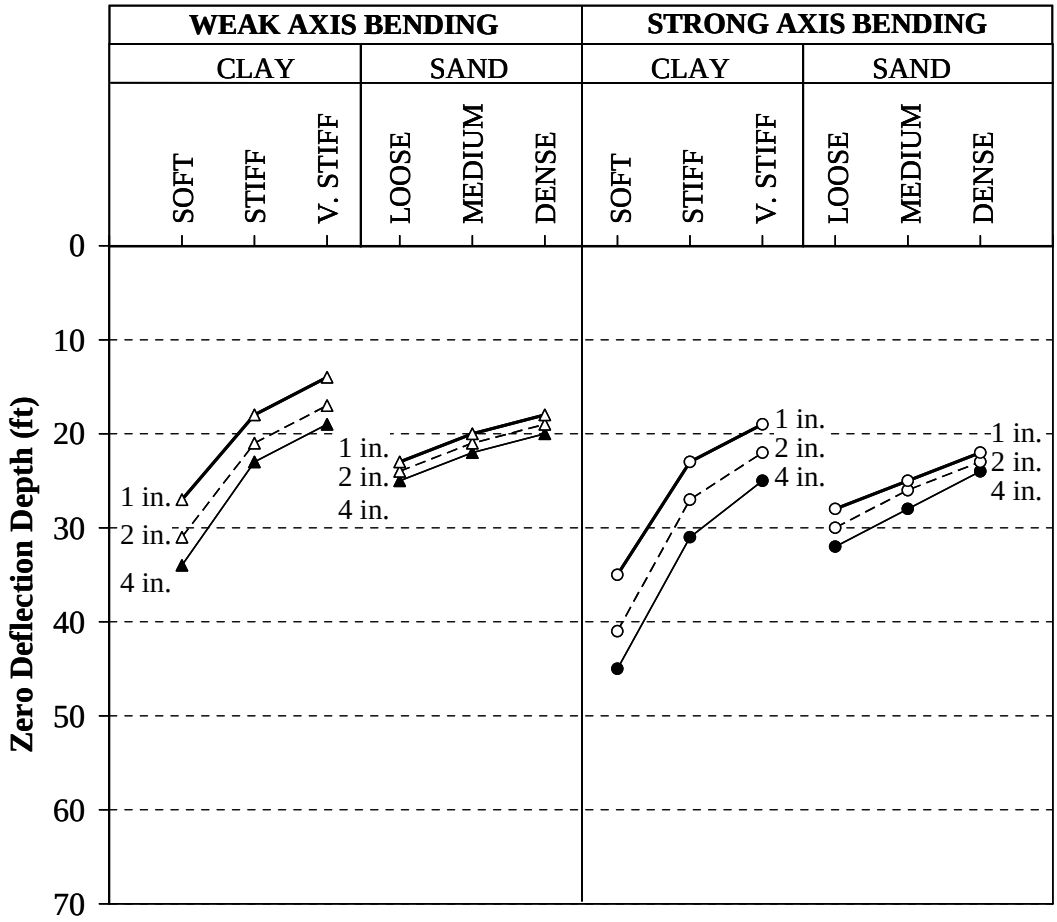

Figure 4.36: Zero Deflection Depth of HP12x53

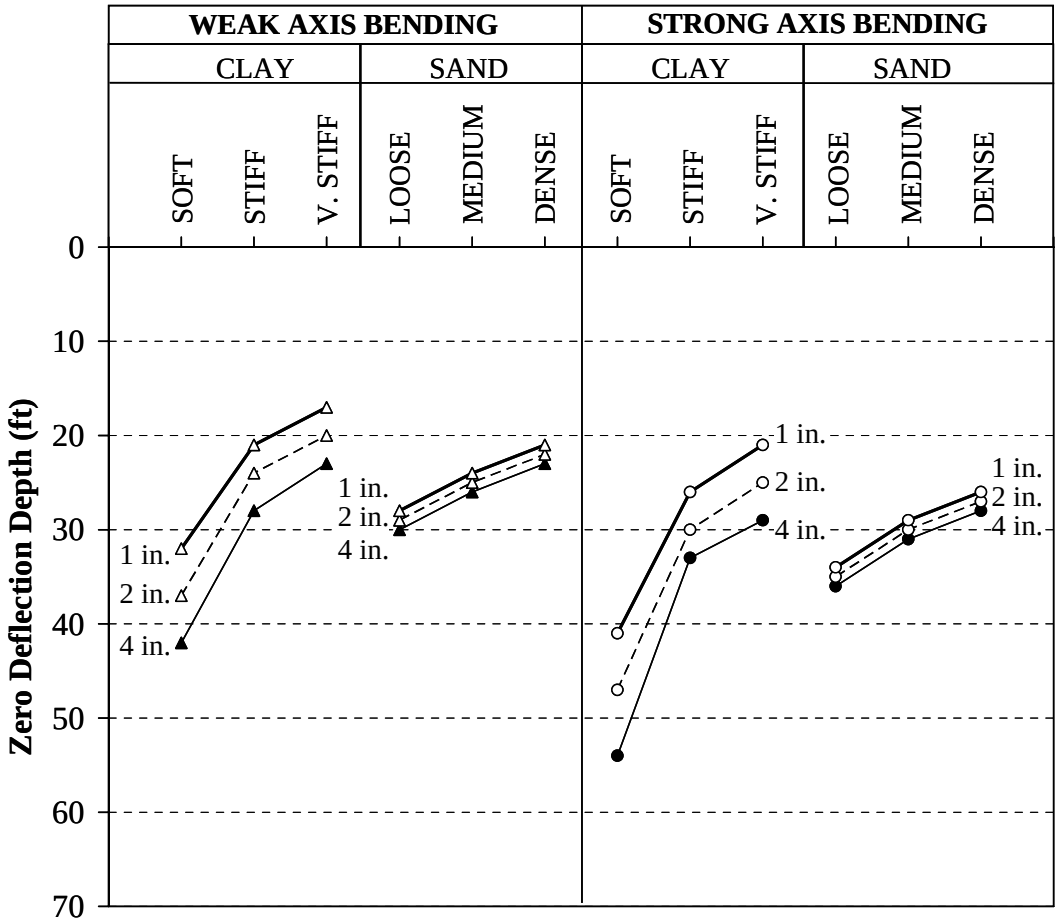

Figure 4.37: Zero Deflection Depth of HP14x89

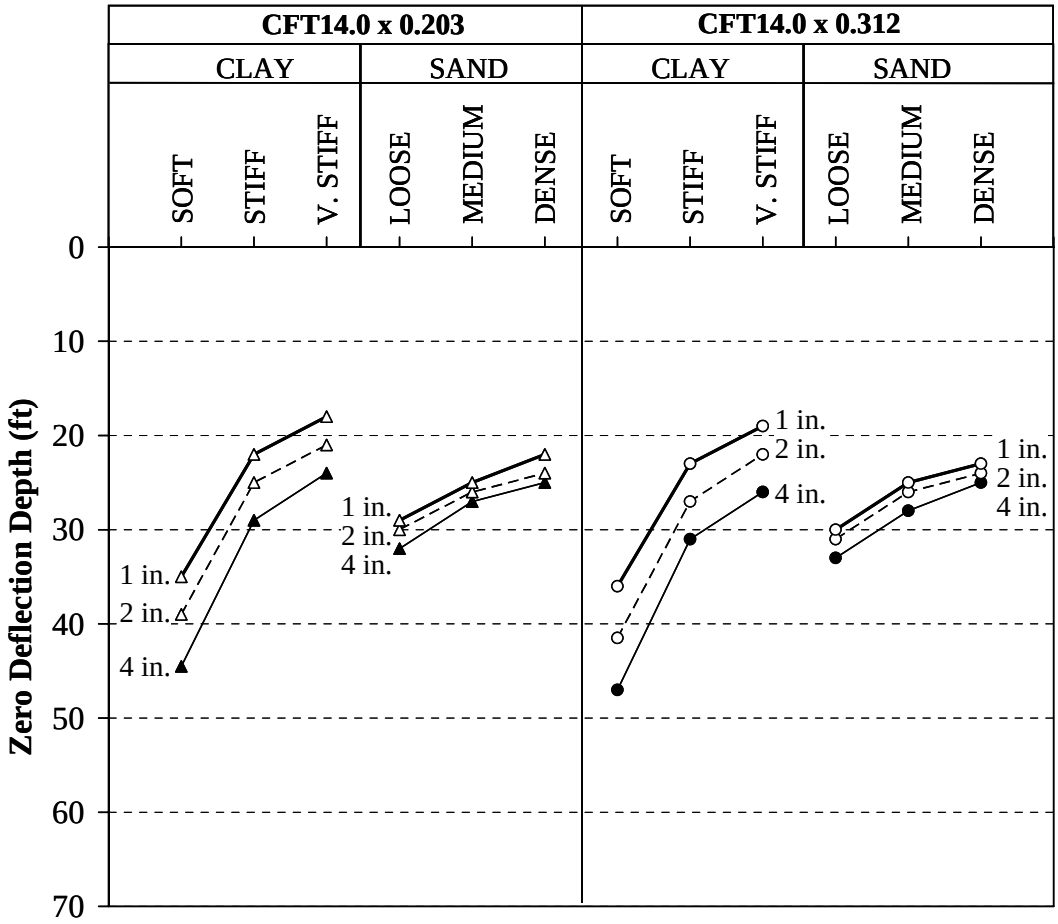

Figure 4.38: Zero Deflection Depth of CFT14

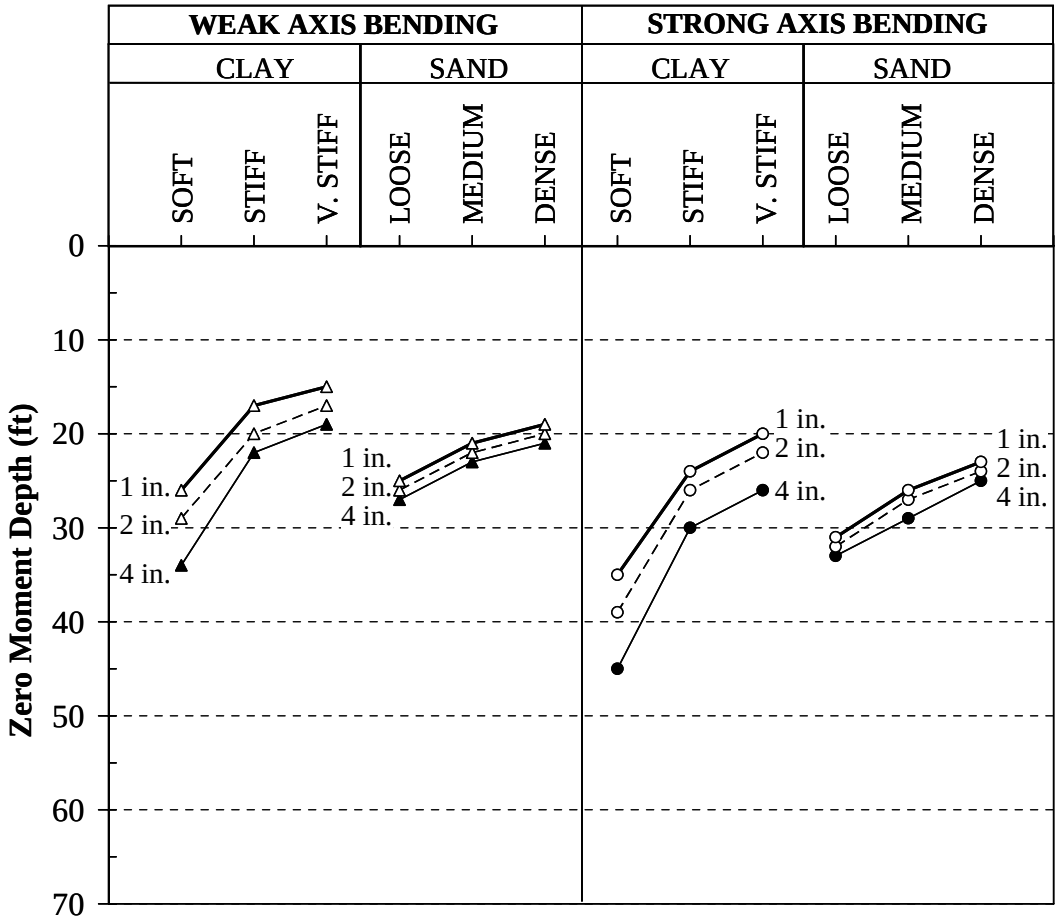

Figure 4.39: Zero Moment Depth of HP10x42

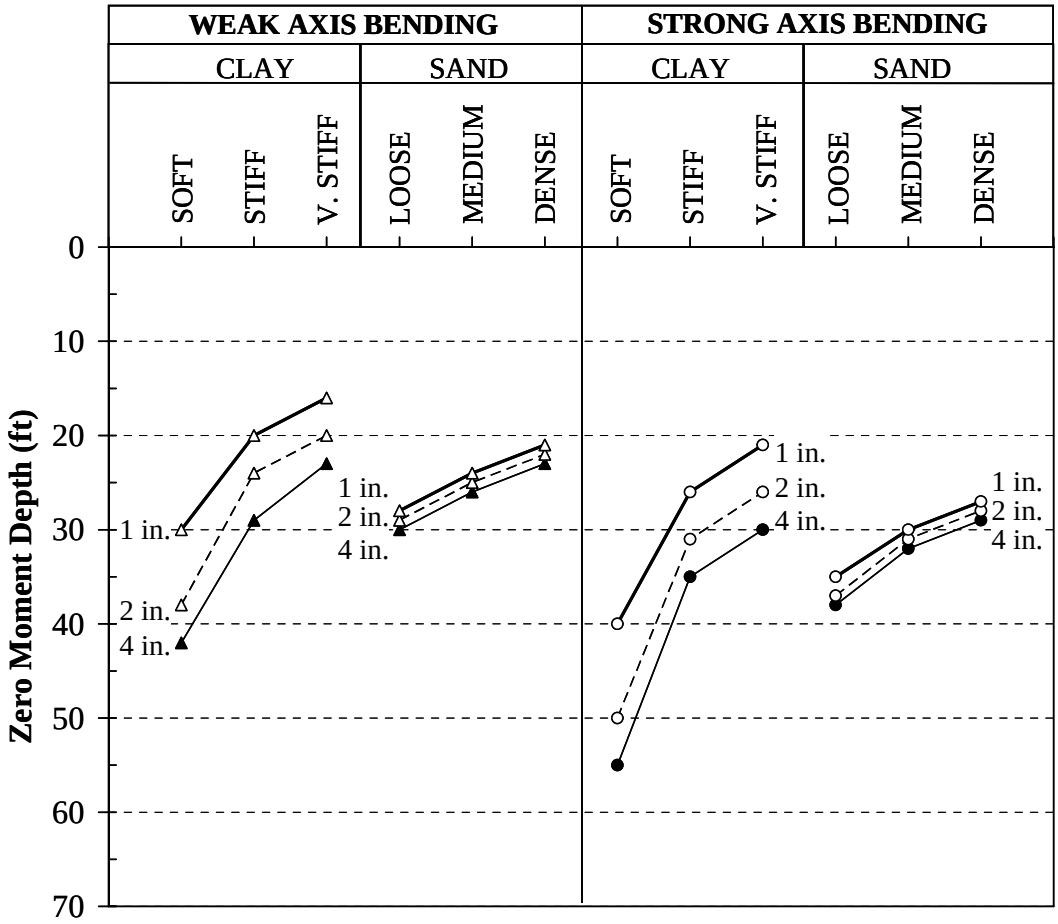

Figure 4.40: Zero Moment Depth of HP12x53

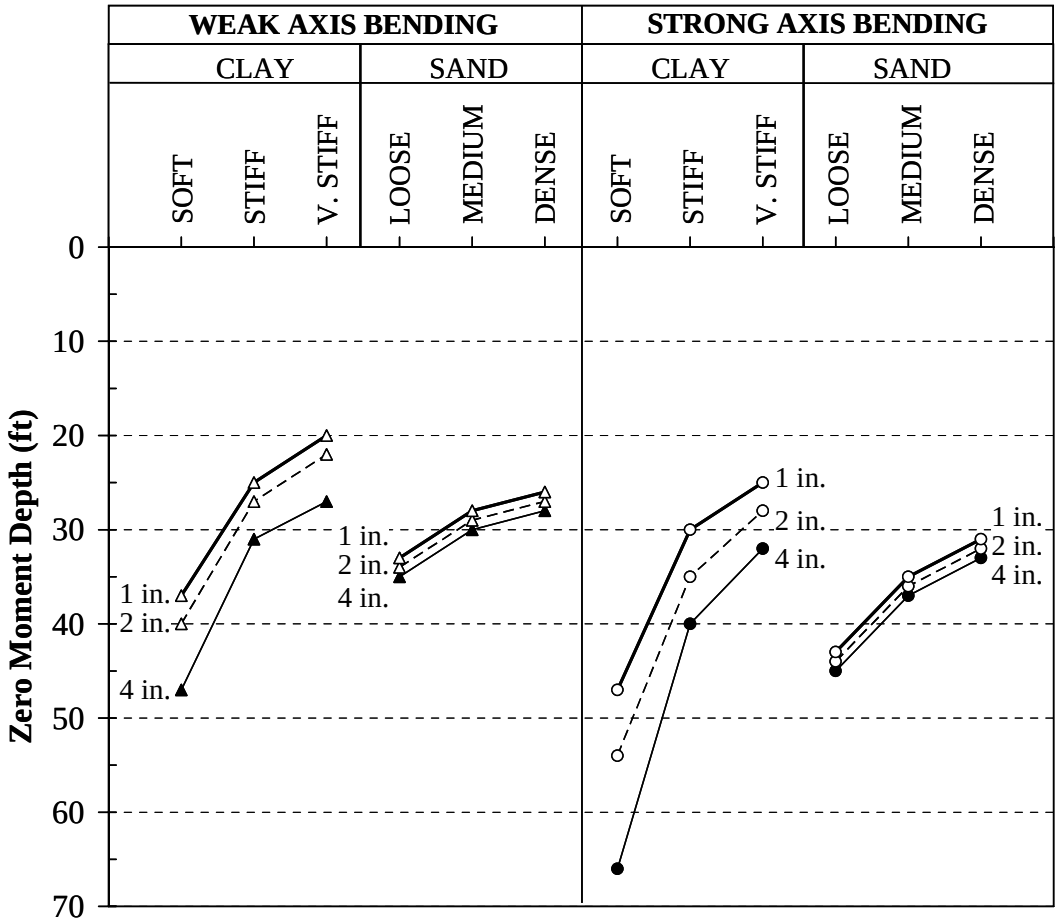

Figure 4.41: Zero Moment Depth of HP14x89

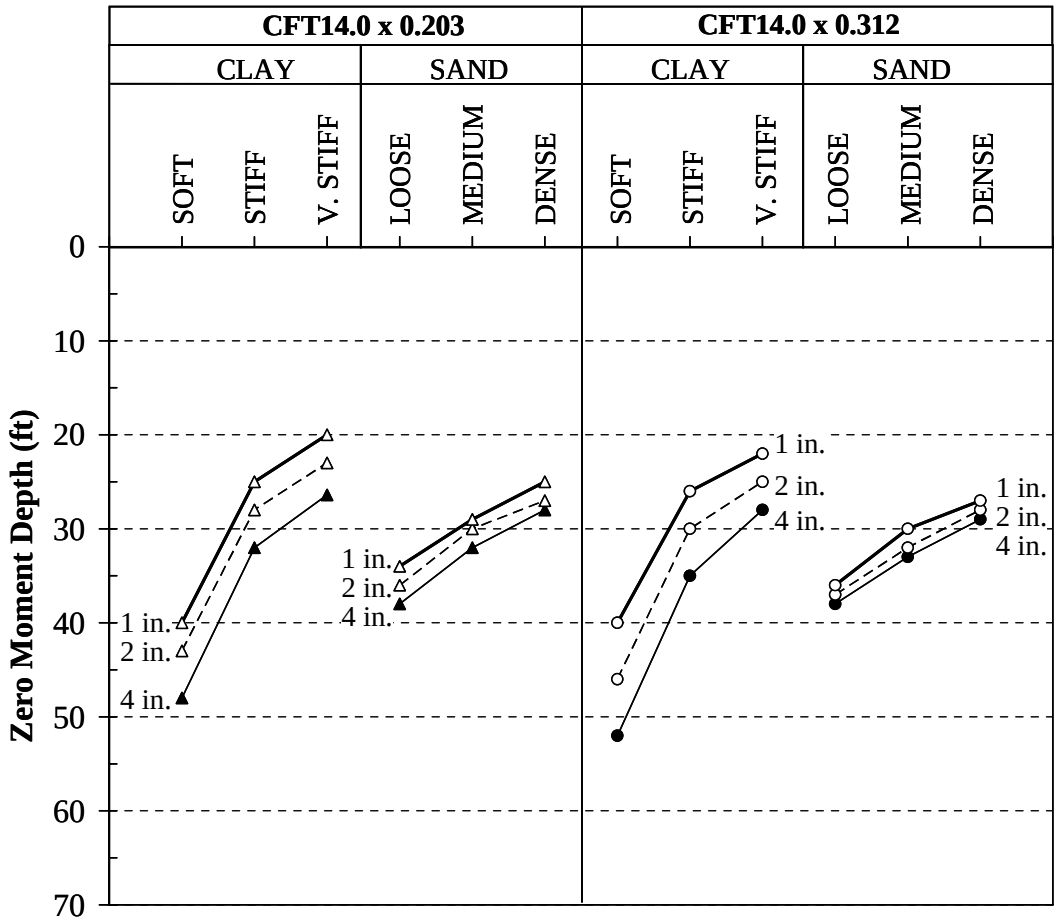

Figure 4.42: Zero Moment Depth of CFT14

The results of these analyses were reviewed and compared. Several findings are provided:

1. Considering the same pile section bending about different axes, the final zero deflection and final zero moment depths are deeper for the stiffer pile orientation.
2. As the stiffness of the pile is increased, the final zero deflection and final zero moment depths increase.
3. Considering different tip displacements, the final zero deflection and final zero moment are deeper as the tip displacement is increased.
4. The final zero deflection depth ranges from 13 ft (HP10x42 Weak, Very stiff clay, Δ = 1 in.) to 54 ft (HP14x89, Strong, Soft Clay, Δ = 4 in.).
5. The final zero moment depth ranges from 15 ft (HP10x42 Weak, Very stiff clay, Δ = 1 in.) to 66 ft (HP14x89, Strong, Soft Clay, Δ = 4 in.).
6. For the same pile embedded in the same soil and subjected to the same tip displacement, the final zero moment depth is 15 to 20 % greater than the final zero deflection depth.

For the selection of a minimum acceptable pile length, however, the final zero deflection depth should be considered rather than the final zero moment depth. Relatively small moments occur below the depth of final zero deflection and small rotations at the base of the pile are considered acceptable. The minimum pile lengths that provide no displacement at the bottom of the pile are listed in Table 4.24. These lengths are based on the analysis presented and are conservative as they were selected based on the critical soil condition.

Table 4.24: The Minimum Pile Length (ft)

Pile	Weak Axis Bending		Strong Axis Bending	
	Clay	Sand	Clay	Sand
HP10x42	30	23	40	28
HP12x53	34	25	45	32
HP14x89	42	30	54	36
CFT14	-	-	47	33

4.8 Conclusions

According to the analysis performed, several conclusions can be drawn.

1. Axial load has minimal influence on the deflected shape and bending moment along the length of the pile.
2. Considering the H and CFT piles recommended by INDOT Memorandums #233 and #243, the inflection point of those piles ranges from 4 to 12 ft below ground level.
3. The inflection point depth, the final zero deflection depth, and the final zero moment depth are dependent upon soil type, bending axis of the pile, stiffness of the pile, and tip lateral displacement. In general, these depths increase as the stiffness of the pile relative to the soil increases. The depths also increase as the tip displacement increase.
4. Considering the H and CFT piles recommended by INDOT, the final zero deflection depth ranges from 13 to 54 ft, while the final zero moment depth ranges from 15 to 66 ft.
5. The final zero deflection depth is considered to provide the minimum acceptable pile length.

4.9 Design Recommendation

Based on the analysis presented in this chapter, it is recommended that a minimum pile length be specified to provide sufficient anchorage to develop the lateral capacity of the pile. These minimum lengths are based on minimizing displacement and rotation at the bottom of the pile. Table 4.25 provides the minimum recommended lengths below ground level.

Table 4.25: Minimum Design Pile Length (ft)

Pile	Weak Axis Bending		Strong Axis Bending	
	Clay	Sand	Clay	Sand
HP10x42	30	25	40	30
HP12x53	35	25	45	30
HP14x89	40	30	55	35
CFT14	-	-	50	35

CHAPTER 5: EXPERIMENTAL INVESTIGATION

5.1 Introduction

To evaluate the behavior of typical piles used in Indiana bridge construction, six steel H piles (HP) and three concrete-filled steel tube piles (CFT) were investigated in the Kettelhut Structural Engineering Laboratory at Purdue University. These tests were used to evaluate the capability of the piles to maintain axial load under low-cycle, large-amplitude lateral displacement expected during thermal movements and to investigate the performance of the abutment-pile connection.

5.2 Specimen Design

The pile supporting the abutment can be represented as a cantilever beam subjected to axial load, P, and cyclic lateral load, H, as shown in Figure 5.1. To determine an appropriate pile length, L, that would provide behavior similar to that experienced in service, a series of analyses were performed using LPILE PLUS (Reese et al., 2000a) as discussed in Chapter 4. Of particular interest was the determination of the inflection point. As the pile responds similar to a cantilever between the abutment and inflection point, the depth to the inflection point was considered as the design cantilever length.

Figure 5.2 illustrates an example analysis for soil conditions similar to the I65 over SR25 site. A medium sand is assumed with its properties provided in Table 5.1 according to Chapter 4. A horizontally-guided support is assumed at the pile top. As shown in Figure 5.2, the inflection depth is fairly stable considering a variety of pile types and sizes. Following additional analyses of various pile types and soil conditions

(Chapter 4), a pile length of 5 ft was selected. Softer soils generally provide for an increase in the inflection depth. As the inflection depth is decreased, increased flexure stresses occur for a given lateral displacement. Therefore, results from using the critical depth of 5 ft are considered conservative.

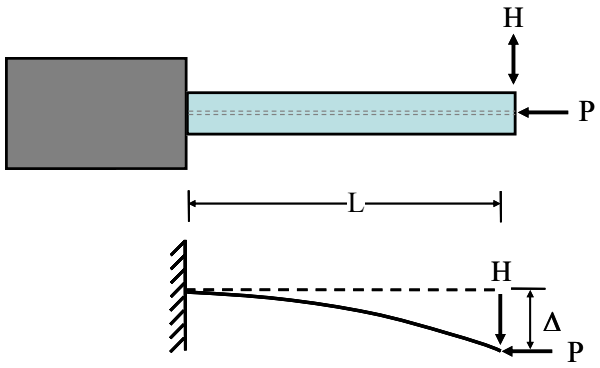

Figure 5.1: Test Design

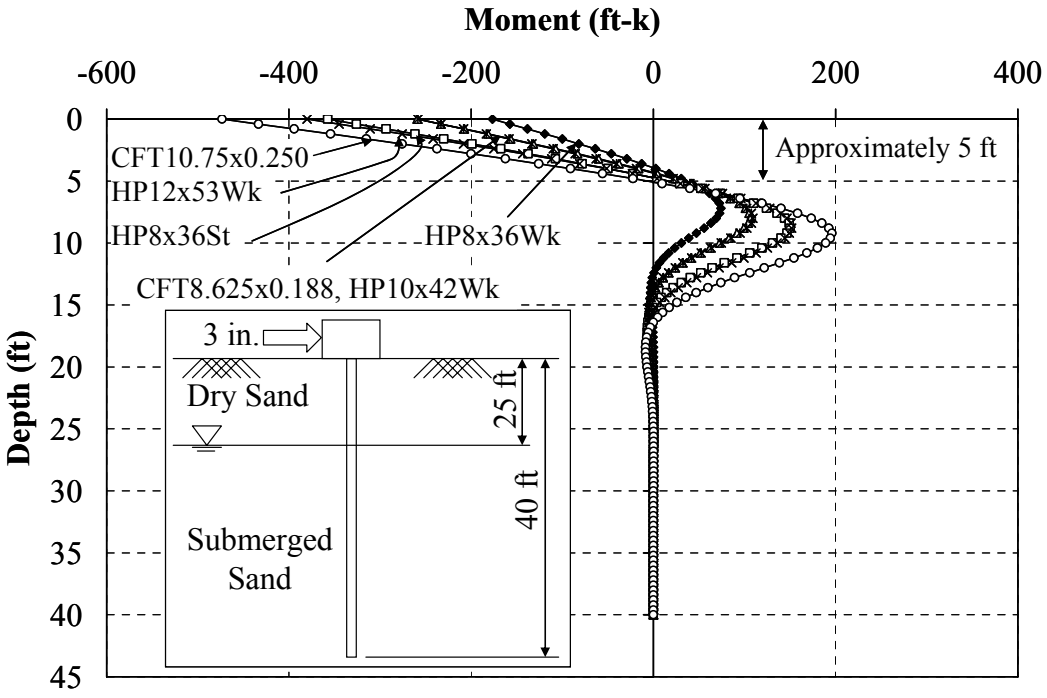

Figure 5.2: Example of Bending Moment versus Depth from LPILE Program

Table 5.1: Soil Properties for LPILE Model

	Dry Sand	Submerged Sand
Unit Weight, γ, pcf	120	60
Relative Density, k, pci	90	60
Angle of Friction, ϕ, deg	35	35

5.3 Test Variables

The experimental program included the following variables: pile type, pile orientation, and axial load. The test matrix is shown in Table 5.2.

Table 5.2: Summary of Test Variables

Specimen	Section	Bending Axis			Axial Load Level	
		Weak	Strong	45°	$0.25f_yA_s + 0.40f_c'A_c$	$0.50f_yA_s + 0.40f_c'A_c$
1	HP8x36	X			X	
2	HP8x36		X		X	
3	HP8x36			X	X	
4	HP8x36	X				X
5	HP10x42	X			X	
6	HP12x53	X			X	
7	CFT8	X*			X	
8	CFT8	X*				X
9	CFT10	X*			X	

*Concrete-Filled Steel Tube (CFT) piles have only one bending axis

5.3.1 Pile Type

Steel H piles (HP) and concrete-filled steel tube (CFT) piles were investigated in the study as these are the only pile types permitted in Indiana according to INDOT Memorandum #233 (INDOT, 1992a). Three steel H pile shapes and two concrete-filled steel tube (CFT) pile shapes were examined: HP8x36, HP10x42, HP12x53, CFT8.625x0.188 (8.625-in. outer diameter and 0.188-in. wall thickness) identified as CFT8, and CFT10.75x0.250 (10.75-in. outer diameter and 0.250-in. wall thickness) identified as CFT10.

These piles were selected considering actual piles used in the field as well as laboratory constraints. HP8x36 was selected because this section is the smallest HP section available; therefore, it can be easily tested in both weak, strong, and 45˚ axis bending as well as for the $0.25f_y$ and $0.5f_y$ axial load cases. HP10x42 was chosen because this section is one of the most commonly-used piles. In addition, results from the HP10x42 could be compared with a similar test conducted by Construction Technology Laboratories (CTL). HP12x53, the last HP section, was tested because this section was used in the I65 over SR25 bridge that has been instrumented. The HP12x53 test was used to correlate with the measured response. Note that even though HP14x89 piles were used in the SR249 over US12 bridge, this section was not tested because of laboratory limitations. The CFT8.625x0.188 sections were selected because they were small enough to test in bending along with the application of the $0.25F_y$ and $0.5F_y$ axial load. In addition, the CFT10.75x0.250 was tested to provide another point of reference.

Note that in INDOT Memorandum #233 (INDOT, 1992a), only 14-in. outer diameter concrete-filled steel tube piles are permitted in integral abutment bridges. Wall thicknesses of 0.203-, 0.250-, and 0.312-in. are typically used according to INDOT Memorandum #243 (INDOT, 1992b). The CFT14 pile, however, could not be investigated because of laboratory capacity limitations. Therefore, a smaller concrete-filled steel tube pile was selected to examine the behavior of this pile type.

5.3.2 Pile Orientation

The HP8x36 section was tested in both weak- and strong- axis bending to evaluate the effect of pile orientation. In addition, it was tested in 45°- axis bending to investigate the effect of skew angle on pile behavior and displacement capacity. Other HP sections were tested in only weak-axis bending. For CFT piles, no orientation exists due to symmetry.

5.3.3 Axial Load Level

Piles were tested under various levels of axial load. The maximum allowable axial stress of steel H piles as given by INDOT Memorandum #233 (INDOT, 1992a) is

9 ksi. This value is based on 25% of the yield strength of 36 ksi as specified by AASHTO (1996). In addition, the maximum allowable stress on a concrete-filled steel tube pipe is specified by AASHTO as 25% of the specified yield strength of the steel shell (35 ksi, A252 Grade 2 steel) plus 40% of the concrete compressive strength ($0.25f_yA_s + 0.4\,f'_c\,A_c$). These axial load levels were examined. Furthermore, higher axial stresses of 50% of the specified yield strength of the steel pile material were tested to determine if these axial load levels could still be maintained under cyclic displacement. Thus, piles were axially loaded to $0.50f_yA_s$ for one HP8x36 and $0.50f_yA_s + 0.4\,f'_c\,A_c$ for one CFT8 where A_s is the area of steel and A_c is the area of concrete.

5.3.4 Embedment Length

The required embedment length was determined based on INDOT design requirements and was checked using Equation 5-1 given by Frosch (1999). The selected embedment length was 1 ft-3 in. which is the minimum provided by INDOT (1992a).

$$\alpha V_n^{Pipe} = \phi\left(0.85f'_c\sqrt{\frac{A_2}{A_1}}\right)\Phi_{OD}\cdot d \qquad (5\text{-}1)$$

where:

α = overstrength factor ≥ 1.25

V_n^{Pipe} = nominal pipe shear strength (= $0.6f_{yw}A_w$ for shear yielding LRFD Eq.(F2-1) and = M_p/L for flexural hinge shear)

ϕ = strength reduction factor = 0.65 (ACI 318-02, Sec. 9.3.2.2)

A_w = shear area (web area for strong-axis bending steel pile, 2 times flange area for weak-axis bending pile, and cross-sectional area of pipe for concrete-filled steel tube pile)

f'_c = compressive strength of concrete, ksi

Φ_{OD} = outside diameter of steel pipe, in.

d = embedment length, in.

$\sqrt{\frac{A_2}{A_1}}$ = confinement factor ≤ 2 (ACI 318-02, Sec. 10.17).

Equation 5-1 provides for the embedment length of steel pipes under cyclic loading. This equation was extended for the calculation of embedment length of both the H and CFT piles. Based on this analysis, embedment length less than 15-in. should be sufficient.

5.4 Construction Materials

5.4.1 Concrete

To represent a pile supported abutment in Indiana bridge construction, INDOT Class C concrete was used for the experimental program. This mix was supplied from Irving Materials Inc. (IMI), a local ready-mix concrete supplier. The mix included a maximum aggregate size of ¾ in. and a water-to-cement ratio of 0.38. The specified slump was 4 in. Specific mix proportions are shown in Table 5.3.

Table 5.3: Mix Design

Material	Quantity
#8 Gravel	1840 pcy
Sand #23	1240 pcy
Cement	655 pcy
Water	250 pcy
Air	6.6 ozcy
Water Reducer	20 ozcy

Compression tests were performed for all concrete used in the testing program. Modulus of elasticity tests were also conducted for the concrete used in the CFT piles since the stiffness of this material is of interest relative to the behavior of these piles. Both the compression and modulus of elasticity tests were performed on 6- by 12-in. cylinders after casting. The compression tests were performed using a 600-kip Forney compression testing machine according to ASTM-C39-01. A 120-kip Baldwin universal testing machine was used to perform the modulus of elasticity tests. The testing procedure followed ASTM-C469-02.

The nine different test specimens presented in Table 5.2 were cast at five different times as listed in Table 5.4. Strength gain curves for the concrete abutments and concrete in the CFT piles are presented in Figures 5.3 and 5.4, respectively. As shown, the specimen compressive strengths at the time of testing are identified by specimen number. The compressive strength, f_c, for all specimens as well as the modulus of elasticity for the CFT piles on the day of testing are tabulated in Table 5.5.

Table 5.4: Casting Sequence

Casting No.	Date	Description
1	2/13/2003	- Support Block Specimen 1 Abutment
2	4/22/2003	- Specimen 2 and 5 Abutments - CFT Piles for Specimens 7, 8 and 9
3	6/11/2003	- Specimen 4 and 6 Abutments
4	7/17/2003	- Specimen 3 and 7 Abutments
5	8/4/2003	- Specimen 8 and 9 Abutments

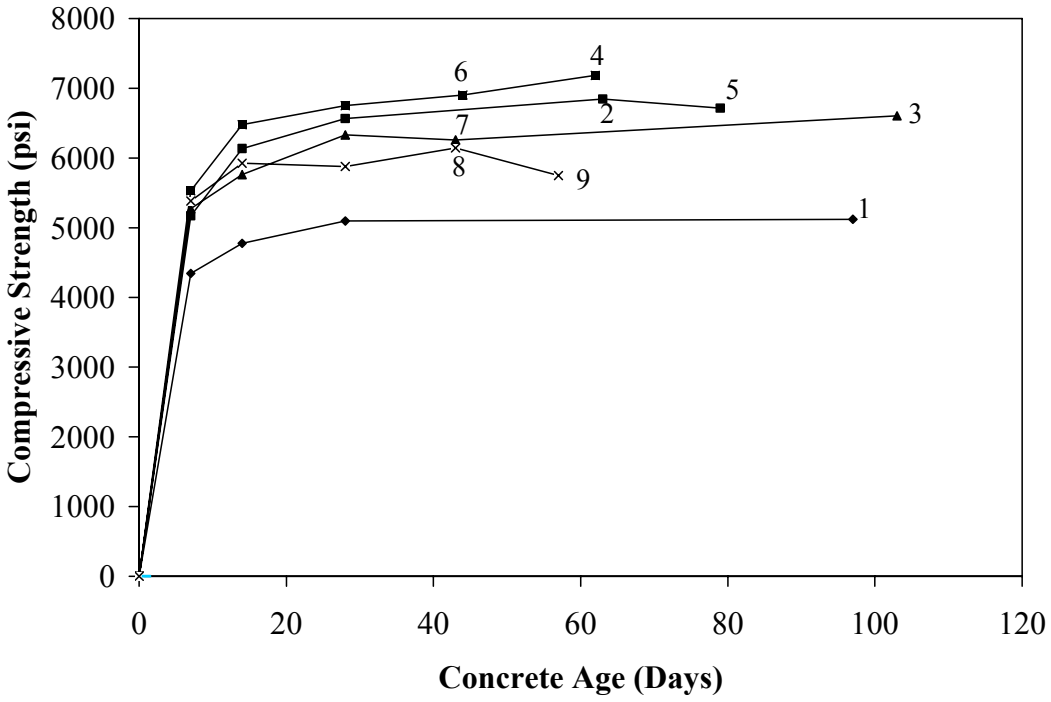

Figure 5.3: Abutment Concrete Compressive Strength Gain

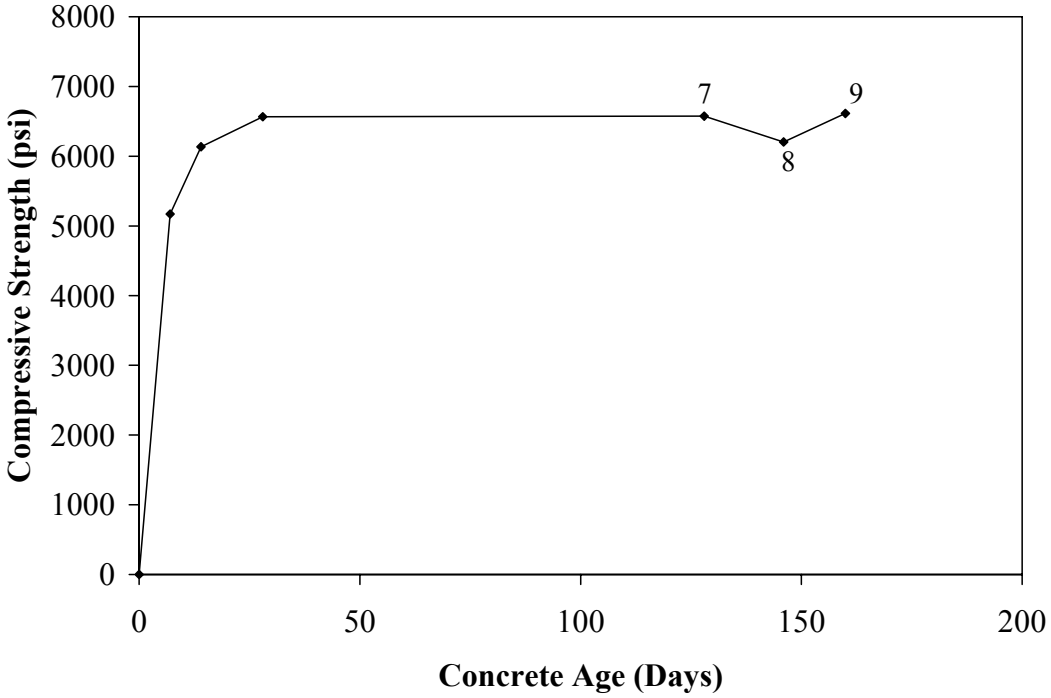

Figure 5.4: Compressive Strength Gain of Concrete in CFT Piles

Table 5.5: Average Concrete Compressive Strength and Modulus of Elasticity

Specimen	Concrete Strength, f_c		Modulus of Elasticity, E_c	Age at Testing	
	Abutment (psi)	CFT Pile (psi)	CFT Pile (psi)	Abutment (days)	CFT Pile (days)
1	5100	-	-	97	-
2	6800	-	-	63	-
3	6600	-	-	103	-
4	7200	-	-	62	-
5	6700	-	-	79	-
6	6900	-	-	44	-
7	6300	6600	4000	43	128
8	6100	6200	4100	43	146
9	5700	6600	4000	57	160

5.4.2 Reinforcing Steel

Grade 60, #4 and #6 reinforcing bars were used in the concrete abutment while #5 reinforcing bars were used in the support block to provide minimum shrinkage and temperature reinforcement. As these material were part of the test setup and not part of the specimen under evaluation, material tests were not performed.

5.4.3 Steel Piles

The steel piles were 7 ft-6 in. long. Coupons that were 22-in. long were cut from each pile. The remaining 5 ft-8 in. long piles were used in the cyclic tests. Tests were conducted on the representative coupons cut from each specimen. A MTS universal test machine (Figure 5.5) was used to perform tensile tests according to ASTM A370-02. The dimensions of strips cut from the H piles and tubular piles (also known as shell/pipe piles) are shown in Figures 5.6 and 5.7, respectively. The total length of the coupons for the HP sections was 1 ft-6 in. while the total length of the tubular pile coupons was 1 ft-10 in. Fifteen steel coupons were cut from the pile flanges (6), webs (6), and pipe walls (3) for evaluating their material properties. Figure 5.8 shows samples of the coupons. Both yield and ultimate tensile strengths were obtained, and the results are presented in Table 5.6. Note that the coupons from the CFT piles presented in Figure 5.9 do not exhibit an obvious yield strength. Therefore, the 0.2% offset yield strength was determined. The stress-strain curves of all coupons are provided in Appendix H.

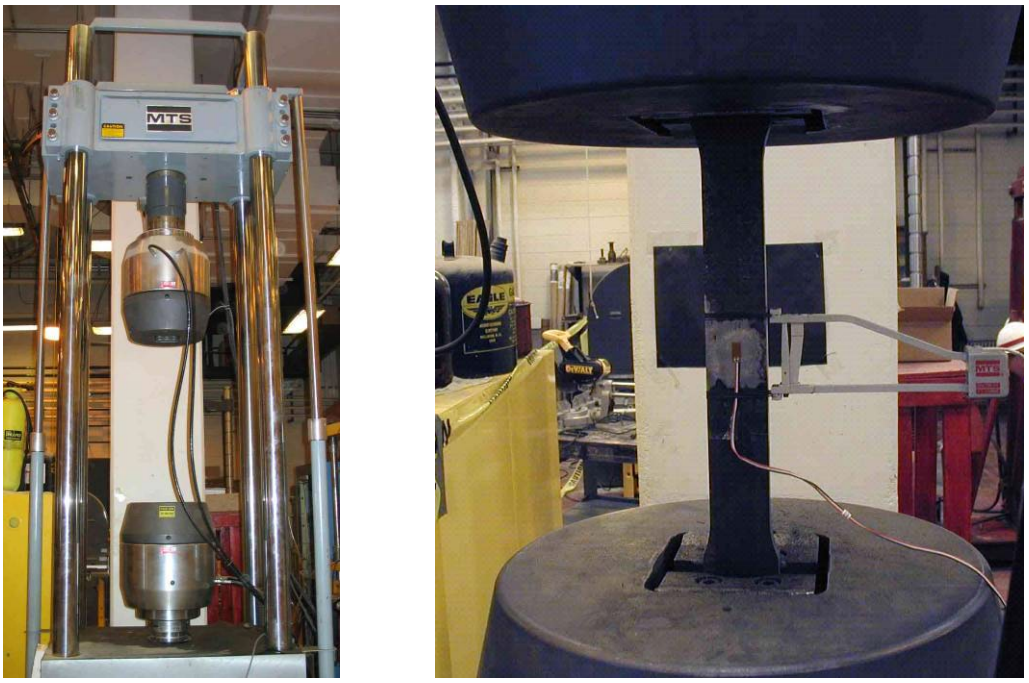

(a) MTS Universal Test Machine **(b) Coupon**

Figure 5.5: Coupon Test

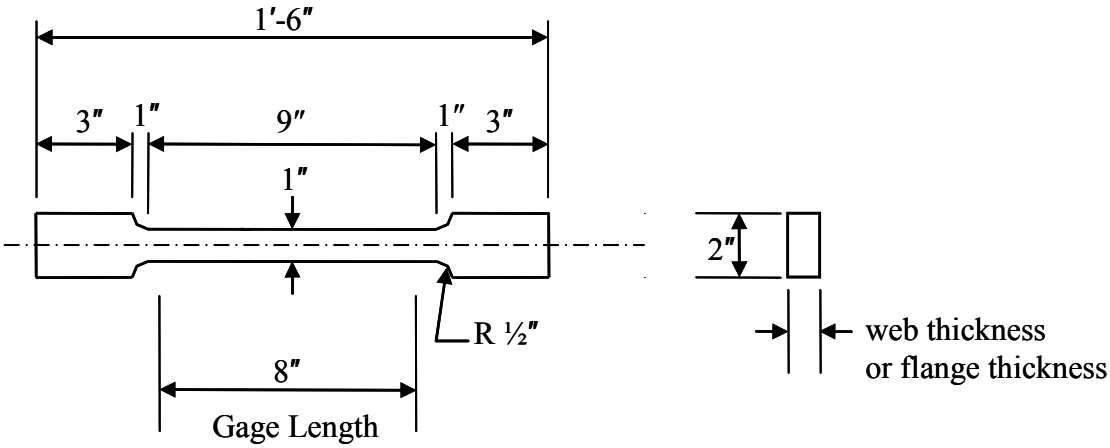

Figure 5.6: Rectangular Tension Test Specimens

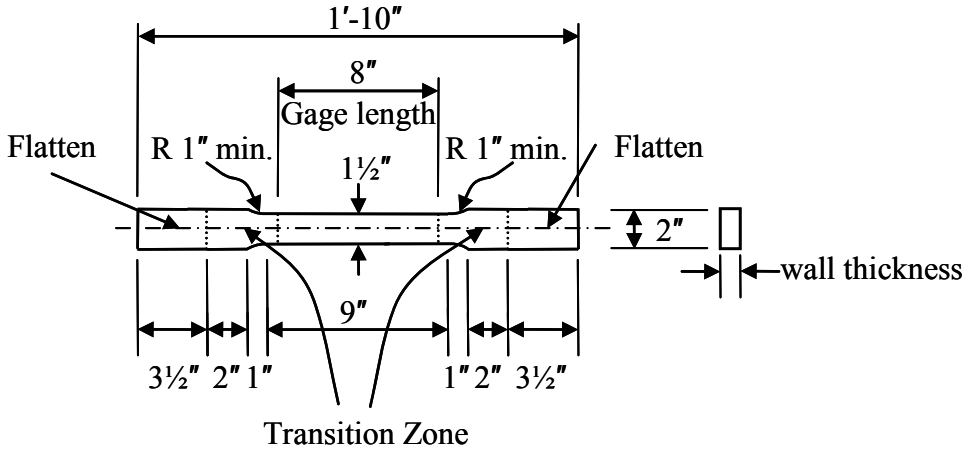

Figure 5.7: Tubular Tension Test Specimens

Figure 5.8: Coupon Specimens

Table 5.7 provides the dimension, and section properties for the steel H piles as obtained from AISC-LRFD (2001). Tables 5.8 and 5.9 provide the dimensions and transformed section properties calculated based on Section 4.3.3 for the CFT piles, respectively.

Table 5.6: The Coupon Test Results

Specimen	Location	Yield Strength (ksi)	Yield Strain (in./in.)	Ultimate Strength (ksi)	Ultimate Strain (in./in.)
1	Flange	48	0.0017	67	0.1821
	Web	46*,**	0.0011	45	0.1892
2	Flange	48	0.0017	66	0.1780
	Web	46	0.0016	66	0.2103
3	Flange	47	0.0016	66	0.1966
	Web	46**	0.0016	66	0.1792
4	Flange	47	0.0016	66	0.1792
	Web	47	0.0016	66	0.1925
5	Flange	40	0.0014	57	0.1981
	Web	38	0.0013	57	0.2429
6	Flange	41	0.0014	61	0.2279
	Web	49	0.0017	71	0.2301
7	-	42	0.0034	65	0.1938
8	-	54	0.0039	68	0.1637
9	-	52	0.0038	68	0.1731

* This was the first coupon test conducted. A problem occurred during testing. A yield strength of 33 ksi was measured; however, a yield strength of 46 ksi was assumed because the yield strengths of the web sections from Specimens 2, 3, and 4 were approximately 46 ksi. These specimens were from the same pile section.

**Fracture did not occur inside the gage length.

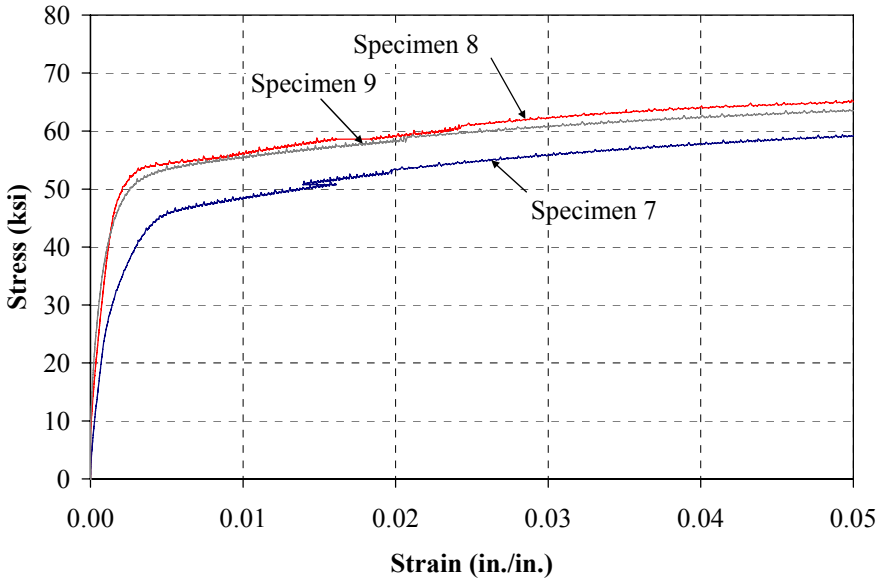

Figure 5.9: Initial Stress-Strain Relationship of Specimens 7, 8, and 9

Table 5.7: Nominal Cross-Sectional Properties of Steel H Piles

Section	A ($in.^2$)	d (in.)	t_w (in.)	b_f (in.)	t_f (in.)	I_x ($in.^4$)	I_y ($in.^4$)	S_x ($in.^3$)	S_y ($in.^3$)	Z_x ($in.^3$)	Z_y ($in.^3$)
HP8x36	10.6	8.02	0.445	8.15	0.445	119	40.3	29.8	9.88	33.6	15.2
HP10x42	12.4	9.70	0.415	10.1	0.420	210	71.7	43.4	14.2	48.3	21.8
HP12x53	15.5	11.8	0.435	12.0	0.435	393	127	66.7	21.1	74.0	32.2

Table 5.8: Dimensions of CFT Piles

Specimen	Outer Diameter (in.)	Inner Diameter (in.)	Wall Thickness (in.)
CFT8.625x0.188	8.625	8.249	0.188
CFT10.75x0.250	10.75	10.25	0.250

Table 5.9: Transformed Section Properties of CFT Piles

Pile Section	A_e ($in.^2$)	d (in.)	$I_{steel\ ring}$ ($in.^4$)	I_e ($in.^4$)
CFT8.625x0.188	11.6	8.625	44.4	72.6
CFT10.75x0.250	18.5	10.75	114	181

5.5 Specimen Construction

5.5.1 Specimen Support Block

A concrete block was used to support the abutment-pile specimens for the testing setup. The dimension of the concrete base was 3.5 x 4.5 x 4.0 ft (W x L x H) as illustrated in Figure 5.10. Twelve-#5 longitudinal reinforcing bars and eight-#5 stirrups were used to provide minimum shrinkage and temperature reinforcement. INDOT Class C concrete (Section 5.4.1) was provided for the block. The assembled formwork for the support block is shown in Figure 5.11.

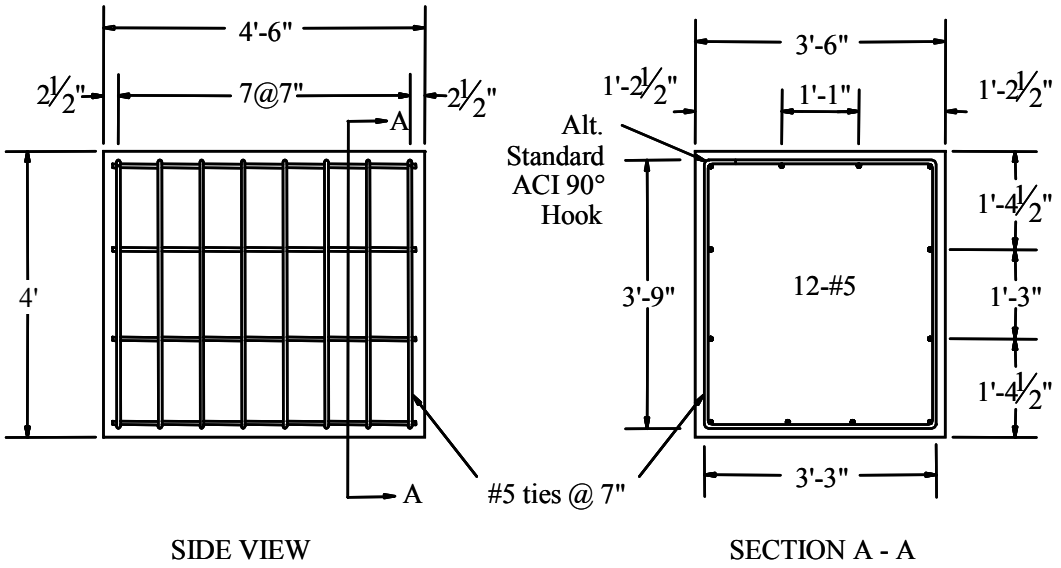

Figure 5.10: Support Block Details

Formwork was constructed by the following sequence. First, the side forms were attached to the base using wood screws. Second, adjacent side forms were bolted together by steel angles. Then, form oil was applied to provide ease in form removal. Then, wales and ties were used to maintain dimensional tolerance and brace the formwork during casting (Figure 5.11). Finally, four single flared loops were attached to the formwork by four coil bolts for lifting the concrete base after casting as shown in Figure 5.12. The support block following casting is shown in Figure 5.13.

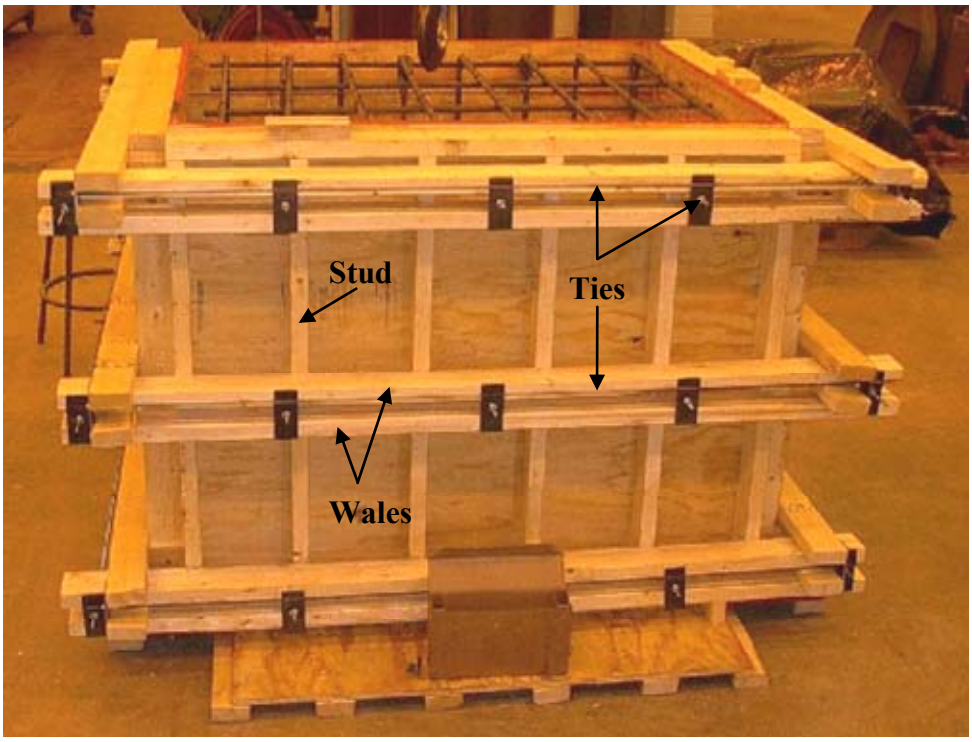

Figure 5.11: Support Block Formwork

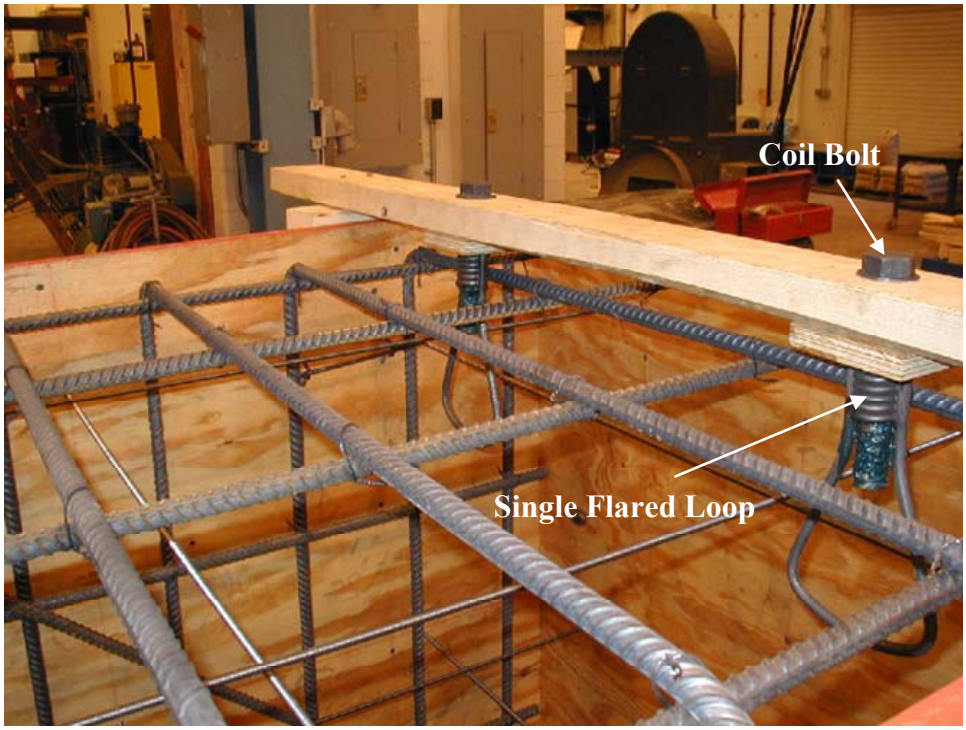

Figure 5.12: Single Flared Loops for Support Block Formwork

Figure 5.13: Support Block

5.5.2 Concrete Abutment Construction

A concrete abutment was cast to represent a fixed connection to the pile specimen. The abutment was 2.5 x 4 x 2.5 ft (W x L x H) as illustrated in Figure 5.14. Figure 5.15 shows the geometry and details of the typical abutment used in the test. The abutment forms were constructed in the same sequence as the support block forms. Wales and ties were also used to resist the lateral pressure during casting (Figure 5.16). Four flared loops were attached to the side of the formwork and coil bolts were then inserted into the flared loops and greased to facilitate in form removal as shown in Figure 5.17. To prevent bowing during casting, ¼″ ∅ rods were inserted through the forms, and the nuts were tightened. Figures 5.18 and 5.19 show the concrete abutment form and concrete abutment after casting.

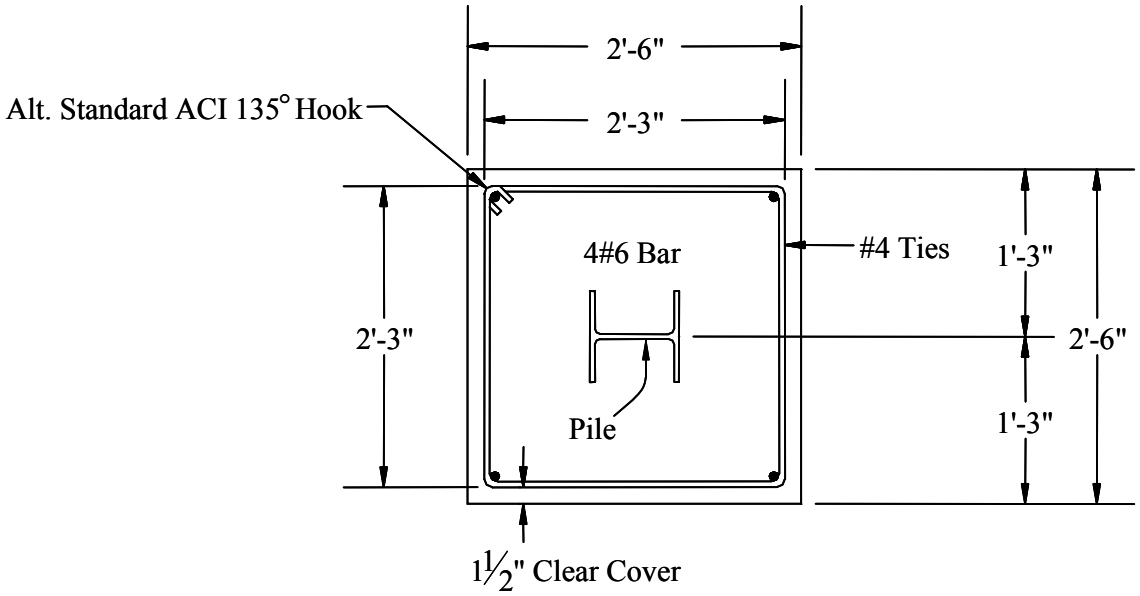

Figure 5.14: Concrete Abutment Cross Section

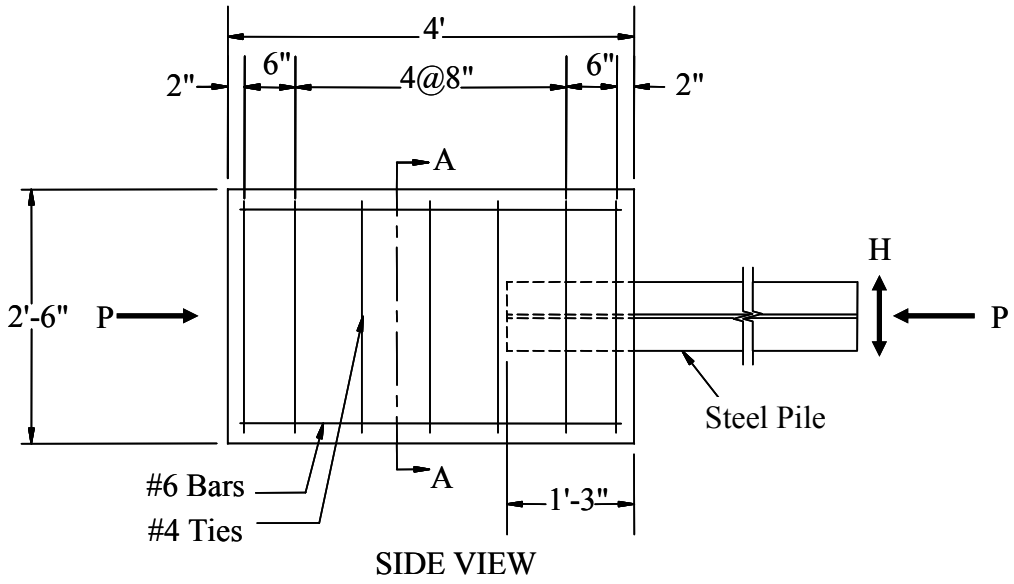

Figure 5.15: Concrete Abutment Details

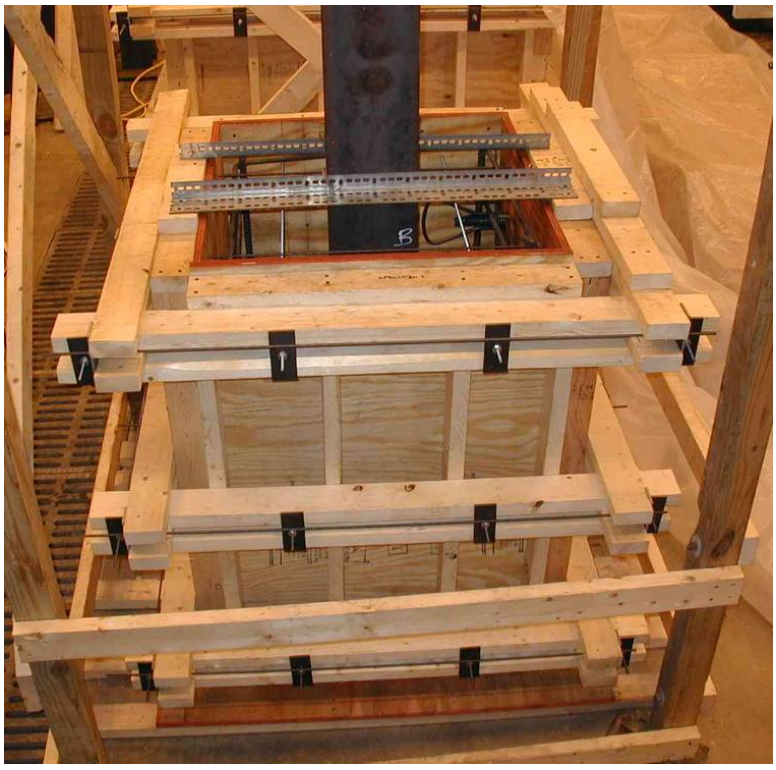

Figure 5.16: Wale and Tie System for Concrete Abutment Form

Figure 5.17: Flared Loop for Concrete Abutment Form

Figure 5.18: Concrete Abutment Form

Figure 5.19: Concrete Abutment after Casting

5.5.3 Steel Pile-Abutment Connection

A steel pile was attached to the concrete abutment form as shown in Figure 5.15. An 18- x 18- x 1-in. steel plate was welded to the steel pile allowing hanging of the pile during casting. The steel pile was lifted and supported by steel angles at the top of a wooden frame as shown in Figure 5.20. The steel pile was braced by two steel angles at the abutment-pile connection to prevent movement during casting (Figure 5.21).

5.5.4 Clamping System

The concrete abutment was clamped to the laboratory floor by two steel beams (W10x100) and sixteen ¾″-∅ Dywidag threadbars. Figure 5.22 illustrates the clamping system of Specimens 1 and 2. Concerns developed regarding confinement at the abutment-pile connection after testing Specimens 1 and 2; therefore, the clamping beams were moved to the middle of the concrete abutment for Specimens 3 to 9 as shown in Figure 5.23 to reduce the effect of confinement on the abutment-pile connection. A clamping force of 80 kips on each end of the beam was applied through four 100-kip hydraulic rams at the top of each beam. The total clamping force, therefore, was 320 kips.

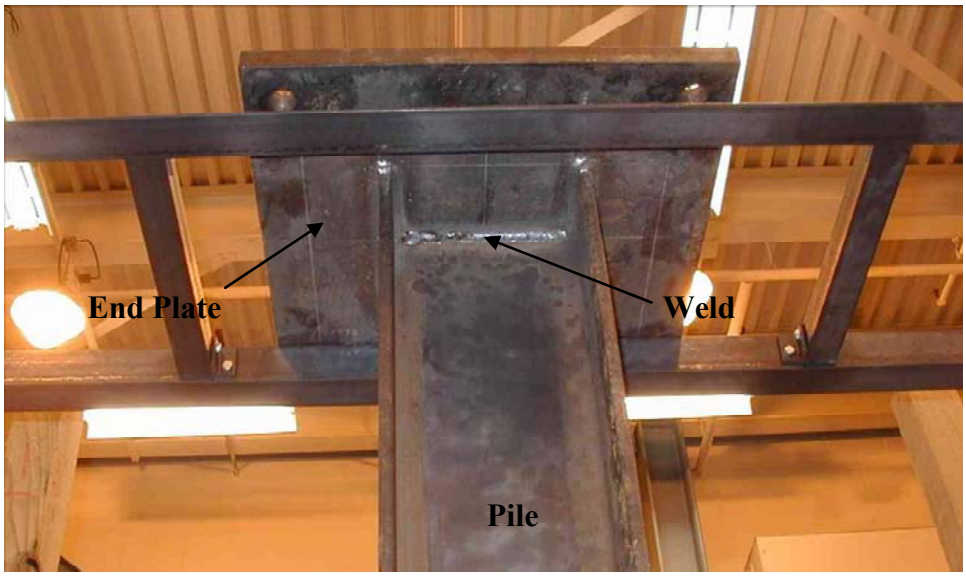

Figure 5.20: Hanging Steel Pile

Figure 5.21: Pile Braced by Steel Angles

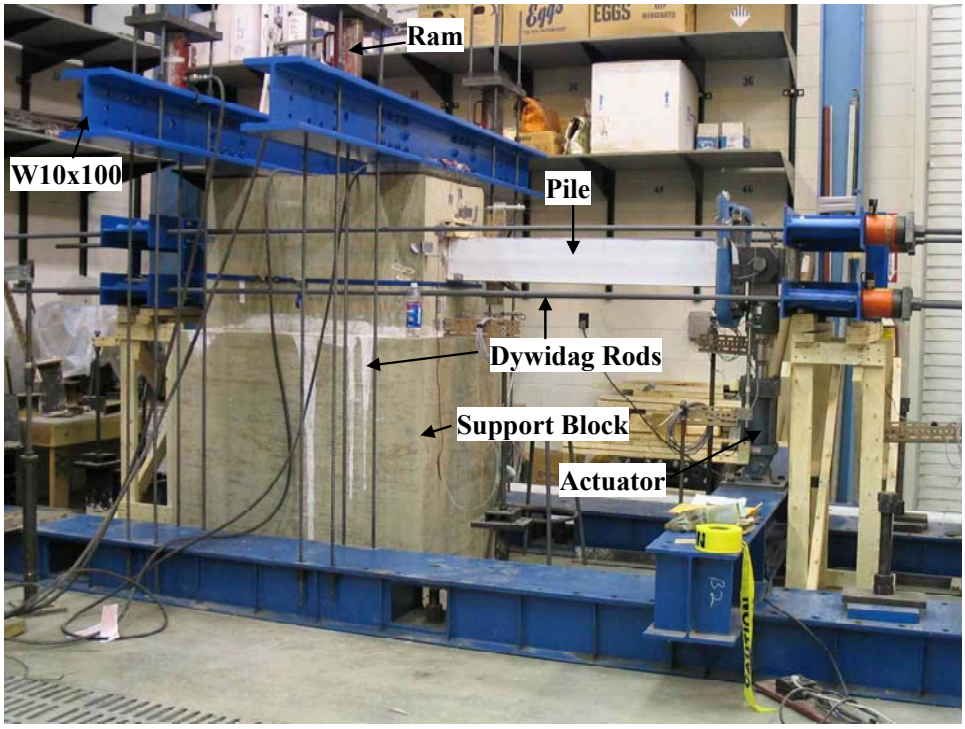

Figure 5.22: Clamping System

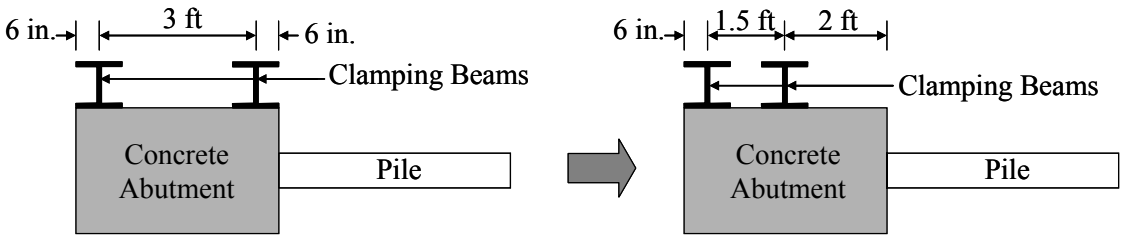

(a) Specimens 1 and 2 (b) Specimens 3 to 9

Figure 5.23: Clamping Beams

5.5.5 Self-Equilibrating Load System

A self-equilibrating load system consisting of four 1-in. ∅ Dywidag threadbars tied through W12x30 beams was used to provide axial load to the specimen. At the back of the concrete abutment, two W12x30 axial beams called "BA1" (Figure 5.24) were connected by two steel angles and WT sections. Four low-friction ball bearings were attached to each WT section to enable vertical movement of the axial load system. This system was designed to provide axial load while minimizing shear produced by the axial system. At the tip of the pile, two W12x30 axial beams called "BA2," were connected by two steel angles and a clevis plate (18 x 18 x 1 in.) as shown in Figure 5.25. Four 1-in. ∅ Dywidag threadbars tied through the axial beams, BA1 and BA2 were used to apply axial load to the pile specimen. The axial load was applied using four 30-ton hydraulic rams that were attached to the axial beams at the back of the concrete abutment. Hexagonal nuts and anchor plates were attached on each side of the Dywidag threadbars. The nuts were tightened when the axial load reached a specified value to maintain a constant axial load.

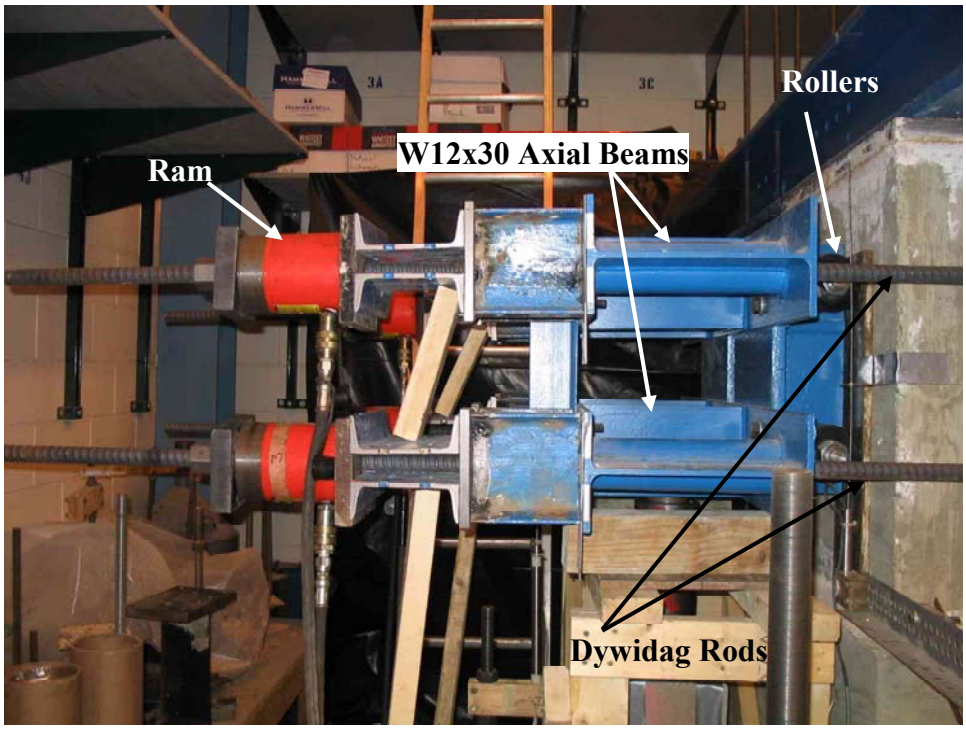

Figure 5.24: Axial Beam behind Concrete Abutment (BA1)

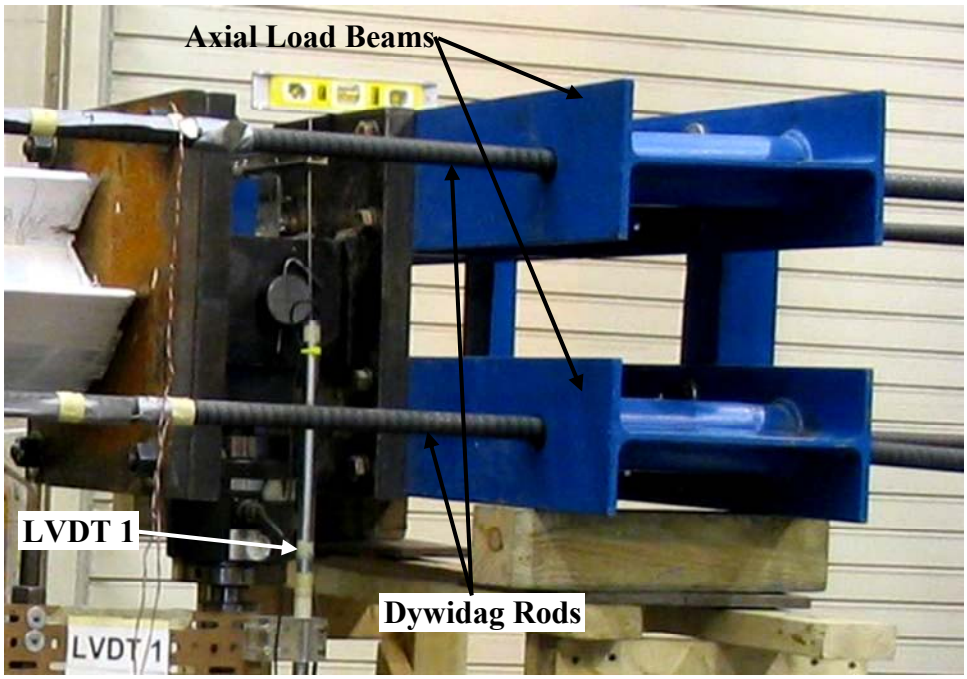

Figure 5.25: Axial Beam at the Pile Tip (BA2)

5.5.6 Casting and Curing

After the concrete had been placed into the forms, the specimen and concrete base were screeded and finished with trowels. The specimens were then allowed to set for two hours before wet burlap and plastic sheeting were used to cover the exposed top surfaces. Both wet burlap and the plastic were removed after a three day wet cure.

5.6 Test Setup

The piles were cyclically tested as a cantilever to simulate in-service behavior (Figure 5.26). As soil resistance was not included over the pile length, this test was considered to provide conservative results. For the HP8x36 bending about its 45° axis, a bracing frame was provided to prevent the pile from moving out-of-plane movement (Figure 5.27).

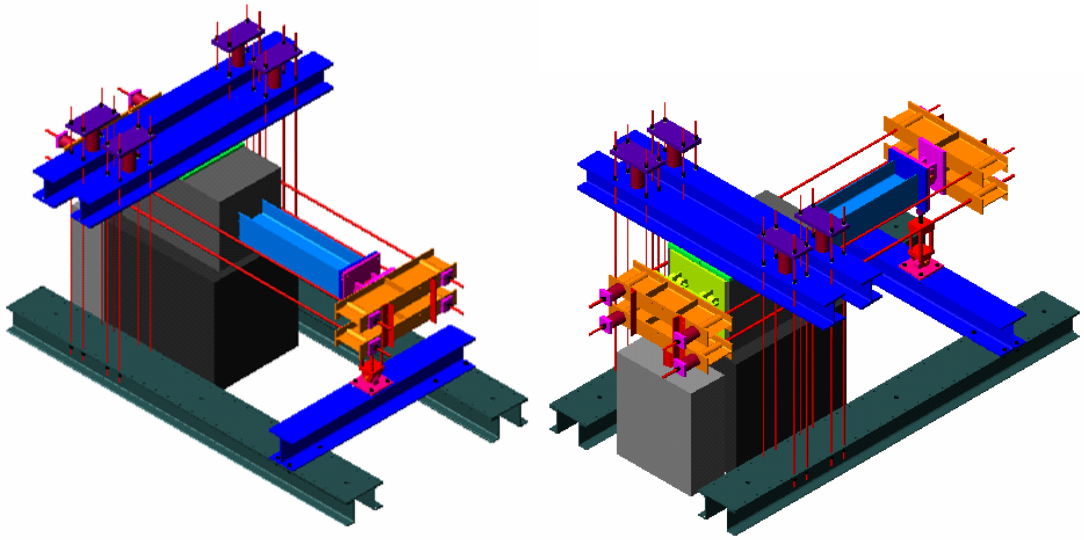

(a) Front View (b) Rear View

Figure 5.26: Scheme of Test Setup

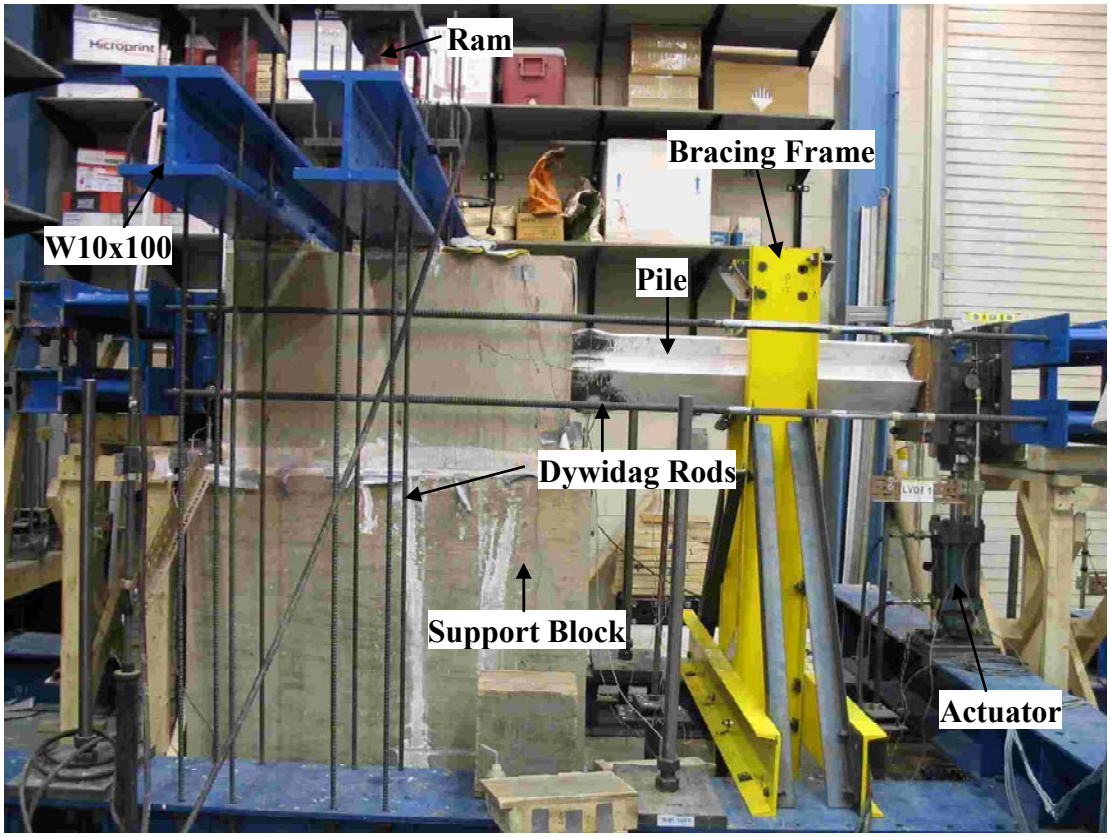

Figure 5.27: Test Setup in the Laboratory

Compressive axial load was applied horizontally to the end of the pile specimen through the self-equilibrating load system. Axial load was provided using four-60 kip hydraulic rams. The axial load was controlled using a 10,000-psi hand pump and monitored by strain gages on each of the 1 in.-∅ Dywidag rods. The axial load capacity of the test system was 240 kips.

Cyclic lateral loads were applied through an actuator capable of both tension and compression. The actuator had a lateral load capacity of 50 kips and a maximum displacement capacity of ±3 in.

Lateral load was monitored through the use of a load cell attached to the actuator. The load cell had a capacity of 100 kips. Lateral displacement, elevation of axial beams, rotation of concrete abutment, and rotation of the pile were monitored by displacement transducers. Additionally, strain gages were attached to the pile 1 in. from the abutment-pile connection to monitor strains.

5.7 Test Instrumentation

Linear voltage differential transducers (LVDT) and strain gages were used to monitor the response of the pile during testing.

5.7.1 Displacement

Figure 5.28 illustrates the locations of the LVDT's that were used to measure displacements.

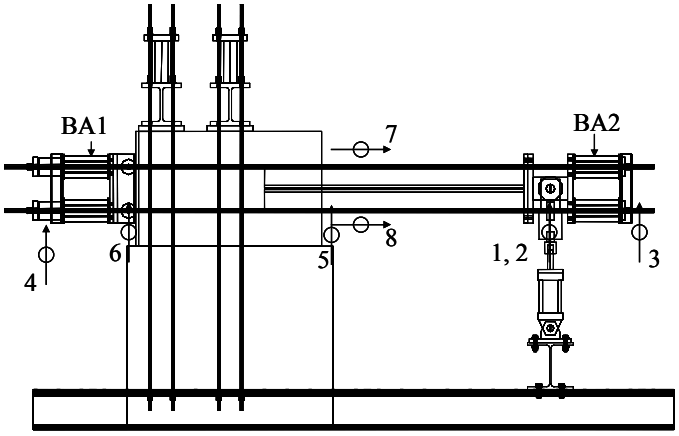

Figure 5.28: LVDT Locations

LVDTs No. 1 and 2 were located at the top of the knuckle connected to the load cell and the actuator to measure overall pile tip displacement. Due to the importance of this measurement, two LVDTs were used at this location to provide redundancy. LVDTs No. 3 and 4 were located at the center of the bottom of the axial beams, BA2 and BA1, respectively to measure the elevation of the Dywidag rods. LVDTs No. 5 and 6 were located at the face of the concrete abutment and were used to measure the rotation of the concrete abutment. LVDTs No. 7 and 8 were located 9 in. from the face of the concrete abutment and only attached to the H piles bending about their weak and strong axes. These LVDTs were used to measure localized connection rotation for the steel H piles. The relative rotation between the pile and the concrete abutment at an approximate distance of 9 in. from the face of the concrete abutment is determined using Equation 5-2.

$$\theta = \frac{\delta_7 - \delta_8}{D_{7-8}} \tag{5-2}$$

where:

δ_7 = displacement measured from LVDTs No. 7.

δ_8 = displacement measured from LVDTs No. 8.

$D_{7\text{-}8}$ = distance between LVDTs No. 7 and 8.

5.7.2 Strain Gages

Strain gages were installed on the piles at the abutment-pile interface. Strain gages were obtained from Measurements Group Inc. Figure 5.29 shows the strain gage locations for the steel piles. For the H piles bending about the weak and 45˚ axes, five gages were installed; four at the tips of the flanges and one at the center of the web. For the H pile bending about the strong axis, only four gages were installed at the tips of the flanges. For the CFT piles, only two gages were installed at the top and bottom of the tube perpendicular to the bending axis.

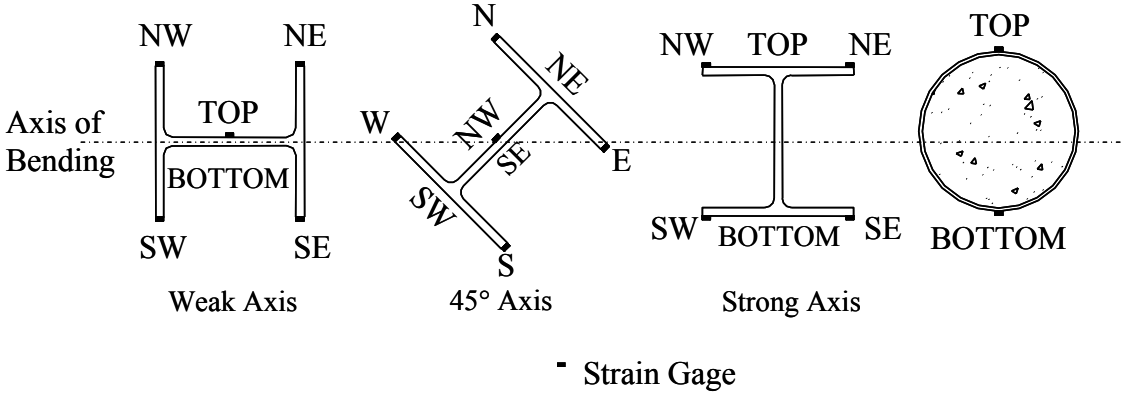

Figure 5.29: Strain Gages Location

The strains measured from these locations were also used to calculate the curvature, ϕ, of the pile cross section at the abutment-pile interface.

For the steel H-pile bending about the weak or strong axis:

$$\phi = \frac{\text{average}(\varepsilon_{SW}, \varepsilon_{SE}) - \text{average}(\varepsilon_{NW}, \varepsilon_{NE})}{D} \tag{5-3}$$

For the steel H pile bending about the 45° axis:

$$\phi = \frac{\varepsilon_S - \varepsilon_N}{D} \tag{5-4}$$

For the CFT piles:

$$\phi = \frac{\varepsilon_{BOT} - \varepsilon_{TOP}}{D} \tag{5-5}$$

where:

ε_{NW} = strain at NW tip of the H pile.

ε_{NE} = strain at NE tip of the H pile.

ε_{SE} = strain at SE tip of the H pile.

ε_{SW} = strain at SW tip of the H pile.

ε_N = strain at N tip of the H pile.

ε_S = strain at S tip of the H pile.

ε_{TOP} = strain at the top of the CFT pile.

ε_{BOT} = strain at the bottom of the CFT pile.

D = flange width for the steel H pile bending about the weak axis, or

D = distance from NW to SE edges for the steel H pile bending about its 45° axis, or

D = depth of the steel H pile bending about the strong axis, or

D = outer diameter of CFT piles.

5.8 Test Procedure

Prior to testing, the pile specimens were white-washed with a mixture of hydrated lime and water in a proportion of 1 lime to 3 water by weight in order to observe yielding of the pile. Next, axial load was applied to the specimen. This load was maintained constant throughout testing. Cyclic lateral loads were then applied to the specimen using displacement control. Both axial and cyclic lateral loads were applied at the pile tip until failure. The test was stopped when the pile could not maintain axial load, the abutment-pile connection deteriorated significantly, or the lateral load of the pile decreased significantly. Loads and lateral displacements were monitored continuously during testing to evaluate the behavior of the specimens.

In general, the pile was cycled using the displacement history listed in Table 5.10. The pile was cycled 0.25 in. for 5 cycles, 0.50 in. for 10 cycles and then 0.75 in. for 25 cycles to ensure that every part of test setup functioned properly before cycling at larger displacements. The piles were then cycled for 50 cycles at increasing displacement increments unless buckling of the pile or steel cracking was observed. Once the onset of buckling or cracking was evident, the pile was cycled for 100 cycles or until failure.

Throughout testing, data from strain gage measurements, displacement transducer readings, and actuator forces were collected. At each displacement stage and at other significant events in the behavior of the specimen, video and photographic recordings were taken.

Table 5.10: History of Testing

Displacement Range (in.)	No. of Cycles
0.25	5
0.50	10
0.75	25
1.00	50
1.25	50
1.50	50
⋮	50
Last	100

CHAPTER 6: EXPERIMENTAL RESULTS

6.1 Introduction

To better understand the behavior of piles for integral abutment bridges, low-cycle, large-amplitude lateral displacement tests were conducted. Nine piles were examined considering various pile types, orientations, and axial loads. The general behavior of the test specimens is discussed, and representative load-displacement relationships are presented. The effect of pile size, axial load, and pile orientation are also discussed. Detailed photographs of the pile response and individual load-displacement responses for each specimen are provided in Appendix I.

Throughout this chapter, the location conventions are as illustrated in Figure 6.1.

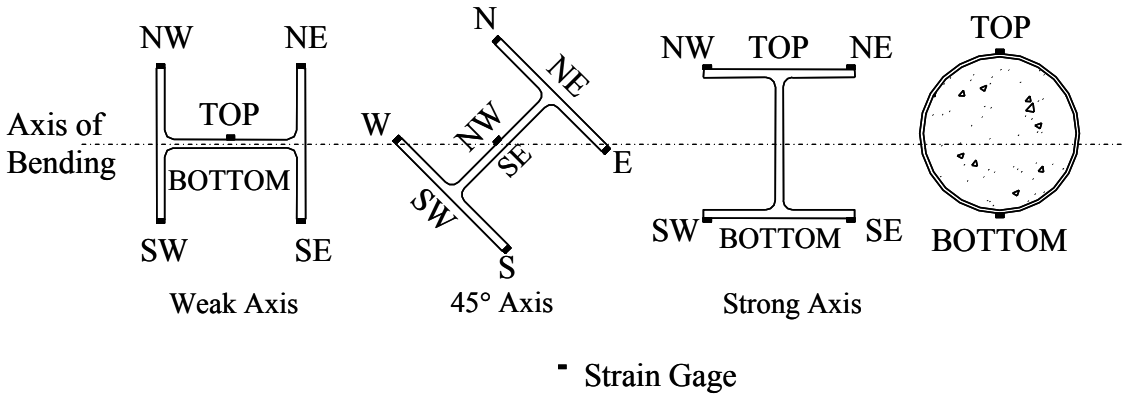

Figure 6.1: Location Conventions

6.2 General Behavior

For all specimens, the piles behaved linearly elastic for the displacement range of ±0.25 in. For displacement ranges of ±0.50 in. and higher, most pile specimens exhibited nonlinear behavior. Regions of the pile located close to the abutment-pile connection yielded. As the lateral displacement range increased, the lateral load increased nonlinearly. After a certain numbers of cycles, a decrease in the lateral load was observed. The pile started buckling and initial cracks occurred. Cracks propagated as the lateral displacement range increased. Finally, most of the piles fractured. Most of the flanges of the pile specimens were fractured except the HP8x36 that was loaded about its strong and 45° axes. In general, the lateral displacement capacity was controlled by the pile's fatigue performance. Table 6.1 shows the numbers of cycles achieved for each lateral displacement range for all specimens.

Table 6.1: Numbers of Cycles

Displacement Range (in.)	Specimens								
	1	**2**	**3**	**4**	**5**	**6**	**7**	**8**	**9**
0.25	5	5	5	5	5	5	5	5	5
0.50	10	10	10	10	10	10	10	10	10
0.75	25	25	25	25	25	25	25	25	25
1.00	50	50	50	50	50	50	50	50	50
1.25	**	**	50	50	50	50	50	50	50
1.50	50	100	50	50	50	100	100	100	50
1.75	**	100	100	50	50	70	33	10	100
2.00	50	-	100	50	50	-	-	-	100
2.25	50	-	-	100	-	-	-	-	-
2.50	100	-	-	66	-	-	-	-	-
2.75	25	-	-	-	-	-	-	-	-
3.00	80	-	-	-	-	-	-	-	-

** This displacement range was not included for the specified specimens.

The behavior of Specimen 5, an HP10x42 pile bending about its weak axis is discussed to illustrate the general behavior experienced by the majority of the specimens. For the displacement range of 0.25 in., the pile behaved linearly elastic and no yielding

was observed. The load-deflection curve remained linear (Figure 6.2) until a displacement range of 0.50 in. when all flanges demonstrated signs of yielding (Figure 6.3). For the displacement range of 0.75 in., the nonlinear behavior of the pile was more noticeable (Figure 6.4). Small local spalling of concrete was observed at the NE flange at the displacement range of 1.00 in. (Figure 6.5); however, the pile maintained its lateral load (Figure 6.6). A loss in lateral load was observed during cycling at a displacement range of 1.25 in. and all flanges started buckling at the end of 1.25 in. cycles (Figure 6.7). As the displacement range was increased to 1.50 in., all flanges showed more obvious signs of buckling and a decrease in lateral load capacity was observed as shown in Figure 6.8. For the displacement range of 1.75 in. (Figure 6.9), the web started yielding. More superficial spalling of concrete occurred on both the east and west sides. Finally, the pile failed by the 50th cycle at a displacement of 2.00 in. The failure was defined by the decrease in the lateral load capacity, which was decreased by 52% in the up direction and 67% in the down direction from the first cycle at the 2.00 in. displacement range (Figure 6.10).

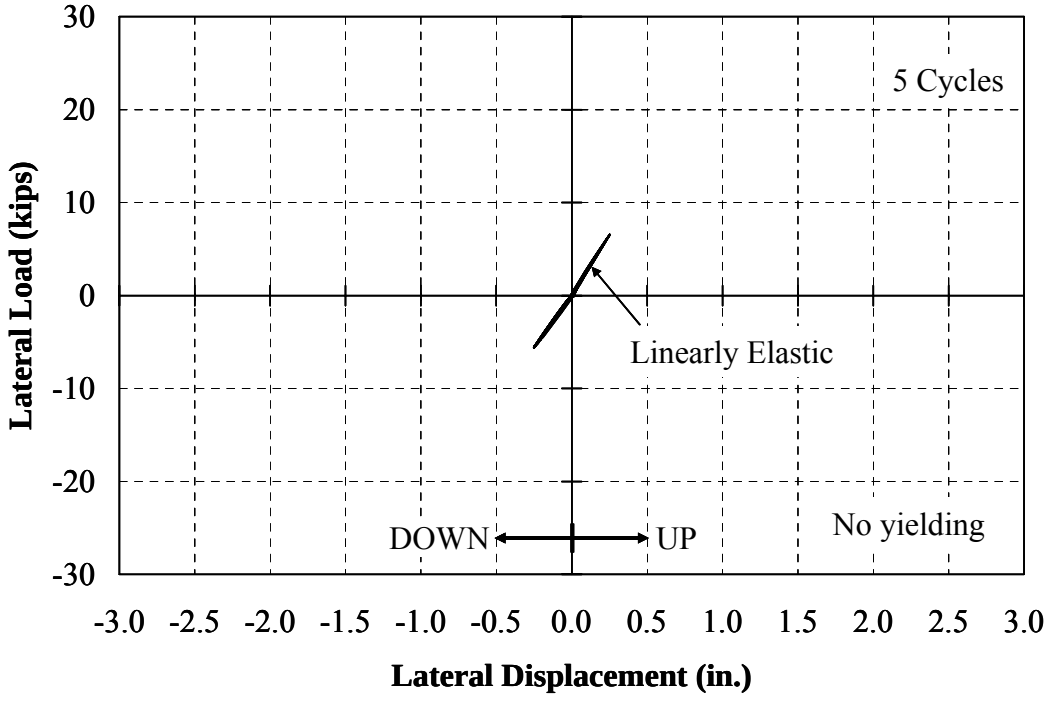

Figure 6.2: Specimen 5 – Load-Deflection Response (±0.25 in. Range)

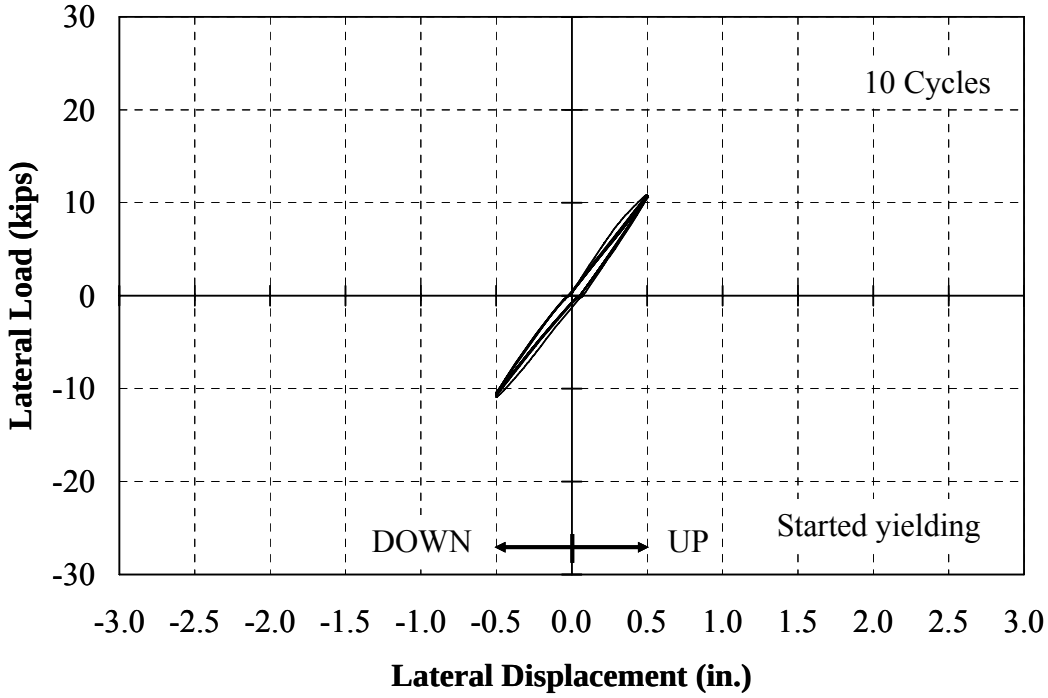

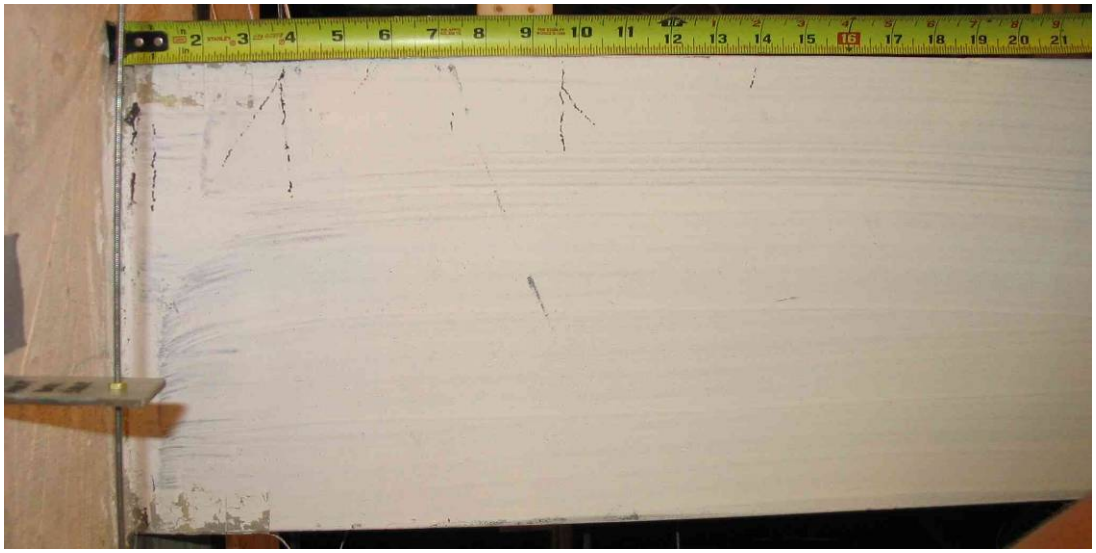

Figure 6.3: Specimen 5 – Load-Deflection Response (±0.50 in. Range)

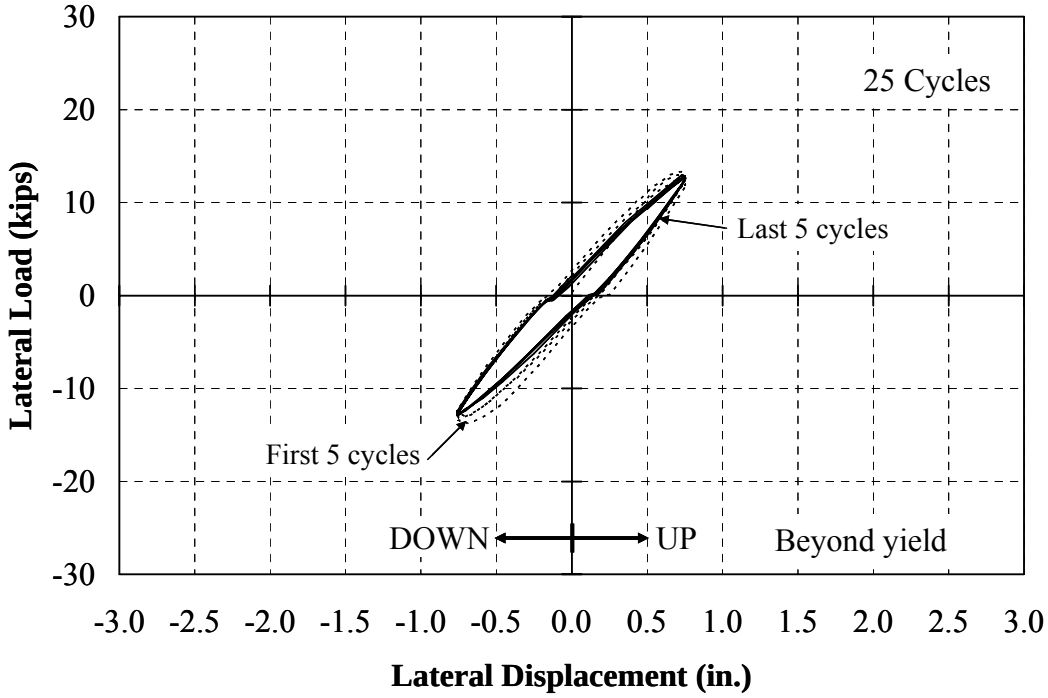

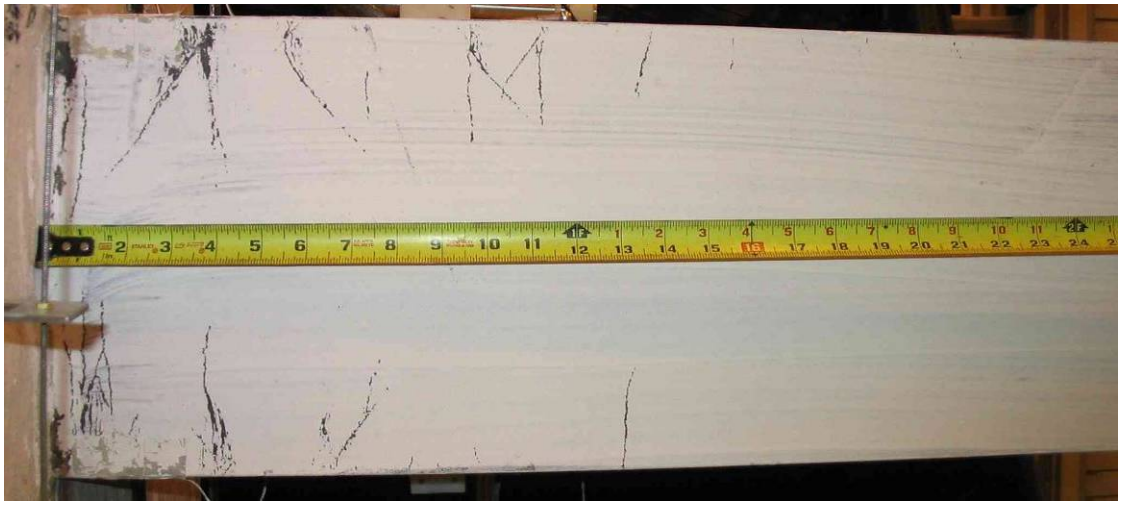

Figure 6.4: Specimen 5 – Load-Deflection Response (±0.75 in. Range)

Figure 6.5: Specimen 5 – Spalling of Concrete at the NE Flange

In summary, the flanges started yielding at a displacement range of 0.50 in. Yield initiated from the fixed end and propagated toward the pile tip. All flanges began buckling at a displacement range of 1.25 in. A series of photographs illustrates the crack propagation that occurred in the NW flange as shown in Figure 6.11. Cracks in the steel flanges grew up to 1/8 in. wide on the NW, NE, and SW flanges while a 1/16 in. crack occurred on the SE flange. The web started yielding during the 1.75 in. displacement range, and significant yielding was evident during the 2.00 in. displacement range (Figure 6.12). Ultimately, all flanges fractured during the 2.00 in. displacement range. Slight deterioration of the abutment-pile connection was observed as illustrated in Figure 6.13 which shows spalling of concrete on both the east and west sides of the pile. The displacement capacity is defined as the capacity of the pile to sustain the axial load until the lateral load started decreasing significantly. For this specimen, the lateral load started decreasing significantly in the 1.75 in. displacement range indicating a displacement capacity of 1.75 in.

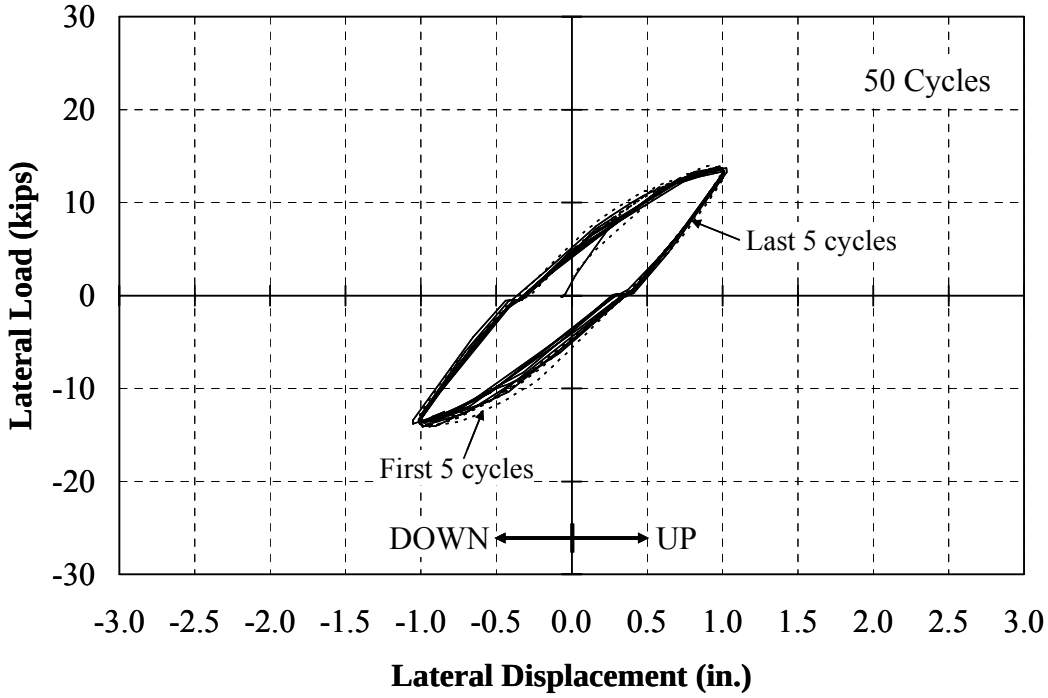

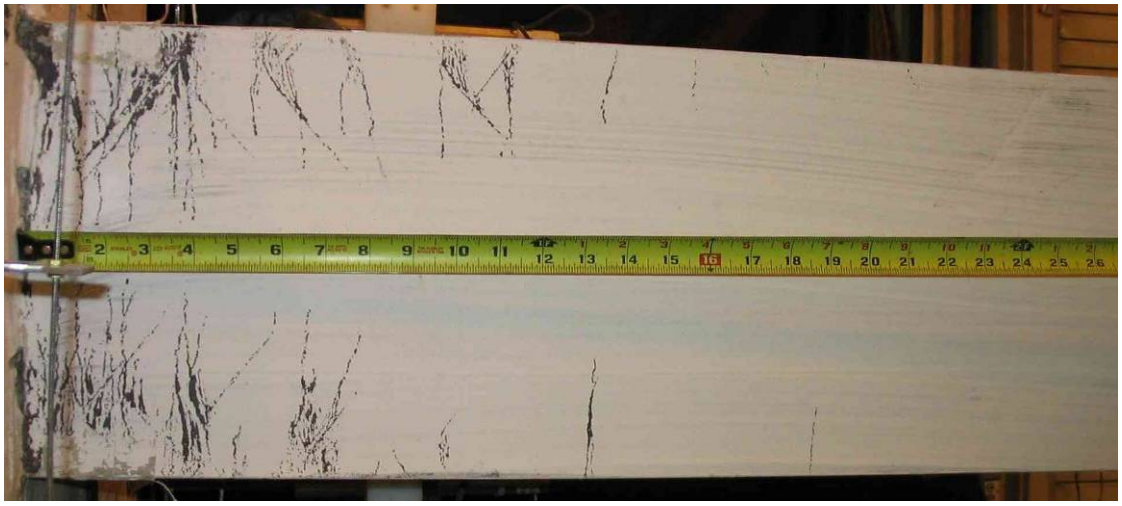

Figure 6.6: Specimen 5 – Load-Deflection Response (±1.00 in. Range)

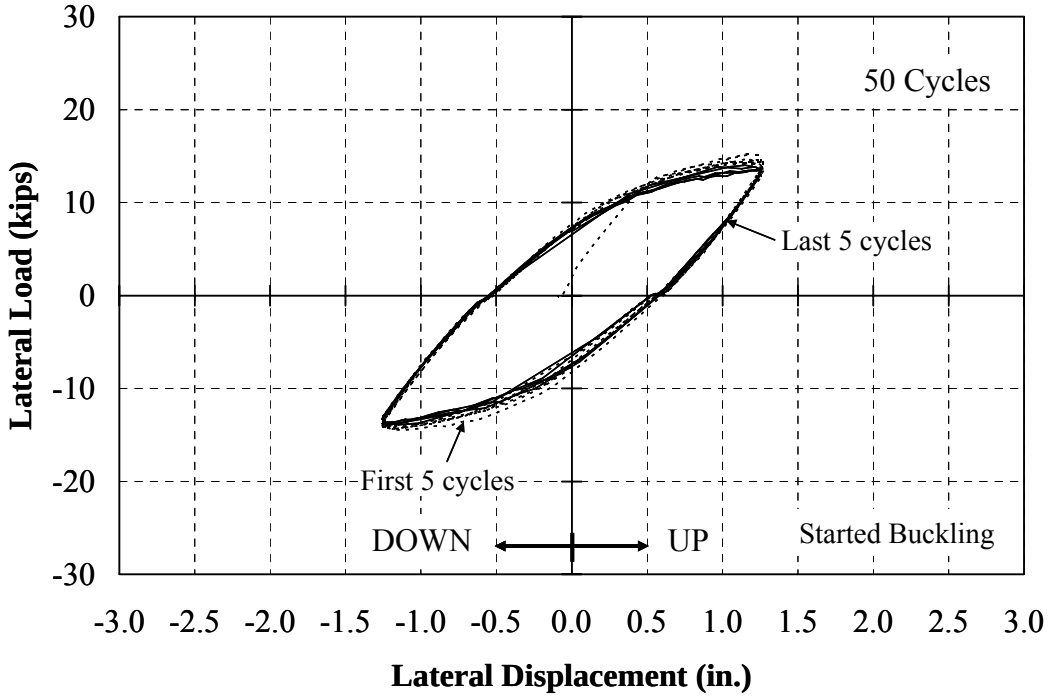

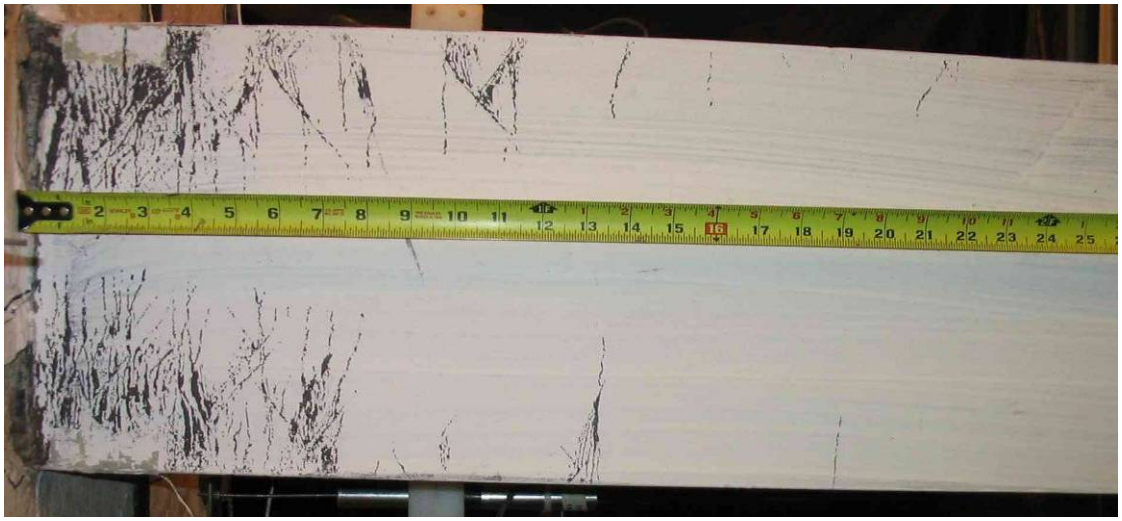

Figure 6.7: Specimen 5 – Load-Deflection Response (±1.25 in. Range)

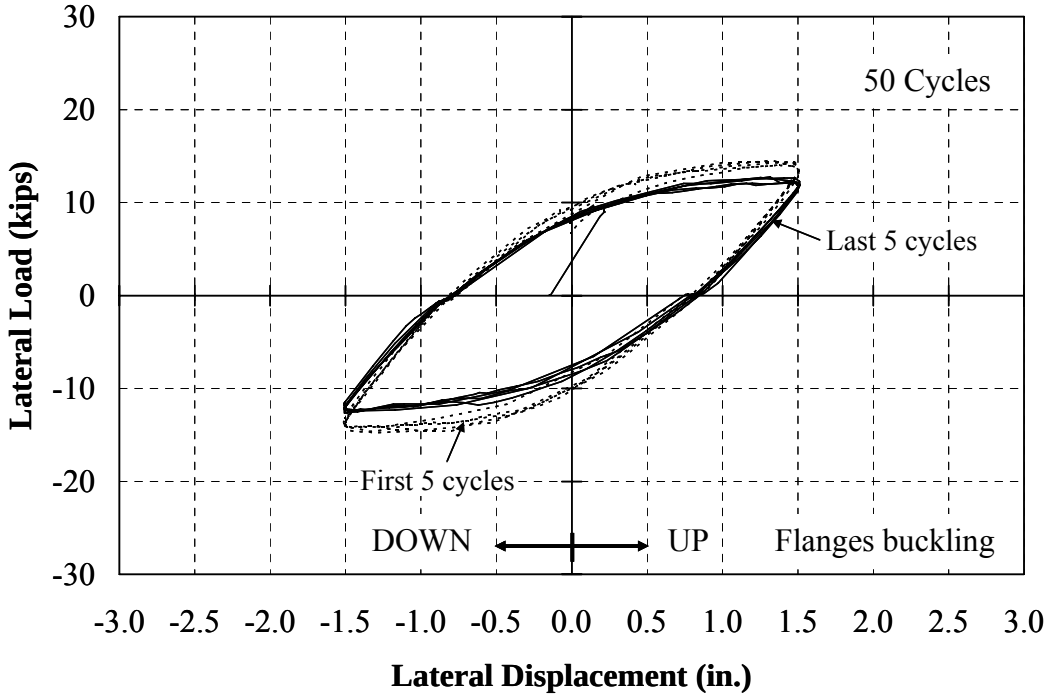

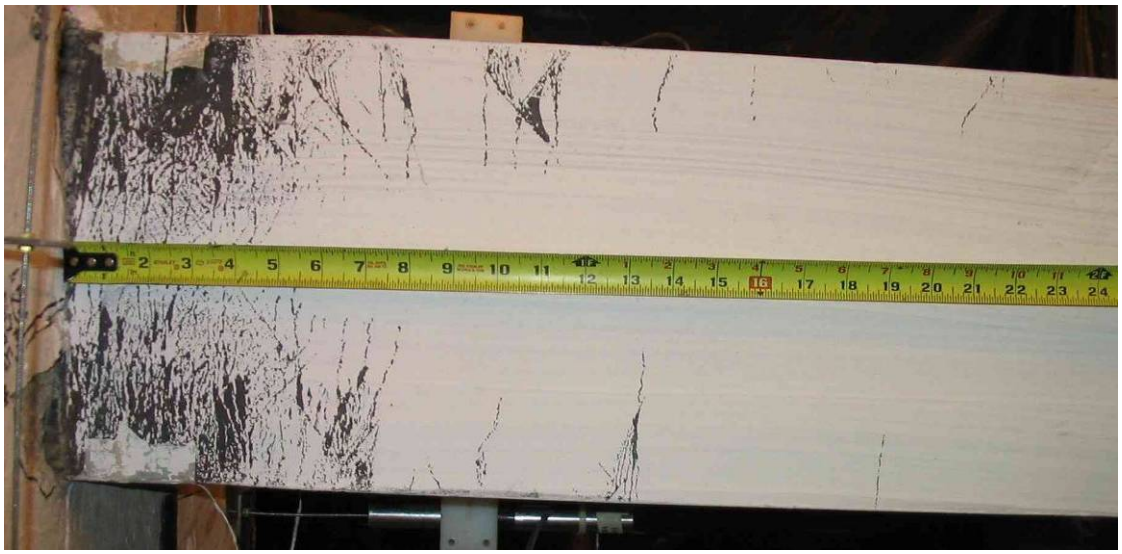

Figure 6.8: Specimen 5 – Load-Deflection Response (±1.50 in. Range)

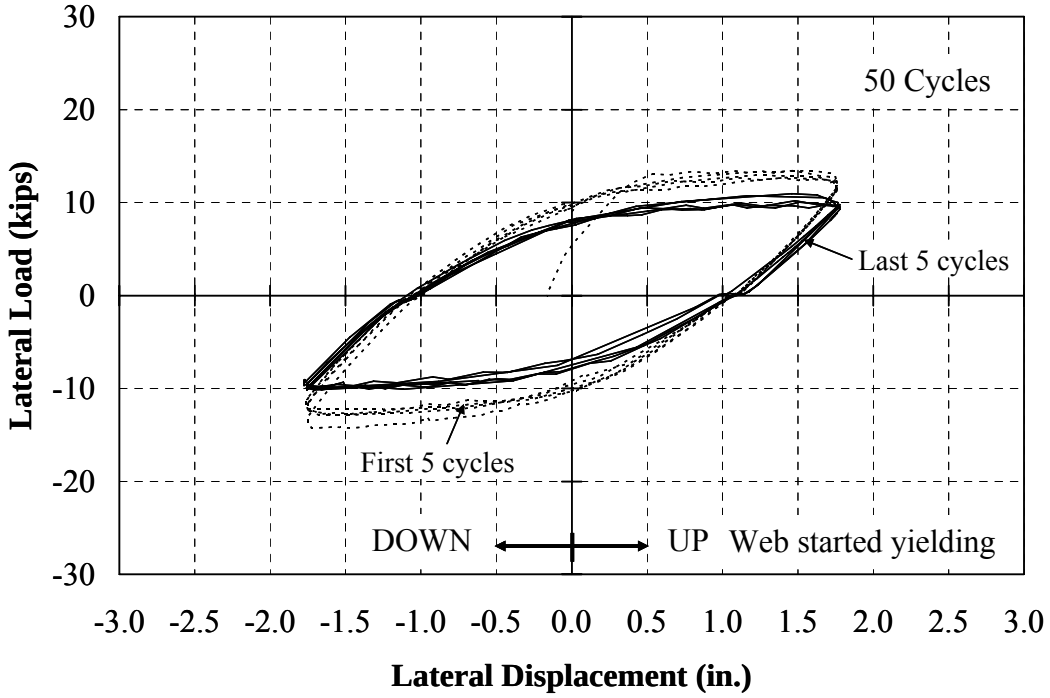

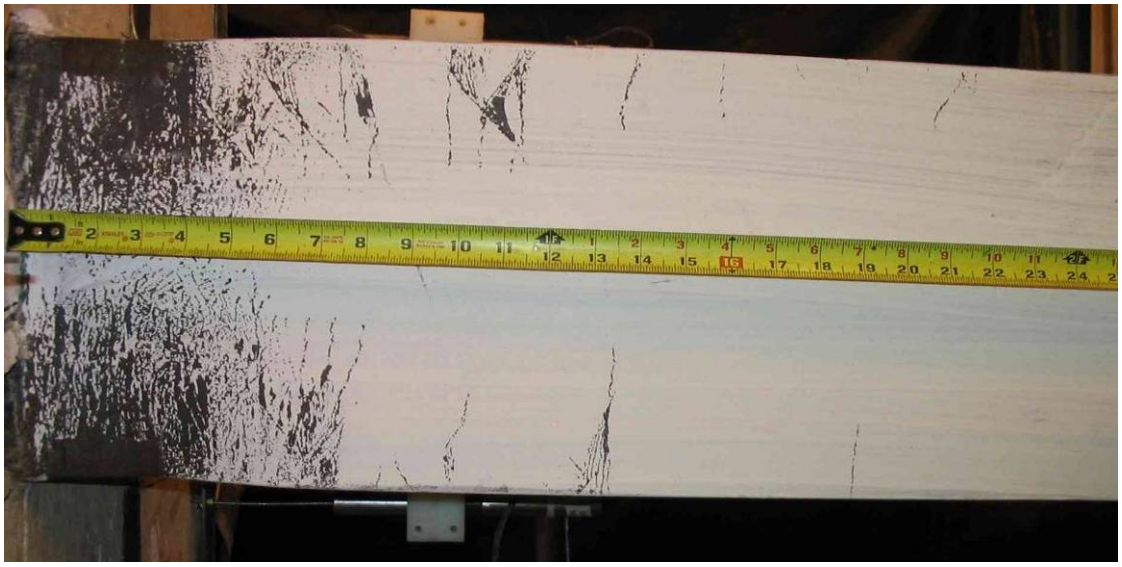

Figure 6.9: Specimen 5 – Load-Deflection Response (±1.75 in. Range)

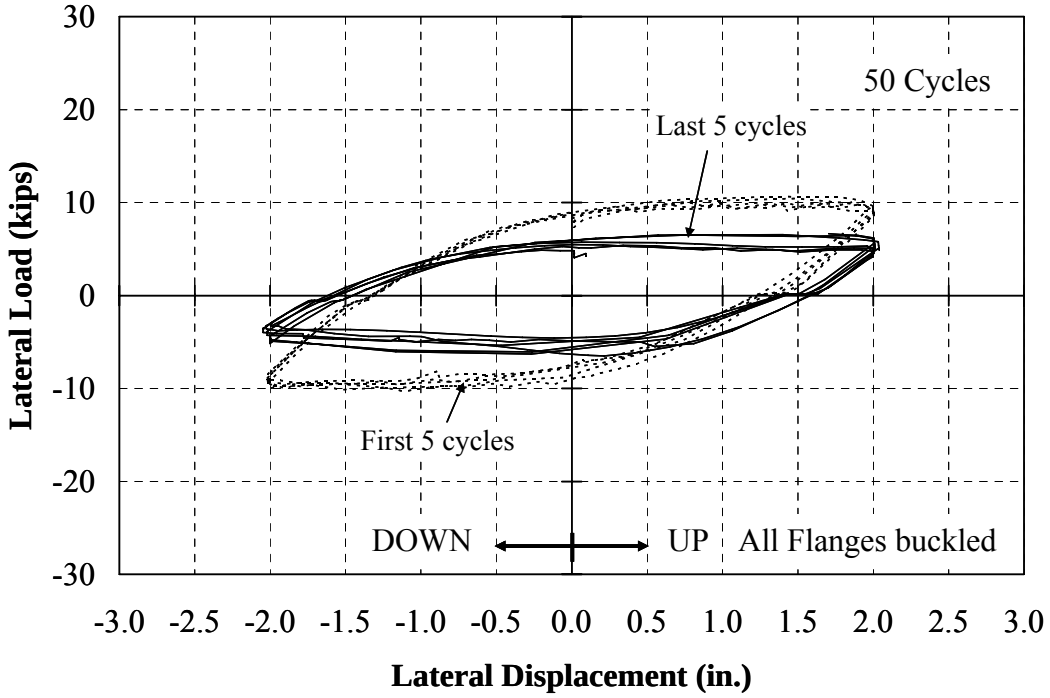

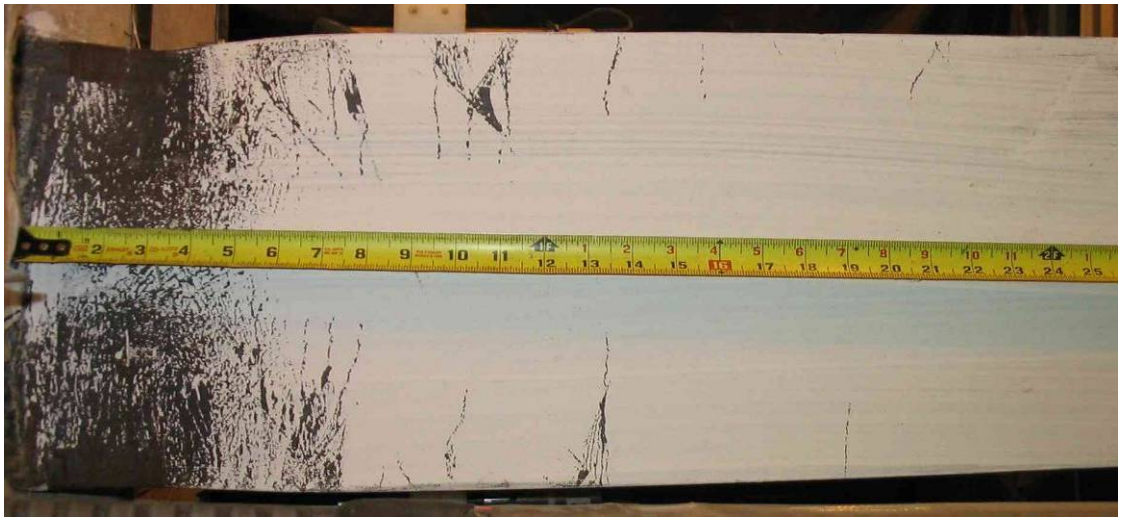

Figure 6.10: Specimen 5 – Load-Deflection Response (±2.00 in. Range)

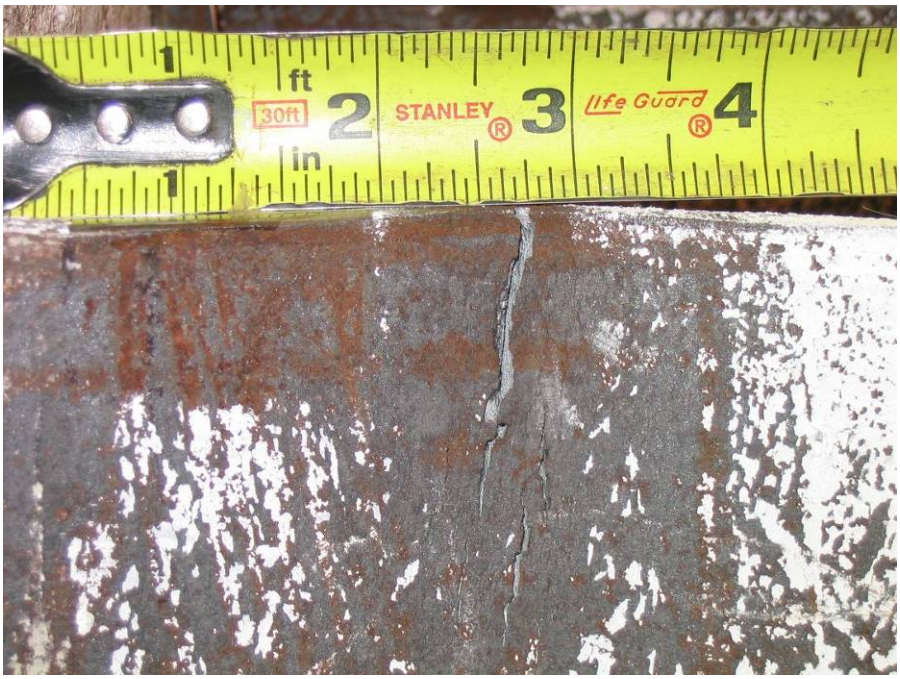

(a) Displacement Range of 1.25 in.

(b) Displacement Range of 1.50 in.

Figure 6.11: Specimen 5 – Crack Propagation

(c) Displacement Range of 1.75 in.

(d) Displacement Range of 2.00 in.

Figure 6.11: Specimen 5 – Crack Propagation (Continued)

(a) Displacement Range of 1.75 in.

(b) Displacement Range of 2.00 in.

Figure 6.12: Specimen 5 – Web Yielding at the Bottom of the Web

(a) 1.75 in. Displacement Range, West Side

(b) 2.00 in. Displacement Range, East Side

Figure 6.13: Specimen 5 – Spalling of Concrete

The axial load of Specimen 5 during the displacement range of 0.50, 1.00, 1.75, and 2.00 in. is shown in Figure 6.14. The axial load was maintained fairly well throughout the test. The axial load was observed to decrease while the pile tip was moved up and down due to shortening of the horizontal Dywidag rods during bending of the pile. The axial load variation during cycling increased as the displacement at the pile tip increased. The axial load at the neutral position (zero deflection) was continuously monitored. When the axial load was observed to decrease after a certain number of cycles (typically every 10 cycles), the axial load was reapplied at the neutral position to the force required to achieve the desired axial stress (9 ksi for Specimen 5).

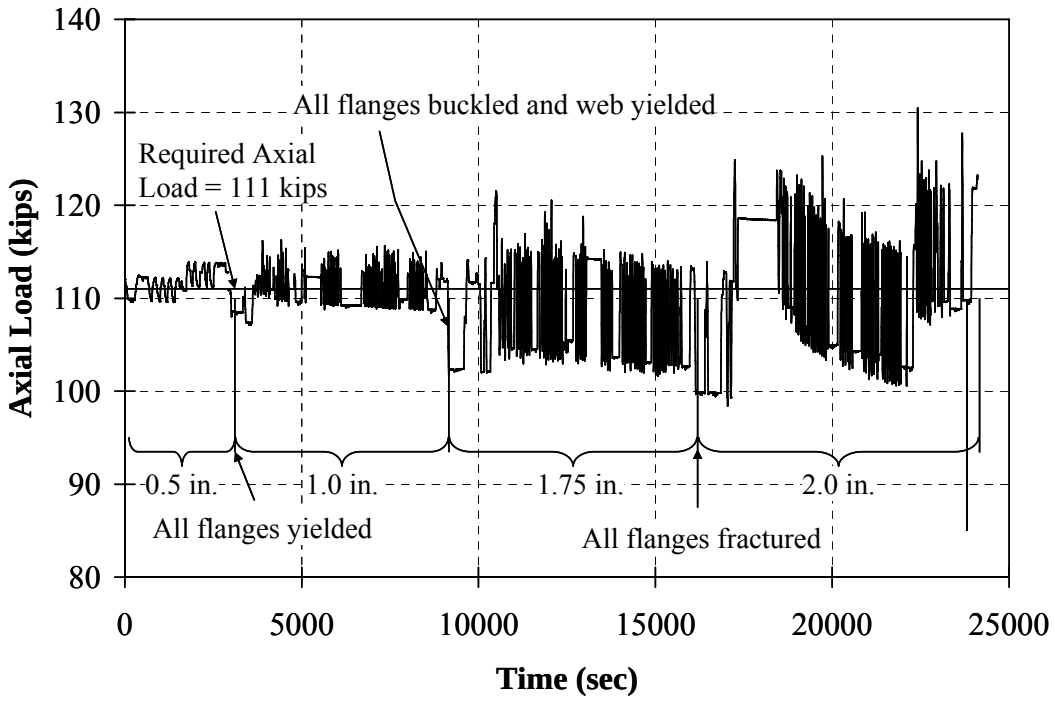

Figure 6.14: Specimen 5 – Axial Load

The abutment rotations of Specimen 5 calculated from LVDTs 5 and 6 during the displacement range of 0.50, 1.00, 1.75, and 2.00 in. are presented in Figure 6.15. As shown, the abutment rotation decreased after local flange buckling. The decrease of the abutment rotation indicated deterioration at the abutment-pile connection or buckling of the pile. The abutment rotation of Specimen 5 is representative of the typical abutment rotation for the other specimens.

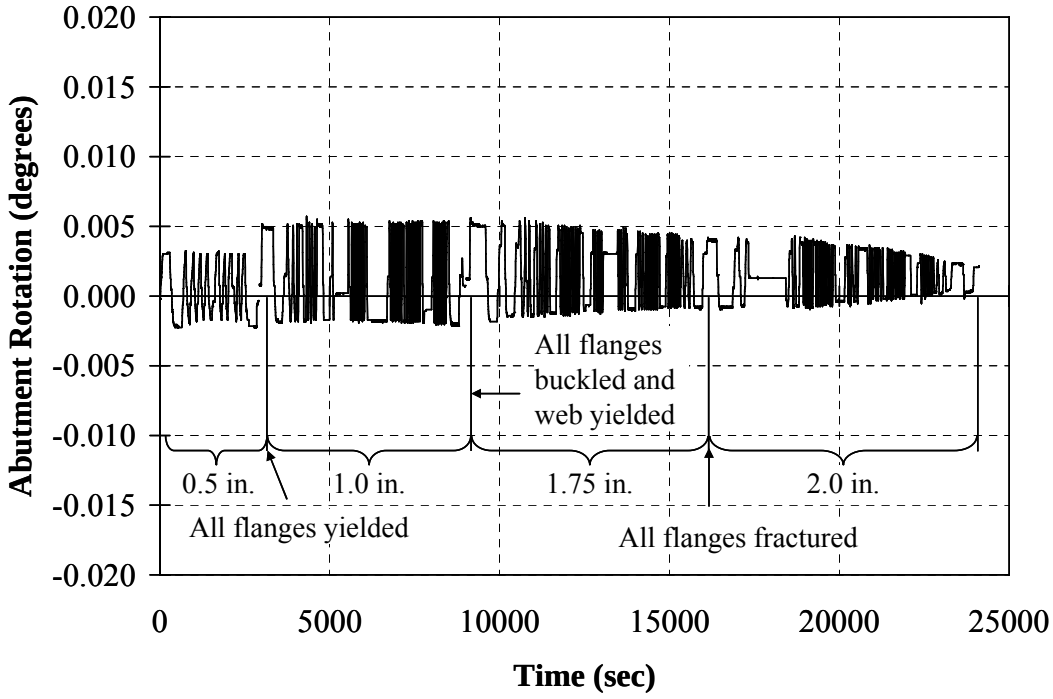

Figure 6.15: Specimen 5 – Abutment Rotation

The pile rotation of Specimen 5 calculated from LVDTs 7 and 8 during the displacement range of 0.50, 1.00, 1.75, and 2.00 in. is presented in Figure 6.16. The pile rotations did not change significantly even after the pile buckled. The pile rotation of Specimen 5 is also representative of the typical pile rotations experienced by the other specimens.

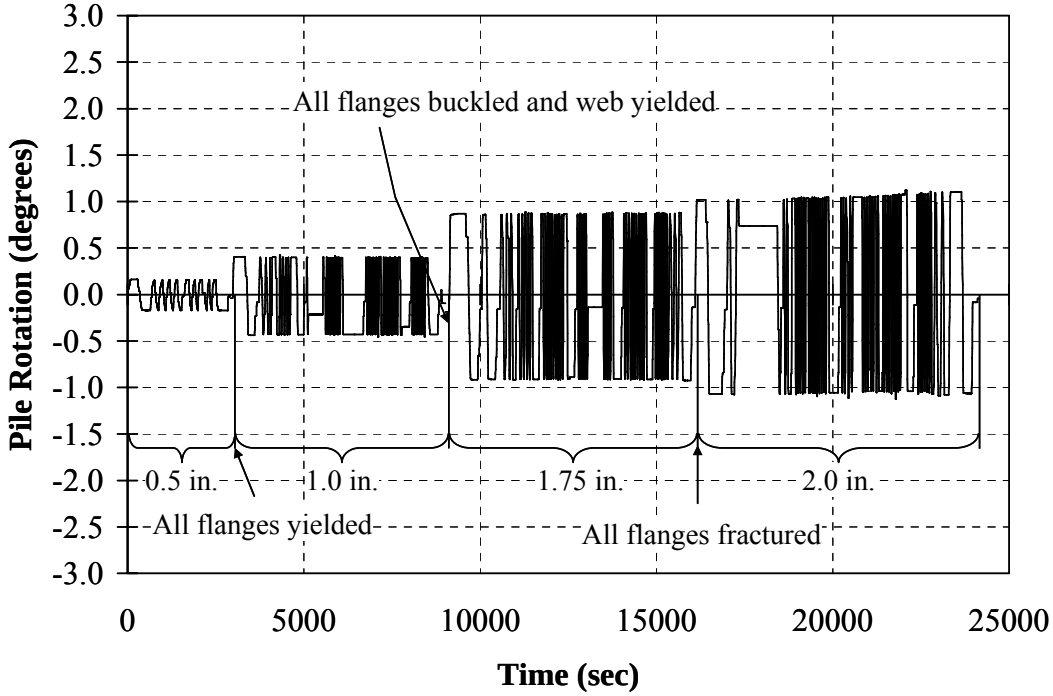

Figure 6.16: Specimen 5 – Pile Rotation

6.3 Experimental Results

6.3.1 Specimen 1 (HP8x36, Weak Axis, 9 ksi)

Specimen 1 was the first H pile tested. An axial load of approximately 95 kips based on 25% of the specified yield strength, f_y, (taken as 36 ksi for all H piles) was applied at the pile tip. This specimen is the reference for the evaluation of the effect of pile size, pile orientation, and axial load on pile behavior.

The NE, SW, and SE flanges of the pile started yielding at the 0.50 in. displacement range while the NW flanges of the pile started yielding at the 1.00 in. displacement range. The NE flange started buckling during the displacement range of 2.00 in., and all flanges buckled during the displacement range of 2.50 in. Figure 6.17 shows buckling of the NW and NE flanges.

Figure 6.17: Specimen 1 – Pile Buckling

Cracks were observed in all flanges that resulted in complete flange fracture by the end of the test. Figure 6.18 shows minor deterioration at the abutment-pile connection along with the NE flange fracture. The lateral load was observed to decrease 19% in the up direction and 43% in the down direction over the course of the 3.00 in.

displacement range. The pile had a lateral load capacity of 14 kips in the up direction and 13 kips in the down direction. The pile reached a deflection of 3.00 in. in the up direction (+3.00 in.) and 2.40 in. in the down direction (-2.40 in.). The pile was limited to a deflection of -2.40 in. because of the range of the actuator. The pile reached +3.00 in. without major damage at the abutment-pile connection. Only small local spalling of the concrete occurred. The axial load measured at the neutral position was observed to be fairly constant during the test. The failure of the pile was denoted by a significant decrease of the lateral load capacity in the 80th cycle of the 3.00 in. displacement range as shown in Figure 6.19.

The overall load-deflection response is presented in Figure 6.20, and a summary of the test is provided in Table 6.2. The displacement ductility is defined as a ratio of the displacement capacity and the displacement at first yield. The displacement ductility of the pile, μ, was approximately 6.0.

Figure 6.18: Specimen 1 – Flange Cracking

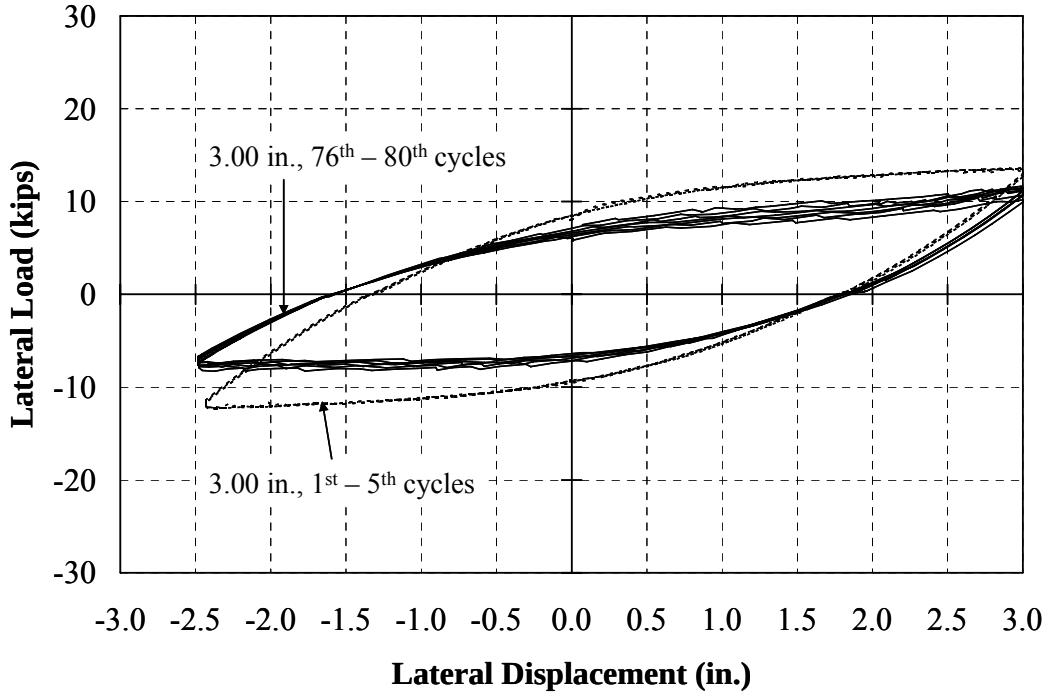

Figure 6.19: Specimen 1 - Load-Deflection Response (±3.00 in. Range)

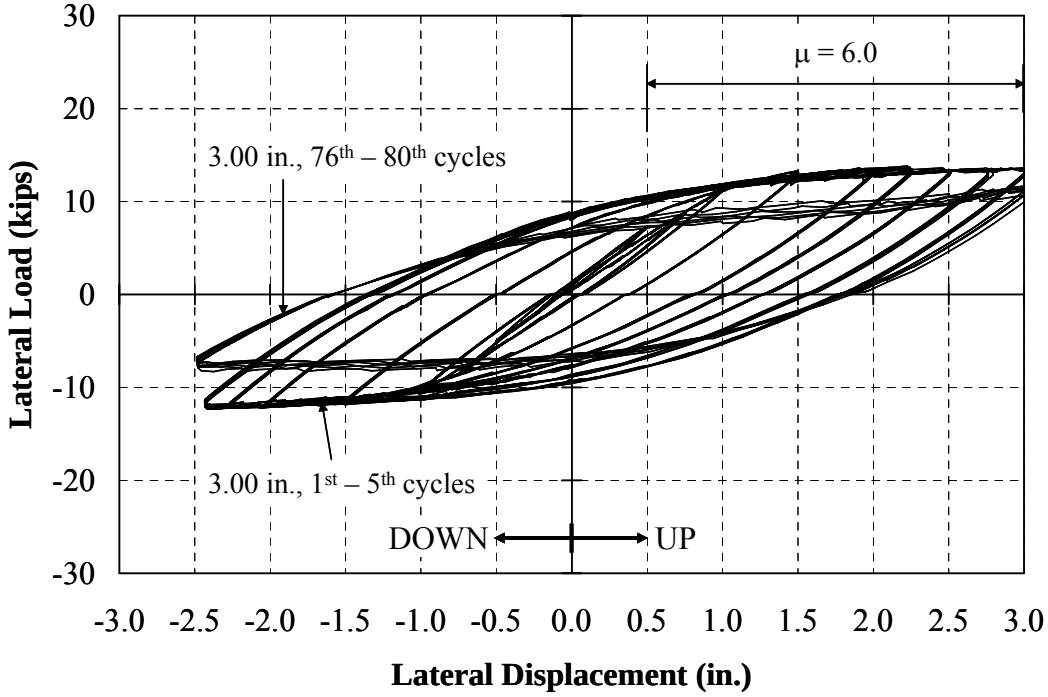

Figure 6.20: Specimen 1 – Overall Load-Deflection Response

Table 6.2: Specimen 1 – Test Summary

Displ. Range (in.)	Total Cycles	Yielding Location from Fixed End (in.)				Avg. Axial Load (kips)			Max. H (kips)		Remark
		NW	NE	SW	SE	UP	Neutral	DOWN	UP	DOWN	
0.25	5	-	-	-	-	-	-	-	4.5	-2.2	- No Yielding
0.50	10	-	-	0.25	0.50	95	-	100	7.4	-5.1	- The NE, SW, and SE flanges yielded
0.75	25	-	-	0.25	3.25	92	94	94	10.1	-8.7	- The NW flange yielded
1.00	50	12.63	15.25	9.25	15.50	93	93	92	11.6	-10.8	
1.50	50	12.63	17.25	11.88	18.13	97	95	93	13.4	-12.1	- Small spalling on the east side of concrete abutment
2.00	50	22.75	21.75	12.75	20.25	90	97	95	14.3	-12.9	- The NE flange buckled
2.25	50	26.50	22.00	12.75	20.75	86	98	91	13.5	-11.6	
2.50	100	22.75	21.75	12.75	23.25	83	95	89	14.3	-12.8	- All flanges buckled - Pile tip could move to only -2.33"
2.75	25	26.50	22.00	12.75	23.25	79	97	88	13.6	-12.3	
3.00	80	26.50	22.00	14.00	23.25	76	97	88	13.6	-12.3 @ -2.33″	- Cracks in all flanges were developed - The NE flange fractured - Lateral load dropped to 11 kips @ 3.00", and -7 kips @ -2.43"

6.3.2 Specimen 2 (HP8x36, Strong Axis, 9 ksi)

Specimen 2 was the same pile size and was subjected to the same axial stress as Specimen 1. This specimen, however, was oriented for strong axis bending to evaluate the effect of pile orientation. By inspection, no yielding was observed until 0.75 in., but strain gages on the flanges indicated yielding of the NW and SW flanges in the 0.50 in. displacement range. Yielding of all flanges was evident and pull-out cracks on the concrete abutment were noted as early as the 0.75 in. displacement range. Pinching of the lateral load-deflection response was evident as early as the 1.00 in. displacement range. The pinching could be attributed to the deterioration of the concrete at the connection. The NW and SW flanges started buckling during the displacement range of 1.50 in. and all flanges buckled during the 1.75 in. displacement range. Figure 6.21 shows buckling of the NE and SE flanges along with deterioration at the abutment-pile connection.

Figure 6.21: Specimen 2 – Flange Buckling on the East Side

The pile response was limited to a displacement of only ± 1.75 in. because of significant deterioration at the abutment-pile connection as shown in Figures 6.22 and 6.23. While the abutment-pile connection of Specimen 2 was more severely deteriorated than that of Specimen 1, only buckling of the pile flanges occurred. No cracks or fractures of flanges were observed. The axial load started to drop while cycling at the 1.75 in. displacement. Axial load was added at the neutral level to ensure that the pile carried approximately 9 ksi. Nevertheless the pile maintained its axial load. The lateral load was observed to slightly decrease 6% in the up direction and 3% in the down direction during the 1.75 in. displacement range. This response indicates that the pile can maintain both axial and lateral load during the final displacement range of 1.75 in. as shown in Figure 6.24.

The overall load-deflection response is shown in Figure 6.25 and a summary of the test is provided in Table 6.3. The pile had a lateral load capacity of 24 kips in the up direction and 23 kips in the down direction. The displacement ductility of the pile, μ, was approximately 3.5. Failure was denoted by significant damage at the abutment–pile connection which was evident in the 100th cycle of the 1.75 in. displacement range.

Figure 6.22: Specimen 2 –Abutment-Pile Connection Damage (West Side)

Figure 6.23: Specimen 2 –Abutment-Pile Connection Damage (East Side)

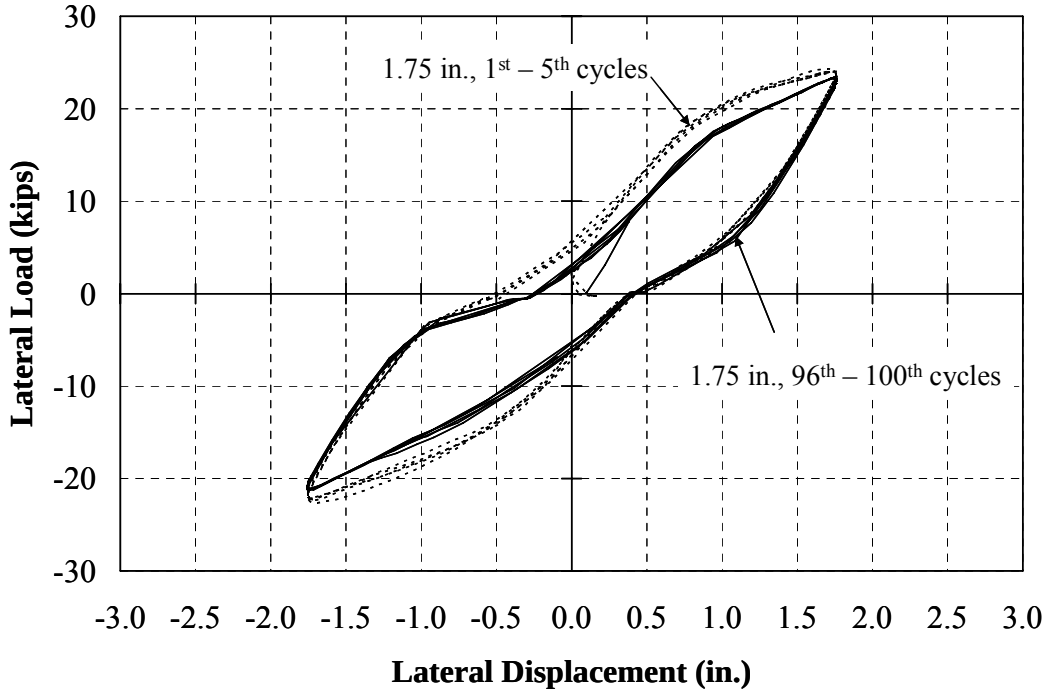

Figure 6.24: Specimen 2 – Load-Deflection Response (±1.75 in. Range)

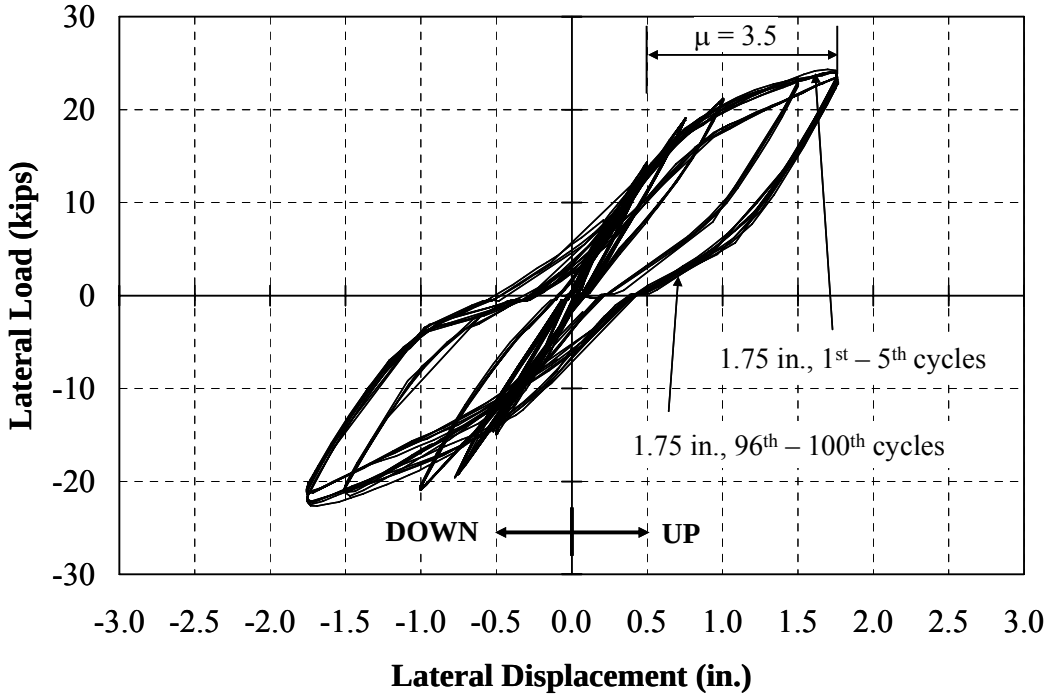

Figure 6.25: Specimen 2 – Overall Load-Deflection Response

Table 6.3: Specimen 2 – Test Summary

Displ. Range (in.)	Total Cycles	Yielding Location from Fixed End (in.)				Avg. Axial Load (kips)			Max. H (kips)		Remark
		NW	NE	SW	SE	UP	Neutral	DOWN	UP	DOWN	
0.25	5	-	-	-	-	93	94	94	8.3	-8.7	- No yielding on pile
0.50	10	-	-	-	-	94	94	96	14.4	-15.0	- The NW and SW flanges yielded
0.75	25	-	-	1.13	-	95	98	101	20.0	-20.4	- Pull-out cracks on concrete abutment were observed - All flanges yielded
1.00	50	2.13	0.50	2.50	5.50	95	97	99	22.1	-22.1	- Abutment-pile connection started deteriorating after 5th cycle
1.50	100	4.00	5.00	7.00	5.75	95	100	104	24.7	-23.5	- @ 81st cycle, the NW flange buckled - @ 91st cycle, the SW flange buckled
1.75	100	4.00	5.00	7.00	5.75	94	107	95	24.1	-20.9	- @1st cycle, the NE flange buckled - @10th cycle, the SE flange buckled - Abutment-pile connection deteriorated significantly to a depth of 6 to 8 in. - Axial load at neutral position was decreased very slightly while cycling

6.3.3 Specimen 3 (HP8x36, 45° Axis, 9 ksi)

Specimen 3 was the same pile size as Specimens 1 and 2, but considered different orientation. Due to its 45° axis bending, the pile tended to move out-of-plane. A bracing frame was established to prevent out-of-plane movement of the pile as shown in Figure 6.26. The frame was designed such that the pile could move ½ in. out-of-plane; however, due to construction tolerance, only 3/8 in. was provided between the pile and the frame.

(a) Bracing Frame (b) 3/8 in. Gap

Figure 6.26: Specimen 3 - Bracing Frame

The north and south flanges started yielding as early as the 0.50 in. displacement range. Cracks in the concrete at the edges of all flanges were noticed during the 1.00 in. displacement range, and the pile slightly moved (1/8 in.) out-of-plane. At the end of the 1.25 in. displacement range, the crack in the concrete at the edge of the west flange extended to the edge of the abutment. At the beginning of the 1.50 in. displacement range, all flanges yielded, and cracks in the concrete at the edges of the north and east flanges extended to the edge of the abutment. The web started yielding and the pile moved 3/8 in. out-of-plane. The north flange started buckling in the 30^{th} cycle of the 1.50 in. displacement range, while the south flange started buckling at the beginning of the 1.75 in. displacement range. These two flanges buckled first because they were at the extreme edges. The crack in the concrete at the south flange extended to the bottom edge of the abutment at the beginning of the 1.75 in. displacement range. Figure 6.27 shows the cracks in the concrete at the edges of the west, north, east, and south flanges extended to the edge of the abutment. Finally, the east and west flanges buckled, and fracture of the north flange was observed during the 2.00 in. displacement range as shown in Figure 6.28. In addition, severe web yielding extended 6 in. outward from the abutment-pile connection as illustrated in Figure 6.29. As indicated in Figure 6.30, the lateral load was observed to reduce 16% in the up direction and 22% in the down direction during the 2.00 in. displacement range. Nevertheless, the abutment-pile connection was only slightly damaged, and the axial load was maintained.

The overall load-deflection response of Specimen 3 is presented in Figure 6.31, and a summary of the test is provided in Table 6.4. A lateral load capacity of the pile was 18 kips in the up direction and 17 kips in the down direction. The displacement ductility, μ, was approximately 4.0. The test was terminated due to loss of the lateral load capacity in the 80^{th} cycle of the 2.00 in. displacement range.

(a) West Flange

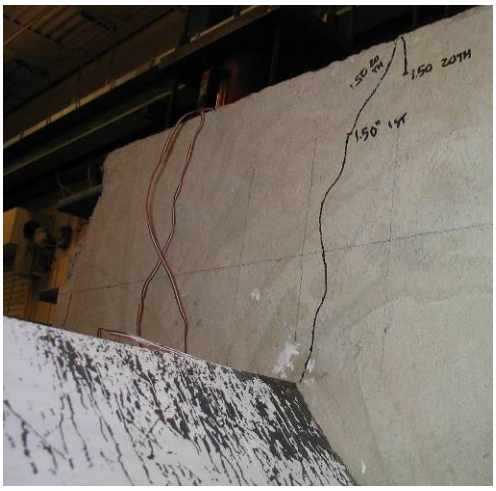

(b) North Flange

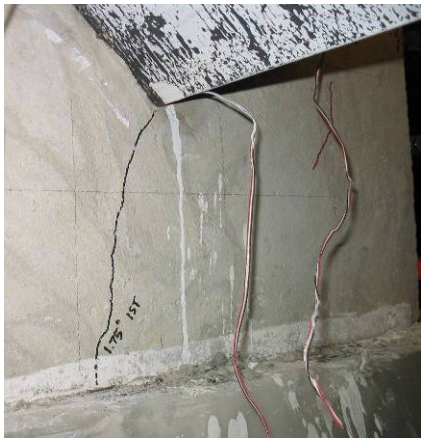

(c) South Flange

(d) East Flange

Figure 6.27: Specimen 3 – Cracks in Concrete

Figure 6.28: Specimen 3 – Fracture of the North Flange

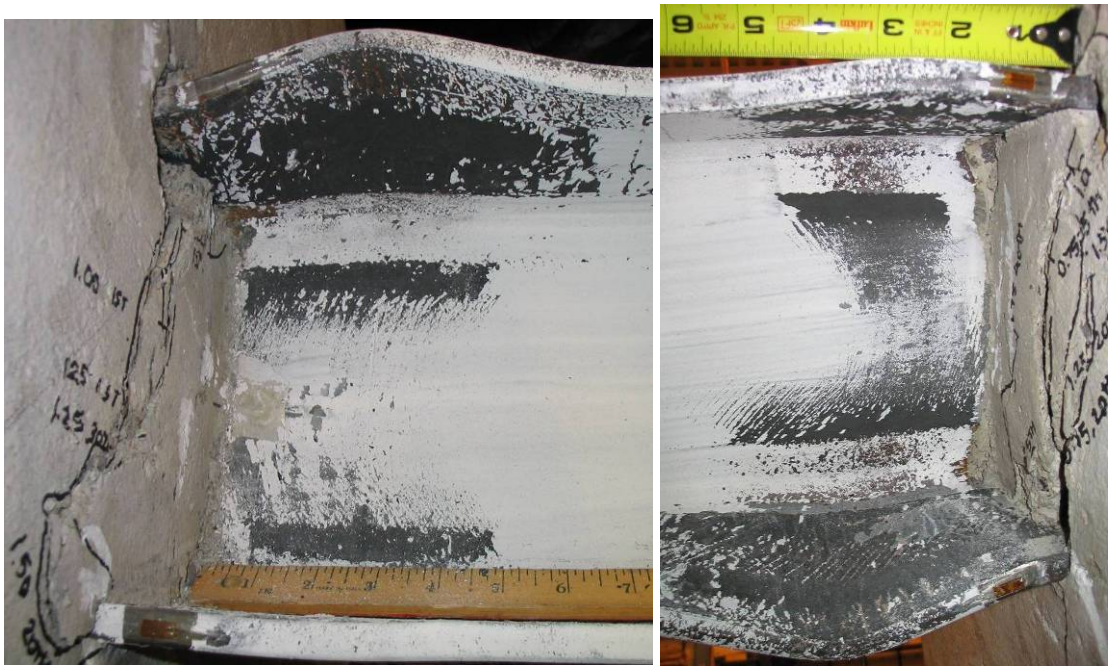

(a) NW Side (b) SE Side

Figure 6.29: Specimen 3 – Web Yielding

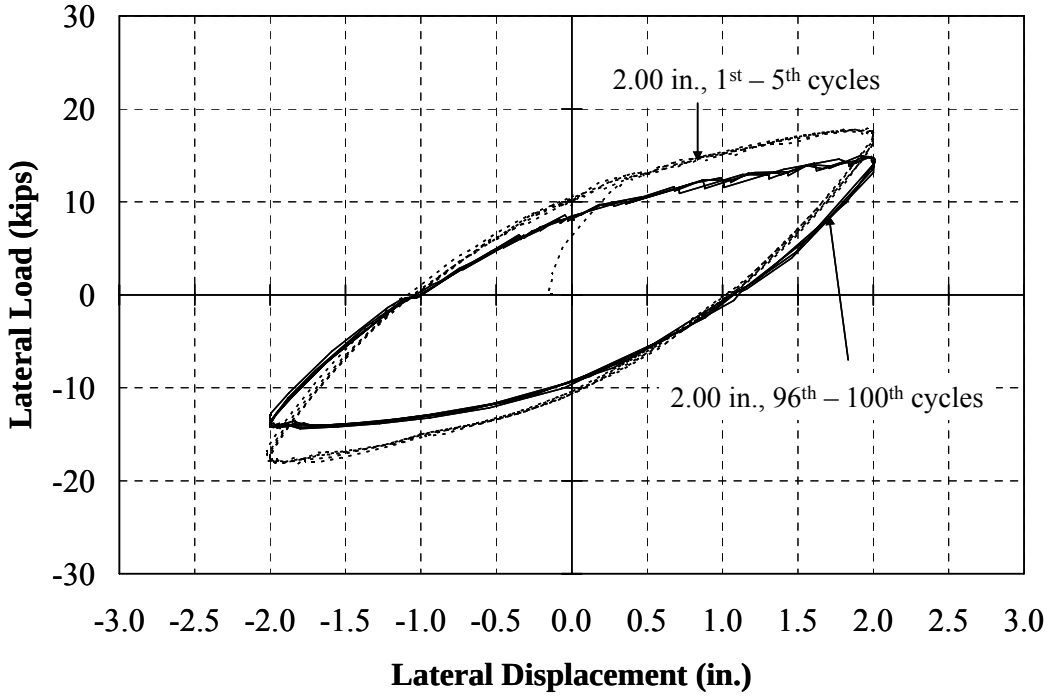

Figure 6.30: Specimen 3 – Load-Deflection Response (±2.00 in. Range)

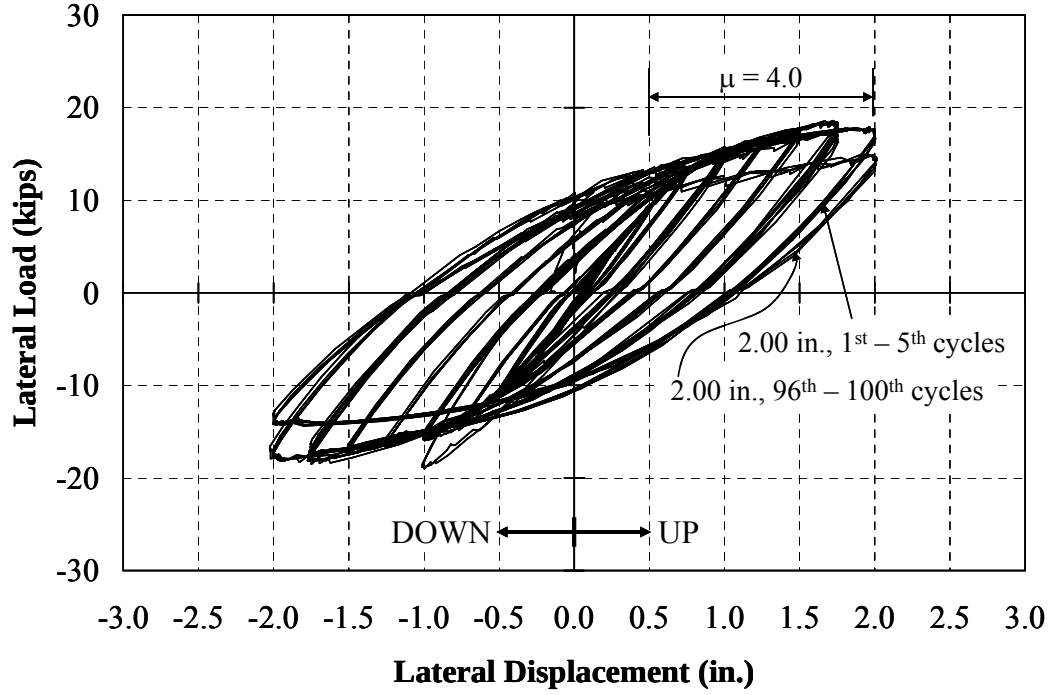

Figure 6.31: Specimen 3 – Overall Load-Deflection Response

Table 6.4: Specimen 3 – Test Summary

Displ. Range (in.)	Total Cycles	Yielding Location from Fixed End (in.)				Avg. Axial Load (kips)			Max. H (kips)		Remark
		W	N	S	E	UP	Neutral	DOWN	UP	DOWN	
0.25	5	-	-	-	-	92	93	93	4.5	-7.2	- No yielding on pile
0.50	10	-	1.00	5.25	-	89	88	89	9.4	-11.1	- The north and south flanges yielded
0.75	25	-	15.00	15.50	-	92	93	94	13.1	-14.1	- Concrete crack on the abutment was found at the edge of the south flange
1.00	50	-	19.50	19.50	-	94	94	96	15.2	-15.6	- All flanges yielded - Concrete cracks on the abutment were found at the edge of all flanges - The pile moved 1/8" out-of-plane
1.25	50	-	19.75	19.75	-	93	94	96	16.6	-16.5	- Concrete spalling at north flange was found - The pile moved 3/8" out-of-plane - Concrete crack grew from the west flange to the edge of abutment
1.50	50	1.00	20.50	22.75	4.75	91	94	94	17.5	-17.2	- Concrete cracks grew to the north and east edges of the abutment - The pile moved 3/8" out-of-plane - @ 10th cycle, web yielded 2.75 in. and 2.00 in. from the abutment-pile connection at the top and bottom of pile, respectively - @ 20th cycle, concrete cracks on the top of the abutment were found - @ 30th cycle, the north flange buckled
1.75	100	1.00	20.50	22.75	4.75	89	95	93	17.9	-17.1	- @ 10th cycle, the south flange buckled - Web yielded 5" and 5.75" from the fixed end on the NW and SE sides, respectively
2.00	100	1.00	20.50	22.75	4.75	83	92	88	16.7	-17.3	- @ 80th cycle, the west and east flanges buckled - @ 100th cycle, the north flange fractured - Web yielded 6" from the fixed end at the NW and SE sides

6.3.4 Specimen 4 (HP8x36, Weak Axis, 18 ksi)

Specimen 4 was the same pile size as Specimen 1; however, it was subjected to twice the axial load to evaluate the effect of axial load on pile behavior. The NW, SW, and SE flanges yielded at the 0.50 in. displacement range. The NE flange and the bottom of the web yielded during the 0.75 in. displacement range, and limited small spalling of concrete was noticed. At the beginning of the 2.00 in. displacement range, the top of the web yielded, and the lateral load capacity was observed to decrease. All flanges buckled during the 2.25 in. displacement range. At the end of the 2.50 in. displacement range, the web was severely buckled as illustrated in Figure 6.32. As indicated in Figure 6.33, the lateral load decreased 29% in the up direction and 23% in the down direction over the course of the 2.50 in. displacement range. Despite of the significant web yielding, the axial load continued to be maintained.

The overall load-deflection response of Specimen 4 is presented in Figure 6.34, and a summary of the test is provided in Table 6.5. The lateral load capacity of Specimen 4 was observed to be 8.5 kips in the up direction and 9.5 kips in the down direction. The displacement ductility, μ, was approximately 5.0. The test was discontinued with flange buckling because of the loss of lateral load capacity and severe web buckling during the 66th cycle of the 2.00 in. displacement range.

Figure 6.32: Specimen 4 – Web Yielding (2.50 in., 66th Cycle)

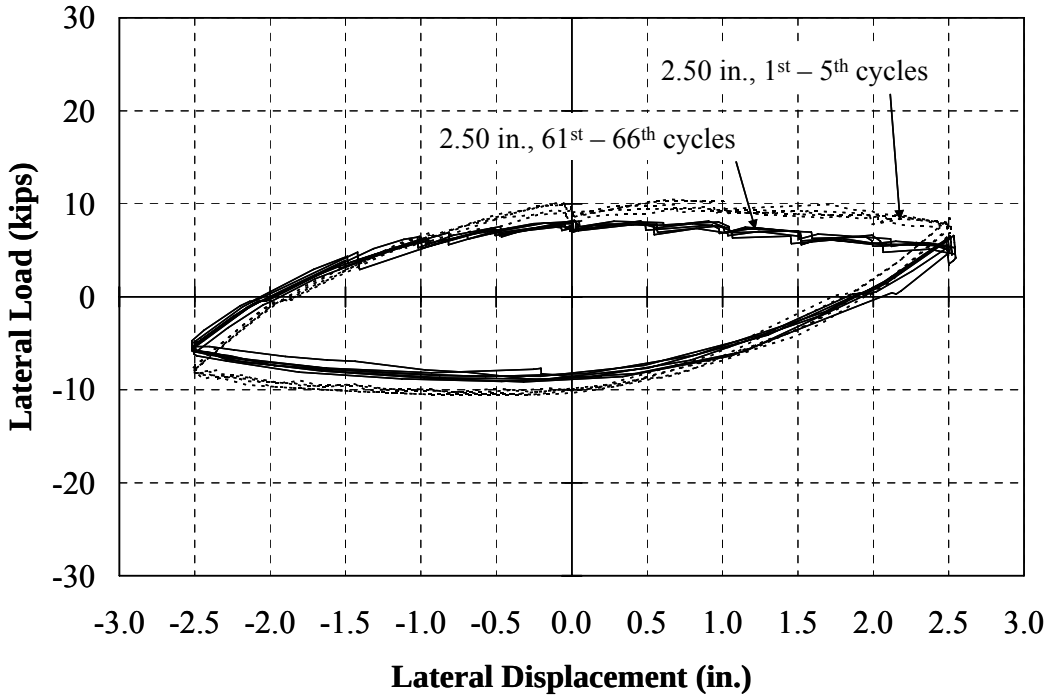

Figure 6.33: Specimen 4 – Load-Deflection Response (±2.50 in. Range)

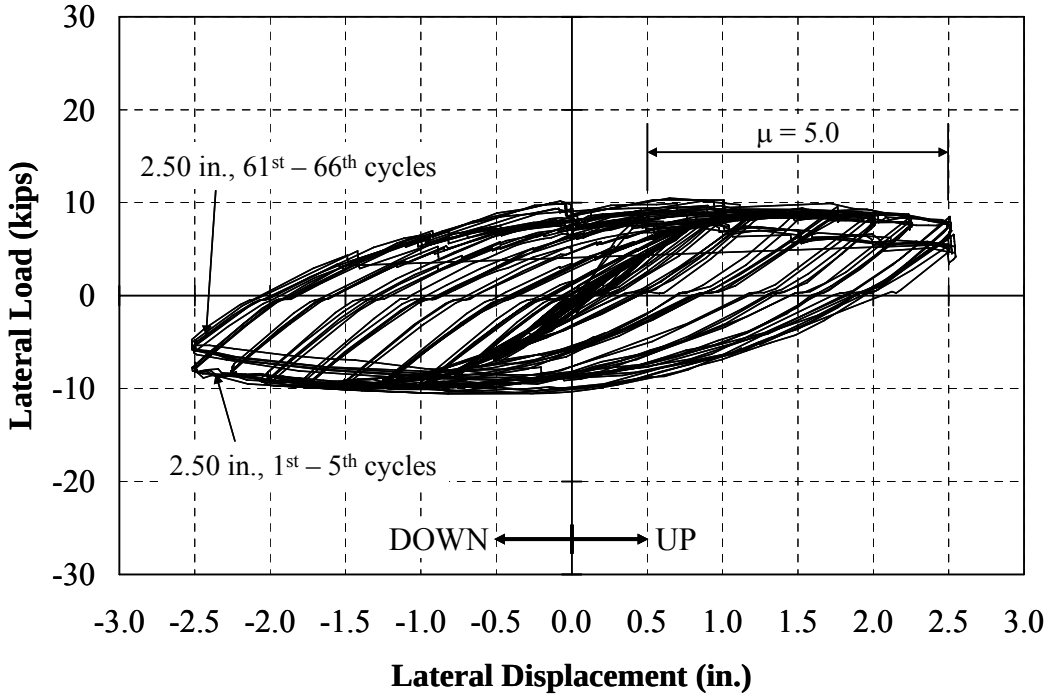

Figure 6.34: Specimen 4 – Overall Load-Deflection Response

Table 6.5: Specimen 4 – Test Summary

Displ. Range (in.)	Total Cycles	Yielding Location from Fixed End (in.)				Avg. Axial Load (kips)			Max. H (kips)		Remark
		NW	NE	SW	SE	UP	Neutral	DOWN	UP	DOWN	
0.25	5	-	-	-	-	190	190	189	2.1	-4.4	- No yielding on pile
0.50	10	-	2.13	10.00	-	191	190	191	4.2	-6.9	- The NW, SW, and SE flanges yielded
0.75	25	20.50	23.13	18.00	16.25	189	190	189	8.5	-6.7	- All flanges yielded
1.00	50	25.25	23.00	23.25	16.25	189	192	188	8.2	-9.4	
1.25	50	26.00	30.50	23.25	18.00	187	192	188	8.5	-9.5	
1.50	50	30.50	30.50	23.25	18.00	187	193	187	8.3	-9.3	
1.75	50	30.50	30.50	23.25	18.00	184	193	184	8.1	-9.1	- @ 1st cycle, some superficial concrete spalling on the NW, NE, and SE flanges fell off - @ 20th cycle, the bottom of the web yielded - @ 50th cycle, small concrete crack on the west side of the abutment
2.00	50	30.50	30.50	23.25	18.00	180	193	182	7.7	-8.7	- @ 5th cycle, pull-out crack was found at the edge of the NW flange - The top of the web yielded and the lateral load started dropping
2.25	100	30.50	30.50	23.25	18.00	178	192	178	7.2	-8.1	-Web yielded 4 in. from the abutment-pile connection - The abutment rotated 0 to 0.004 degrees - @ 50th cycle, the SW flange buckled - @ 60th cycle, the NW and NE flanges buckled - @ 100th cycle, the SE flange buckled
2.50	66	30.50	30.50	25.00	21.75	170	189	171	7.0	-7.4	- Web buckled severely - The abutment rotated 0.0005 to 0.004 degrees - Lateral load dropped from 7 to 5 kips or 28.5% in the up direction - Lateral load dropped from -7.4 to -5.7 kips or 23% in the down direction

6.3.5 Specimen 5 (HP10x42, Weak Axis, 9 ksi)

Specimen 5 was previously described in Section 6.2. The pile was larger than Specimens 1 to 4, and an axial load of approximately 112 kips was applied and maintained during the test. This pile was tested to evaluate the effect of pile size compared to Specimens 1 and 6. As indicated in Figure 6.10, the lateral load was observed to decrease 52% in the up direction and 67% in the down direction during the displacement range of 2.00 in. while the axial load continued to be maintained.

The overall load-deflection response of Specimen 5 is presented in Figure 6.35, and a summary of the test is provided in Table 6.6. The pile had a lateral load capacity of 15 kips in both the up and down directions. The displacement ductility, μ, was approximately 3.5, which was lower than that of Specimen 1. The significant reduction of the lateral load capacity led to the test being terminated at the 50th cycle of the 2.00 in. displacement range.

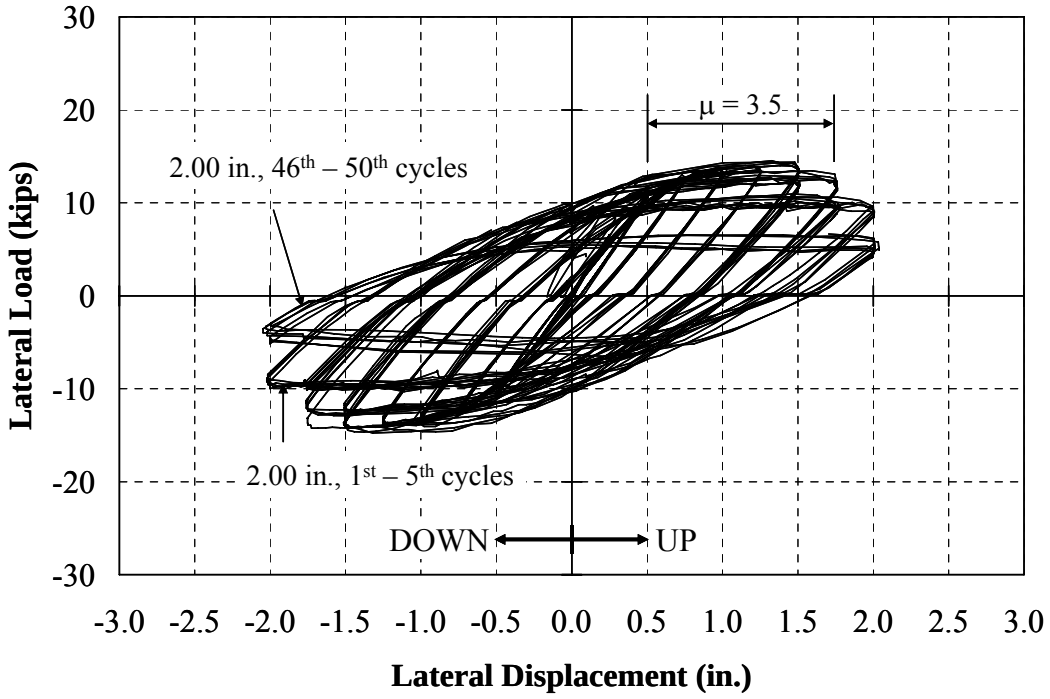

Figure 6.35: Specimen 5 – Overall Load-Deflection Response

Table 6.6: Specimen 5 – Test Summary

Displ. Range (in.)	Total Cycles	Yielding Location from Fixed End (in.)				Avg. Axial Load (kips)			Max. H (kips)		Remark
		NW	NE	SW	SE	UP	Neutral	DOWN	UP	DOWN	
0.25	5	-	-	-	-	112	111	113	6.6	-5.7	- No yielding on pile
0.50	10	13.75	7.00	6.88	13.00	112	110	113	10.8	-10.9	- All flanges yielded
0.75	25	21.25	16.88	13.25	21.50	112	110	110	13.4	-13.8	- Superficial crack spalling at the NW and NE flanges
1.00	50	21.25	16.88	13.25	21.50	112	110	110	14.8	-14.6	- Small concrete spalling at the NW flange
1.25	50	21.88	16.88	18.38	22.00	114	110	109	15.1	-13.6	- @ 10th cycle, superficial crack at the NE flange - Small concrete spalling at the west and east sides - Crack at the NE flange grew
1.50	50	21.88	16.88	18.38	22.00	113	107	106	13.2	-13.8	- @ 1st cycle, all flanges buckled
1.75	50	21.88	16.88	18.38	22.00	114	104	103	12.4	-13.8	- More superficial concrete spalling on the east side - Web yielded - @ 20th cycle, small cracks on the NE flange were found - @ 30th cycle, concrete spalling on the east side
2.00	50	21.88	16.88	18.38	22.00	113 118 115	100 105 103	100 105 102	9.3	-10.0	- @ 6th cycle, crack was found on the SE flange - @ 20th cycle, the NW flange fractured 1/16" wide and more web yielding was found - @ 25th cycle, the SE flange fractured - @ 30th cycle, the NW flange fractured 1/8" wide - @ 40th cycle, the crack on the NW, NE, and SE flanges grew 3/16", 1/16", and 1/16" wide, respectively - @ 50th cycle, crack on the SW flange was more evident and crack on SE flange was through 1/8" wide - @ 50th cycle, crack on the NE flange grew 1/8" wide - The top of the web yielded and more web yielding was found at the bottom

6.3.6 Specimen 6 (HP12x53, Weak Axis, 9 ksi)

Specimen 6 was tested to provide another reference to evaluate the effect of pile size. An axial load of approximately 140 kips was applied and maintained during the test. The SW and SE flanges yielded as early as the 0.50 in. displacement range while the NW and NE flanges yielded in the 0.75 in. displacement range. Concrete cracks were noted on the west and east sides of the abutment. All flanges buckled during the 1.25 in. displacement range. Figure 6.36 shows buckling of the top flanges. Cracks on the NW, NE, and SW flanges initiated in the 20th cycle of the 1.75 in. displacement range while a crack on the SE flange initiated in the 30th cycle.

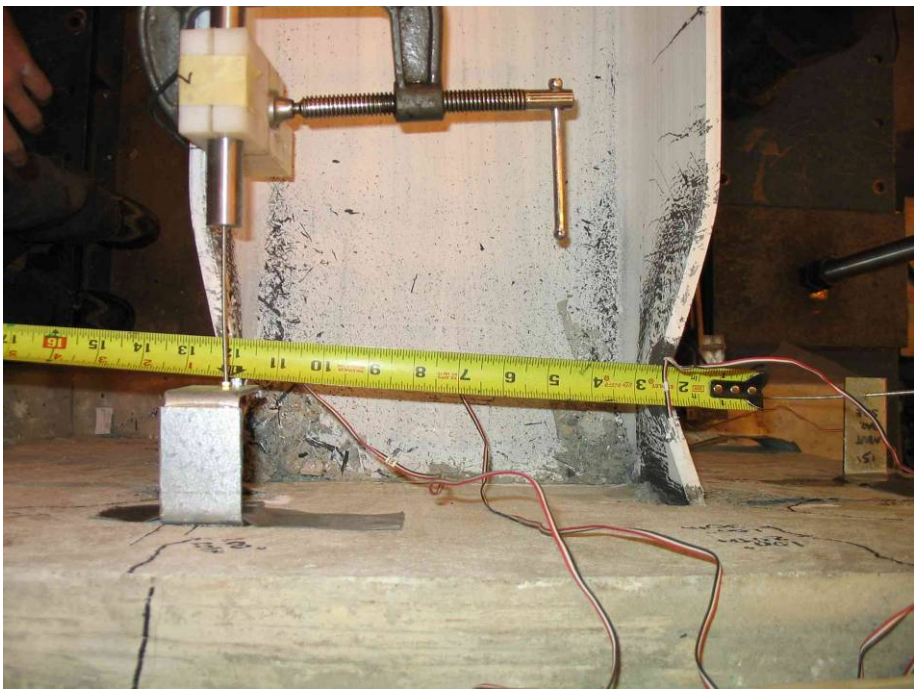

Figure 6.36: Specimen 6 – The NW and NE Flange Buckling

At the end of the 1.75 in. displacement range, all flanges were fractured. Figure 6.37 shows the fracture of the NE flange. The pile maintained the axial load despite the deterioration experienced at the abutment-pile connection (Figure 6.38). As illustrated in Figure 6.39, the lateral load was observed to decrease 55% in the up direction and 75% in the down direction.

The overall load-deflection response is presented in Figure 6.40 and a summary of the test is provided in Table 6.7. The pile had a lateral load capacity of 22.3 kips in the up direction and 18.9 kips in the down direction. The displacement ductility, μ, was approximately 3.0, which is lower than that of Specimens 1 and 5, respectively. The loss of lateral load caused the termination of the test in the 70th cycle of the 1.75 in. displacement range.

Figure 6.37: Specimen 6 – Flange Fracture (NE Flange)

Figure 6.38: Specimen 6 – Deterioration at the Abutment Pile Connection

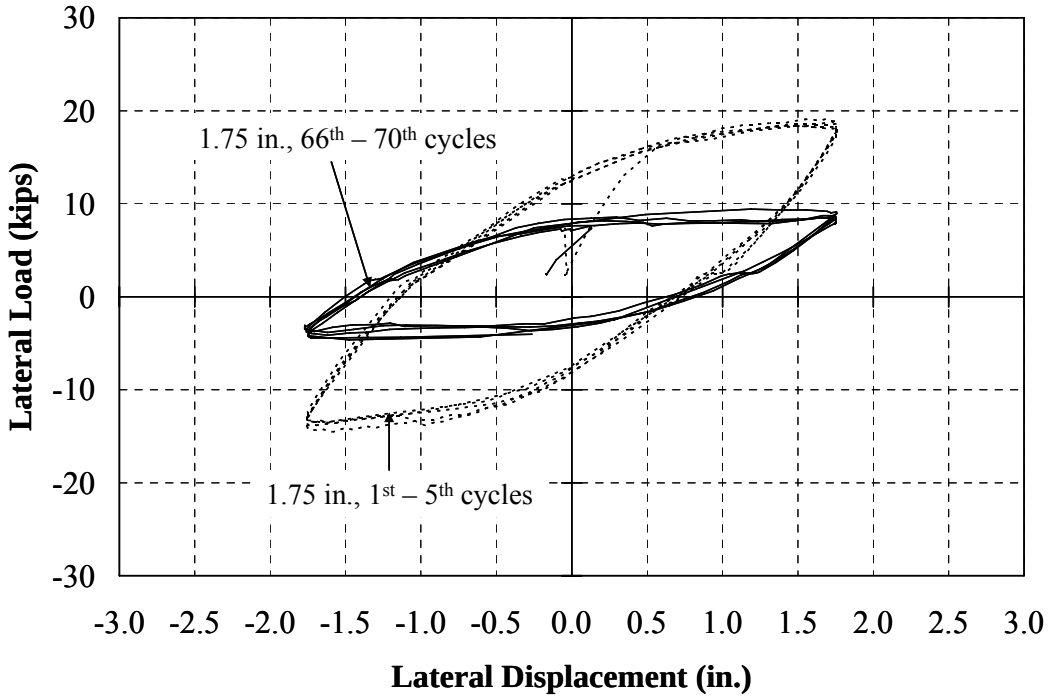

Figure 6.39: Specimen 6 – Load-Deflection Response (±1.75 in. Range)

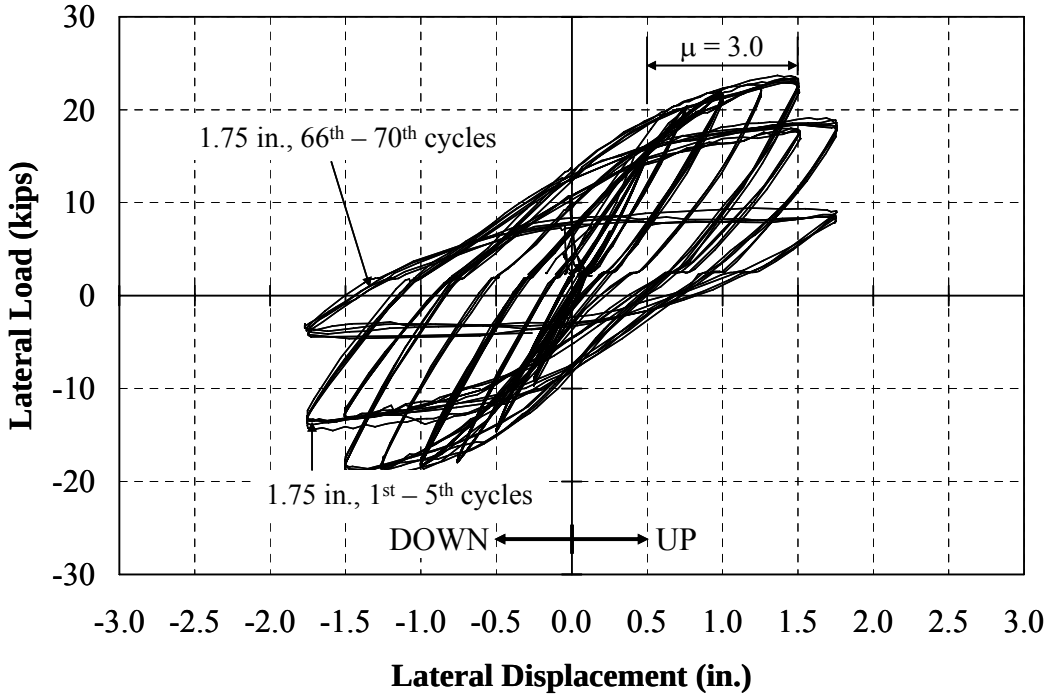

Figure 6.40: Specimen 6 – Overall Load-Deflection Response

Table 6.7: Specimen 6 – Test Summary

Displ. Range (in.)	Total Cycles	Yielding Location from Fixed End (in.)				Avg. Axial Load (kips)			Max. H (kips)		Remark
		NW	NE	SW	SE	UP	Neutral	DOWN	UP	DOWN	
0.25	5	-	-	-	-	138	137	138	6.8	-8.9	- No yielding observed
0.50	10	-	-	11.00	11.00	137	140	139	15.1	-14.4	- Bottom flanges yielded
0.75	25	15.00	15.25	20.50	15.38	139	140	142	20.3	-17.8	- @ 10th cycle, pull-out concrete cracks at the edge of the NW and NE flanges were found - The top flanges yielded - Concrete cracks on the west and east sides of the abutment were found
1.00	50	22.25	15.25	20.25	15.38	137	141	140	21.7	-18.4	- @ 20th cycle, concrete cracks were found at the top of the abutment
1.25	50	22.25	15.25	20.25	15.38	138	142	141	22.3	-18.6	- @ 40th cycle, all flanges buckled - Pull-out cracks were found
1.50	100	22.25	15.25	20.25	15.38	133	141	138	22.2	-18.9	- Crack on the east side of the abutment grew to 11 in., while crack on the west side of the abutment grew to 12 in.
1.75	70	22.25	15.25	20.25	15.38	131	142	137	17.8	-13.2	- @ 20th cycle, cracks on the NW, NE, and SW flanges were found - @ 30th cycle, crack on the SE flanges was found, and the NE flange fractured - @ 50th cycle, the NW flange fractured - @ 60th cycle, the SW flange fractured - @ 70th cycle, the SE flange fractured - No further concrete crack on the abutment was found - Lateral load decreased 55% from 17.8 kips to 8.1 kips in the up direction - Lateral laod decreased 75% from -13.2 kips to -3.3 kips in the down direction

6.3.7 Specimen 7 (CFT8, 9 ksi)

Specimen 7 was the first CFT pile tested. The specified yield strength, f_y, was 35 ksi based on ASTM A252, Grade 2. The specified concrete compressive strength, f'_c, was 4,000 psi based on INDOT Class C concrete. Steel area, A_s, and concrete area, A_c, were calculated to be 4.98 and 53.4 in.^{2}, respectively. An axial load of 43.6 kips was attributed to steel area considering $0.25f_yA_s$, and an axial load of 85.4 kips was attributed to the concrete core area considering $0.4\,f'_c\,A_c$. Therefore, the total axial load is applied at the pile tip was 43.6 + 85.4 = 129 kips. Nevertheless, the axial loads distributed to the steel area and the concrete core area calculated based on strain compatibility and a concrete modulus of elasticity of 4,500 ksi were approximately 49.0 and 80.0 kips, respectively. The actual stress on the steel area was approximately 9.8 ksi, while the stress on the concrete was approximately 1.5 ksi. The "9 ksi" axial load is denoted as the axial load of $0.25f_yA_s + 0.4\,f'_c\,A_c$.

By inspection, no yielding was observed until the 1.00 in. displacement range; however, strain gages indicated that the top and bottom of the pile were yielded as early as the 0.50 in. displacement range. During the 1.00 in. displacement range, the lateral load started dropping. During the 50th cycle of the 1.25 in. displacement range, a small amount of concrete spalling was observed near the abutment-pile connection. The pile buckled at the top and bottom during the 1.50 in. displacement range. Cracks at the top and bottom of the steel shell formed during the 30th cycle of the 1.75 in. displacement range, and fracture of the top and bottom of the steel shell was noticed during the 33rd cycle as illustrated in Figure 6.41.

(a) Buckling on the East Side (b) Crack at the bottom of the Steel Shell

Figure 6.41: Specimen 7 – Pile at Failure (1.75 in., 33rd Cycle)

A significant drop in the lateral load was observed between the 30th and 33rd cycles of the 1.75 in. displacement range while the axial load was maintained. As presented in Figure 6.42, the lateral load was observed to decrease 38% in the up direction and 18% in the down direction. The overall load-deflection response is provided in Figure 6.43, and a summary of the test is provided in Table 6.8. The pile had a lateral load capacity of 13.3 kips in the up direction and 14.2 kips in the down direction. The displacement ductility, μ, was approximately 3.5. Due to the decrease in the lateral load capacity, the test was terminated in the 33rd cycle of the 1.75 in. displacement range. Only minor deterioration of the abutment-pile connection as shown in Figure 6.44 was evident.

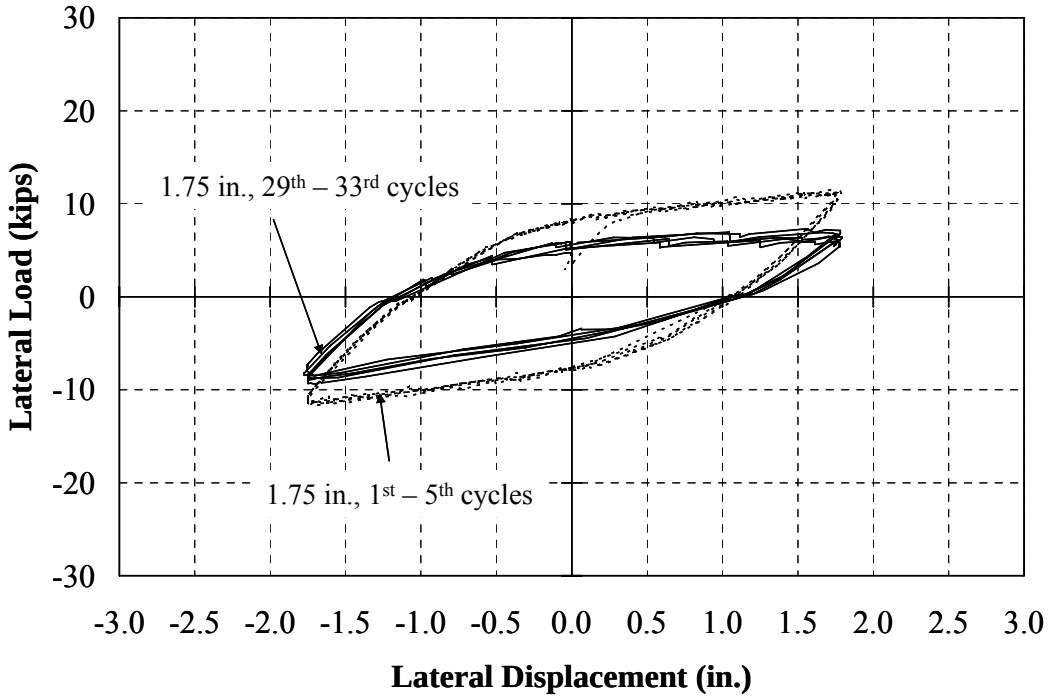

Figure 6.42: Specimen 7 –Load-Deflection Response (±1.75 in. Range)

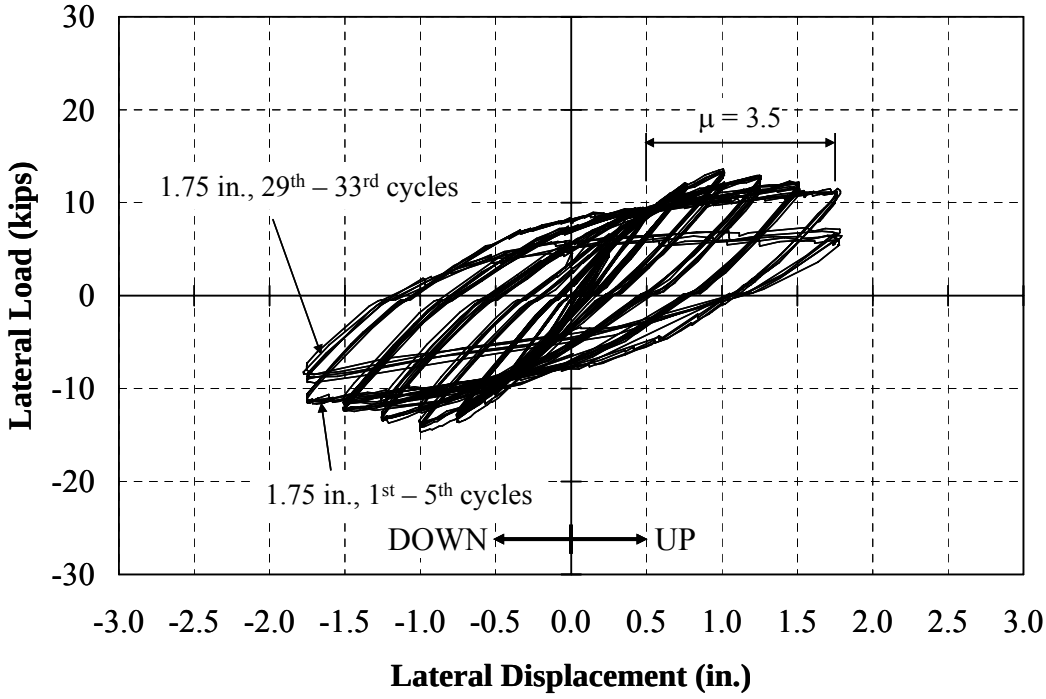

Figure 6.43: Specimen 7 – Overall Load-Deflection Response

Figure 6.44: Specimen 7 –Deterioration at the Abutment-Pile Connection

Table 6.8: Specimen 7 – Test Summary

Displ. Range (in.)	Total Cycles	Yielding Location from Fixed End (in.)		Avg. Axial Load (kips)			Max. H (kips)		Remark
		TOP	BOTTOM	UP	Neutral	DOWN	UP	DOWN	
0.25	5	-	-	130	130	130	4.7	-6.9	- No pile yielding
0.50	10	-	-	130	129	130	8.7	-10.7	- The top and bottom of the pile yielded
0.75	25	-	-	131	130	131	12.1	-13.6	
1.00	50	2.00	2.00	131	130	131	13.3	-14.2	- Lateral load dropped to 11.7 kips and -12.0 kips in the up and down directions, respectively
1.25	50	3.50	3.50	130	130	130	12.7	-13.2	- @ 50th cycle, concrete cracks on the abutment were found - Very small concrete cracks in the abutment were found near the pile - Lateral load dropped to 11.3 kips and -11.4 kips in the up and down direction, respectively
1.50	100	9.00	9.00	128	128	126	11.7	-12.1	- @ 1st cycle, the top and bottom of the pile buckled - @ 20th cycle, another concrete crack was found on the abutment - Lateral load dropped to 10.4 kips and -10.5 kips in the up and down direction, respectively
1.75	33	9.50	9.50	126	128	122	10.1	-11.0	- @ 30th cycle, initial cracks were found on steel shell - Significant cracks were found at the top and bottom of steel shell - @ 33rd cycle, significant drop in the lateral and axial load was noticed - Lateral load dropped to 6.2 kips (-38%) in the up direction and -9.0 kips (-18%) in the down direction

6.3.8 Specimen 8 (CFT8, 18 ksi)

Specimen 8 was the same size as Specimen 7 but was subjected to a higher axial load of approximately 172 kips. This pile was tested to evaluate the effect of axial load on CFT pile behavior. This level of axial load was determined based on the stress level $0.5f_y$ for the steel + $0.4f'_c$ for the concrete. Therefore, the steel was assumed to resist $0.5f_yA_s = 87.1$ kips while the concrete was assumed to resist $0.4f'_cA_c = 85.5$ kips. The total axial load was therefore equal to $87.1 + 85.5 \cong 172$ kips. Based on strain compatibility and a concrete modulus of elasticity of 4,500 ksi, the load distributed to the steel area and concrete area were approximately 65.4 and 106.6 kips, respectively. The actual stress on the steel area was approximately 13.1 ksi, and the stress on the concrete area was approximately 2.0 ksi. The "18 ksi" axial load is defined as the axial load of $0.5f_yA_s + 0.4f'_cA_c$.

Based on whitewash flaking, the pile did not yield until the 1.00 in. displacement range. Strain gages, however, indicated that the top and bottom of the pile yielded as early as the 0.50 in. displacement range. Cracks at the top of the abutment were noticeable at the beginning of the 1.25 in. displacement range. In the 1st cycle of the 1.50 in. displacement range, the top and bottom of the pile buckled. A crack at the bottom of the steel shell was noticeable in the 1st cycle of the 1.75 in. displacement range and propagated very quickly to a length of 4.75 in. within 10 cycles as shown in Figure 6.45.

Figure 6.45: Specimen 8 – Steel Shell Fracture at the Bottom of the Pile

Only minor deterioration of the abutment-pile connection was observed as illustrated in Figure 6.46. While the cracking was more than that of Specimen 7, it was still only minor. As indicated in Figure 6.47, the lateral load decreased 26% in the up direction and 9.5% in the down direction in the course of the 1.75 in. displacement range. The overall load-deflection response is provided in Figure 6.48, and a summary of the test is provided in Table 6.9. The pile had a lateral load capacity of 12 kips in the up direction and 13 kips in the down direction. The displacement ductility, μ, of Specimen 8 was approximately 3.0, which is lower than that of Specimen 7. The test was stopped a little earlier than that of Specimen 7 due to the higher axial load. The test was terminated in the 10^{th} cycle of the 1.75 in. displacement range because of the decrease in the lateral load.

Figure 6.46: Specimen 8 –Deterioration at the Abutment-Pile Connection

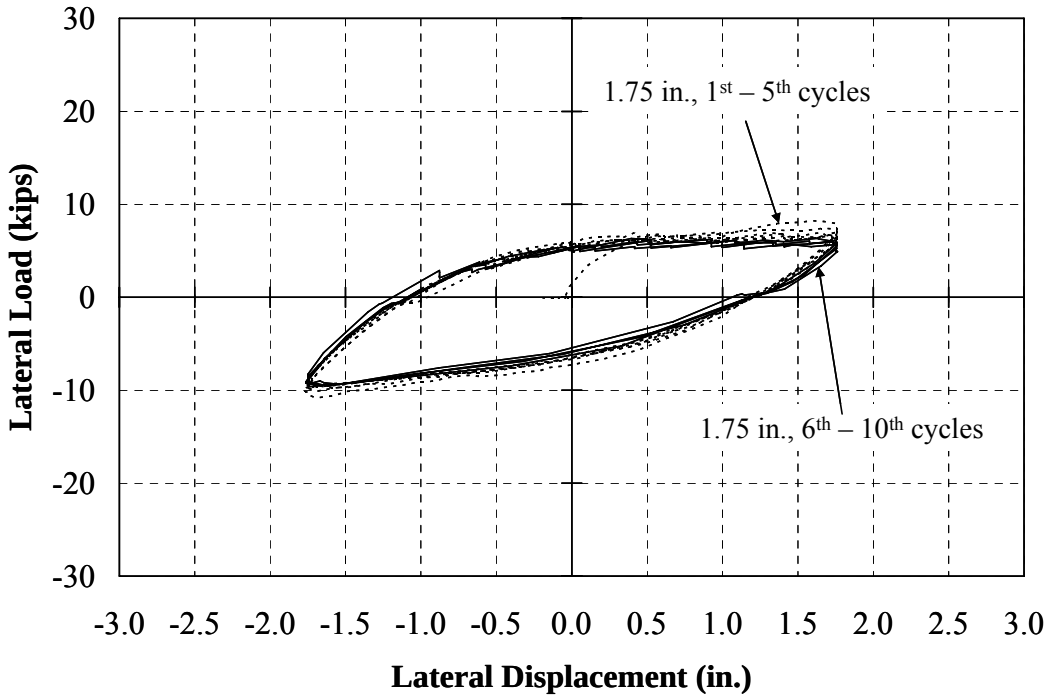

Figure 6.47: Specimen 8 – Load-Deflection Response (±1.75 in. Range)

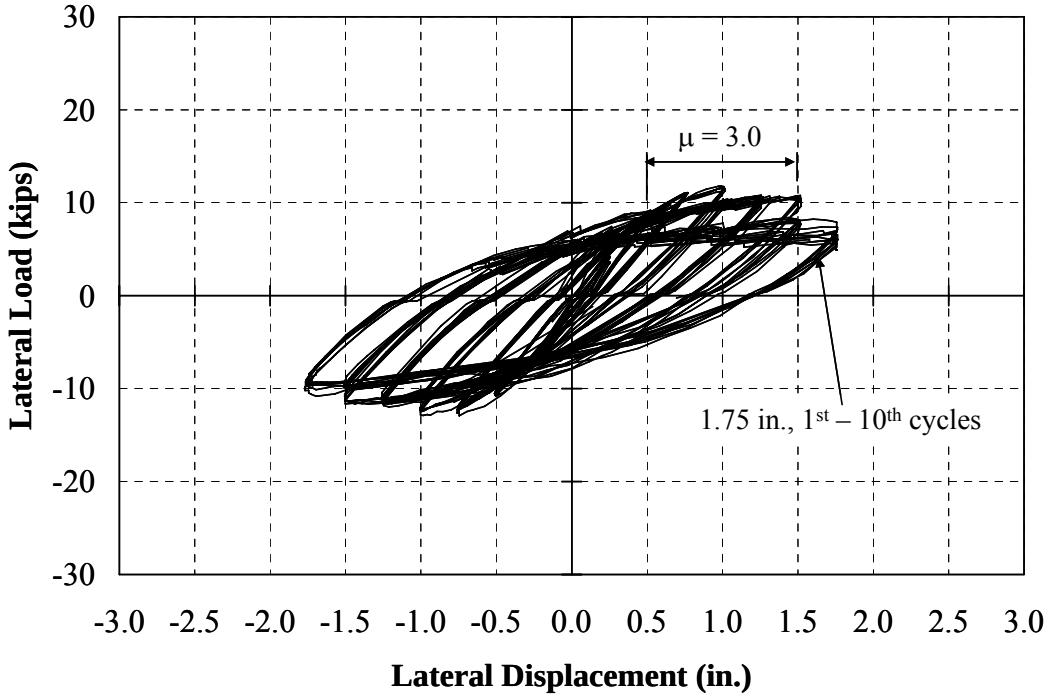

Figure 6.48: Specimen 8 – Overall Load-Deflection Response

Table 6.9: Specimen 8 – Test Summary

Displ. Range (in.)	Total Cycles	Yielding Location from Fixed End (in.)		Avg. Axial Load (kips)			Max. H (kips)		Remark
		TOP	BOTTOM	UP	Neutral	DOWN	UP	DOWN	
0.25	5	-	-	173	172	173	3.5	-7.2	- No yielding on pile
0.50	10	-	-	172	172	173	8.3	-10.1	- The top and bottom of the pile yielded
0.75	25	-	-	173	174	175	11.3	-12.9	
1.00	50	2.50	2.50	172	173	173	11.8	-12.9	- @ 5th cycle, the top of the pile yielded - @ 22nd cycle, the bottom of the pile yielded - No significant change in the axial load
1.25	50	7.00	8.00	169	172	173	10.3	-11.3	- @ 5th cycle, some minor concrete cracks on the abutment was found - Whitewash flaked off at the bottom more than at the top of the steel shell - @ 10th cycle, concrete crack was found on the top of the abutment
1.50	100	8.00	8.00	165	168	168	10.0	-11.1	- @ 1st cycle, the top and bottom of the pile buckled - Most of whitewash flaked off from zero to 2.75" from the fixed end
1.75	10	8.00	8.00	165	169	164	7.3	-9.5	- @ 1st cycle, crack at the bottom was found - @ 4th cycle, crack at the bottom grew to 2.5 in. long - @ 5th cycle, crack at the bottom grew to 3.75 in. long - @ 10th cycle, crack at the bottom grew to 4.75 in. long - Severe cracking on the bottom shell was observed

6.3.9 Specimen 9 (CFT10, 9 ksi)

Specimen 9 consisted of a larger pile than the two previous CFT piles tested. This pile was subjected to an axial load of approximately 204 kips which was calculated according to the same equation as Specimens 7, $0.25f_yA_s + 0.4\,f'_c\,A_c$. The specified yield strength and concrete compressive strength were the same as those of Specimens 7 and 8. Steel area, A_s, and concrete area, A_c, were calculated to be 8.25 and 53.4 $in.^2$, respectively. An axial load of 72.0 kips was calculated for the steel area, and an axial load of 132 kips was calculated for the concrete core. Thus, the total axial load is equal to $72.2 + 132.0 \cong 204$ kips. The axial loads distributed to the steel area and concrete area were approximately 81.6 and 122.4 kips based on strain compatibility and a concrete modulus of elasticity of 4,300 ksi. The stresses on steel area and concrete were calculated to be equal to approximately 9.9 and 1.5 ksi. The "9 ksi" axial load is defined as the axial load of $0.25f_yA_s + 0.4\,f'_c\,A_c$ for this specimen.

By inspection, yielding at the bottom of the pile was not noticeable until the 1.25 in. displacement range, and yielding at the top of the pile was not noticed until the 1.75 in. displacement range. The strain gages, however, indicated that the top and bottom of the pile yielded at the beginning of the 0.50 in. displacement range. At the 0.50 in. displacement range, concrete cracks at the top and east sides of the abutment were visible. The lateral load started dropping during the 0.75 in. displacement range suggesting deterioration at the abutment-pile connection. Several cracks formed around the abutment-pile connection and grew radially to the sides of the abutment. In the 25^{th} cycle of the 1.75 in. displacement range, the steel shell at the bottom buckled, and the lateral load continued to drop. The top of the pile buckled at the beginning of the 2.00 in. displacement range. In the 90^{th} cycle of the 2.00 in. displacement range, a crack at the bottom of the steel shell initiated and grew quickly from 1.75 in. to 3.75 in. in length wide within 5 cycles as illustrated in Figure 6.49. Despite of damage at the abutment-pile connection shown in Figure 6.50, the axial load was still maintained during the course of the 2.00 in. displacement range. However, the lateral load significantly decreased 23% in the up direction and 31% in the down direction (Figure 6.51).

The overall load-deflection response is presented in Figure 6.52, and a summary of the test is provided in Table 6.10. The pile had a lateral load capacity of 23 kips in the up direction and 31 kips in the down direction. The difference in the lateral load capacity between the up and down directions is likely due to the self-weight of the pile and the deterioration at the abutment-pile connection. The displacement ductility was approximately 4.0, which is higher than that of Specimens 7 and 8. The test was terminated at a lateral displacement of 2.00 in. due to the significant drop in the lateral load.

Figure 6.49: Specimen 9 – Crack on the Pile (±2.00 in. Range, 100th Cycle)

Figure 6.50: Specimen 9 – Deterioration of the Abutment-Pile Connection

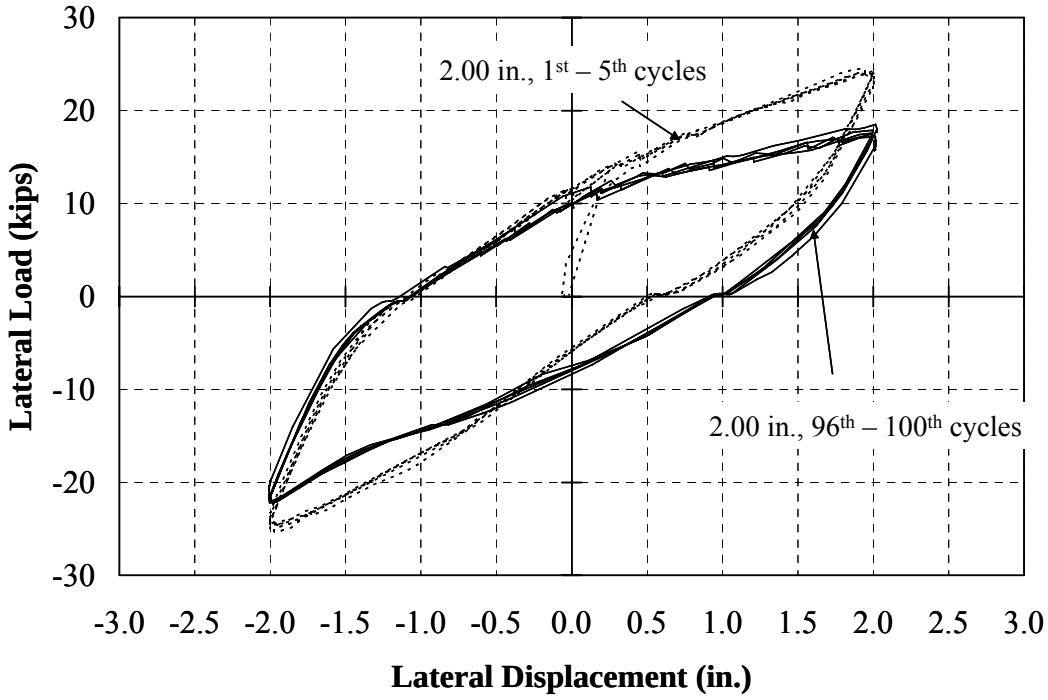

Figure 6.51: Specimen 9 – Load-Deflection Response (±2.00 in. Range)

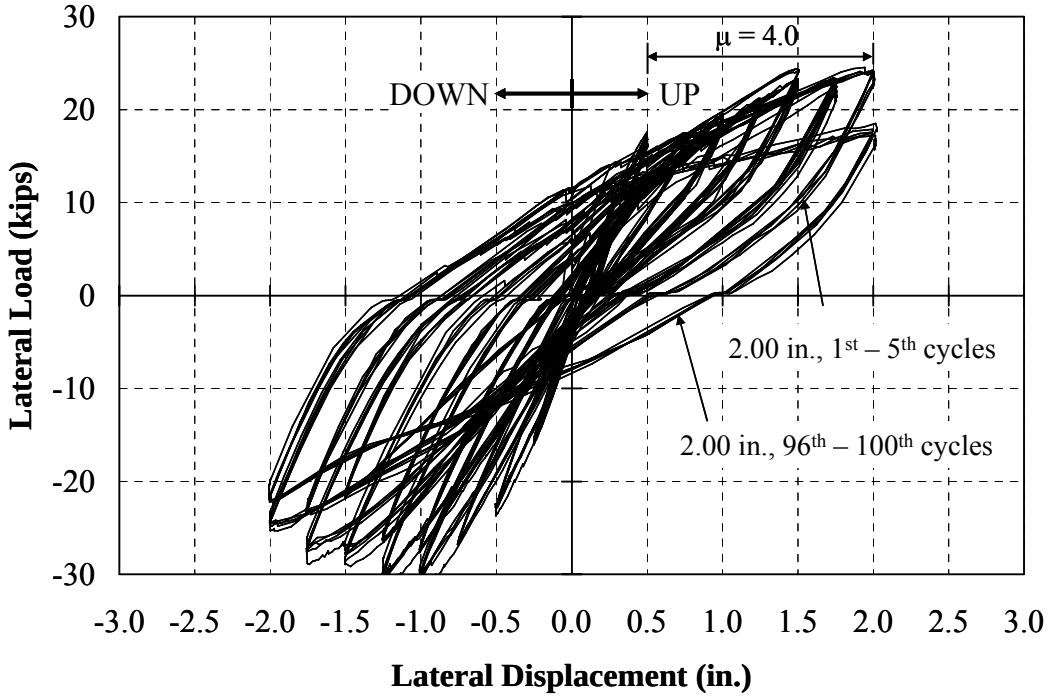

Figure 6.52: Specimen 9 – Overall Load-Deflection Response

Table 6.10: Specimen 9 – Test Summary

Displ. Range (in.)	Total Cycles	Yielding Location from Fixed End (in.)		Avg. Axial Load (kips)			Max. H (kips)		Remark
		TOP	BOTTOM	UP	Neutral	DOWN	UP	DOWN	
0.25	5	-	-	200	199	200	8.7	-15.6	- No yielding on pile
0.50	10	-	-	203	201	204	17.5	-23.3	- The top and bottom of the pile yielded - Concrete cracks were found on the abutment at the top and east side - Lateral load dropped to 15.8 and -22.1 kips in the up and down directions, respectively
0.75	25	-	-	206	203	207	18.5	-28.1	- Concrete cracks were found on the west side - New cracks were found until 25th cycle - Lateral load dropped to 16.4 and -26.2 kips in the up and down directions, respectively
1.00	50	-	-	209	205	210	19.2	-31.0	- New cracks continued to form - Superficial concrete spalling at the top of the pile was observed
1.25	50	-	-	212	206	212	20.7	-30.5	- @ 10th cycle, the bottom of the pile yielded - Additional cracks formed
1.50	50	-	3.00	212	205	209	23.0	-28.4	
1.75	100	2.50	4.00	210	204	206	21.8	-27.3	- @ 10th cycle, steel shell yielded at the top - @ 25th cycle, steel shell buckled at bottom - @ 40th cycle, SG23 offscaled -Lateral load dropped to 22.3 and -22.2 kips in the up and down directions, respectively
2.00	100	3.50	3.75	205.3	204.3	204.0	23.3	-23.9	- @ 5th cycle, the top of the pile buckled - @ 90th cycle, the pile shell started to crack at the bottom - Crack grew from 1.75" to 3.75" within 5 cycles - Lateral load dropped to 16.4 and -20.4 kips in the up and down directions, respectively

6.4 Evaluation of Results

Based on the experimental results, the effect of the pile size, axial load, and pile orientation on the behavior of abutment-pile system are discussed.

6.4.1 Effect of Pile Size

To evaluate the effect of pile size on the pile-abutment response, the behavior of Specimens 1, 5, and 6 are compared. These specimens were oriented for bending about their weak axis under an axial stress of 9 ksi, and the only variable was the size of the pile. The lateral load-deflection responses of these specimens (HP8x36, HP10x42, and HP12x53) are presented in Figure 6.53 along with their displacement ductilities, μ.

Furthermore, a comparison between pile sizes for CFT piles is also evaluated (Specimens 7 and 9). The lateral load-deflection response of these piles (CFT8 and CFT10) piles under the same axial stress of "9 ksi" are shown in Figure 6.54 along with their displacement ductilities, μ.

The moments of inertia of the HP8x36, HP10x42, and HP12x53 bending about their weak axis are 40.3, 71.7, and 127 in.^{4}, respectively. Based on the specified yield strength of 35 ksi and the specified concrete strength of 4,000 psi, the transformed moments of inertia of CFT8 and CFT10 including the concrete are 72.6 and 181.1 in.^{4}, respectively. It can be observed in both Figures 6.53 and 6.54 that as the size of the H and CFT sections are increased (stiffness increased), the lateral load capacity of both pile types is increased. In addition, more deterioration occurs at the abutment-pile connection. While this trend occurs for both H and CFT sections, the trend for lateral displacement capacity is different. For H sections, the lateral displacement capacity decreased with increased stiffness while it increased slightly for CFT sections. Furthermore, the onset of buckling for the H sections occurred earlier as the stiffness increased while it was delayed for the CFT sections.

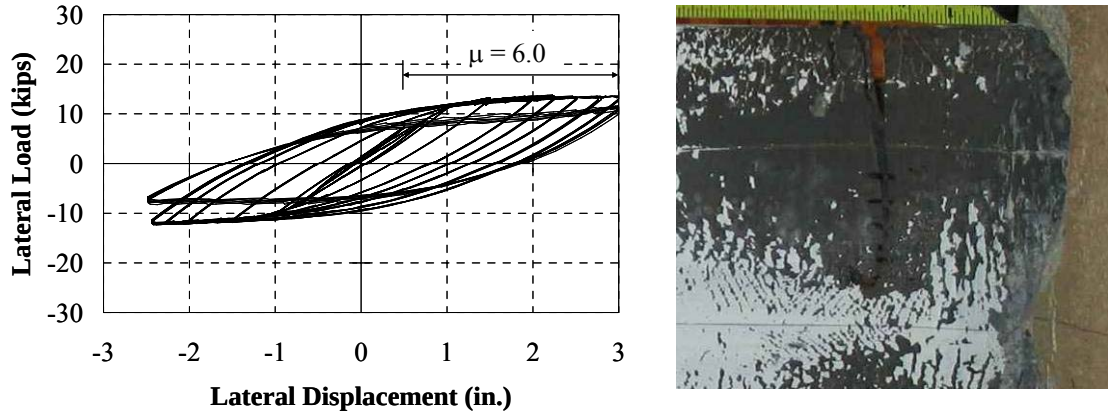

(a) HP8x36 (Specimen 1)

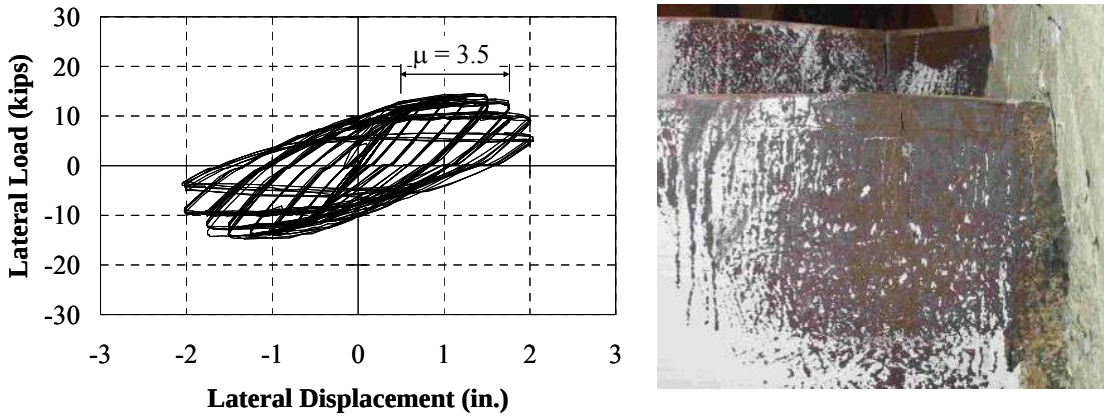

(b) HP10x42 (Specimen 5)

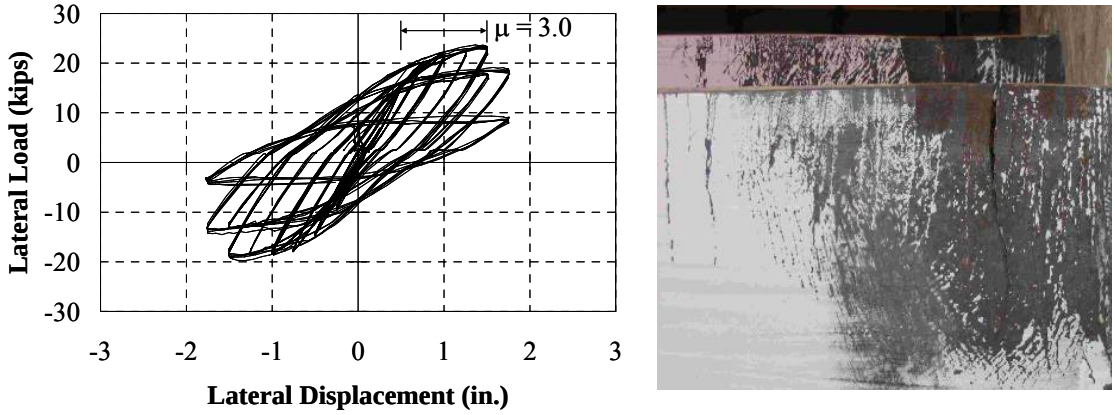

(c) HP12x53 (Specimen 6)

Figure 6.53: Lateral Load-Deflection Responses for H Piles

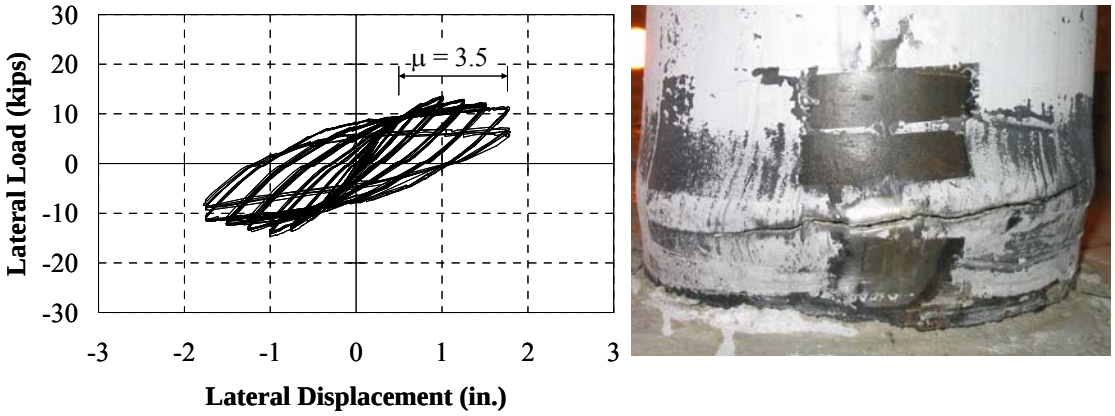

(a) CFT8 (Specimen 7)

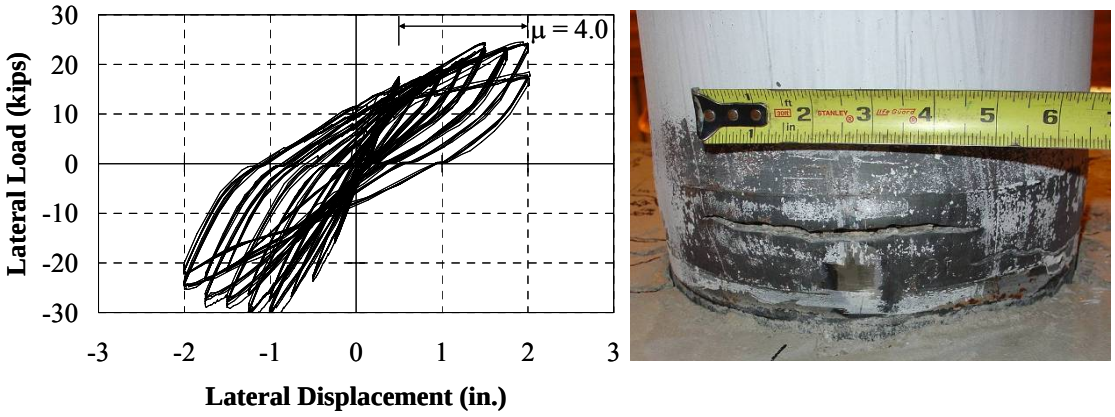

(b) CFT10 (Specimen 9)

Figure 6.54: Lateral Load-Deflection Responses for CFT Piles

The CFT sections were further analyzed to evaluate this behavior. A 1 ft cut section of the CFT8 and CFT10 was considered to evaluate the concrete confinement as shown in Figure 6.55. It should be realized that the axial stress provided to both the steel shell (9.8 ksi and 9.9 ksi) and the concrete (1.5 ksi for both specimens) was essentially identical. Considering the yield strength of the steel shell based on the 0.2% offset steel strength (42 ksi for CFT8 and 52 ksi for CFT10), the transverse forced provided by the steel shell is approximately 189.5 and 312.0 kips for the CFT8 and CFT10 sections, respectively. By equilibrium, this tension or hoop force is resisted by compression of the concrete core. The stress on the concrete core was calculated to be approximately 1.9 ksi for the CFT8 and 2.5 ksi for the CFT10. Therefore, the confinement increased by 32%

which can explain the improved performance of the CFT10, especially the increase in lateral capacity that was observed with increasing displacement. This increase was not evident for the CFT8. It is also important to note that the wall thickness of the CFT10 section (0.250 in.) is approximately 33% thicker than that of the CFT8 section (0.188 in.) Besides being responsible for the increase in confinement stress, the increased wall thickness improved the local buckling behavior and is likely responsible for the increase ductility exhibited prior to buckling.

A summary of the lateral load capacity, lateral displacement capacity, lateral displacement ductility, and displacement at first buckling of Specimens 1, 5, 6, 7, and 9 is provided in Table 6.11.

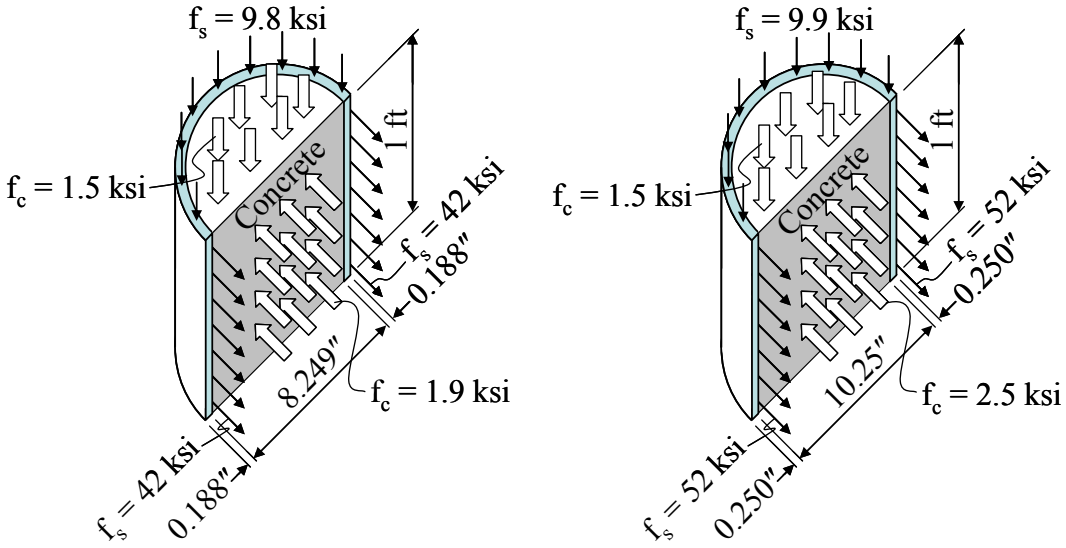

(a) CFT8 (Specimen 7) (b) CFT10 (Specimen 9)

Figure 6.55: Effect of Confinement

Table 6.11: Effect of Pile Size (Specimens 1, 5, vs. 6, and 7 vs. 9)

Specimen	Lateral Load Capacity (kips)	Lateral Displacement Capacity (in.)	Lateral Displacement Ductility, μ	First Buckling (in.)
1	14	3.00	6.0	2.00
5	15	1.75	3.5	1.25
6	22	1.50	3.0	1.25
7	13	1.75	3.5	1.50
9	23	2.00	4.0	1.75

6.4.2 Effect of Axial Load

The effect of axial load on the pile-abutment response was evaluated for both H and CFT piles. This effect is important as the axial load is currently limited to a maximum steel stress of 9 ksi for these pile types due to concerns regarding combined axial and lateral loading. To evaluate the axial load effect on H piles, the lateral load-deflection responses of Specimens 1 and 4 were compared as shown in Figure 6.56.

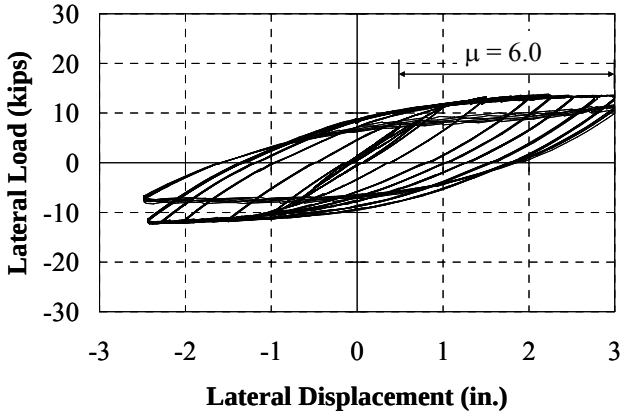

(a) 9 ksi (Specimen 1)

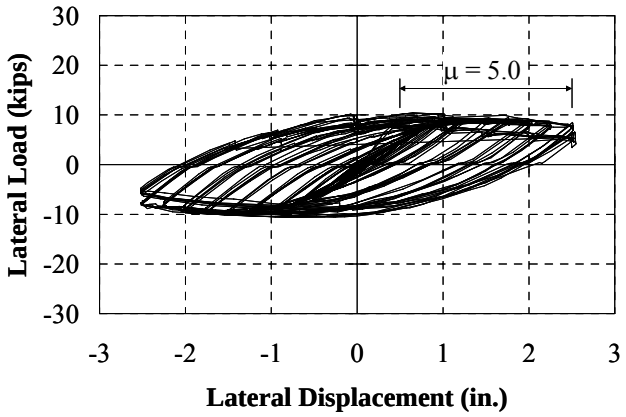

(b) 18 ksi (Specimen 4)

Figure 6.56: Load-Deflection Responses in HP8x36 under Different Axial Stresses

It can be observed that the H pile subjected to a stress of 18 ksi provided a lower lateral load and lateral displacement capacity than that of the pile subjected to 9 ksi. Even though significant deterioration of the concrete at the abutment-pile connection of both specimens did not occur and the axial load was maintained, the web of the pile with higher axial load yielded severely. The lower load and displacement capacity, therefore, was likely due to the effect of web yielding as shown in Figure 6.57. It can be seen that the web of the pile carrying higher axial load buckled while no buckling of the web occurred at the 9 ksi level. It can also be noticed that as the axial load applied is increased, the lateral displacement ductility is decreased from 6.0 to 5.0, while the onset of local buckling is slightly delayed from the 2.00 to 2.25 in. displacement range as presented in Table 6.12. Moreover, it should be noted from the load-displacement response (Figure 6.56 (b)), a small loss of lateral load capacity occurred while the displacement was increased. This degradation was not evident for the 9 ksi specimen (Figure 6.56 (a)).

(a) 9 ksi (Specimen 1) (b) 18 ksi (Specimen 4)

Figure 6.57: Web Yielding of HP8x36 Bending about Weak Axis

Table 6.12: Effect of Axial Load (Specimens 1 vs. 4)

Specimen	Lateral Load Capacity (kips)	Lateral Displacement Capacity (in.)	Lateral Displacement Ductility, μ	First Buckling (in.)
1	14	3.00	6.0	2.00
4	9	2.50	5.0	2.25

The lateral load-deflection responses of the CFT8 piles subjected to stress levels of "9 ksi" and "18 ksi" are shown in Figure 6.58. It is to be noted that the actual steel stress was increased from 9.8 ksi to 13.1 ksi and the concrete stress in the tube was increased from 1.5 ksi to 2.0 ksi. As tabulated in Table 6.13, the CFT pile subjected to an axial stress of "9 ksi" had approximately the same lateral load and lateral displacement capacity as the CFT pile with an axial stress of "18 ksi." According to the experiment results, the CFT pile with an axial load of "9 ksi" started buckling at the same displacement range as the CFT pile with an axial load of "18 ksi." However, the CFT pile with "9 ksi" axial load failed in the 33rd cycle of the 1.75 in. displacement range, while the CFT pile with "18 ksi" axial load failed in the 10th cycle of the same displacement range. It was observed that as the axial load was increased, the displacement ductility decreased from 3.5 to 3.0, and more deterioration was observed at the abutment-pile as illustrated in Figure 6.59. The higher axial stress in the pile caused slightly earlier buckling.

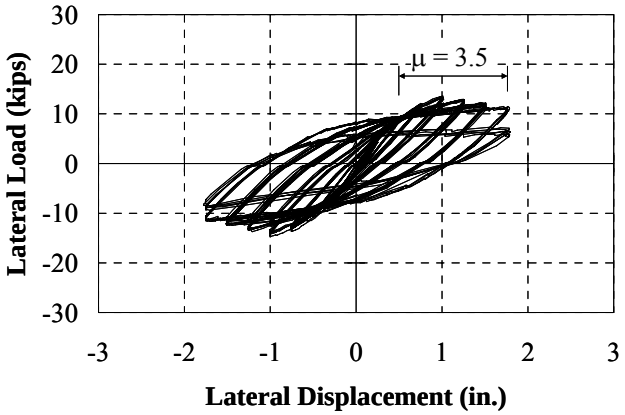

(a) "9 ksi" (Specimen 7)

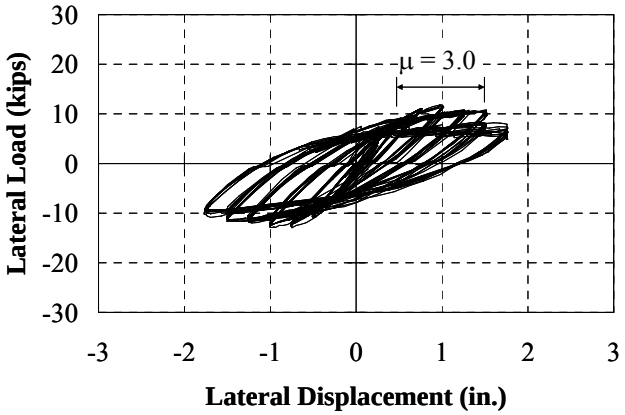

(b) "18 ksi" (Specimen 8)

Figure 6.58: Load-deflection Responses in CFT8 Piles under Different Axial Stress

(a) “9 ksi” (Specimen 7) (b) “18 ksi” (Specimen 8)

Figure 6.59: Abutment-Pile Connection of CFT8 Piles under Different Axial Stress

Table 6.13: Effect of Axial Load (Specimens 7 vs. 8)

Specimen	Lateral Load Capacity (kips)	Lateral Displacement Capacity (in.)	Lateral Displacement Ductility, μ	First Buckling (in.)
7	13	1.75	3.5	1.50
8	12	1.50	3.0	1.50

6.4.3 Effect of Pile Orientation

The lateral load-deflection responses of HP8x36 piles bending about weak-, 45°-, and strong-axes are shown in Figure 6.60. A summary of the lateral load capacity, displacement capacity, and displacement ductility is provided in Table 6.14. The lateral displacement capacity of the pile bending about its weak-, 45°-, and strong-axes are 3.00, 2.00, and 1.75 in., respectively. Moreover, the lateral load capacity of the pile bending about its weak-, 45°-, and strong-axes are approximately 14, 18, and 25 kips, respectively. From this trend, it can be observed that the ultimate displacement decreased while the lateral load increased as the stiffness of the section increased due to the pile orientation. It can also be observed that the lateral displacement capacity of the pile bending about its weak axis is higher than that of the pile bending about the 45°- and strong-axes, respectively. However, the lateral load capacity of weak axis bending was lower than that of the 45°- and strong-axis bending pile, respectively. Perhaps more importantly, the amount of deterioration of the abutment-pile connection increased as the orientation changed from weak to 45° to strong. This deterioration is evident in the load-deflection response where significant pinching is observed for the strong-axis specimen. It must be noted that, whereas, the behavior of the weak- and 45°-axis specimens was dominated by the pile response, the strong-axis specimen was dominated by the deterioration of the abutment-pile connection. In fact, this deterioration limited its response and lateral load capacity. Improvement of the strong-axis connection may improve the response and lateral load capacity of the pile in this orientation.

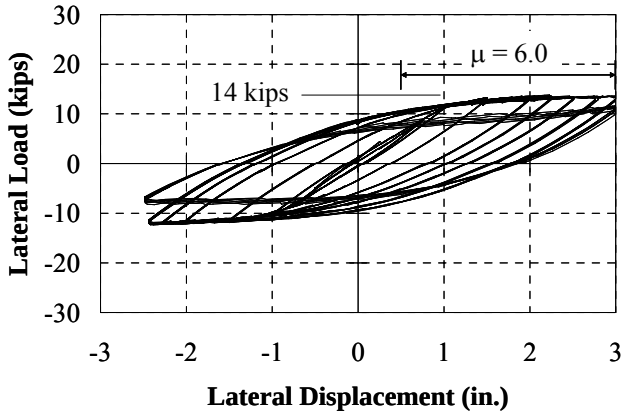

(a) Weak Axis (Specimen 1)

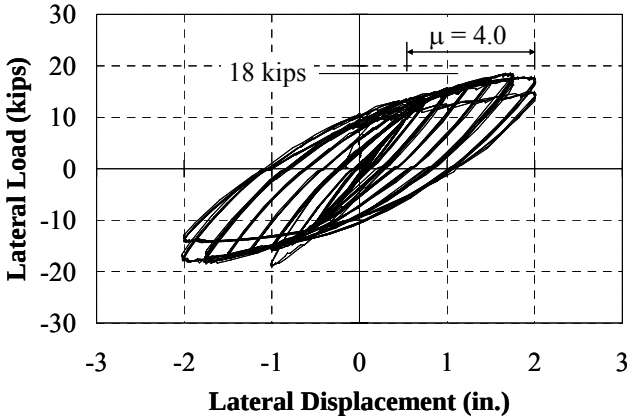

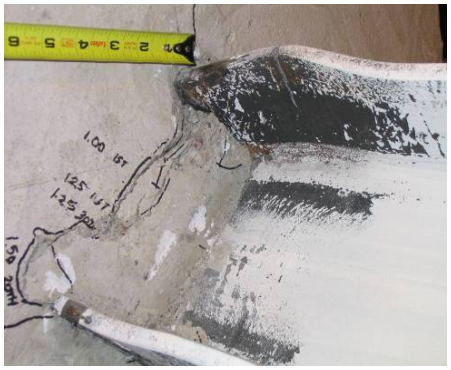

(b) 45° Axis (Specimen 3)

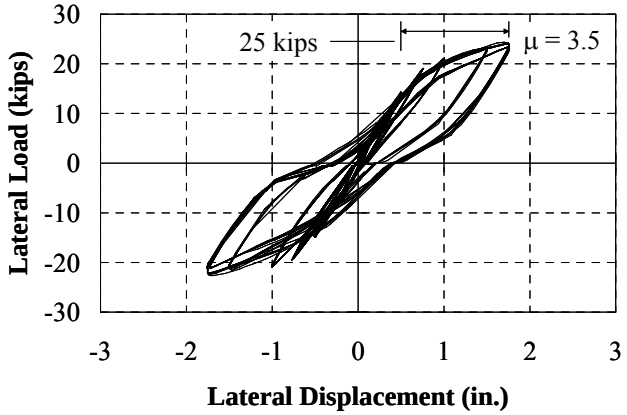

(c) Strong Axis (Specimen 2)

Figure 6.60: Lateral Load-Deflection Responses in HP8x36

Table 6.14: Effect of Pile Orientation (Specimens 1, 2, vs. 3)

Specimen	Lateral Load Capacity (kips)	Lateral Displacement Capacity (in.)	Lateral Displacement Ductility, μ	First Buckling (in.)
1	14	3.00	6.0	2.00
3	18	2.00	4.0	1.50
2	25	1.75	3.5	1.50

6.5 Conclusions from Experimental Results

A summary of the test results is tabulated in Table 6.15. A summary of the test variables was previously presented in Table 5.2. "Complete yielding" means all flanges or both the top and bottom of steel shell yield and "complete buckling" means all flanges or both the top and bottom of steel shell buckle. Conclusions regarding, axial load, pile orientation, pile stiffness, abutment-pile connection, and bridge length are discussed. A recommended length for integral abutment bridges, calculated based on the experimental results is also discussed.

Table 6.15: Summary of Test Results

Specimen	Axial Load (kips)	First Yielding	Complete Yielding	First Buckling		Complete Buckling		Failure	
		Displ. (in.)	Displ. (in.)	Displ. (in.)	Cycle	Displ. (in.)	Cycle	Displ. (in.)	Cycle
1	95.4	0.50	0.75	2.00	50	2.50	100	3.00	80
2	95.4	0.50	0.75	1.50	80	1.75	10	1.75	100
3	95.4	0.50	1.00	1.50	30	2.00	80	2.00	100
4	191	0.50	0.75	2.25	50	2.25	100	2.50	66
5	112	0.50	0.50	1.25	10	1.50	1	2.00	50
6	140	0.50	0.75	1.25	5	1.25	50	1.75	70
7	129	0.50	0.50	1.50	1	1.50	1	1.75	33
8	173	0.50	0.50	1.50	1	1.50	1	1.75	10
9	204	0.50	0.75	1.75	25	2.00	5	2.00	100

6.5.1 Axial Load

For H sections, axial load has a detrimental effect on both lateral load and lateral displacement capacities. Even though, deterioration at the abutment-pile connection of piles with different axial loads was not significantly different, the pile with higher axial load could not maintain lateral load and failed earlier than the pile with a lower axial load. For example, the HP8x36 bending about its weak axis subjected to an axial stress of 9 ksi failed in the 80^{th} cycle of the 3.0 in. displacement range, while it failed in the 66^{th} cycle of the 2.5 in. displacement range when it was subjected to an axial load of 18 ksi.

For CFT sections, axial load has only a minor effect on both the lateral load and lateral displacement capacities. However, as the axial load increases, the lateral displacement ductility decreased from approximately 3.5 to 3.0.

6.5.2 Pile Orientation

For H sections, as indicated in Figure 6.60, the abutment-pile connection of the HP8x36 bending about its strong axis deteriorated much more than that of the pile bending about its 45° and weak axes. The weak axis provided higher lateral displacement capacity and ductility than for the 45° and strong axes.

6.5.3 Pile Stiffness

According to INDOT Memorandum #233, an H section with a depth of 14 in. is recommended for integral abutment bridges, for example, HP14x117, HP14x102, HP14x89, and HP14x73. Furthermore, according to INDOT Memorandum #243, a CFT section with an outer diameter of 14 in. and a wall thickness of 0.203, 0.250, and 0.312 in. is recommended. Table 6.16 provides steel area, moment of inertia about the weak axis of the H piles and moment of inertia of steel transformed section for the CFT piles along with axial load capacity calculated based on the axial stress of 9 ksi distributed on steel area. One can note that the transformed section of the CFT piles is based on the compressive strength of concrete of 4,000 psi and the yield strength of steel of 35 ksi. HP14x117 and CFT14x0.250 are used to compare the effect of pile stiffness. It appears

that for approximately the same moment of inertia, the H pile allows approximately three times higher axial load capacity than the CFT pile. In other words, for the same equivalent cross sectional area, H piles provide lower bending stiffness than CFT piles.

Table 6.16: H Piles vs. CFT Piles

Section	A ($in.^2$)	I_y ($in.^4$)	P (kips)
HP14x117	34.4	443	310
HP14x102	30.0	380	270
HP14x89	26.1	326	235
HP14x73	21.4	261	193
CFT14x0.312	13.4	510	121
CFT14x0.250	10.8	458	97
CFT14x0.203	8.8	418	79

6.5.4 Abutment-Pile Connection

As the pile size or stiffness of the pile increased, the deterioration at the abutment-pile connection also increased. According to INDOT Memorandum #233 and #243, an H section with a depth of 14 in. and a CFT section with an outer diameter of 14 in. are recommended for integral abutment bridges. These two sections are larger than the largest H and CFT sections that were tested. Based on the results of Specimens 6 (HP12x53) and 9 (CFT10.75x0.250), however, the abutment-pile connections were cracked at the time that the piles started yielding and deteriorated significantly by the end of the test.

6.5.5 Bridge Length

Since the pile length used in the experimental study represents the typical distance from the abutment-pile connection to the inflection point, the abutment movement of the bridge is approximately twice the lateral displacement that occurred in the test. For example, the HP12x53 pile model for the I65 over SR25 bridges has the inflection point depth located at a depth of 5.6 ft below ground level (Figure 6.61). The lateral

displacement at the inflection point is 0.32 in., which is approximately half of the tip displacement of 0.55 in. The total bridge movement that can be accommodated is approximately four times the lateral displacement measured during testing. For instance, if the lateral displacement capacity measured during testing is 0.5 in., the abutment movement that can be accommodated is 1.0 in., with an overall bridge movement of 2.0 in.

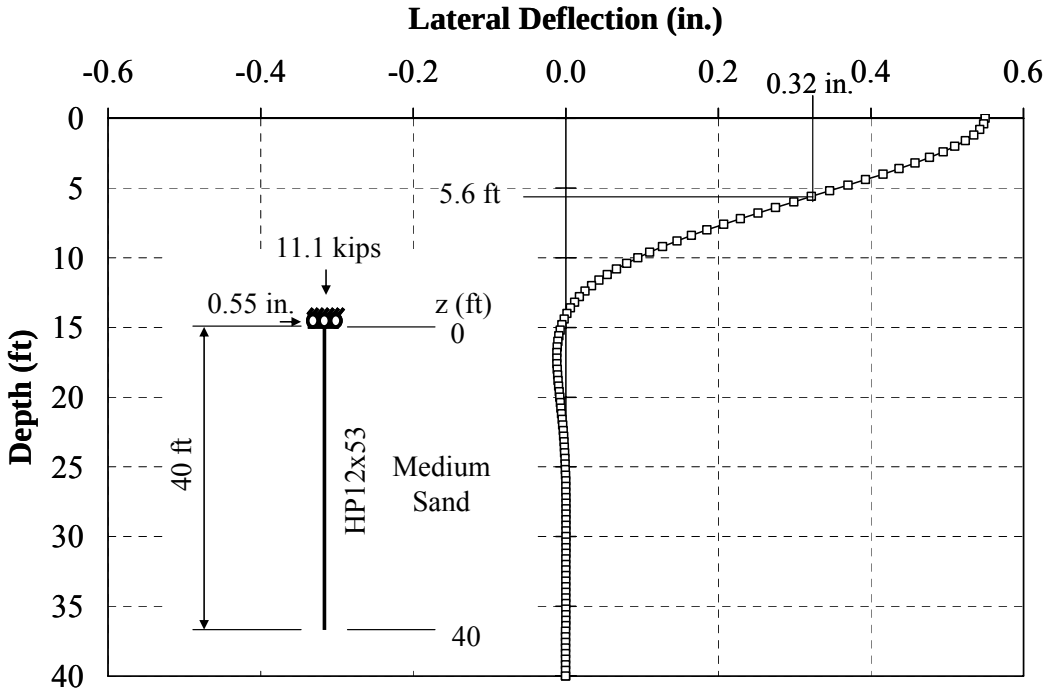

Figure 6.61: Inflection Point Depth of the HP12x53 on I65 over SR25

In general, piles except HP8x36 bending about its strong axis (Specimen 2) and CFT10 (Specimen 9) yielded without cracking at the abutment-pile connection at the 0.5 in. displacement range. Typically, piles experienced yielding on all flanges or both the top and bottom shell in the displacement range between 0.5 in. and 0.75 in. Beyond this displacement until 1.0 in., even though the piles yielded, the axial load and lateral load were maintained for fifty cycles which is equivalent to approximately 50 years. After the 1.0 in. displacement range, local buckling occurred, steel cracks started to initiate, and the lateral load capacity began to decrease. This indicates that piles should be limited to a displacement range of approximately 1.0 in. which allows pile yielding but prevents local

buckling. This movement allows for a total end bent movement in each direction of 2.0 in. Considering a temperature change, ΔT, equal to 100° F and the coefficient of thermal expansion of steel, α, equal to 6.5 x 10^{-6} /°F, an overall bridge length of 500 ft can be provided without buckling of the pile.

6.6 Recommendations

Based on the experimental results, the following recommendations are made:

1. H sections are recommended due to relatively higher displacement capacity and ductility. In addition, H piles can provide equivalent axial load capacity, but decreased bending stiffness causing lower stress at the abutment-pile connection. Therefore, the abutment-pile connection of H sections can deteriorate less than that of CFT sections.
2. To maximize lateral displacement and minimize deterioration at the abutment-pile connection, piles should be oriented for weak axis bending. This orientation minimizes stresses at the abutment-pile connection.
3. Axial load should be limited to 9 ksi for H piles and $0.25f_yA_s + 0.4\,f'_c\,A_c$ for CFT piles.
4. Based on the observed deterioration of the connection, confinement reinforcement and/or deeper embedment length should be provided to control cracks and prevent or reduce deterioration at the abutment-pile connection. While additional research is needed to quantify the optimum amounts and lengths, any amounts provided would enhance the behavior of the connection.
5. The end abutment can be designed considering abutment movement up to 1.0 in. with no other treatment than embedment into the concrete. Displacement up to this range for the piles tested did not result in local pile buckling. Therefore, the maximum overall bridge length can easily be extended to 500 ft.

CHAPTER 7: ANALYTICAL INVESTIGATION

7.1 Introduction

In calculating the load-deflection relationship, the development of moment-curvature diagrams for sections subjected to simultaneous flexure and axial compressive load is essential. A strain compatibility/equilibrium model was developed to calculate the moment-curvature relationship of both steel H piles and concrete-filled steel tube (CFT) piles. The curvature is integrated over the length of the pile to obtain the load-deflection relationship. In this chapter, the steel and concrete models used to calculate the moment-curvature relationship and load-deflection relationship are presented. The results from the analysis are also discussed. The analytical results are compared to the experimental results and extended to evaluate typical piles used in integral abutment practice. Recommendations are provided based on this analysis for the maximum length of integral abutment bridges utilizing this foundation and correction system.

7.2 Material Modeling of Steel Strength and Failure Criteria

In this research, tri-linear models were employed for steel H piles while bilinear models were utilized for the steel shell of the CFT piles. These two steel models take into account strain hardening. The steel behaves elastically below the yield strain, ε_y. The modulus of elasticity, or Young's modulus, E_s, is taken as 29,000 ksi. For steels exhibiting a yield point such as for H piles, steel in the plastic range deforms at a constant stress of f_y up to the certain strain, denoted as the strain at the onset of strain hardening, ε_{st}. Salmon and Johnson (1996) state that ε_{st} typically ranges from 15 to 20 times the yield strain, ε_y. For strains greater than ε_{st}, the stress increases but with a much flatter

slope than the original elastic slope, E_s. The slope of the stress-strain curve beyond the plastic range is known as the strain-hardening modulus, E_{st}. The steel stress increases to the ultimate strength, f_u. This stress-strain curve is adopted for both compression and tension. The yield strain of steel can be calculated using Equation 7-1. The ultimate strain is limited to 0.05.

$$\varepsilon_y = \frac{f_y}{E_s} \tag{7-1}$$

where:

E_s = Young's modulus of steel section, ksi.

ε_y = strain of steel section at yield, in./in.

f_y = yield stress of steel section, ksi.

7.2.1 Steel Model for H Piles

For all A36 steel H piles, the average value of the strain at the onset of the strain hardening, ε_{st}, is taken as 0.014 in./in. (Salmon and Johnson, 1996) and the strain hardening modulus of steel, E_{st}, is assumed to be 300 ksi to correspond with the coupon test results. A typical stress-strain curve for the H pile models is presented in Figure 7.1.

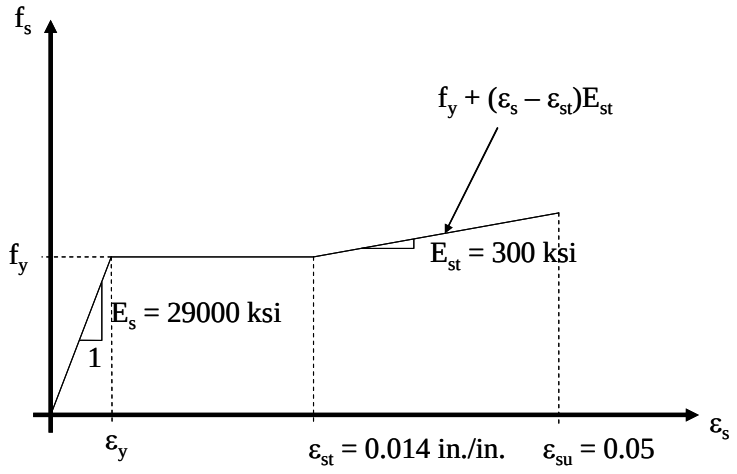

Figure 7.1: Stress-Strain Curves of H Piles

To provide perspective, the stress-strain curves obtained from the coupon tests of the HP10x42 section compared with the analytical stress-strain curve are presented in Figure 7.2. The actual yield strain is equal to 0.00134 calculated from the average yield strength of 39 ksi divided by Young's modulus taken as 29,000 ksi. The strain at the onset of strain hardening was assumed to be 0.014, and the strain hardening modulus was taken as 300 ksi as described in Section 7.2. Figure 7.3 shows a complete stress-strain relationship compared to the proposed stress-strain relationship.

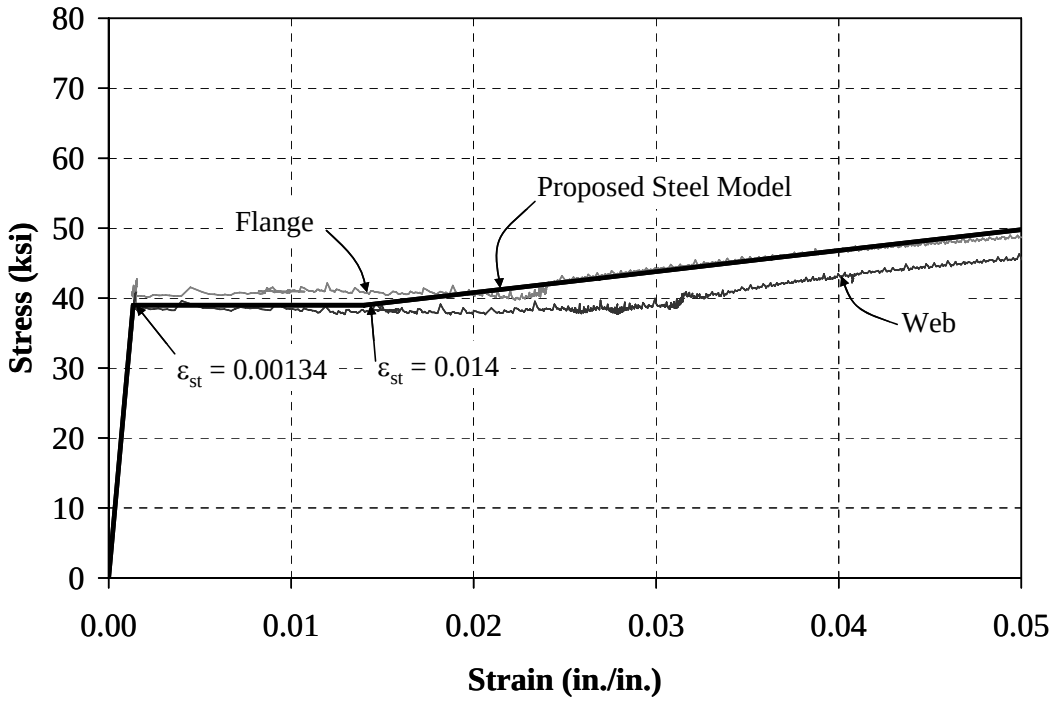

Figure 7.2: Specimen 5 – Stress-Strain Curve of Steel

7.2.2 Steel Model for Steel Shell of CFT Piles

Stress-strain curves for the steel shells of the CFT piles do not exhibit an obvious yield plateau; therefore, a bilinear stress-strain relationship was established. A steel shell is assumed to behave linear elastically with an initial modulus of 29,000 ksi up to yield followed by a linear relationship with a strain hardening modulus of 300 ksi as illustrated in Figure 7.4. The yield strength was calculated considering coupon results and based on the bilinear model.

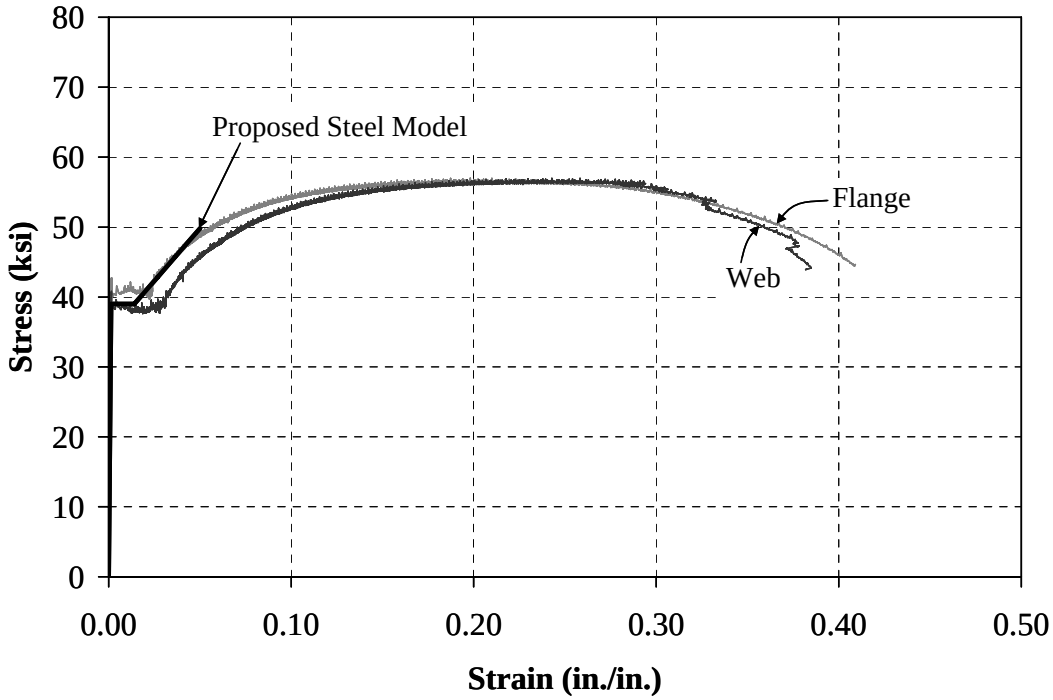

Figure 7.3: Specimen 5 – Complete Stress-Strain Curve

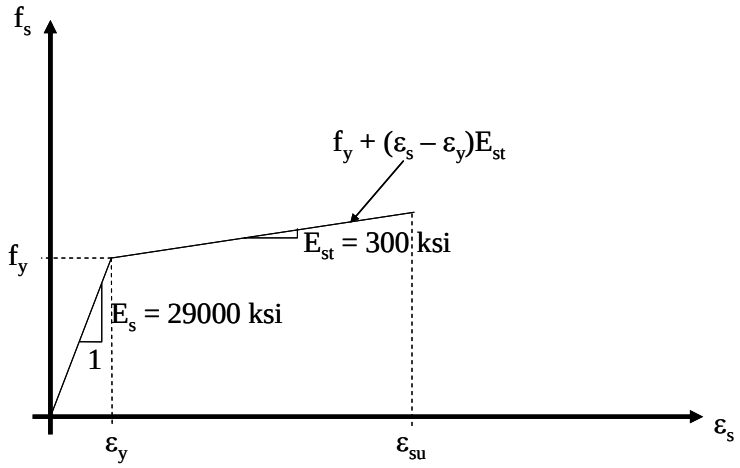

Figure 7.4: Stress-Strain Curve for Steel Shell of CFT Pile

The proposed stress-strain curves for a steel shell of the CFT piles are slightly different from those of the H piles. The proposed stress-strain curve of Specimen 7, for example, is presented in Figure 7.5. It can be noticed that the 0.2% offset yield strength was 42 ksi but a yield strength of 46 ksi was used in this model to fit the strain hardening portion of the curve. The yield strengths of Specimens 8 and 9 used in the models were approximately the same values as the yield strength obtained from the coupon test results based on the 0.2% offset and equal to 54 and 52 ksi, respectively. Figures 7.6 and 7.7 present the proposed stress-strain relationship for the steel shell of Specimens 8 and 9, respectively.

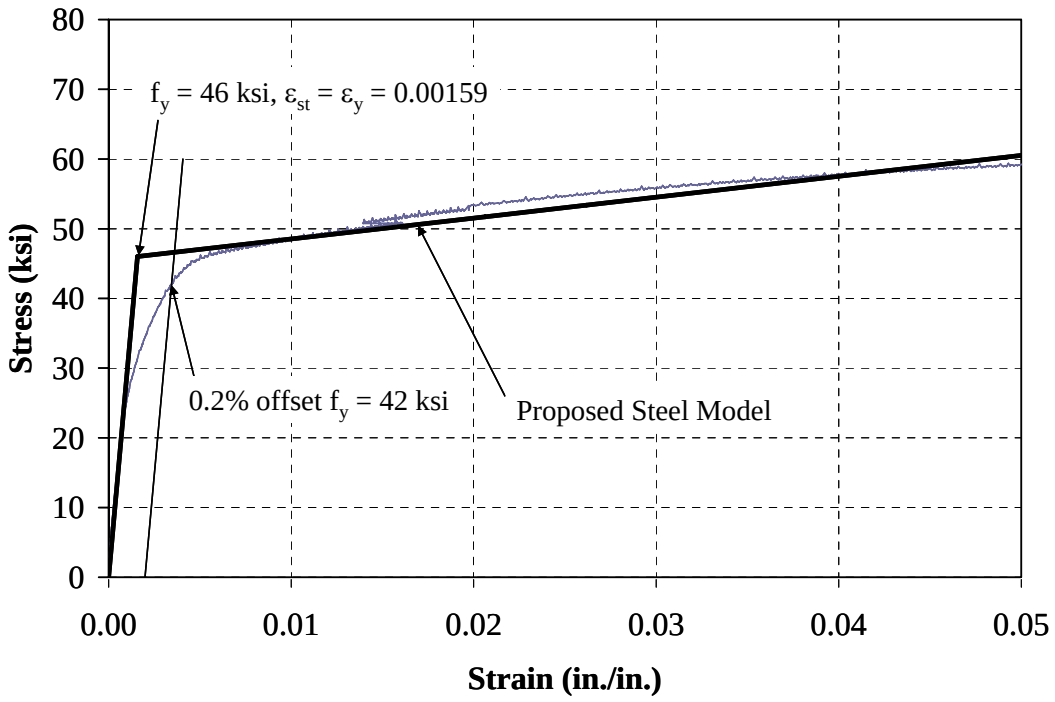

Figure 7.5: Specimen 7 – Stress-Strain Curve of Steel Shell

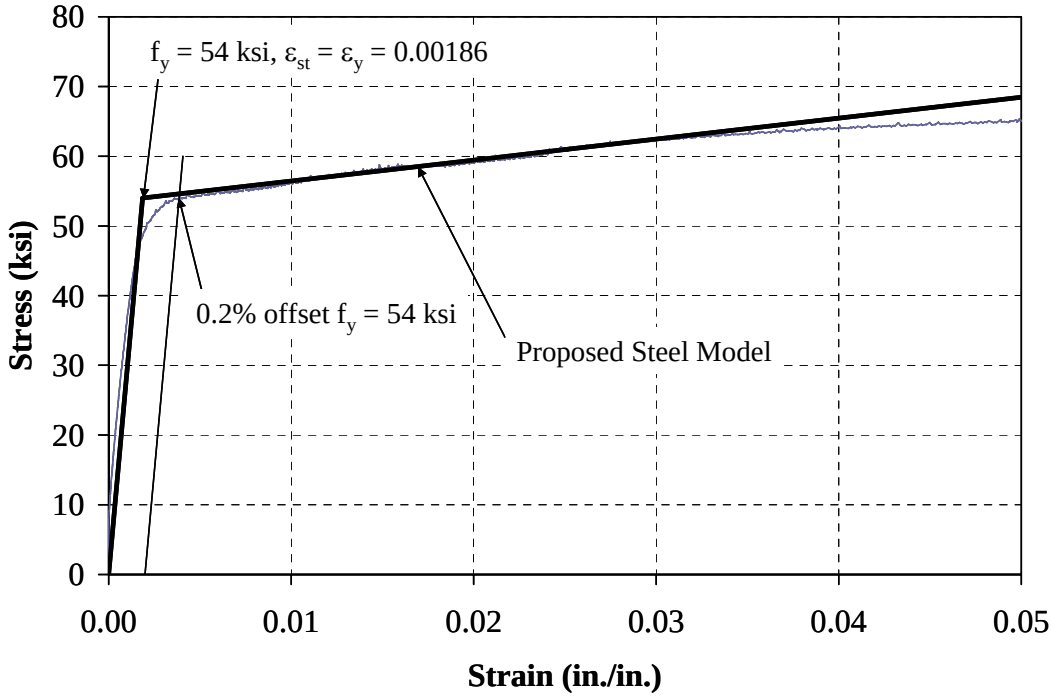

Figure 7.6: Specimen 8 – Stress-Strain Curve of Steel Shell

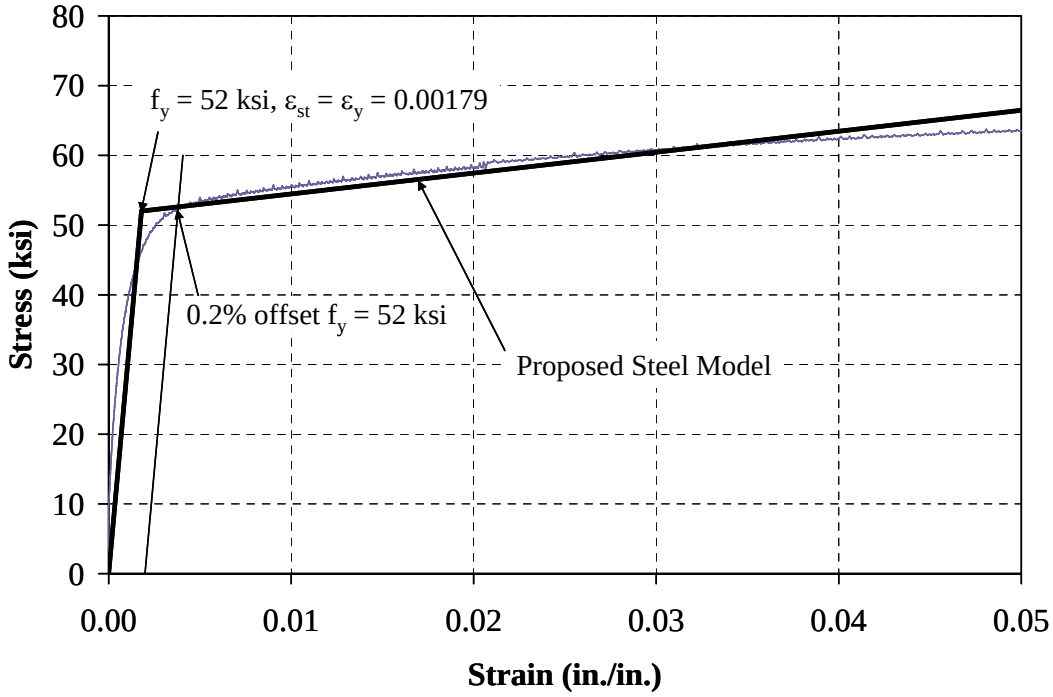

Figure 7.7: Specimen 9 – Stress-Strain Curve of Steel Shell

7.3 Material Modeling of Concrete Strength and Failure Criteria

Because the concrete core was confined by a steel shell, a confined concrete stress-strain model should be considered. Several concrete models such as the Modified Hognestad model (1951), Kent and Park model (1971), and Modified Mander et al model (Elremaily and Azizinamini, 2002) are discussed.

7.3.1 Modified Hognestad Model (Hognestad, 1951)

The modified Hognestad stress-strain curve consists of a second-degree parabola followed by the linear line shown in Figure 7.8. The stress corresponding to any given strain is given by $f_c = f_c''\left[2\frac{\varepsilon_c}{\varepsilon_0} - \left(\frac{\varepsilon_c}{\varepsilon_0}\right)^2\right]$. The strain at the maximum stress, f_c'', is assumed to be equal to $0.85 f_c'$. The strain, ε_0, corresponding to the maximum stress is given as $2\frac{f_c'}{E_c}$ where E_c is the modulus of concrete, taken as $57,000\sqrt{f_c'}$. The ultimate concrete strain is limited to 0.003 for unconfined concrete. The ultimate concrete strain, ε_{cu}, of 0.050 was assumed for confined concrete (Ashour et al, 2001). The stress corresponding with the ultimate strain is equal to $0.85 f_c'' = 0.72 f_c'$. The equation of the line past ultimate can be calculated as $f_c = f_c''\left[1 - 0.15\left(\frac{\varepsilon_c - \varepsilon_0}{\varepsilon_{cu} - \varepsilon_0}\right)\right]$.

One of the objectives of this research is to develop a simplified model that can calculate the behavior of the pile. Therefore, this model is used to analyze the moment-curvature relationship due to its simplicity with the obvious goal of providing good correlation with the experiment results.

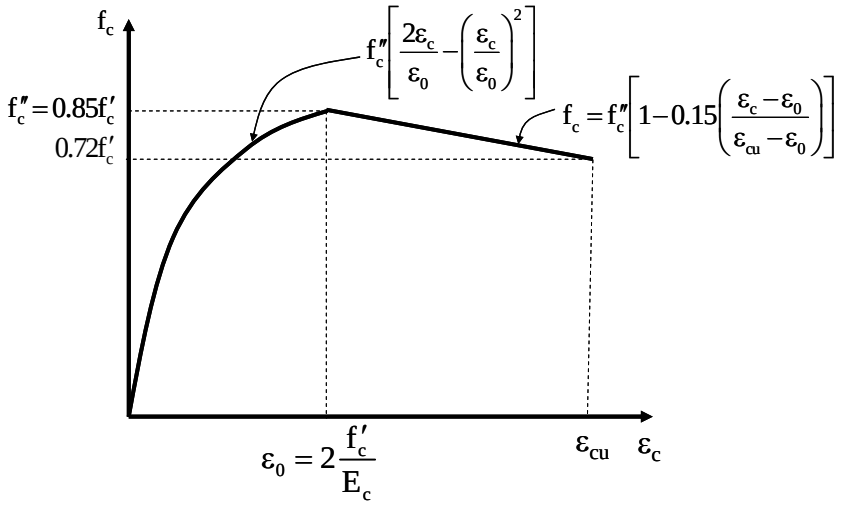

Figure 7.8: Modified Hognestad Model

7.3.2 Kent and Park Model (Kent and Park, 1971)

This concrete model is widely used for concrete confined with spirals. The model assumes that the confined steel has no effect on the second-degree parabola curve until a concrete strain, ε_{co}, of 0.002. Following this strain, the concrete stress decreases linearly to 20 percent of f_c' at a strain of ε_{20c} upon which it becomes constant. The Kent and Park stress-strain curve is presented in Figure 7.9. The equation of the line, $f_c = f_c'\left[1 - Z_c\left(\varepsilon_c - \varepsilon_0\right)\right]$, is a function of the spacing of spirals. Because this model was developed for concrete confined with spirals, this model is not readily applicable to the CFT piles, and was not used in this research.

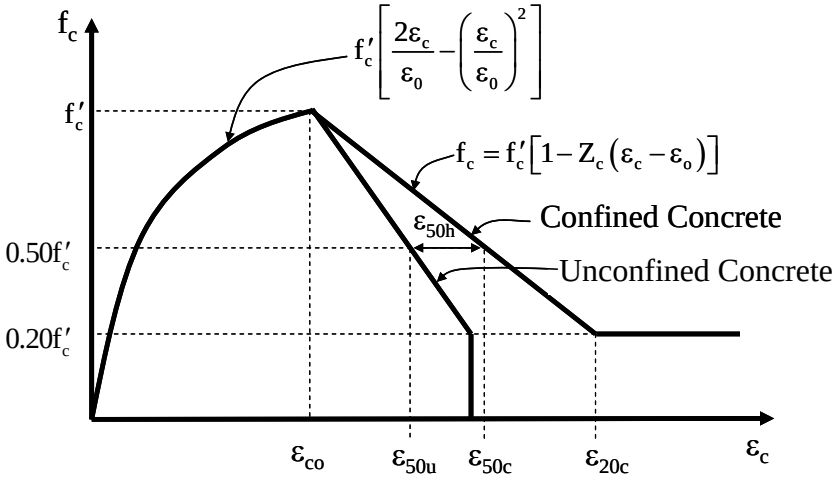

Figure 7.9: Kent and Park Model (Kent and Park, 1971)

7.3.3 Modified Mander et al. Model (Elremaily and Azizinamini, 2002)

Mander et al. (1988) adopted a confined concrete model for both circular and rectangular concrete sections as shown in Figure 7.10. Elremaily and Azizinamini (2002) modified the Mander et al. model to apply to the CFT sections by considering the effective lateral confining stress provided to the concrete by the steel tube. The stress-strain relationship of the steel tube is represented by an elastic-perfectly plastic relationship with different yield stresses in the tension and compression regions. Strain hardening of the steel is ignored in the computation of the hoop stress using Von Mises' yield criterion. The Modified Mander et al. (1988) model is relatively more complex than the concrete models previously described. As previously noted, one of the objectives of this research is to develop a simplified model that can evaluate realistically the pile behavior. Therefore, due to its complexity, the Modified Mander et al. model is not practical for this application.

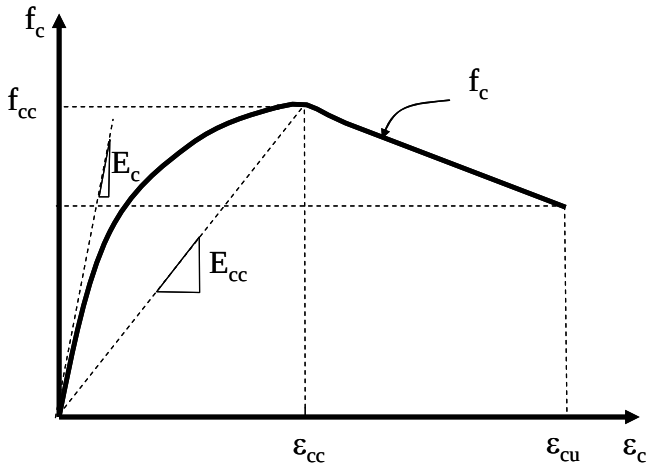

Figure 7.10: Modified Mander et al. Model (Elremaily and Azizinamini, 2002)

7.4 Analysis

7.4.1 Moment-Curvature Analysis

The moment-curvature relationships of steel H piles subjected to different levels of axial load were obtained. The moment-curvature relationships are used to estimate the displacement capacity of H and CFT piles under cyclic lateral loading. These relationships of both the steel and composite sections under combined axial load, P, and bending moment, M, are analyzed using a fiber-based method. The cross section is divided into a number of slices as shown in Figure 7.11. The steel tube is discretized into steel fibers and the concrete infill is discretized into concrete fibers. Each fiber has an associated area, distance from the centroid of the section, and a uniaxial stress-strain ($\sigma-\varepsilon$) curve.

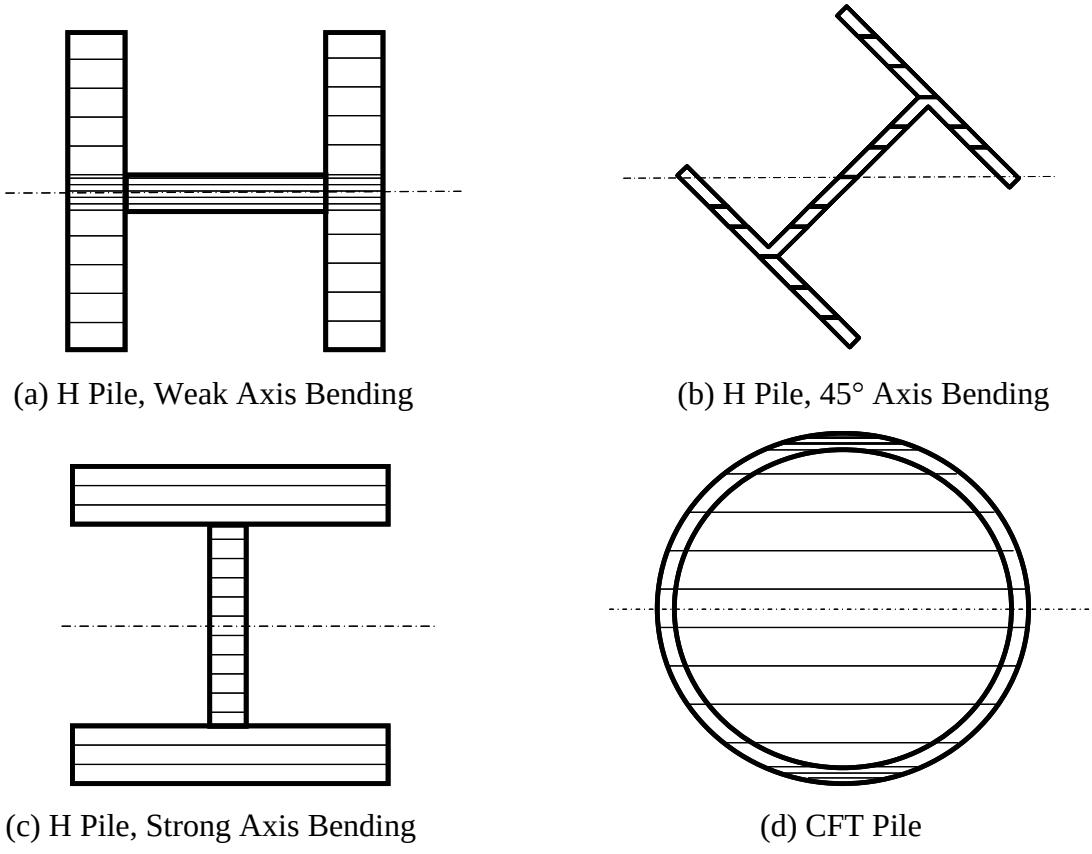

(a) H Pile, Weak Axis Bending

(b) H Pile, 45° Axis Bending

(c) H Pile, Strong Axis Bending

(d) CFT Pile

Figure 7.11: Fiber Discretization

For the CFT models, the modified Hognestad stress-strain relationship for concrete given in Figure 7.8 was used. The following assumptions were made.

1. The contribution of concrete in tension is neglected.
2. No slip occurs between the steel tube and the concrete core (perfectly composite).
3. Plane sections perpendicular to the axis of bending before bending remain plane after bending.
4. Concrete creep and shrinkage are ignored. As stated by Hajjar and Gourley (1996), concrete-filled steel tubes rarely exhibit flexural-torsional or lateral–torsional buckling, these failure modes are thus not considered.

For a given strain profile, the stresses of each slice can be determined using the steel and concrete models described in Sections 7.2 and 7.3. The given axial load, P, and the corresponding bending moment, M, on the section can be calculated by Equations 7-1 and 7-2.

$$P = \sum_{i=1}^{n} f_{si} \cdot A_{si} + \sum_{i=1}^{n} f_{ci} \cdot A_{ci} \tag{7-1}$$

$$M = \sum_{i=1}^{n} f_{si} \cdot A_{si} \cdot y_i + \sum_{i=1}^{n} f_{ci} \cdot A_{ci} \cdot y_i \tag{7-2}$$

where:

n = number of slices.

y_i = distance measured from the centroidal axis of the section to the centroid of i^{th} slice, in.

f_{si}, = stress of steel in i^{th} slice, ksi.

f_{ci} = compressive stress of concrete in i^{th} slice, ksi.

A_{si}, = area of steel in i^{th} slice, $in.^2$

A_{ci} = area of concrete in i^{th} slice, $in.^2$

P = axial load corresponding to the axial stress level of $0.25f_yA_s + 0.4f'_cA_c$, and $0.50f_yA_s + 0.4f'_cA_c$, kips.

M = bending moment corresponding to the fixed end moment.

A_s = area of steel = $\sum_{i=1}^{n} A_{si}$, in.^{2}

A_c = area of concrete = $\sum_{i=1}^{n} A_{ci}$, in.^{2}

f_y = specified yield strength of steel, ksi.

f'_c = specified compressive strength of concrete, ksi.

For a given strain at the top fiber, ε_t, the location of the neutral axis, c, measured from the extreme top fiber was determined using trial-and-error to satisfy Equation 7-1. The curvature for a given top fiber strain is calculated by $\phi = \frac{\varepsilon_t}{c}$, and the corresponding moment can be calculated by Equation 7-2. Using this method, the moment-curvature relationship can be developed as shown in Figure 7.12.

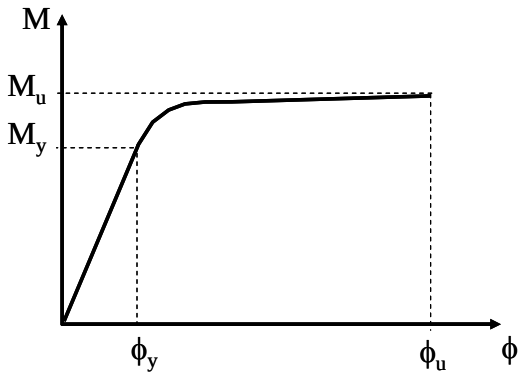

Figure 7.12: Moment-Curvature Relationship

7.4.2 Load–Deflection Relationship

The pile specimen was modeled as a cantilever beam subjected to an axial load, P, and a lateral load, H, at the free end as illustrated in Figure 7.13. The load-deflection relationship of the pile was analyzed using the moment-curvature relationship as described in Section 7.4.1.

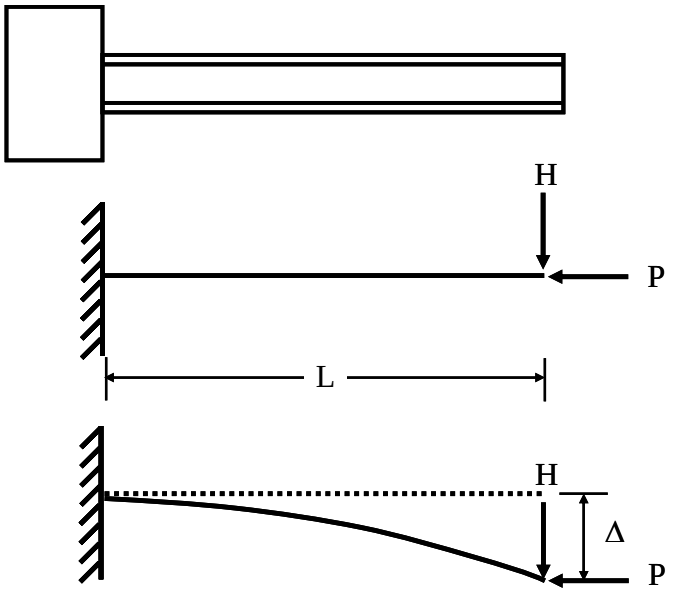

Figure 7.13: Cantilever Beam with Axial Load

For a given moment-curvature relationship, the displacement along the pile length can be calculated using following algorithm. Full details of the calculation of load-deflection response are presented in Appendix J.

1. Determine the ultimate moment, M_u, from the given moment-curvature relationship.
2. Determine the corresponding lateral load, $H = M_u/L$.
3. Calculate the moment along the pile length.
4. Determine the corresponding curvature along the pile length from a given moment-curvature relationship.
5. Calculate the lateral displacement at the pile tip by integrating the moment of area under the curvature curve. The deflections, along the length of the cantilever pile can be calculated using the Moment-Area method.
6. Plot the first-order load-deflection curve.

7.5 Analysis Results

The analytical load-deflection curves of all specimens were compared to the experimental load-deflection curves. The analytical displacements and strains were calculated at significant behavioral events, namely, yield, buckling, and failure.

The strain at first yield, ε_{yield}, was determined based on the stress-strain relationship obtained from coupon tests. The displacement at first yield was determined by assuming the extreme compression fiber of the section yields. The corresponding displacement at first yield was calculated using the moment-curvature relationship up to the curvature at first yield, ϕ_y. Strains at first buckling, $\varepsilon_{buckling}$, and strains at failure, $\varepsilon_{failure}$, were determined using the trial-and-error method. The strain at the extreme compression fiber was varied until the analytical lateral displacement was equal to the displacements at first buckling and at failure as observed from the experiments.

The models were calibrated based on the experimental results. In particular, the strains required to achieve local buckling and failure were calculated. Based on this calibration, the models were used to estimate the behavior of piles that were not tested, but are commonly used in integral bridge design. The models were used to estimate the load-deflection relationships of H piles with a depth of 14 in. and CFT piles with an outer diameter of 14 in. as recommended by INDOT Memorandums #233 and #243 (INDOT, 1992a and INDOT, 1992b), respectively.

7.5.1 H Piles

The analytical results of the load-deflection curves of Specimens 1 through 6 are presented in Figures 7.14 to 7.19. In general, the analytical results correlate well with the experimental results. The lateral load-deflection relationship of Specimen 1 was estimated fairly well. The analytical lateral load capacities of Specimens 2, 3, 4, and 6 are slightly overestimated because of the deterioration that occurred at the abutment-pile connection during testing. Since Specimens 5 and 6 are non-compact sections according to the AISC-LRFD specification (2001), these sections reach the yield stress in compression elements before local buckling occurs, but do not resist inelastic local buckling at the strain level required for a fully plastic stress distribution. This means that

the cross-section can locally buckle prior to reaching the full plastic moment. One of the assumptions of the moment-curvature relationship is that the piles are compact. As a result, the lateral load capacity was slightly overestimated. It should also be noted that the analysis does not consider residual stresses. Therefore, for all sections, the yield transition is slightly more pronounced than the actual response. Finally, despite the deterioration of the abutment-pile connection of Specimen 5, the analytical load-deflection curve provides a good correlation with the load-deflection curves obtained from test results up to the 1.50 in. displacement range. The calculated strains and curvatures along with the displacements at first buckling and failure of the H piles are summarized in Table 7.1.

Table 7.1: Strains at First Buckling and at Failure of the H Specimens

Specimen	Buckling				Failure			
	Δ_{test} (in.)	ε (in./in.)	$\varepsilon/\varepsilon_y$	ϕ (rad/in.)	Δ (in.)	ε (in./in.)	$\varepsilon/\varepsilon_y$	ϕ (rad/in.)
1	2.00	0.031	19	0.0073	3.00	0.041	25	0.0096
2	1.50	0.031	19	0.0052	1.75	0.034	21	0.0059
3	1.50	0.036	22	0.0057	2.00	0.045	28	0.0073
4	2.25	0.034	21	0.0075	2.50	0.037	23	0.0082
5	1.25	0.026	20	0.0050	2.00	0.036	27	0.0070
6	1.25	0.029	19	0.0048	1.75	0.037	24	0.0060

In summary, the results of the analytical models correlate well with the load-deflection curves of the piles that had little or no deterioration at the abutment-pile connection, but slightly overestimated the response if the abutment-pile connection was damaged. This overestimation is expected since deflection due to the softening of the connection was not included in the analysis procedure.

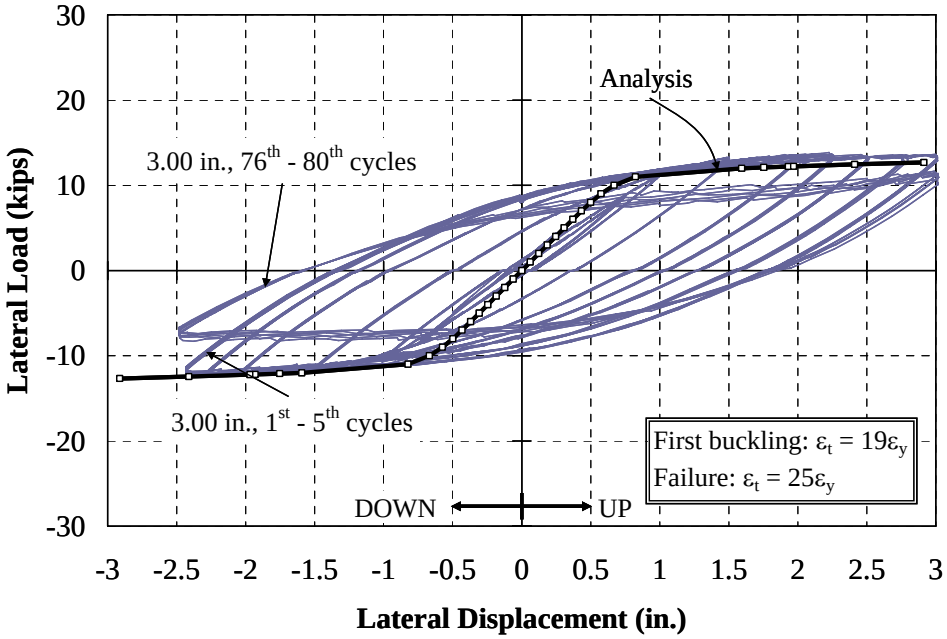

Figure 7.14: Specimen 1 – Load-Deflection Curve

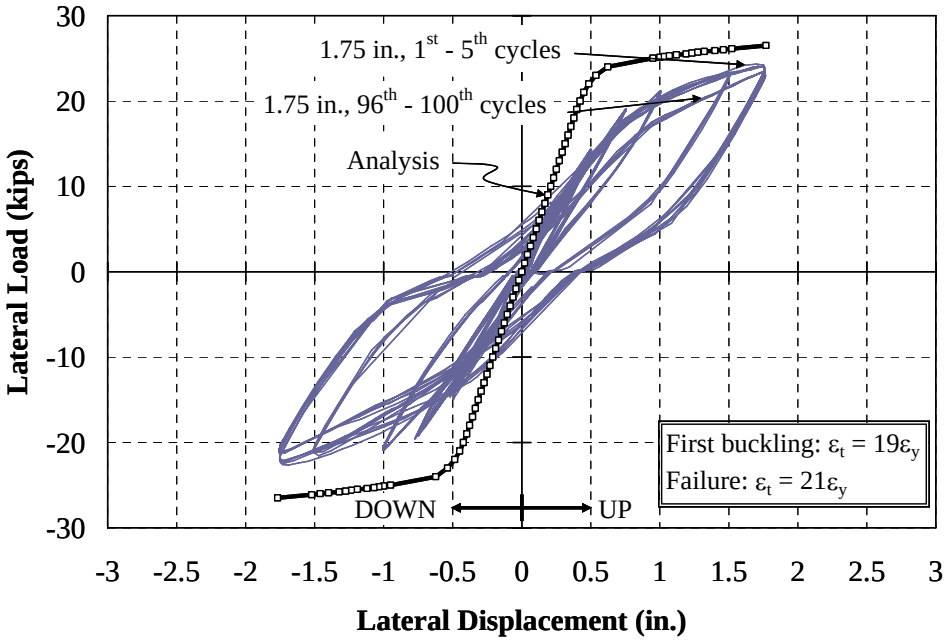

Figure 7.15: Specimen 2 – Load-Deflection Curve

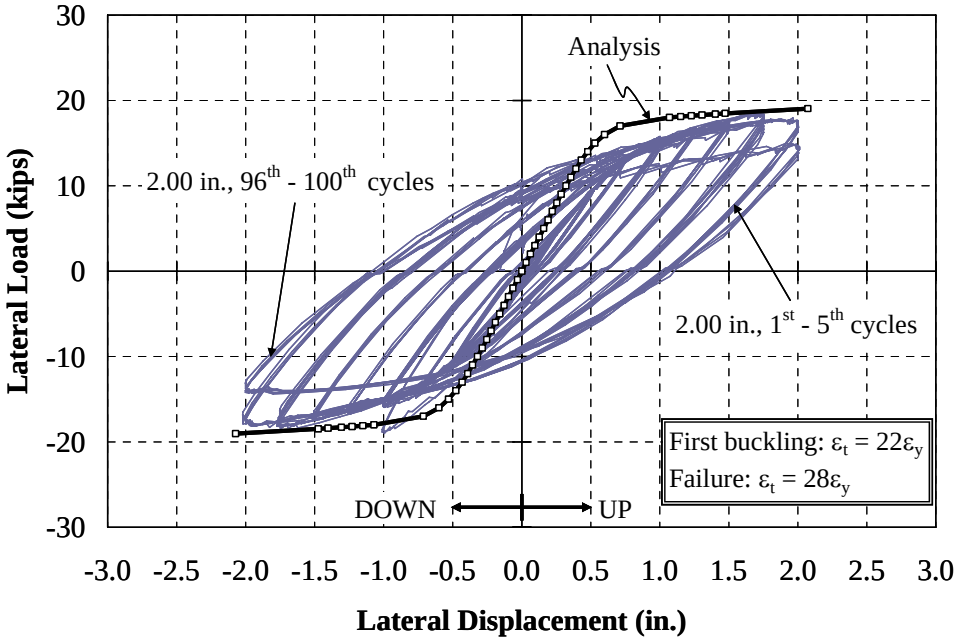

Figure 7.16: Specimen 3 – Load-Deflection Curve

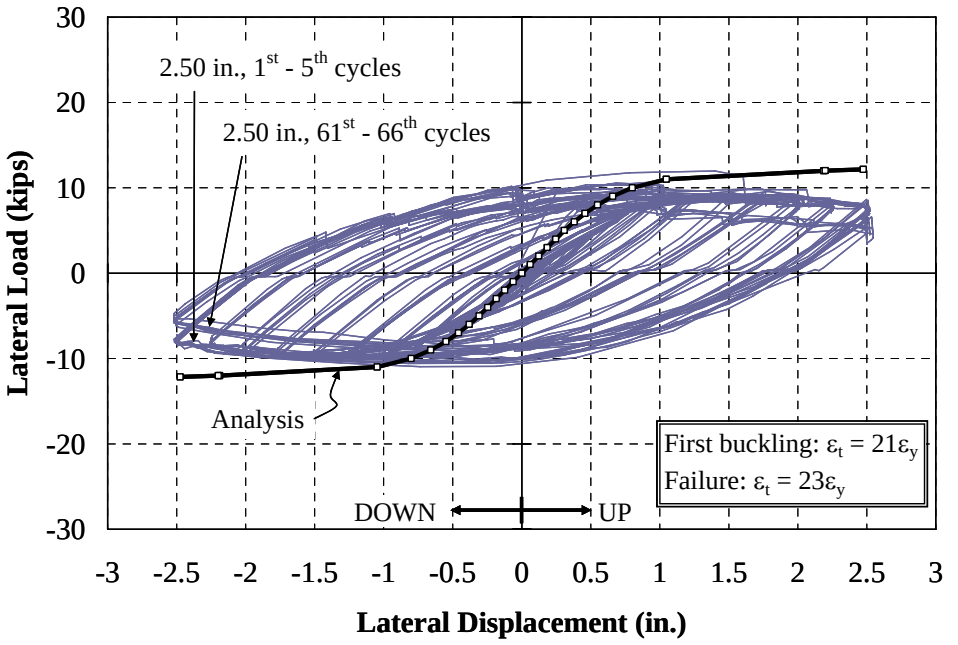

Figure 7.17: Specimen 4 – Load-Deflection Curve

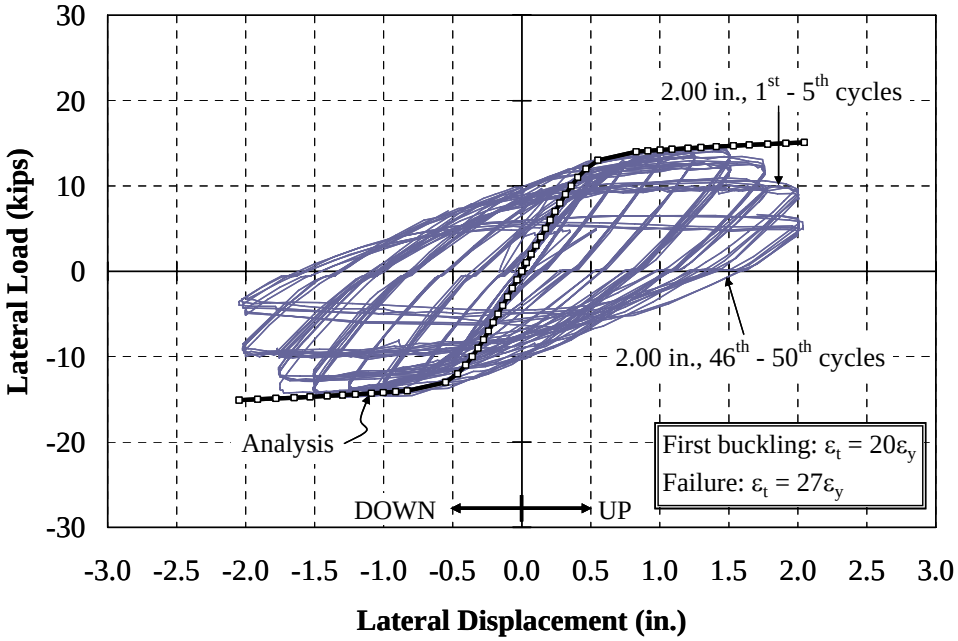

Figure 7.18: Specimen 5 – Load-Deflection Curve

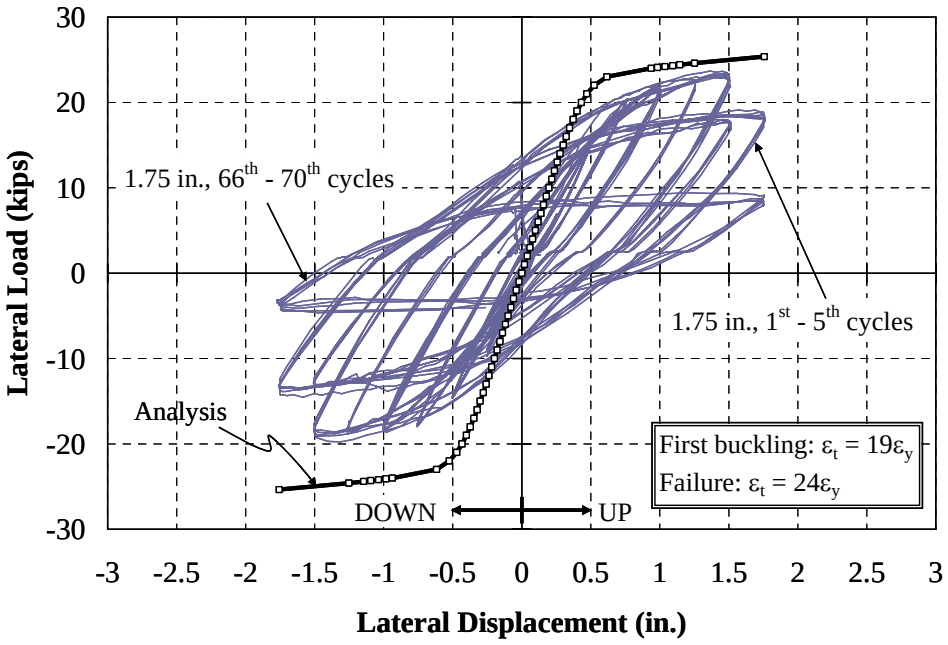

Figure 7.19: Specimen 6 – Load-Deflection Curve

7.5.2 CFT Piles

The calculated strains and curvatures along with the displacements at first buckling and failure of Specimens 7 through 9 are provided in Table 7.2. The analytical load-deflection curves of the CFT piles are presented in Figures 7.20 to 7.22. Two models were analyzed to estimate the load-deflection curves of the CFT piles. The first model is the composite concrete-steel model and another is the steel-only model. While a coupon cut from Specimen 8 indicated a yield strength of approximately 54 ksi as shown in Figure 7.6, this value was inconsistent with Specimen 7. Specimens 7 and 8 were obtained from the same pile; therefore, these yield strengths should be similar if not identical. Both yield strengths were evaluated, and it was found that a yield of 46 ksi was more appropriate based on the experimental results. This yield was used for Specimens 7 and 8. The stress-strain curve shown in Figure 7.5 was used. The yield strength of Specimen 9 was 52 ksi as previously described in Section 7.2.2. The load-deflection curve obtained by the composite (concrete + steel) model correlates fairly well for Specimen 7. The composite model slightly overestimates the load-deflection curves of Specimens 8 and 9 due to deterioration that occurred at the abutment-pile connection. As the deterioration of the connection increases, the concrete-steel model provided a greater overestimation. It can be noticed that the composite model overestimates the capacity in the up direction more than in the down direction. The difference in the load and displacement capacity of the pile was likely due to its self weight and deterioration at the abutment-pile connection as described in Section 6.3.9. Due to deterioration at the connection and the lower confinement provided on top of the abutment from the location of the clamping system, the lateral load required to displace the pile in the up direction was lower than that in the down direction. On the other hand, the steel-only model correlates well with all of the final cycles of the last displacement range of Specimens 7 and 8. The steel-only model slightly overestimates the final cycle of Specimen 9 because of significant deterioration of the abutment-pile connection as well as fracture of the pile.

Table 7.2: Strains at First Buckling and at Failure of the CFT Specimens

Specimen	Model	Buckling				Failure			
		Δ (in.)	ε (in./in.)	$\varepsilon/\varepsilon_y$	ϕ (rad/in.)	Δ (in.)	ε (in./in.)	$\varepsilon/\varepsilon_y$	ϕ (rad/in.)
7	Steel-Only Model	1.50	0.022	14	0.0030	1.75	0.025	16	0.0035
8		1.50	0.017	11	0.0022	1.75	0.021	13	0.0026
9		1.75	0.034	19	0.0040	2.00	0.039	22	0.0047
7	Composite Model	1.50	0.025	16	0.0060	1.75	0.029	18	0.0068
8		1.50	0.021	18	0.0043	1.75	0.025	21	0.0053
9		1.75	0.036	20	0.0068	2.00	0.041	23	0.0078

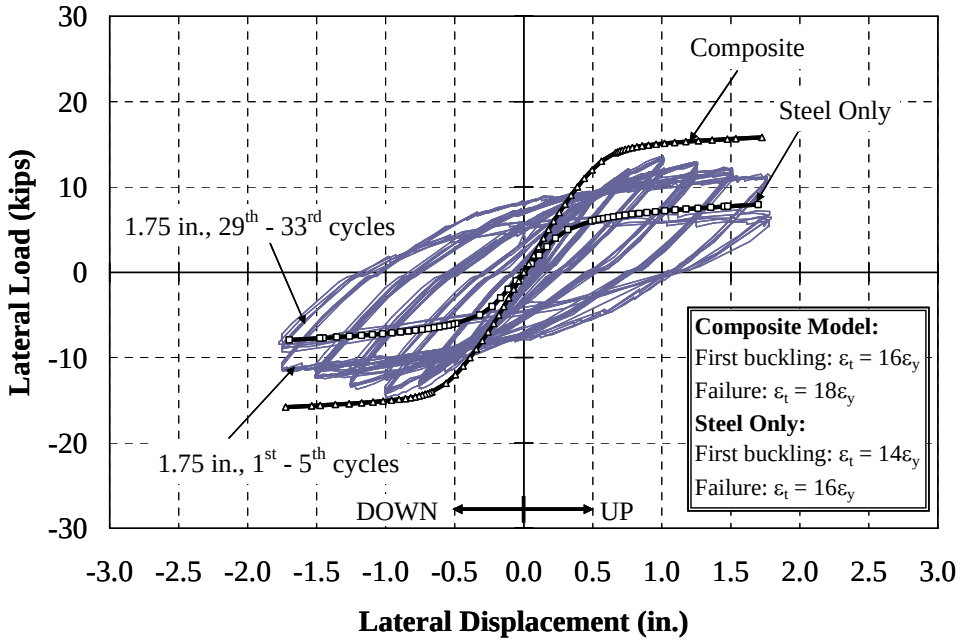

Figure 7.20: Specimen 7 – Load-Deflection Curve

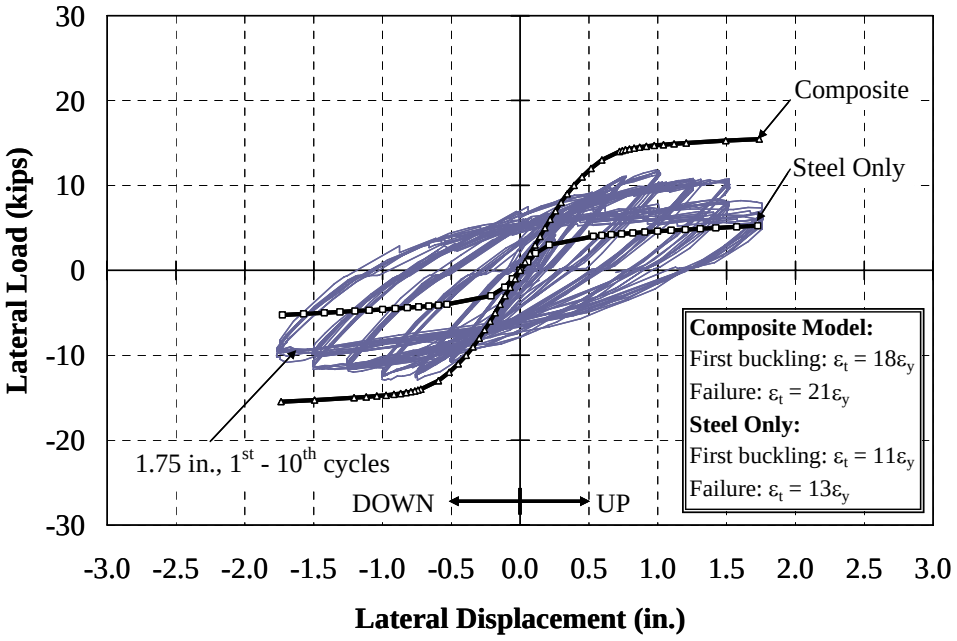

Figure 7.21: Specimen 8 – Load-Deflection Curve

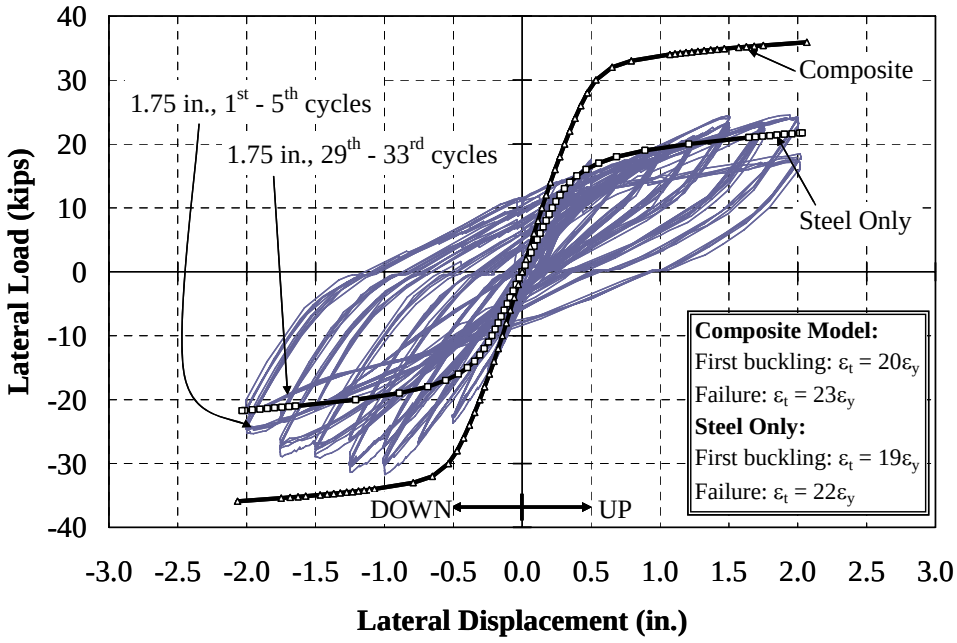

Figure 7.22: Specimen 9 – Load-Deflection Curve

7.5.3 Ductility Ratio

In this research, the ratio of strain at first buckling to the strain at yield, $\varepsilon_{buckling}/\varepsilon_{yield}$, is defined as the buckling ductility ratio. The AISC-LRFD specification (2001) denotes the ratio of strain at fracture to strain at yield, $\varepsilon_{failure}/\varepsilon_{yield}$, as the inelastic ductility ratio. The buckling and inelastic ductility ratios of all specimens using the steel model for the H piles and a composite model for the CFT piles along with their width/thickness ratios (b/t) are summarized in Figure 7.23.

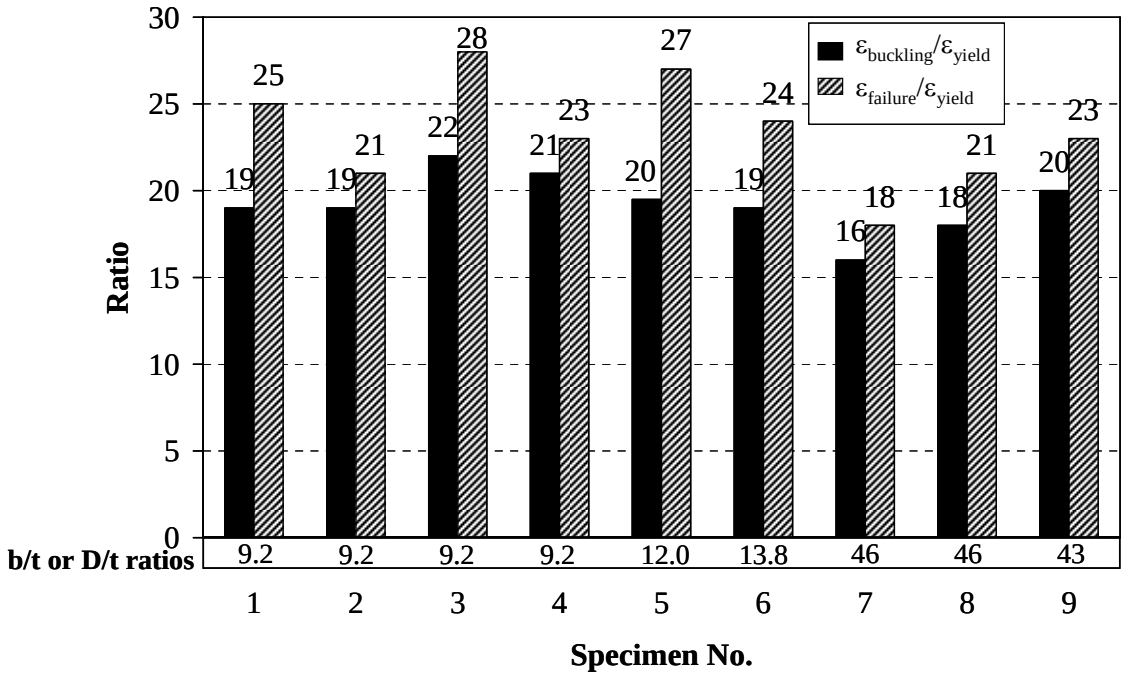

Figure 7.23: Ductility Ratios

In general, the buckling ductility ratios of the H piles are between approximately 19 and 22, while the buckling ductility ratios of the CFT piles vary from approximately 16 to 20. As the b/t ratio increases for the H piles, meaning the flange is more slender, both the buckling ductility and inelastic ductility ratios remain fairly constant, while as the D/t ratio increases for the CFT piles, both the buckling ductility and inelastic ductility ratios decrease. On average, the value of the strain at first buckling for the H piles was

approximately $20\varepsilon_y$, while it was approximately $18\varepsilon_y$ for the CFT piles. The buckling and inelastic ratios are used to discuss the effect of pile size, axial load level, and pile orientation.

7.5.3.1 Effect of Pile Size on Ductility Ratio

The buckling ductility and inelastic ductility ratios of Specimens 1, 5, and 6 were compared to evaluate the effect of pile size on these ratios. One can note that the clamping system of Specimens 1 and 2 was placed differently from the other specimens, that is, the clamping beams of Specimens 1 and 2 were placed at the edges of the concrete abutment, while for the other specimens, one of clamping beams was placed at the middle of the concrete abutment as illustrated in Figure 7.24. The reason that the beam was moved after testing Specimens 1 and 2, was to reduce confinement provided at the abutment-pile connection as much as possible. Even though the confinement at the abutment-pile connection is reduced in the up direction, the concrete support block provides confinement in the down direction. This difference in the clamping system was considered in the evaluation; however, as evident, both ductility ratios remained approximately the same regardless of pile size.

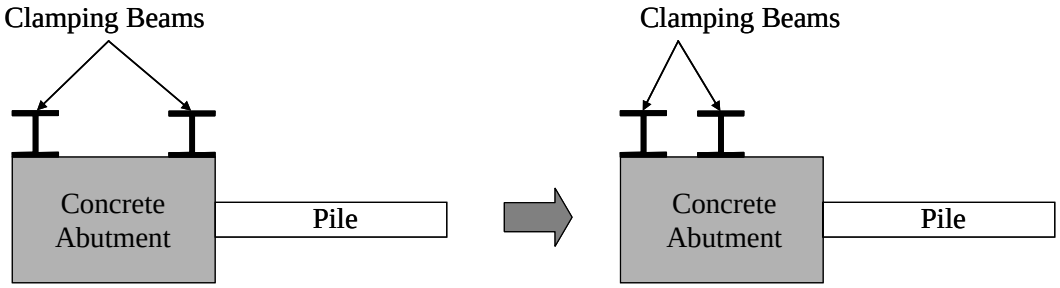

(a) Specimens 1 and 2 (b) Other Specimens

Figure 7.24: Clamping Beams

Unlike the trend of the H piles, the CFT piles behaved differently. As the D/t ratio decreased from 46 to 43, both buckling and inelastic ductility ratios increased. Specimen 9 has a lower D/t, and a higher percentage of steel (7%) than Specimens 7 and 8. This increase in ductility is likely a result of the increased wall thickness (33% greater) that assists in preventing local buckling.

7.5.3.2 Effect of Axial Load Level on Ductility Ratio

The buckling and inelastic ductility ratios of Specimens 1 and 4 as well as Specimens 7 and 8 were compared to evaluate the effect of axial load level on these ratios. In general, it is expected that as the axial load increases, there would be a decrease in the ductility ratios. This comparison indicated that the H pile with a higher axial load had a lower inelastic ductility ratio but the buckling ductility ratio remained fairly constant. On the other hand, for the CFT piles, as the axial load increased, both ductility ratios increased. The pile with a higher axial load was expected to buckle and fail earlier than that with a lower axial load. Both Specimens 7 and 8 were able to achieve a displacement of 1.50 in. prior to buckling. The difference in buckling ductilities may be an artifact of the 0.25 in. displacement increment. Regardless, the higher axial load did not significantly affect the ductility of the CFT pile.

7.5.3.3 Effect of Pile Orientation on Ductility Ratio

Specimens 1, 2, and 3 were considered to evaluate the effect of pile orientation. The analytical results indicate that the pile orientation has only a minor effect on the buckling ductility ratio, but a significant effect on the inelastic ductility ratio. This difference in inelastic ductility ratio is likely caused by the deterioration that occurred at the abutment-pile connection of Specimen 2. Failure of this specimen was limited by deterioration of the connection rather than by failure of the pile. However, comparing weak- and 45°-axis bending piles (Specimens 1 and 3), the pile bending about its 45° axis was observed to have a slightly higher inelastic ductility ratio than the pile bending about its weak axis. This difference is not significant. In general, the buckling ductility capacities were similar.

7.6 Previous Research

Only two tests on H piles were obtained from the literature that are similar to those conducted here. Ravat (1997) performed tests on A36, HP14x89 piles, with a length of 20 ft under combined axial and lateral loads. The piles were oriented for weak, 45°, and strong axes bending. The axial load, however, was varied throughout the test to simulate seismic loading. Construction Technology Laboratories (CTL) (Oesterle et al., 1998) also conducted a test on a HP10x42 section, with a length of 6.7 ft under a constant axial load of 90 kips or 7.3 ksi subjected to lateral load. The pile was oriented for weak axis bending.

Several tests have been conducted for CFT columns under combined flexure and axial loads. These have been reported by Furlong (1967), Knowles and Park (1969), Neogi et al. (1969), Rangan and Joyce (1992), Boyd et al. (1995), Morino et al. (1996), Elremaily and Azizinamini (2000), and Kilpatrick and Rangan (1999). Except for the studies by Boyd et al. (1995), Morino et al. (1969), and Elremaily and Azizinamini (2000), all of the tested columns had a small diameter that ranged from 3 to 6 in. Boyd et al. (1995) tested columns with a diameter of 8 in., while Morino et al. (1996) tested columns with diameters ranging from 4 to 17 in. The diameter of the columns tested by Elremaily and Azizinamini (2000) was 12.75 in. Analytical models have been proposed by Neogi et al. (1969) and Rangan and Joyce (1992). These models, however, ignore the effect of confinement on the concrete strength, and the predicted capacities were conservative for columns with a length-to-diameter ratio (L/O.D.) less than 15 and with a small eccentricity. One can note that the piles tested in this research have length-to-diameter ratios of 5.5 and 7.0 and diameter-to-thickness ratios (O.D./t) of 43 and 46.

7.7 CTL Research

Construction Technology Laboratories (CTL) (Oesterle et al., 1998) conducted a test on an H pile similar to that performed in this research. The results from this test were also compared with the model described in Section 7.2.1 to evaluate its applicability beyond the tests conducted here.

7.7.1 Test Setup (CTL Specimen)

The steel pile cross section used in the CTL test was a HP10x42. The dimensions and section properties are shown in Table 7.3, and the material properties for this pile are provided in Table 7.4. It should be noted that the actual modulus of elasticity of steel is approximately 29,000 ksi, but the measured modulus of elasticity of steel is reported as 26,850 ksi in the CTL research. This difference is likely due to measurement error. The total length of the pile was 9 ft-7 in., and the pile was embedded 2 ft into a concrete abutment. The pile was bent about its weak axis with lateral load applied at a distance of 80 in. from the face of the concrete abutment. An axial load of 90 kips (7.25 ksi) was applied horizontally at the end of the pile and remained horizontal and in line with the pin at the end of the pile using a low-friction ball bearing assembly as illustrated in Figure 7.25. The specimen was subjected to cyclic loading at three different displacement ranges. One hundred (100) cycles were applied at a displacement range of 0.6 in. while 50 cycles were applied at a displacement range of 1.2 and 2.4 in. The pile was expected to experience first yielding during the 0.6 in. displacement range and first buckling during the 2.4 in. displacement range. First buckling was calculated based on an expression by Abendroth et al. (1989).

Table 7.3: Nominal Cross-Sectional Properties of HP10x42

Section	A ($in.^2$)	d (in.)	t_w (in.)	b_f (in.)	t_f (in.)	I_x ($in.^4$)	I_y ($in.^4$)	S_x ($in.^3$)	S_y ($in.^3$)	Z_x ($in.^3$)	Z_y ($in.^3$)
HP10x42	12.4	9.70	0.415	10.1	0.420	210	71.7	43.4	14.2	48.3	21.8

Table 7.4: Material Properties*

Modulus of Elasticity (ksi)	Yield Strength (ksi)	Ultimate Strength (ksi)
26,850	43.25	64.3

* Reported by Oesterle et al. (1998)

7.7.2 Experimental Results (CTL Specimen)

As reported by Oesterle et al. (1998), it was apparent that there was no significant degradation for 100 cycles at the 0.6 in. displacement range. Small concrete cracks were observed radiating from the four corners of the pile and propagating outward during the 1.2 in. displacement range as shown in Figure 7.26. During the tenth cycle of the 2.4 in. displacement range, local buckling was observed on the top and bottom sides of the flanges as shown in Figure 7.27. The abutment-pile connection exhibited minor cracking and spalling; however, the pile maintained axial load in the 50th cycle. The selected load-deflection curves of the 0.6, 1.2, and 2.4 in. displacement ranges are provided in Figure 7.28.

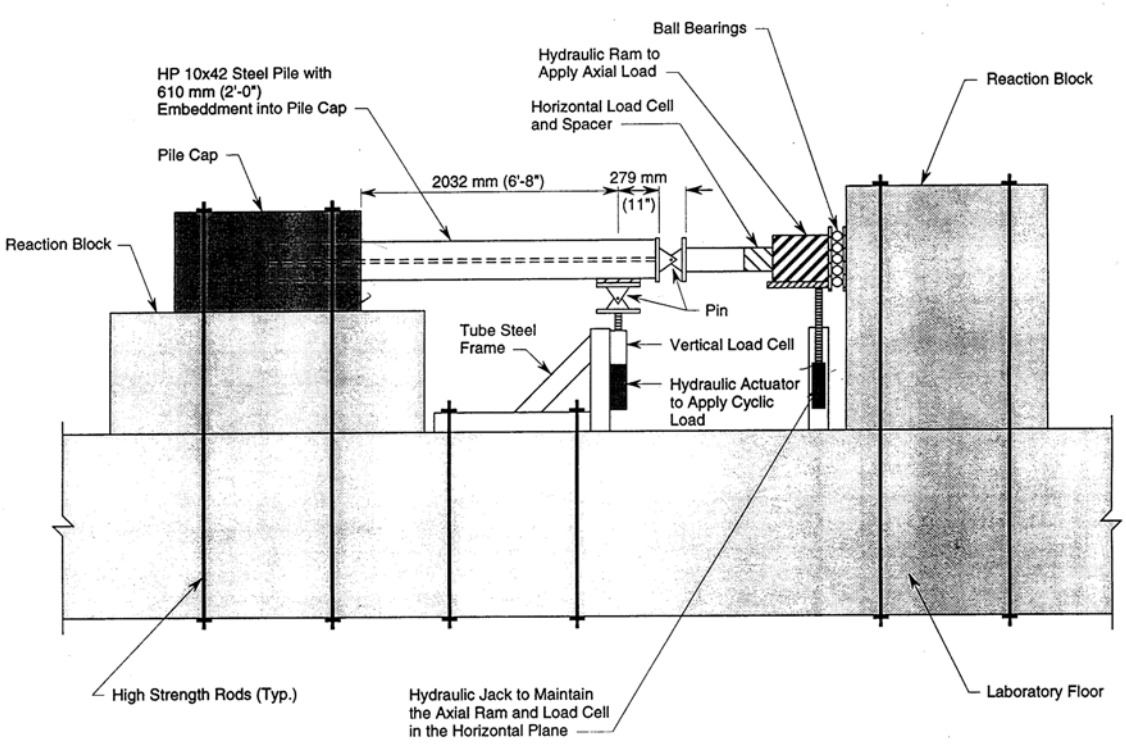

Figure 7.25: CTL Test Setup (Oesterle et al., 1998)

7.7.3 Pile Model (CTL Specimen)

The pile was modeled as a cantilever beam subjected to an axial load of 90 kips along with a lateral load at the pile tip. The pile length was 80 in. The model used the trilinear stress-strain model for steel as described in Section 7.2.1. A modulus of

elasticity of 29,000 ksi and a yield strength of 43.25 ksi were used. The strain at the onset of strain-hardening was assumed to be 0.014 in./in., and the modulus of strain hardening was taken as 300 ksi. Based on the previous analyses, the strain at first buckling was assumed to equal to $20\varepsilon_y$.

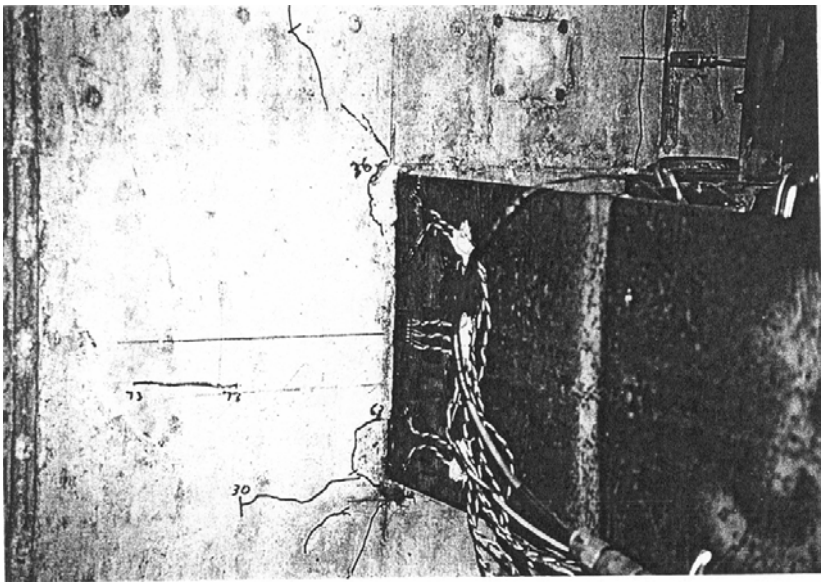

Figure 7.26: Cracks on Concrete Abutment (1.2 in. Cycle)

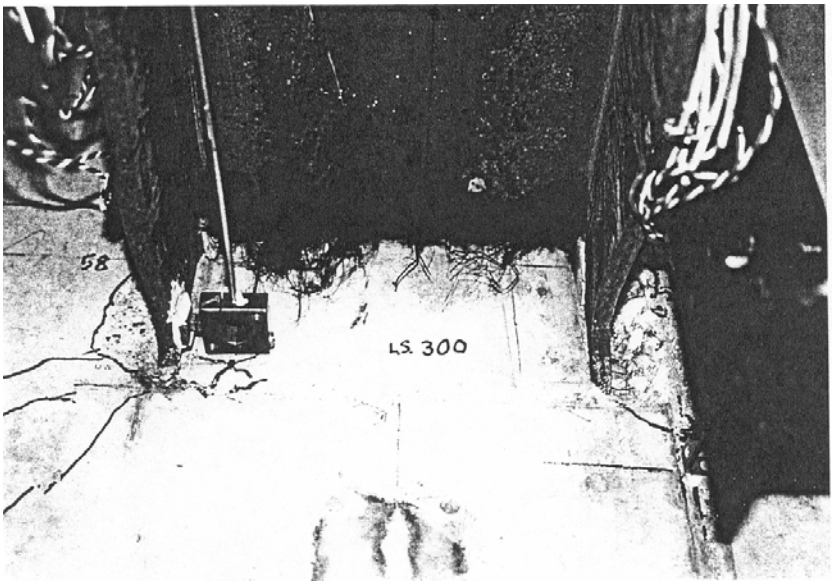

Figure 7.27: Buckling at the Bottom of the Flanges (2.4 in. Cycle)

7.7.4 Analytical Results (CTL Specimen)

The analytical load-deflection curve is plotted in Figure 7.28. In general, the analysis provides a reasonable prediction of the pile response. Using a strain of $20\varepsilon_y$ estimated the displacement at first buckling as 2.7 in. which slightly overestimates the observed behavior. The difference in the lateral load capacity at larger displacements is caused by the deterioration that occurred at the abutment-pile connection.

7.7.5 Comparison between Test Results

The CTL results were compared with the experimental results from Specimen 5 (HP10x42) as this was the same pile size. The difference in the lateral load capacity and lateral displacement capacity is caused by the difference in material properties and the length of the pile. The CTL specimen had a yield strength of approximately 43 ksi, while that of Specimen 5 was approximately 39 ksi. The distance from the fixed support to the location of the applied load of the CTL specimen was 80 in., while that of Specimen 5 was 60 in. One should also note that the embedment length of the CTL test is 6 in. deeper than that of Specimen 5. The lower lateral load capacity is caused by the larger moment arm used in the CTL test.

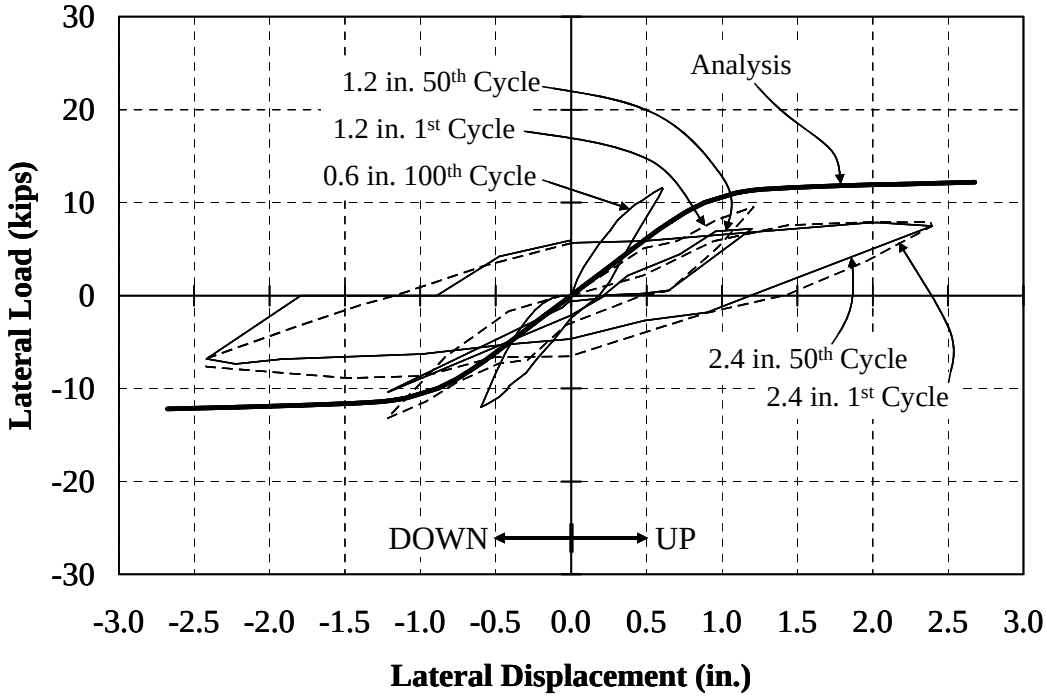

Figure 7.28: Load-Deflection Curves for CTL Specimen

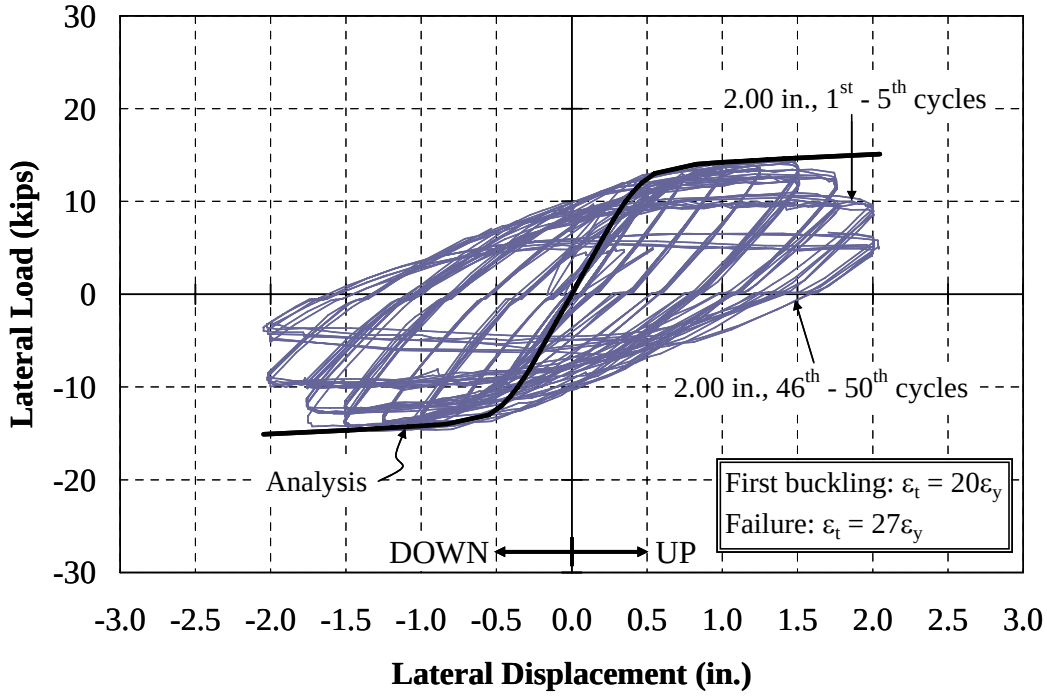

Figure 7.29: Load-Deflection Curves for Specimen 5 (HP10x42)

7.7.6 Comparison of Abendroth et al. (1989) and Buckling Strain Analysis Model

Abendroth et al. (1989) proposed an equation for determining the displacement capacity of the pile based on plastic redistribution. Oesterle et al. (1998) adopted the Abendroth et al. method to calculate the theoretical lateral displacement at local flange buckling for H piles as given in Equations 7-3 and 7-4. A fixed-headed, equivalent cantilever pile with the length of the pile equal to L/2 was assumed as shown in Figure 7.30. A pile was assumed to be an elastic-perfectly plastic material where the plastic hinge moment remains constant and equal to the plastic moment capacity, M_p. Displacement relative to the inflection point at the local flange buckling limit is one-half of Δ calculated using Equation 7-3.

$$\Delta = \Delta_p(0.6 + 2.25C_i) \tag{7-3}$$

$$C_i = \frac{19}{6} - \frac{b_f\sqrt{f_y}}{60t_f} \tag{7-4}$$

where:

Δ = lateral displacement at pile tip, in.

f_y = yield strength of steel, ksi

b_f = width of flange, in.

t_f = thickness of flange, in.

$$\Delta_p = \frac{M_pL^2}{6EI} \tag{7-5}$$

$$M_p = f_yZ \tag{7-6}$$

Z = plastic modulus, in.^{3}

E = modulus of elasticity, ksi

I = moment of inertia, in.^{4}

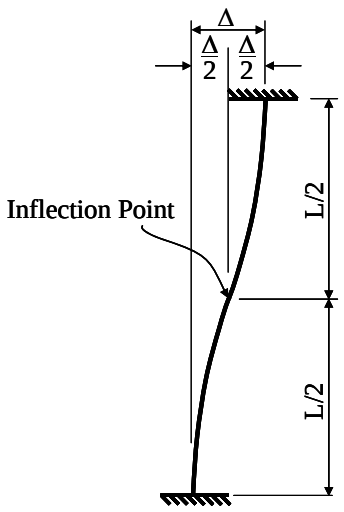

Figure 7.30: Equivalent Cantilever Pile

The theoretical displacement at buckling using the Abendroth equation and using the pile model developed based on the strain of $20\varepsilon_y$ were calculated and compared with the displacement at buckling observed from the experimental results as presented in Table 7.5. As the section increases, the theoretical displacement using the Abendroth equation is underestimated significantly. It was found that the use of a strain capacity of $20\varepsilon_y$ to estimate pile buckling capacity provides better results. Furthermore, the Abendroth equation was developed for H sections and is not applicable for CFT sections.

Table 7.5: Comparison of the Theoretical Displacement at Buckling

Specimen	f_y (ksi)	Δ_{test} (in.)	M_p (ft-k)	Abendroth Δ_{calc} (in.)	$\Delta_{calc}/\Delta_{test}$	At $20\varepsilon_y$ Δ_{calc} (in.)	$\Delta_{calc}/\Delta_{test}$
1	47	2.00	59.5	2.21	1.11	2.11	1.06
2	47	1.50	131.6	1.66	1.10	1.63	1.09
3	47	1.50	96.4	1.81	1.21	1.29	0.86
4	47	2.25	59.5	2.21	0.98	2.07	0.92
5	39	1.25	70.9	1.03	0.82	1.29	1.03
6	45	1.25	120.8	0.37	0.30	1.35	1.08
				Average	0.92	Average	1.01

7.8 Recommended Pile Sections

7.8.1 H Sections

Based on the comparison of the results of the analytical model with experimental results, it was determined that the simplified analysis method could reasonably estimate the response up to first buckling of the pile system. First buckling was considered the maximum desired displacement range as increased cycling following local buckling eventually results in fracture of the pile. The analytical model was then used to evaluate all standard H sections as provided in the AISC-LRFD specification (2001). These sections were analyzed based on the following assumptions:

1. The specified yield strength of steel, f_y, equals 36 ksi.
2. Deterioration of the abutment-pile connection is prevented. The connection is assumed as fixed.
3. The lateral deflection at yield, Δ_y, was determined using the yield strain, ε_y, assumed based on f_y = 36 ksi.
4. The lateral deflection at buckling, $\Delta_{buckling}$, was determined using a strain value of $20\varepsilon_y$.
5. The pile length is 5 ft. This is assumed to be the inflection point of the pile and is constant for all H sections.
6. All piles can achieve the plastic moment, M_p, prior to local buckling.
7. All piles are subjected to an axial stress of 9 ksi.

H sections included HP14x117, HP14x102, HP14x89, HP14x73, HP12x84, HP12x74, HP12x63, HP12x53, HP10x57, HP10x42, and HP8x36. The moment-curvature relationships and the lateral load-deflection relationships of all H piles are presented in Figures 7.31 and 7.32, respectively. The lateral displacements at a strain of 20 times the yield strain based on above assumptions along with the compact section criteria ($b_f/2t_f$ and h/t_w ratios) are summarized in Table 7.6. The compact section criterion is provided by Table B5.1 in AISC-LRFD specification (2001).

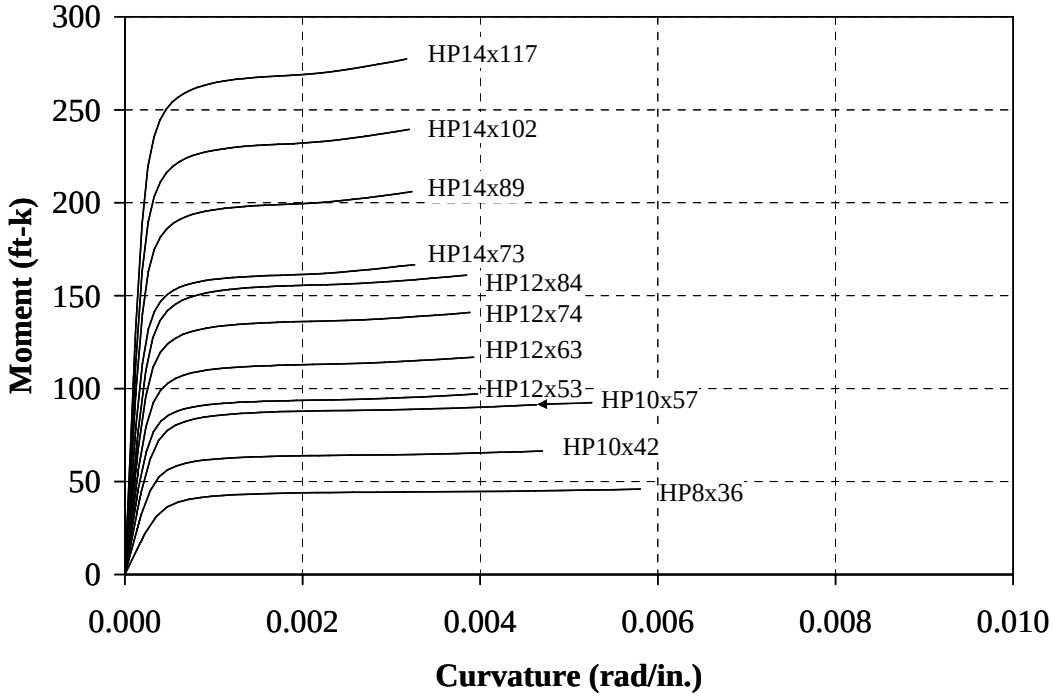

Figure 7.31: Moment-Curvature Relationships of All H Piles

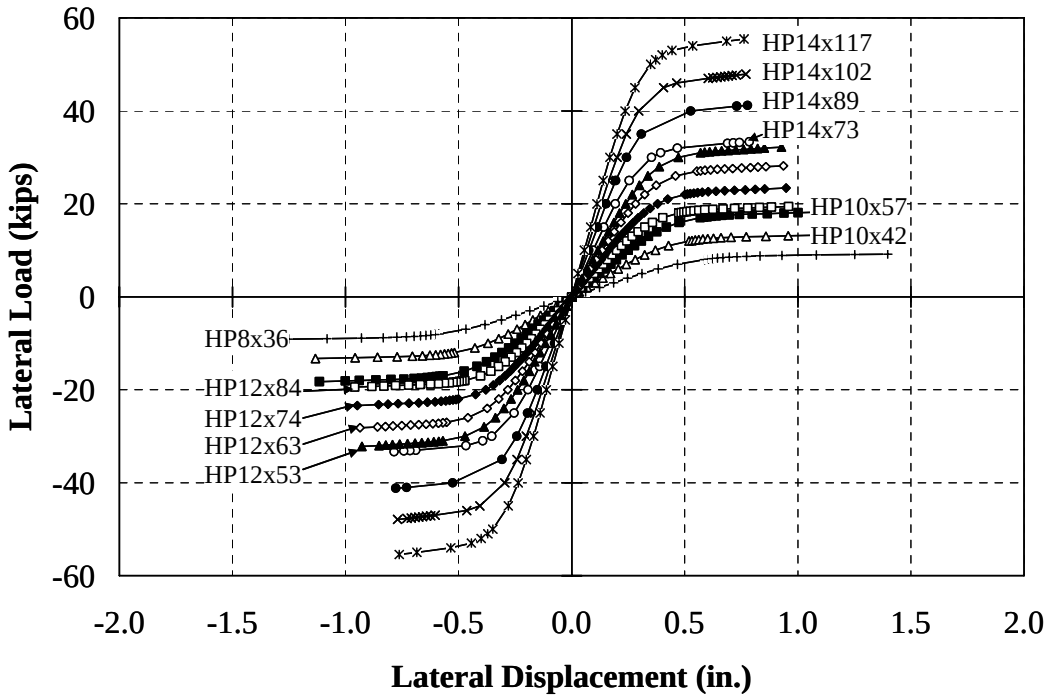

Figure 7.32: Load-Deflection Relationships of All H Piles

Table 7.6: Displacement at $20\varepsilon_y$

Section	Compact Section Criteria*			Axial Load (kips)	$\Delta@20\varepsilon_y$ (in.)
	$b_f/2t_f$	h/t_w			
HP14x117	9.25	14.2	Compact	310	0.76
HP14x102	10.5	16.2	Compact	270	0.77
HP14x89	11.9	18.5	Noncompact	235	0.78
HP14x73	14.4	22.6	Noncompact	193	0.79
HP12x84	8.97	14.2	Compact	221	0.93
HP12x74	10.0	16.1	Compact	196	0.94
HP12x63	11.8	18.9	Noncompact	166	0.95
HP12x53	13.8	22.3	Noncompact	140	0.96
HP10x57	9.05	13.9	Compact	151	1.12
HP10x42	12.0	18.9	Noncompact	112	1.13
HP8x36	9.16	14.2	Compact	95.4	1.40

* Flange: $\lambda_p = 0.38\sqrt{E/F_y} = 10.8$ and $\lambda_r = 0.83\sqrt{E/F_y} = 27.6$;
Web: $\lambda_p = 3.76\sqrt{E/F_y} = 107$ and $\lambda_r = 5.70\sqrt{E/F_y} = 162$

For a pile length of 5 ft, the piles with the same cross-sectional depth, d, have approximately the same lateral displacement capacity. However, the length of the pile which represents the depth to the inflection point of the pile in soil actually varies depending upon the soil type and pile size. Consequently, the pile length should vary to account for these parameters. The inflection point of 5 ft is reasonable for the HP10, but too shallow for HP12 and HP14 sections. HP10x42, HP12x53, and HP14x89 were further analyzed because they are commonly used in the field. HP12x84 and HP14x117 sections were also analyzed to conservatively represent the family of HP12 and HP14 sections. All piles were assumed to be embedded in stiff clay and medium sand. The pile lengths for the analysis based on the inflection point depth were determined using LPILE PLUS, and the displacements at first yield, Δ_y, and at buckling, $\Delta_{buckling}$, were calculated as presented in Table 7.7. The load-deflection curves of those piles were calculated and are shown in Figure 7.33. As the length of the pile increases, the lateral load decreases, but the lateral displacement capacity increases. Due to the adjustment in the pile length to reflect the stiffness changes in the pile, larger displacement capacities result as compared to considering only a fixed pile length (Table 7.6).

Table 7.7: Length of the H Piles Based on LPILE PLUS

Section	Soil Type	Pile Length (ft)	Δ_y (in.)	$\Delta_{buckling}$ (in.)
HP14x117	Med. Sand	7.0	0.30	1.50
	Stiff Clay	7.4	0.33	1.67
HP14x89	Med. Sand	6.5	0.26	1.31
	Stiff Clay	6.9	0.29	1.47
HP12x84	Med. Sand	6.1	0.27	1.38
	Stiff Clay	6.3	0.28	1.42
HP12x53	Med. Sand	5.6	0.23	1.20
	Stiff Clay	5.7	0.24	1.25
HP10x42	Med. Sand	5.0	0.22	1.13
	Stiff Clay	5.0	0.22	1.13

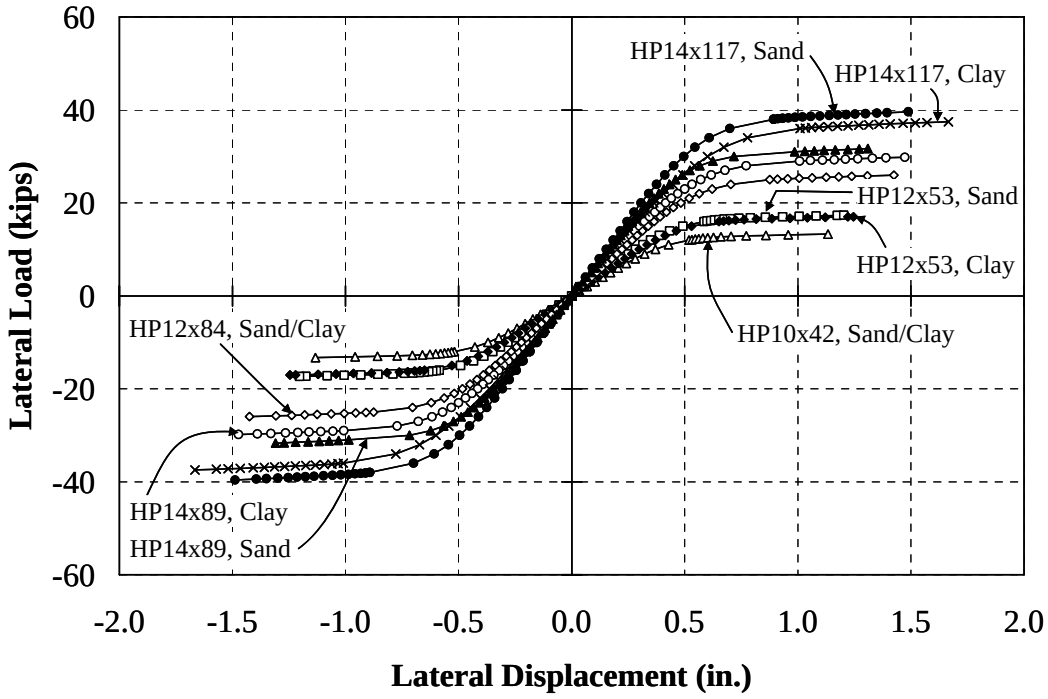

Figure 7.33: Displacement at $20\varepsilon_y$ Based on the Inflection Point using LPILE

7.8.2 CFT Sections

Similar as Section 7.8.1, CFT sections recommended by INDOT Memorandum #243, were analyzed based on the following assumptions:

1. The specified yield strength of steel, f_y, is assumed to be 35 ksi.
2. Deterioration of the abutment-pile connection is prevented. The connection is assumed fixed.
3. The lateral deflection at yield, Δ_y, was determined using the yield strain, ε_y, assumed based on f_y = 35 ksi.
4. The lateral deflection at buckling, $\Delta_{buckling}$, was determined using a strain value of $15\varepsilon_y$. This value was conservatively selected based on the analytical results.
5. The pile length is 5 ft. This is assumed to be the inflection point of the pile and is constant for all CFT sections.
6. All piles can achieve the plastic moment, M_p, prior to local buckling.
7. All piles are subjected to an axial stress of $0.25f_yA_s + 0.4f'_cA_c$.

CFT sections included CFT14.0x0.203, CFT14.0x0.250, and CFT14.0x0.312. The moment-curvature relationships and the lateral load-deflection relationships of all CFT piles are presented in Figures 7.34 and 7.35, respectively. The lateral displacements at a strain of 15 times the yield strain based on above assumptions along with the compact section criteria (D/t ratios) are summarized in Table 7.8. The compact section criterion is provided by Table B5.1 of AISC-LFRD specification (2001).

For a pile length of 5 ft, the piles have approximately the same lateral displacement capacity. As mentioned in Section 7.8.1, the pile length should vary to account for the soil type and pile thickness. The CFT14.0x0.203 and CFT14.0x0.312 sections were further analyzed to evaluate the boundaries of the family of CFT14 sections. Both piles were assumed to be embedded in stiff clay and medium sand. The lengths of the pile for the analysis based on the inflection point depth were determined using LPILE PLUS, and the displacements at first yield, Δ_y, and at buckling, $\Delta_{buckling}$, were calculated as presented in Table 7.9. The load-deflection curves of those piles were calculated and are shown in Figure 7.36. Similar to the H pile behavior, as the length of

the pile increases, the lateral load decreases, but the lateral displacement capacity increases. Due to the adjustment in the pile length to reflect the stiffness changes in the pile, larger displacement capacities result as compared to considering only a fixed pile length (Table 7.8).

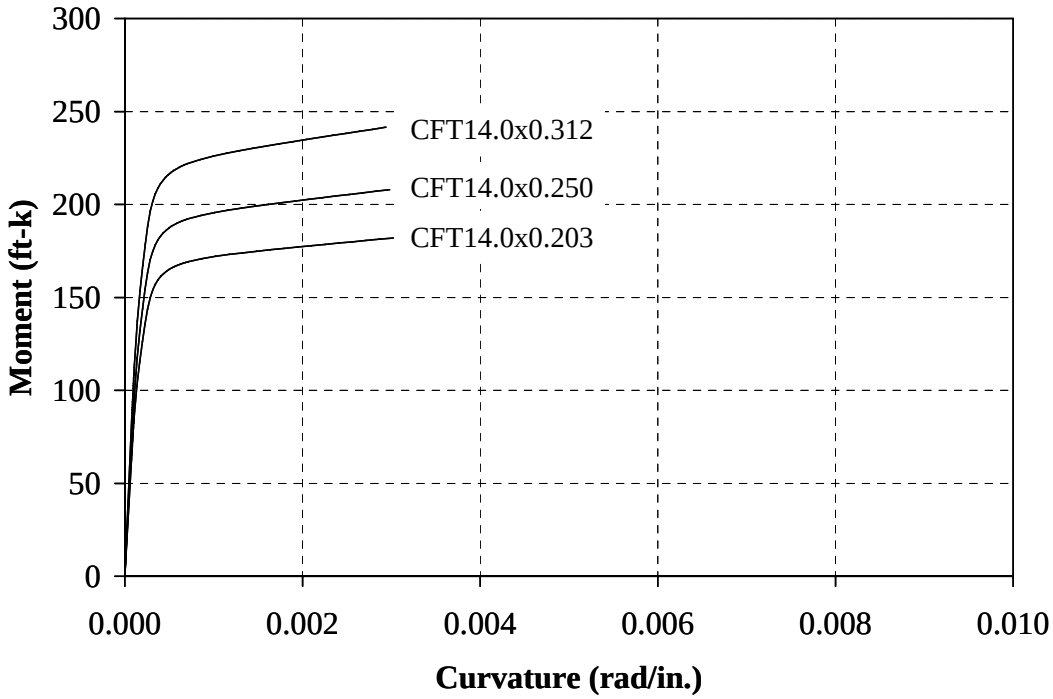

Figure 7.34: Moment-Curvature Relationships of CFT14 Piles

The same method was applied to piles embedded in a very stiff clay and a dense sand to calculate their displacement capacities. Soil properties of a very stiff clay and a dense sand are given in Chapter 4. The displacements at first yield, Δ_y, and at buckling, $\Delta_{buckling}$, were calculated as presented in Table 7.10.

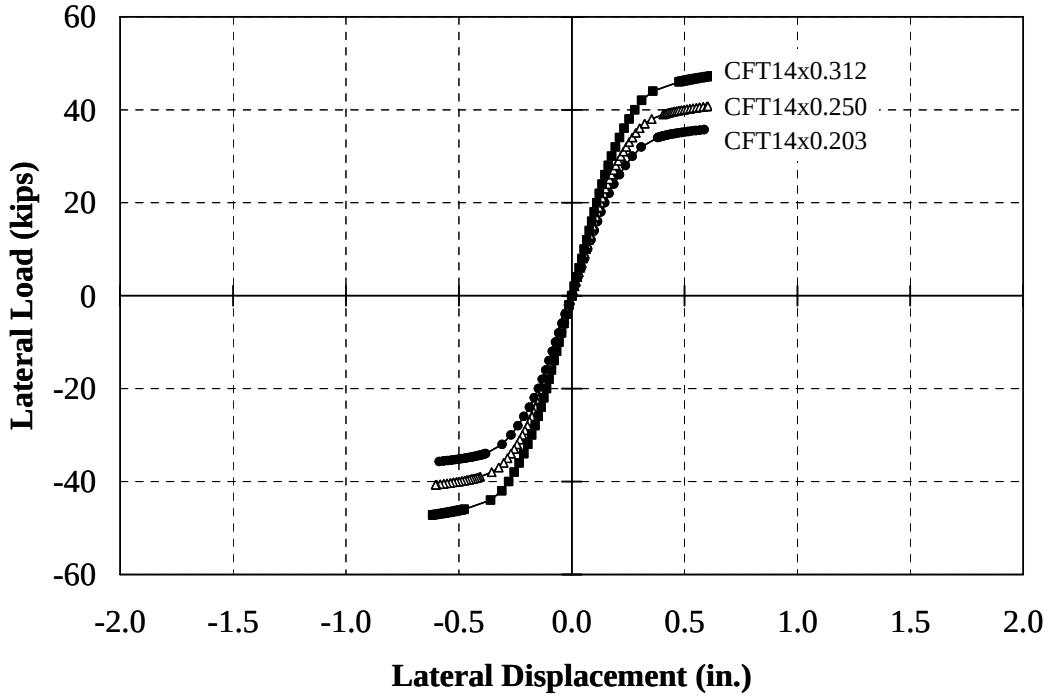

Figure 7.35: Load-Deflection Relationships of CFT14 Piles

Table 7.8: Displacement at $15\varepsilon_y$

Section	Compact Section Criterion*		Axial Load (kips)	$\Delta@15\varepsilon_y$ (in.)
	D/t			
CFT14.0x0.203	69	Noncompact	309	0.59
CFT14.0x0.250	56	Compact	324	0.60
CFT14.0x0.312	45	Compact	342	0.62

* $\lambda_p = 0.07E/F_y = 58$ and $\lambda_r = 0.31E/F_y = 257$

Table 7.9: Length of the CFT Piles based on LPILE PLUS

Section	Soil Type	Pile Length (ft)	Δ_y (in.)	$\Delta_{buckling}$ (in.)
CFT14.0x0.312	Med. Sand	7.1	0.25	1.21
	Stiff Clay	7.6	0.30	1.46
CFT14.0x0.203	Med. Sand	6.8	0.22	1.09
	Stiff Clay	7.4	0.27	1.29

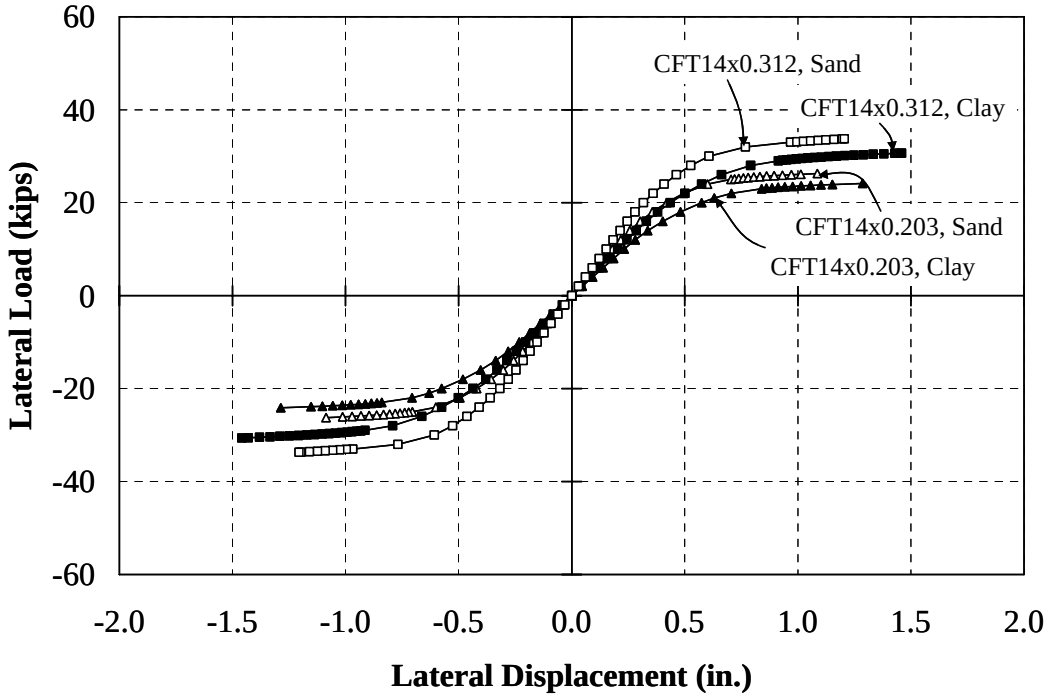

Figure 7.36: Displacement at $15\varepsilon_y$ Based on the Inflection Point using LPILE

Table 7.10: Length of the Piles Embedded in Very Stiff Clay and Dense Sand

Section	Soil Type	Pile Length (ft)	Δ_y (in.)	$\Delta_{buckling}$ (in.)
HP14x117	Dense Sand	6.5	0.25	1.29
	V. Stiff Clay	6.1	0.22	1.13
HP14x89	Dense Sand	6.0	0.22	1.12
	V. Stiff Clay	5.7	0.20	1.01
HP12x84	Dense Sand	5.6	0.23	1.17
	V. Stiff Clay	5.2	0.20	1.01
HP12x53	Dense Sand	5.1	0.19	1.00
	V. Stiff Clay	4.7	0.16	0.84
HP10x42	Dense Sand	4.6	0.18	0.96
	V. Stiff Clay	4.1	0.15	0.76
CFT14x0.312	Dense Sand	6.5	0.22	1.04
	V. Stiff Clay	6.4	0.21	1.01
CFT14x0.203	Dense Sand	6.2	0.19	0.90
	V. Stiff Clay	6.0	0.17	0.85

7.9 Calculated and Measured Movements

The pile models described in the previous sections were used to predict the behavior of the piles supporting the abutments of the I65 and SR18 bridges. The CFT14x5x0.250 and HP12x53 piles embedded in a wet medium sand as well as the CFT14.0x0.312 piles embedded in a dry medium sand and a dry stiff clay were evaluated as shown in Figures 7.37 and 7.38. The measured abutment movement is approximately twice the tip displacement calculated using the pile model. For I65 over SR25, the expansion and contraction abutment movements obtained from the longitudinal linear potentiometer (Figure 3.18) are approximately 0.2 and 0.7 in., respectively. Therefore, the lateral displacements provided in the pile model are approximately 0.10 and 0.35 in., respectively. For SR18 over the Mississinewa River, the expansion and contraction abutment movements measured from a displacement meter (Figure 3.28) are approximately 0.00 and 0.46 in., respectively. Therefore, the lateral displacements provided in the pile model are approximately 0.00 and 0.23 in., respectively. These displacement ranges are superimposed in Figures 7.37 and 7.38 to illustrate the range of pile behavior exhibited in service. As noted, the response is well within the capacity of the piles. Table 7.11 presents the measured movements compared with the calculated movements (displacement at first yield and at buckling) of both bridges. The table indicates that during contraction, the piles supporting abutments of the I65 bridge yielded but did not buckle, while during expansion, the piles did not yield. The piles of the SR18 bridge did not yield during both expansion and contraction.

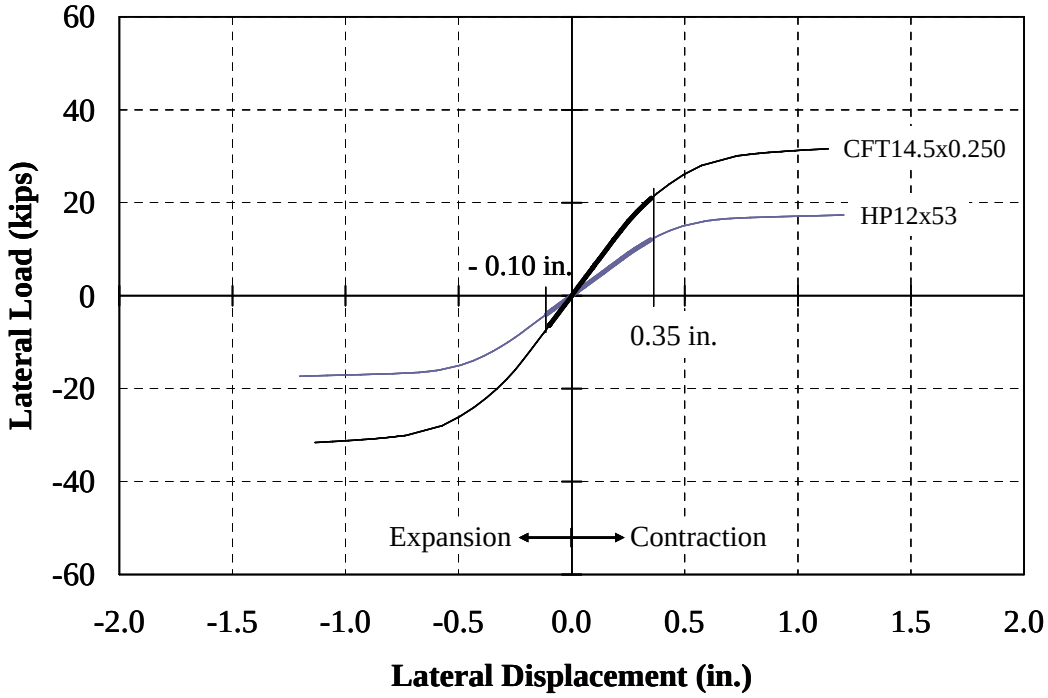

Figure 7.37: Load-Deflection Curves for Piles on I65

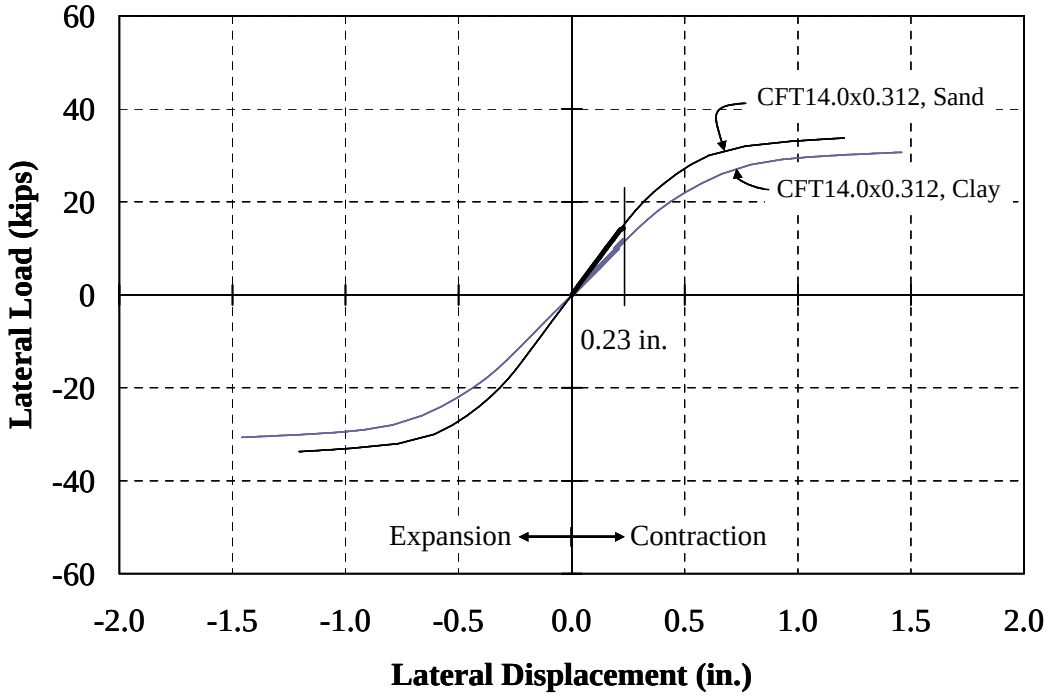

Figure 7.38: Load-Deflection Curves for Piles on SR18

Table 7.11: Measured and Calculated Movements

Pile Section	$\Delta_{Measured}$		$\Delta_{Calculated}$	
	Contraction	Expansion	$\Delta_{First\ Yield}$	$\Delta_{Buckling}$
HP12x53	0.35	0.10	0.23	1.20
CFT14.5x0.250	0.35	0.10	0.23	1.13
CFT14.0x0.312 Sand	0.23	0.00	0.26	1.21
CFT14.0x0.312 Clay	0.23	0.00	0.29	1.42

7.10 Recommended Bridge Length

The lateral displacements calculated in Section 7.8 were used to calculate the maximum bridge length that these piles can accommodate. As previously discussed in Section 6.5.5, the movement that can be accommodated by the end bent is approximately twice the calculated lateral displacement capacity of the pile since only the depth to the inflection point is considered in the analysis. The total thermal movement of the bridge is, therefore, four times the lateral displacement calculated in Section 7.8. The total bridge lengths are solved using Equation 7-8 are presented in Figure 7.39.

$$\Delta L = \alpha(\Delta T)L \qquad (7\text{-}8)$$

where:

ΔL = four times the displacement calculated in Section 7.8, ft.

α = coefficient of thermal expansion, taken as 6.5×10^{-6} /°F.

ΔT = temperature change, assumed to be 100° F.

L = total bridge length, ft.

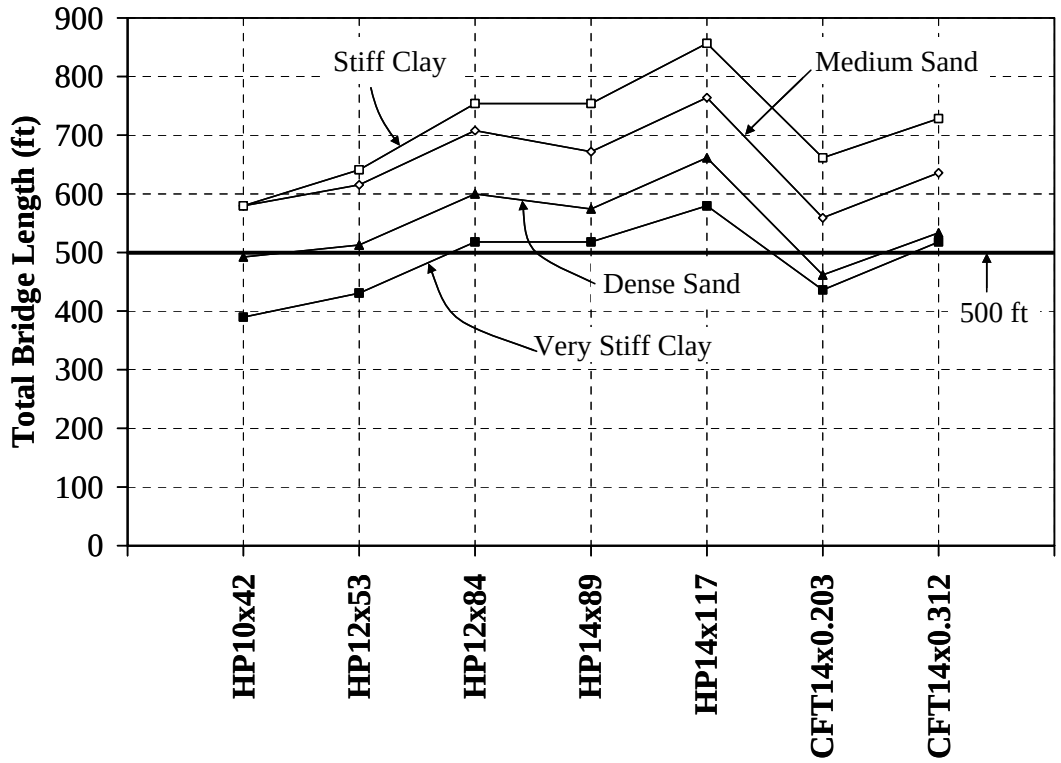

Figure 7.39: Expected Total Bridge Length

It should be noted that the change in temperature, ΔT, is assumed as 100° F. This large temperature variation is used as typical bridge construction in Indiana occurs in the summer. Therefore, average construction temperatures are likely around 80° F. This temperature change accommodates contraction to -20° F and is considered reasonable. The temperature change considered varies from that provided by AASHTO. According to AASHTO, Indiana is located in a cold climate and provides temperature limits of -30 to 120° F for steel and 0 to 80 ° F for concrete design.

It is important to note that this analysis assumes minimal deterioration of the abutment-pile connection. Therefore, to achieve the proposed total bridge length, the abutment-pile connection must be detailed to prevent or minimize damage. It can be concluded that as the pile size increases, the total bridge length can be increased. Based on this analysis, Table 7.12 provides the recommended maximum bridge length where the pile is integrally connected to the abutment. This analysis considered embedment in medium and dense sand as well as stiff and very stiff clay. As noted the soil type

influences the maximum bridge length as well as the stiffness of the pile relative to the soil.

Table 7.12: Recommended Bridge Length

Section	Bridge Length (ft)			
	Clay		Sand	
	Stiff	V. Stiff	Medium	Dense
HP14x117	860	580	760	660
HP14x89	750	520	670	570
HP12x84	750	520	710	600
HP12x53	640	430	610	510
HP10x42	580	390	580	490
CFT14x0.312	730	520	640	530
CFT14x0.203	660	440	560	460

To provide simplicity, it is recommended that a maximum bridge length of 500 ft can be used without regard to pile type (Figure 7.39). This recommendation is provided for several reasons. First, the stiffnesses provided analytically for very stiff clays and dense sands are uncommon in practical field applications. Second, cyclic response tends to reduce the stiffness (soften) of the soil. Third, the pile sections that provide lengths below 500 ft shown in Figure 7.39 are not typically used in bridge construction. Fourth, these lengths are based on the entire thermal movement being accommodated by the end bent. Field measurements indicate that this displacement is lower than the computed value due to restraint provided by the backfill, pile lateral resistance, and friction from the approach slab. This recommendation, therefore, is considered conservative.

CHAPTER 8: SUMMARY AND CONCLUSIONS

8.1 Introduction

Integral abutment bridges have been used in the United States for decades. These structures eliminate expensive expansion joints by utilizing the end bent to accommodate the total thermal movement of the bridge. Due to their complexity of response, these bridges are designed based upon experience, and a rational design specification has not been developed. Furthermore, the interaction of the abutment, pile, and soil remains uncertain. A better understanding regarding the behavior of this system is needed. The objective of this research is to evaluate the behavior of the integral abutment-pile system and evaluate any limitations of its use. A goal of the research is to develop minimum design and detailing recommendations. Two phases were conducted: a field investigation and an experimental investigation. In both phases, analytical and parametric studies were performed to further understand the behavior of this structural system. Based on the research performed here, design recommendations are provided regarding the design of the pile system as well as limitations on the overall length for this structural type.

8.2 Conclusions

8.2.1 Field Investigation

Four integral abutment bridges were instrumented to investigate the in-service behavior of integral abutment bridges as well as the behavior of the piles. Based on the results of the field instrumentation, several conclusions were made:

1. The abutment responds to temperature changes, and its movement can be estimated conservatively using the theoretical thermal expansion/contraction of the superstructure, $\Delta L = \alpha(\Delta T)L$. The actual displacement is expected to be slightly less due to backfill restraint, pile resistance, and approach slab friction.
2. The abutment primarily translates or "slides" longitudinally in response to thermal expansion and contraction of the bridge. Only minor rotations of the abutment occur and for analysis purposes can be ignored.
3. Piles integrally connected with the abutment bend in double curvature. Lateral displacements in the soil correspond directly with temperature changes. Measures to eliminate the integral abutment-pile connection can be used such as in the SR249 structure to provide for a pinned connection. This connection eliminated the double curvature response.
4. For satisfactory bridge performance, the structure must be detailed and constructed properly.
    a. Piles must be constructed and oriented as designed.
    b. Intermediate piers should be designed to accommodate lateral displacement or the connection must be detailed to minimize lateral force transfer. If the piers are not designed for the lateral displacement, locking of the superstructure to the intermediate piers must be prevented through isolation.

8.2.2 Analysis of Field Investigation

Analytical models were calibrated using the field results. These models were then used to perform a parametric study to evaluate the effect of the primary variables involved in the pile-soil interaction. Based on this study, the following conclusions were reached:

1. Pile axial load does not have a significant effect on the behavior of the pile in the soil. The deflected shape and moment distribution along the pile were not significantly affected.
2. A minimum pile length must be provided below ground level in order to prevent displacement at the base of the pile.

3. For the same soil type, as the pile stiffness increases due to size or orientation, the deflected shape of the pile is affected. The inflection point, the final zero deflection, and the final zero moment depths increase.
4. For the same pile type and orientation, as the soil stiffness increases, the deflected shape of the pile is affected. The inflection point, the final zero deflection, and the final zero moment depths decrease.

8.2.3 Experimental Investigation

Six steel H piles and three concrete-filled steel tube piles (CFT) were tested to evaluate the capability of the piles to maintain axial load under low-cycle, large amplitude lateral displacement and to investigate the performance of the abutment-pile connection. Variables included the pile size, axial load, and pile orientation. Based on the results of the experimental instrumentation, several conclusions were made:

1. The pile was able to maintain axial loads while undergoing cyclic lateral displacements post-yield. In general, no degradation in the load-displacement response was evident. The piles demonstrated that they can be loaded past the yield displacement and provide for a 50-100 year bridge life.
2. Once local buckling of the pile was observed, significant deterioration and damage occurred in the local region of the pile. Damage accumulation was observed and noted in the load-deflection response. Cycling at the displacement level that initiated local buckling eventually led to fracture of the section. Therefore, local buckling should be prevented to provide for a 50-100 year bridge life.
3. Significant deterioration occurred at the abutment-pile connection that can prevent achievement of design life. This deterioration was more severe as the pile stiffness increased.
4. As the pile size was increased, the lateral load resistance increased while the displacement capacity and ductility decreased.
5. As the axial load was increased, the lateral load resistance decreased along with the displacement capacity.

6. As the pile orientation was rotated from weak axis to strong axis, the lateral load resistance increased while the displacement capacity decreased. Severe deterioration of the strong axis specimen was observed that limited its performance.

8.2.4 Analysis of Experimental Investigation

Analytical models were developed for the piles tested in the experimental program. The models were compared with the measured response and calibrated. A goal of the analysis was to provide a model that could estimate the load-displacement response and predict local buckling of the pile. Both bilinear and trilinear steel models and the modified Hognestad concrete model were utilized to develop these simplified models. Based on this analysis, the following conclusions were reached:

1. For the H piles, a simple, trilinear steel model could be used to estimate the response. For the CFT piles, a composite model using a bilinear steel model and the modified Hognestad model could be used to estimate the response.
2. Local pile buckling could be reasonably estimated based on the extreme fiber strain. It was determined that a strain capacity of $20\varepsilon_y$ could be used to estimate local buckling for H piles while a strain capacity of $15\varepsilon_y$ could be used for CFT piles.

8.3 Design Recommendations

Based on the results of the field, experimental, and analytical studies, the following recommendations are provided. In general, these recommendations are directed towards the pile behavior.

1. Piles sizes should be selected to provide adequate axial capacity while minimizing their bending resistance along the longitudinal axis of the bridge. This selection provides for maximum ductility response while minimizing stresses at the abutment-pile connection.
2. Piles should be oriented about their weak axis. This orientation provides for maximum ductility response while minimizing stresses at the abutment-pile connection.

3. Axial load should be limited to $0.25f_yA_s$ for H piles and $0.25f_yA_s + 0.4\,f'_c\,A_c$ for CFT piles. This axial load level which is currently stipulated by AASHTO based on pile driving stresses provides adequate displacement response and ductility. Higher stress levels demonstrate a lower ductility capacity.
4. The minimum embedment length of 15 in. often specified for pile embedment should be increased and/or confinement steel should be provided. Additional research in this regard is needed to quantify the effect, but it is recommended that a minimum of 24 in. be provided at this time. Significant deterioration of the pile-abutment connection occurred for the larger pile sections that can limit the response and behavior of the pile-abutment system.
5. A minimum pile length below ground is required to prevent displacement at the pile base. The minimum length depends on pile size as well as soil type and is provided as follows:

Table 8.1: Minimum Pile Length

Pile Size	Minimum Depth (ft)	
	Clay	Sand
HP10	30	25
HP12	35	25
HP14	40	30
CFT14	50	35

6. Bridges designed considering the above recommendations can be constructed up to a maximum total length of 500 ft for both steel and concrete superstructures. This recommendation is based on consideration of structures with skews less than 30 degrees. The length limit was selected to limit local pile buckling and provide for a bridge life of 100 years. Lengths longer than this limit are possible if the bridge deck casting which provides continuity for the integral bridge is conducted at temperatures less than 60° F. For temperatures in the range of 40 - 50° F, the bridge length can be extended to 770 ft. Casting at moderate temperatures should be encouraged.

8.4 Recommendations for Further Research

Several recommendations are provided regarding further research that should be conducted to further understand the behavior of this structural system.

1. Bridges instrumented as part of this study should be continued to be monitored to evaluate long term performance. Of particular interest is the effect of annual cycle on abutment ratcheting.
2. The current research provides information on the behavior of integral bridges with a small skew. Field instrumentation should be performed on integral bridges with greater skews to determine the effects of this parameter on the behavior of these bridges and in particular the pile response.
3. Due to laboratory restraints, the experimental study involved relatively small H and CFT piles relative to the piles widely used in typical integral bridges in Indiana. Full-scale laboratory experiments should be performed on larger H and CFT sections (for example, HP14x89 and CFT14.0x0.312). These tests should evaluate the effect of embedment length and confinement to provide additional guidance regarding this aspect of the design of the abutment-pile connection.
4. Additional piles should be instrumented in the field to further determine the effect of the soil on the pile behavior. It was be advantageous to embed in different soil types to refine analytical models and further understand the soil-structure interaction.
5. Nonlinear finite element models for the piles supporting integral abutment should be developed to improve the prediction of pile local buckling.
6. Integral bridges subjected to seismic loading should be evaluated.

LIST OF REFERENCES

LIST OF REFERENCES

1. AASHTO (1996), *Standard Specifications for Highway Bridge,* 16th Edition, American Association of State Highway and Transportation Officials, Washington, D.C., 1996.

2. Abendroth, R.E., Greimann, L.F., Ebner, P.B. (1989), "Abutment Pile Design for Jointless Bridges," *Journal of Structural Engineering,* Vol. 115, No. 11, November 1989, pp. 2914-2929.

3. ACI Committee 318 (2002), "Building Code Requirements for Structural Concrete (318-02)," American Concrete Institute, Farmington Hills, MI, 443 pp.

4. AISC-LRFD Specification (2001), "Manual of Steel Construction, Load and Resistance Factor Design", 3rd edition, American Institute of Steel Construction, 2001.

5. Arsoy, S. et al. (1999), "The Behavior of Integral Abutment Bridges," Final Contract Report, Virginia Transportation Research Council, Charlottesville, Virginia, November 1999.

6. ASTM A252-98 (Reapproved 2002), "Standard Specification for Welded and Seamless Steel Pipe Piles," West Conshohocken, PA: ASTM, 1998, 7 pp.

7. ASTM A370-02 (2002), "Standard Test Methods and Definitions for Mechanical Testing of Steel Product," West Conshohocken, PA, ASTM, 2002, 52 pp.

8. ASTM C39/C39M-01 (2001), "Standard Test Method for Compressive Strength of Cylindrical Concrete Specimens," West Conshohocken, PA, ASTM, 2001, 5 pp.

9. ASTM C469-02 (2002), "Standard Test Method for Static Modulus of Elasticity and Poisson's Ratio of Concrete in Compression," West Conshohocken, PA, ASTM, 2002, 4 pp.

10. Ashour, M., Norris, G., and Shamsabadi, A. (2001), "Effect of the Non-Linear Behavior of Pile Material on the Response of Laterally Loaded Piles," *Proceedings*, Fourth International Conference on Recent Advances in Geotechnical Earthquake Engineeing and Soil Dynamics and Symposium in Honor of Professor W.D. Liam Finn, San Diego, California, March 26-31, 2001, pp. 1-8.

11. Bowman, E.R., (1958), "Investigation of the Lateral Resistance to Movement of a Plate in Cohesionless Soil," Thesis submitted to the University of Texas at Austin, 1958.

12. Boyd, P.F., Cofer, W.F., and McLean, D.I. (1995), "Seismic Performance of Steel-Encased Concrete Columns under Flexural Loading," *ACI Structural Journal*, Technical Paper, Title No. 92-834, May-June 1995, pp. 355-364.

13. Burdette, E.G., Ingram, E.E., Goodpasture, D.W., and Deatherage, J.H. (2002), "Behavior of Concrete Integral Abutments," *Concrete International*, July 2002, pp.49-53.

14. Burke, M. P. Jr. (1993), "The Design of Integral Concrete Bridges," *Concrete International: Design and Construction*, Vol. 15, No. 6, June 1993, pp. 37-42.

15. Davisson, M. T. (1970), "Lateral Load Capacity of Piles," Highway Research Record No. 333, National Academy of Sciences, Washington, D.C., 1970, pp. 104-112.

16. Durbin, K.O. (2001), "Investigation of the Behavior of an Integral Abutment Bridge," M.S. Thesis, Purdue University, West Lafayette, IN, 2001, 138 pp.

17. Elremaily, A., and Azizinamini, A. (2000), "Behavior of Circular Concrete-Filled Steel Tube Columns," Composite Construction in Steel and Concrete IV, Proceedings of the Conference, May 28-June 2, 2000, Banff, Alberta, Canada; sponsored by United Engineering Foundation, Inc., by Jerome F. Hajjar, (editor), Mel Hosain, (editor), W. Samuel Easterling, (editor), and Bahram M. Shahrooz, (editor), 2002, pp. 573-583.

18. Federal Highway Administration (1980), "Integral, No-Joint Structures and Required Provisions for Movement," FHWA Technical Advisory T5140.13, U.S. Department of Transportation, Washington, D.C., January 28, 1980.

19. Frosch, R. J. (1999), "Shear Transfer between Concrete Elements Using Steel Pipe Connection," *ACI Structural Journal*, Technical Paper, November-December 1999, pp. 1003-1008.

20. Furlong, R.W. (1967), "Strength of Steel-Encased Concrete Beam Columns," *Journal of the Structural Division*, Proceedings of the American Society of Civil Engineers, Vol. 93, No. ST5, October 1967, pp. 113-124.

21. Girton, D.D., Hawkinson, T.R., and Greimann, L.F. (1991), "Validation of Design Recommendations for Integral-Abutment Piles," *Journal of Structural Engineering*, ASCE, Vol. 117, No. 7, July 1991, pp. 2117-2134.

22. Greimann, L.F., et al. (1987), "Pile Design and Tests for Integral Abutment Bridges," Final Report, Department of Civil Engineering, Engineering Research Institute, Iowa State University, Ames, Iowa, December 1987, 302 pp.

23. Greimann, L.F., Yang, P.S., and Wolde-Tinsae, A.M. (1986), "Nonlinear Analysis of Integral Abutment Bridges," *Journal of Structural Engineering*, ASCE, Vol. 112, No. 10, 1986, pp. 2263-2280.

24. Hajjar, J. F. and Gourley, B. C. (1996), "Representation of Concrete-Filled Steel Tube Cross-Section Strength," *Journal of Structural Engineering*, Vol. 122, No. 11, November 1996, pp. 1327-1336.

25. Hognestad, E., (1951), "A Study of Combined Bending and Axial Load in Reinforced Concrete Members," Bulletin 399, The Reinforced Concrete Research Council of the Engineering Foundation, University of Illinois Engineering Experiment Station, Urbana, Illinois, November 1951, 128 pp.

26. Indiana Department of Transportation (1992a), Inter-Department Communication, *Bridge Design Memorandum #233 Revised.* Indiana, November 1992, 5 pp.

27. Indiana Department of Transportation (1992b), Inter-Department Communication, *Bridge Design Memorandum #243 Revised*, Indiana, December 1992, 3 pp.

28. Indiana Department of Transportation (1992c), Inter-Department Communication, *Bridge Design Memorandum #246 Revised*, Indiana, October 1992, 13 pp.

29. Indiana Department of Transportation (1999), Standard Specifications, 1999, 888 pp.

30. Kent, D.C., and Park, R. (1971), "Flexural Members with Confined Concrete," *ASCE Journal*, Vol. 97, No. ST7, July 1971.

31. Kilpatrick, A., and Rangan, V. (1999), "Tests on High-Strength Concrete-Filled Steel Tubular Columns," *ACI Structural Journal*, March-April 1999, pp. 268-274.

32. Knowles, B. and Park, R. (1969), "Strength of Concrete Filled Steel Tubular Columns," *Journal of the Structural Division*, ASCE, Vol. 95, No. ST12, December 1969, pp. 2565-2587.

33. Mander, J.B., Priestley, J.N., and Park, R. (1988), "Theoretical Stress-Strain Model for Confined Concrete," *Journal of Structural Engineering*, Vol. 114, No. 8, August 1988, pp.1804-1826.

34. Matlock, H. (1970), "Correlations for Design of Laterally Loaded Piles in Soft Clay," *Proceedings*, the Second Annual Offshore Technology Conference, Houston, Texas, Vol. I, Paper No. 1204, 1970, pp. 577-594.

35. Neogi, P.K., Sen, H.K., and Chapman, J.C. (1969), "Concrete-Filled Tubular Steel Columns under Eccentric Loading," *Journal of Structural Engineering*, Vol. 47, No. 5, May 1969, pp. 187-195.

36. Oesterle, R.G., Tabatabai, H., Lawson, T.J., Refai, T.M., Volz, J.S., and Scanlon, A. (1998), "Jointless and Integral Abutment Bridges: Summary Report," Final Report Summitted by Construction Technology Laboratories, Inc. of Skokie, IL, to be published, FHWA, Contract No. DTFH61-92-C-00154, 2002.

37. Parker, F. Jr. and Reese, L.C. (1971), "Experimental and Analytical Studies of Behavior of Single Piles in Sand under Lateral and Axial Loading," *Research Report 117-2*, Center for Highway Research, the University of Texas at Austin, 1971.

38. Rangan, V. and Joyce, M. (1992), "Strength of Eccentrically Loaded Slender Steel Tubular Columns Filled with High-Strength Concrete," *ACI Structural Journal*, November-December 1992, pp. 676-681.

39. Ravat, S.V. (1997), "Low Cycle Fatigue Behavior of Steel Piles," Master Thesis Submitted to the University of California at Berkeley, December 1997.

40. Reese, L.C. (1958), Discussion of "Soil Modulus for Laterally Loaded Piles," by McClelland and Focht, *Transactions*, American Society of Civil Engineers, Vol. 123, 1958, pp. 1071-1074.

41. Reese, L.C. and Welch, R.C. (1975), "Lateral Loading of Deep Foundations in Stiff Clay," *Journal of the Geotechnical Engineering Division*, American Society of Civil Engineers, Vol. 101, No. GT7, February 1975, pp. 633-649.

42. Reese, L.C., Cox, W.R., and Koop, F.D. (1974), "Analysis of Laterally Loaded Piles in Sand," *Proceedings*, Offshore Technology Conference, Houston, Texas, Vol. II, Paper No. 2080, 1974, pp. 473-484.

43. Reese, L.C., et al., (2000a), "Computer Program LPILE Plus Version 4.0 - A Program for the Analysis of Piles and Drilled Shafts under Lateral Loads-Technical Manual," ENSOFT, INC., October 2000, 278 pp.

44. Reese, L.C., et al. (2000b), "Computer Program LPILE Plus Version 4.0 - A Program for the Analysis of Piles and Drilled Shafts under Lateral Loads-User's Manual," ENSOFT, INC., October 2000, 305 pp.

45. Russell, H. G. and Gerken, L. J. (1994), "Jointless Bridges – the Knowns and the Unknowns," *Concrete International*, Vol. 16, No. 4, April 1994, pp. 44-48.

46. Salmon, C.G. and Johnson J.E., (1996), "Steel Structures Design and Behavior," Fourth Edition, HarperCollins Publishers Inc., 1996, 1024 pp.

47. Steel Bridges (1993), "Why Integral Bridges?," Steel Bridges, News and Information from the Steel Bridge Forum, Summer/Fall, 1993, pp.1-6.

48. Terzaghi, K. (1955), "Evaluation of Coefficients of Subgrade Reaction," *Geotechnic*, Vol. 5.5, December 1955, pp. 297-326.

49. Wasserman, E. P. and Walker, J. H. (1996), "Integral Abutments for Steel Bridges," Highway Structures Design Handbook, Tennessee Department of Transportation, Volume II, Chapter 5, American Iron and Steel Institute, October 1996.

50. Welch, R.C. and Reese, L.C., "Laterally Loaded Behavior of Drilled Shafts," Research Report No. 3-5-65-89, Center for Highway Research, the University of Texas at Austin, May 1972.

51. Wolde-Tinsae, A.M., Greimann, L.F., and Yang, P.S. (1982), "Nonlinear Pile Behavior in Integral Abutment Bridges," Iowa DOT Project HR-227, ERI Project 1501, ISU-ERI-Ames 82123, February 1982.

APPENDIX A

INDOT BRIDGE DESIGN MEMORANDUMS

A. D. 114

INDIANA DEPARTMENT OF TRANSPORTATION

INDIANAPOLIS, INDIANA 46204-2249

INTER-DEPARTMENT COMMUNICATION

November 2, 1992

BRIDGE DESIGN MEMORANDUM # 233 Revised

TO: All Design, Operations, and District Personnel, and Consultants

THRU: Cristine M. McFatridge

Cristine M. McFatridge
Design Services Manager,
Division of Design

FROM: John R. Szabo

John R. Szabo
Design Standards Engineer, Design Services Section
Division of Design

SUBJECT: Integral End Bents.

SUPERSEDES: Bridge Memorandum #233, Revised April 14, 1989.

EFFECTIVE: The revisions concerning reinforcing steel lap lengths shall be effective on all applicable bridge projects which are being designed using Grade 60 reinforcing steel in accordance with Bridge Design Memorandum #246, issued October 1, 1992. The revisions concerning the correction of the welding symbols shall be effective immediately.

November 2, 1992 Revisions and Additions

The November 2, 1992 revisions to this memorandum are on the attached Suggested Integral End Bent Details. The welding symbols have been corrected on both sets of details. Also, the lap lengths have been increased on both sets of details to correspond to the Department's changeover to the exclusive use of Grade 60 reinforcing steel, in accordance with Bridge Design Memorandum #246, issued October 1, 1992. The sections concerning the effective date for beginning the use of integral end bent design, and the background of integral end bent design, have been deleted. The Sections concerning the special provisions and pay items have been revised. The remainder of this memorandum is identical to the version issued on April 14, 1989.

APPLICATION TO NEW BRIDGES

(March 10, 1989 & April 14, 1989)

The use of integral end bents for new steel beam or girder, and prestressed concrete I-beam and box beam bridges should be considered, and their use is strongly recommended at structures which meet the following geometric limitations;

1) **Maximum Bridge Length:**

   a) **Steel Structures** - 250 feet (125 feet from the structure fixed point to the end bent);
   b) **Prestressed Concrete Structures** - 300 feet (150 feet from the structure fixed point to the end bent);

2) **Maximum Bridge Skew:** 30 degrees.

The maximum lengths indicated above may be increased, subject to approval, if a rational analysis of induced pile stresses indicates that the piles are not over-stressed. Two rational analysis methods are presented in the report, "Pile Design and Tests for Integral Abutment Bridges", available from the Iowa Department of Transportation.

Integral end bents will continue to be used for reinforced concrete slab structures, regardless of the skew, using the same details as have been used in the past, but the maximum bridge length has been increased to 200 feet.

APPLICATION TO BRIDGE REPAIR PROJECTS

(March 10, 1989 & April 14, 1989)

The conversion of existing bridges to integral end bent structures should also be considered for repair projects. Due to the many different types of bridges and the type of repair, no definite criteria can be suggested for when to make the conversion . However, when the mudwalls of the existing end bents are to be removed, conversion should be actively pursued, using the criteria for new bridges as a guideline.

GENERAL DESIGN CRITERIA

(March 10, 1989 & April 14, 1989)

The following requirements must be satisfied in all cases where integral end bents are used;

1) "B" Borrow for Structure Backfill must be specified behind the end bents for a distance of 1'-6" at the base of the cap, as shown on Bridge Standard S1. This fill must be drained with a 6" perforated pipe;

2) A reinforced concrete bridge approach, anchored to the end bent with #6 bars spaced at 9" centers, shall be used at all integral end bents regardless of the traffic count. Two layers of 6 mil (minimum) polyethylene shall be specified between the concrete bridge approach and the subgrade. A rigid approach is necessary to prevent compaction of the backfill behind the end bent. Bituminous bridge approaches shall not be specified;

3) A 2'-0" wide terminal joint or pavement relief joint shall be used at the roadway end of the concrete bridge approach slab if any portion of the adjacent pavement section is concrete. No such joint is required if the entire adjacent pavement section is bituminous.

SUPERSTRUCTURE AND INTERIOR SUBSTRUCTURE DESIGN CRITERIA
(March 10, 1989 & April 14, 1989)

There will be no changes in the usual design methods for the superstructure or the interior piers when integral end bents are used. Although the ends of the superstructure are monolithically attached to the end bents, it shall be assumed that enough rotation occurs in the piling to provide a pinned end condition. The following design assumptions shall be made;

1) The ends of the superstructure are free to rotate and translate longitudinally;

2) The restraining effect of passive earth pressure behind the end bents shall be neglected when considering superstructure longitudinal force distribution to the interior piers;

3) When steel beam or girders are used, an interior diaphragm should be placed within 10 feet of the end support to provide beam stability during the deck pour.

END BENT DESIGN CRITERIA
(March 10, 1989 & April 14, 1989)

1) Only vertical loads shall be considered when designing end bent piling for structures having lengths below the maximum values designated herein. Pile bending stresses due to temperature, shrinkage, and horizontal soil pressure forces shall be neglected;

2) Only steel H piles or steel encased concrete piles will be permitted at integral end bents. The use of steel H piles is preferred. When the H pile is used as a friction pile and soil conditions permit, the allowable bearing pressure shall be increased above the usual 40 tons when economically feasible, but the pile shall be stressed to no more than 9 ksi. Steel H pile webs shall be placed perpendicular to the centerline of the structure to minimize pile bending stresses. All end bent piling shall be driven vertically and only one row of piling will be permitted;

3) When an existing cohesive earth stratum, with a standard penetration resistance (N) exceeding 35 blows per foot, is located within the 10 foot interval below the bottom of the cap, the pile shall be placed in an oversized predrilled hole before driving. The predrilled hole shall extend 8 feet below the bottom of the cap. The minimum diameter of the oversized hole shall be 4 inches greater than the maximum cross sectional dimension of the pile. The hole shall be backfilled with uncrushed coarse aggregate size #12 (pea gravel) following the pile driving operation;

END BENT DESIGN CRITERIA - CONT'D.

(March 10, 1989 & April 14, 1989)

4) The connection between the wingwall and the end bent cap should be given special attention. In general, the wingwall should extend no more than 10 feet behind the rear face of the cap. If longer extensions are necessary, stresses in the connection between the wingwall and cap, and in the wingwall itself, shall be investigated and adequate reinforcing steel provided.

END BENT DETAILS

(March 10, 1989 & April 14, 1989)

Integral end bents may be designed and detailed using either of the following methods:

METHOD A: The superstructure beams may be placed on, and attached directly to the end bent piling. The entire end bent shall then be poured integrally with the superstructure slab. This is the preferred method.

METHOD B: The superstructure beams may be set in place and anchored to the previously cast-in-place end bent.

Regardless of the method used, the end bent details shall conform to the following minimum requirements:

1) The minimum end bent width shall be 2'-6";

2) The piling shall extend a minimum of 2'-0" into the cap when using Method A, and a minimum of 1'-3" into the cap when using Method B;

3) The beams must be physically attached to the end bent piling when using Method A, and to the cast-in-place cap when using Method B;

4) The beams must extend at least 1'-9" into the bent, measured along the centerline of the beam;

5) Concrete cover beyond the farthest most edge of the beam at the rear face of the bent shall be a minimum of 4 inches. This minimum cover shall also apply to the pavement ledge area. The top flange of steel beams and prestressed I-beams may be coped to meet this requirement. When the 4 inch minimum cover cannot be maintained using a 2'-6" cap, the cap shall be widened;

6) Steel beams and girders shall have 1/2" stiffener plates welded to both sides of the web and to the flanges over the supports, to anchor the beams into the concrete. In addition, a minimum of three holes shall be provided thru the webs of steel beams and girders, and two holes thru prestressed I-beam webs near the front face of the bent, to allow #6 bars to be inserted to further anchor the beam to the cap. Box beams shall have two 3/4 inch inserts placed in each side panel for anchorage purposes;

END BENT DETAILS - CONT'D.
(March 10, 1989 & April 14, 1989)

7) The minimum size and spacing of stirrups shall be #6 @ 1'-0". Longitudinal cap reinforcing shall be #7 @ 1'-0" maximum spacing along both faces of the bent;

8) The use of continuous corner bars extending from the rear face of the cap into the top of the slab at approximately 1'-0" spacing (as shown on the attached details) is mandatory.

DETAILS FOR PLANS
(Revised November 2, 1992)

The attached details are only suggested details. They are not intended as absolute detailing requirements. Other reinforcing and connection details should be considered and used when they are structurally sound and afford a definite advantage over those shown on the attached sheets. The November 2, 1992 revisions to these details were changes to the welding symbols and the bar lap lengths.

ADDITIONAL SOILS INFORMATION REQUIREMENTS
(Added April 14, 1989)

The Geotechnical Section of the Division of Materials and Tests will provide the additional soils information needed for integral end bent I-beam structures. This additional information is an estimated pile tip elevation for steel H piles, when the H pile is loaded to 55 and 70 tons. These are the capacities of the smallest 10 inch and 12 inch steel H piles, respectively, when the gross area is stressed to 9 ksi. These additional pile tip elevations will only be required for steel H piles used at the end bents of integral end bent I-beam structures. The following note shall be added to the soil boring location plan sheet, on those plans requiring this additional information:

"Pile tip elevations for steel H piles loaded to 40, 55, and 70 tons should be evaluated at Bents ___ and ___."

The designer shall be responsible for determining when the use of the longer, higher capacity piles, is economical.

SPECIAL PROVISIONS AND PAY ITEMS
(Revised November 2, 1992)

Special Provision 701-B-078, "Oversized Predrilled Pile Holes For Integral End Bent Structures" which was distributed with the April 14, 1989 issuance of this memorandum is now contained in the Department's Recurring Special Provisions Book. This special provision shall still be included in those contracts for integral end bent structures where the blow counts (N) exceed 35 blows per foot within the 10 foot interval below the bottom of the cap. The piles will be paid for in accordance with the Standard Specifications. The oversized predrilled pile holes and the uncrushed gravel backfill will be paid for in accordance with Special Provision 710-B-078.

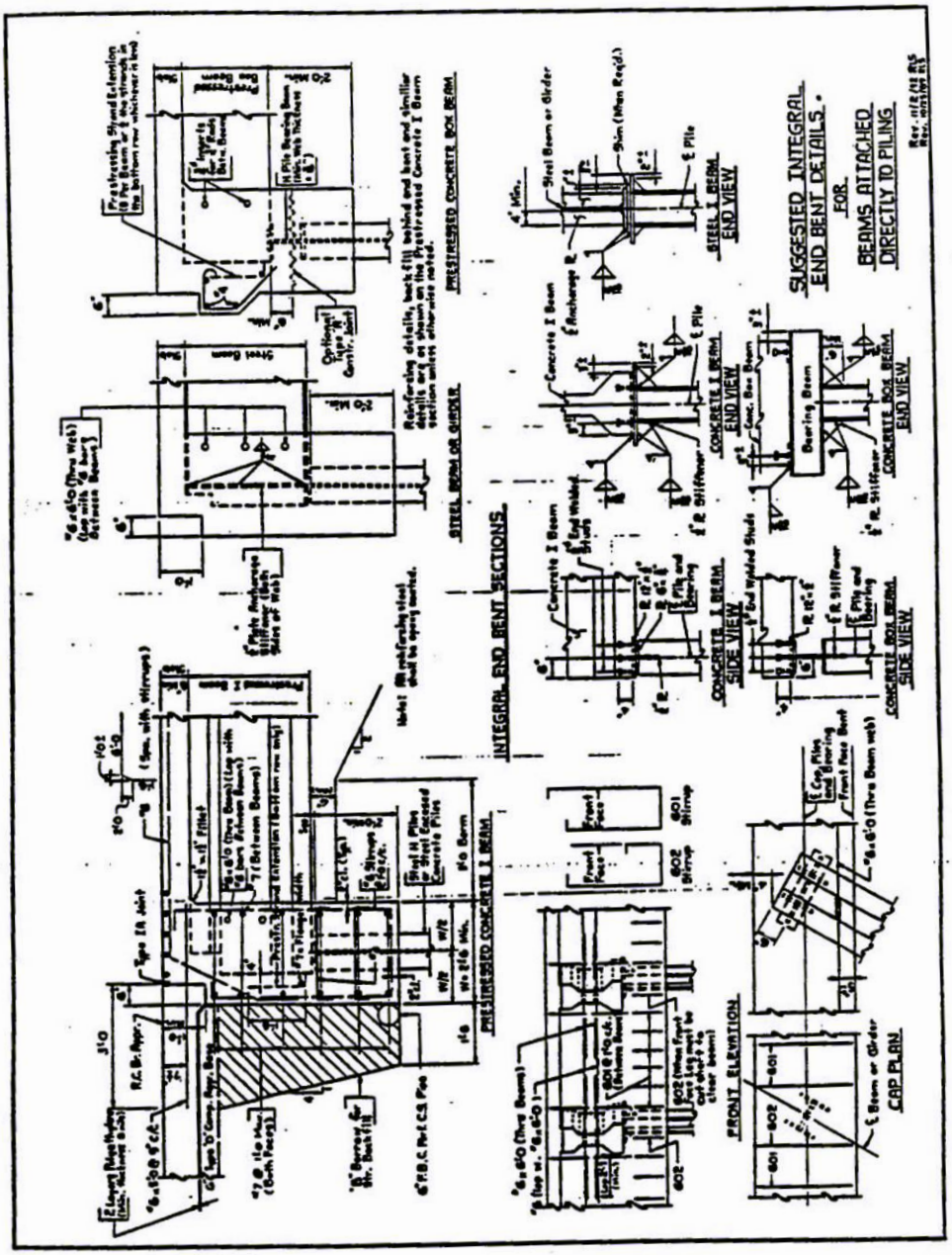
INTEGRAL END BENT SECTIONS
PRESTRESSED CONCRETE I BEAM
STEEL BEAM OR GIRDER
PRESTRESSED CONCRETE BOX BEAM
SUGGESTED INTEGRAL END BENT DETAILS FOR BEAMS ATTACHED DIRECTLY TO PILING
FRONT ELEVATION
CAP PLAN
STEEL I BEAM END VIEW
CONCRETE I BEAM END VIEW
CONCRETE I BEAM SIDE VIEW
CONCRETE BOX BEAM END VIEW
CONCRETE BOX BEAM SIDE VIEW

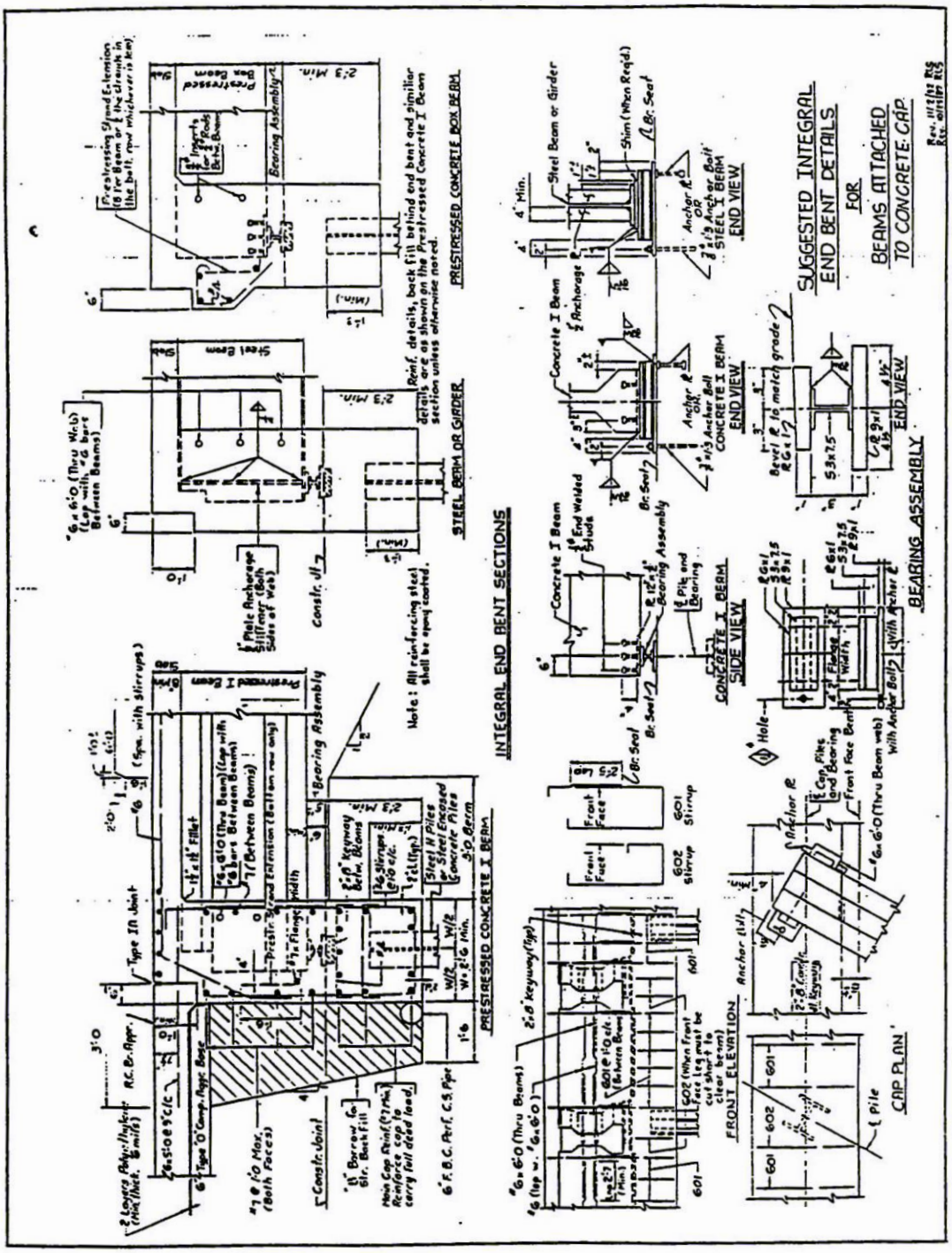
INTEGRAL END BENT SECTIONS
PRESTRESSED CONCRETE I BEAM
STEEL BEAM OR GIRDER
PRESTRESSED CONCRETE BOX BEAM
Type IA Joint
Type 'O' Comp. Joint Seal
Construction Joint
Bearing Assembly
Steel H Piles or Steel Encased Concrete Piles
Pile Anchorage Stiffener (Both Sides of Web)
Concrete I Beam
End Welded Studs
Steel Beam or Girder
Anchorage
Shim (When Reqd.)
Anchor Bolt
Pile and Bearing
Hole
Cap Pile and Bearing
Front Face Bent
Anchor Bolt With Anchor Plate
Pile
CAP PLAN
FRONT ELEVATION
CONCRETE I BEAM SIDE VIEW
CONCRETE I BEAM END VIEW
STEEL I BEAM END VIEW
BEARING ASSEMBLY
SUGGESTED INTEGRAL END BENT DETAILS FOR BEAMS ATTACHED TO CONCRETE CAP

A. D. 114

INDIANA DEPARTMENT OF TRANSPORTATION

INDIANAPOLIS, INDIANA 46204-2249

INTER-DEPARTMENT COMMUNICATION

DECEMBER 1, 1992

BRIDGE MEMORANDUM # 243 REVISED

TO: All Design, Operations, and District Personnel, and Consultants

THRU: Cristine M. McFatridge
Cristine M. McFatridge
Design Services Manager,
Division of Design

FROM: John R. Szabo
John R. Szabo
Design Standards Engineer,
Design Services Section,
Division of Design

SUBJECT: Epoxy Coated Steel (Metal) Shell Encased Piles, Epoxy Coated Steel H Piles, and Revised Pay Items for All Pile Types.

EFFECTIVE: Immediately on all bridge projects.

SUPERSEDES: Bridge Memorandum #243, dated October 1, 1991; Item #1 of Bridge Memorandum #226 dated August 24, 1987; Section 8-335.03 Metal Shell and the third paragraph of Section 8-355.12 Pile Bents of the Bridge Design Manual.

A) CARRY-OVER: The following items are a carry-over from Bridge Memorandum #243, dated October 1, 1991:

1) Only fusion bonded (powdered epoxy resin) epoxy coating shall be used to coat all epoxy coated piles. The liquid applied coal tar epoxy will no longer be allowed for this application;

2) Steel shell piles shall be fourteen (14) inch diameter only, and the 12" diameter shall no longer be allowed as an alternate.

3) The reinforced concrete portion of the steel shell pile shall extend to a depth of ten (10) feet below the flow line elevation.

4) The payment for steel shell pile shall be in accordance with the type of shell coating and the type of concrete filling;

5) Item #1 of Bridge Memorandum #226 dated August 24, 1987 is deleted;

6) Section 8-355.12, Paragraph Three, Pile Bents, of the Bridge Design Manual is deleted;

7) The specified wall thickness of the steel pile shell shall be the minimum wall thickness that the contractor will be permitted to use;

CARRY-OVER - Continued:

8) Exposed/Buried Piles: A pile which is composed of an "exposed portion" and a "buried portion", as shown on Bridge Standard C-1, Adopted December 1992, shall be paid for in two parts. For example, the buried portion of a steel H pile would be paid for as Steel H Pile, and the exposed portion would be paid for as Epoxy Coated Steel H Pile.

9) The pay item(s) for the pile(s) shall reflect the actual pile being specified. The pay item(s) will include such things as the pile diameter/size, the type of encasement, reinforcing steel requirements, and the wall thickness of the steel shell;

10) Except for timber piles, the "furnished and driven" phrase, previously contained in the pay item name, is now contained in the descriptive text preceding the pay item designations;

11) Pile encasement, reinforcing steel, and concrete filling will not be paid for separately, but will be included in the pay item for the pile(s);

B) REVISIONS: These revisions are a result of the recent meetings of the Joint INDOT-ICI Sub-Committee on Bridges, co-chaired by Thomas Seeman, Division of Design. These revisions involve a change in the following:

1) Allowable wall thicknesses of steel shell piles;

2) The limit of the epoxy coating of steel shell piles now extends to only two (2) feet below the flow line elevation;

3) A change to the use of plain, instead of epoxy coated, reinforcing steel in the reinforced portion of the concrete filling;

4) A table of suggested bearing capacities for minimum steel shell wall thickness is now provided;

5) New details on Bridge Standard C-1, adopted December 1992, showing the limits of the reinforced concrete filling and the limits of the epoxy coating on the pile shell, previously contained in Bridge Memorandum #243, dated October 1, 1991.

6) Section 8-335.03, Metal Shell, of the Bridge Design Manual is hereby deleted

C) DESIGN REQUIREMENTS: The Geotechnical Section will routinely investigate bearing capacities of 40, 55, and 70 tons for shell piles, and/or 45, 55, and 70 tons for H-piles, for most projects. The designer shall perform a preliminary feasibility analysis when bearing capacities other than these are desired, and shall notify the Geotechnical Section of the desired bearing capacity prior to the beginning of the soils

C) DESIGN REQUIREMENTS - Continued:

investigation. The table below gives suggested bearing values for a range of available steel shell wall thicknesses. The designer shall use these combinations of values only as a starting point in their analysis.

Shell Wall Thickness vs. Bearing	
Minimum Shell Wall Thickness (Inches)	Suggested Bearing Capacity (Tons)
.203	40 to 50
.250	55 to 65
.312	70 to 90

All high capacity pile designs shall be verified by engineering analysis and shall require the concurrence of the geotechnical engineer assigned to the project. Consideration shall be given to the economics of using a single steel shell wall thickness on projects where the piling for the different substructure elements fall into different bearing capacity ranges. Other wall thicknesses are subject to limited availability and shall not be used without justification and assurance of availability.

D) SPECIFICATIONS: The revised specifications distributed with Bridge Memorandum #243, dated October 1, 1991, in the form of Special Provision 701-B-089, Revised 9/19/91, have since been acted upon by the Specifications Committee, and are now part of the Standard Specifications via the current Supplemental Specifications.

The pile specifications which have been revised to reflect the changes detailed in this memorandum are now contained in the attached copy of *Special Provision 701-B-089, Revised 12/1/92*. This special provision shall be utilized by all designers on applicable bridge projects until such time as this information is incorporated into the Standard Specifications by the Specifications Committee.

[b2431291.wp]
attachment: 701-B-089 [12/1/92]

12-1-92

STEEL SHELL ENCASED CONCRETE PILES

DESCRIPTION. This work shall consist of furnishing and driving steel shell encased concrete filled piles of the size, location, and bearing as shown on the plans.

MATERIALS. Materials shall be in accordance with the following:

Epoxy Coating for Piles	914.01(d)
Steel Encased Concrete Piles	914.01
Structural Concrete	702
Reinforcing Steel	703

Powdered epoxy resin shall be used to coat the epoxy coated portion of the steel shell encased concrete piles.

CONSTRUCTION REQUIREMENTS. The construction requirements shall be in accordance with 701 except as noted herein. The specified steel shell wall thicknesses shall be the minimum allowable. The Contractor may furnish and drive thicker walled steel shells with no additional payment. The limits of the epoxy coated steel shell portion of the pile, and the limits of the reinforced concrete shall be as shown on the plans.

METHOD OF MEASUREMENT. Steel shell encased concrete piles will be measured by the linear foot complete in place. Reinforcing steel, class A concrete filling, and epoxy coating will not be measured for payment.

BASIS OF PAYMENT. Epoxy coated steel shell encased reinforced concrete piles and steel shell encased concrete piles will be paid for at the contract unit price per linear foot for the shell thickness and diameter specified, complete in place.

Payment will be made under:

Pay Item	Pay Unit
Pile, Reinforced Concrete, Steel Shell Encased, Epoxy Coated, _____ (shell thickness) in., _____ (diameter) in.	Linear Foot
Pile, Concrete, Steel Shell Encased, _____ (shell thickness) in., _____ (diameter) in.	Linear Foot

The costs of furnishing and driving piles, and all necessary incidentals shall be included in the cost of this work. The cost of the reinforcing steel which extends beyond the limits of the epoxy coating as shown on the plans shall be included in the cost of the epoxy coated steel shell encased reinforced concrete pile.

==========

701-B-089

A. D. 114

INDIANA DEPARTMENT OF TRANSPORTATION

INDIANAPOLIS, INDIANA 46204-2249

INTER-DEPARTMENT COMMUNICATION

October 1, 1992

BRIDGE DESIGN MEMORANDUM #246

TO: All Design, Operations, and District Personnel, and Consultants

THRU: Cristine M. McFatridge
Cristine M. McFatridge
Design Services Manager,
Division of Design

FROM: John R. Szabo
John R. Szabo
Design Standards Engineer, Design Services Section
Division of Design

AUTHOR: John J. White
Plan Development Manager,
Division of Design

SUBJECT: Allowable Design Stresses for Concrete and Reinforcing Steel.

EFFECTIVE: Immediately on all bridge projects which have not reached the Structure Size and Type due date as of October 1, 1992.

SUPERSEDES: Figure 8-401.02, entitled "FLOOR SLAB CONTINUOUS OVER STRINGERS", dated May 1975 in Section 8-401.02 of the Department's Bridge Design Manual; the applicable portions of the Department's Bridge Design Manual Sections 8-215.03, 8-250.08, 8-250.09, 8-255.03, 8-255.07, 8-401.02, 8-410.04 c, 8-410.04 d, 8-410.09(pg. 8-410.09A), and Figure 8-250.12B dated May 1975 in Section 8-250.12; Bridge Memorandum #172, entitled "Reinforcing Bar Lap And Embedment Lengths", issued September 2, 1976

IMPLEMENTATION: Designers shall implement this policy no later than the effective date stated above. The designer shall design the entire structure using one set of design stresses. Projects underway using the old design stresses shall not be revised, nor shall the new design stresses be applied to the undesigned components of these structures.

A) - BACKGROUND

Jack White has recommended that INDOT use higher allowable design stresses for concrete and reinforcing steel in structures. Mr. White based his recommendations on the following:

1) The concrete materials currently used exceed the recommended ultimate yield stresses by at least 500 psi. This was verified by R. K. Smutzer of our Materials and Tests Division.

2) The reinforcing steel currently stocked by our fabricators is Grade 60, and it is being placed in our structures whether we design for it or not. In fact, the Grade 40 steel now used in design was eliminated from the ASTM A615 Specs. in sizes above # 6 almost ten years ago.

3) This change brings the Department in line with the practice of most states throughout the country.

4) AASHTO's new upcoming Load Resistance Factor Design Specification (LRFD) will be used as the basis for structural design in the Department's upcoming new Design Manual. Several design provisions of the LRFD require a minimum concrete compressive strength of 4000 psi and the use of Grade 60 Reinforcing Steel. These design allowables must be established before the LRFD is introduced in order to utilize these design provisions fully .

B) - NEW ALLOWABLE DESIGN STRESSES

The new design stresses are as follows:

Class C Concrete	f'c =	4000 psi
Class A Concrete	f'c =	3500 psi
Class B Concrete	f'c =	3000 psi
Reinforcing Steel (Grade 60)	fy =	60,000 psi

C) - EFFECTS OF INCREASE IN ALLOWABLE DESIGN STRESSES

1) **Specifications:** No immediate changes in the specifications are required. The concrete mixes currently used provide compressive strengths that are more than ample to meet the suggested stress levels. However, several changes related to reinforcing steel that will align the specifications with the new design stresses will be implemented in near future. The specifications currently state: *"Unless otherwise specified, bars for concrete reinforcement shall be deformed billet steel, grade 40 or 60; rail steel, grade 50 or 60; or axle steel, grade 40 or 60.*

The bars for cement concrete pavement shall be deformed billet steel, rail steel, or axle steel of the grades set out above except tie bars that are to be bent and subsequently straightened during construction shall be deformed bars conforming to ASTM A 615, grade 40. Tie bar assemblies used in lieu of bent tie bars shall meet the minimum total ultimate strength and minimum total yield strength requirements specified for bent tie bars; bend test and elongation will not be required. Steel splicing systems shall be as specified in 703.06.

Reinforcing steel used in precast prestressed concrete structural members include deck panels shall be in accordance with ASTM A 615, grade 60."

The specifications will be changed to state that only Grade 60 steel shall be supplied unless Grade 40 is specified on the plans. Until the specification can be changed, the attached Special Provision 703-B-097, *"Reinforcing Steel Type and Grade"*, shall be required for all plans designed in accordance with these new design stresses.

2) Standards Sheets: The following Standards Sheets will be revised as indicated, in time for the designers to utilize them in the plans that are designed with the new allowable stresses:

a) Bridge Standards Sheet C-1: Revise table of dimensions for standard hooks based on new design stresses for concrete and reinforcing steel; Delete table of dimensions for special hooks.

b) Bridge Standards Sheet C-3: Optional Railing Reinforcing Splice.

c) Road Standards Sheet Joint Sheet B: Revise R. C. Bridge Approach reinforcing steel lap and bar lengths in Tables I and II based on new lap splices for grade 60 reinforcing steel.

d) Road Standards Sheet ME-1A: Revise reinforcing steel lap lengths in multiple pipe concrete anchor details based on new lap splices for grade 60 reinforcing steel.

e) Road Standards Sheet ME-3 thru ME-6: Revise reinforcing steel bending diagrams, Note #3, and reinforcing steel quantities in tables for grated box end sections based on new lap splices for grade 60 reinforcing steel

3) Reinforcing Steel Detailing: These new higher allowable design stresses will result in longer reinforcing steel lap lengths. The lap distance is related to the concrete compressive stress as well as the reinforcing steel yield strength. Theoretically, three different sets of required lap lengths will be needed if three concrete stress levels are used. Attached are new *TENSION LAP SPLICE TABLES I thru VI* for the designers use when designing with these new stresses. Detailing of all reinforcing bar lap and embedment lengths shall continue as was required by Bridge Design Memorandum #172, issued September 2, 1976, and superseded by this memorandum.

4) Continuous Floor Slab Design: *Figure 8-401.02*, entitled *"FLOOR SLAB CONTINUOUS OVER STRINGERS"*, dated May 1975 and contained in **Section 8-401.06** of the Department's **Bridge Design Manual** has been replaced with the attached *"CONTINUOUS FLOOR SLAB DESIGN CHART"*, dated October 1, 1992.

D) - CLASS OF SUBSTRUCTURE CONCRETE

All substructure concrete above the footing shall be Class A. The cost of Class A over that of Class B in pier stems is insignificant - one bag of cement per cubic yard. The increased durability, workability, and higher compressive strength in what is essentially a column element more than offsets the slight additional cost. The present item "Concrete, Class B above Footing", shall be replaced with "Concrete, Class A, in Substructure". "Concrete, Class B, in Footing" shall continue to be used as in the past.

E) - TRANSITION PERIOD

During the transition period to convert all of the Department's structural designs to these new design stresses, the designer shall place the following table on the general plan sheet for bridge projects:

ALLOWABLE DESIGN STRESSES	
Class C Concrete	f'c = 4000 psi
Class A Concrete	f'c = 3500 psi
Class B Concrete	f'c = 3000 psi
Reinforcing Steel (grade 60)	fy = 60,000 psi

This table will identify those plans which were designed using the higher allowable design stresses.

APPENDIX B

PILE DRIVING RECORD

Appendix B: Pile Driving Record

Table B.1: Pile Driving Record of Bent 1 (SR249 over US12)

Form IC 225

INDIANA DEPARTMENT OF TRANSPORTATION

CONTRACT NO. B-23891

STRUCTURE NO. 1-12-64-2673

PROJECT NO. NH N343

DES # 9502610

TYPE STRUCTUE

PILE DRIVING RECORD

Bent 1

DATE 5/11/99

RECORD NO.

FOR H Pile

TYPE OF PILING

Delmag D30-32

TYPE HAMMER

Found. and Pile Number	Length Put in Leads	Length Cut off	Length Below Cut off	Total Penetration Last ___ Blows	Weight and Drop Beats Per 300MM B P M and Energy		Bearing Value in Tons	Remarks Bearing Required, Etc.
					10.5 Drop 39 Beats			2182KN
					Elev. at Bottom of Pile			
(1)	45.897	5.410	40.487	-	(1)	149.724		Top of Pile Elev.
(2)	45.921	9.220	36.701	-	(2)	153.51		190.211
(3)	45.872	5.892	39.980		(3)	150.231		
(4)	45821	6.05	39.77		(4)	150.441		
(5)	45.92	5.105	40.816		(5)	149.395		
(6)	45.872	5.486	40.386		(6)	149.825		
	275.304	37.164	283.140		TOTALS THIS REPORT			ALLOWABLE SPLICES
	267.233	17.803	249.43		TOTALS LAST REPORT			
	542.537	54.967	487.57		TOTALS TO DATE			

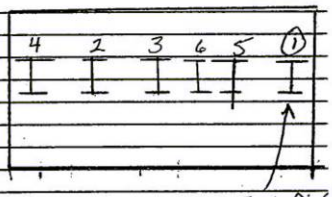

NOTE: — On the back of this sheet make a sketch of each foundation reported on, numbering each pile and showing the points of the compass and the direction of flow of stream.

State Form 4287

SIGNED Ricky D. Hammons

TITLE EAT

Table B.2: Pile Driving Record of Bent 11 (SR249 over US12)

Form IC 225

INDIANA DEPARTMENT OF TRANSPORTATION

CONTRACT NO. B 23291 ITEM NO 0086 DATE 4/29/99

STRUCTURE NO. I-12-64-2673 RECORD NO.

PROJECT NO. NHN 343 FOR H-Pile

DES # TYPE STRUCTUE 9502610

PILE DRIVING RECORD Bent 11

TYPE OF PILING: Delmag TYPE HAMMER: 30-32

Found. and Pile Number	Length Put in Leads	Length Cut off	Length Below Cut off	Total Penetration Last ___ Blows	Weight and Drop or B P M and Energy	Elev. of Bottom of Pile	Bearing Value in Tons	Remarks Bearing Required, Etc.
								2,143 KN.
①	53.492	2.844	50.648		①	141.155		6 Beats Per 300 MM Drop 10'
②	53.492	2.91	50.582		②	141.221		To P of Pile El.
③	53.34	4.548	48.792		③	143.011		191.803
④	53.34	3.453	49.887		④	141.916		
⑤	53.569	4.039	49.53		⑤	142.273		
	(53.447)							

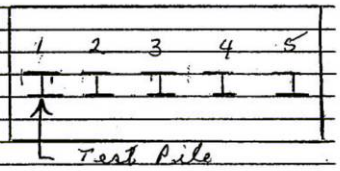

	267.233	17.803	249.430	TOTALS THIS REPORT
	0	0	0	TOTALS LAST REPORT
	267.233	17.803	249.430	TOTALS TO DATE

ALLOWABLE SPLICES

NOTE: — On the back of this sheet make a sketch of each foundation reported on, numbering each pile and showing the points of the compass and the direction of flow of stream.

State Form 4287

SIGNED Ricky D. Hammons

TITLE EAI

Table B.3: Pile Driving Record of Bent 1, North Bound (I65 over SR25)

128-1

Form IC 225 Rev. 6-6-60 State Form 4287

INDIANA DEPARTMENT OF HIGHWAYS

CONTRACT NO. B-24138 DATE 6-27-2000

STRUCTURE NO. I65-176-5543C RECORD NO. 1

PROJECT NO. IM-65-6 (059) 176 FOR 12X53 H-PILING (TYPE OF PILING)

TYPE STRUCTURE STEEL Beam HERA 1500 (TYPE HAMMER)

PILE DRIVING RECORD

BENT 1 N.B.L.

Found. and Pile Number	Length Put in Leads	Length Cut off	Length Below Cut off	Total Penetration Last 20 Blows	Weight and Drop or B P M and Energy		Bearing Value in Tons	Remarks Bearing Required, Etc.
NB1-1	45.25'		38.5	4 1/8	7	3300#	60.4	100 TON
			40	3 1/4	7 1/2		75.4	
			41	2 3/4	7 1/2		83.4	
			42	2 3/8	7 1/2		90.6	
				2 1/2	7 1/2		88.0	
			43	2 3/8	7 1/2		90.6	
				2 1/2	7 1/2		88.0	
				2 3/4	7		77.8	
				3	7		73.9	
				2 5/8	7		80.0	
				2 1/2	7		82.1	
				2 1/4	7		87.0	
				2 3/4	7		77.8	
				2 1/8	7 1/2		96.1	
				2	7 1/2		99.0	
		0	45.25	1 3/4	7 1/2		105.6	
NB1-2	45.25		41.5	3 1/8	7		89.7	
				2 1/8	7		89.7	
			42	2 1/8	7		89.7	
				2	7		92.4	
				2 1/8	7		89.7	
			42.5	2	7		92.4	
				2 1/8	7		89.7	
				2 1/8	7		89.7	
				2 1/4	7 1/2		93.2	
				2 1/4	7		87.0	
				2 1/4	7		87.0	
				2 1/4	7		87.0	
				2 1/8	7		89.7	
				1 7/8	7		95.4	
				1 7/8	7		95.4	
		0.83	44.42	1 1/2	7		105.6	
NB1-3	45.25		38	2 3/4	7		77.8	
				2 3/8	7		84.6	
				2 1/4	7		87.0	
				2 1/8	7		89.7	
				2	7		92.4	
				1 3/4	7		98.6	
				1 5/8	7		102.0	
		5.33	39.92	1 1/2	7		105.6	
	135.75	6.16	129.59	TOTALS THIS REPORT			129.59	
	0	0	0	TOTALS LAST REPORT			0	→ ALLOWABLE SPLICES
	135.75	6.16	129.59	TOTALS TO DATE			129.59	

Table B.3: Pile Driving Record of Bent 1, North Bound (I65 over SR25) (Continued)

128-2

m JC 225
v. 6-6-60 State Form 4287

INDIANA DEPARTMENT OF HIGHWAYS

CONTRACT NO. B-24138 DATE 6-27-2000

STRUCTURE NO. I65-126-5543C RECORD NO. B

PROJECT NO. IM-65-6 (059) 176 FOR 12X53 H-PILING (TYPE OF PILING)

TYPE STRUCTURE STEEL BEAM TYPE HAMMER HERA 1500

PILE DRIVING RECORD

BENT 1 N.BL.

Found. and Pile Number	Length Put in Leads	Length Cut off	Length Below Cut off	Total Penetration Last 20 Blows	Weight and Drop or B P M and Energy		Bearing Value in Tons	Remarks Bearing Required, Etc.
N81-4	45.25		40.5	2 3/8	6 1/2	3300		100 TON
				2 1/4	6 1/2		80.9	
				2	6 1/2		85.5	
				2	7		92.4	
				1 3/4	7		98.6	
				1 3/4	7		98.6	
				1 5/8	7		102.0	
				1 5/8	7		102.0	
				1 3/8	7		109.5	
		3.67	41.58	1 3/8	7 1/2		117.3	
N81-5	45.25		41	2	6 1/2		85.8	
				1 7/8	6 1/2		88.6	
			42.5	1 3/4	6 1/2		91.5	
				1 5/8	6 1/2		94.7	
				1 5/8	7		102.0	
				1 5/8	7		102.0	
		3.08	42.17	1 1/2	7		105.6	
N81-6	45.25		41	2 1/8	6 1/2			
				2	6 1/2		85.8	
				2	6 1/2		85.8	
				1 7/8	6 1/2		88.6	
				1 7/8	7		95.4	
				2	7		92.4	
				1 5/8	7		102.0	
				1 3/4	7		98.6	
				1 3/4	7		98.6	
				1 1/2	7		105.6	
				1 1/4	7		113.7	
		2.58	42.67	1 1/4	7		113.7	

135.75	9.33	126.42	TOTALS THIS REPORT	126.42	
135.75	4.16	129.59	TOTALS LAST REPORT	0	→ ALLOWABLE SPLICES
271.50	13.49	256.01	TOTALS TO DATE	256.01	

Table B.4: Pile Driving Record of Bent 3, North Bound (I65 over SR25)

128-3

Form IC 225 Rev. 6-6-60 State Form 4287

INDIANA DEPARTMENT OF HIGHWAYS

CONTRACT NO. B-24138 DATE 7-11-2000

STRUCTURE NO. I65-176-5543C RECORD NO. 3

PROJECT NO. IM 65-6 (059) 176 FOR 12x53 H-PILING (TYPE OF PILING)

TYPE STRUCTURE STEEL BEAM

PILE DRIVING RECORD

BENT 3 NBL

TYPE HAMMER: HERA 1500

Found. and Pile Number	Length Put in Leads	Length Cut off	Length Below Cut off	Total Penetration Last 20 Blows	Weight and Drop or B P M and Energy	Bearing Value in Tons	Remarks Bearing Required, Etc.
NB3-6	45.25		41	4	7'	61.6	
				3 3/4	7	64.3	
				3 1/4	7	70.4	
			42	3	7	73.9	
				3 1/8	7	72.2	
				3	7	73.9	
				2 3/4	7	77.8	
				2 5/8	7	80.0	
				2 1/2	7	82.1	
				2 1/2	7	82.1	
				2 1/4	7	87.0	
				2 1/4	7	87.0	
				2	7	92.4	
				2	7	92.4	
				2	7 1/2	99.0	
				2	7 1/2	99.0	
				1 3/4	7 1/2	105.6	
		- 1.09	44.16	1 3/4	7 1/2	105.6	
NB3-5	45.25		40.5	1 7/8	6 1/2	88.6	
				1 3/4	6 1/2	91.5	
				1 1/2	6 1/2	98.1	
				1 1/2	6 1/2	98.1	
				1 5/8	6 1/2	94.7	
				1 1/2	7	105.6	
			41	1 1/2	7	105.6	
				1 5/8	7	102.0	
				1 5/8	7 1/2	109.2	
				1 5/8	7 1/2	109.2	
		- 3.48	41.77	1 3/8	7 1/2	117.3	
NB3-4	45.25 (WEST PIER)		42	3 1/4	7	70.4	
				3 1/4	7	70.4	
				3 1/8	7	72.2	
				3	7	73.9	
				3	7	73.9	
			43	2 3/4	7	77.8	
				2 3/4	7	77.8	
				2 5/8	7	80.0	
				2 1/2	7	82.1	
			44	2 1/2	7	82.1	
				2 3/8	7 1/2	90.6	
	90.50	4.57	85.93	TOTALS THIS REPORT		85.93	
	271.50	15.49	256.01	TOTALS LAST REPORT			→ ALLOWABLE SPLICES
	362.00	20.06	341.94	TOTALS TO DATE		362.00	

Table B.4: Pile Driving Record of Bent 3, North Bound (I65 over SR25) (Continued)

128-4

Form IC 225 Rev. 6-6-60 State Form 4287

INDIANA DEPARTMENT OF HIGHWAYS

CONTRACT NO. B-24138 DATE 7-11-2000

STRUCTURE NO. I65-176-5543C RECORD NO. 4

PROJECT NO. IM 65-6 (059) 176 FOR 12x53 H-PILING (TYPE OF PILING)

TYPE STRUCTURE STEEL BEAM

PILE DRIVING RECORD

BENT 3 N.B.L

HERA 1500 (TYPE HAMMER)

Found. and Pile Number	Length Put in Leads	Length Cut off	Length Below Cut off	Total Penetration Last 20 Blows	Weight and Drop or B P M and Energy	Bearing Value in Tons	Remarks Bearing Required, Etc.
NB3-4	45.25		≈ 44	2 3/8	7 1/2	90.6	
				2 1/8	7 1/2	96.1	
				2 1/8	7 1/2	96.1	
				2 1/4	7 1/2	93.2	
				2	7 1/2	99.0	
			45	2	7 1/2	99.0	
				1 3/4	7 1/2	105.6	
		(+.25)	45.50	1 3/4	7 1/2	105.6	
NB3-3	45.25		41	2	6 1/2	85.8	
				1 7/8	6 1/2	88.6	
				2	6 1/2	85.8	
				1 7/8	6 1/2	88.6	
				1 3/4	6 1/2	91.5	
				1 3/4	7	98.6	
				1 1/2	7	105.6	
				1 1/2	7	105.6	
			42	1 1/2	7	105.6	
				1 5/8	7	95.4	
				1 5/8	7	95.4	
				1 7/8	7	95.4	
				1 7/8	7	95.4	
				1 7/8	7	95.4	
				1 3/4	7	98.6	
				1 3/4	7	98.6	
				1 5/8	7	102.0	
				1 5/8	7	102.0	
				1 5/8	7	102.0	
				1 1/4	7	113.7	
		-1.10	44.15	1 1/4	7	113.7	
NB3-2	45.25 (NEXT PAGE)			2	6 1/2	85.8	
			43	2 1/4	6 1/2	80.1	
				2	6 1/2	85.8	
				2	6 1/2	85.8	
				2	6 1/2	85.8	
			44	1 3/4	6 1/2	91.5	
				2	6 1/2	85.8	
				1 7/8	6 1/2	88.6	
				2	6 1/2	85.8	
				1 7/8	7	95.4	
				1 7/8	7	95.4	

90.50	0.85	89.65	TOTALS THIS REPORT	89.65	ALLOWABLE SPLICES
362.00	20.06	341.94	TOTALS LAST REPORT		
452.50	20.91	431.59	TOTALS TO DATE	431.59	

Table B.4: Pile Driving Record of Bent 3, North Bound (I65 over SR25) (Continued)

128-S

Form IC 225
Rev. 8-6-60

State Form 4287

INDIANA DEPARTMENT OF HIGHWAYS

CONTRACT NO. 8-24138 DATE 7-11-2000

STRUCTURE NO. I65-176-55436 RECORD NO. 5

PROJECT NO. IM 65-6 (059) 176 FOR 12 & 53 H-PILING
TYPE OF PILING

TYPE STRUCTURE STEEL BEAM

PILE DRIVING RECORD

HERA 1500
TYPE HAMMER

Found. and Pile Number	Length Put in Leads	Length Cut off	Length Below Cut off	Total Penetration Last 20 Blows	Weight and Drop or B P M and Energy	Bearing Value in Tons	Remarks Bearing Required, Etc.
N83-2	45.25			1 7/8	7	95.4	
				1 7/8	7	95.4	
				1 7/8	7	95.4	
				2	7 1/2	97.0	
				1 3/4	7 1/2	105.4	
		(+.92)	46.17	1 1/2	7 1/2	113.1	
N83-1	45.25		40	2 7/8	6 1/2	70.5	
				2 5/8	6 1/2	74.3	
				2 3/4	6 1/2	72.3	
			41	2 3/4	6 1/2	72.3	
				2 3/4	6 1/2	72.3	
			42	2 1/2	6 1/2	76.3	
				2 1/8	6 1/2	83.4	
				2 1/8	6 1/2	83.4	
			43	2	6 1/2	95.8	
				1 7/8	6 1/2	88.6	
				1 7/8	6 1/2	88.6	
				2	6 1/2	95.8	
				1 3/4	6 1/2	91.5	
				1 3/4	6 1/2	91.5	
				1 1/2	6 1/2	98.1	
				1 5/8	6 1/2	94.7	
				1 1/2	7	105.6	
				1 5/8	7	102.0	
				1 5/8	7	102.0	
		-.33	44.92	1 1/2	7	105.6	

90.50	- 0.59	91.09	TOTALS THIS REPORT	91.09	
452.50	20.98	931.59	TOTALS LAST REPORT	—	→ ALLOWABLE SPLICES
543.00	20.32	522.68	TOTALS TO DATE	522.68	

Table B.5: Pile Driving Record of Bent 1 (SR18)

Form IC 225 Rev. 6-6-60 State Form 4287

INDIANA DEPARTMENT OF HIGHWAYS

5M 8-81

CONTRACT NO. B-26342 DATE 7-9-03

STRUCTURE NO. 18-27-4518D RECORD NO.

PROJECT NO. 1325037 FOR SEC - SHELL (TYPE OF PILING)

TYPE STRUCTURE Bridge MKT - DE 30/20 R (TYPE HAMMER)

Des. No. 0013030

PILE DRIVING RECORD

Found. and Pile Number	Length Put in Leads	Length Cut off	Length Below Cut off	Total Penetration Last 20 Blows	Weight and Drop or B P M and Energy		Bearing Value in Tons	Remarks Bearing Required, Etc.
1-10	40.16	19.50	20.66	4.0	2800	5.0		
				4.0	2800	5.0		
				3.5	2800	5.0		
				2.25	2800	5.5	162	112.5 TONS REQUIRED
1-9	40.16	21.25	18.91	7.0	2800	5.0		
				3.0	2800	5.0		
				2.5	2800	5.0		
				2.5	2800	5.5	157	112.5 TONS REQUIRED
1-8	40.16	17.08	23.08	4.5	2800	5.5		
				4.0	2800	5.5		
				3.5	2800	6.0		
				3.0	2800	6.0	157	112.5 TONS REQUIRED
1-7	40.16	18.25	21.91	5.0	2800	5.0		
				5.0	2800	5.0		
				3.0	2800	5.0		
				2.0	2800	5.0	157	112.5 TONS REQUIRED
1-5	40.16	17.25	22.91	5.0	2800	5.0		
				4.5	2800	5.5		
				4.0	2800	5.0		
				3.0	2800	5.5	148	112.5 TONS REQUIRED
1-4	40.16	21.75	18.41	4.0	2800	5.0		
				4.0	2800	5.0		
				3.0	2800	5.0		
				2.0	2800	5.5	167	112.5 TONS REQUIRED
1-3	40.16	22.33	17.83	6.0	2800	6.0		
				4.5	2800	6.0		
				3.0	2800	6.0		
				2.5	2800	6.0	165	112.5 TONS REQUIRED
1-2	40.16	22.08	18.08	5.0	2800	6.0		
				4.0	2800	6.5		
				3.5	2800	6.5		
				3.0	2800	6.5	165	112.5 TONS REQUIRED
	321.28	159.49	161.79	TOTALS THIS REPORT				ALLOWABLE SPLICES
				TOTALS LAST REPORT				
				TOTALS TO DATE				

Table B.5: Pile Driving Record of Bent 1 (SR18) (Continued)

Form IC 225 Rev. 6-6-60 State Form 4287

INDIANA DEPARTMENT OF HIGHWAYS

5M 8-81 CONTRACT NO. B-26342 DATE 7-9-03

STRUCTURE NO. 18-27-45181 RECORD NO.

PROJECT NO. 1325037 PILE DRIVING RECORD FOR SEC - SHELL (TYPE OF PILING)

TYPE STRUCTURE Bridge MKT - DE 30/20 B (TYPE HAMMER)

DES. No. 0013030

Found. and Pile Number	Length Put in Leads	Length Cut off	Length Below Cut off	Total Penetration Last 20 Blows	Weight and Drop or B P M and Energy		Bearing Value in Tons	Remarks Bearing Required, Etc.
1-1	40.16	18.58	21.58	4.5	2800	6.0		
				7.0	2800	5.0		
				4.0	2800	5.0		
				3.0	2800	5.5	148	112.5 TONS REQUIRED
1-11	40.16	18.66	21.50	4.0	2800	5.0		
				4.0	2800	5.0		
				4.0	2800	5.0		
				4.0	2800	5.0	125	112.5 TONS REQUIRED
1-6	26.25	2.75	23.50	6.5	2800	5.0		
				5.0	2800	5.0		
				4.5	2800	5.0		
				3.5	2800	5.0	132	112.5 TONS REQUIRED
	106.57	39.99	66.58	TOTALS THIS REPORT				ALLOWABLE SPLICES
				TOTALS LAST REPORT				
				TOTALS TO DATE				

Table B.6: Pile Driving Record for Pile 6, Bent 1 (SR18)

Form IC 225 Rev. 6-6-60 State Form 4287

INDIANA DEPARTMENT OF HIGHWAYS

5M 8-81 CONTRACT NO. B-26342 DATE 6-12-03

STRUCTURE NO. 18-27-45180 RECORD NO.

PROJECT NO. 1325037 PILE DRIVING RECORD FOR SEC - SHELL (TYPE OF PILING)

TYPE STRUCTURE Bridge MKT-DE30/20B (TYPE HAMMER)

DES. No. 0013030

Found. and Pile Number	Length Put in Leads	Length Cut off	Length Below Cut off	Total Penetration Last 20 Blows	Weight and Drop or B P M and Energy		Bearing Value in Tons	Remarks Bearing Required, Etc.
6-12	28.83	7.25	27.58	7.0	2800	4.5		
				6.0	2800	4.5		
				5.5	2800	5.5		
				3.5	2800	5.5	140.8	100 TONS REQUIRED
6-6	40.16	12.33	27.83	7.0	2800	4.5		
				7.0	2800	4.5		
				5.0	2800	5.0		
				4.0	2800	5.5	134.0	100 TONS REQUIRED
6-5	40.16	11.16	29.00	5.5	2800	4.5		
				5.5	2800	4.5		
				5.0	2800	5.0		
				4.5	2800	5.5	129.0	100 TONS REQUIRED
6-4	40.16	10.25	29.91	5.0	2800	5.0		
				4.75	2800	5.0		
				4.50	2800	5.5		
				4.0	2800	5.5	134.0	100 TON REQUIRED
6-3	29.50	2.58	26.92	4.0	2800	5.0		
				4.0	2800	5.0		
				3.0	2800	5.0		
				3.0	2800	5.5	148.1	100 TON REQUIRED
6-2	29.00	1.42	27.58	6.0	2800	4.5		
				6.0	2800	5.0		
				5.5	2800	5.5		
				5.0	2800	5.5	124.0	100 TON REQUIRED
6-1	29.08	2.83	26.25	6.0	2800	5.0		
				6.0	2800	5.5		
				5.5	2800	5.5		
				5.0	2800	6.0	131.0	100 TON REQUIRED
6-11	29.33	2.25	27.08	6.5	2800	4.5		
				6.5	2800	5.0		
				6.0	2800	5.5		
				6.0	2800	5.5	115.4	100 TON REQUIRED
				TOTALS THIS REPORT				ALLOWABLE SPLICES
				TOTALS LAST REPORT				
				TOTALS TO DATE				

℄ → ROADWAY

Table B.6: Pile Driving Record for Pile 6, Bent 1 (SR18) (Continued)

Form IC 225 Rev. 6-6-66 State Form 4287

INDIANA DEPARTMENT OF HIGHWAYS

5M 8-81

CONTRACT NO. B-26342 DATE 6-11-03

STRUCTURE NO. 18-27-4518D RECORD NO.

PROJECT NO. 1325037 FOR SEC - SHELL (TYPE OF PILING)

TYPE STRUCTURE Bridge MKT-DE-30/20B (TYPE HAMMER)

DES. No. 0013030

PILE DRIVING RECORD

Found. and Pile Number	Length Put in Leads	Length Cut off	Length Below Cut off	Total Penetration Last 20 Blows	Weight and Drop or B P M and Energy		Bearing Value in Tons	Remarks Bearing Required, Etc.
6-10	40.16	14.42	25.74	10.0	2800	4.0		
				9.5	2800	5.0		
				6.0	2800	5.0		
				3.0	2800	5.5	148.1	100 TONS REQUIRED
6-9	40.16	15.67	24.49	8.0	2800	3.5		
				7.5	2800	4.0		
				7.0	2800	5.0		
				3.0	2800	5.5	148.1	100 TONS REQUIRED
6-8	40.16	14.33	25.83	7.0	2800	5.0		
				4.0	2800	5.5		
				4.0	2800	6.0		
				4.0	2800	6.0	142.0	100 TONS REQUIRED
6-7	40.16	13.67	26.49	5.0	2800	5.5		
				4.5	2800	6.0		
				5.0	2800	6.0		
				4.5	2800	6.0	137.0	100 TONS REQUIRED
				TOTALS THIS REPORT				ALLOWABLE SPLICES
				TOTALS LAST REPORT				
				TOTALS TO DATE				

APPENDIX C

CONSTRUCTION PLANS

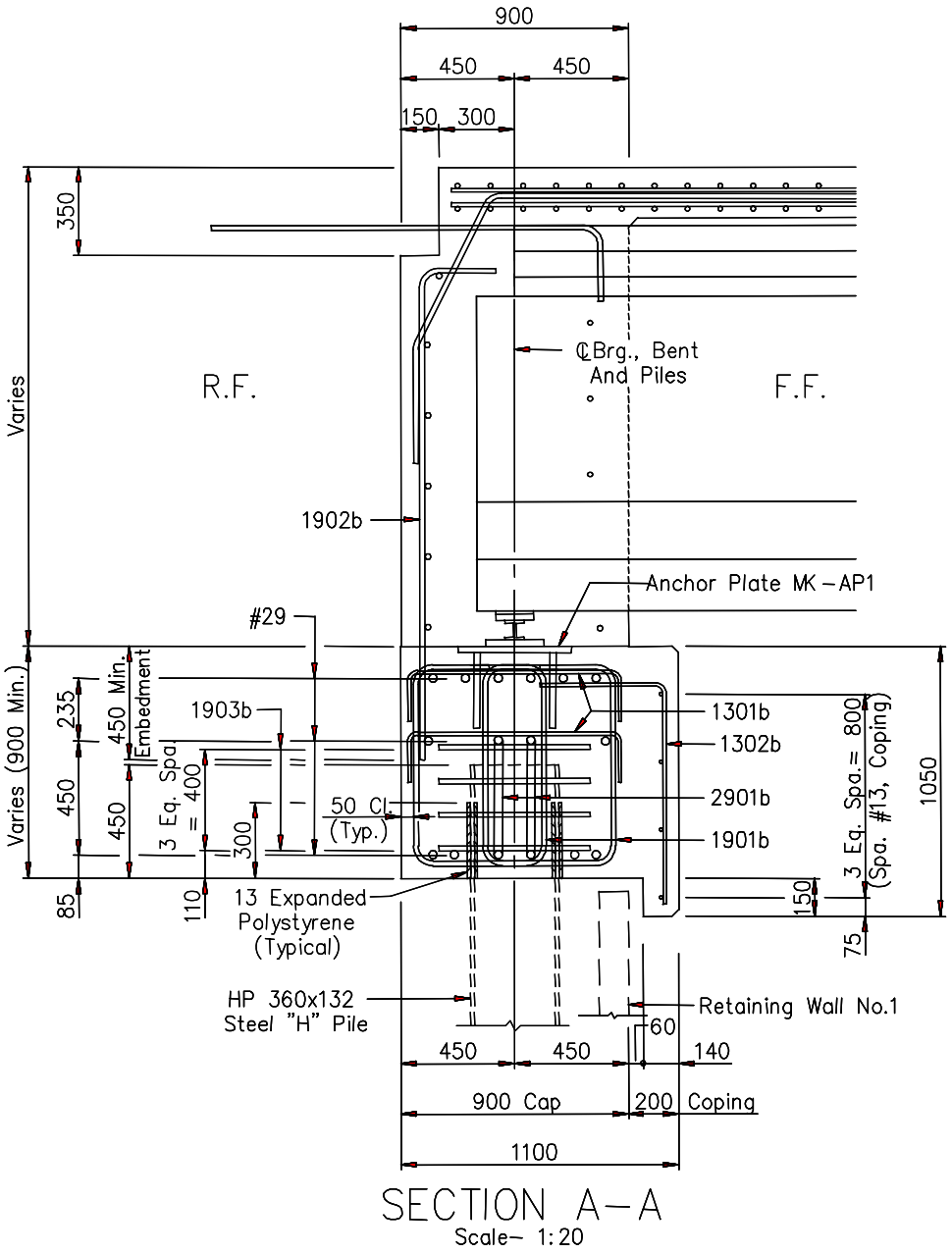

Figure C.1: End Bent Details of Bent 1 (SR249 over US12)

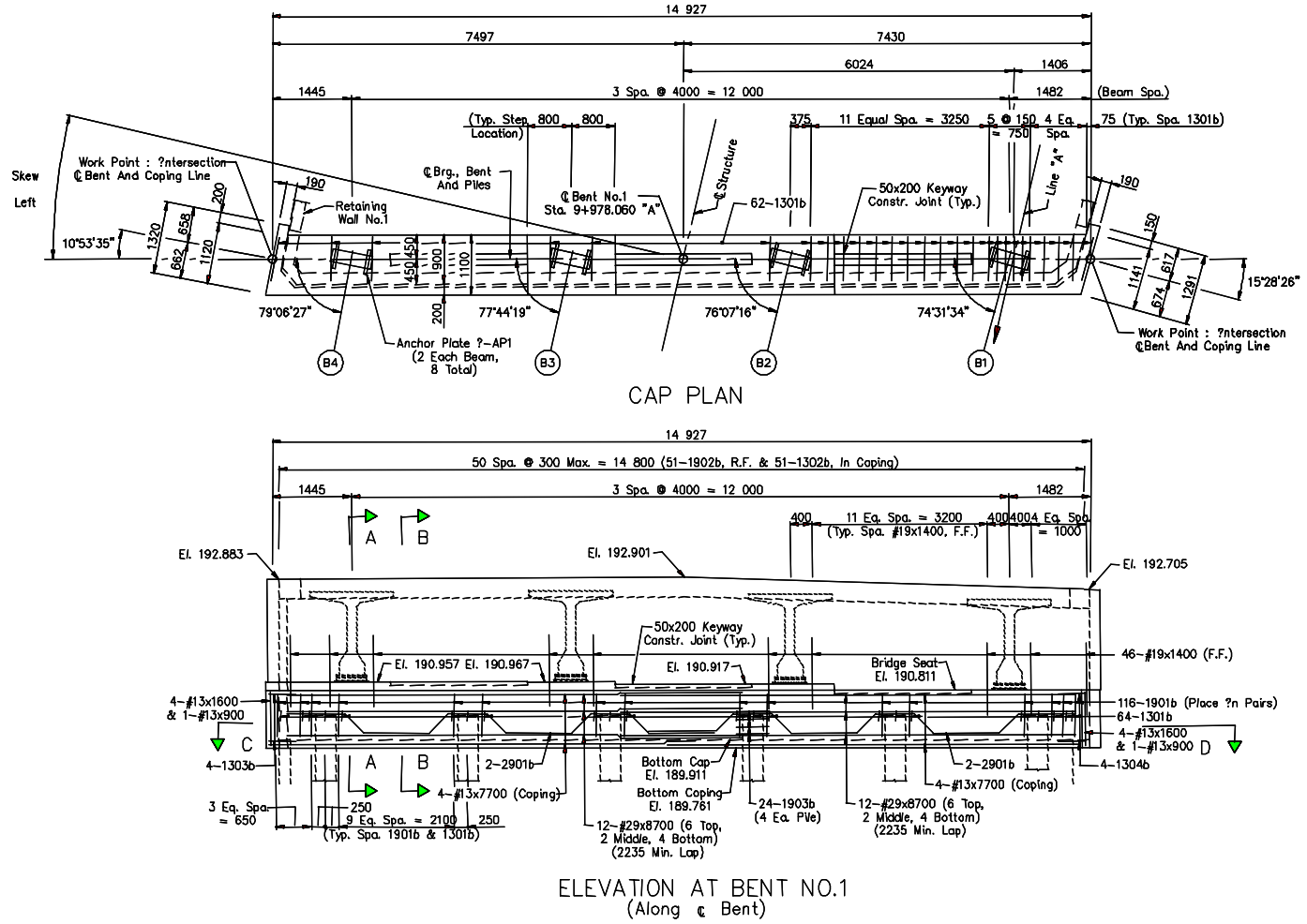

Figure C.2: Plan and Elevation Views of Bent 1 (SR249 over US12)

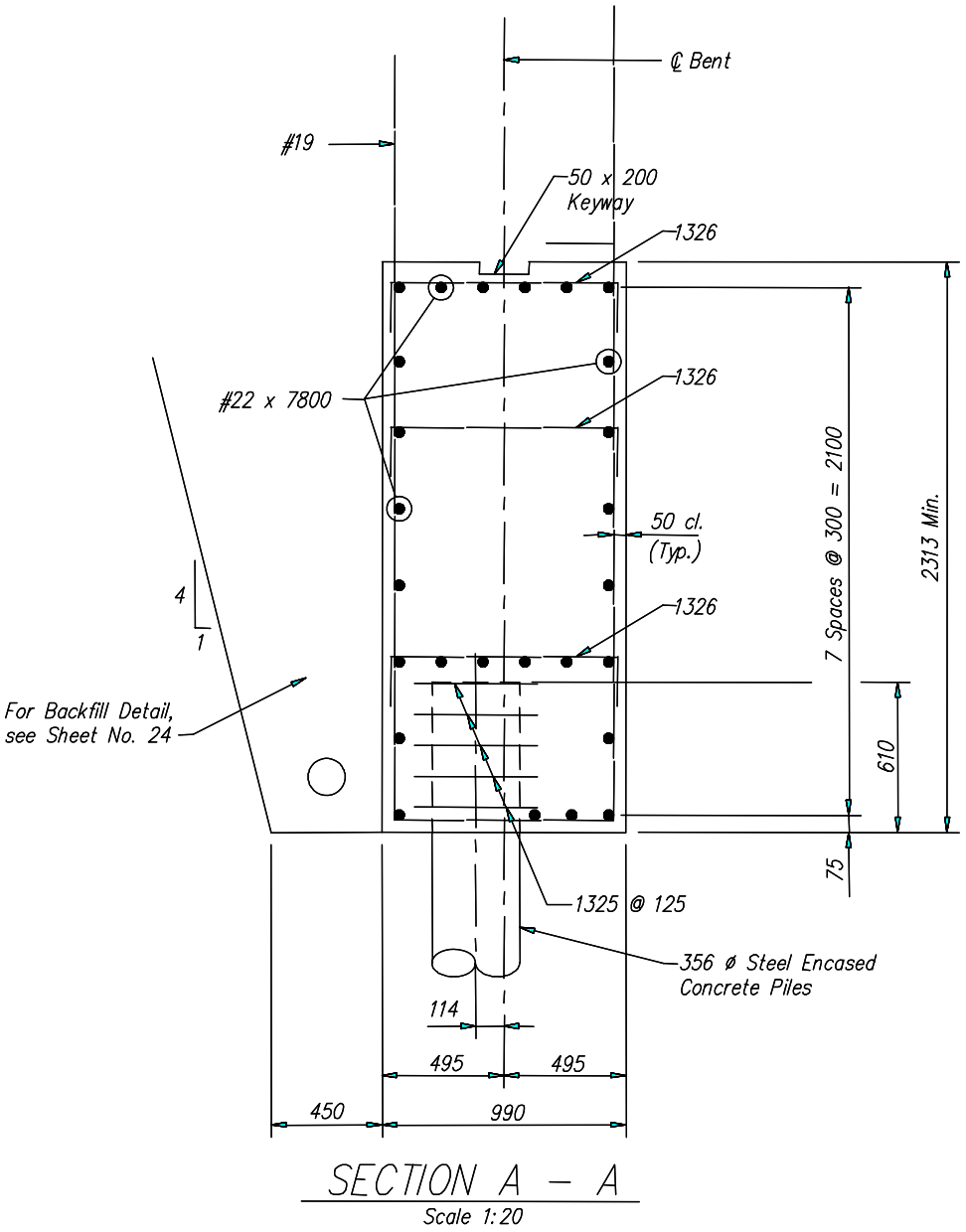

Figure C.3: End Bent Details of Bent 1 (I65 over US25)

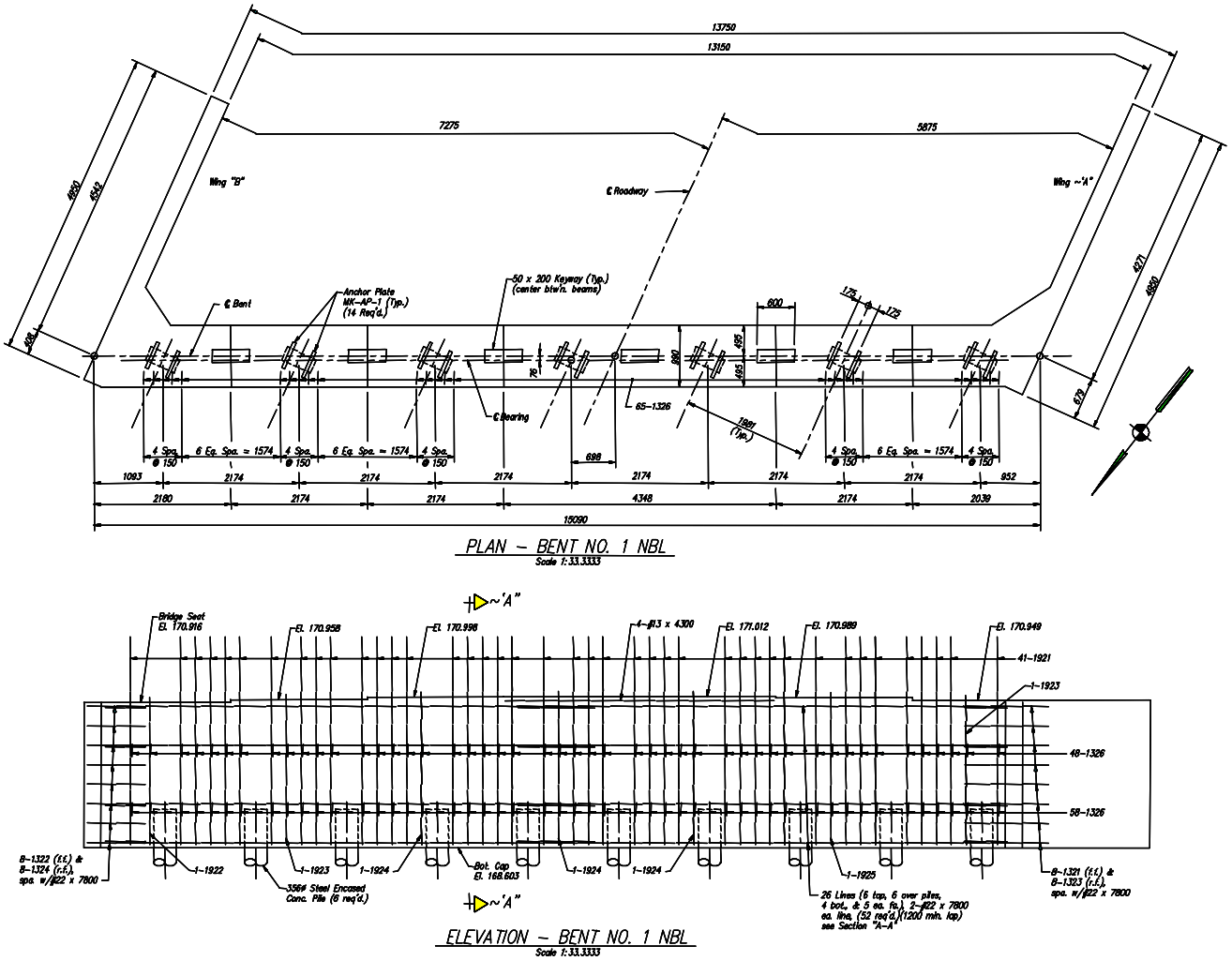

Figure C.4: Plan and Elevation Views of Bent 1 (I65 over US25)

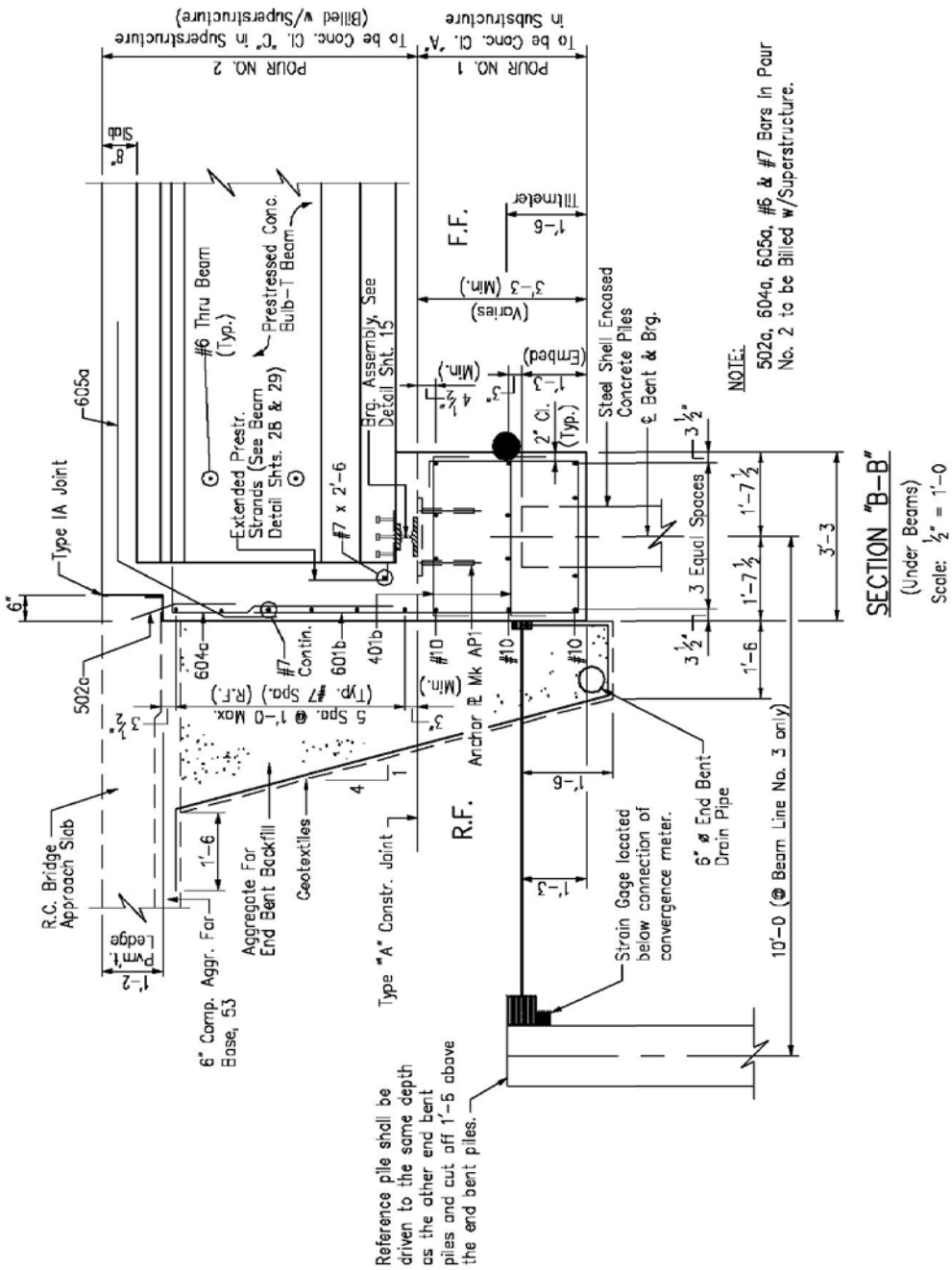

Figure C.5: End Bent Details of Bent 1 (SR18 over Mississinewa River)

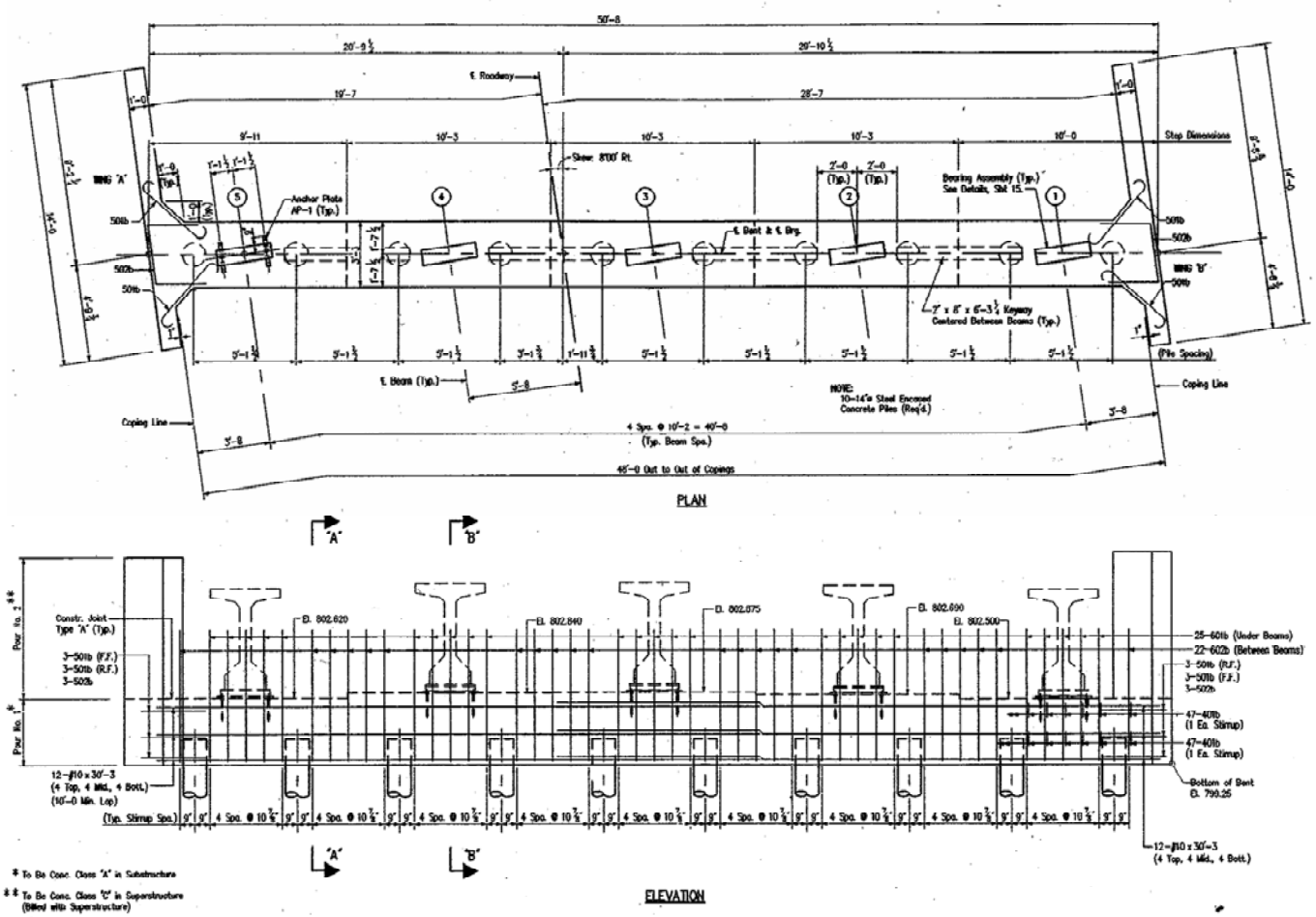

Figure C.6: Plan and Elevation Views of Bent 1 (SR18 over Mississinewa River)

APPENDIX D

CONSTRUCTION SEQUENCE

Appendix D: Construction Sequence

Table D.1: Construction Sequence (SR249 over US12)

Date	Event
5/5/1999	Driving HP at Bent 11
5/10/1999	Driving HP at Bent 1
5/11/1999	Still driving HP at Bent 1
5/12/1999	Driving piles at Pier 10
5/19/1999	Driving piles at Piers 9 and 10
5/24/1999	Began installing the instrumentation on Pier 10
5/26/1999	Driving piles at Piers 8 and 9, poured footing at Pier 9
5/27/1999	Driving piles at Pier 7
6/1/1999	Poured Pier 10 (Stem)
6/2/1999	Poured Footing at Pier 7
6/3/1999	Flexural beam test on Pier 10, 551 psi, driving piles at Pier 6
6/4/1999	Poured Pier 9, driving piles at Pier 5
6/7/1999	Poured Footing at Pier 8
6/8/1999	Poured Pier 8 (Stem)
6/9/1999	Poured Pier 10 (Pier Cap)
6/10/1999	Poured Pier 7 (Stem)
6/14/1999	Driving piles at Pier 5, poured Pier 6
6/16/1999	Poured Pier 9 (Pier Cap)
6/18/1999	Poured Pier 8 (Pier Cap)
6/22/1999	Poured Footing at Pier 5
6/23/1999	Poured Pier 7 (Pier Cap), Pier 5 (Stem)
6/28/1999	Driving piles at Pier 2
6/30/1999	Poured Footing at Pier 2
7/2/1999	Poured Pier 6 (Pier Cap)
7/6/1999	Poured Pier 2 (Stem)
7/7/1999	Driving piles at Pier 4
7/12/1999	Poured Pier 2 (Pier Cap)
7/13/1999	Poured Pier 5 (Pier Cap)
7/15/1999	Poured Footing at Pier 4
7/15/1999	Foundation worked on Bent 1
7/17/1999	Poured Pier 4 (Stem)
7/20/1999	Poured Pier 4 (Pier Cap)
7/24/1999	Driving Piles at Pier 3
7/27/1999	Placing EPS fills at Bent 1
8/4/1999	Poured Pier 3 (Stem)

Table D.1: Construction Sequence (SR249 over US12) (Continued)

Date	Event
8/9/1999	Poured Pier 3 (Pier Cap)
8/13/1999	Poured Bent 1 (1st pour)
8/17/1999	Set Beams on Span B
8/19/1999	Set Beams on Spans A and C
8/20/1999	Poured Span C Diaphragm
8/22/1999	Set Beams on Span D
8/23/1999	Set Beams on Span E, poured Span B Diaphragm
8/24/1999	Set Beams on Span F, poured Span A Diaphragm
8/25/1999	Poured foundation on Bent 11, set Beams on Span G, poured Span D Diaphragm
8/26/1999	Set Beams on Span H, poured Spans F Diaphragms
8/27/1999	Set Beams on Span I, poured Span G Diaphragm
8/28/1999	Poured Spans H and I Diaphragms
8/31/1999	Began placing deck pan
9/2/1999	Placing EPS fills at Bent 11
9/9/1999	Began placing reinforcing steel for deck
9/10/1999	Poured Bent 1 (2nd pour)
9/16/1999	Poured Span A (East half of Phase #1)
9/20/1999	Poured Bent 11 (1st pour), , poured Span B (Phase #2)
9/20/1999	Poured Span A (West Half of Phase #1)
9/23/1999	Poured Deck on Spans C and D, poured diaphragm on Pier 3, set Beams on Span J
9/27/1999	Poured Span J Diaphragm
10/1/1999	Poured Deck on Spans E and F, poured diaphragm on Piers 2 and 5, installed inclinometer on Bent 1
10/4/1999	Poured Diaphragm on Pier 4
10/5/1999	Poured Diaphragm on Pier 6
10/6/1999	Poured Deck on Spans G and H, poured diaphragm on Pier 7
10/8/1999	Poured Deck on Span J
10/11/1999	Poured Deck on Span I
10/12/1999	Poured Diaphragm on Pier 9, poured pavement north end of the bridge
10/13/1999	Poured the sleeper slab south end of the bridge
10/15/1999	Poured the approach slab south end of the bridge
10/21/1999	Poured the pavement south end of the bridge
10/22/1999	Poured he pavement north end of the bridge, poured gap in pavement south end of the bridge
10/23/1999	Poured the sleeper slab north end of the bridge
10/26/1999	Poured the approach slab north end of the bridge

Table D.1: Construction Sequence (SR249 over US12) (Continued)

Date	Event
11/9/1999	Opened to traffic northbound
11/24/1999	Opened to traffic for both bounds
3/20/2000	Began placing conduit for the instrumentation wires, placing instrumentation cabinet
3/28/2000	Hawk Inc. installed crackmeters
3/29/2000	Began placing wire through conduit
4/3/2000	Finished pulling wire through conduit
4/12/2000	Hooked up the cabinet
5/17/2000	Installed the instrumentation software
6/7/2000	All strain gages and crackmeters began reading
8/18/2000	Cellular modem was installed (no data obtained from 8/18/2000 to 12/8/2000)

Table D.2: Northbound Lanes Construction Sequence (I65 over SR25)

Date	Event
5/24/2000	Drilling bridge deck to locate edge of beams
5/25/2000	Drilling bridge deck to locate edge of beams
5/26/2000	Drilling bridge deck to locate edge of beams
5/29/2000	Memorial Day
5/30/2000	Started to remove barrier wall
5/31/2000	Removing barrier wall
6/1/2000	Removing barrier wall
6/2/2000	Removing barrier wall
6/5/2000	Sawing bridge deck into sections for removal
6/6/2000	Sawing bridge deck into sections for removal
6/7/2000	Sawing bridge deck into sections for removal
6/8/2000	Removing deck
6/9/2000	Removing deck
6/12/2000	Removing deck/hauling deck off site
6/13/2000	Removing deck/hauling deck off site
6/14/2000	Removing deck/hauling deck off site
6/15/2000	Breaking approach slabs and sleeper slabs; breaking slopewall on south side
6/16/2000	Driving temporary piling in Bent 3
6/17/2000	Driving temporary piling in Bents 1 and 3
6/19/2000	Driving temporary piling in Bent 1
6/20/2000	Jacking and supporting beams
6/21/2000	Jacking and supporting beams
6/22/2000	Jacking and supporting beams
6/23/2000	Removing Bent 1
6/24/2000	Removing Bent 1
6/26/2000	Removing Bent 1
6/27/2000	Drove piling in Bent 1
6/28/2000	Forming Bent 1 and wingwalls
6/29/2000	Forming Bent 1 and wingwalls
6/30/2000	Removing debris from old bent; Placed and tied steel in Bent 1
7/3/2000	Forming Bent 1 and wingwalls
7/4/2000	Independence Day
7/5/2000	Setting plates for Bent 1 pour/Forming Bent1 and wingwalls
7/6/2000	Poured Bent 1/Removing Bent 3
7/7/2000	Removing Bent 3
7/8/2000	Removing Bent 3
7/10/2000	Removing Bent 3/Removing forms, Bent 1

Table D.2: Northbound Lanes Construction Sequence (I65 over SR25) (Continued)

Date	Event
7/11/2000	Drove piling Bent 3; Finished removing forms, Bent 1; Grinding seats for bearing assemblies
7/12/2000	Forming Bent 3 and wingwalls
7/13/2000	Forming Bent 3 and wingwalls and backfilled Bent 1
7/14/2000	Placed and tied steel in Bent 3
7/15/2000	Clean-up on Bent 3; Grading and forming Bent 1 (top portion); Finished forming Bent 3
7/17/2000	Poured Bent 3
7/18/2000	Removing forms, Bent 3, setting beams
7/19/2000	Backfilled Bent 3
7/20/2000	Preparing to remove damaged beams
7/21/2000	Grading; Removing old drain pipe; Removed damaged beams and diaphragms (span B)
7/24/2000	Tying re-steel in crash steel
7/25/2000	Set two new beams (span B); Tying resteel for crashwall
7/26/2000	Resetting diaphragms
7/27/2000	Forming crashwall; Finished setting beams; Bolting diaphragms
7/28/2000	Bolting diaphragms
7/31/2000	Forming Bent 1; Drilling and bolting splices and diaphragms
8/1/2000	Forming Bent 1; Setting deck pans; Finished bolting diaphragms and checking torque
8/2/2000	Grading for sleeper slabs; Forming end bents
8/3/2000	Installing deck pans and forming end bents
8/4/2000	Installing deck pans, replacing damaged shear studs and forming end bents
8/5/2000	Installing deck pans, installing new shear studs and forming end bents
8/7/2000	Installing deck pans and forming end bents
8/8/2000	Placing reinforcement in deck and forming end bents
8/9/2000	Placing reinforcement in deck and forming deck
8/10/2000	Placing reinforcement in deck and end bents
8/11/2000	Placing reinforcement in deck and end bents
8/12/2000	Forming end bents
8/14/2000	Forming/getting ready for deck pour
8/15/2000	Poured deck (began at 7:00 am at Bent 1 and proceeded north to Bent 3; finished pouring around 2:00 pm; placed burlene that evening)
8/16/2000	Stripping bents; Wet burlene
8/17/2000	Forming South Approach Slab and placing rebar in South Approach Slab (rained in evening)

TableD.2: Northbound Lanes Construction Sequence (I65 over SR25) (Continued)

Date	Event
8/18/2000	Finished shoulders and placing rebar in South Approach
8/21/2000	Sealing joints; Clean up on bridge superstructure; Forming North Approach
8/22/2000	Placing rebar in North Approach Slab
8/23/2000	Working on shoulders
8/24/2000	Sealed deck
8/25/2000	Slip-formed barrier walls
8/28/2000	Traffic switched to Northbound lanes at 2:25 pm
8/31/2000	Began work on SBL

Table D.3: Southbound Lanes Construction Sequence (I65 over SR25)

Date	Event
8/28/2000	Switched traffic to northbound lanes
8/31/2000	Removed asphalt overlay and overhead sign
9/1/2000	Began breaking pavement and removing concrete deck; removed barrier wall
9/2/2000	Continuing deck removal
9/4/2000	Continuing deck removal
9/5/2000	Continuing deck removal
9/6/2000	Completed deck removal
9/7/2000	Began jacking and supporting beams
9/8/2000	Continued jacking and supporting beams and drove temporary piles
9/12/2000	Finished jacking and supporting beams
9/13/2000	Removing end bents
9/14/2000	Removing end bents
9/15/2000	Finished removing bents and drove steel H piles for Bent 1
9/16/2000	Forming Bent 1 and drove steel H piles for Bent 3
9/18/2000	Forming Bent 2 and placing steel in Bent 1
9/19/2000	Placing steel in Bent 3
9/20/2000	Grading subbase and forming Bents No. 1 and 3; Placing steel in Bents No. 1 & 3
9/21/2000	Grading subbase; Forming Bents No. 1 and 3; Placing steel in Bents No. 1 and 3
9/22/2000	Poured concrete for Bents No. 1 and 3
9/23/2000	Stripping forms on Bents No. 1 and 3; Placed geotextile fabric
9/25/2000	Backfilled abutments; Preparing sleeper areas for concrete; Placed end bent drains
9/26/2000	Setting beams
9/27/2000	Setting beams
10/2/2000	Grading subbase for sleeper slabs
10/3/2000	Poured crashwall footing; Welding bearing assembly in place; Bolting end diaphragms
10/4/2000	Bolting end diaphragms
10/5/2000	Stripping forms for crashwall; Forming Bents No. 1 and 3
10/6/2000	Installing deck pans and forming Bents No. 1 and 3
10/7/2000	Installing deck pans and replacing damaged shear studs
10/8/2000	Installing deck pans and installing new shear studs
10/9/2000	Placing reinforcement in deck
10/10/2000	Placing reinforcement in deck
10/11/2000	Placing reinforcement in deck and end bents

Table D.3: Southbound Lanes Construction Sequence (I65 over SR25) (Continued)

Date	Event
10/12/2000	Placing reinforcement in deck; Forming end bents and coping line
10/13/2000	Placing reinforcement in deck; Forming end bents
10/14/2000	Placing reinforcement in deck; Forming end bents
10/16/2000	Finished deck steel; Forming end bents
10/17/2000	Removing median asphalt; Forming end bents
10/18/2000	Poured deck – began at Bent 3 at 7:30AM (38°F, foggy); Finished at Bent 1 around 1:30PM (60°F, sunny); Placed burlene over deck around 9:00PM
10/19/2000	Stripping end bent forms; Wet burlene
10/20/2000	Forming approach slabs
10/21/2000	Poured South Approach Slab (7:00-11:00AM)
10/23/2000	Poured North Approach Slab (AM)
10/24/2000	Placed base in terminal joints/Placing steel in bridge railing/Stripping coping forms
10/25/2000	Folded burlene
10/26/2000	Poured curbs; Removed burlene
10/27/2000	Working on shoulders
10/28/2000	Sealed deck
10/29/2000	Slip-formed barrier walls
10/30/2000	Clean-up
10/31/2000	Southbound traffic switched to Southbound lanes at 9:30AM

Table D.4: Construction Sequence (SR18)

Date	Event
5/6/2003	Removal of existing deck and beams began
5/28/2003	Removed Pier 5 Cap
6/5/2003	Removed Bent 6 and old piling
6/6/2003	Poured Bent 5 Stem
6/11/2003	Bent 6 Piles Driven
6/12/2003	Pier 5 cap poured, Bent 6 pile driving completed
6/13/2003	Began forming Pour #1 of Bent 6
6/16/2003	Bent 6 Pile Strain gages attached to piles, pressure cells installed
6/17/2003	Bent 6 instrumentation conduit ran. East datalogger programmed and uploaded and tested. Problems observed with readings
6/18/2003	Continued working program for East datalogger
6/19/2003	Poured Pour #1 on Bent 6 and Wing walls
6/20/2003	Installed Bent 6 Tiltmeter and convergence meters. Backfill Bent 6 up to Pour #1
6/23/2003	Placed 3 of 5 beams on Span E
6/24/2003	Placed last 2 beams of Span E
6/27/2003	Poured Span E Midspan diaphragm. Installed Pier 5 gages
6/30/2003	Poured Pour #2 on Bent 6 and Wing Walls
7/1/2003	Continued demolition of Spans B, C, D. Began SIP deck forms on Span E
7/2/2003	Removal of Pier 4 Cap
7/3/2003	Removal of Pier 3 Cap
7/7/2003	Completed SIP forms on Span E. Removed Bent 1. Began new Bent 1 excavation.
7/9/2003	Bent 1 piles driven. Strain gages attached to Pile 6 prior to driving. Tested with readout box.
7/14/2003	Swapped east datalogger out today for one with modem. Strain gages and pressure cells on Bent 1.
7/15/2003	Completed removing pier caps 2, 3, and 4. Wiring for Bent 1 instruments. Awaiting West Datalogger
7/17/2003	Wired Multiplexers into West Datalogger
7/18/2003	Poured pour 1 on Bent 1 and wing walls
7/21/2003	Poured Pier 4 stem
7/22/2003	Tiltmeter and convergence meter at Bent 1
7/23/2003	Backfilled Bent 1
7/24/2003	Poured Pier 4 Cap
7/31/2003	Placed beams on Span D. Poured Pier 3 Stem
8/5/2003	Poured Pier 3 Cap
8/7/2003	Poured Span D midspan diaphragms

Table D.4: Construction Sequence (SR18) (Continued)

Date	Event
8/12/2003	Placed beams on Span C
8/13/2003	Poured Pier 2 Stem
8/15/2003	Poured Span C midspan diaphragms
8/19/2003	Poured Pier 2 Cap
8/21/2003	Began work on SIP deck forms for Spans C, D, and E
9/2/2003	Finished SIP deck forms for Spans C, D, and E
9/3/2003	Began deck reinforcement for Spans D and E
9/4/2003	Continued placing deck steel Spans C, D, and E
9/8/2003	Placed Beams on Spans A and B
9/9/2003	Poured Span B midspan diaphragms
9/10/2003	Poured Pour #2 on Bent 1 and wing walls. Reinforcing steel on Span B
9/12/2003	Poured Span A Midspan Diaphragm. Tiltmeter and Crackmeter on Pier 2, but problems with readout box so installation stopped.
9/16/2003	Completed SIP deck forms and continued deck reinforcing steel. More East End bent backfilling
9/18/2003	Placed aggregate base on east approach. Poured west sleeper slab.
9/19/2003	Placed aggregate base on west approach
9/20/2003	Recompacted east approach
9/22/2003	Completed deck steel. Started approach steel
9/26/2003	Cast the deck
9/27/2003	Saw cut the approaches
10/3/2003	Poured concrete curb on south side of bridge
10/7/2003	Poured concrete sidewalk on north side of bridge
10/13/2003	Poured bridge rail on north side
10/17/2003	Poured rail transition on North side
11/11/2003	Move East instrumentation from temporary cabinet to permanent
11/12/2003	Move West instrumentation from temporary cabinet to permanent
11/19/2003	Power lines run to instrumentation cabinets
11/25/2003	Bridge opened to traffic
12/3/2003	Power lines connected to dataloggers
12/19/2003	Phone line connected on west box, but not working
12/23/2003	Went to bridge for final inspection. West phone line repaired by LSI. Was able to download using modem.

APPENDIX E

COMPUTATION OF DEFLECTED SHAPE OF PILE 6 (SR18)

Appendix E: Computation of Deflected Shape of Pile 6 (SR18)

Curvatures along the depth of Pile 6 as shown in Figure E.1were determined from the strain gage measurement. The bottom of the pile was assumed to be fixed. Deflections, $\Delta_1(z)$, along the pile depth, z, were computed by integrating the moment of the area under the curvature relationship as illustrated in Figure E.2. It is assumed that the bottom of the pile behaves as a hinged support. Thus, a rotation, θ, can occur at the bottom of the pile. The previously calculated deflections, $\Delta_1(z)$, were calibrated with the value measured by a convergence meter, $\Delta_{cv}(0)$, at the ground level (z = 0). By assuming the values from the convergence meter is correct, the rotation at the bottom of the pile was determined by solving Equation E-1 for θ.

$$\Delta_1(0) = \Delta_{cv}(0) + \theta L \qquad \text{(E-1)}$$

where:

$\Delta_1(0)$ = deflection at the top of the pile calculated by moment-area method assumed fixed end at the bottom of the pile, in.

$\Delta_{cv}(0)$ = deflection at the center of Bent 1 measured by a convergence meter, in.

θ = rotation at the bottom of the pile, radian.

L = length of the pile below ground surface, in.

For example, at $\Delta T = -60°$ F, $\Delta_1(0) = 0.59$ in., $\Delta_{cv}(0) = 0.21$ in., and L = 22.25 ft (267 in.), θ can be solved by Equation E-1 to be equal to 0.00079 rad.

The final deflected shape can be calculated by subtracting the value of θx from the previously calculated deflection, $\Delta_1(z)$ where x is the distance from the bottom of the pile to a specific depth (x = 22.25 – z). For instance, at a depth of 8 ft from the ground surface, $\Delta_1(8) = 0.26$ in., $\theta x = (0.00079 \text{ rad})(22.25 \text{ ft} - 8 \text{ ft})(12 \text{ in./ft}) = 0.13$ in. Therefore, adjusted $\Delta(8) = 0.26$ in. – 0.13 in. = 0.13 in.

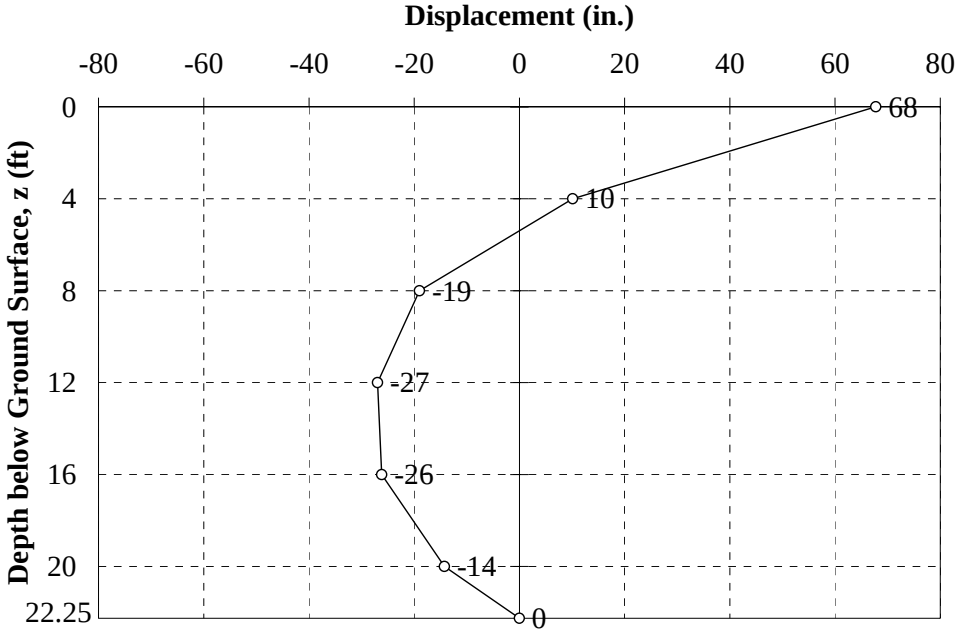

Figure E.1: Curvature of Pile 6 on Bent 1 (SR18) at ΔT = -60° F

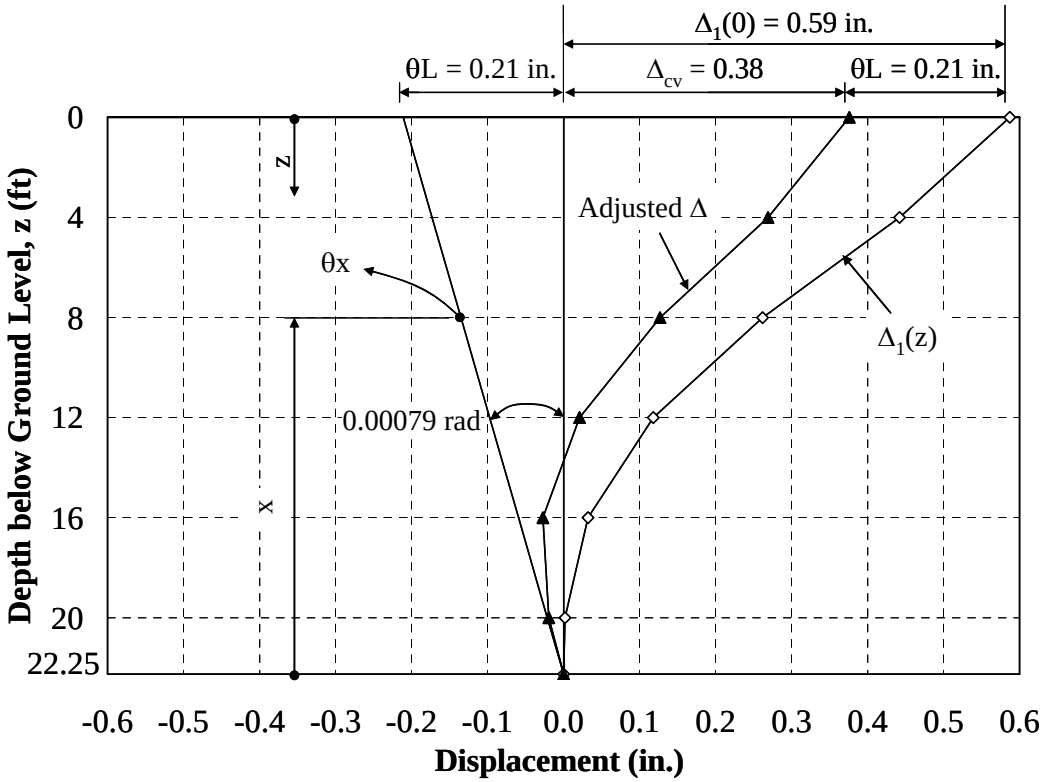

Figure E.2: Deflected Shape at ΔT = -60° F

APPENDIX F

LPILE SOIL MODEL

Appendix F: LPILE Soil Model

The p-y curves for sand below ground surface illustrated in Figure F.1 can be created by the following procedure (Reese et al., 1974).

1. Obtain value for the angle of internal friction, ϕ, the soil unit weight, γ, and pile diameter, B.
2. Compute the preliminary values.

$$\alpha = \frac{\phi}{2}$$

$$\beta = 45° + \frac{\phi}{2}$$

$K_0 = 0.4$; and $K_A = \tan^2\left(45° - \frac{\phi}{2}\right)$

3. Compute the ultimate soil resistance per unit length of pile, psi, using the smaller of the values given by Equations F-1, and F-2.

$$p_{st} = \gamma z\left[\frac{K_o z \tan\phi \sin\beta}{\tan(\beta-\phi)\cos\alpha} + \frac{\tan\beta}{\tan(\beta-\phi)}(B + z\tan\beta\tan\alpha)\right.$$
$$\left. + K_0 z \tan\beta(\tan\phi\sin\beta - \tan\alpha) - K_A B\right] \quad \text{(F-1)}$$

$$p_{sd} = K_A B\gamma z(\tan^8\beta - 1) + K_0 B\gamma z\tan\phi\tan^4\beta \quad \text{(F-2)}$$

4. Find the intersection, x_t, by equating Equations F-1 and F-2. Above this depth, use Equation F-1 for the ultimate soil resistance near the ground surface. Below this depth, use Equation F-2 for the ultimate soil resistance well below the ground surface.
5. Select a depth at which a p-y curve is desired.
6. Establish y_u as 3B/80. Compute p_u by Equation F-3

$$p_u = A_s p_s \text{ or } p_u = A_c p_s \quad \text{(F-3)}$$

The values of A_s or A_c, coefficients for static and cyclic cases, respectively, can be obtained from Figure F.2.

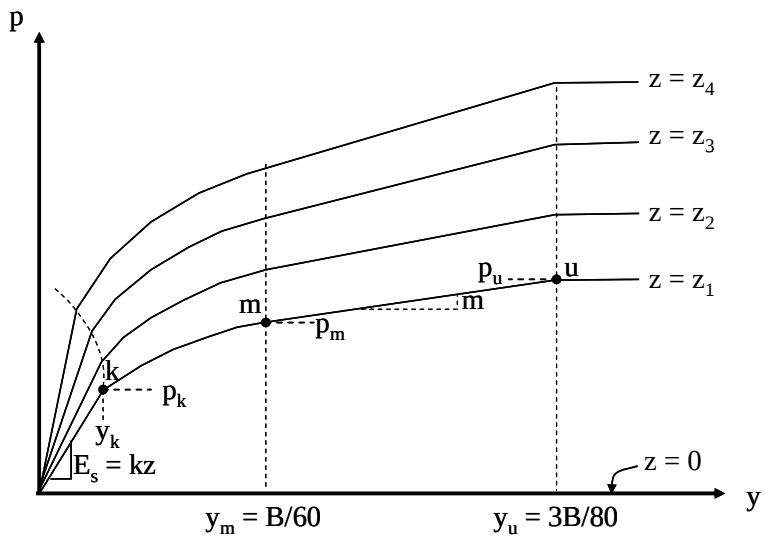

where: z = depth below ground level and $z_1 < z_2 < z_3 < z_4$.

Figure F.1: Characteristic Shape of a Family of p-y Curves for Static and Cyclic Loading in Sand (Reese et al., 1974)

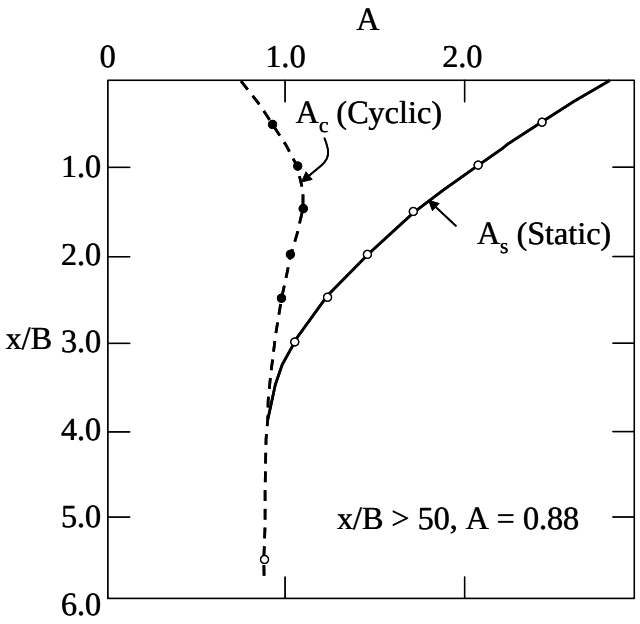

Figure F.2: Values of Coefficients A_s and A_c (Reese et al., 1974)

7. Establish y_m as B/60. Compute p_m by Equation F-4.

$$p_m = B_s p_s \text{ or } p_m = B_c p_s \qquad \text{(F-4)}$$

The values of B_s or B_c, coefficients for static and cyclic cases, respectively, can be obtained from Figure F.3.

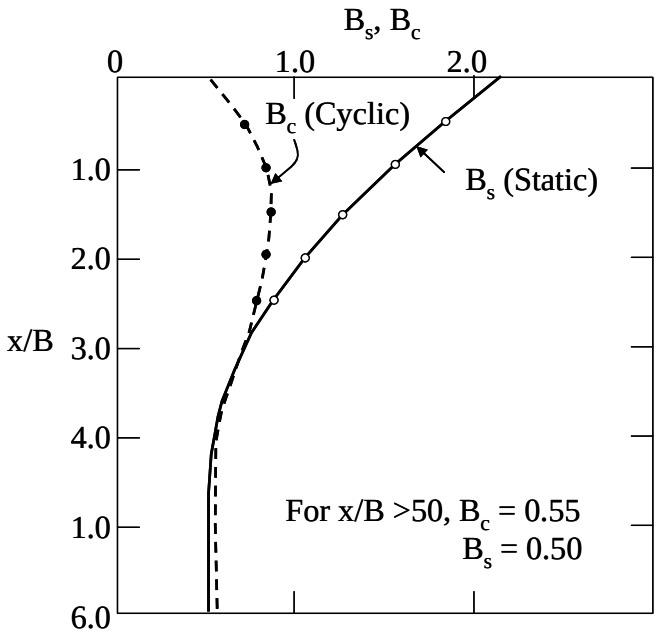

Figure F.3: Values of Coefficients B_s and B_c (Reese et al., 1974)

8. Establish the initial slope of the p-y curve, k from Table F.1

Table F.1: Recommended Values of k for Sand (lb/in.^{3})

Sand	Relative Density		
	Loose	Medium	Dense
Submerged	20	60	125
Dry	25	90	225

9. Fit a parabola between points k and m as follows:
   a. Obtain the slope of the line between points m and u by,

$$m = \frac{p_u - p_m}{y_u - y_m} \tag{F-5}$$

   b. Obtain the power of the parabolic section by,

$$n = \frac{p_m}{m y_m} \tag{F-6}$$

   c. Obtain the coefficient C as follows:

$$C = \frac{y_m}{y_m^{1/n}} \tag{F-7}$$

d. Determine point k as,

$$y_k = \left(\frac{C}{kz} \right)^{\frac{n}{n-1}} \tag{F-8}$$

10. Establish the parabolic section of the p-y curve between points k and m.

$$p = Cy^{1/n} \tag{F-9}$$

APPENDIX G

SOIL SPRING STIFFNESS VALUES

Appendix G: Soil Spring Stiffness Values

Table G.1: Soil Spring Stiffness Values for Piles (SR249 over US12)

Depth below ground surface (ft)	Bent 1 Spring Stiffness, k (k/ft)	Bent 11 Spring Stiffness, k (k/ft)
0	0	0
1	5	5
2	9	9
3	14	14
4	19	19
5	24	24
6	93	28
7	108	33
8	123	38
9	139	42
10	154	47
11	67	67
12	67	67
13	67	67
14	67	67
15	67	67
16	67	247
17	67	262
18	67	278
19	67	293
20	67	309
21	567	324
22	567	340
23	567	355
24	567	370
25	567	386
26	123	401
27	127	417
28	132	432
29	137	448
30	141	463

Depth below ground surface (ft)	Bent 1 Spring Stiffness, k (k/ft)	Bent 11 Spring Stiffness, k (k/ft)
31	146	478
32	151	494
33	156	509
34	160	525
35	495	1620
40	335	335
45	503	503
55	8488	8488
65	10031	10031
75	11574	11574
85	13117	13117
95	14660	14660
105	16204	16204
115	(fixed end)	17747
125		19290
135		20833
145		(fixed end)

Table G.2: Soil Spring Stiffness Values for Piles (I65 over SR25)

Depth below ground surface (ft)	Spring Stiffness, k (k/ft)
0	0
1	15
2	31
3	46
4	62
5	77
6	93
7	108
8	123
9	139
10	231
12	370
14	432
16	494
18	556
20	617
22	679
24	741
26	802
28	864
30	926
32	988
34	1049
36	1111
38	1759
40	(fixed end)

Table G.3: Soil Spring Stiffness Values for Piles (SR18 over Mississinewa River)

Depth below ground surface	Spring Stiffness, k (k/ft)	
	Stiff Clay	Medium Sand
0	0	0
1	211	53
2	241	107
3	271	160
4	301	213
5	331	267
6	361	320
7	391	373
8	421	427
9	451	480
10	481	533
11	511	587
12	541	640
13	541	693
14	541	747
15	541	800
16	541	853
17	541	907
18	541	960
19	541	1013
20	541	1067
21	541	1120
22	406	880
22.25	(fixed end)	(fixed end)

APPENDIX H

COUPON TEST RESULTS

APPENDIX H :Coupon Test Results

(a) Flange

(b) Web

Figure H.1: Specimen 1 – Coupons

(a) Flange

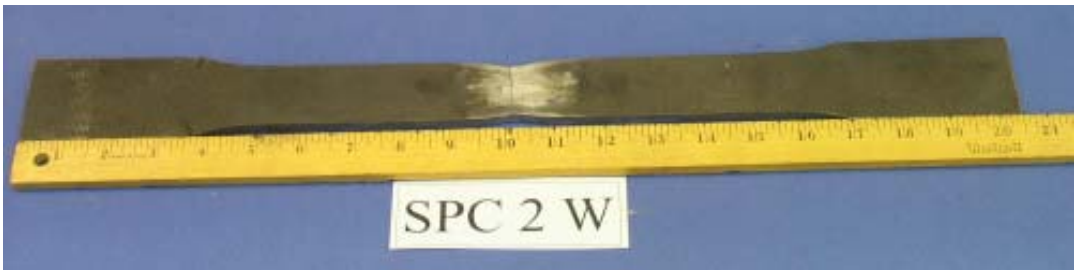

(b) Web

Figure H.2: Specimen 2 – Coupons

(a) Flange

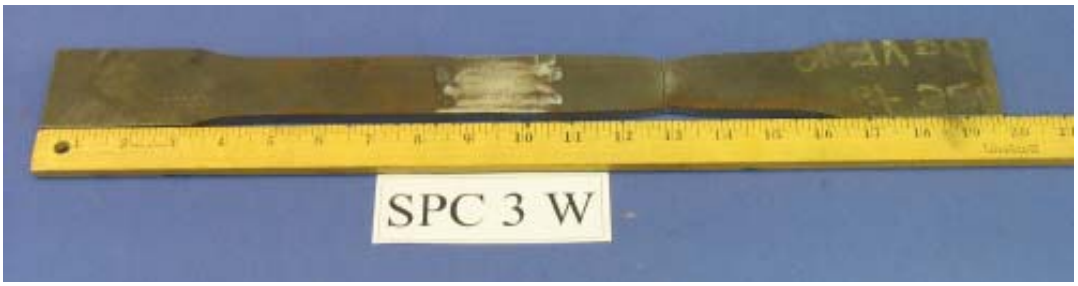

(b) Web

Figure H.3: Specimen 3 – Coupons

(a) Flange

(b) Web

Figure H.4: Specimen 4 – Coupons

(a) Flange

(b) Web

Figure H.5: Specimen 5 – Coupons

(a) Flange

(b) Web

Figure H.6: Specimen 6 – Coupons

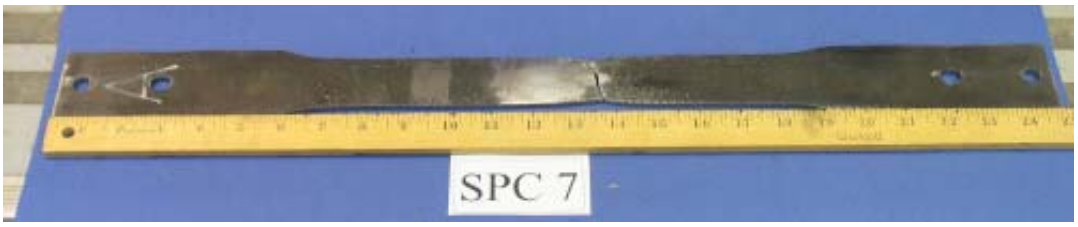

Figure H.7: Specimen 7 – Coupon

Figure H.8: Specimen 8 – Coupon

Figure H.9: Specimen 9 – Coupon

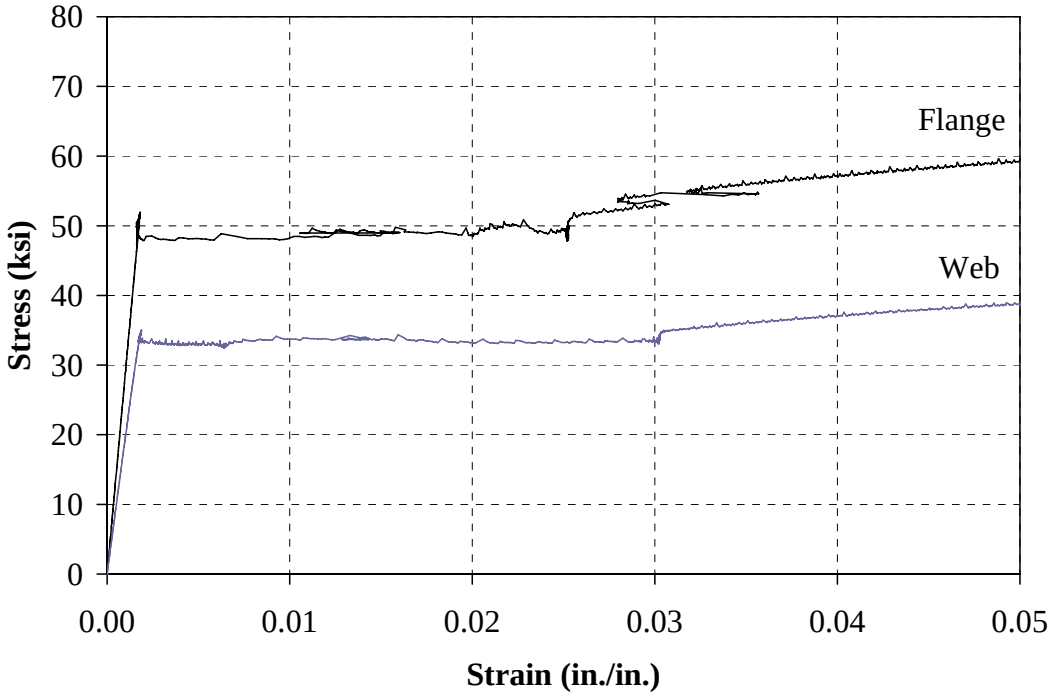

(a) Initial Curve

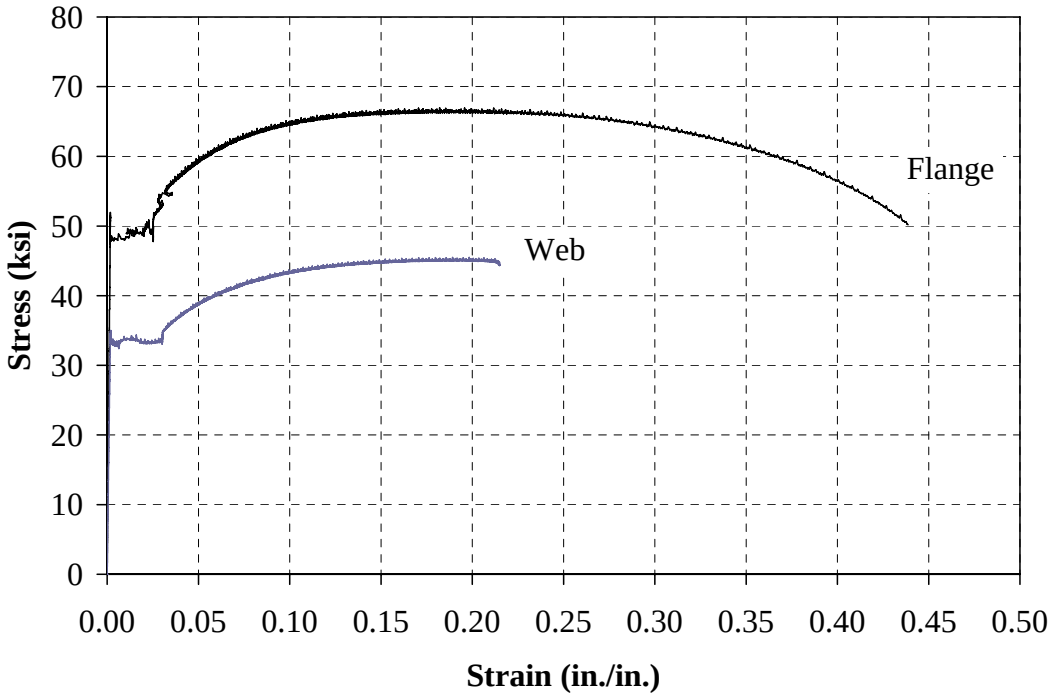

(b) Complete Curve

Figure H.10: Specimen 1 – Stress-Strain Relationship

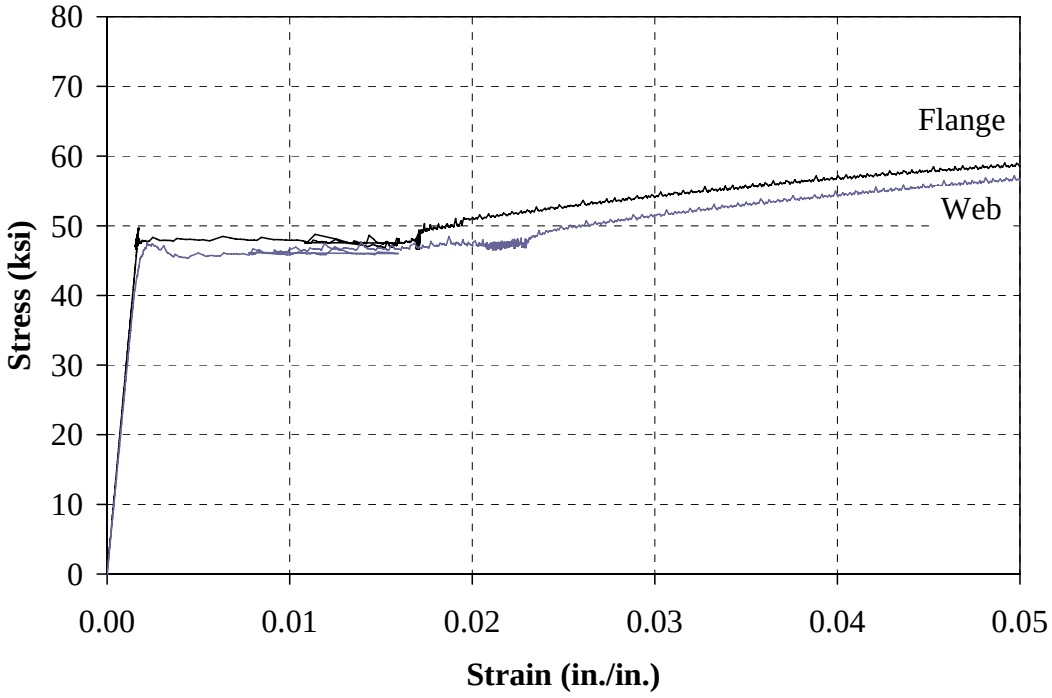

(a) Initial Curve

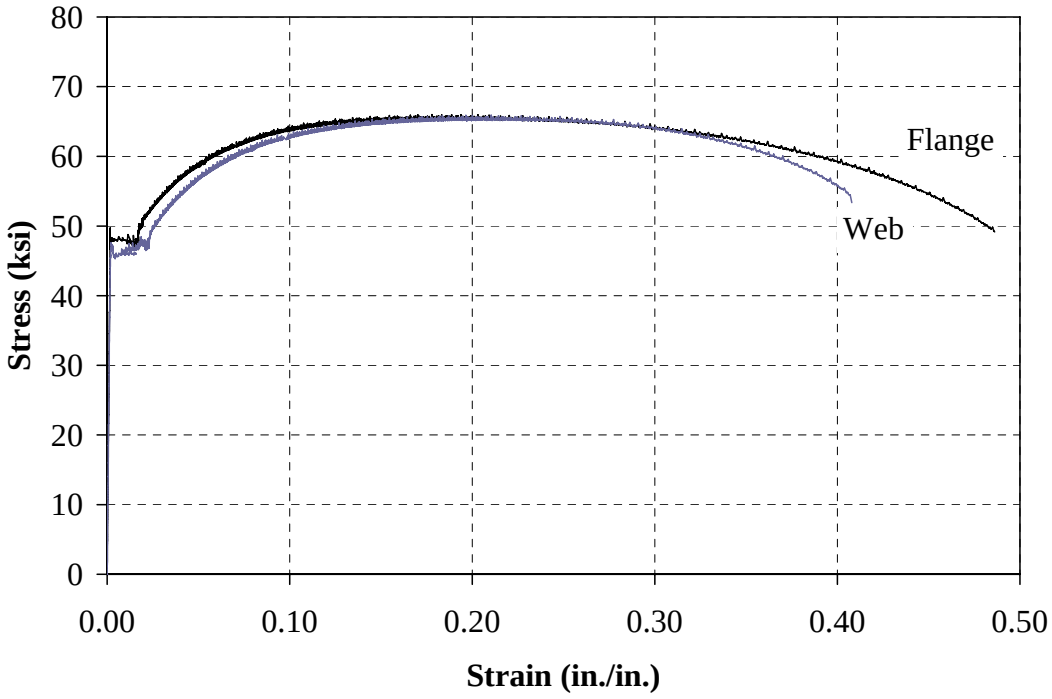

(b) Complete Curve

Figure H.11: Specimen 2 – Stress-Strain Relationship

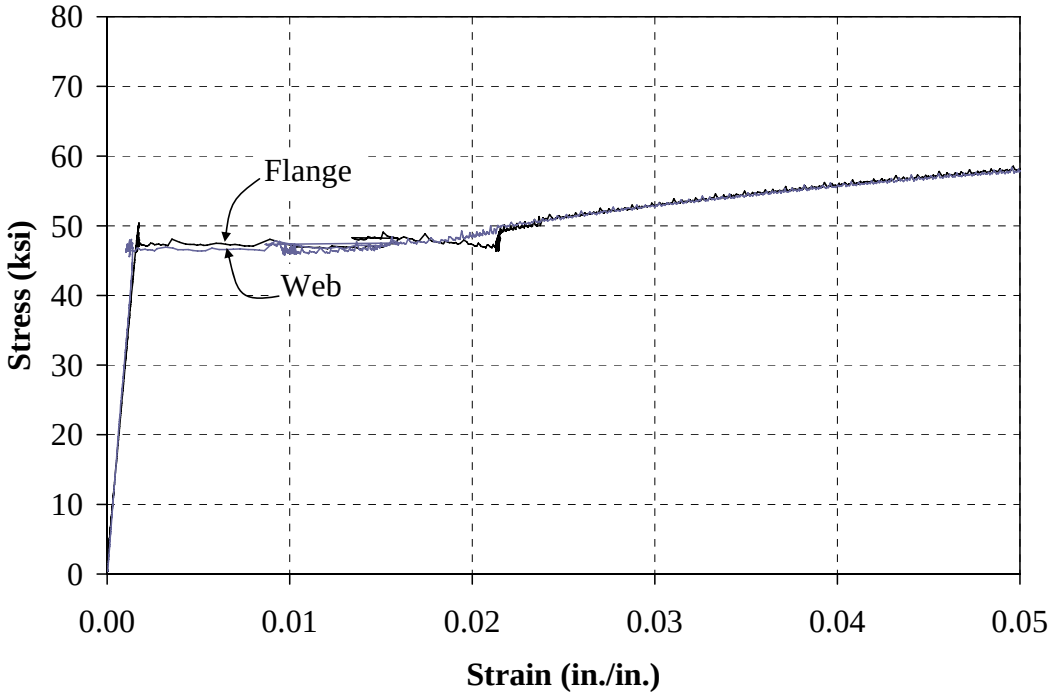

(a) Initial Curve

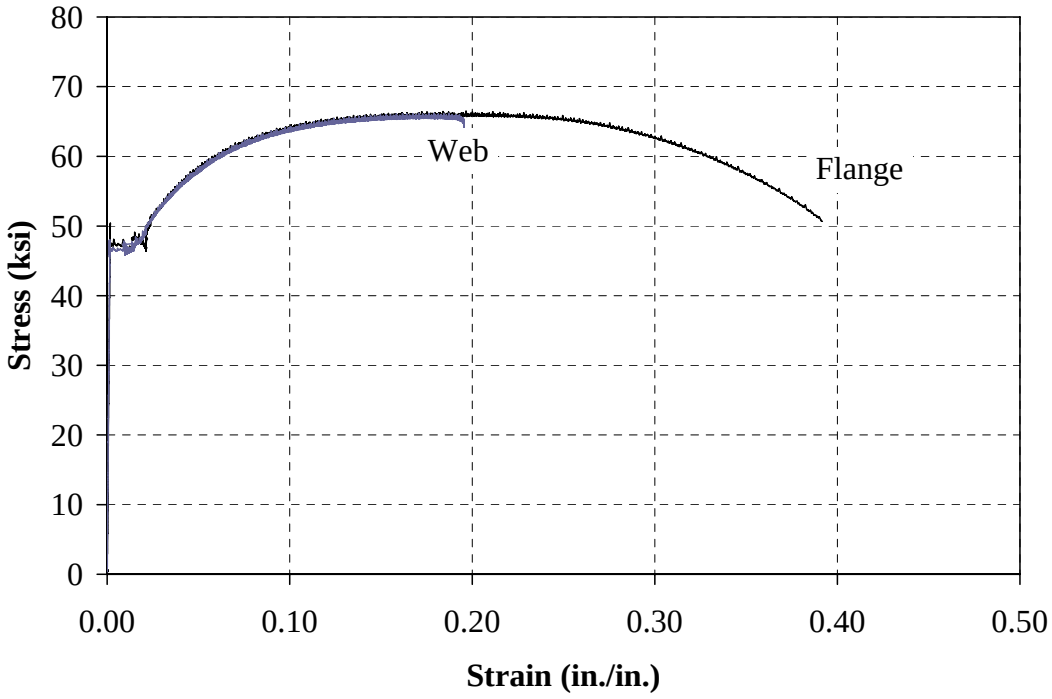

(b) Complete Curve

Figure H.12: Specimen 3 – Stress-Strain Relationship

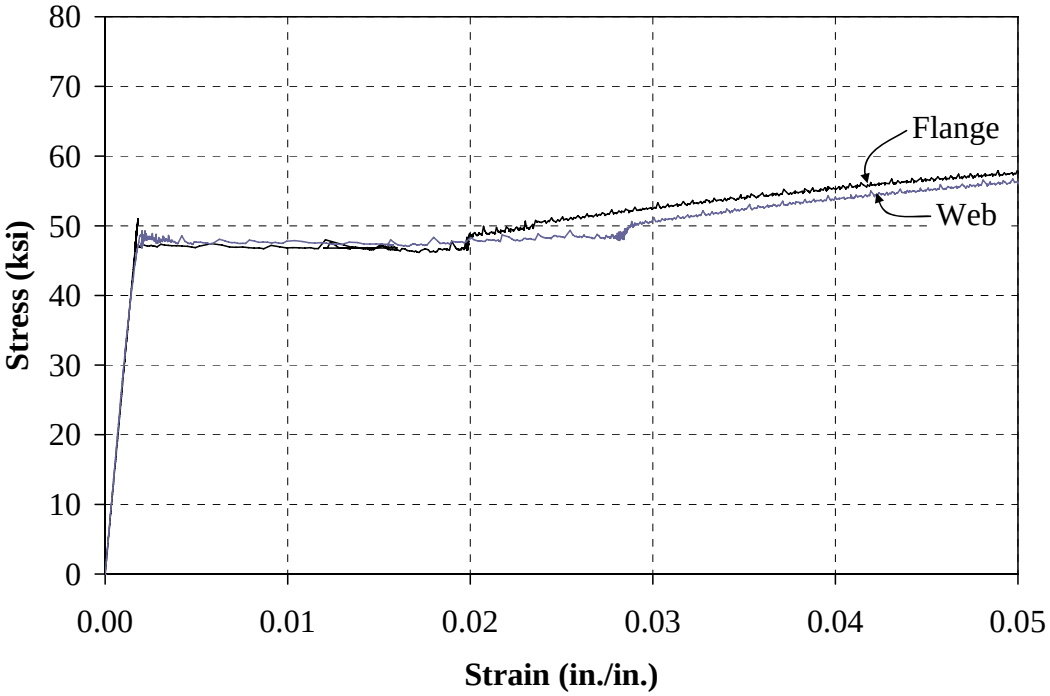

(a) Initial Curve

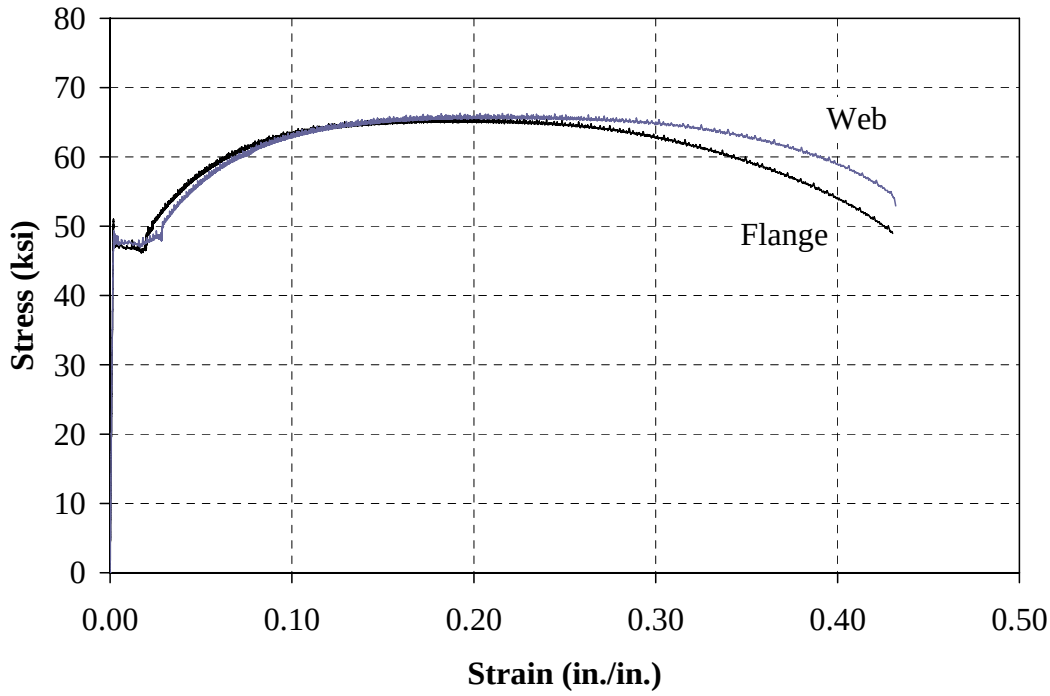

(b) Complete Curve

Figure H.13: Specimen 4 – Stress-Strain Relationship

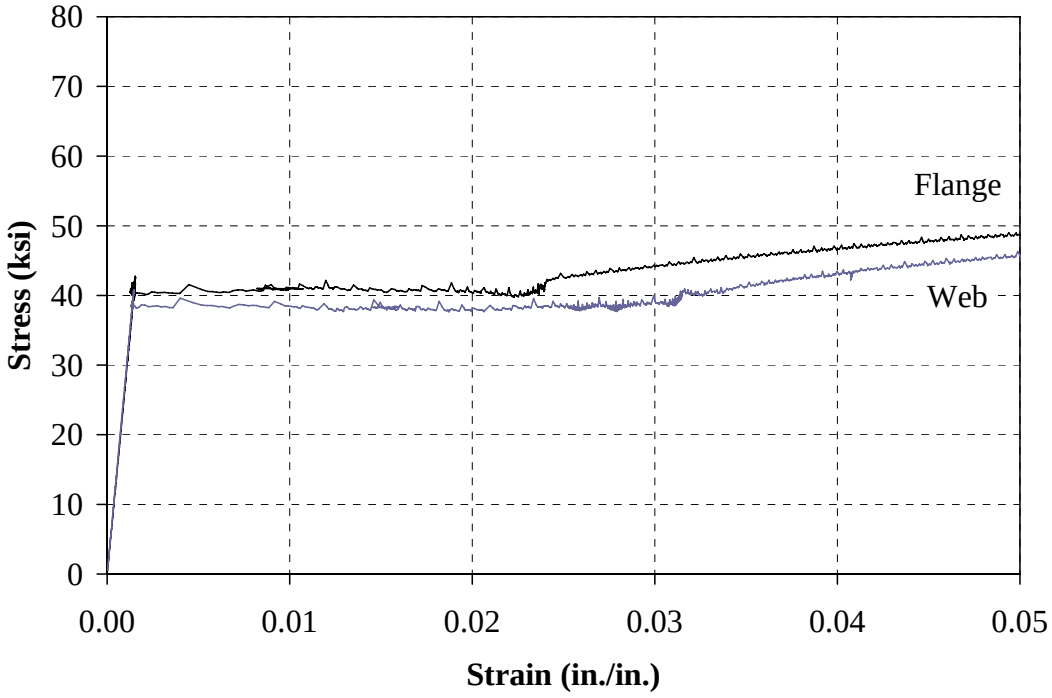

(a) Initial Curve

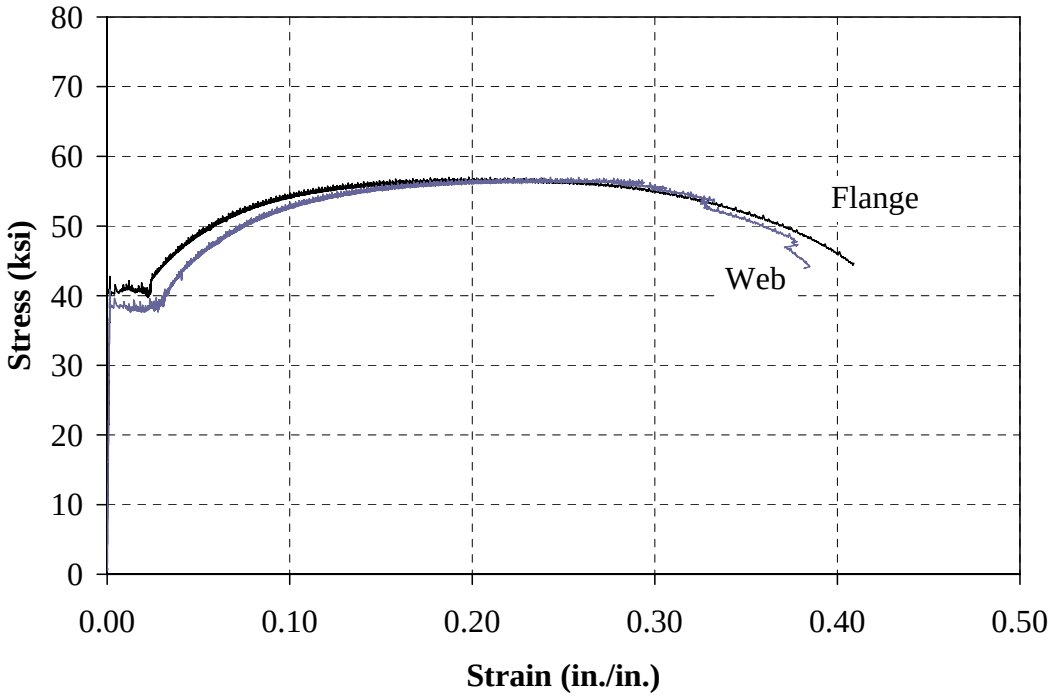

(b) Complete Curve

Figure H.14: Specimen 5 – Stress-Strain Relationship

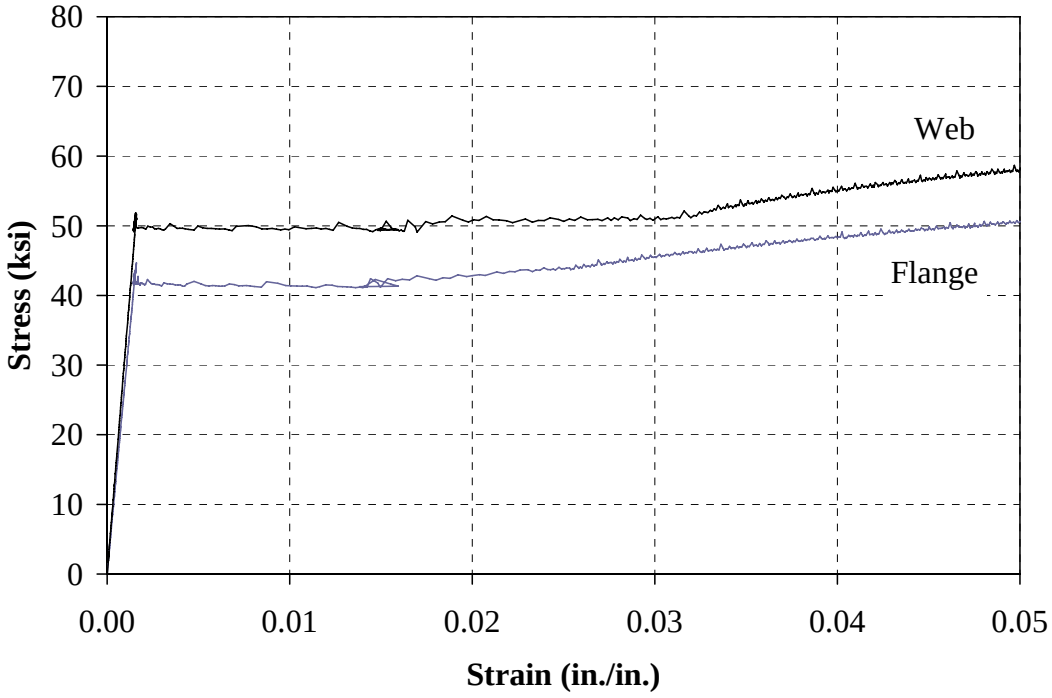

(a) Initial Curve

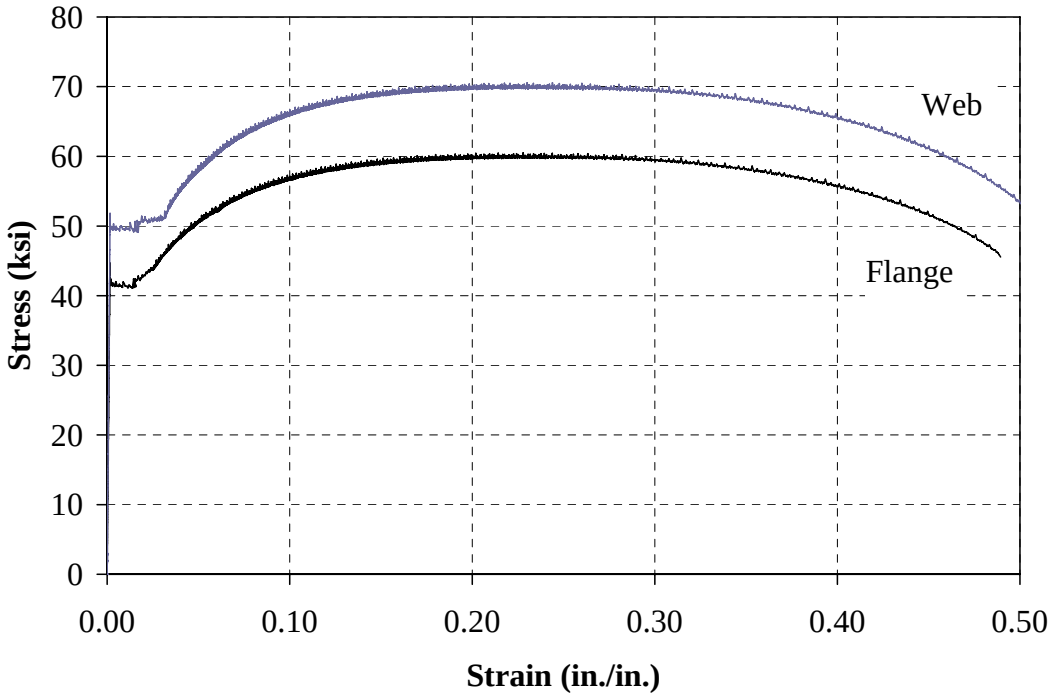

(b) Complete Curve

Figure H.15: Specimen 6 – Stress-Strain Relationship

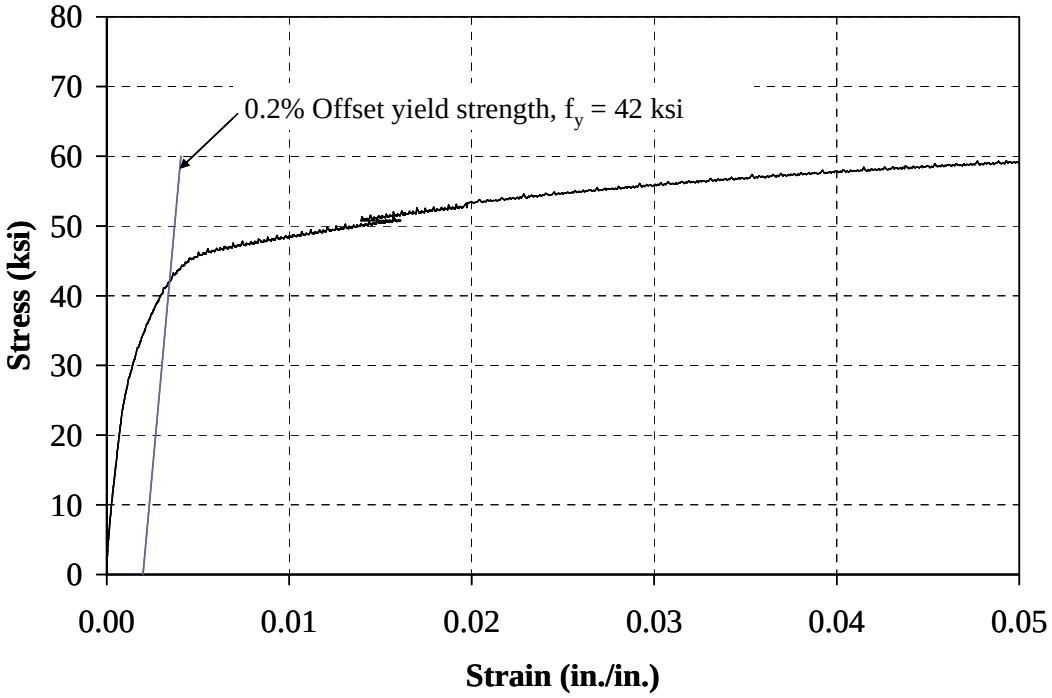

(a) Initial Curve

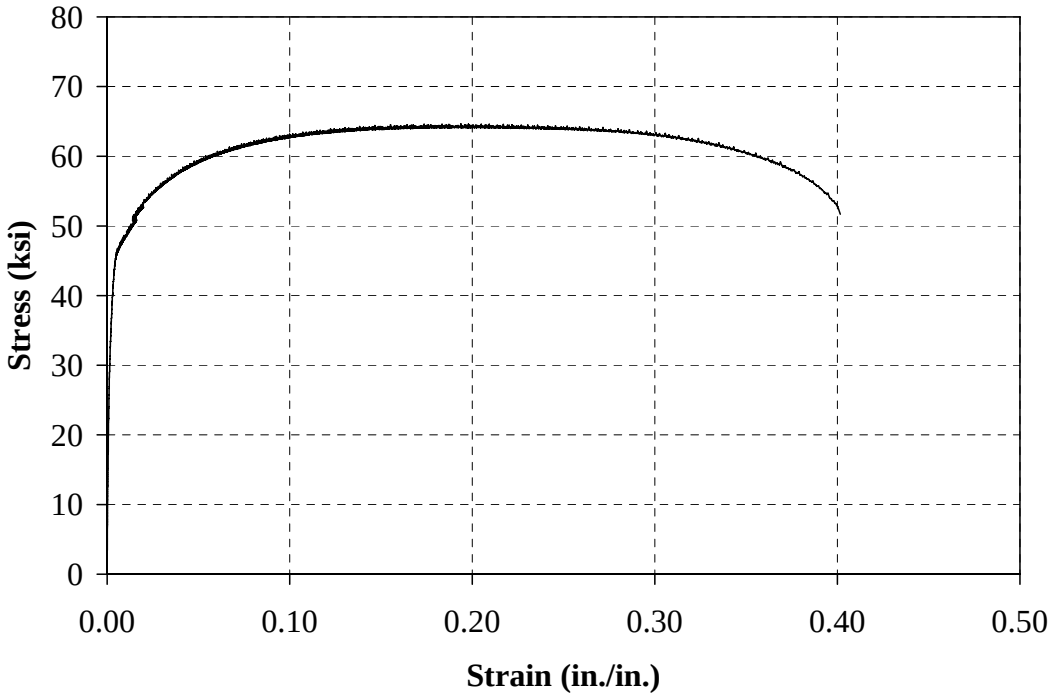

(b) Complete Curve

Figure H.16: Specimen 7 – Stress-Strain Relationship

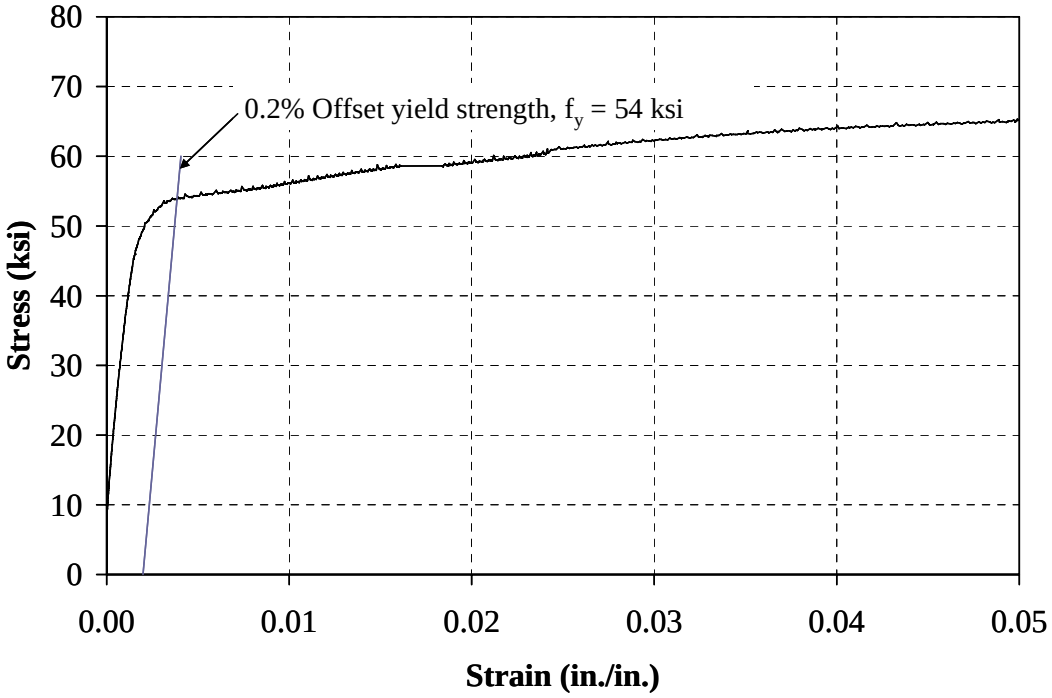

(a) Initial Curve

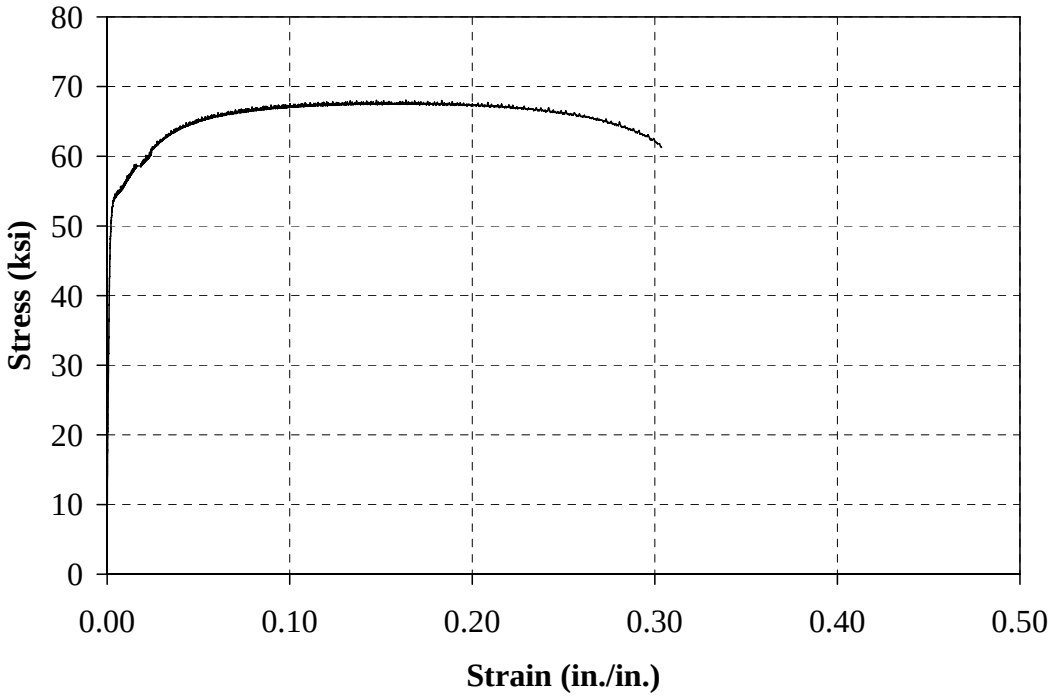

(b) Complete Curve

Figure H.17: Specimen 8 – Stress-Strain Relationship

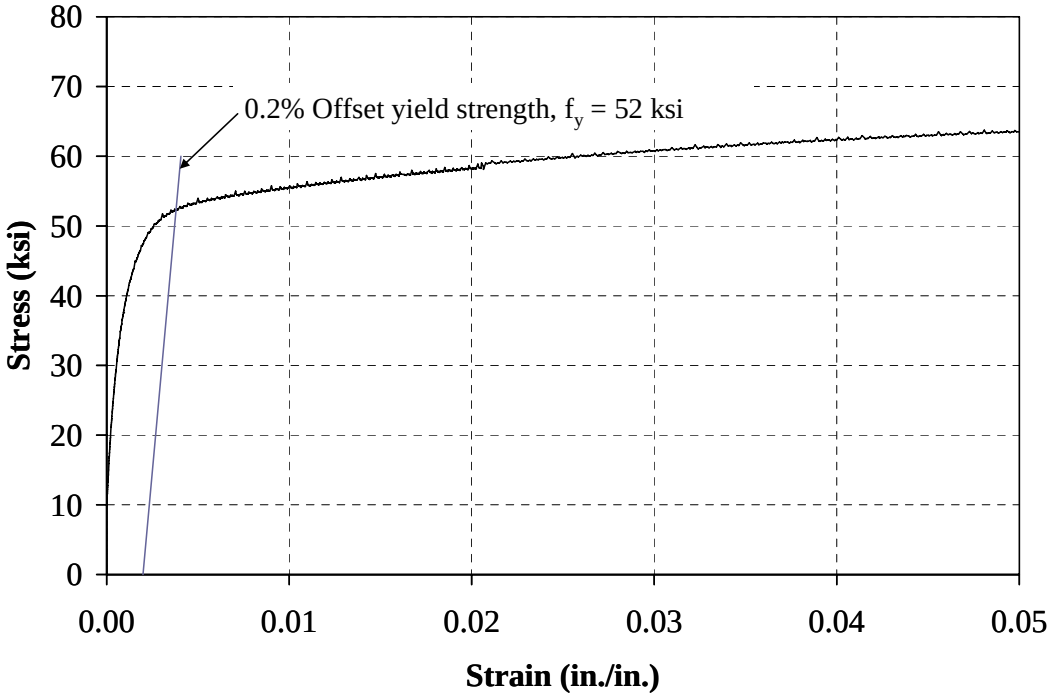

(a) Initial Curve

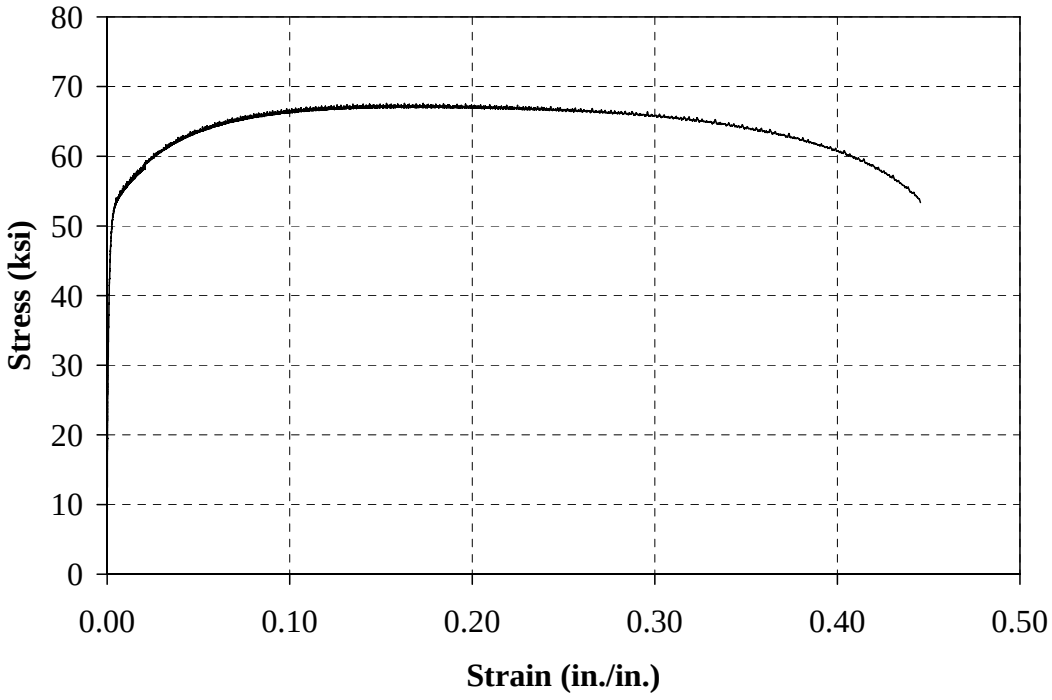

(b) Complete Curve

Figure H.18: Specimen 9 – Stress-Strain Relationship

APPENDIX I

EXPERIMENTAL RESULTS

Appendix I: Experimental Results

Specimen 1 (HP8x36, Weak, 9 ksi)

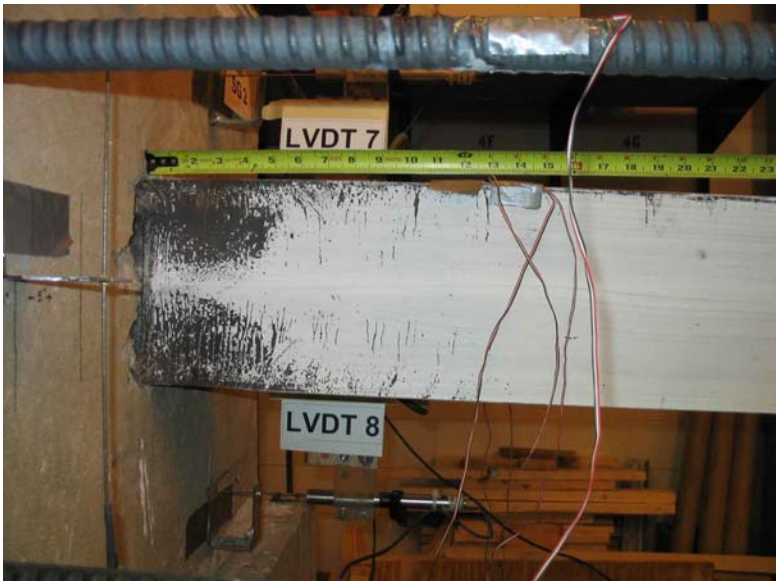

(a) West Side

(b) East Side

Figure I.1: Specimen 1 – Yielding (3.00 in., 80th Cycle)

(a) Top

(b) Bottom

Figure I.2: Specimen 1 – Flange Buckling (3.00 in., 80th Cycle)

(a) NW Flange

(b) NE Flange

Figure I.3: Specimen 1 – Crack on Steel Pile (3.00 in., 80th Cycle)

(c) SW Flange

(d) SE Flange

Figure I.3: Specimen 1 – Crack on Steel Pile (3.00 in., 80th Cycle) (Continue)

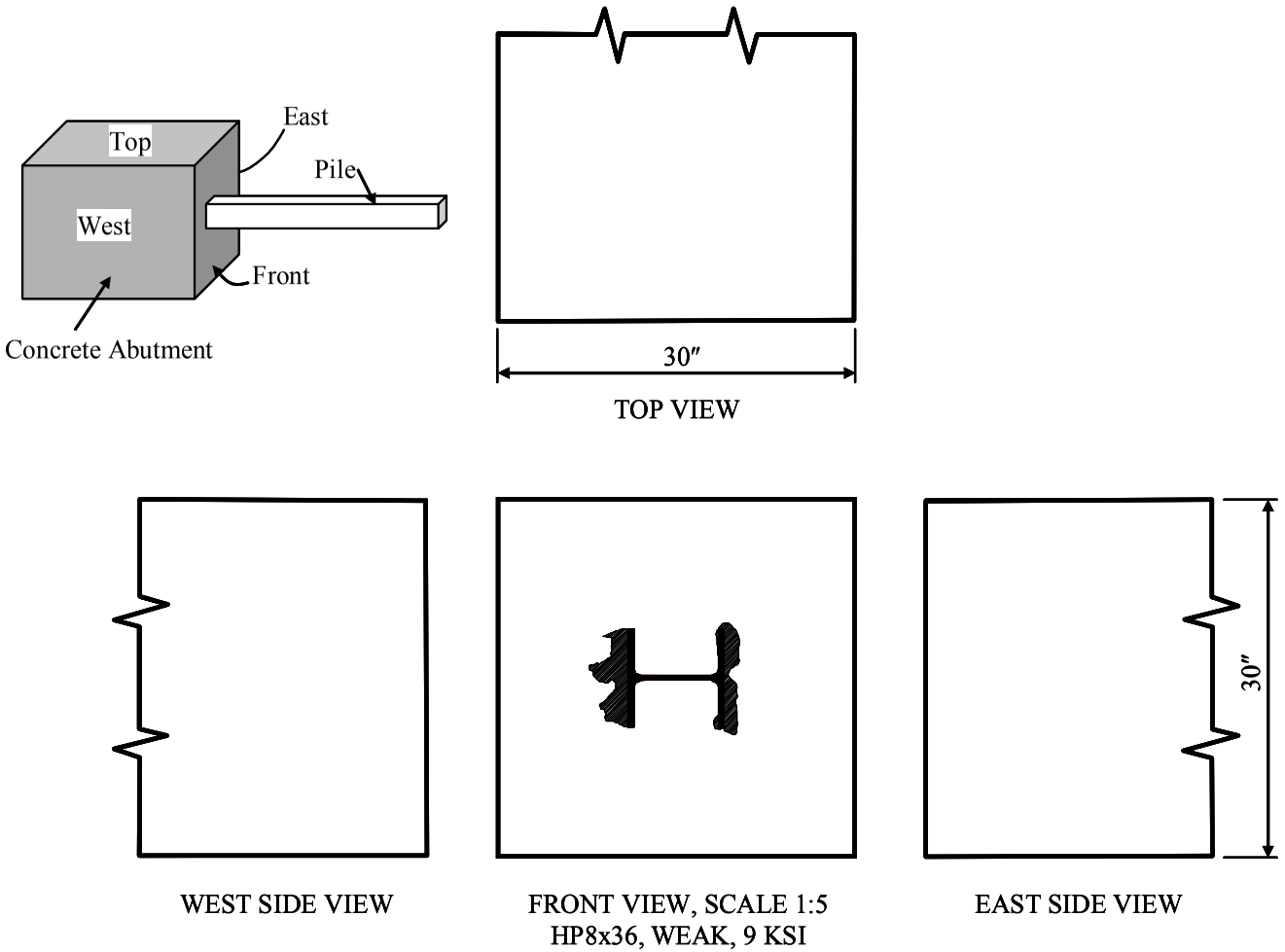

Figure I.4: Specimen 1 – Crack on Concrete Abutment (Overall)

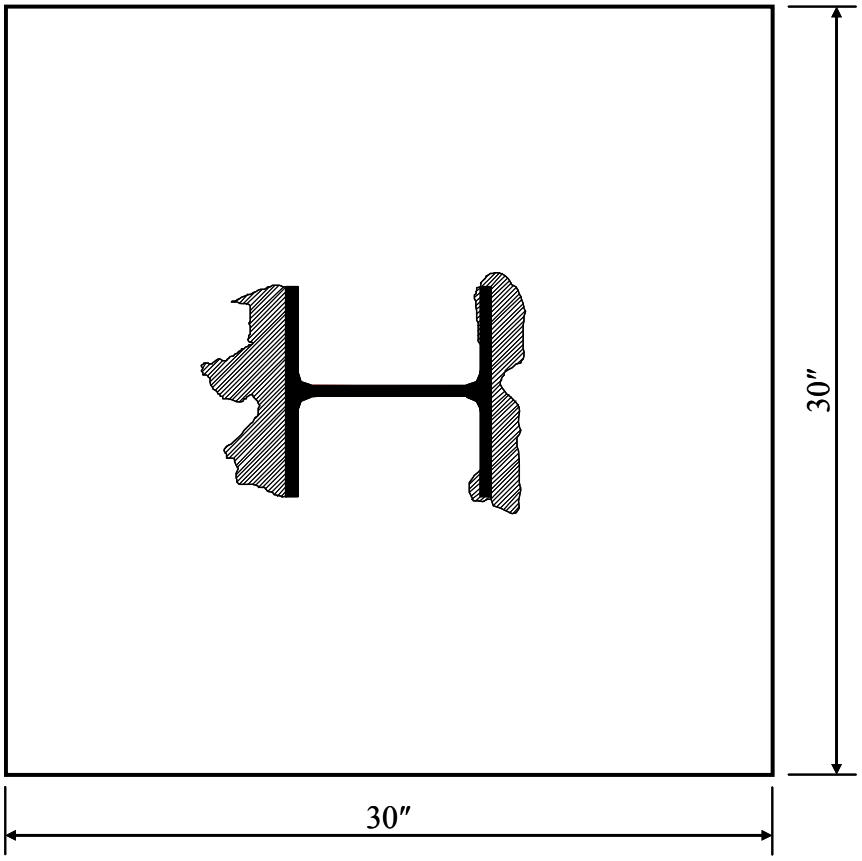

Figure I.5: Specimen 1 – Crack on Concrete Abutment (Front View)

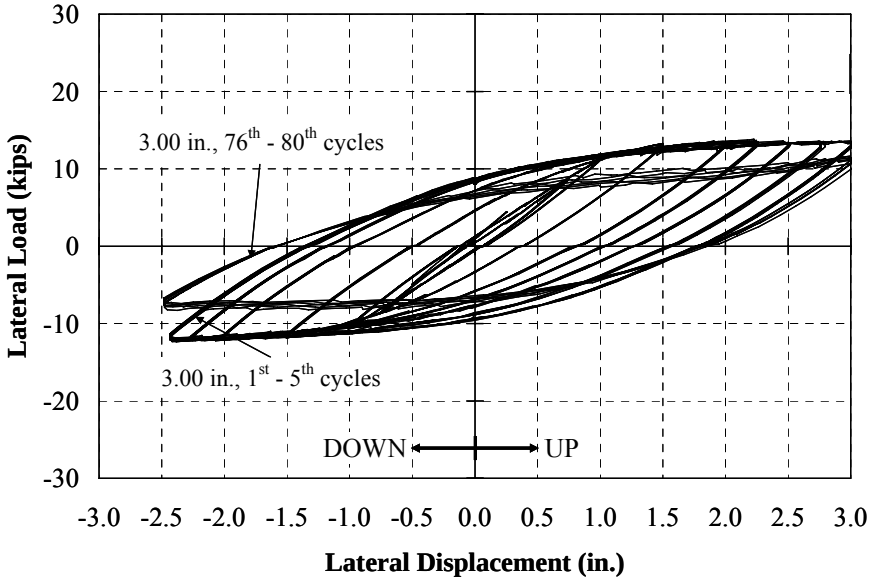

Figure I.6: Specimen 1 – Summary of Lateral Load-Deflection Curves

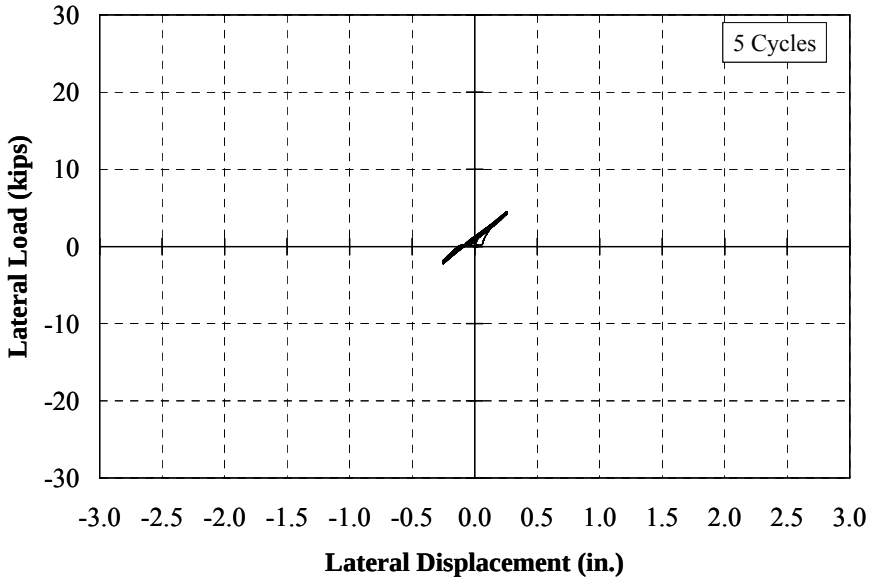

Figure I.7: Specimen 1 – Lateral Load-Deflection Response (±0.25 in.)

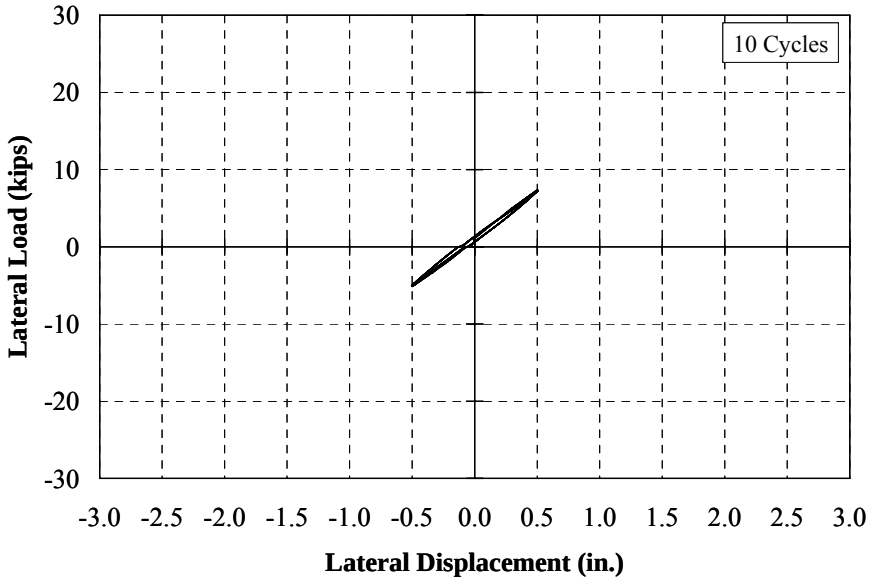

Figure I.8: Specimen 1 – Lateral Load-Deflection Response (±0.50 in.)

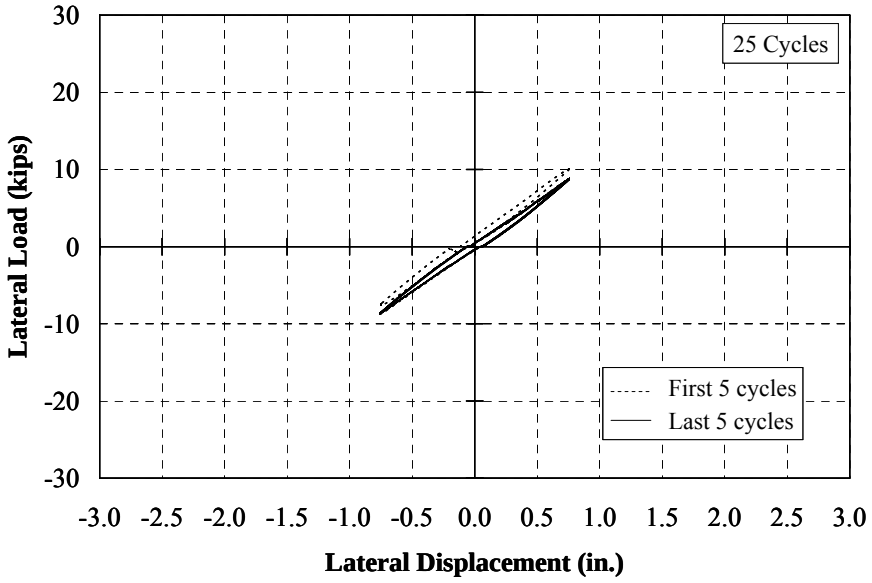

Figure I.9: Specimen 1 – Lateral Load-Deflection Response (±0.75 in.)

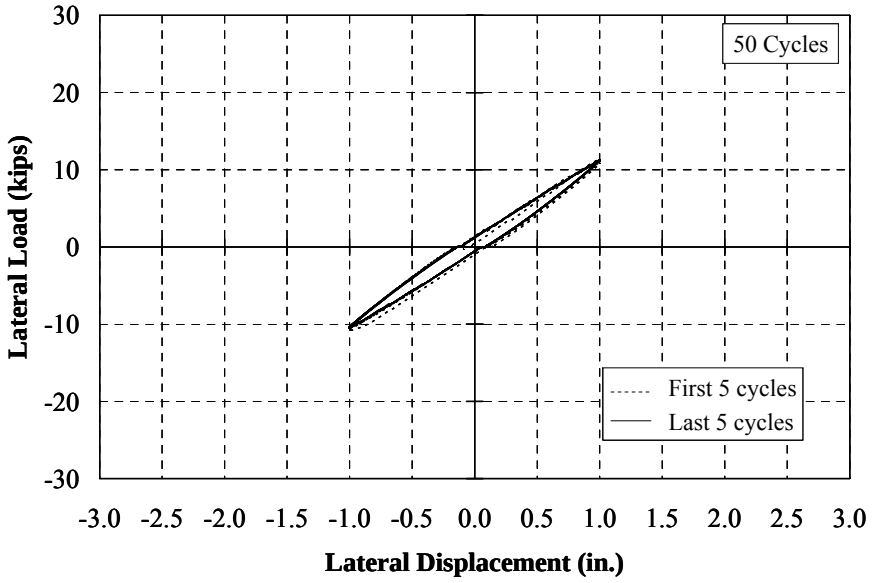

Figure I.10: Specimen 1 – Lateral Load-Deflection Response (±1.00 in.)

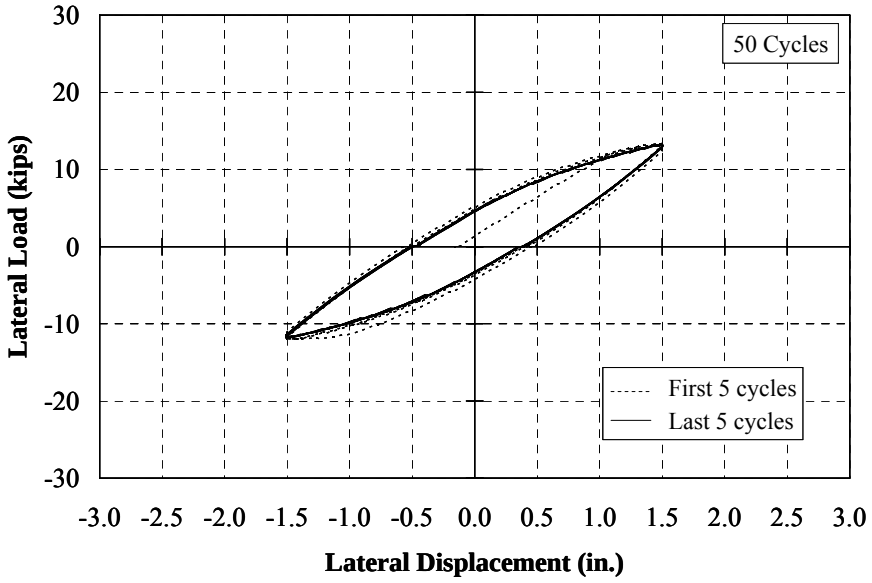

Figure I.11: Specimen 1 – Lateral Load-Deflection Response (±1.50 in.)

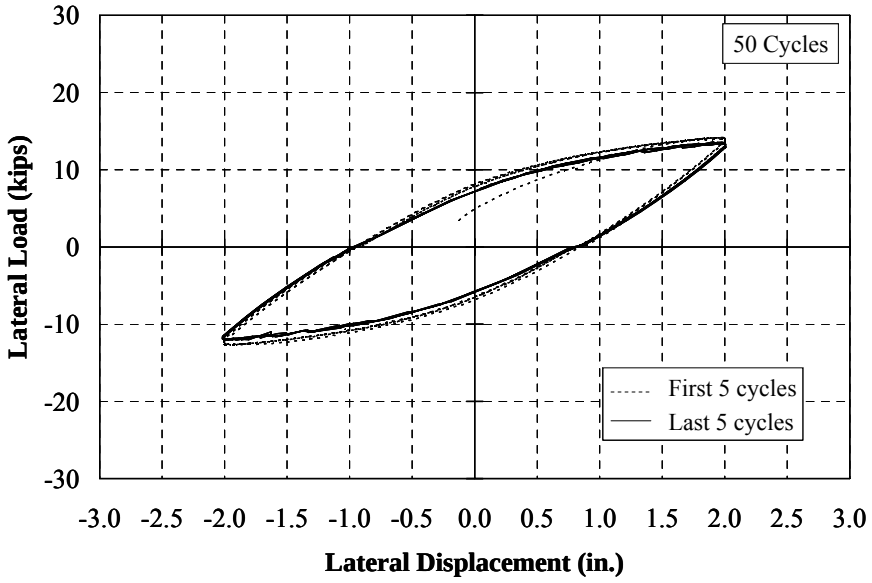

Figure I.12: Specimen 1 – Lateral Load-Deflection Response (±2.00 in.)

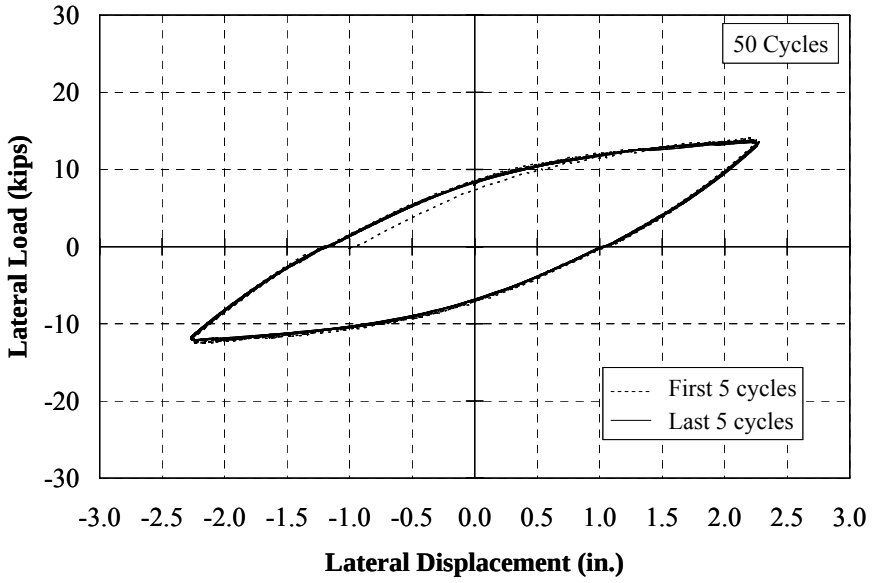

Figure I.13: Specimen 1 – Lateral Load-Deflection Response (±2.25 in.)

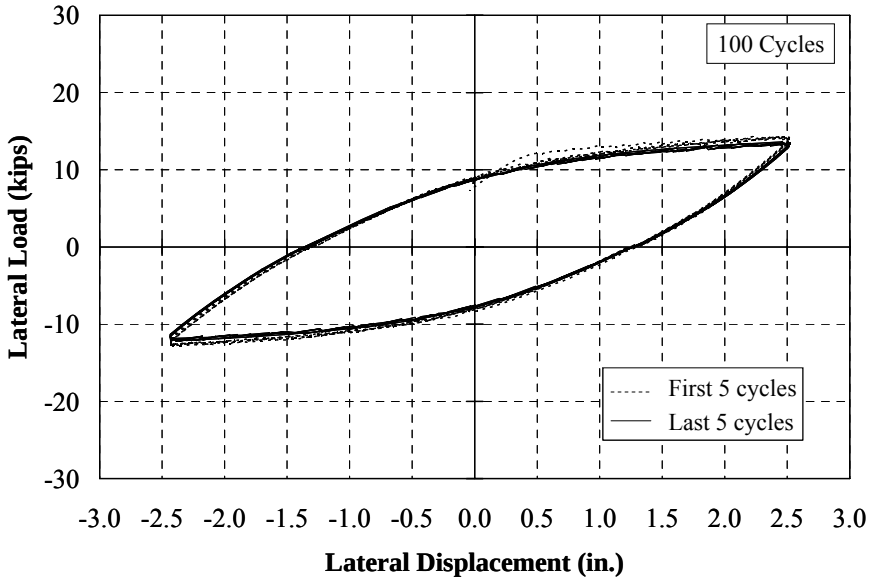

Figure I.14: Specimen 1 – Lateral Load-Deflection Response (±2.50 in.)

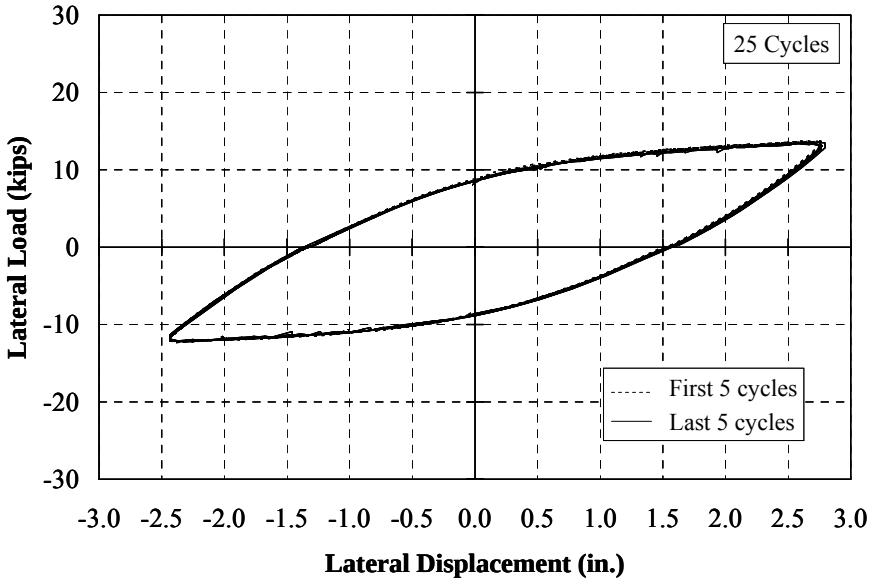

Figure I.15: Specimen 1 – Lateral Load-Deflection Response (±2.75 in.)

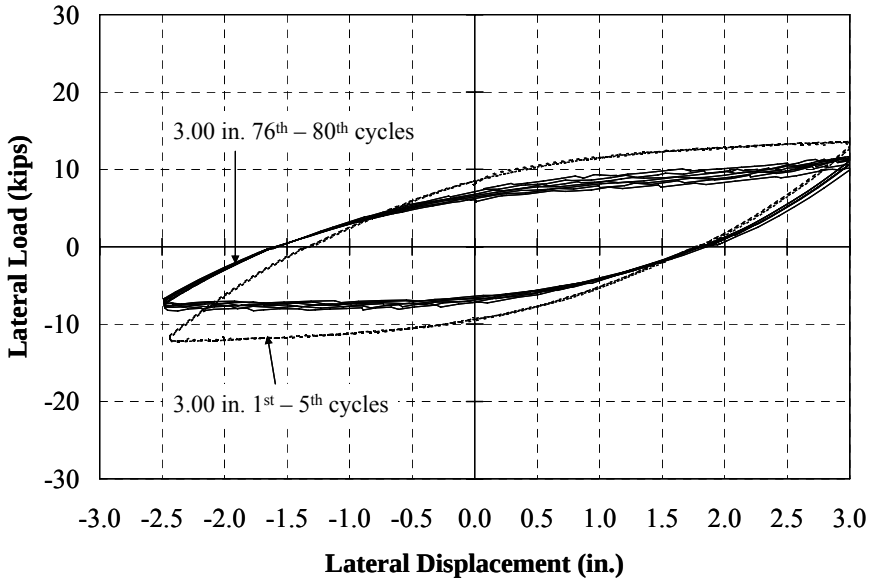

Figure I.16: Specimen 1 – Lateral Load-Deflection Response (±3.00 in.)

Specimen 2 (HP8x36, Strong, 9 ksi)

(a) West Side

(b) East Side

Figure I.17: Specimen 2 – Cracking (1.75 in., 100th Cycle)

(a) West Side

(b) East Side

Figure I.18: Specimen 2 – Deterioration at the Abutment-Pile Connection (1.75 in., 100th Cycle)

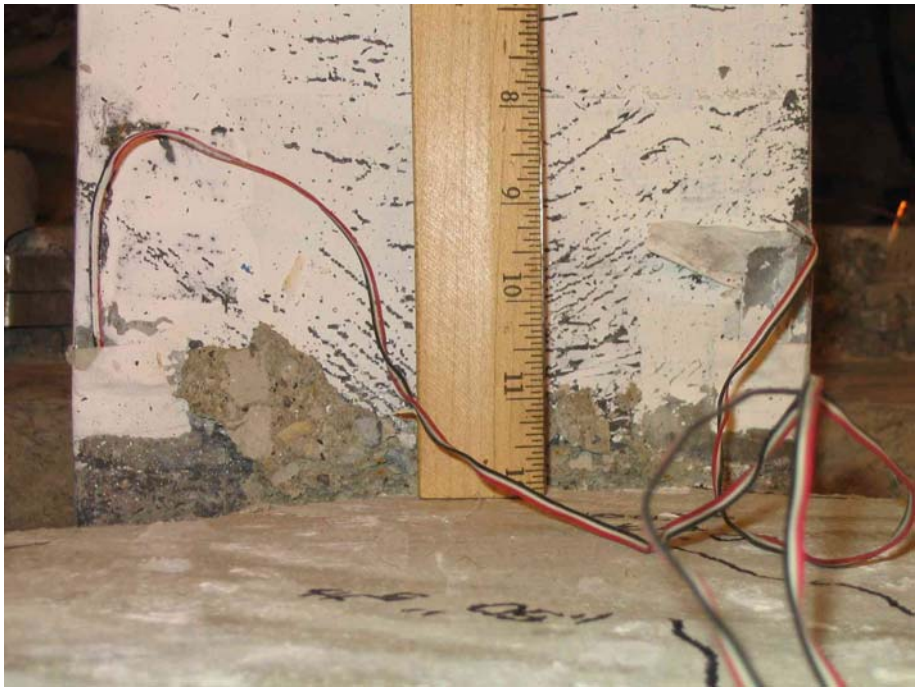

(a) Top Flange

(b) Bottom Flange

Figure I.19: Specimen 2 – Pile Yielding – (1.75 in., 100th Cycle)

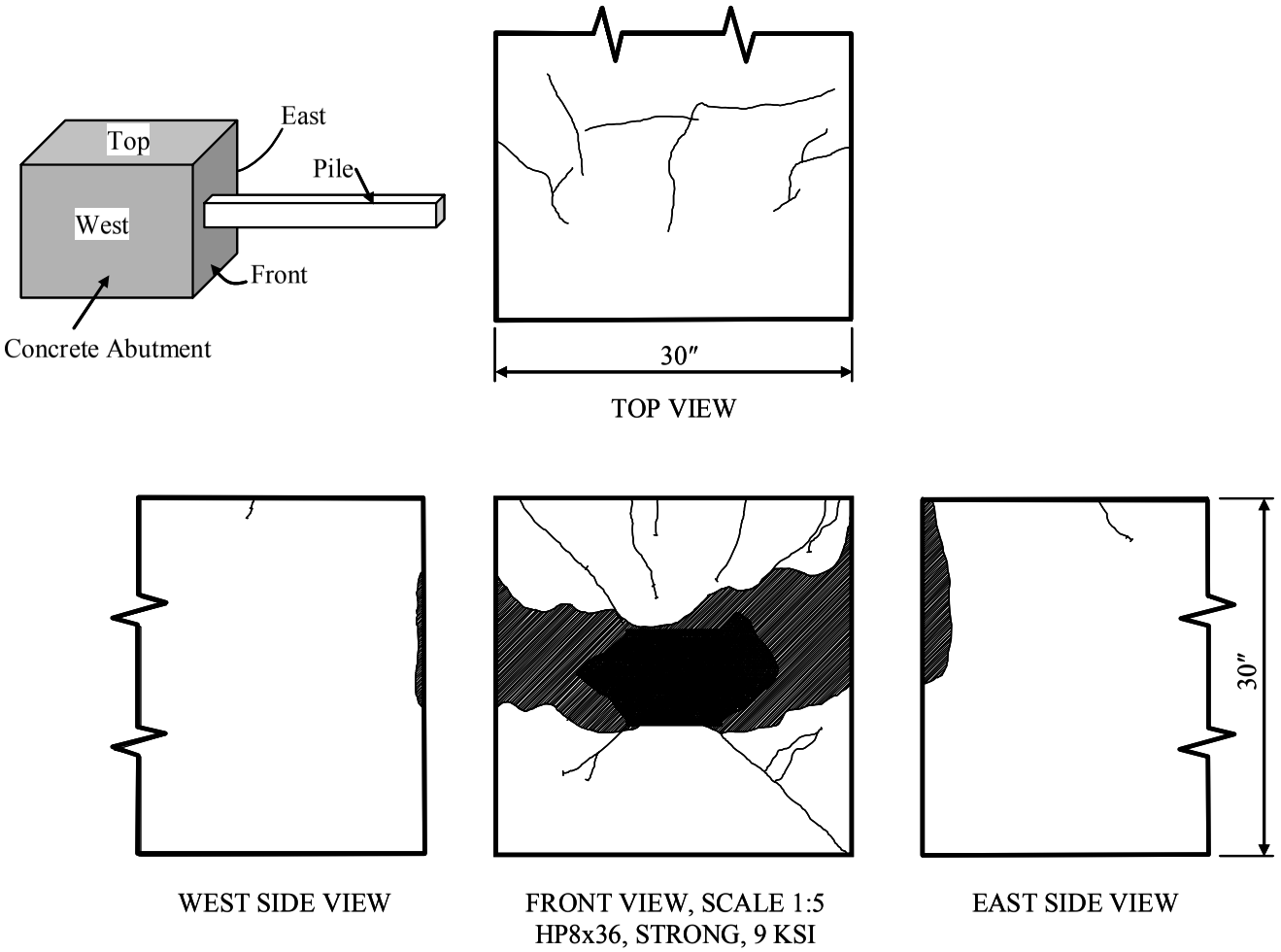

Figure I.20: Specimen 2 - Crack on Concrete Abutment (Overall)

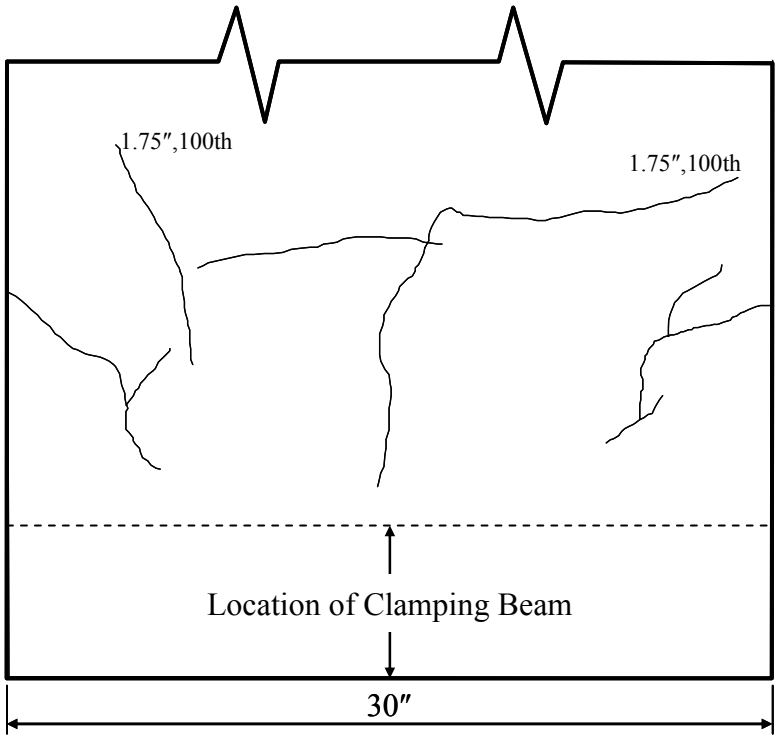

Figure I.21: Specimen 2 – Crack on Concrete Abutment (Top View)

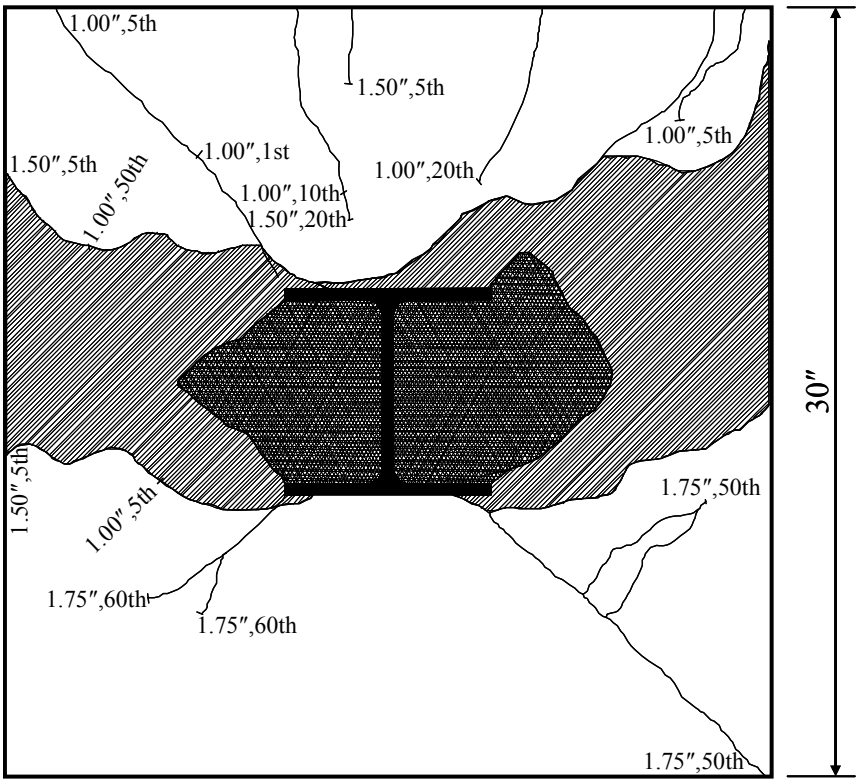

Figure I.22: Specimen 2 – Crack on Concrete Abutment (Front View)

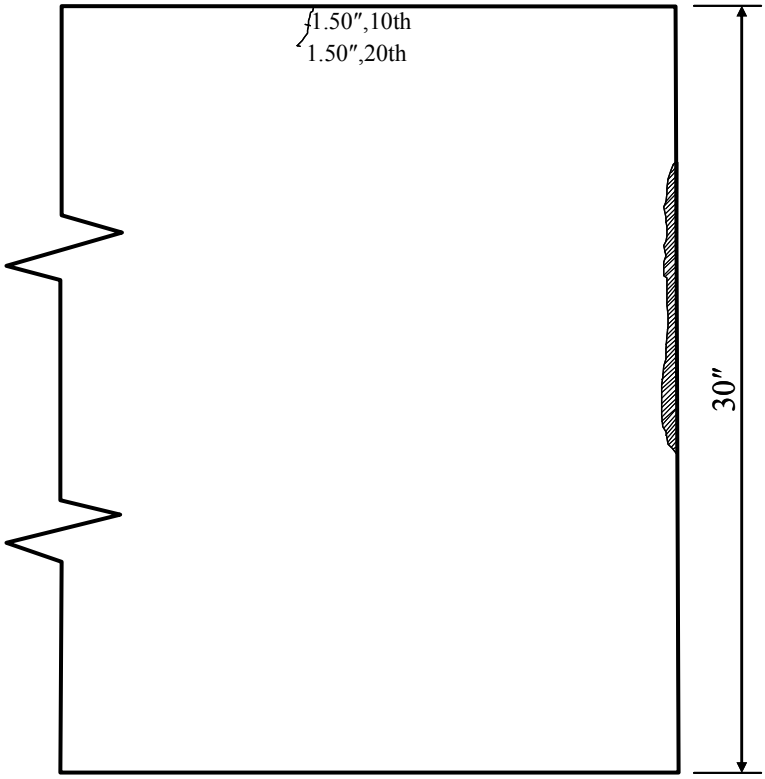

Figure I.23: Specimen 2 – Crack on Concrete Abutment (West View)

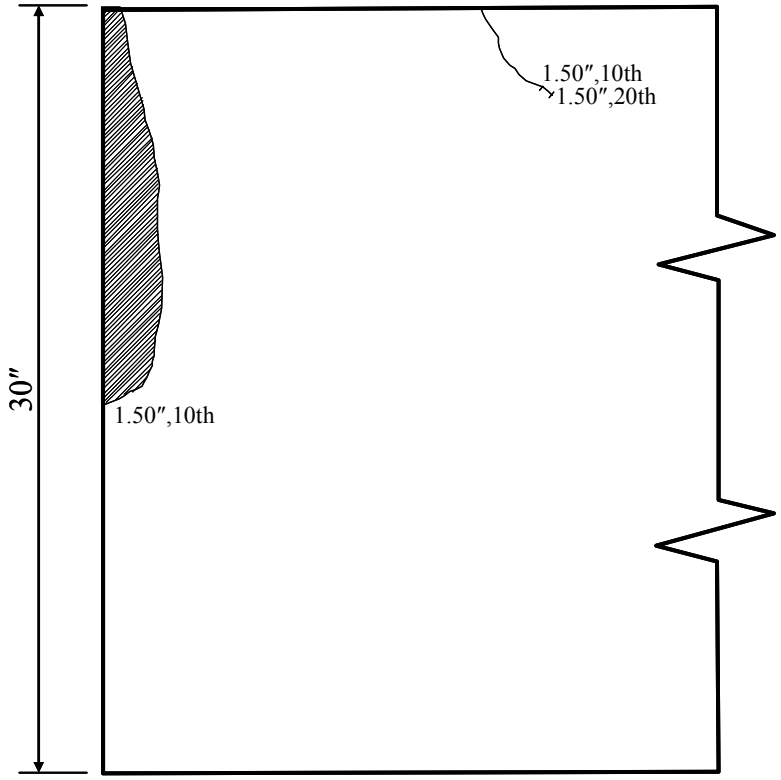

Figure I.24: Specimen 2 – Crack on Concrete Abutment (East View)

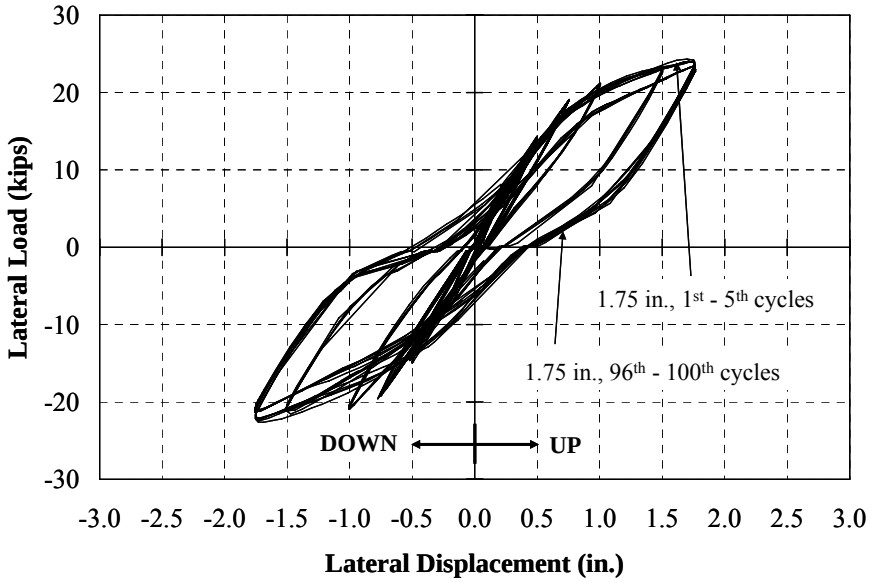

Figure I.25: Specimen 2 – Summary of Lateral Load-Deflection Curves

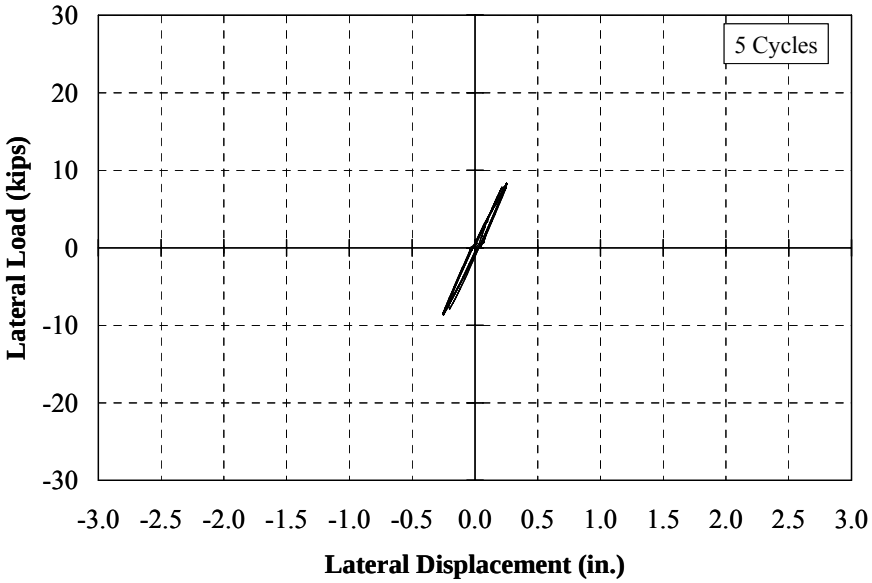

Figure I.26: Specimen 2 – Lateral Load-Deflection Response (±0.25 in.)

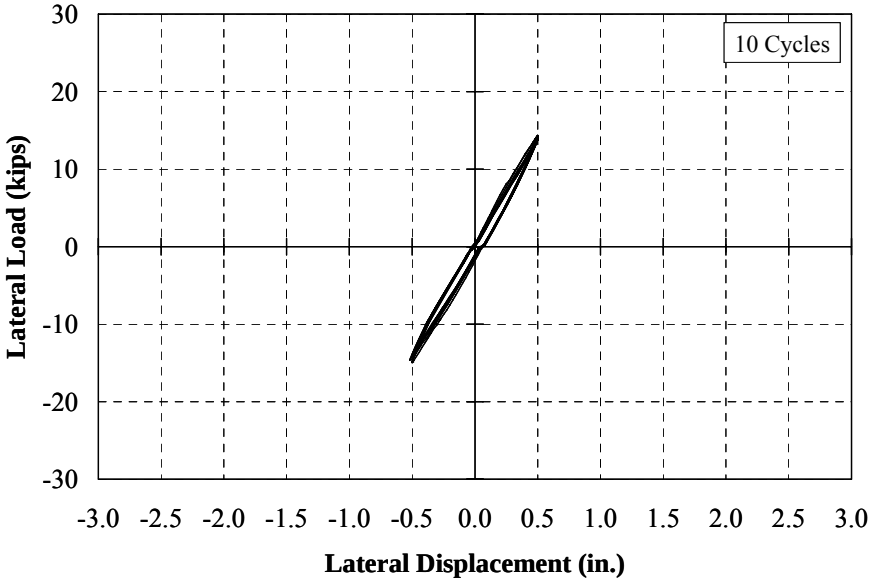

Figure I.27: Specimen 2 – Lateral Load-Deflection Response (±0.50 in.)

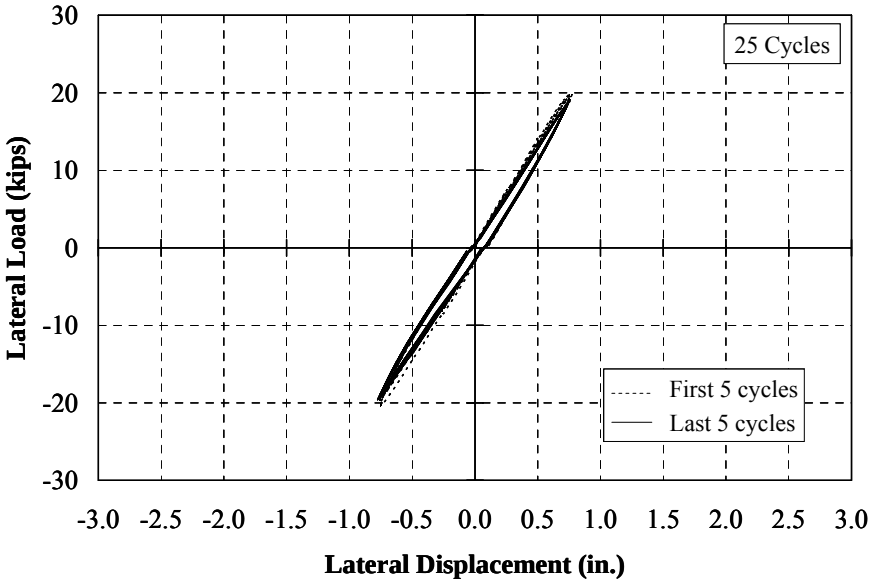

Figure I.28: Specimen 2 – Lateral Load-Deflection Response (±0.75 in.)

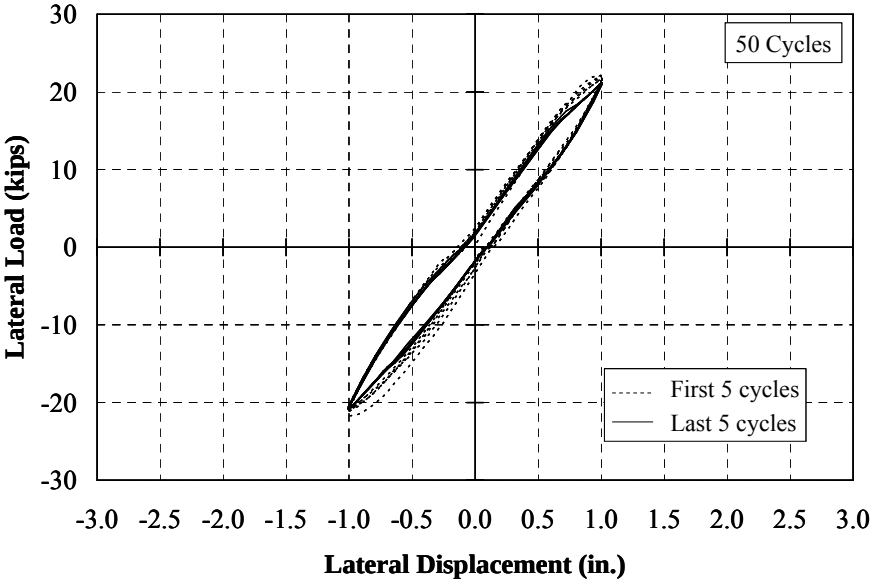

Figure I.29: Specimen 2 – Lateral Load-Deflection Response (±1.00 in.)

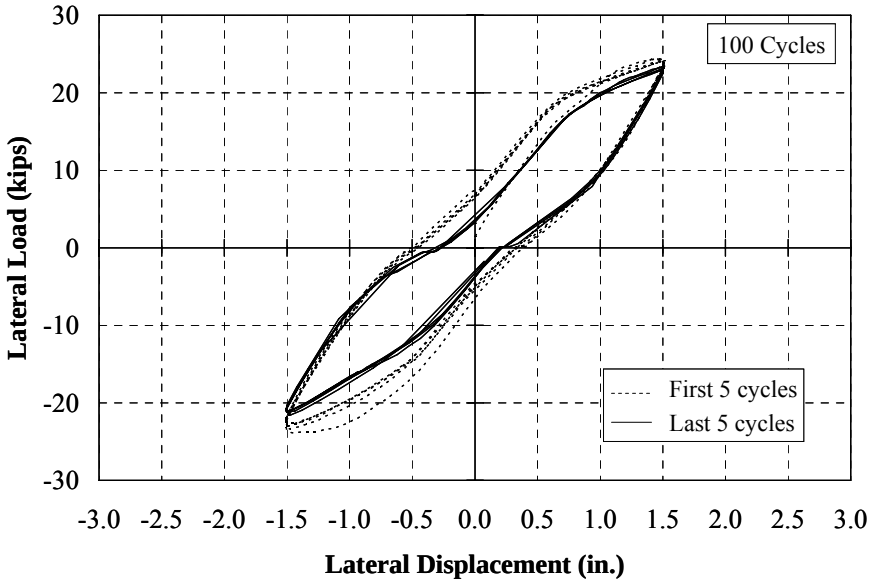

Figure I.30: Specimen 2 – Lateral Load-Deflection Response (±1.50 in.)

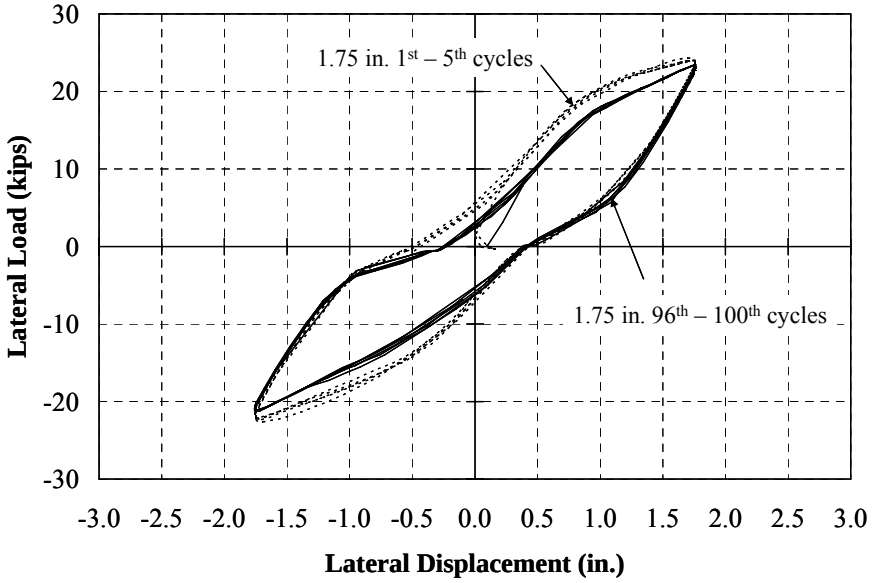

Figure I.31: Specimen 2 – Lateral Load-Deflection Response (±1.75 in.)

Specimen 3 (HP8x36, 45°, 9 ksi)

(a) West Side

(b) East Side

Figure I.32: Specimen 3 – Cracking (2.00 in., 100th Cycle)

(c) Bottom

Figure I.32: Specimen 3 – Cracking (2.00 in., 100th Cycle) (Continue)

(a) West Side

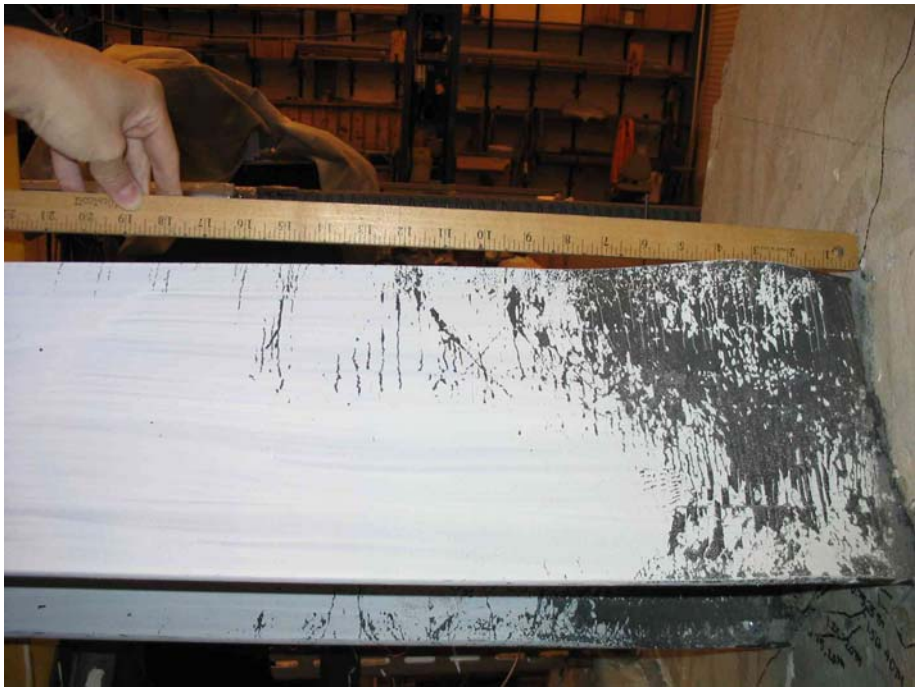

(b) East Side

Figure I.33: Specimen 3 – Pile Yielding (2.00 in., 100th Cycle)

(a) Top

(b) Bottom

Figure I.34: Specimen 3 – Flange Buckling and Web Yielding (2.00 in., 100th Cycle)

(a) North

(b) South

Figure I.35: Specimen 3 – Flange Buckling along with Crack on Pile (2.00 in., 100th Cycle)

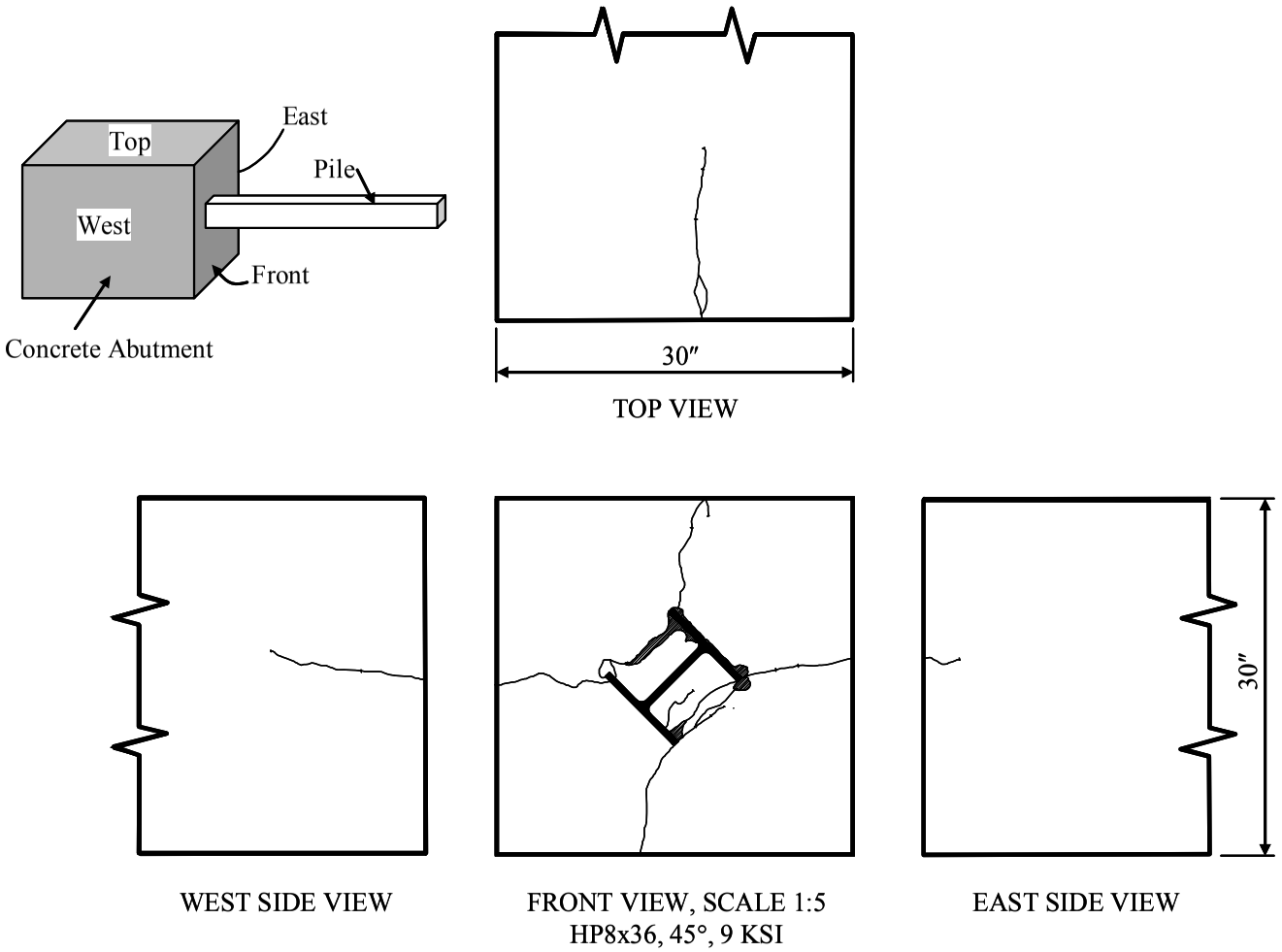

Figure I.36: Specimen 3 – Crack on Concrete Abutment (Overall)

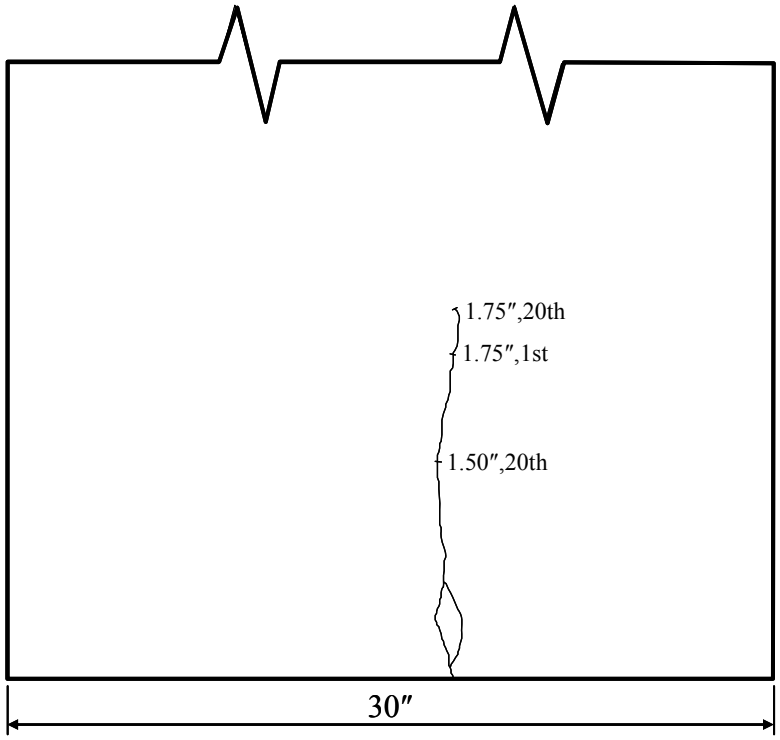

Figure I.37: Specimen 3 – Crack on Concrete Abutment (Top View)

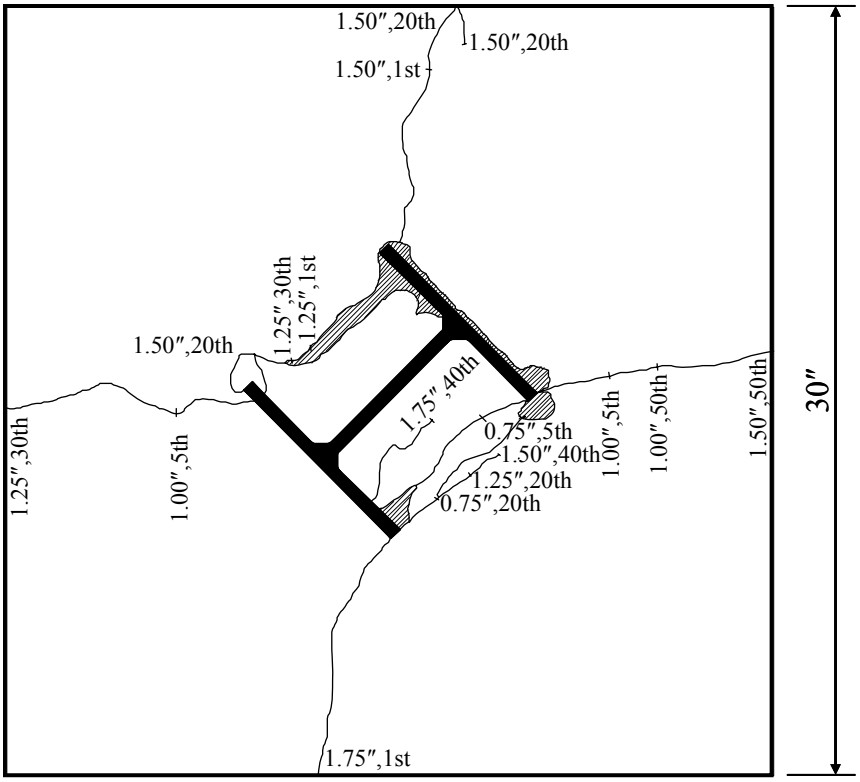

Figure I.38: Specimen 3 – Crack on Concrete Abutment (Front View)

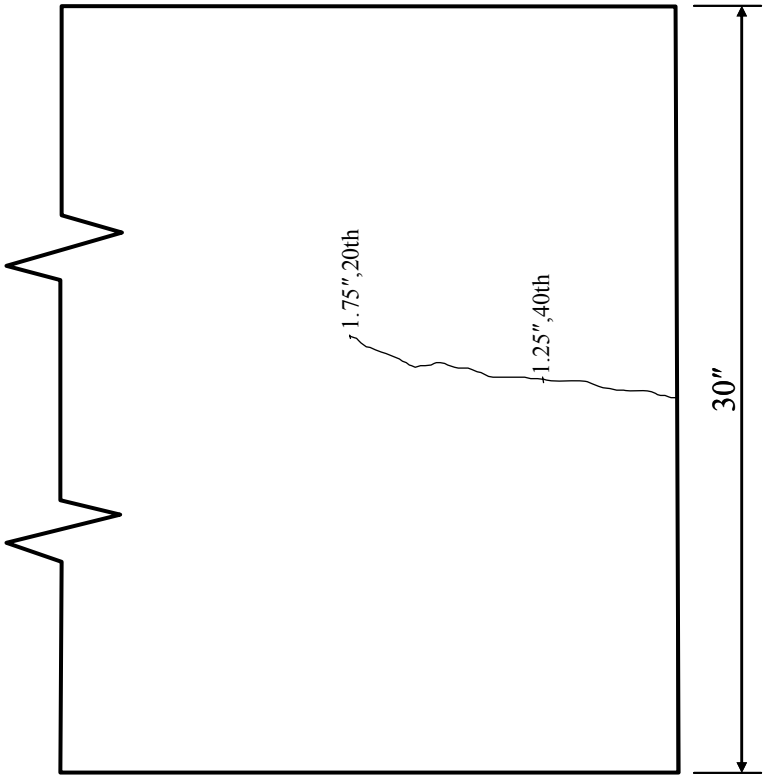

Figure I.39: Specimen 3 – Crack on Concrete Abutment (West View)

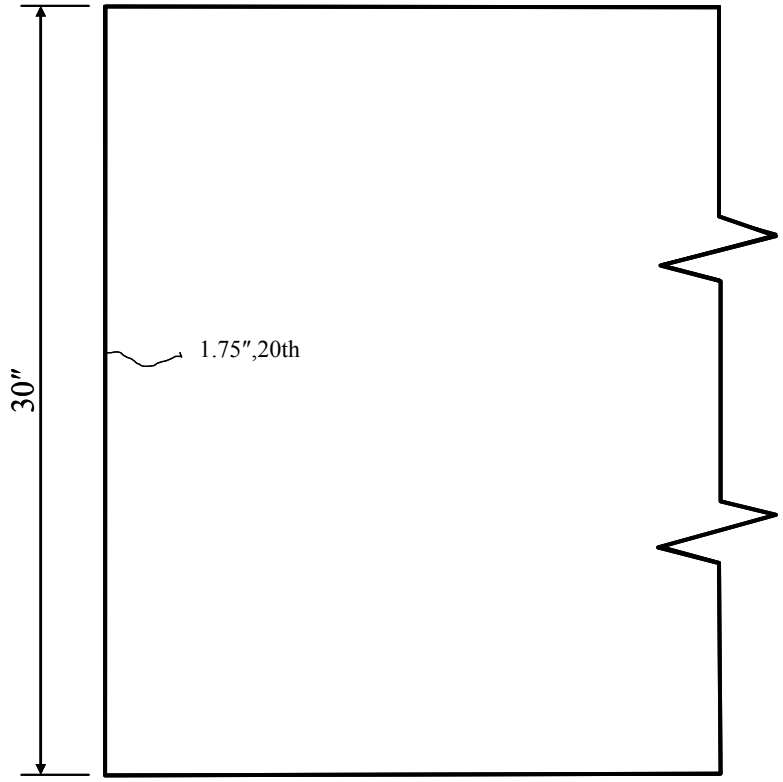

Figure I.40: Specimen 3 – Crack on Concrete Abutment (East View)

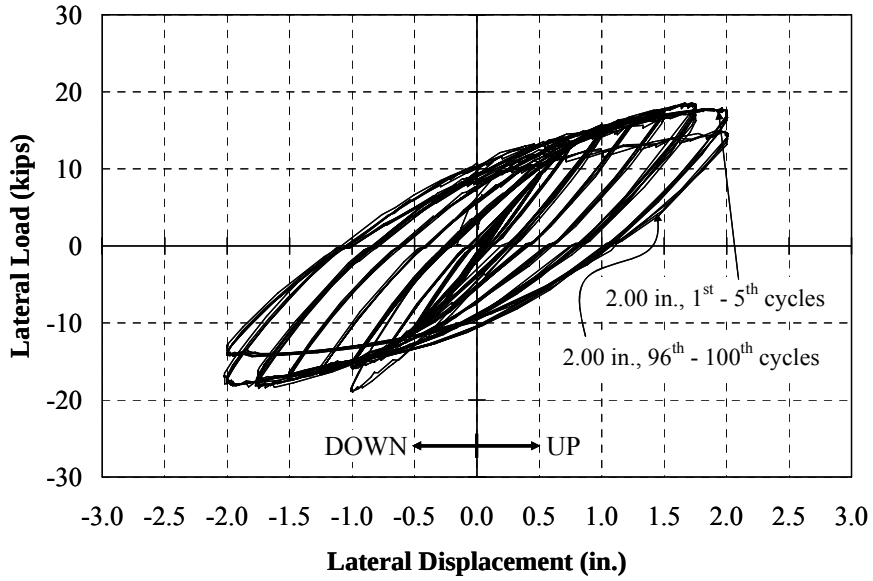

Figure I.41: Specimen 3 – Lateral Load-Deflection Curves

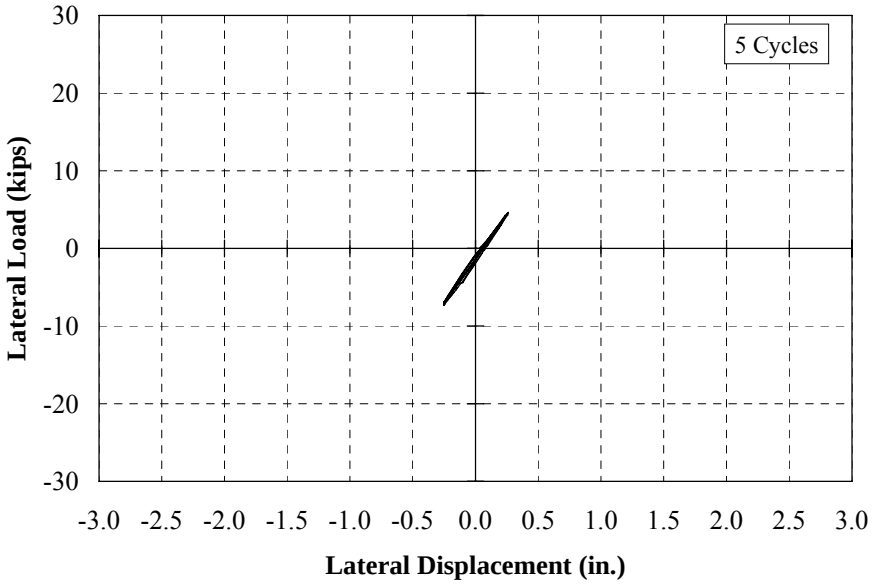

Figure I.42: Specimen 3 – Lateral Load-Deflection Response (±0.25 in.)

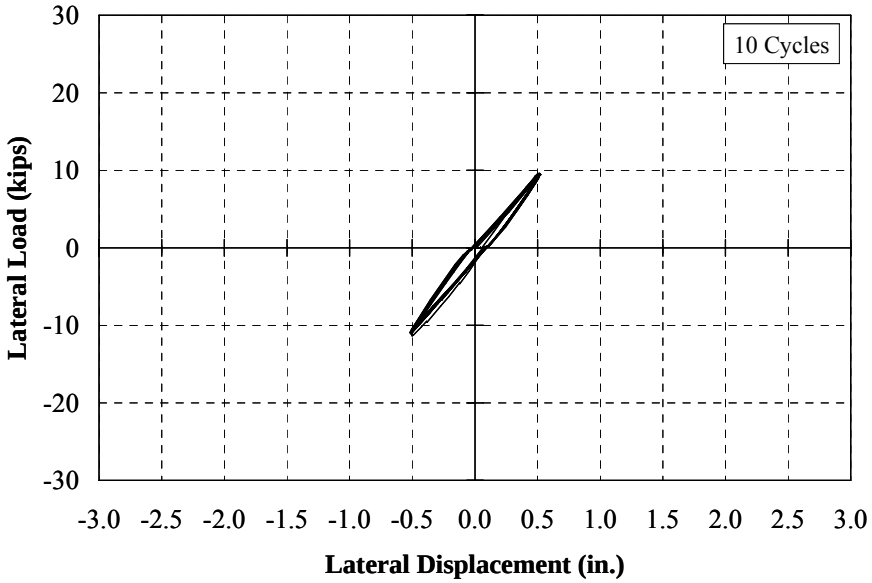

Figure I.43: Specimen 3 – Lateral Load-Deflection Response (±0.50 in.)

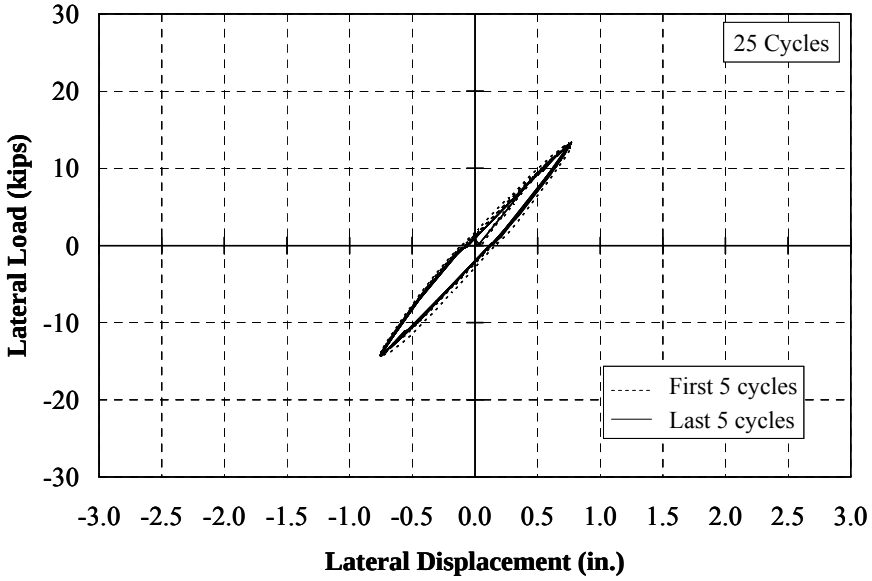

Figure I.44: Specimen 3 – Lateral Load-Deflection Response (±0.75 in.)

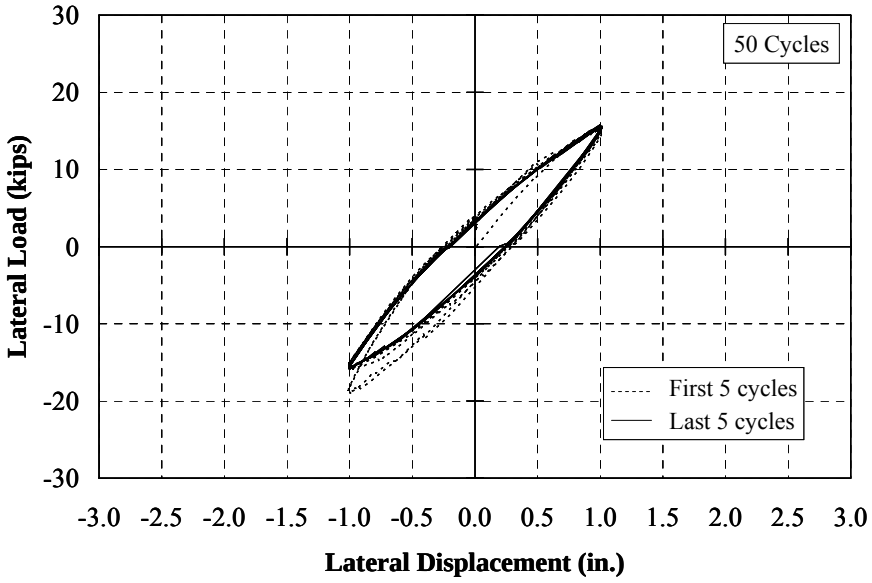

Figure I.45: Specimen 3 – Lateral Load-Deflection Response (±1.00 in.)

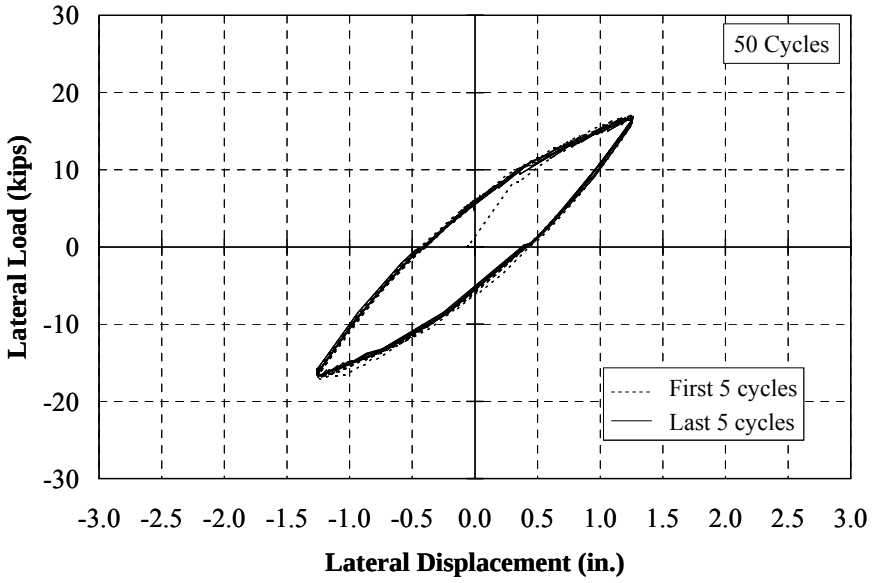

Figure I.46: Specimen 3 – Lateral Load-Deflection Response (±1.25 in.)

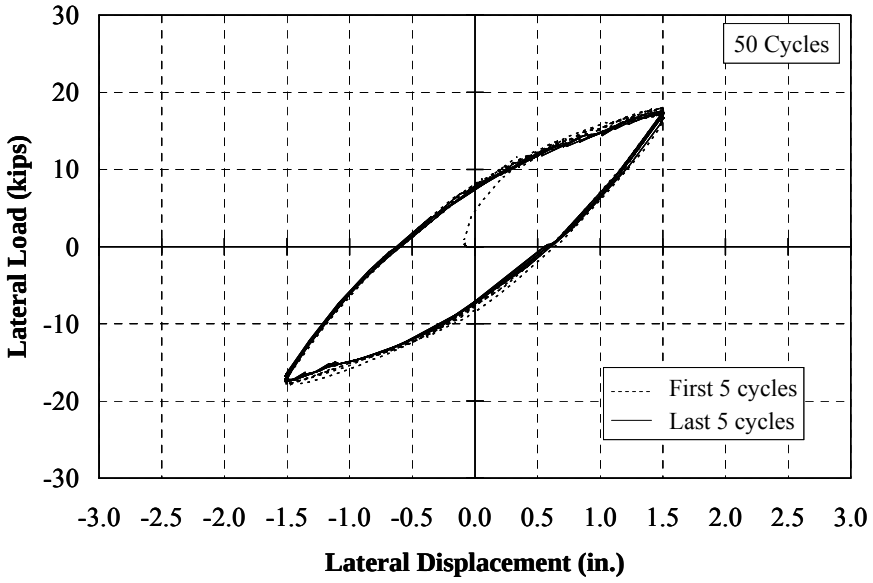

Figure I.47: Specimen 3 – Lateral Load-Deflection Response (±1.50 in.)

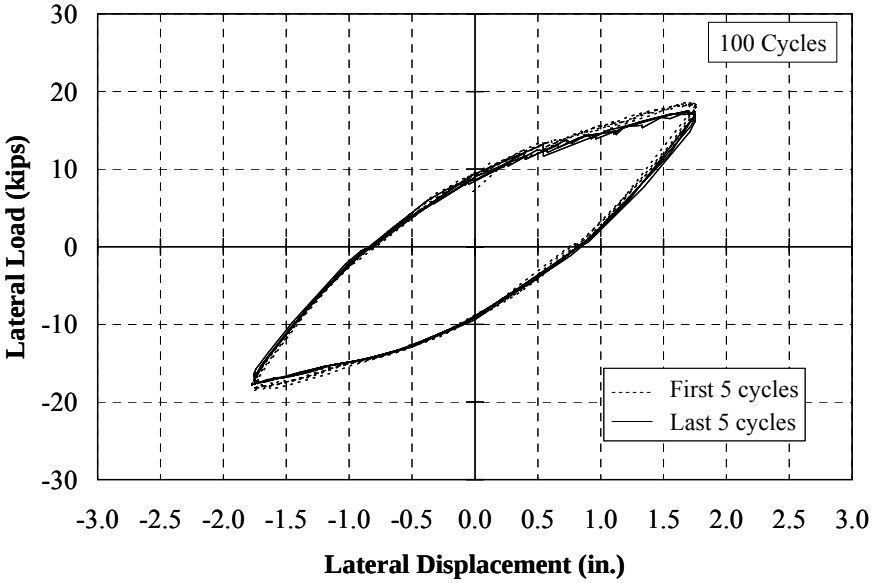

Figure I.48: Specimen 3 – Lateral Load-Deflection Response (±1.75 in.)

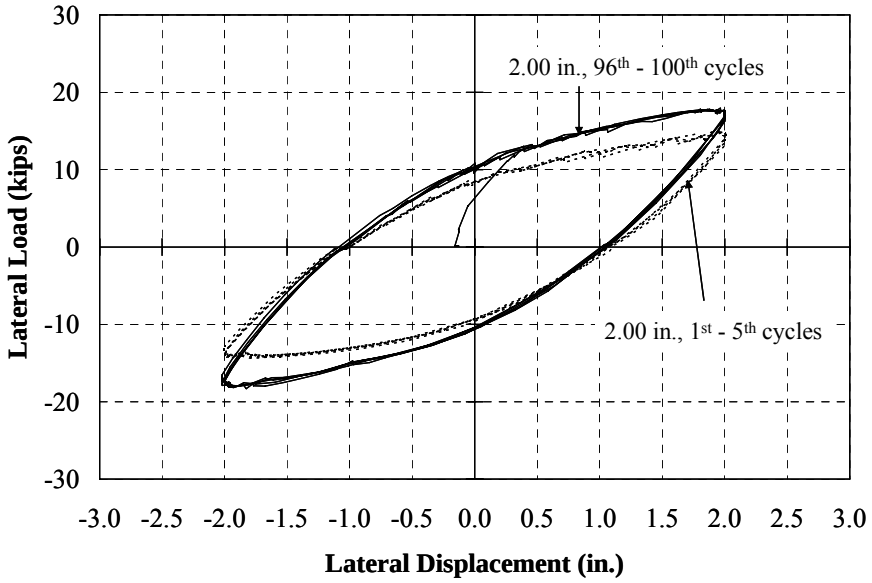

Figure I.49: Specimen 3 – Lateral Load-Deflection Response (±2.00 in.)

Specimen 4 (HP8x36, Weak, 18 ksi)

(a) West Side

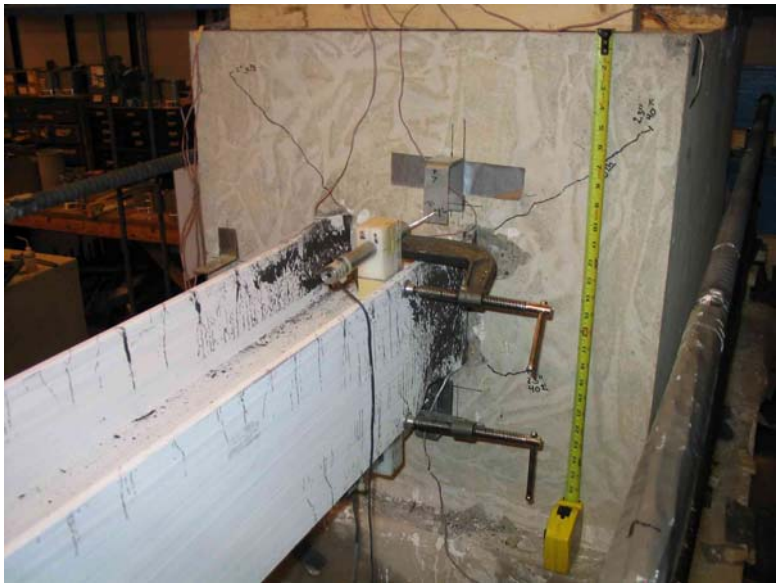

(b) East Side

Figure I.50: Specimen 4 – Cracking (2.50 in., 66th Cycle)

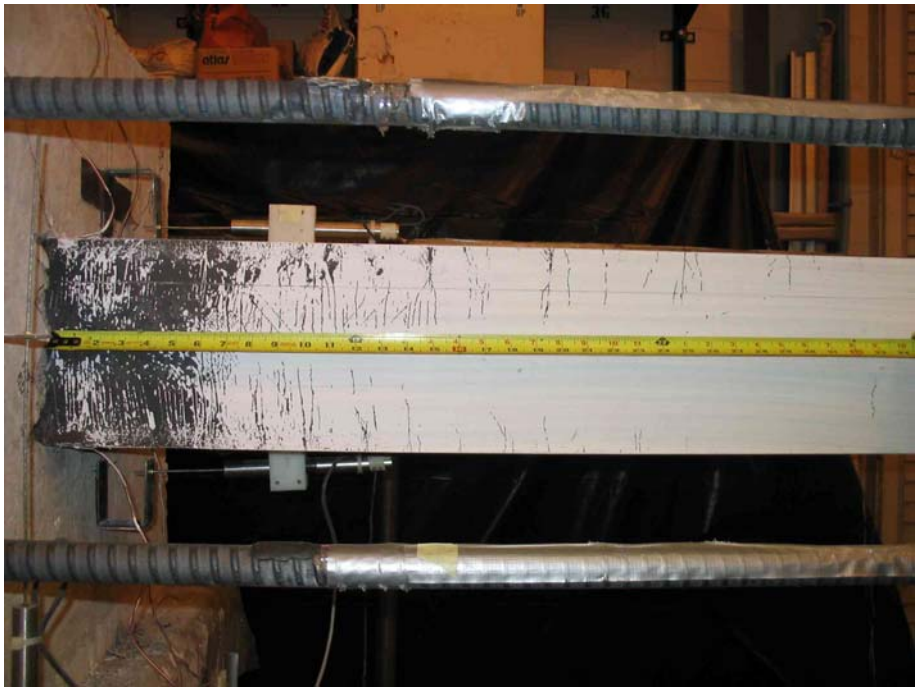

(a) West Side

(b) East Side

Figure I.51: Specimen 4 – Yielding (2.50 in., 66th Cycle)

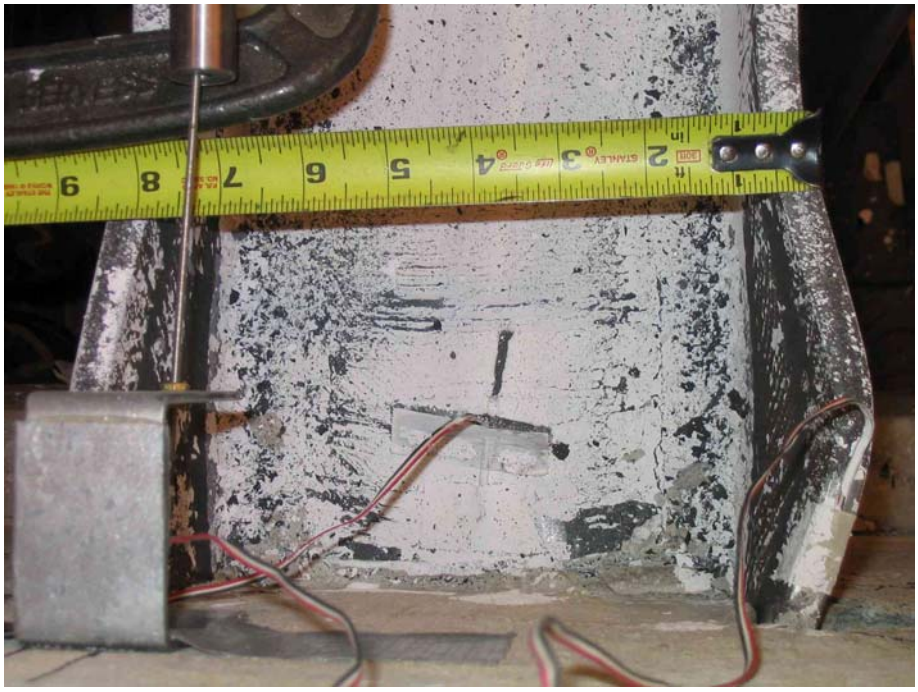

(a) Top

(b) Bottom

Figure I.52: Specimen 4 – Flange Buckling and Web Yielding (2.50 in., 66th Cycle)

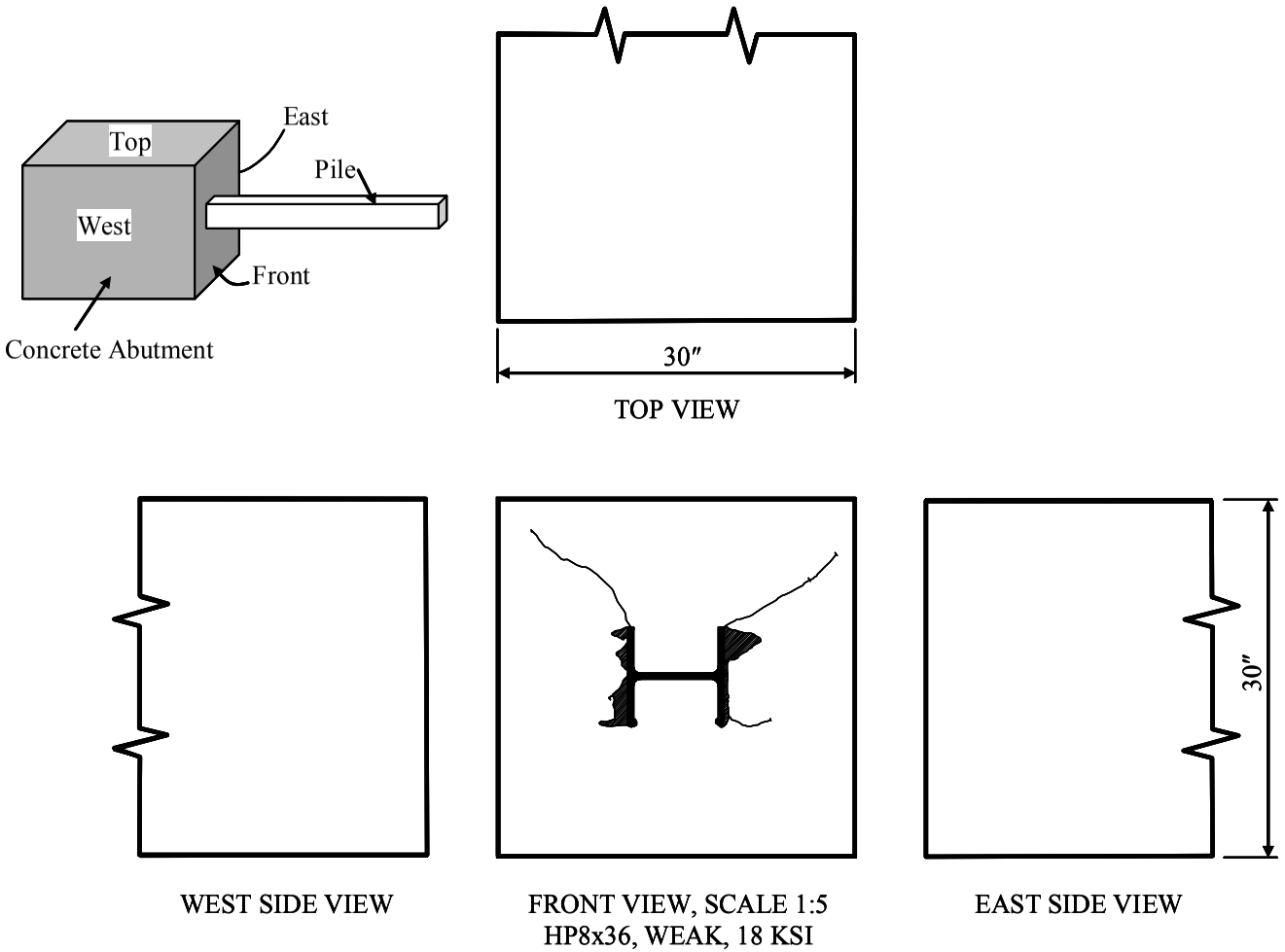

Figure I.53: Specimen 4 – Crack on Concrete Abutment (Overall)

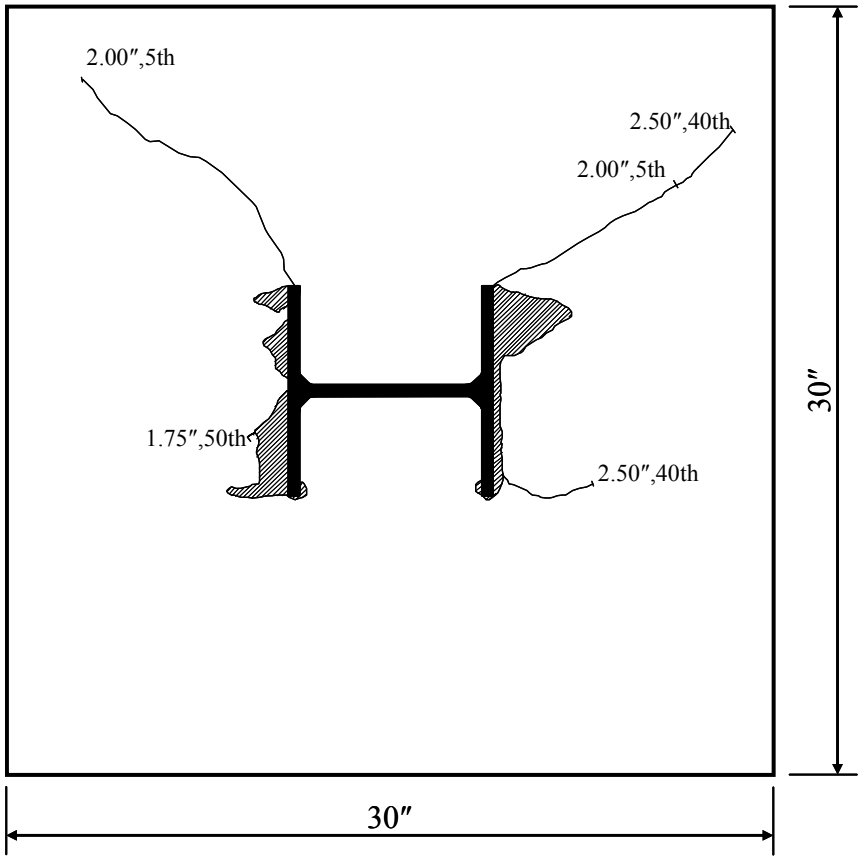

Figure I.54: Specimen 4 – Crack on Concrete Abutment (Front View)

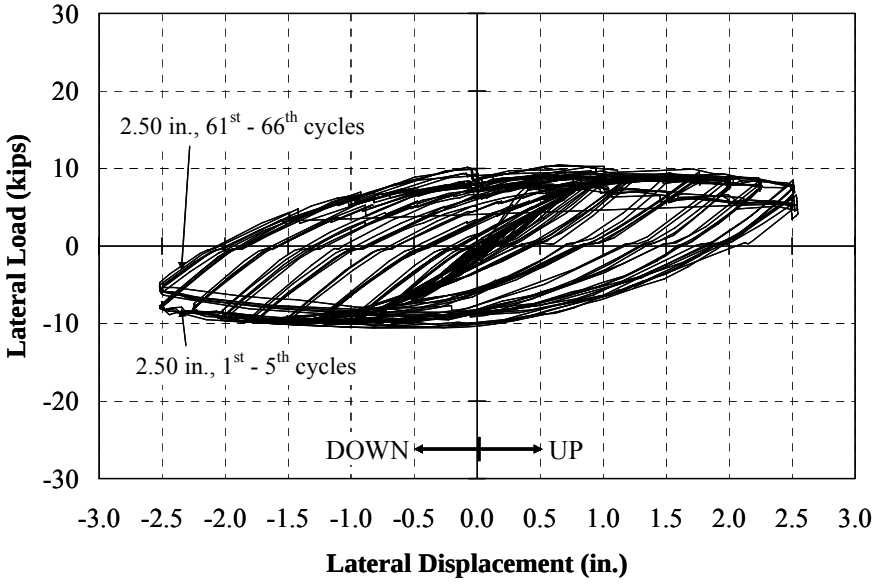

Figure I.55: Specimen 4 – Summary of Lateral Load-Deflection Curves

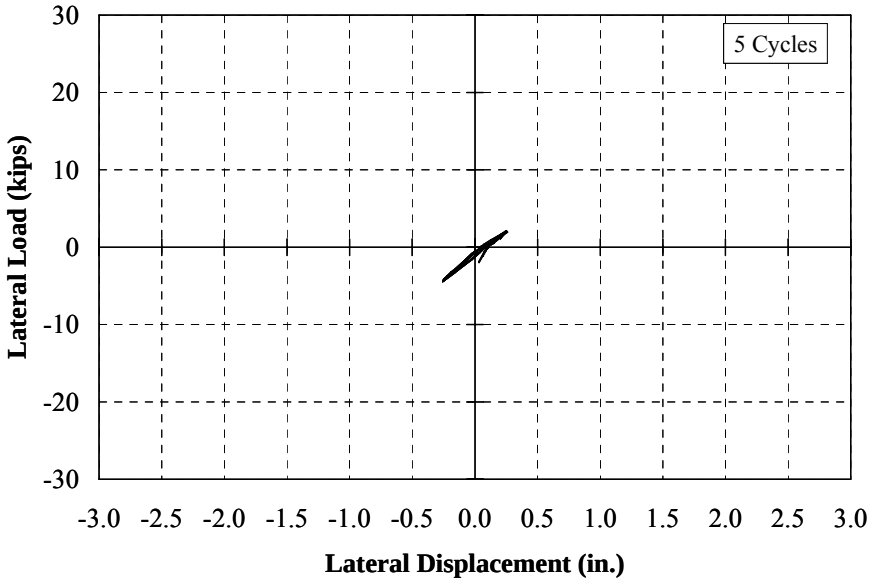

Figure I.56: Specimen 4 – Lateral Load-Deflection Response (±0.25 in.)

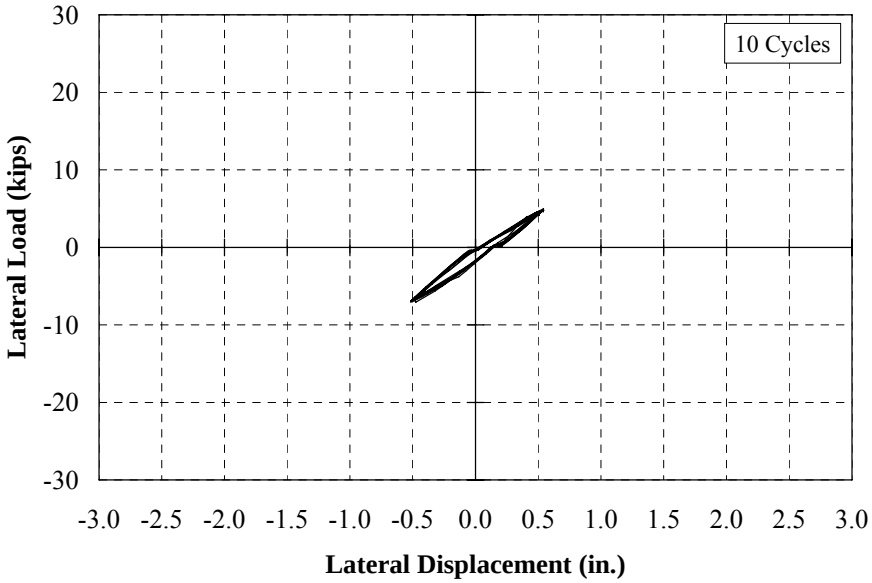

Figure I.57: Specimen 4 – Lateral Load-Deflection Response (±0.50 in.)

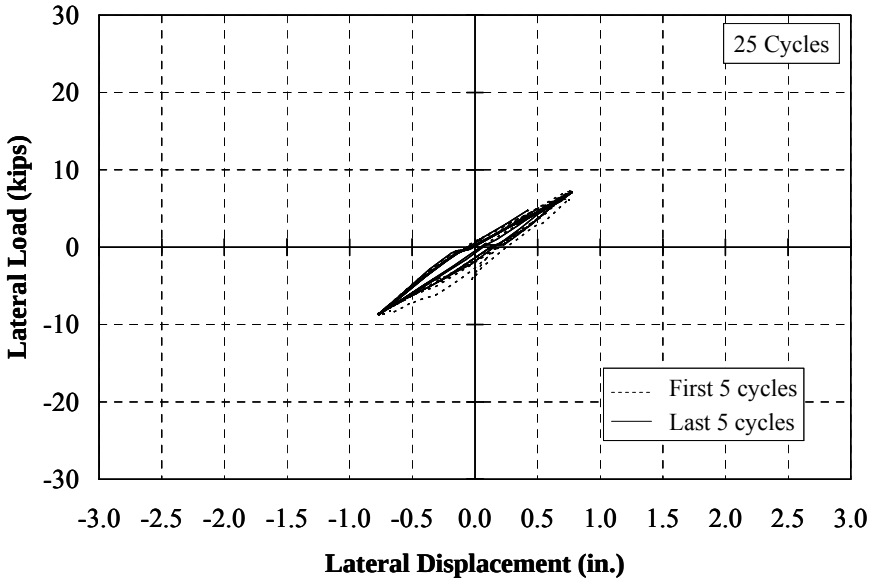

Figure I.58: Specimen 4 – Lateral Load-Deflection Response (±0.75 in.)

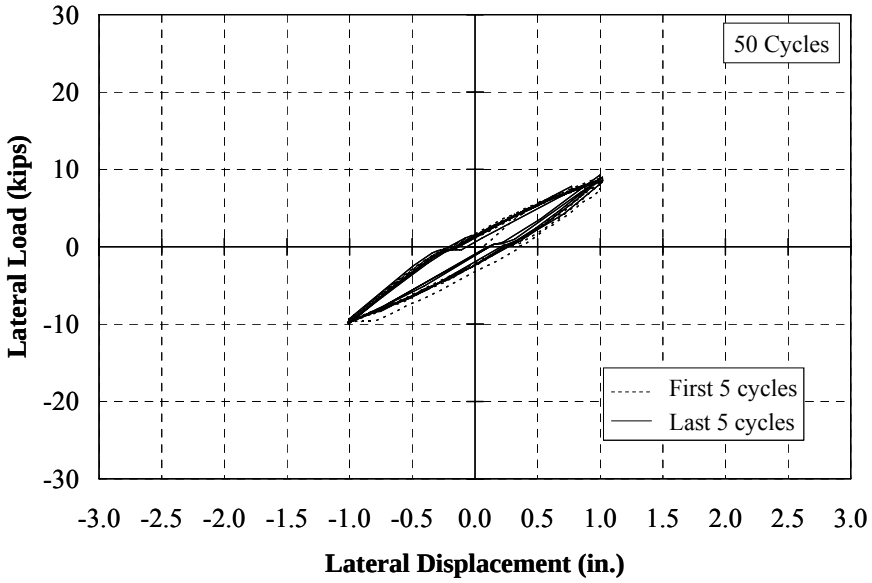

Figure I.59: Specimen 4 – Lateral Load-Deflection Response (±1.00 in.)

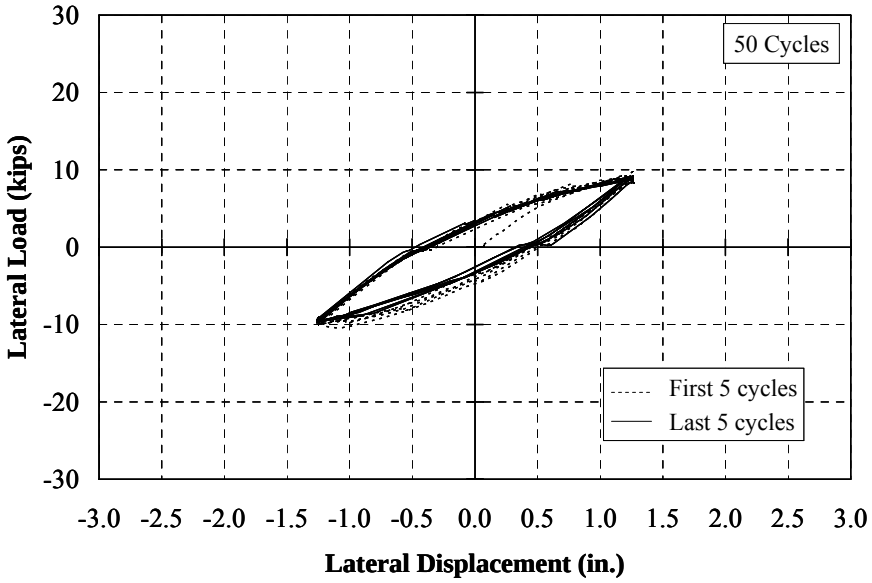

Figure I.60: Specimen 4 – Lateral Load-Deflection Response (±1.25 in.)

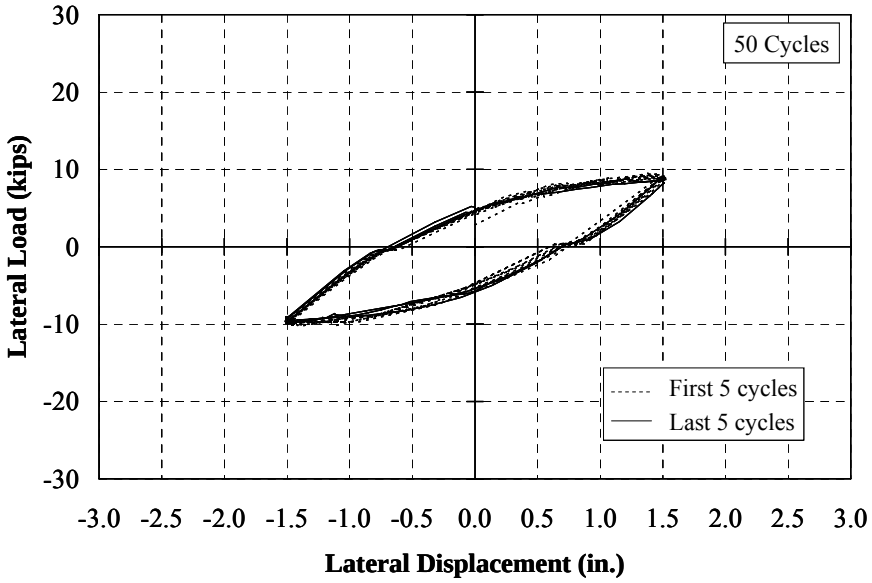

Figure I.61: Specimen 4 – Lateral Load-Deflection Response (±1.50 in.)

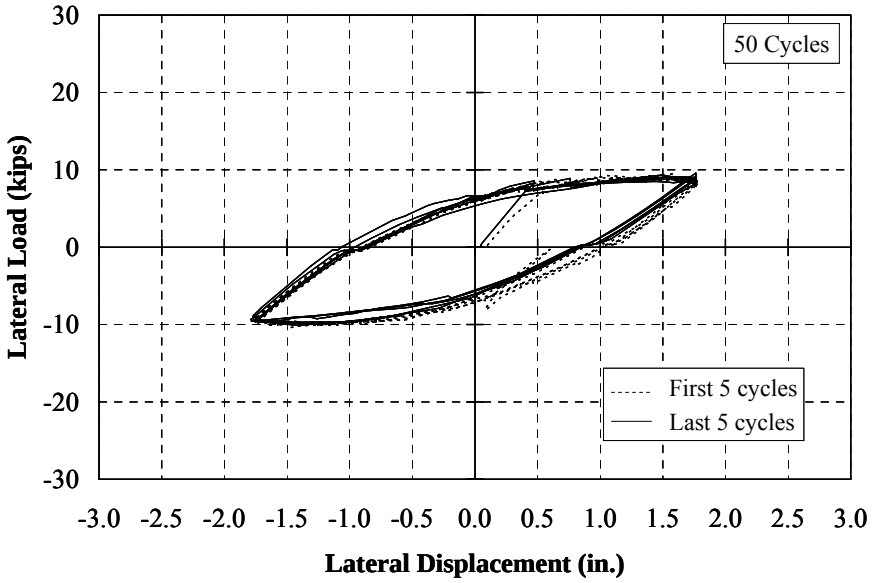

Figure I.62: Specimen 4 – Lateral Load-Deflection Response (±1.75 in.)

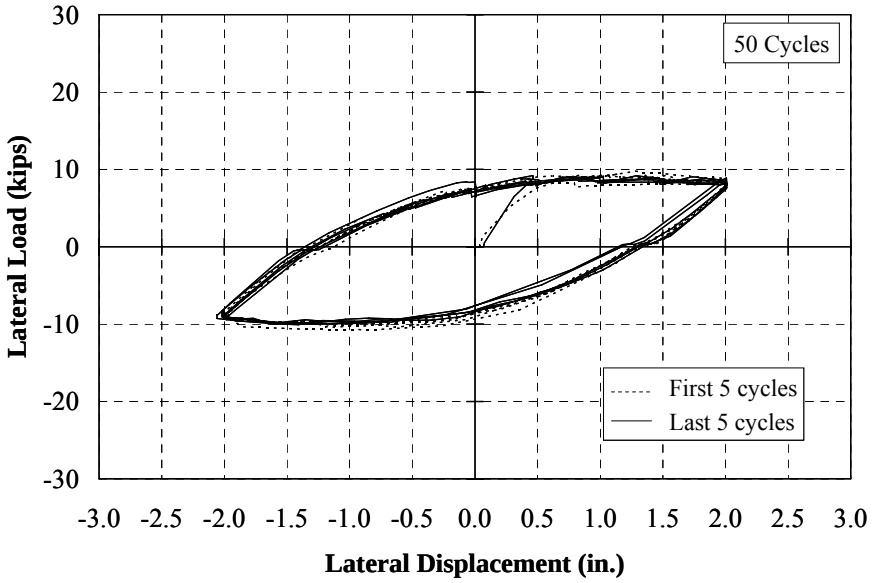

Figure I.63: Specimen 4 – Lateral Load-Deflection Response (±2.00 in.)

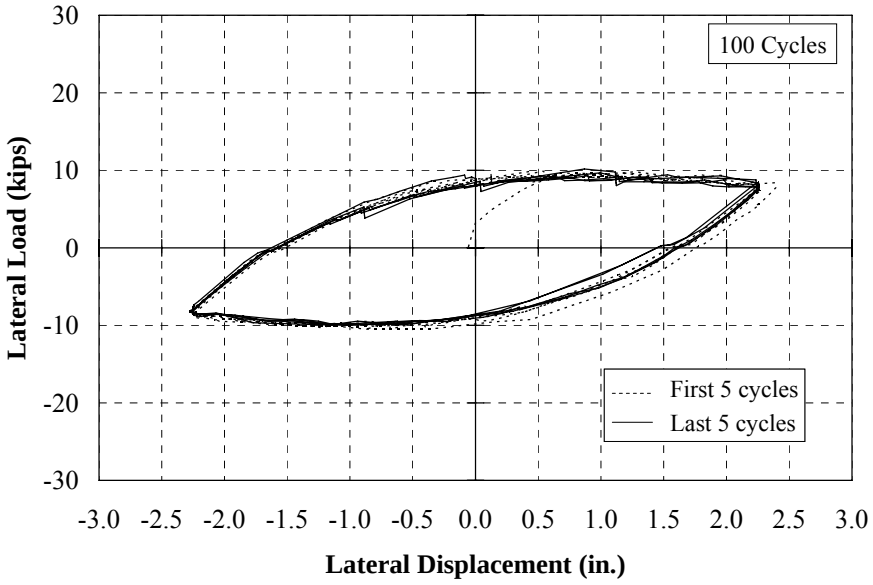

Figure I.64: Specimen 4 – Lateral Load-Deflection Response (±2.25 in.)

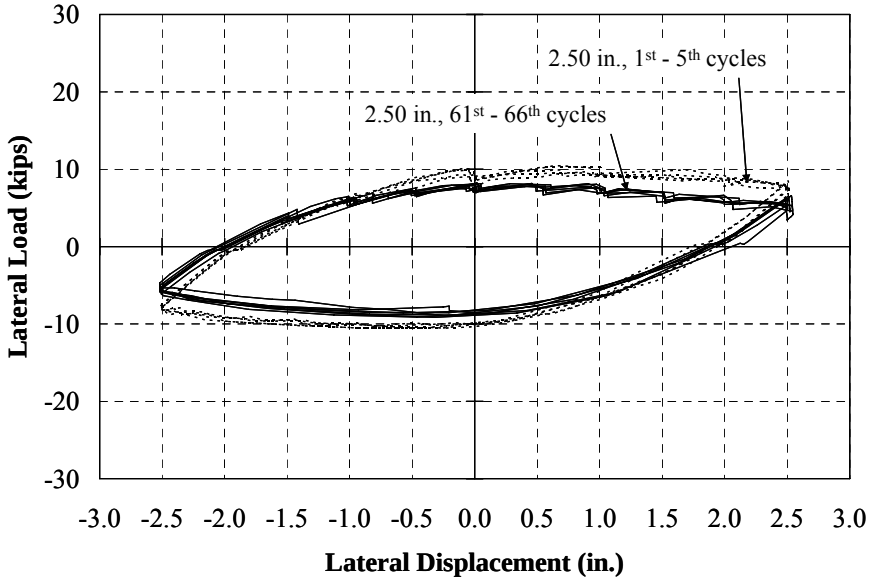

Figure I.65: Specimen 4 – Lateral Load-Deflection Response (±2.50 in.)

Specimen 5: HP10x42, Weak, 9 ksi

(a) West Side

(b) East Side

Figure I.66: Specimen 5 – Cracking (2.00 in., 50th Cycle)

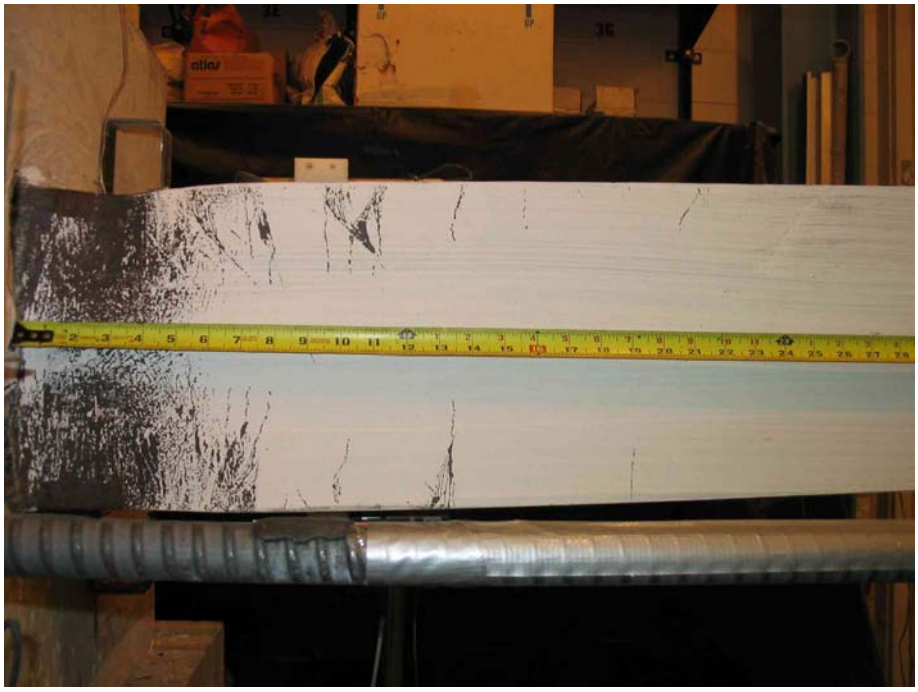

(a) West Side

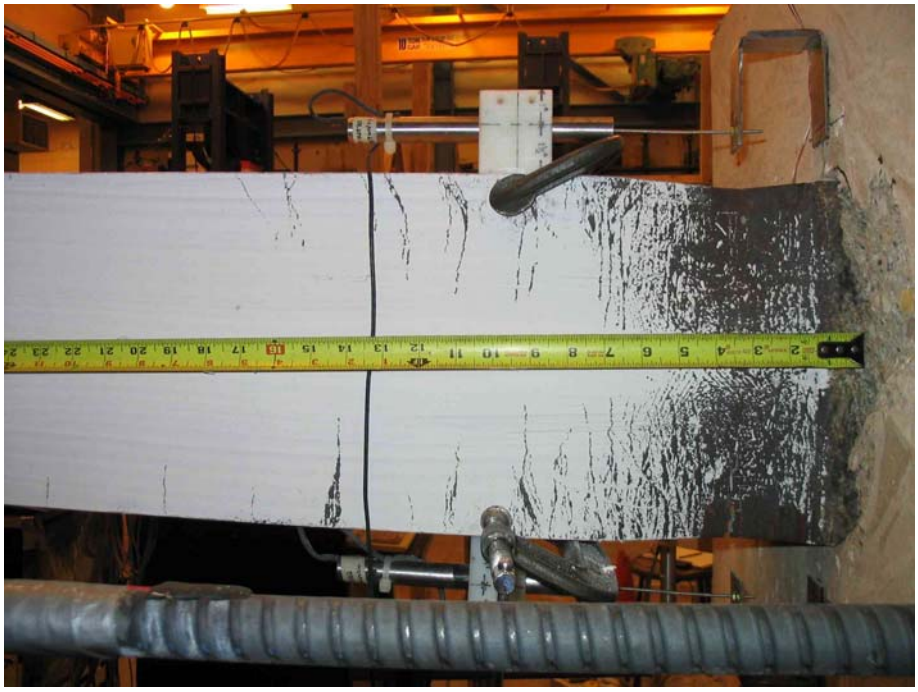

(b) East Side

Figure I.67: Specimen 5 – Pile Yielding (2.00 in., 50th Cycle)

(a) Top

(b) Bottom

Figure I.68: Specimen 5 – Pile Flange Buckling and Web Yielding (2.00 in., 50th Cycle)

(a) NW Flange

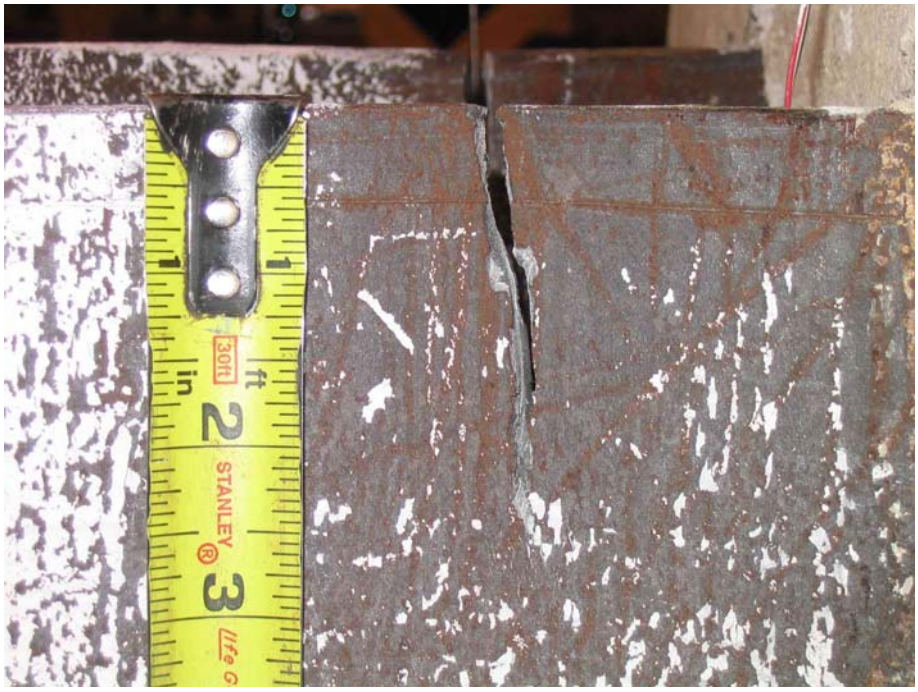

(b) NE Flange

Figure I.69: Specimen 5 – Crack on Steel Pile (2.00 in., 50th Cycle)

(c) SW Flange

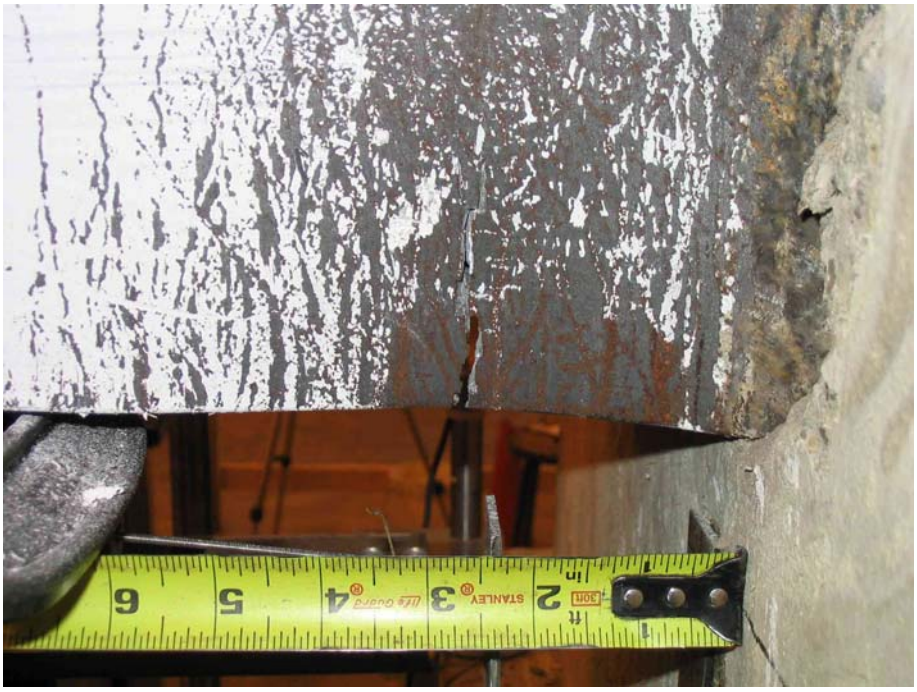

(d) SE Flange

Figure I.69: Specimen 5 – Crack on Steel Pile (2.00 in., 50th Cycle) (Continue)

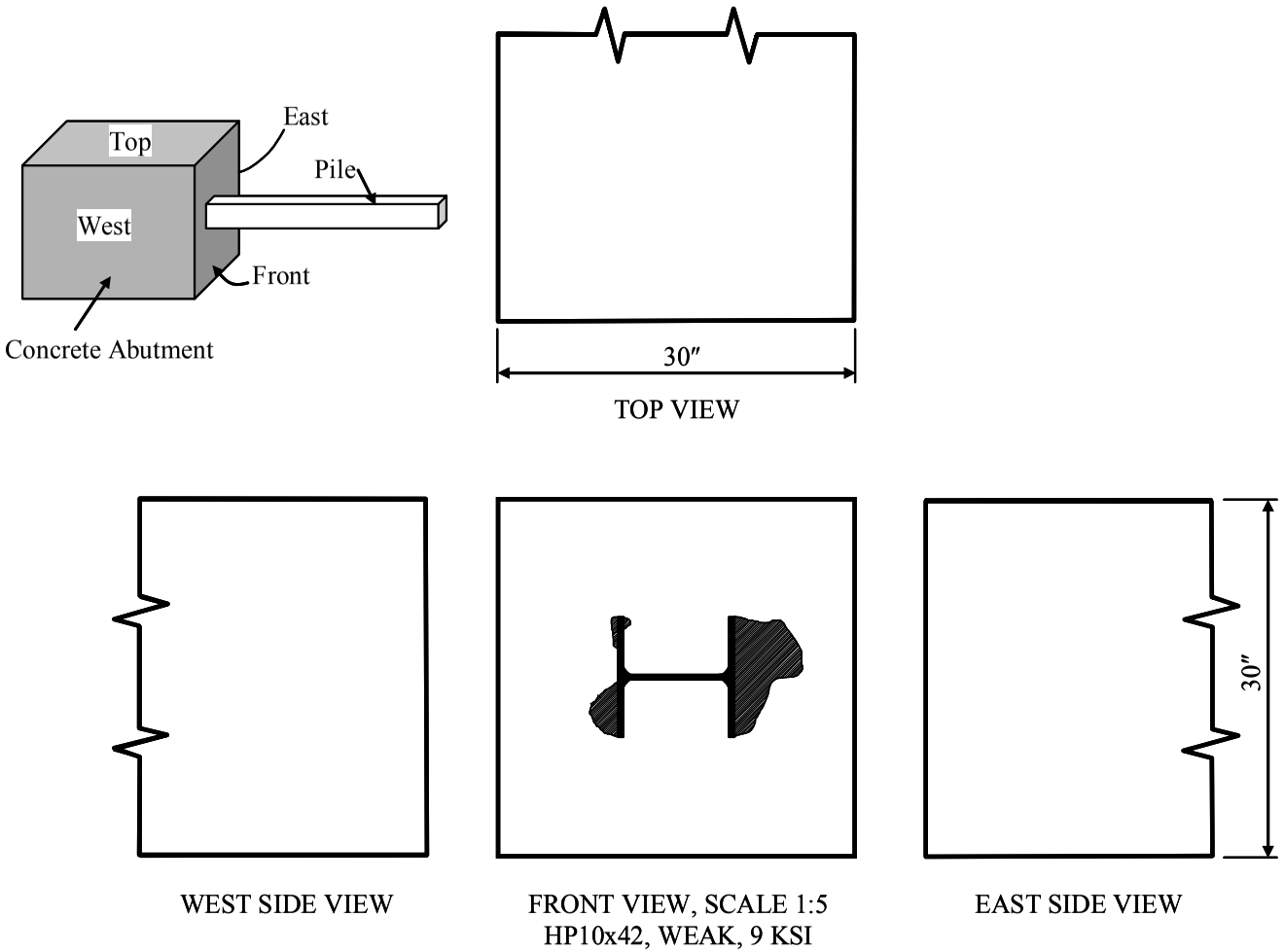

Figure I.70: Specimen 5 – Crack on Concrete Abutment (Overall)

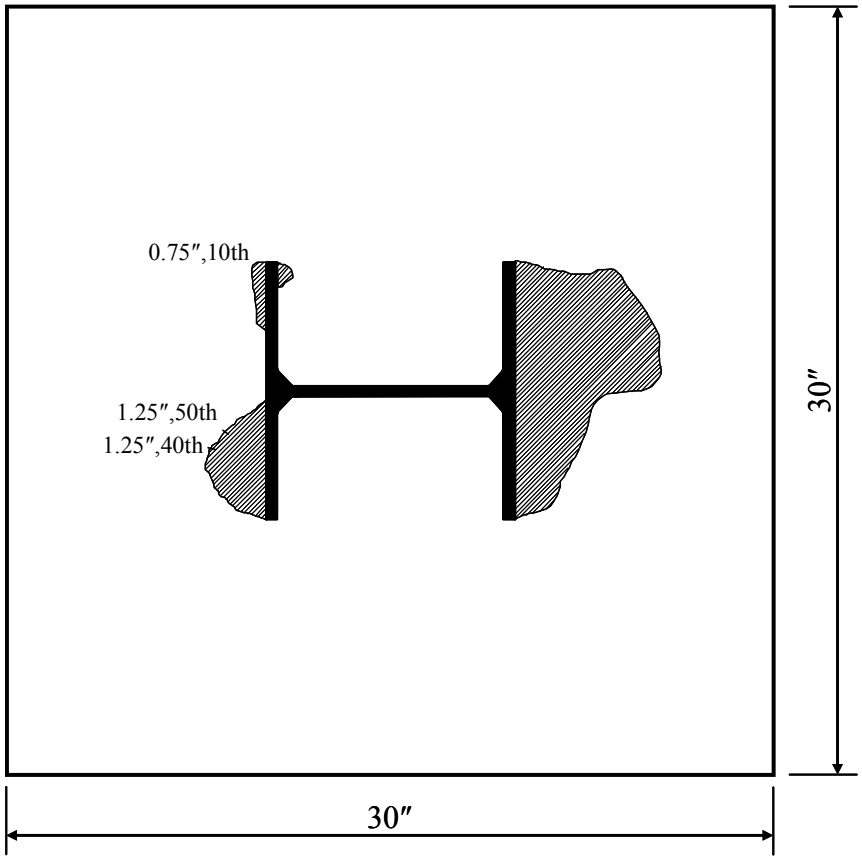

Figure I.71: Specimen 5 – Crack on Concrete Abutment (Front View)

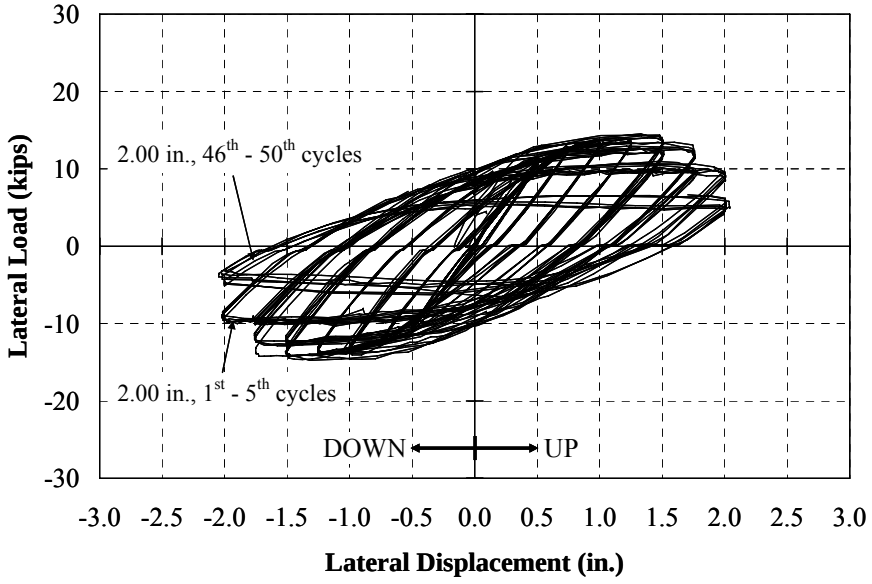

Figure I.72: Specimen 5 – Summary of Lateral Load-Deflection Curves

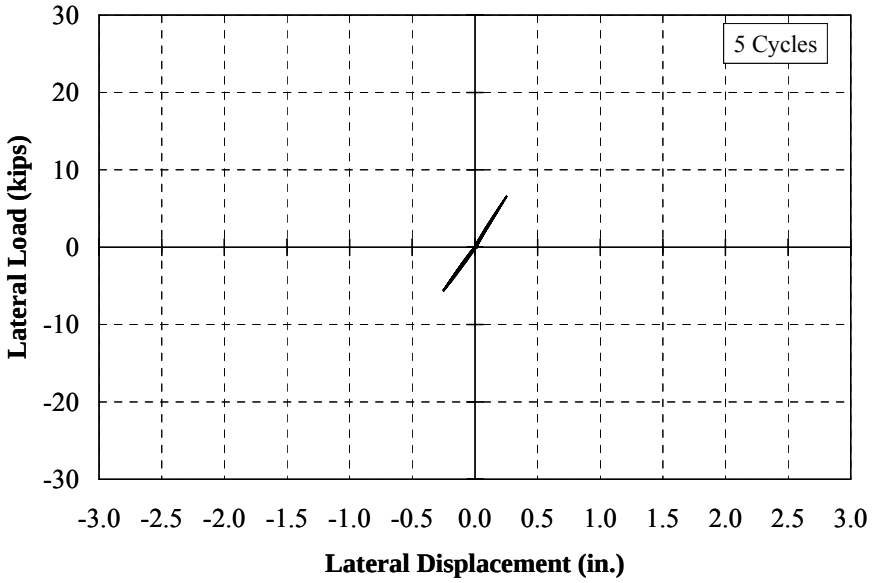

Figure I.73: Specimen 5 – Lateral Load-Deflection Response (±0.25 in.)

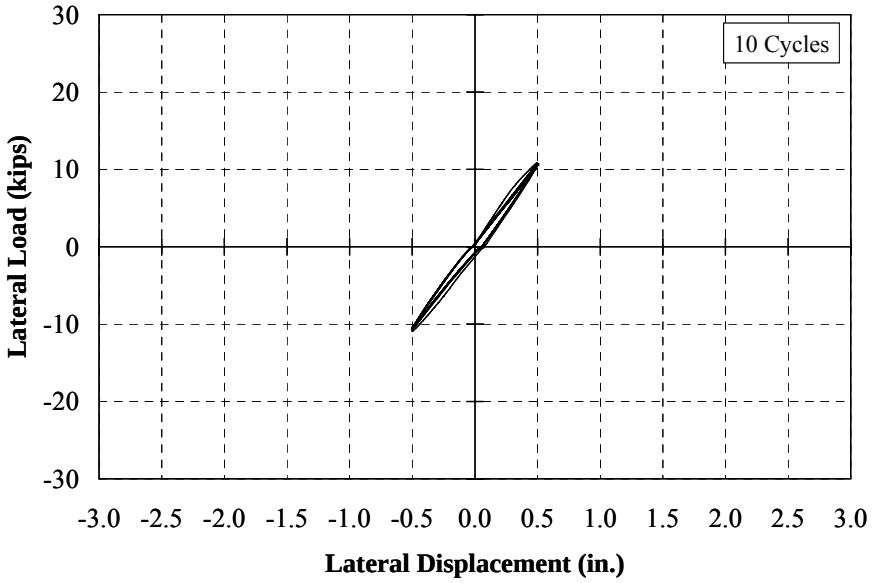

Figure I.74: Specimen 5 – Lateral Load-Deflection Response (±0.50 in.)

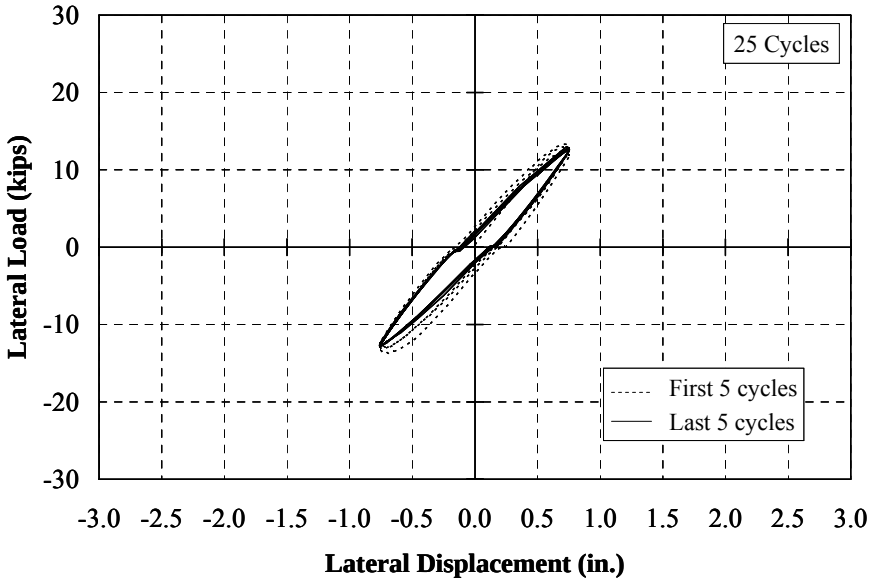

Figure I.75: Specimen 5 – Lateral Load-Deflection Response (±0.75 in.)

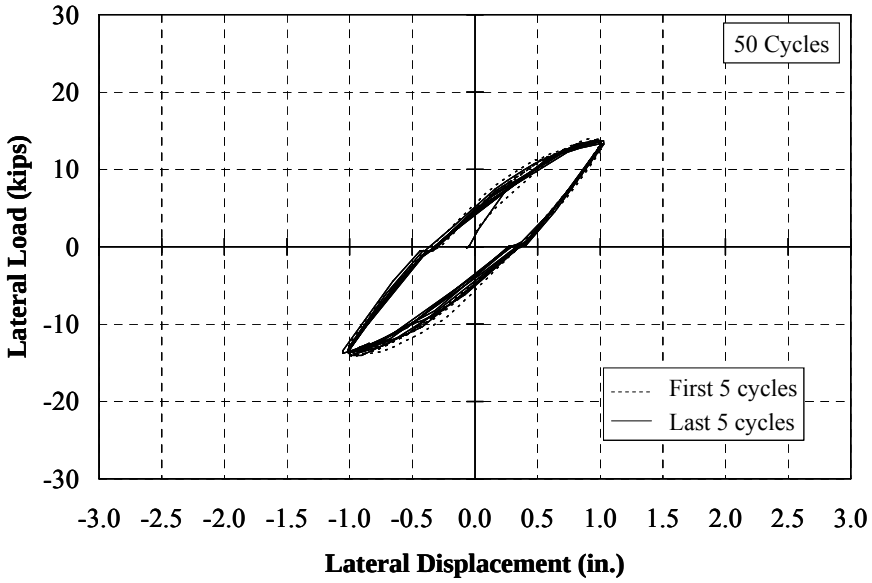

Figure I.76: Specimen 5 – Lateral Load-Deflection Response (±1.00 in.)

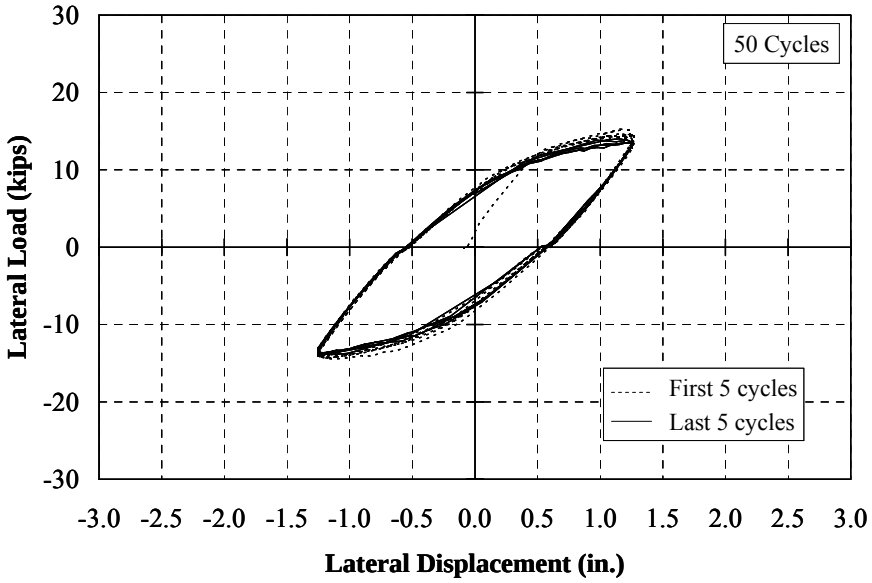

Figure I.77: Specimen 5 – Lateral Load-Deflection Response (±1.25 in.)

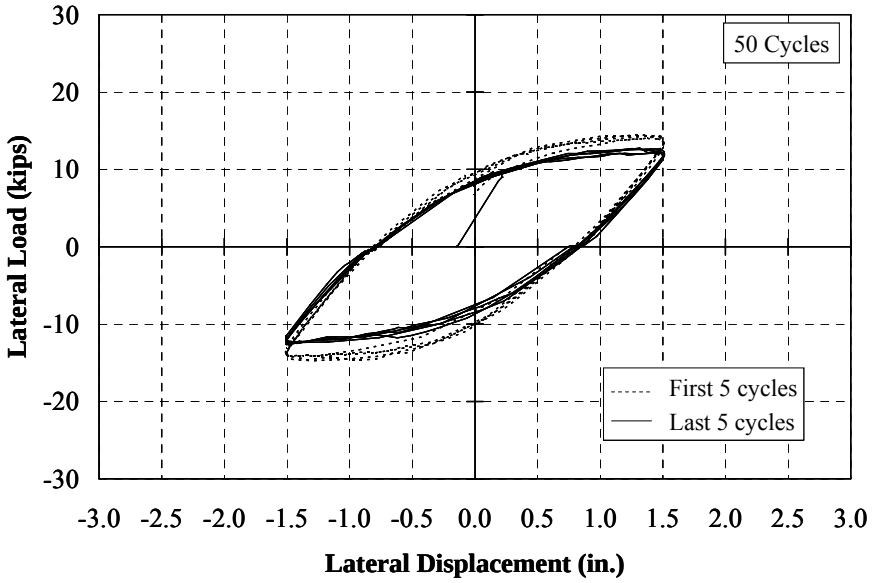

Figure I.78: Specimen 5 – Lateral Load-Deflection Response (±1.50 in.)

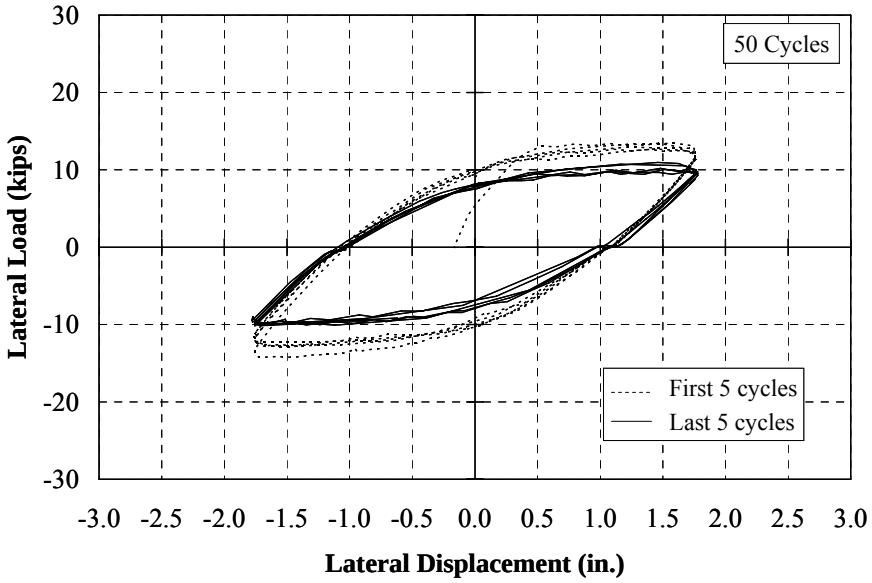

Figure I.79: Specimen 5 – Lateral Load-Deflection Response (±1.75 in.)

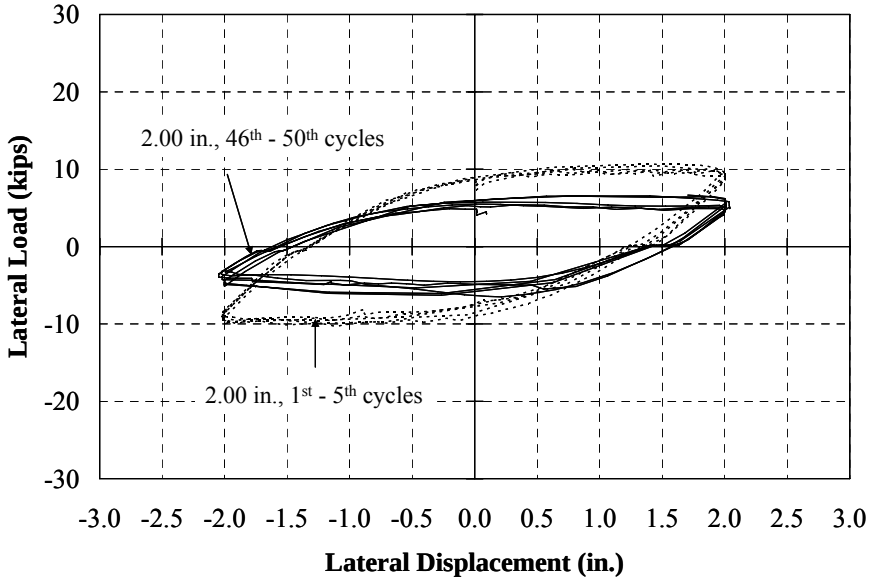

Figure I.80: Specimen 5 – Lateral Load-Deflection Response (±2.00 in.)

Specimen 6: HP12x53, Weak, 9 ksi

(a) West Side

(b) East Side

Figure I.81: Specimen 6 – Cracking (1.75 in., 70th Cycle)

(a) West Side

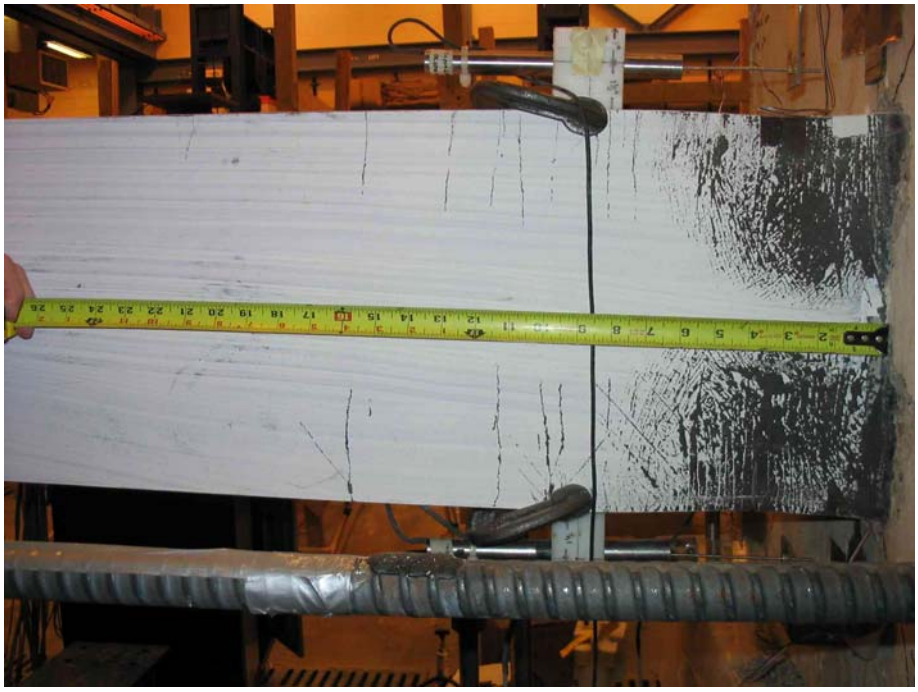

(b) East Side

Figure I.82: Specimen 6 – Pile Yielding (1.75 in., 70th Cycle)

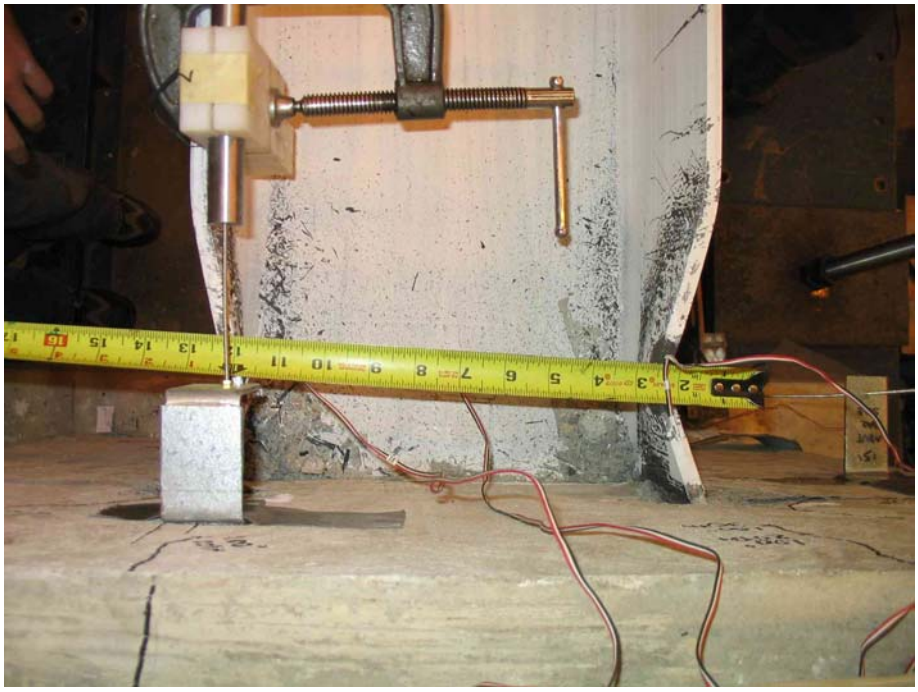

(a) Top

(b) Bottom

Figure I.83: Specimen 6 – Pile Flange Buckling (1.75 in., 70th Cycle)

(a) NW Flange

(b) NE Flange

Figure I.84: Specimen 6 – Crack on Steel Pile (1.75 in., 70th Cycle)

(c) SW Flange

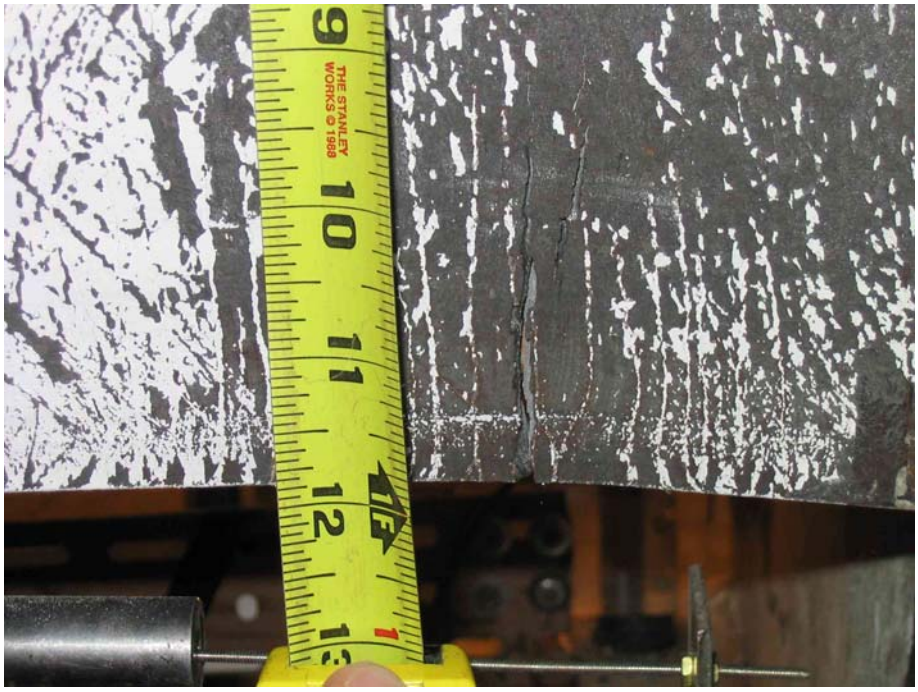

(d) SE Flange

Figure I.84: Specimen 6 – Crack on Steel Pile (1.75 in., 70th Cycle) (Continue)

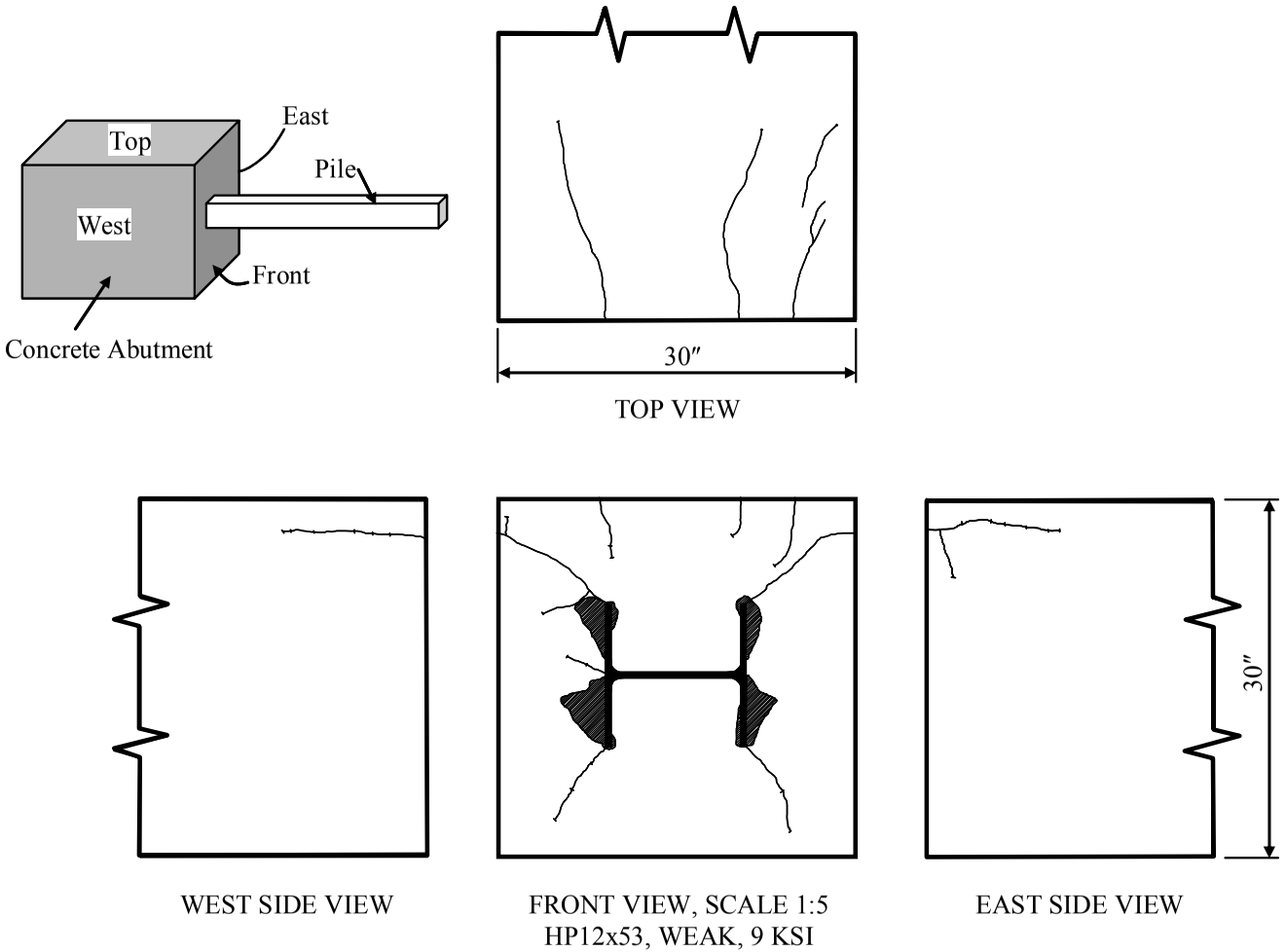

Figure I.85: Specimen 6 – Crack on Concrete Abutment (Overall)

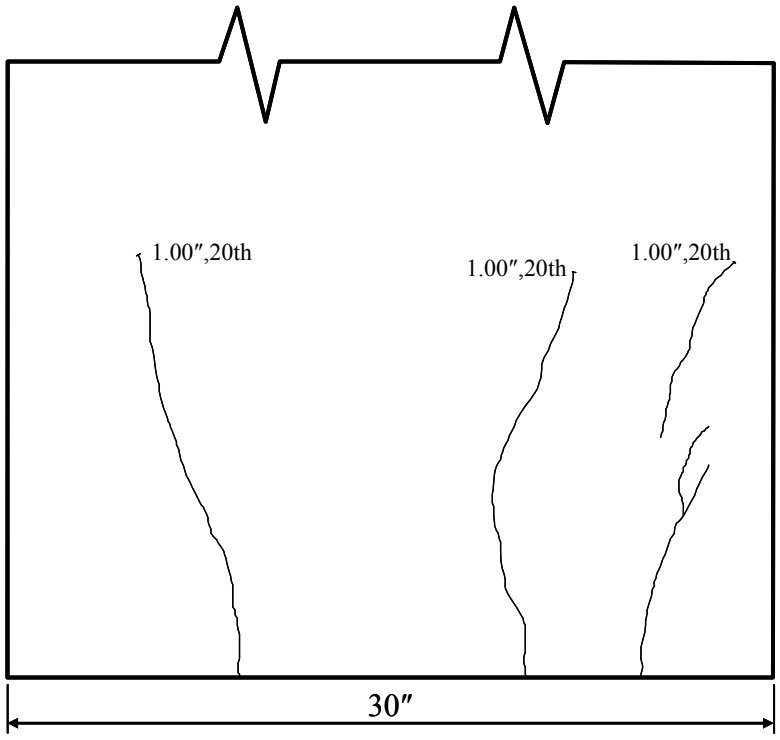

Figure I.86: Specimen 6 – Crack on Concrete Abutment (Top View)

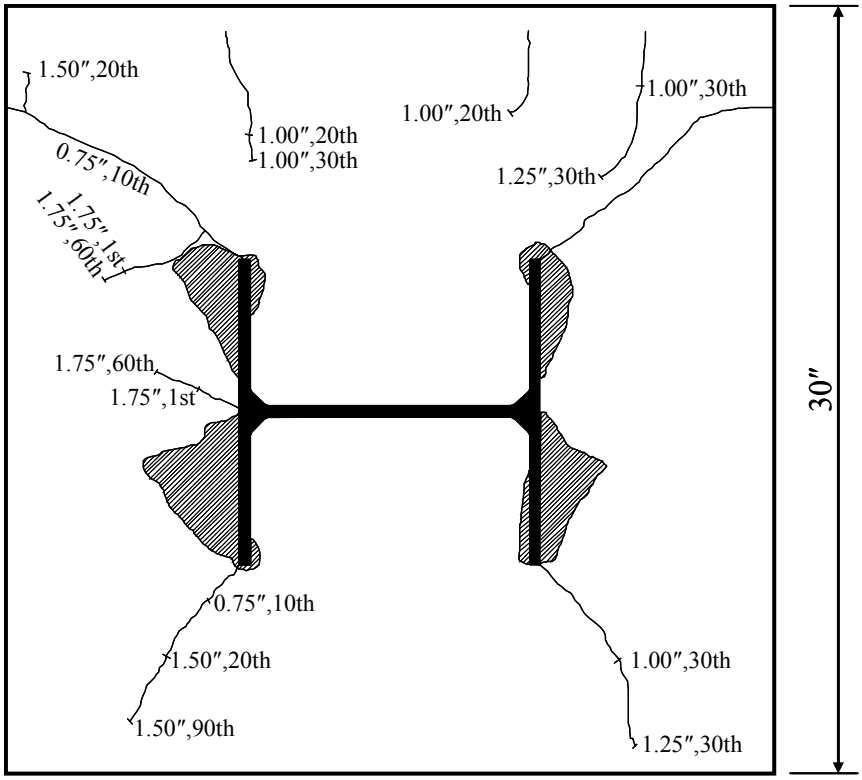

Figure I.87: Specimen 6 – Crack on Concrete Abutment (Front View)

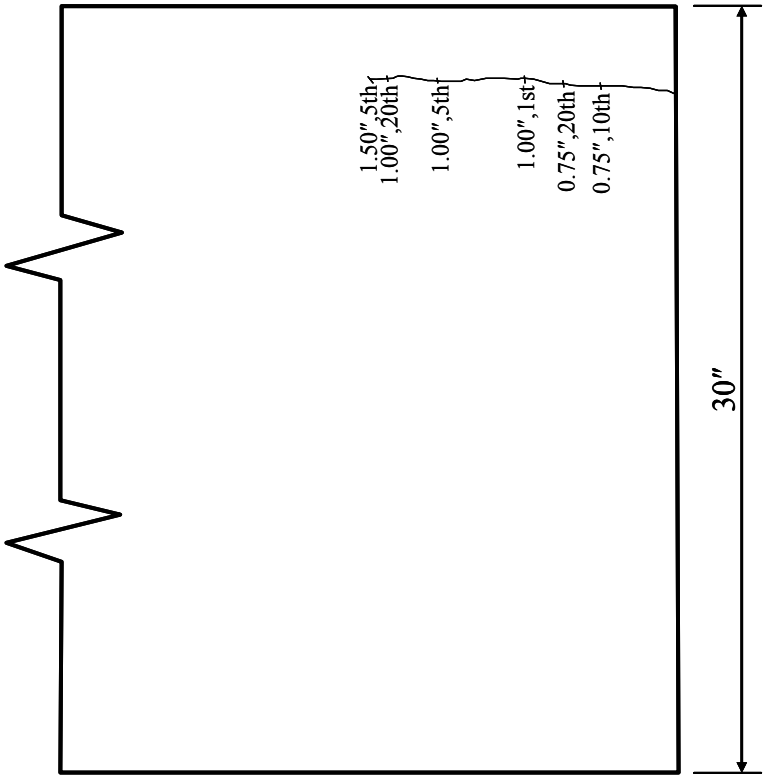

Figure I.88: Specimen 6 – Crack on Concrete Abutment (West View)

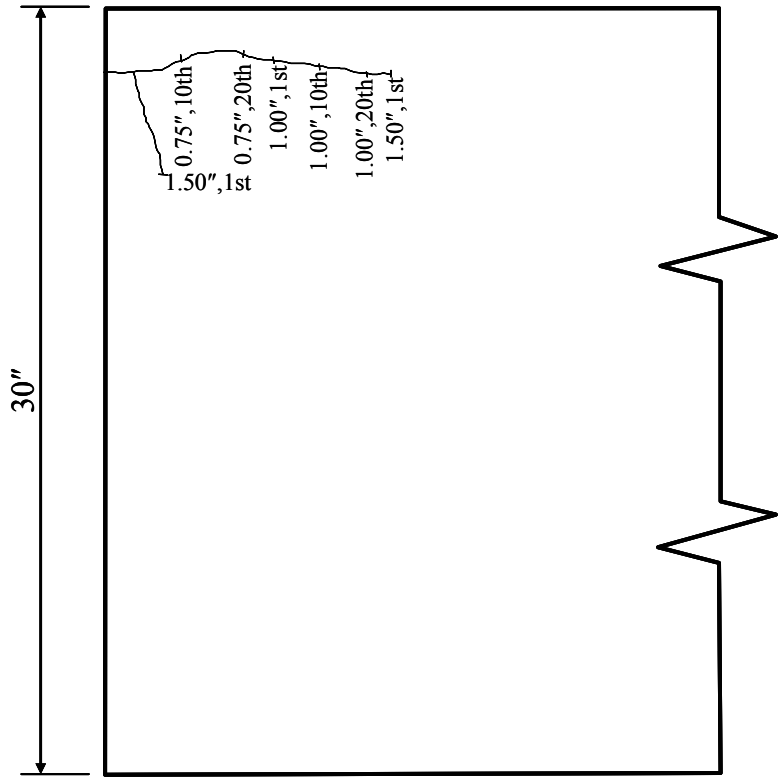

Figure I.89: Specimen 6 – Crack on Concrete Abutment (East View)

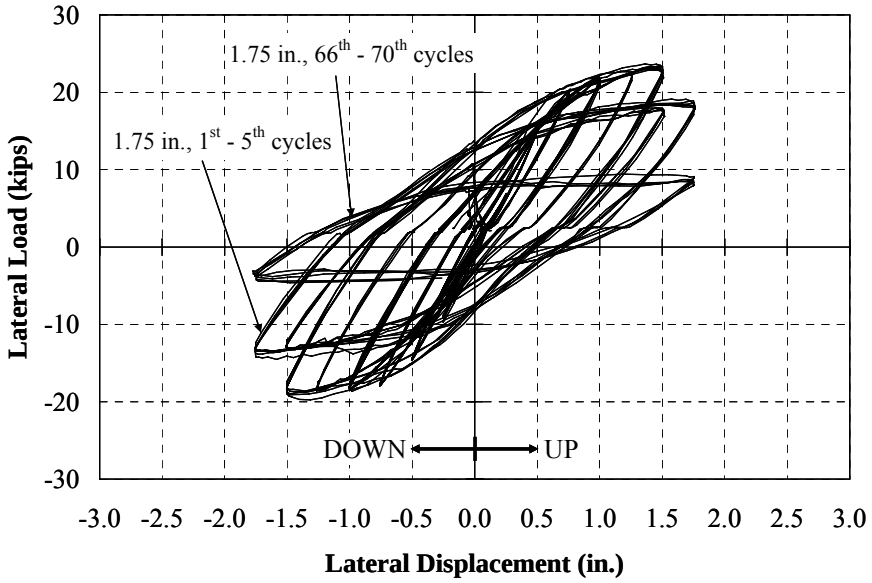

Figure I.90: Specimen 6 – Summary of Lateral Load-Deflection Curves

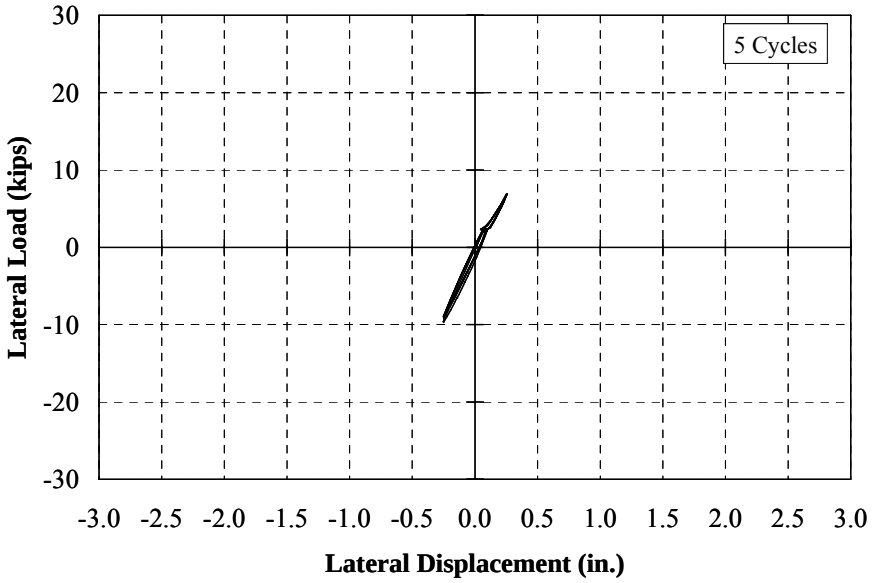

Figure I.91: Specimen 6 – Lateral Load-Deflection Response (±0.25 in.)

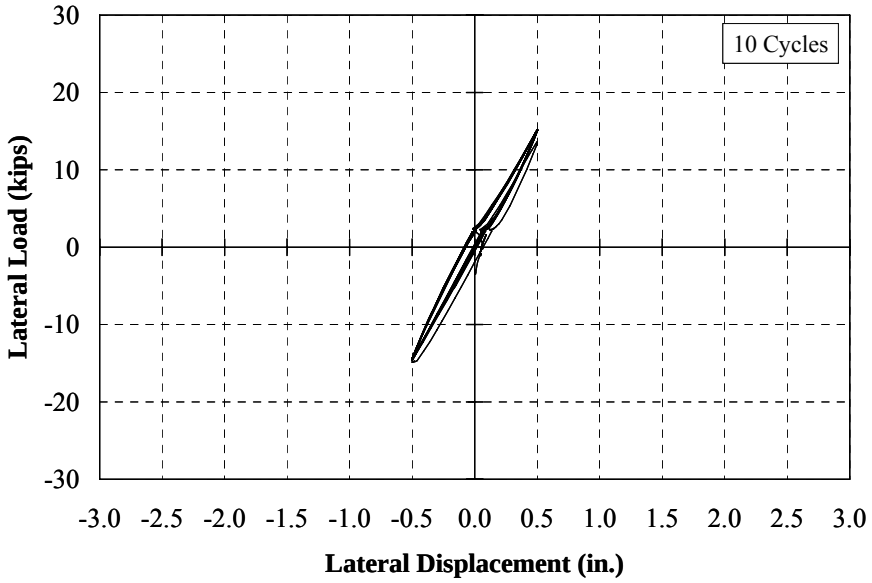

Figure I.92: Specimen 6 – Lateral Load-Deflection Response (±0.50 in.)

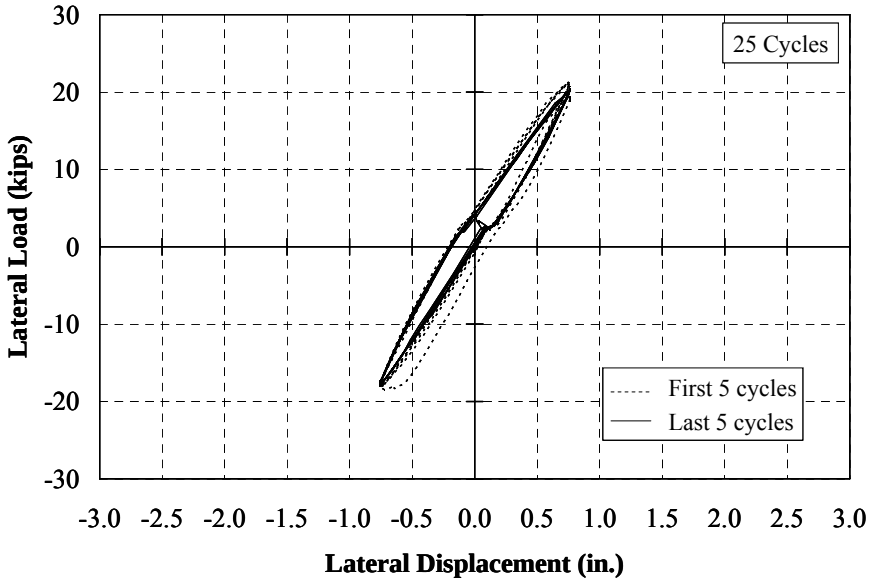

Figure I.93: Specimen 6 – Lateral Load-Deflection Response (±0.75 in.)

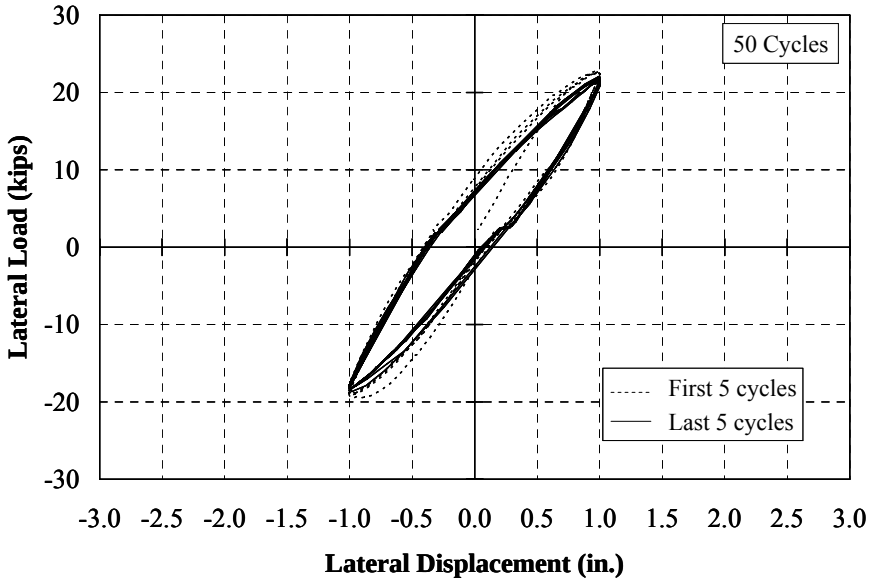

Figure I.94: Specimen 6 – Lateral Load-Deflection Response (±1.00 in.)

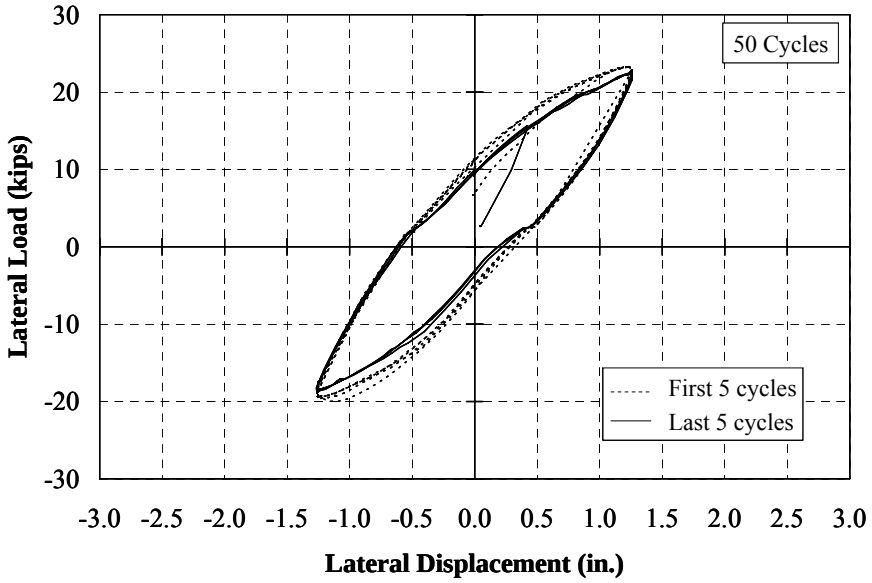

Figure I.95: Specimen 6 – Lateral Load-Deflection Response (±1.25 in.)

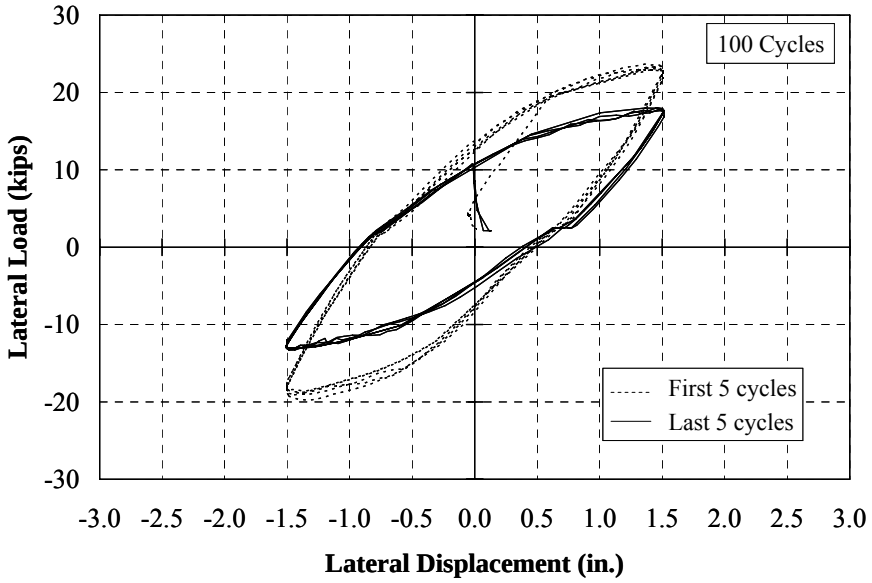

Figure I.96: Specimen 6 – Lateral Load-Deflection Response (±1.50 in.)

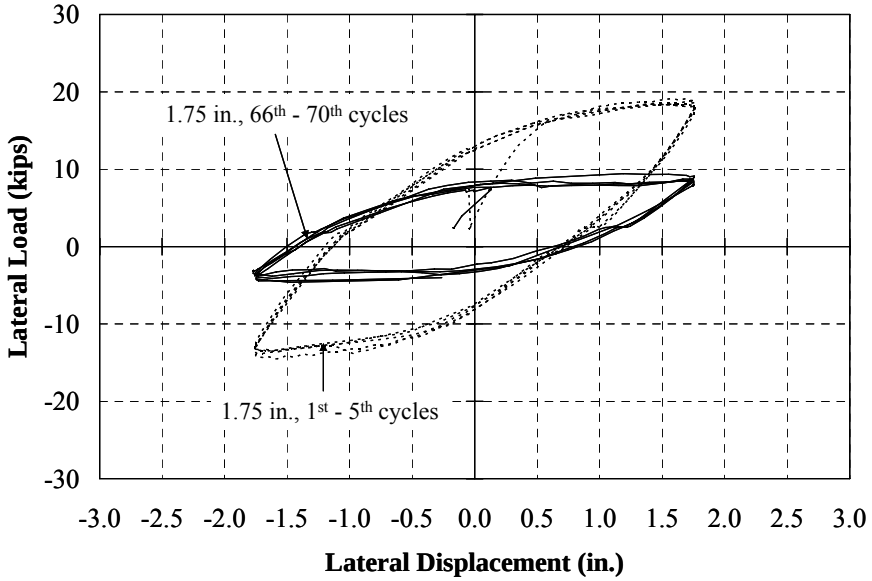

Figure I.97: Specimen 6 – Lateral Load-Deflection Response (±1.75 in.)

Specimen 7: CFT8.625x0.188, “9 ksi”

(a) West Side

(b) East Side

Figure I.98: Specimen 7 – Cracking (1.75 in., 33rd Cycle)

(a) West Side

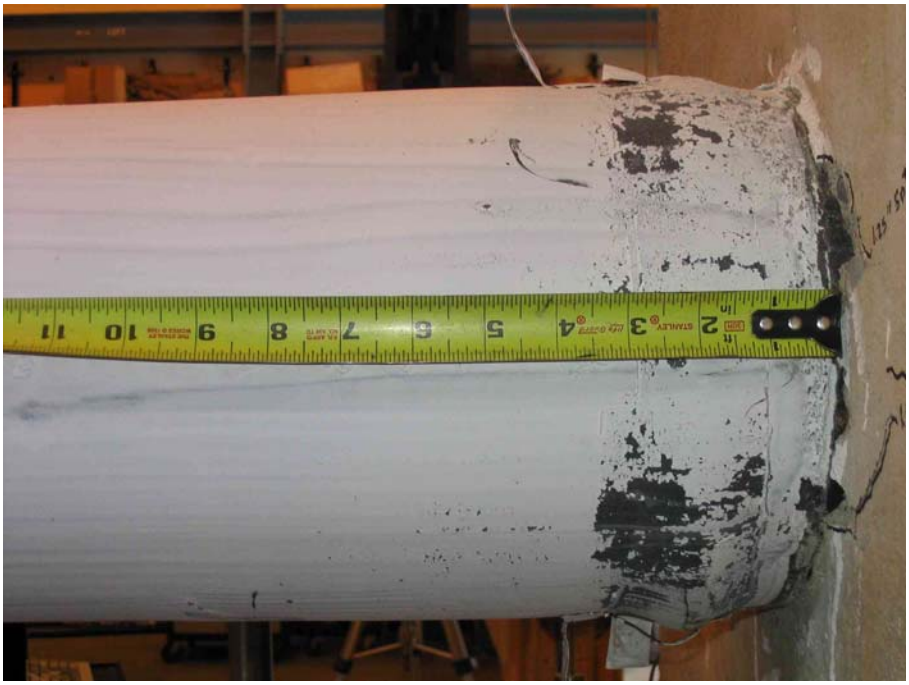

(b) East Side

Figure I.99: Specimen 7 – Pile Yielding (1.75 in., 33rd Cycle)

(c) Top

(d) Bottom

Figure I.99: Specimen 7 – Pile Yielding (1.75 in., 33rd Cycle) (Continue)

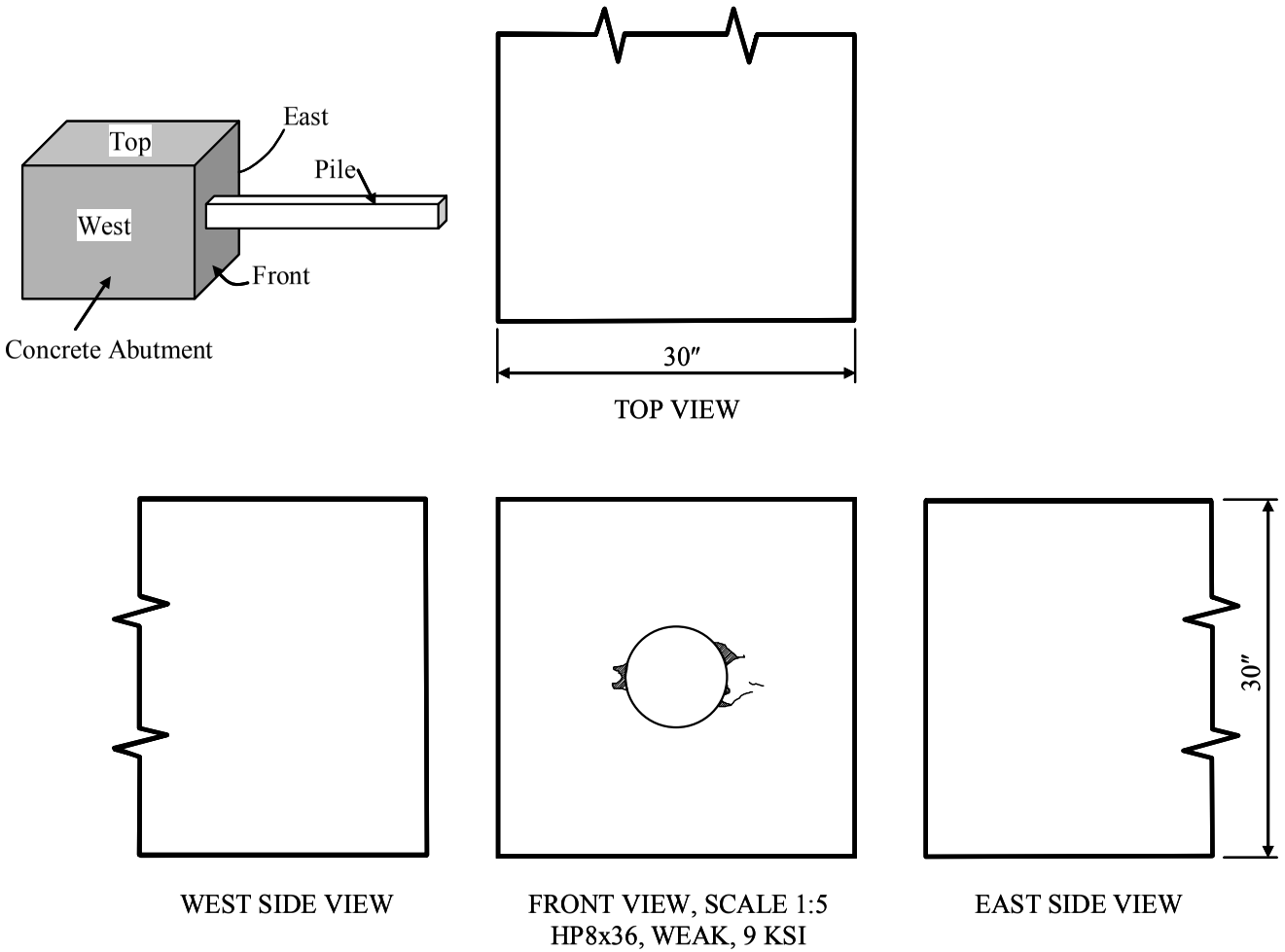

Figure I.100: Specimen 7 – Crack on Concrete Abutment (Overall)

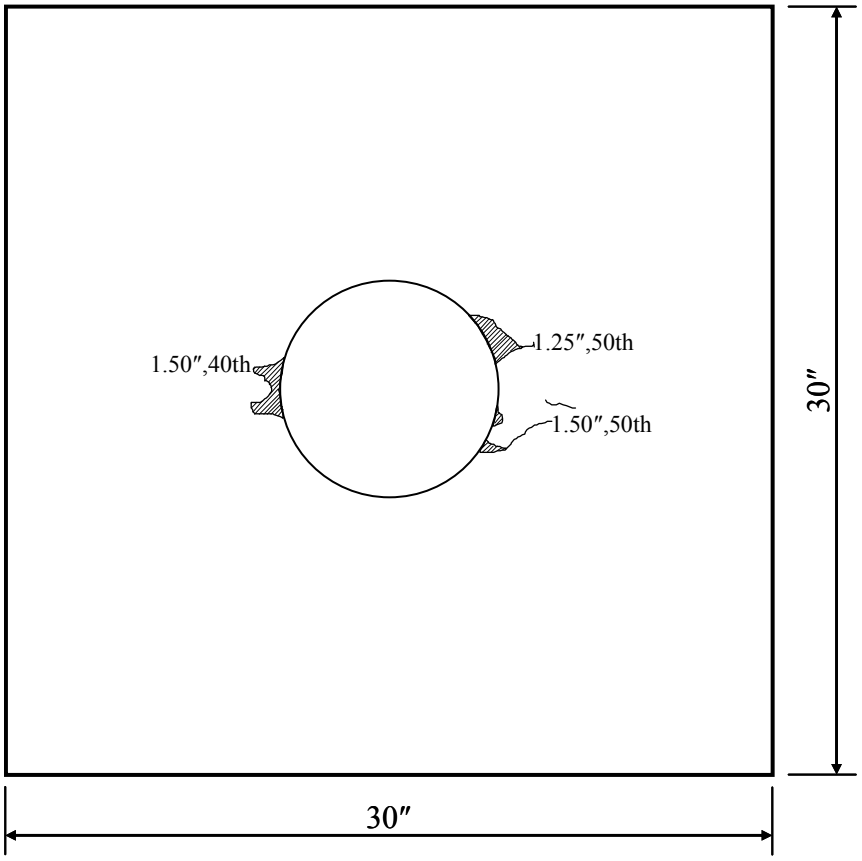

Figure I.101: Specimen 7 – Crack on Concrete Abutment (Front View)

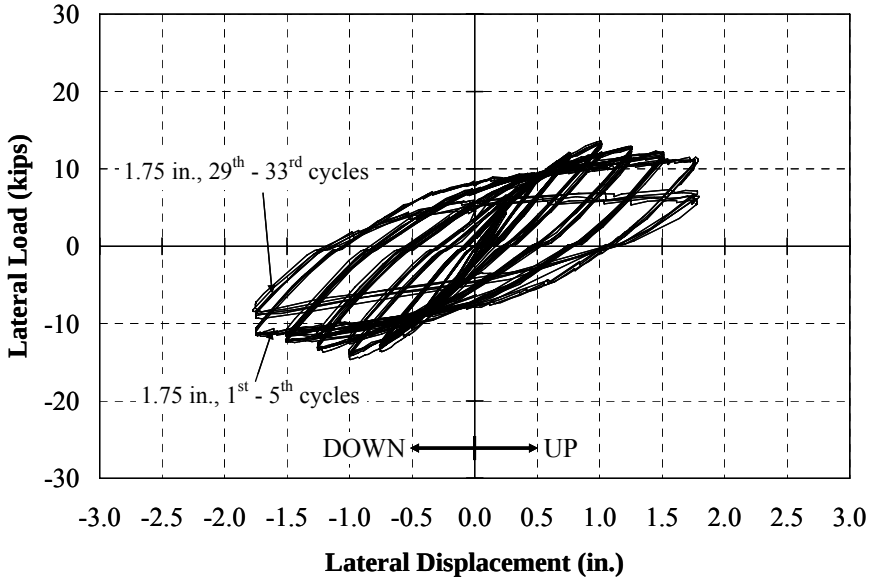

Figure I.102: Specimen 7 – Summary of Lateral Load-Deflection Curves

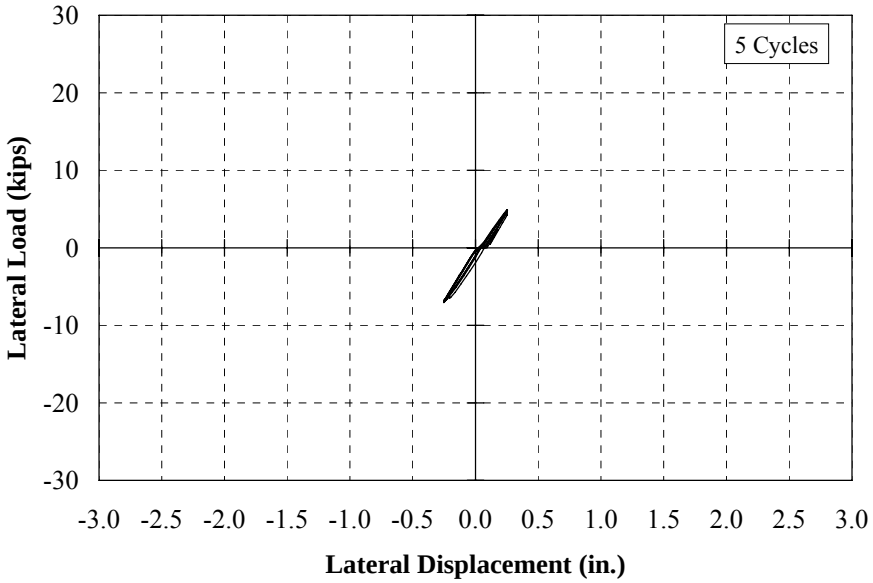

Figure I.103: Specimen 7 – Lateral Load-Deflection Response (±0.25 in.)

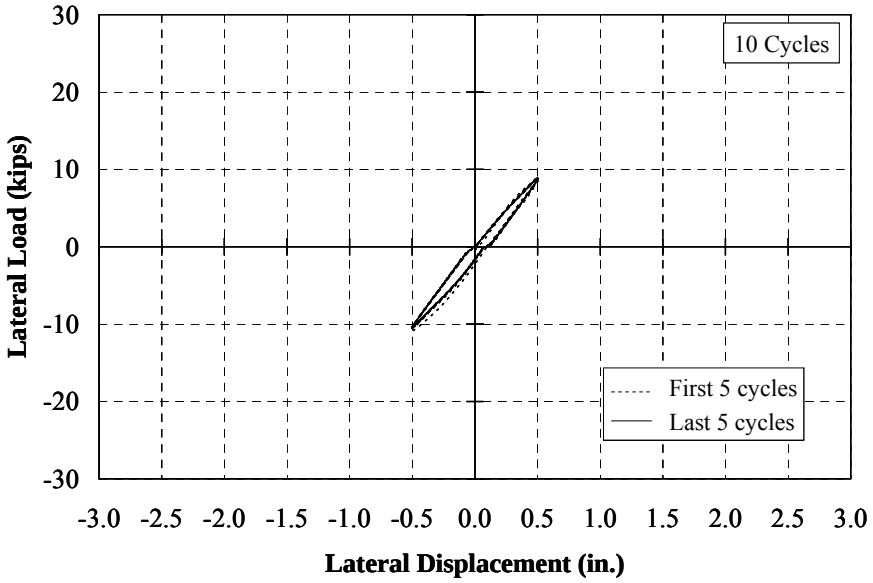

Figure I.104: Specimen 7 – Lateral Load-Deflection Response (±0.50 in.)

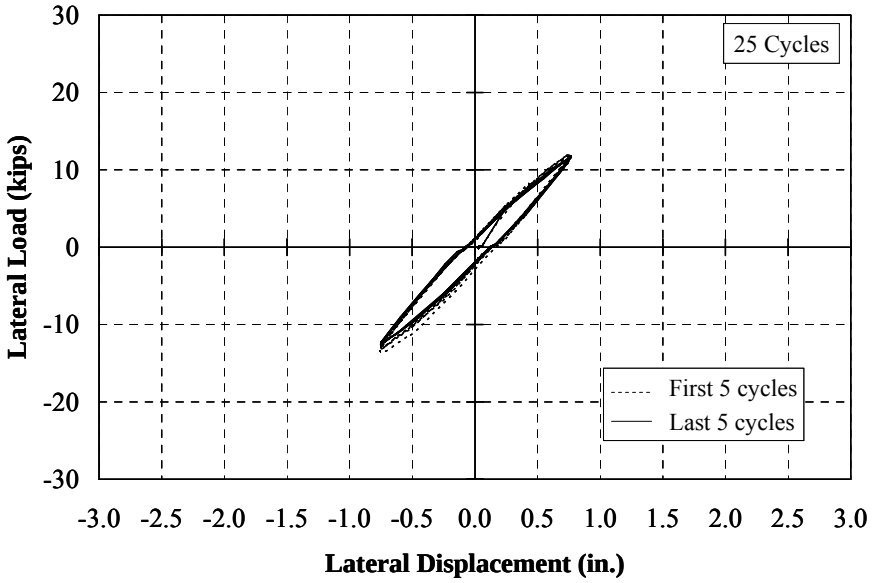

Figure I.105: Specimen 7 – Lateral Load-Deflection Response (±0.75 in.)

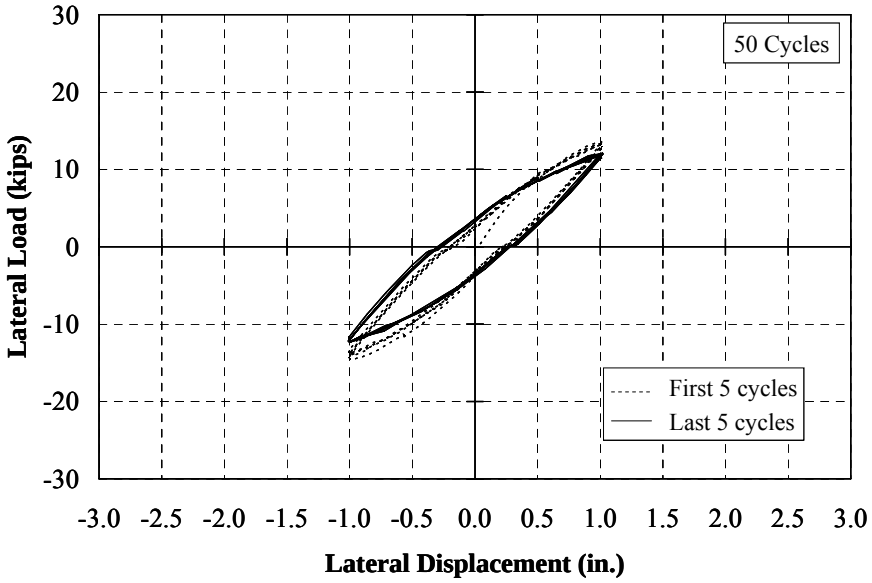

Figure I.106: Specimen 7 – Lateral Load-Deflection Response (±1.00 in.)

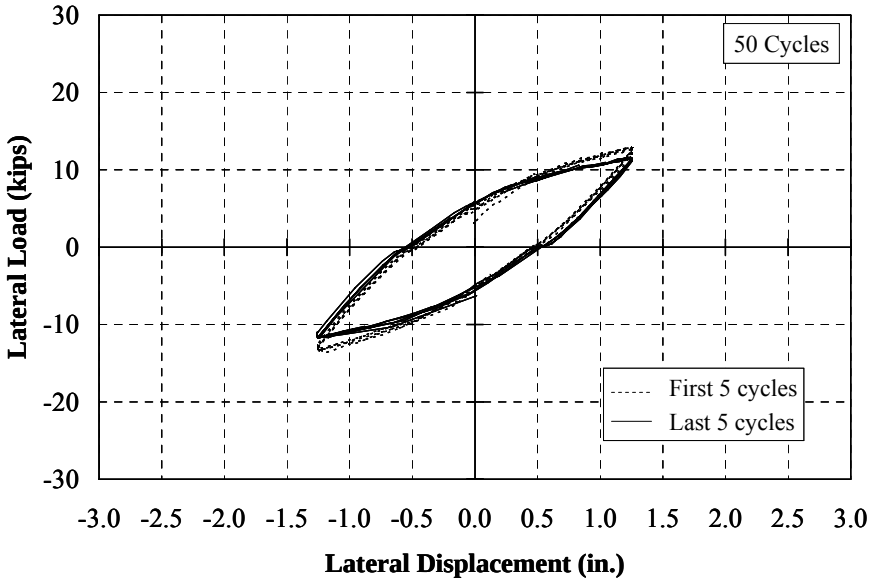

Figure I.107: Specimen 7 – Lateral Load-Deflection Response (±1.25 in.)

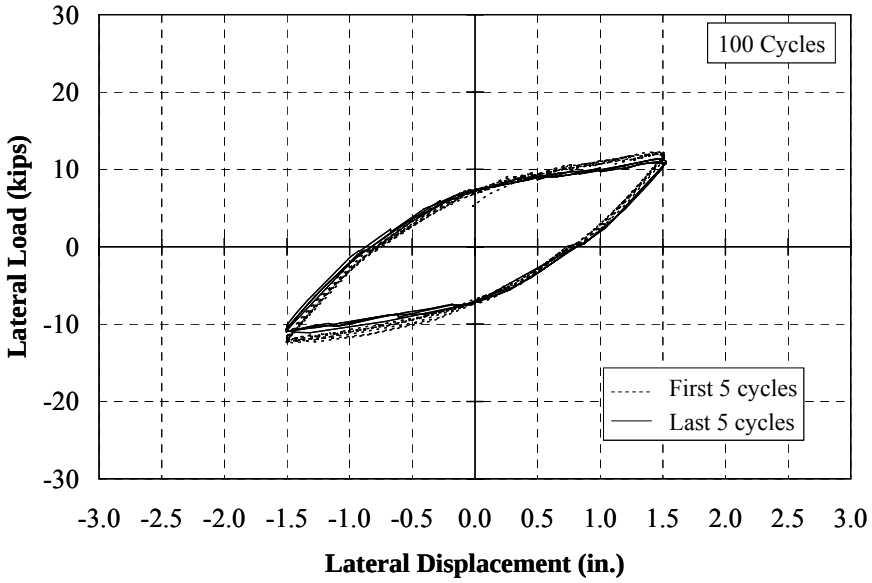

Figure I.108: Specimen 7 – Lateral Load-Deflection Response (±1.50 in.)

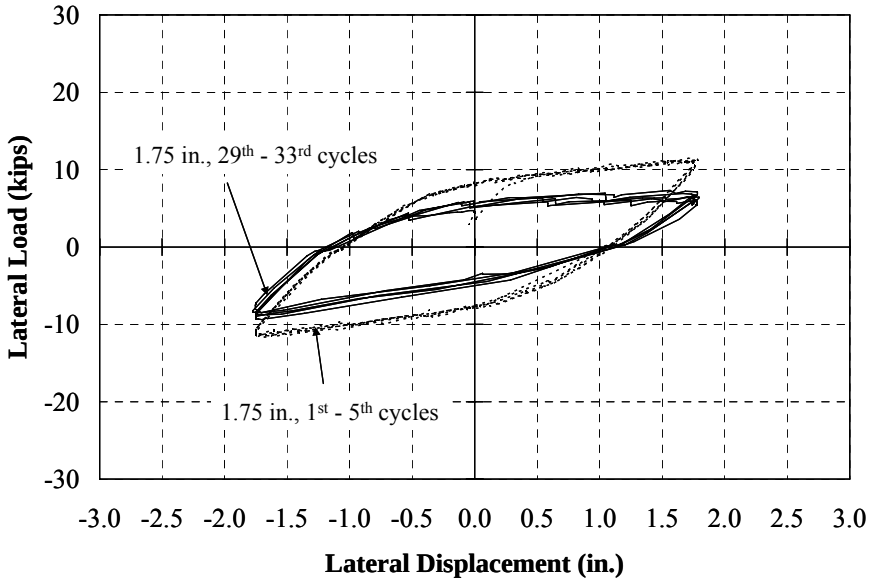

Figure I.109: Specimen 7 – Lateral Load-Deflection Response (±1.75 in.)

Specimen 8: CFT8.625x0.188, “18 ksi”

(a) West Side

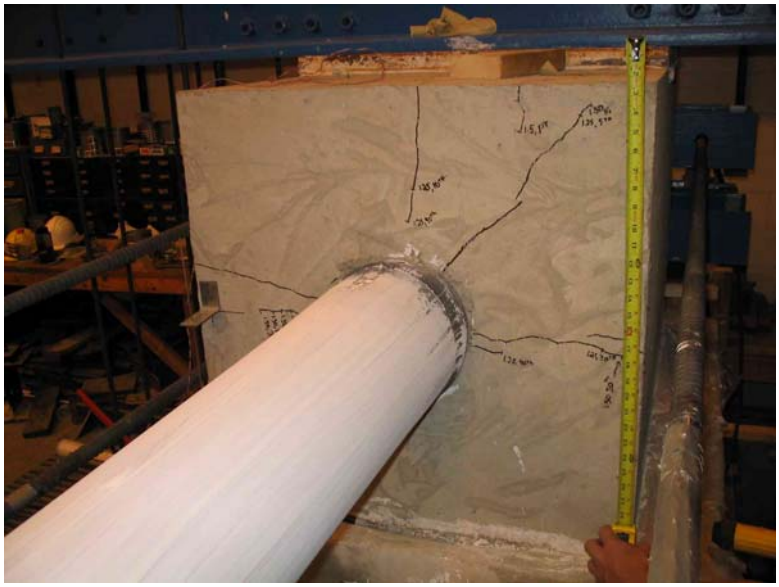

(b) East Side

Figure I.110: Specimen 8 – Cracking (1.75 in., 10th Cycle)

(a) West Side

(b) East Side

Figure I.111: Specimen 8 – Pile Yielding (1.75 in., 10th Cycle)

(c) Top

(d) Bottom

Figure I.111: Specimen 8 – Pile Yielding (1.75 in., 10th Cycle) (Continue)

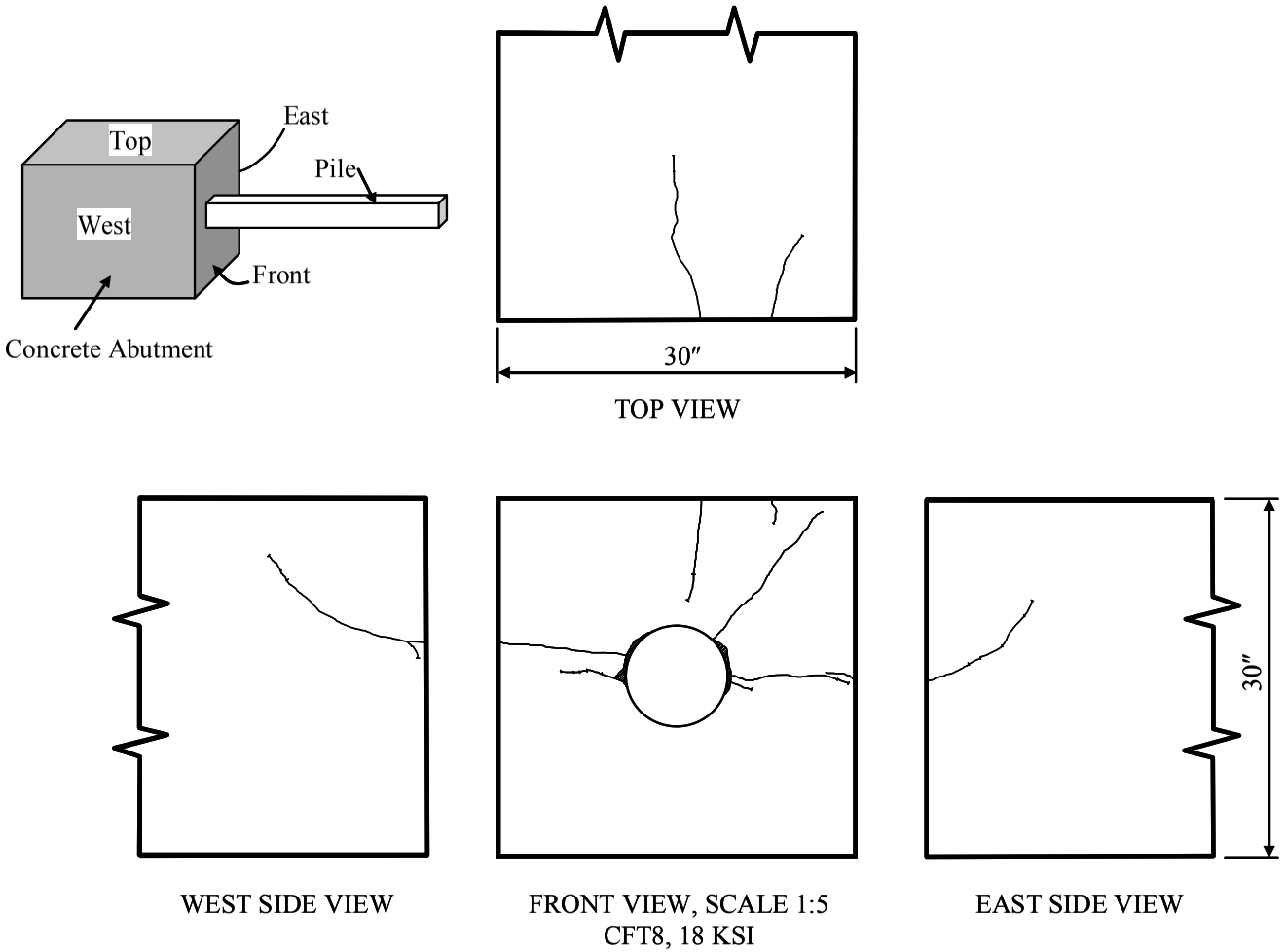

Figure I.112: Specimen 8 – Crack on Concrete Abutment (Overall)

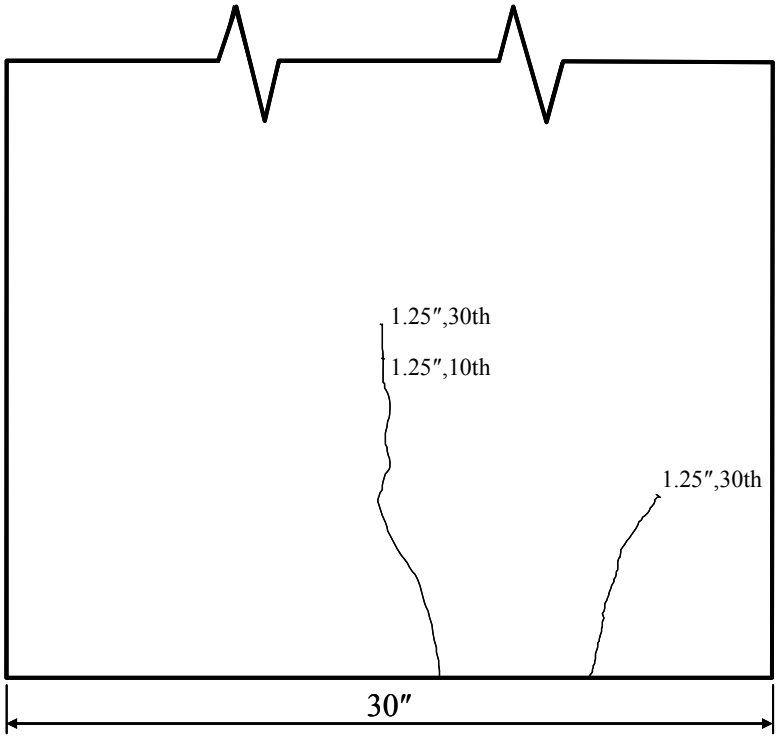

Figure I.113: Specimen 8 – Crack on Concrete Abutment (Top View)

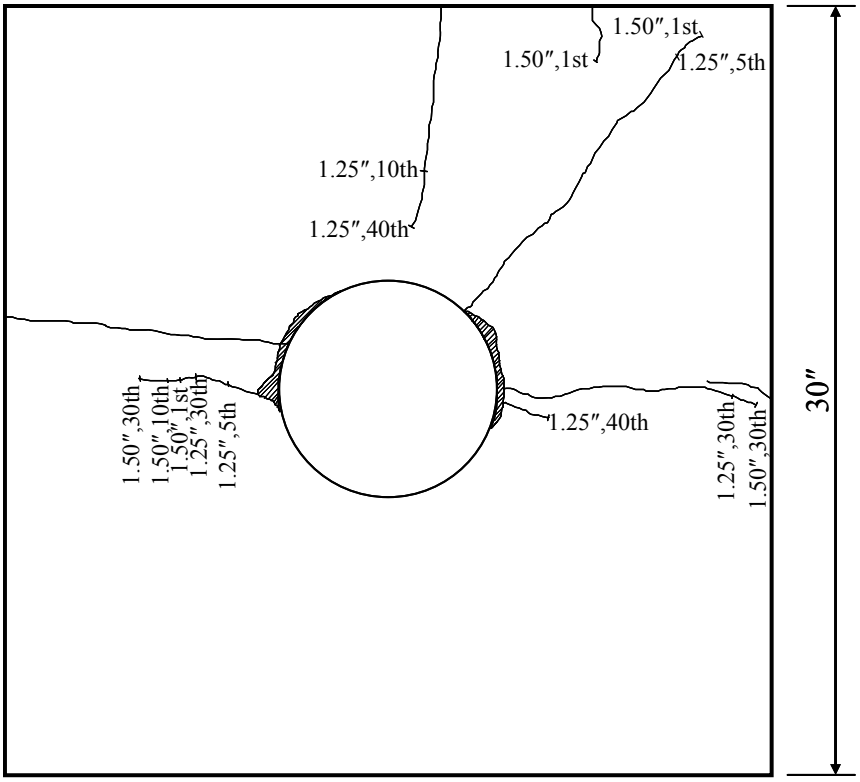

Figure I.114: Specimen 8 – Crack on Concrete Abutment (Front View)

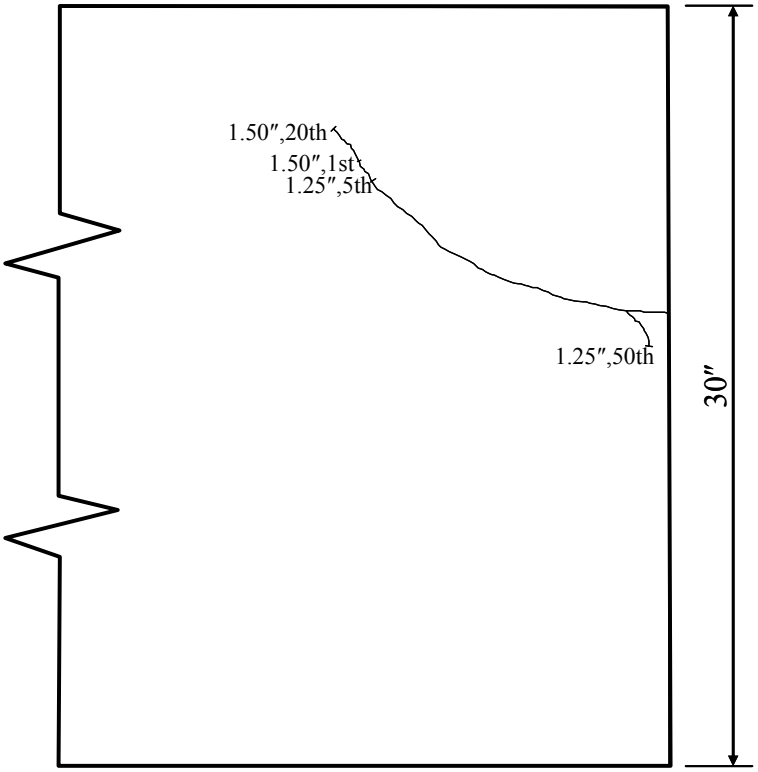

Figure I.115: Specimen 8 – Crack on Concrete Abutment (West View)

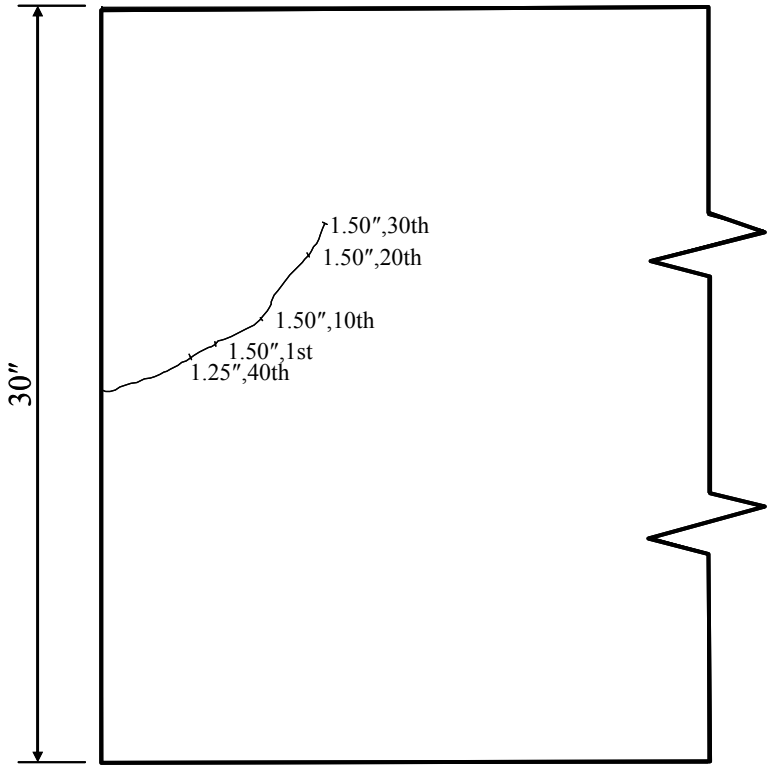

Figure I.116: Specimen 8 – Crack on Concrete Abutment (East View)

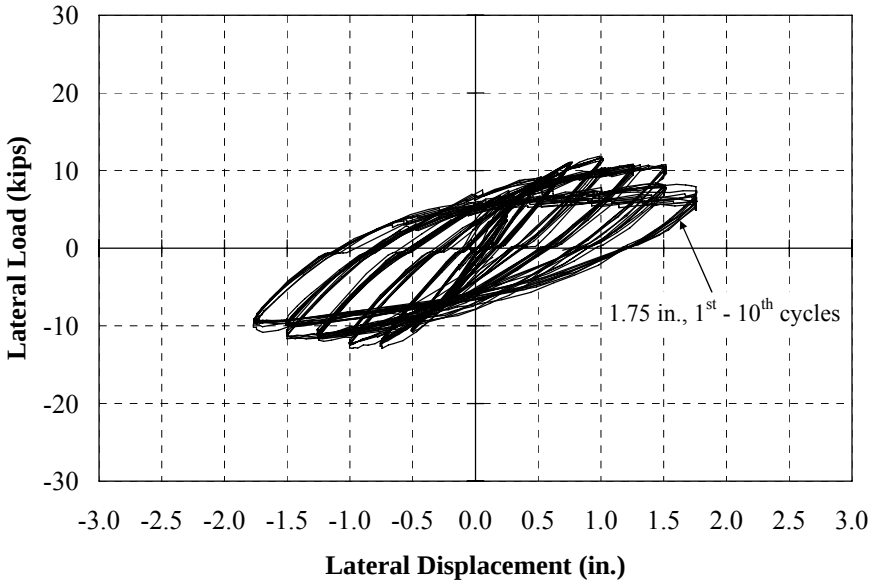

Figure I.117: Specimen 8 – Summary of Lateral Load-Deflection Curves

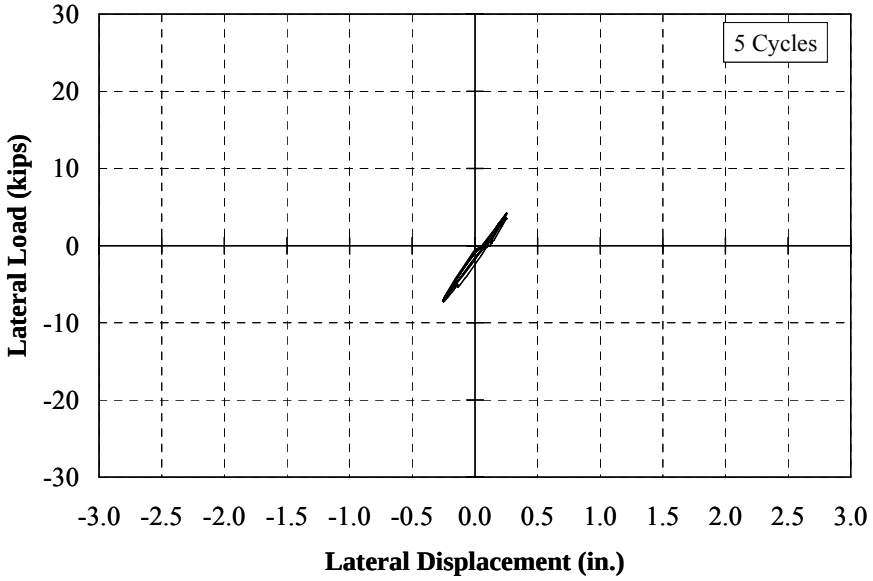

Figure I.118: Specimen 8 – Lateral Load-Deflection Response (±0.25 in.)

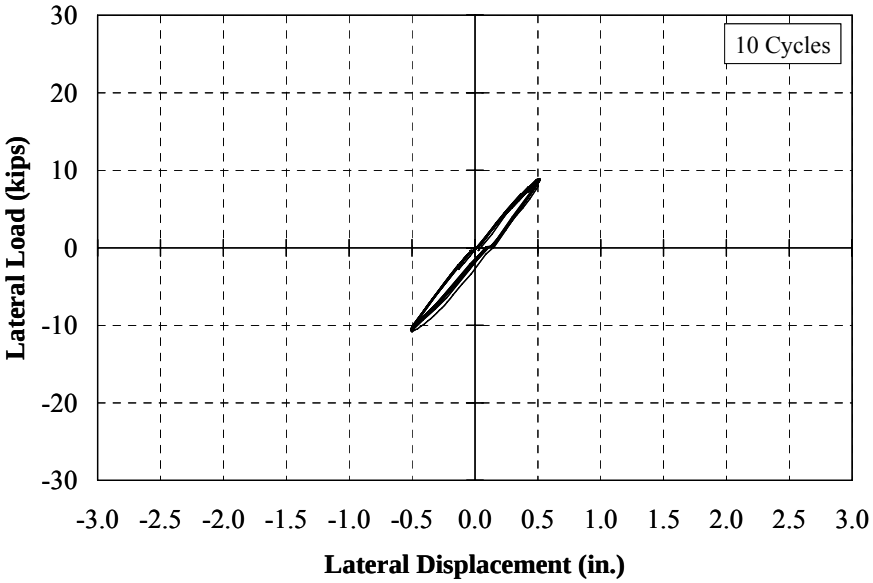

Figure I.119: Specimen 8 – Lateral Load-Deflection Response (±0.50 in.)

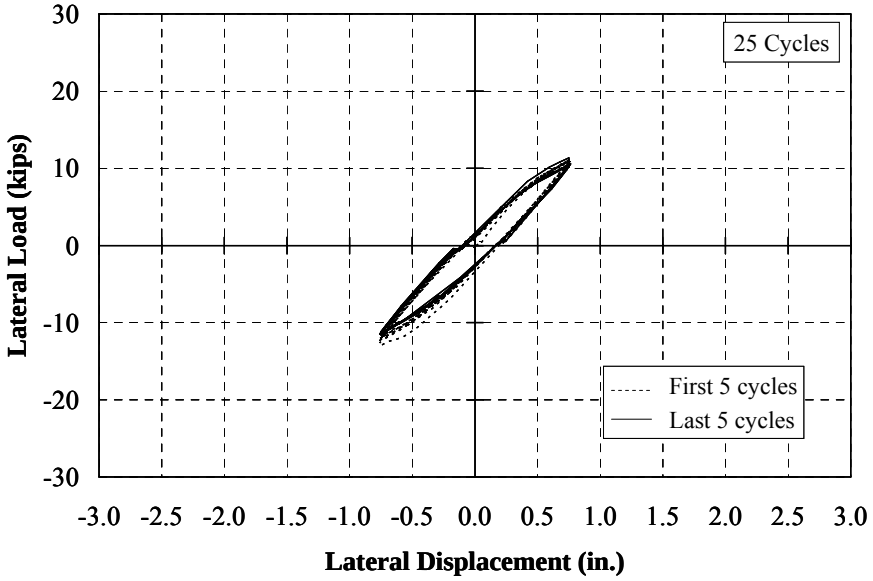

Figure I.120: Specimen 8 – Lateral Load-Deflection Response (±0.75 in.)

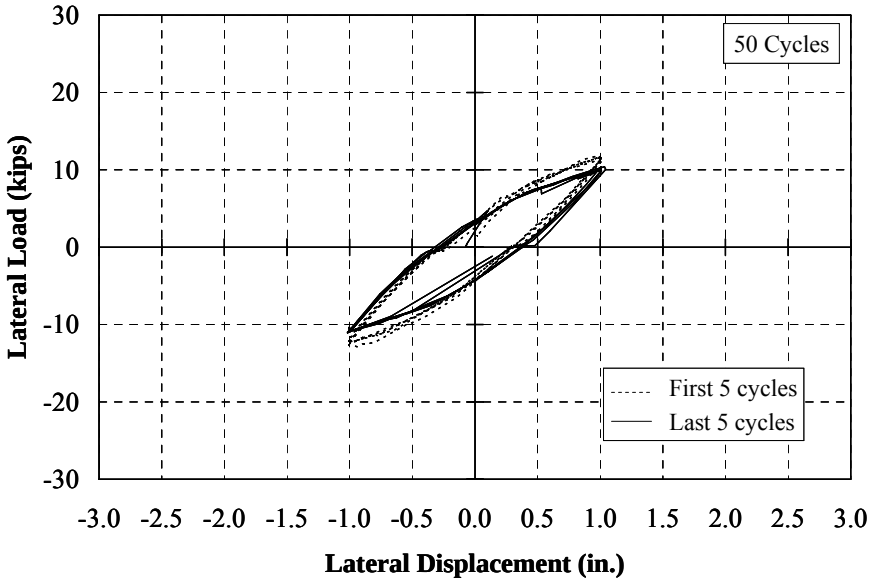

Figure I.121: Specimen 8 – Lateral Load-Deflection Response (±1.00 in.)

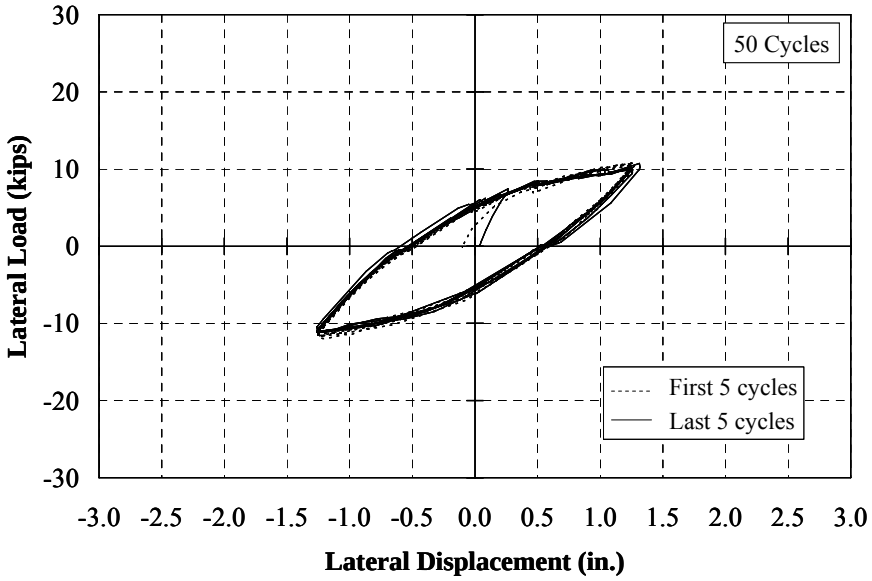

Figure I.122: Specimen 8 – Lateral Load-Deflection Response (±1.25 in.)

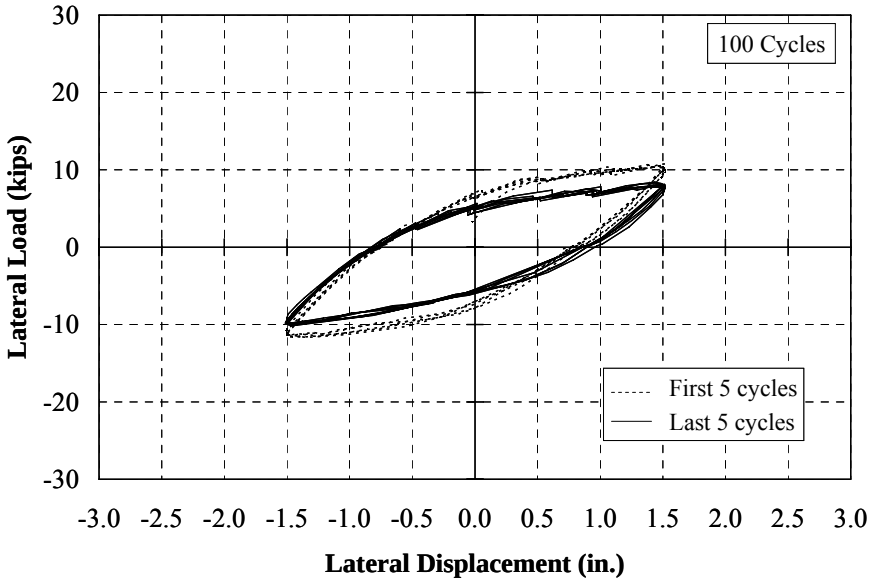

Figure I.123: Specimen 8 – Lateral Load-Deflection Response (±1.50 in.)

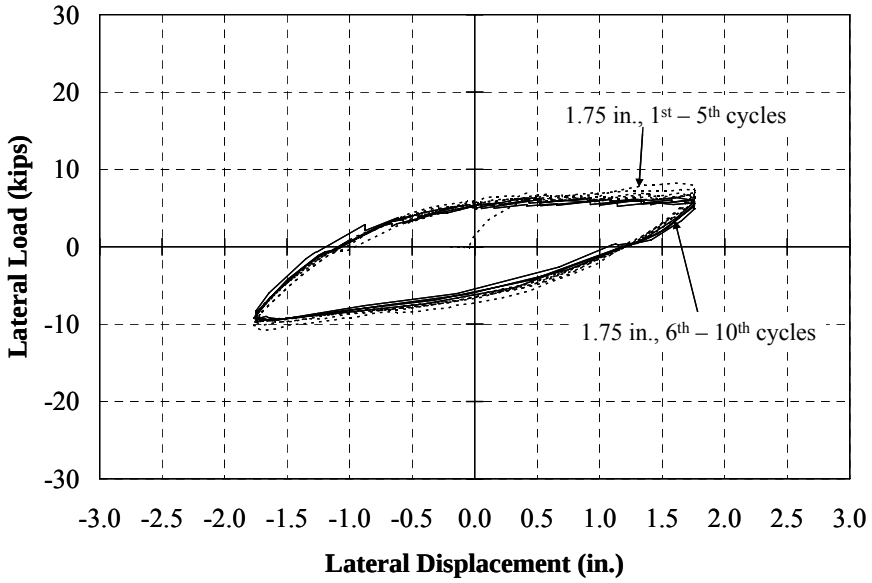

Figure I.124: Specimen 8 – Lateral Load-Deflection Response (±1.75 in.)

Specimen 9: CFT10.75x0.250, 9 ksi

(a) West Side

(b) East Side

Figure I.125: Specimen 9 – Cracking (2.00 in., 100th Cycle)

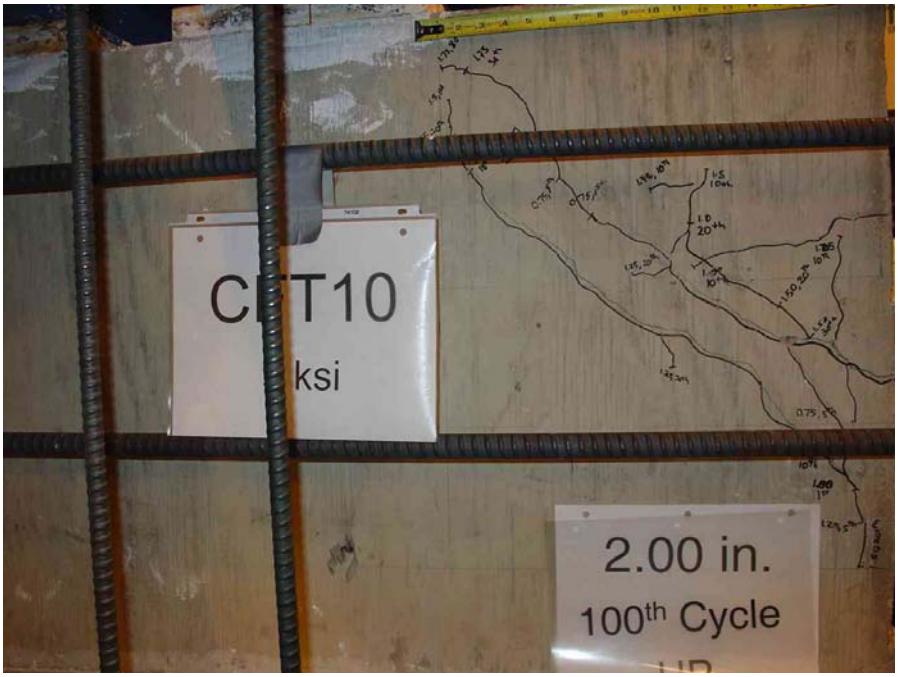

(a) West Side

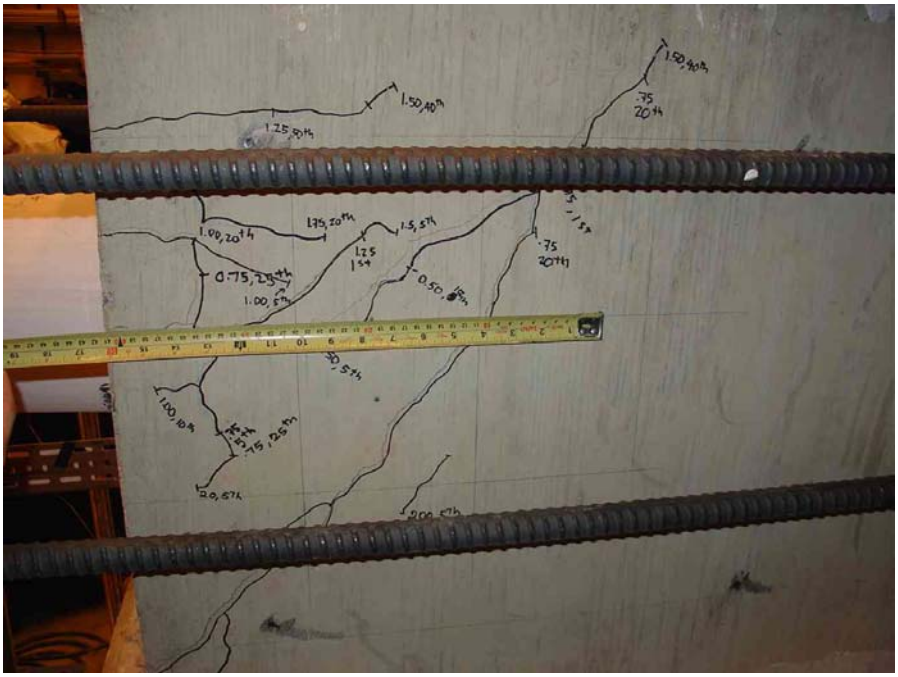

(b) East Side

Figure I.126: Specimen 9 – Crack on Concrete Abutment (2.00 in., 100th Cycle)

(a) West Side

(b) East Side

Figure I.127: Specimen 9 – Pile Yielding (2.00 in., 100th Cycle)

(c) Top

(d) Bottom

Figure I.127: Specimen 9 – Pile Yielding (2.00 in., 100th Cycle) (Continue)

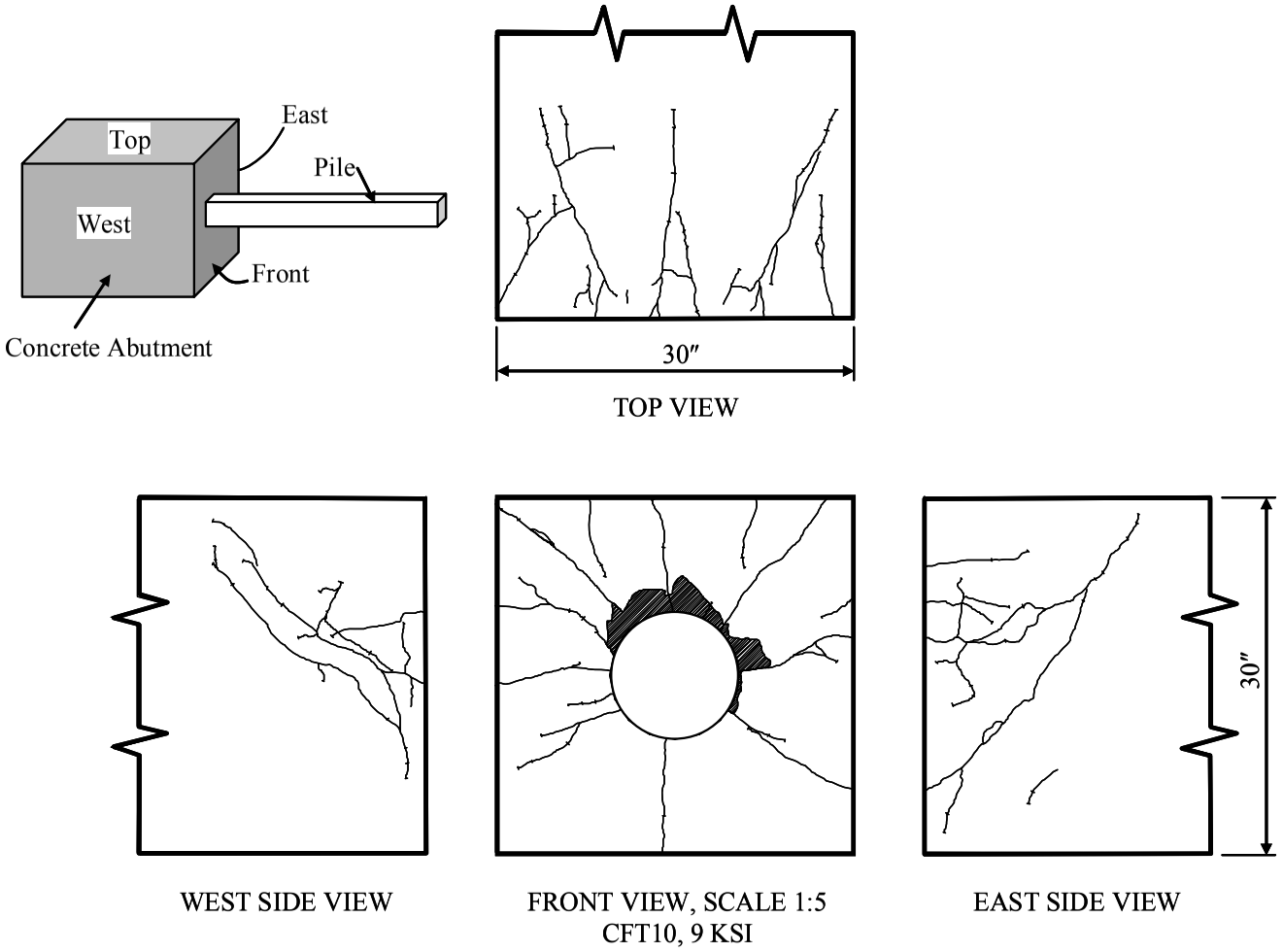

Figure I.128: Specimen 9 – Crack on Concrete Abutment (Overall)

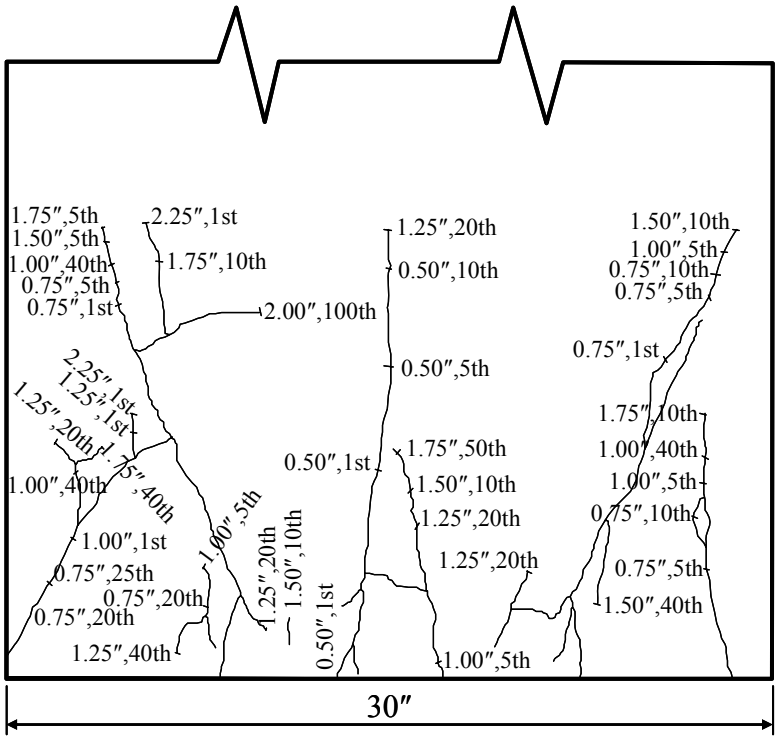

Figure I.129: Specimen 9 – Crack on Concrete Abutment (Top View)

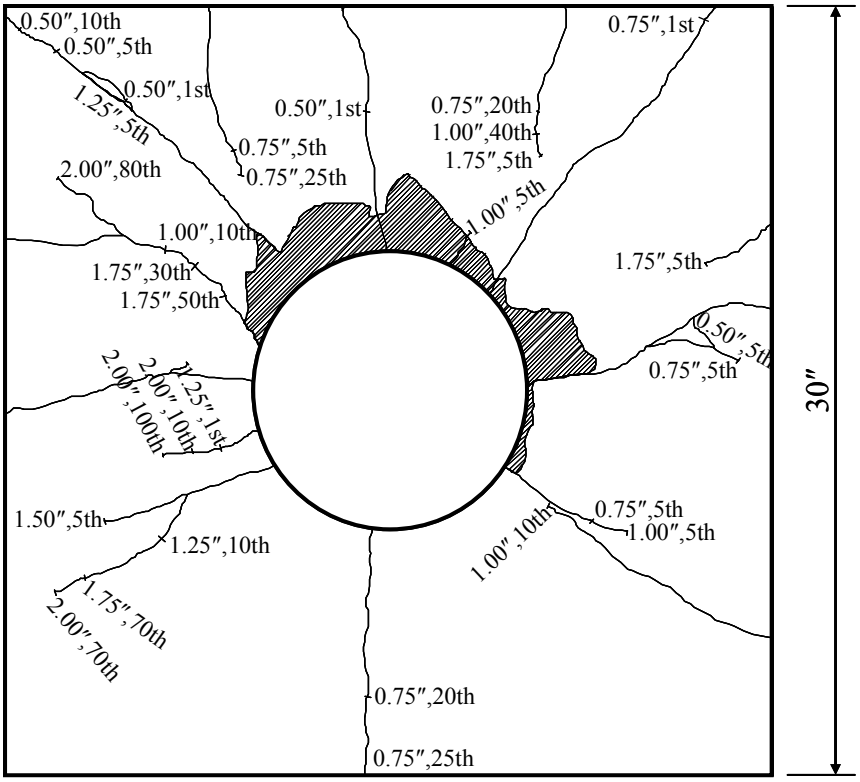

Figure I.130: Specimen 9 – Crack on Concrete Abutment (Front View)

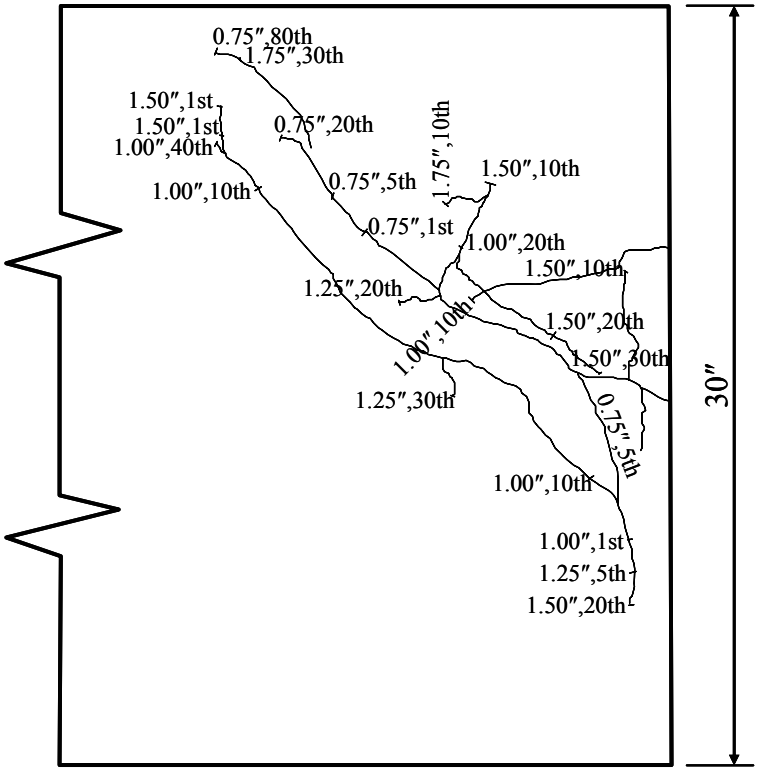

Figure I.131: Specimen 9 – Crack on Concrete Abutment (West View)

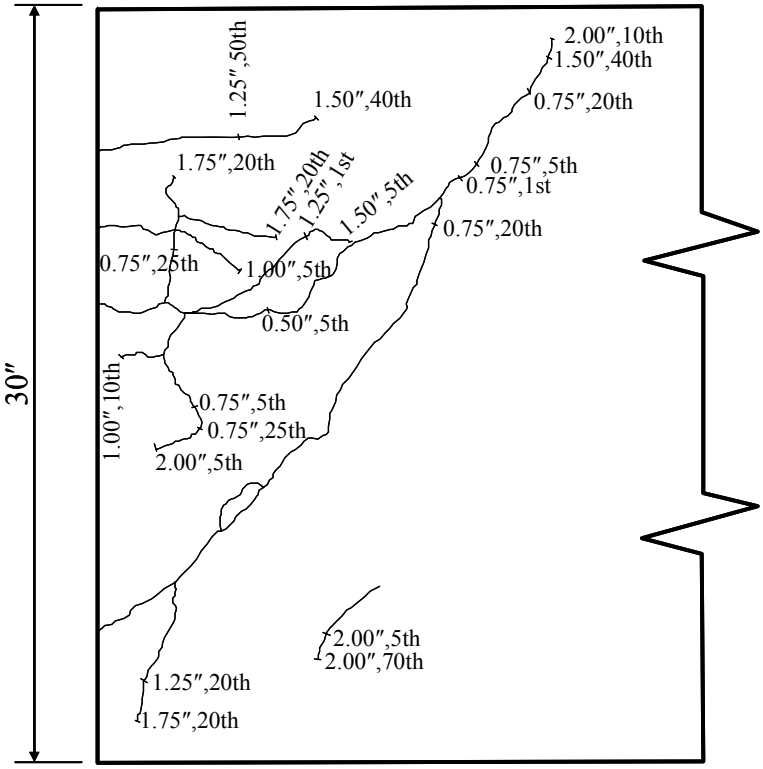

Figure I.132: Specimen 9 – Crack on Concrete Abutment (East View)

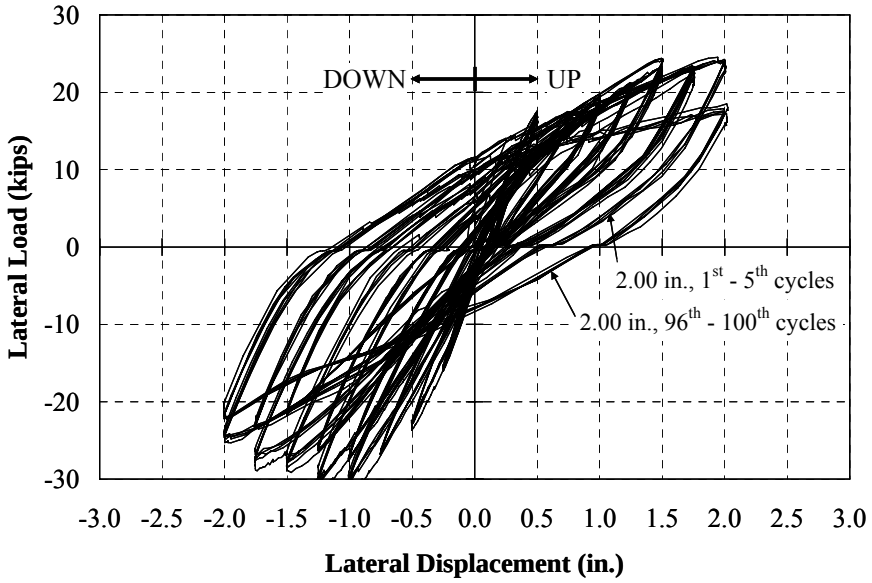

Figure I.133: Specimen 9 – Summary of Lateral Load-Deflection Curves

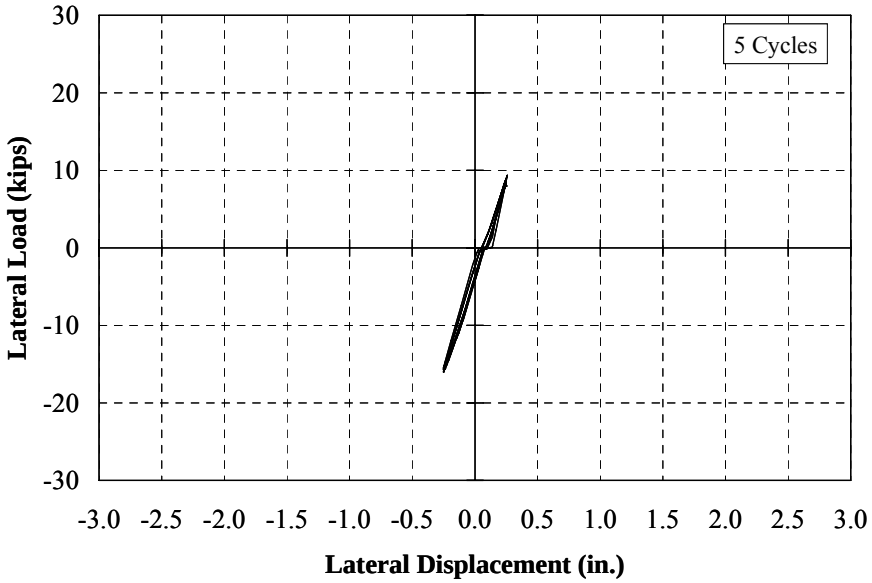

Figure I.134: Specimen 9 – Lateral Load-Deflection Response (±0.25 in.)

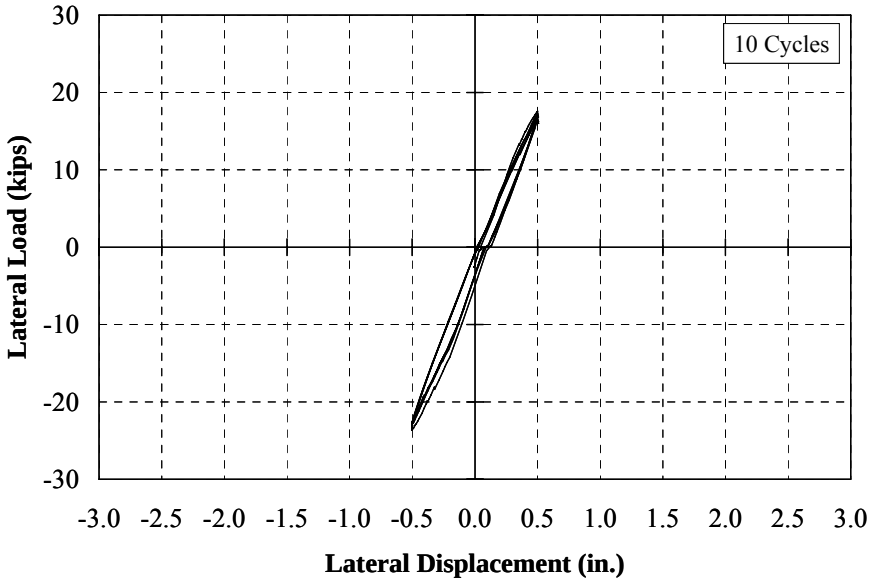

Figure I.135: Specimen 9 – Lateral Load-Deflection Response (±0.50 in.)

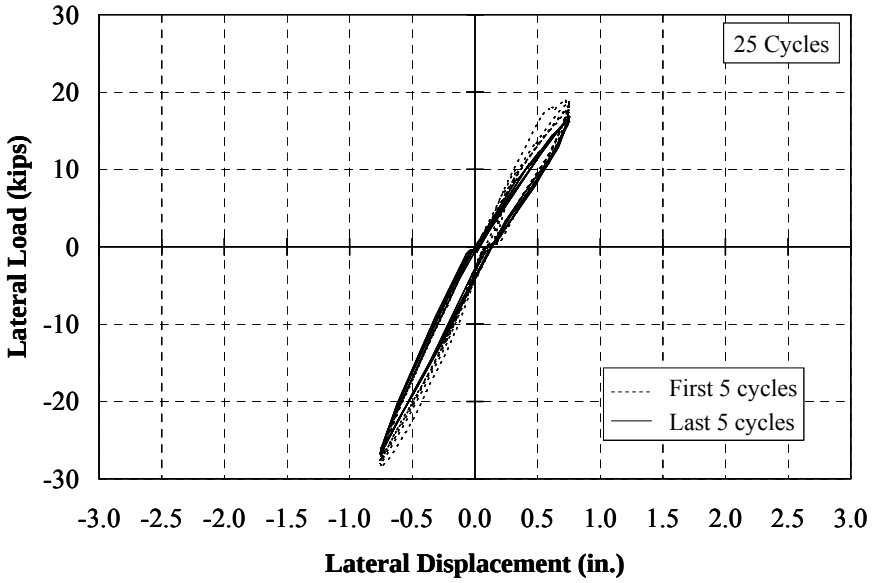

Figure I.136: Specimen 9 – Lateral Load-Deflection Response (±0.75 in.)

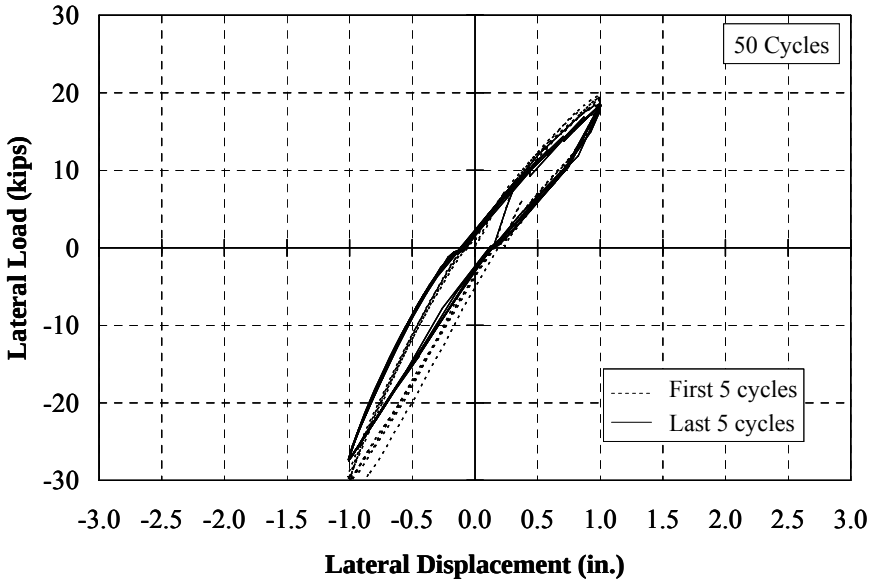

Figure I.137: Specimen 9 – Lateral Load-Deflection Response (±1.00 in.)

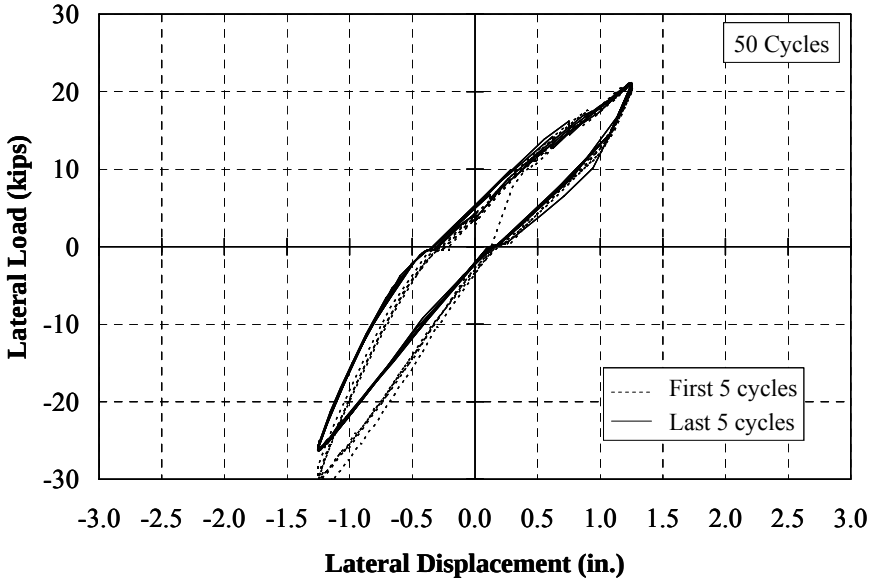

Figure I.138: Specimen 9 – Lateral Load-Deflection Response (±1.25 in.)

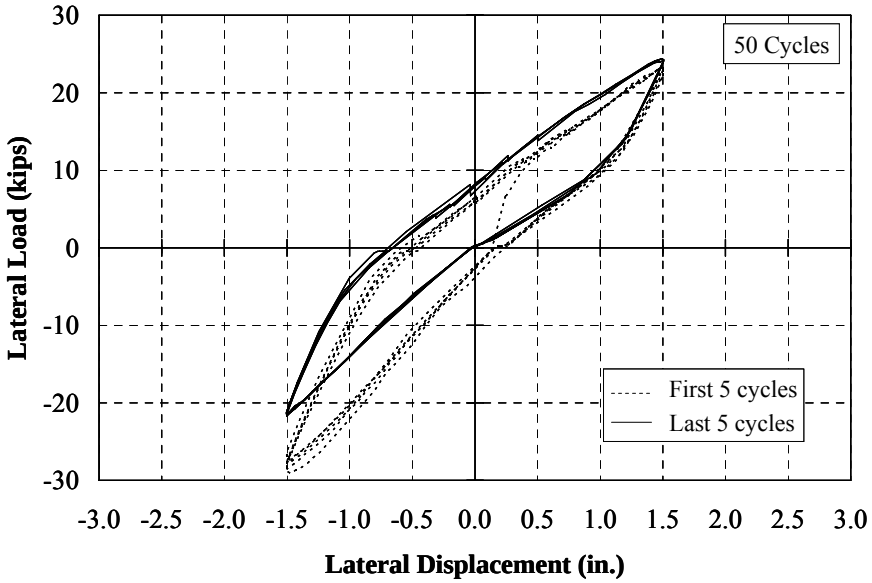

Figure I.139: Specimen 9 – Lateral Load-Deflection Response (±1.50 in.)

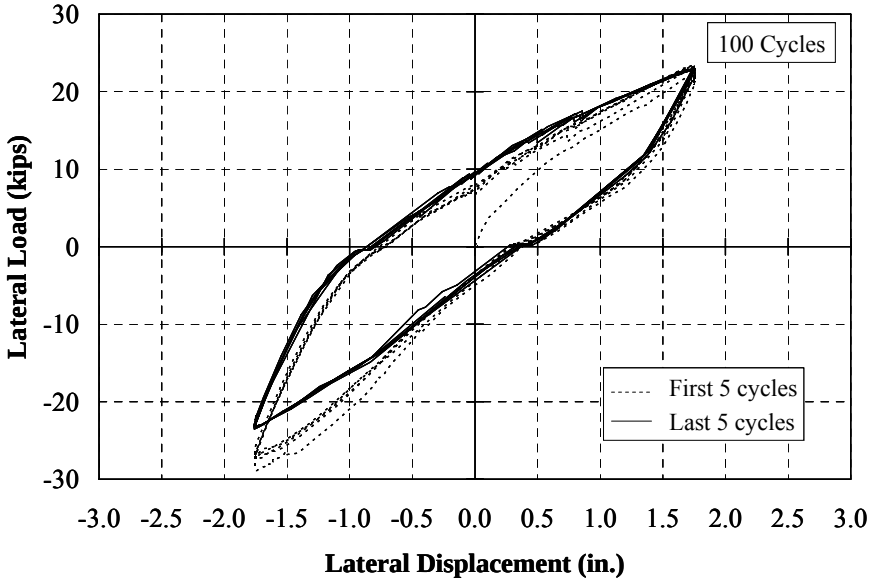

Figure I.140: Specimen 9 – Lateral Load-Deflection Response (±1.75 in.)

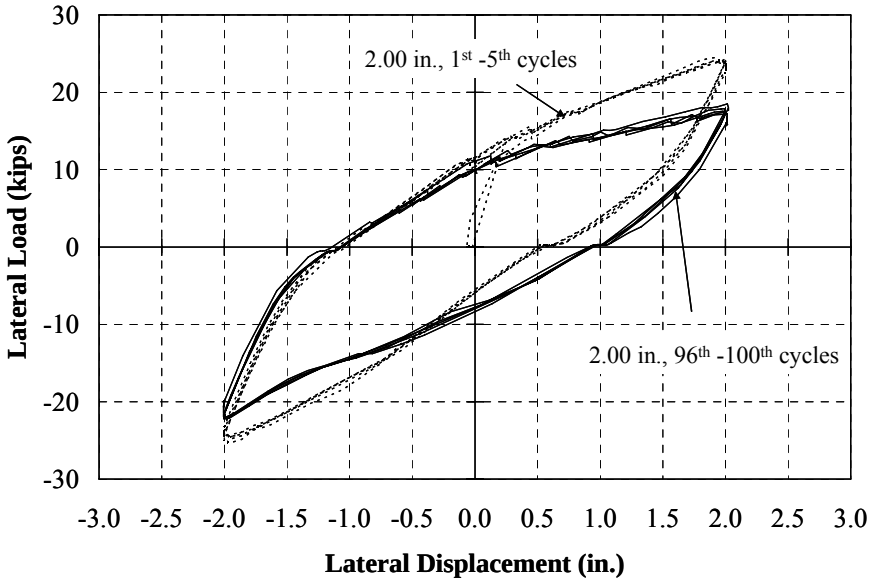

Figure I.141: Specimen 9 – Lateral Load-Deflection Response (±2.00 in.)

APPENDIX J

MOMENT-CURVATURE ANALYSIS AND LOAD-DEFLECTION ANALYSIS

Appendix J: Moment-Curvature Analysis and Load-Deflection Analysis

Moment-Curvature Analysis

Steel and concrete sections are divided into a numbers of slices as illustrated in Figure J.1.

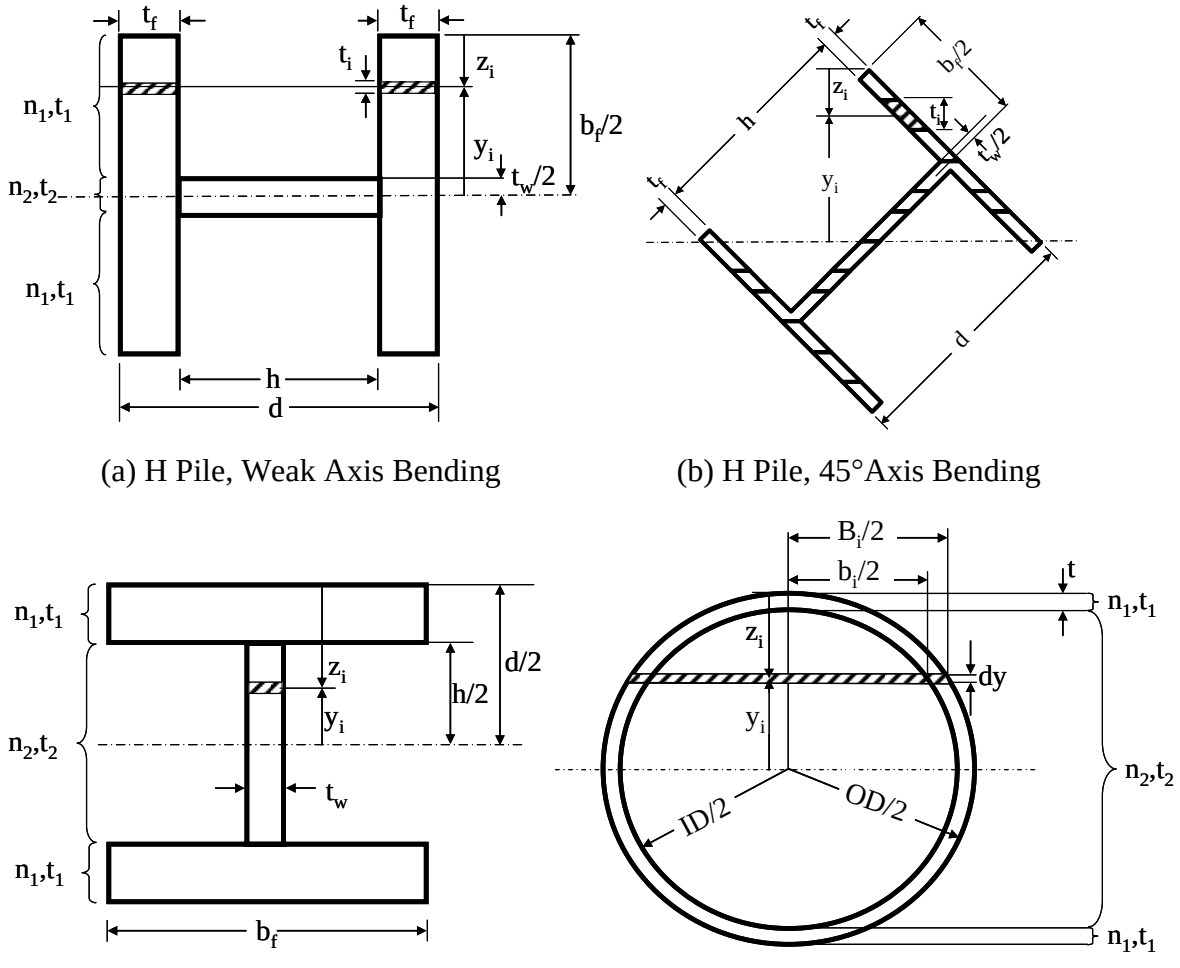

(a) H Pile, Weak Axis Bending (b) H Pile, 45°Axis Bending

(c) H Pile, Strong Axis Bending (d) CFT Pile

Figure J.1: Fiber Discretization

where:

n_1, t_1 = number and thickness of segment 1, respectively.

n_2, t_2 = number thickness of segment 2, respectively.

$$n_1 = \begin{cases} 1000;\ \text{weak-axis bending pile} \\ 40;\ \text{strong-axis bending pile} \\ 40;\ \text{CFT pile} \end{cases}$$

$$n_2 = \begin{cases} 80;\ \text{weak-axis bending pile} \\ 2000;\ \text{strong-axis bending pile} \\ 2000;\ \text{CFT pile} \end{cases}$$

$$t_1 = \begin{cases} \dfrac{(b_f - t_w)}{2n_1};\ \text{weak-axis bending pile} \\ \dfrac{(d-h)}{2n_1} = \dfrac{t_f}{n_1};\ \text{strong-axis bending pile} \\ \dfrac{(OD-ID)}{2n_1};\ \text{CFT pile} \end{cases}$$

$$t_2 = \begin{cases} \dfrac{t_w}{n_2};\ \text{weak-axis bending pile} \\ \dfrac{h}{n_2};\ \text{strong-axis bending pile} \\ \dfrac{ID}{n_2};\ \text{CFT pile} \end{cases}$$

One can note that for 45° axis pile bending, the pile was divided into 12 slices. The area, A_{si}, and centroid, y_i, of each slice were determined using AutoCAD program.

z_i = distance measured from the top fiber to the centroid of the slice i^{th}

$$z_i = \begin{cases} 0; i = 0 \\ \dfrac{t_1}{2} + (i-1)t_1; 1 \le i \le n_1 \\ n_1 t_1 + \dfrac{t_2}{2} + (i - n_1 - 1)t_2; n_1 < i \le n_1 + n_2 \\ n_1 t_1 + n_2 t_2 + \dfrac{t_1}{2} + (i - n_1 - n_2 - 1)t_1; n_1 + n_2 < i \le 2n_1 + n_2 \\ 2n_1 t_1 + n_2 t_2; i = 2n_1 + n_2 + 1 \end{cases}$$

y_i = distance measured from the centroidal axis of the section to the centroid of the i^{th} slice; $y_i = D/2 - z_i$

t_i = thickness of the i^{th} slice

b_f, t_f = flange width and thickness of H pile, respectively

d = depth of H pile

h, t_w = web depth and thickness of H pile, respectively

ID, OD = inner diameter and outer diameter, respectively

b_i = width of the i^{th} slice

For H piles bending about their weak and strong axes:

$$\text{For weak axis bending, } b_i = \begin{cases} d; 0 \le |y_i| < \dfrac{t_w}{2} \\ zt_f; \dfrac{t_w}{2} \le |y_i| \le \dfrac{b_f}{2} \end{cases}$$

$$\text{For strong axis bending, } b_i = \begin{cases} t_w; 0 \le |y_i| < \dfrac{h}{2} \\ b_f; \dfrac{h}{2} \le |y_i| \le \dfrac{d}{2} \end{cases}$$

For CFT piles:

$$B_i = 2\sqrt{\left(\frac{OD}{2}\right)^2 - y_i^2}\ ;\ b_i = 2\sqrt{\left(\frac{ID}{2}\right)^2 - y_i^2}; 0 \le |y_i| \le \frac{ID}{2}$$

$$\text{Steel ring width} = \begin{cases} B_i - b_i; 0 \le |y_i| < \dfrac{ID}{2} \\ B_i; \dfrac{ID}{2} \le |y_i| \le \dfrac{OD}{2} \end{cases}$$

Concrete core width = b_i

The strains of the steel slice, ε_{si}, and of concrete slice, ε_{ci}, can be evaluated according Equations J-1 and J-2, respectively:

$$\varepsilon_{si} = \left(\frac{c - \frac{d_p}{2} + y_i}{c} \right) \cdot \varepsilon_t \tag{J-1}$$

$$\varepsilon_{ci} = \begin{cases} \left(\frac{c - \frac{d_p}{2} + y_i}{c} \right) \cdot \varepsilon_t ; z_i \le c \\ 0 ; z_i > c \end{cases} \tag{J-2}$$

where:

ε_t = strain at the top fiber of the section;

c = distance from the neutral axis to the top fiber of the section;

d_p = flange width, b_f, of H section bending about weak axis, or

d_p = depth, d, of H section bending about strong axis, or

d_p = outer diameter, OD, for circular pipe section

Hence, for a given strain profile, the stresses can be determined for each slice using the steel and concrete models in Section 7.2. The total axial load, P, and the total bending moment, M, on the section can be calculated as follows:

$$P = \sum_{i=1}^{n} f_{si} \cdot A_{si} + \sum_{i=1}^{n} f_{ci} \cdot A_{ci} \tag{J-3}$$

$$M = \sum_{i=1}^{n} f_{si} \cdot A_{si} \cdot y_i + \sum_{i=1}^{n} f_{ci} \cdot A_{ci} \cdot y_i \tag{J-4}$$

where:

n = number of segments.

y_i = distance measured from the centroidal axis of the section to the centroid of the i^{th} slice, in.

f_{si} = stress of steel in the i^{th} slice, ksi

f_{ci} = stress of concrete in the i^{th} slice, ksi

A_{si} = area of steel in the i^{th} slice, $in.^2$

A_{ci} = area of concrete in the i^{th} slice, $in.^2$

P = axial load, kips.

M = bending moment corresponding to the fixed end moment.

Load –Deflection Relationship

Notations:

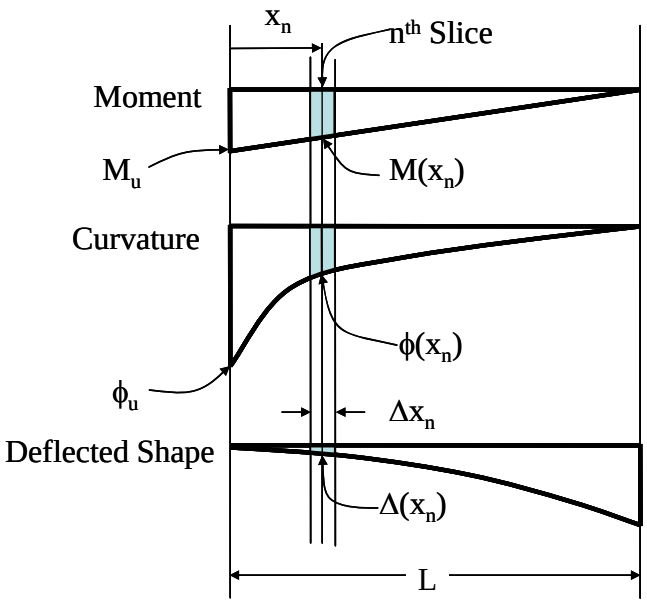

Figure J.2: Notations

where:

n = number of slices (the 0^{th} slice to the n^{th} slice).

L = distance from the fixed end to the applied load, taken as 60 in.

x_n = location of the n^{th} slice, measured from the fixed end to the centroid of the slice, in.

H = lateral load, kips.

P = axial load, kips.

M_u = ultimate moment, ft-kips.

ϕ_u = ultimate curvature corresponding to M_u, rad/in..

$M_{i-1}(x_n)$= first-order moment at the location x_n, ft-kips.

$\phi_{i-1}(x_n)$ = curvature at the location x_n, rad/in.

$\Delta_{i-1}(x_n)$ = deflection, in.

Δx_n = thickness of the slice n^{th}, in.

Algorithm:

For a given moment-curvature relationship, the tip displacement can be calculated by the following algorithm:

1. Determine the ultimate moment, M_u, (or the plastic moment, M_p) from the given moment-curvature relationship.
2. Determine the corresponding lateral load, $H = M_u/L$.
3. Calculate the moment at the location x from the fixed end, M(x), along the pile length and define $M_{i-1}(x) = \frac{M_u}{L}(L - x_n)$ or $M_{i-1}(x_n) = H(L-x_n)$, ft-k.
4. Determine the corresponding curvature along the pile length, $\phi_{i-1}(x)$, from a given moment-curvature relationship as illustrated in Figure J.3.

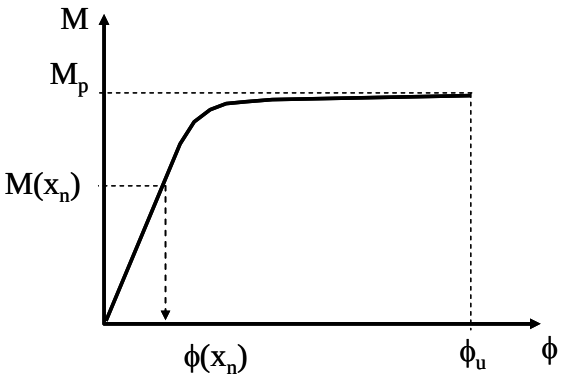

Figure J.3: Curvature Interpolation

5. Calculate the summation of the moment of area under the curvature curve; that is the lateral displacement at the pile tip. The first-order deflections, $\Delta_{i-1}(x_n)$ along the length of the cantilever pile can be calculated as follow:

   First-order deflection = (Curvature)(Thickness of slice)(Moment arm)

$$\Delta_{i-1}(x_n) = \sum_{j=1}^{n} \phi_{i-1}(x_j) \cdot \Delta x_j \cdot x_j \qquad \text{(J-5)}$$

For example, as shown in Figure J.4, the deflection at location x_4 can be determined as follows:

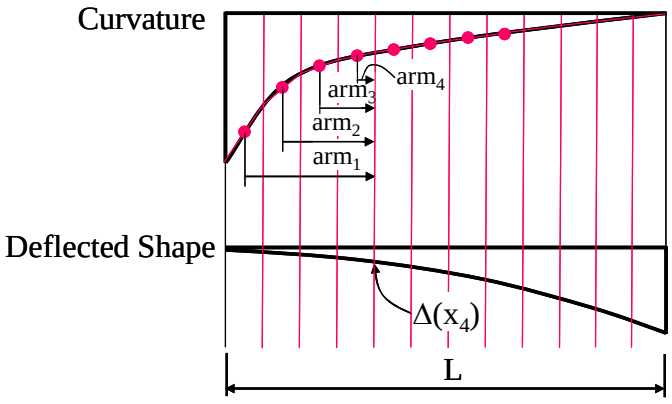

Figure J.4: Deflection Calculation Example

$$\Delta(x_4) = \phi(x_1)\Delta x_1(x_1) + \phi(x_2)\Delta x_2(x_2) + \ldots + \phi(x_4)\Delta x_4(x_4)$$

and $\Delta x_1 = \Delta x_2 = \ldots = \Delta x_4 = \Delta x$